BEILSTEIN JOURNAL OF NANOTECHNOLOGY

Self-assembly of nanostructures and nanomaterials II

Edited by Isabelle Berbezier, Maurizio De Crescenzi and Simona Boninelli

Imprint

Beilstein Journal of Nanotechnology
www.bjnano.org
ISSN 2190-4286
Email: journals-support@beilstein-institut.de

The *Beilstein Journal of Nanotechnology* is published by the Beilstein-Institut zur Förderung der Chemischen Wissenschaften.

Beilstein-Institut zur Förderung der Chemischen Wissenschaften
Trakehner Straße 7–9
60487 Frankfurt am Main
Germany
www.beilstein-institut.de

BEILSTEIN JOURNAL OF NANOTECHNOLOGY

Filled and empty states of Zn-TPP films deposited on Fe(001)-*p*(1×1)O

Gianlorenzo Bussetti*, Alberto Calloni, Rossella Yivlialin, Andrea Picone, Federico Bottegoni and Marco Finazzi

Full Research Paper

Open Access

Address:
Department of Physics, Politecnico di Milano, p.za Leonardo da Vinci 32, 20133 Milano, Italy

Email:
Gianlorenzo Bussetti* - gianlorenzo.bussetti@polimi.it

* Corresponding author

Keywords:
inverse photoemission; metal-oxide film; OMBE; porphyrin

Beilstein J. Nanotechnol. **2016,** *7,* 1527–1531.
doi:10.3762/bjnano.7.146

Received: 01 July 2016
Accepted: 14 October 2016
Published: 27 October 2016

This article is part of the Thematic Series "Self-assembly of nanostructures and nanomaterials II".

Guest Editor: I. Berbezier

Abstract

Zn-tetraphenylporphyrin (Zn-TPP) was deposited on a single layer of metal oxide, namely an Fe(001)-*p*(1×1)O surface. The filled and empty electronic states were measured by means of UV photoemission and inverse photoemission spectroscopy on a single monolayer and a 20 monolayer thick film. The ionization energy and the electron affinity of the organic film were deduced and the interface dipole was determined and compared with data available in the literature.

Introduction

Thin organic films can be realized by depositing single molecules on surfaces, which is the first step for the so-called bottom-up assembly of devices based on organic compounds. The molecule–surface interaction, however, can alter the electronic properties of the organic compound and/or the functionality of the electronic device. This effect is enhanced in molecules showing catalytic activity when the catalytic sites directly interact with the substrate [1]. A characteristic example is offered by metal-tetraphenylporphyrins (M-TPPs). These molecules have been studied in many research fields [2-6] because a specific change in their peripheral groups or inner metal ion can induce enormous variations in the porphyrin reactivity [1]. In particular, the metal atom is placed in the middle of the main cavity of the porphyrin, which has a planar structure, allowing the metal atom to interact from both sides of the molecule. The molecule–substrate interaction can be interpreted in terms of a bond between a special ligand (the surface) and the porphyrin (the so-called surface trans effect (STE)) [1,7]. In order to avoid this problem, porphyrin films are usually grown on passivated surfaces [1] or, conversely, thick (on the order of a few nanometers) films are exploited [8]. A possible alternative is the use of ultrathin metal oxide (MO) films [9]. Here, a single layer of oxygen atoms can decouple, or at least reduce, the interaction between the grown molecules and the buried metal substrate.

The mechanisms involved during the film growth on the oxide layer are still under debate. In this respect, we have recently studied the growth of Zn-TPP (the molecular structure is reported in Figure 1), a well-characterized and studied porphyrin, on a prototypical ultrathin MO substrate, namely Fe(001)-*p*(1×1)O [10]. On this surface, oxygen atoms are placed between four metal atoms, slightly above the Fe(001) uppermost layer, making an ultrathin Fe monoxide layer. From our data we observe an increase of the porphyrin diffusivity on the MO layer [12]. This allows molecules to assemble in an ordered square super-lattice showing a (5 × 5) reconstruction, as observed by low-energy electron diffraction. An X-ray photoemission analysis proves that Zn-TPP molecules are deposited flat on the surface and the molecular skeleton is not significantly distorted, as observed when Zn-TPP is grown on other substrates for comparison.

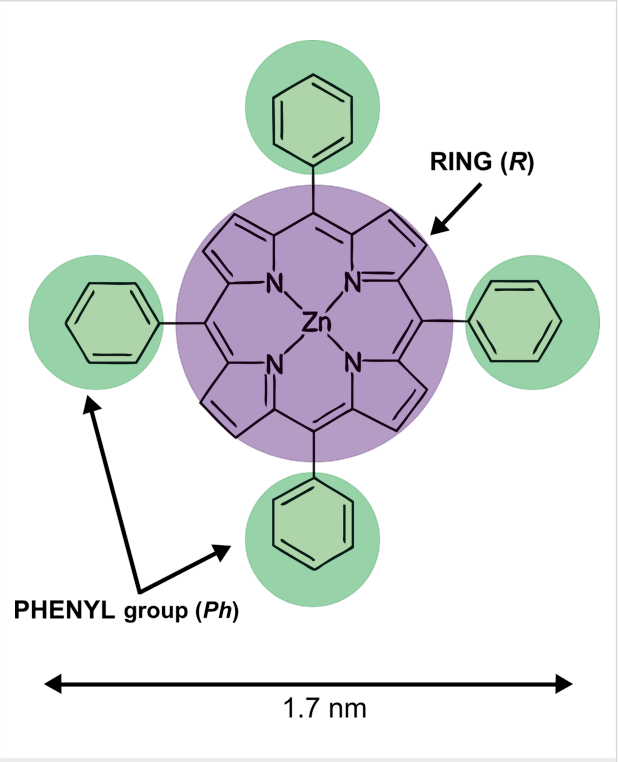

Figure 1: The structure of the Zn-tetraphenylporphyrin molecule. The main inner cavity of the porphyrin (ring) as well as the four phenyl groups have been marked in the image.

In this paper, we investigate the electronic structure of a Zn-TPP film, studying both normally occupied and unoccupied molecular levels by using ultraviolet photoemission (UPS) and inverse photoemission spectroscopy (IPES), respectively. A comparison between filled and empty states can help to reveal the creation and the value of an interface dipole, which shifts the sample vacuum energy level with respect to the pristine Fe(001)-*p*(1×1)O substrate. The determination of such an interface dipole, its direction with respect to the sample surface, and its dependence on the porphyrin film thickness are important in view of possible applications in electronic device prototypes. In such devices, the band alignment between molecular levels and substrate bands plays a key role in the transport properties.

Results and Discussion

From a technological point of view, the 1 monolayer (ML) thick sample is the most interesting and appealing, due to its ordered (5 × 5) reconstruction [10] that can be exploited (i) as a template for the deposition of other organic molecules or (ii) as a buffer layer in flat organic devices. On the other hand, a detailed analysis of the electronic properties of the porphyrin single layer requires a reference sample for comparison. Generally, as well as in this paper, a thick (typically 20 ML) porphyrin film is used for this purpose [10,11]. There, the substrate is almost completely covered by porphyrins. The spectra acquired on thick films can be considered representative of the electronic properties of a hypothetical isolated molecule, since molecule–molecule interactions are limited to weak van der Waals forces [11]. Consequently, changes in the energy position of the different spectroscopic features of the 1 ML film with respect to the reference layer are usually interpreted in terms of intensity strength of the molecule–substrate interaction.

In Figure 2, we report the filled (black line) and empty (red line) states of the Fe(001)-*p*(1×1)O substrate. The filled states are characterized by an intense peak at about 4.5 eV, due to the O 2p states of the oxygen layer [12]. On the other hand, the empty states are dominated by two peaks, close to the Fermi energy level, which are distinctive structures well known for their spin-polarized character [13]. The small feature at about 4.0 eV is usually attributed to an image state resonance that demonstrates the very good quality of the surface preparation [14].

The 20 ML thick sample shows the main features of the Zn-TPP molecule, where the different peaks are visible in the filled states. The first structure, close to the Fermi energy, is related to the HOMO level of the main molecular ring (at 1.76 eV with respect to the Fermi level and labelled R in the figure), while the intense structures at 4.0 eV and 6.7 eV are linked to the phenyl groups (Ph) of the molecule [10]. In the empty states, we recognize two features, one at about 1.5 eV (onset at 0.75 eV), and the second at 3.7 eV. We ascribe them to R-LUMO and Ph-LUMO, respectively. These results, and the states assignments, are in close agreement with data reported on a comparable molecule, Zn-phthalocyanine (Zn-Pc) [14]. In the Zn-Pc film, a gap of about 1.94 eV [14] is measured between the onset of the *R*-HOMO peak and the onset of the R-LUMO feature, in very good agreement with our data (1.95 eV). As discussed in

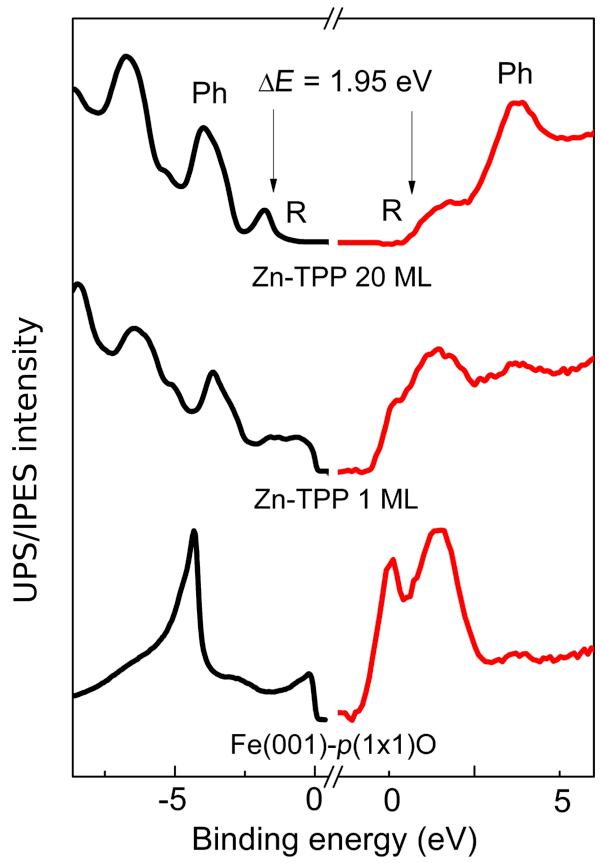

Figure 2: Filled (black lines) and empty (red lines) states acquired on freshly prepared Fe(001)-*p*(1×1)O for 1 ML and 20 ML thick Zn-TPP samples.

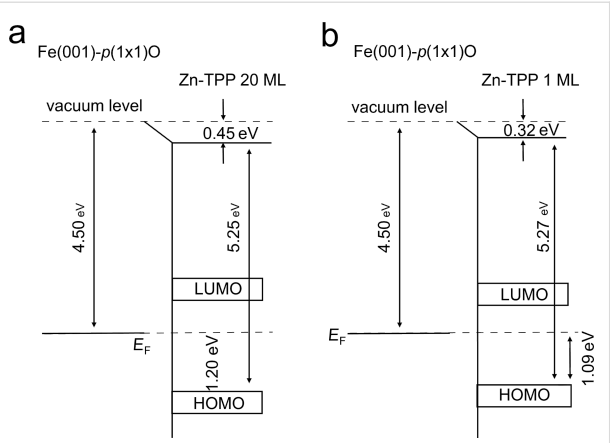

Figure 3: Energy of molecular levels near the interface between Fe(001)-*p*(1×1)O and the (a) 20 ML thick Zn-TPP film and (b) 1 ML thick Zn-TTP film. The interface dipole, work function of the bare substrate, and Zn-TPP ionization energy are indicated.

detail in [10], the porphyrin R-HOMO and Ph-HOMO are already visible in the 1 ML thick sample. The empty states of the ultrathin layer are affected however by the signal arising from the buried substrate. The IPES spectrum of the 1 ML thick sample is dominated by structures close to the Fermi energy, which are similar to the two peaks of the clean substrate. At 3.6 eV, a quite large feature appears. Considering the observed energy shift of the Zn-TPP peaks between 1 ML and 20 ML structures [10], we attribute this structure to the Ph-LUMO state.

From the data acquired with UPS and IPES measurements, the ionization energy (the difference between the vacuum level, E_{vac}, and the leading edge of the HOMO) and the electron affinity (the difference between E_{vac} and the LUMO) of the condensed organic film can be deduced. For this purpose, we have measured the sample work function from the energy position of the low-energy secondary electron cutoff edge that, compared with the work function (WF) of the pristine Fe(001)-*p*(1×1)O (4.50 eV [13]), allows the determination of the interface dipole, as reported in Figure 3.

The results obtained for the 20 ML film are in good agreement with those reported for Zn-Pc [14] deposited on a gold substrate. The measured ionization energy (5.25 eV, see Figure 3a) is directly comparable with the value obtained for Zn-Pc (5.28 eV) [14], confirming that Zn-TPP and Zn-Pc have a comparable electronic as well as chemical structure. Conversely, the interface dipole of the Zn-TPP film (0.45 eV, see Figure 3a) is about 300 meV smaller with respect to the Zn-Pc film (0.76 eV, as reported in [14]), suggesting a different (lower) molecule–substrate interaction. The sample belongs to the large organic/metal interface group at which the vacuum level alignment rule breaks down [15] and chemical bonds play a key role in tuning the barrier height [16]. With these interfaces, the sign of the dipole is deduced from the decreasing substrate work function and interpreted in terms of a (partial) electron transfer from the organic material to the Fe(001)-*p*(1×1)O surface [14]. In this picture, the direction of the dipole vector points from the substrate into the (positive) organic film. In Figure 3b, a similar analysis is reported for the 1 ML sample. In this case, an interface dipole of about 0.32 meV is found. This means that its value increases as a function of the deposited organic film thickness (0.32 meV at 1 ML vs 0.45 meV at 20 ML) in agreement with data reported in the literature [17]. The determination of the LUMO level is here more critical, because, as mentioned above, the IPES spectra are partially affected by the substrate photoemission signal. The LUMO energy position has been assessed after an analysis of the acquired spectra, the details of which are reported in Supporting Information File 1. As recently reported by the authors [10], the Zn-TPP sample undergoes a phase transition (from a (5 × 5) to a (√5 × √5) reconstruction) for film thicknesses larger than 1 ML. Generally speaking, a change in the molecular packing could influence the energy levels of the film. However, the band

alignment at the molecule/substrate interface is mainly due to a charge transfer between the organic layers and the substrate and a consequent modification of the electron density, as reported in the literature [18]. The changes of the interface dipole, as a function of the film thickness, can thus give a first characterization to evaluate possible barriers that affect the transport properties of the junction. Finally, we summarize in the Table 1 the main energy positions of the R/Ph-HOMO and R/Ph-LUMO molecular levels as measured and/or deduced from our data.

Table 1: Binding energy position of both filled and empty molecular levels as a function of the porphyrin film thickness.

	1 ML thick sample	20 ML thick sample
R-HOMO	1.50 ± 0.01 eV	1.76 ± 0.01 eV
Ph-HOMO	3.80 ± 0.01 eV	4.00 ± 0.01 eV
R-LUMO	0.6 ± 0.3 eV	0.8 ± 0.3 eV
Ph-LUMO	3.6 ± 0.3 eV	3.7 ± 0.3 eV

Conclusion

An organic Zn-TPP film was grown under UHV conditions in a special chamber devoted to the sublimation of molecules. The porphyrin films were deposited at RT on a freshly prepared Fe(001)-*p*(1×1)O substrate, whose topmost layer can be considered prototypical of the wide class of thin MO films. The ultrathin oxide layer is able to decouple the molecules from the buried iron substrate. The reduced molecule–substrate interaction allows preservation of the main electronic properties of the Zn-TPP porphyrins. This means that the HOMO and LUMO levels of the organic film are placed close to the characteristic energy values of the unperturbed molecule. In this paper, the filled and empty states of the organic film were studied and the formation of the interface dipole was analyzed. These results are interesting in view of applications of ultrathin Zn-TPP films in organic devices, where the alignment of the HOMO and LUMO levels of the molecule with the substrate bands play a crucial role in charge transport.

Experimental

The experimental apparatus consists of a multichamber ultra-high vacuum (UHV, base pressure in the 10^{-8} Pa range) system described elsewhere [19], coupled to a chamber devoted to organic molecular beam epitaxy (OMBE). The OMBE chamber was designed and built in collaboration with 5Pascal srl. (via Boccaccio 108, 20090 Trezzano sul Naviglio, Milano, Italy). The OMBE system is equipped with four Knudsen cells, whose crucibles are controlled within 0.5 °C. One of the cells is filled with Zn-TPP molecules provided by Sigma-Aldrich and purified in vacuum by several cycles of annealing at 150 °C and flashes at 310 °C, until the pressure in the OMBE chamber was stable in the low 10^{-7} Pa range. The molecule sublimation was achieved at a temperature of 300 °C and the molecular flux (0.5 ML/min, where 1 ML is 3.06 Å [11]) was measured by a quartz microbalance. The Fe(001) substrate was kept at room temperature during the porphyrin sublimation.

The Fe(001)-*p*(1×1)O fresh surface was prepared by exposing the clean Fe(001) surface to few Langmuir of molecular oxygen followed by annealing at 630 °C, as reported in the literature [20,21].

Ultraviolet photoemission spectroscopy (UPS) was performed by exciting electrons out of the sample at normal emission with a UV radiation ($h\nu$ = 21.2 eV) and detecting them by means of a 150 mm hemispherical analyzer (SPECS GmbH) [11], having an energy resolution of about 50 meV. A GaAs(001) photocathode, prepared according to standard procedures [22,23], was used for inverse photoemission spectroscopy (IPES), operating in the isochromatic mode, by detecting 9.6 eV photons with a band-pass detector [24-26]. The IPES energy resolution is about 700 meV. All the experiments reported here were achieved under negligible charging conditions during electron spectroscopy data acquisition. The position of the vacuum level was obtained by adding the photon energy to the low-energy secondary electron cutoff acquired with the sample at negative bias (−10 V).

Supporting Information

Supporting Information File 1

Additional experimental information.
[http://www.beilstein-journals.org/bjnano/content/supplementary/2190-4286-7-146-S1.pdf]

Acknowledgements

The authors are grateful to G. Berti, A. Brambilla and M. Celeri for useful discussions. Support of this work by the FIRB project no. RBAP115AYN is gratefully acknowledged.

References

1. Gottfried, J. M. *Surf. Sci. Rep.* **2015,** *70,* 259–379. doi:10.1016/j.surfrep.2015.04.001
2. Szyszko, B.; Latos-Grażyński, L. *Chem. Soc. Rev.* **2015,** *44,* 3588–3616. doi:10.1039/C4CS00398E
3. Pratviel, G. *Coord. Chem. Rev.* **2016,** *308,* 460–477. doi:10.1016/j.ccr.2015.07.003
4. Auwärter, W.; Écija, D.; Klappenberger, F.; Barth, J. V. *Nat. Chem.* **2015,** *7,* 105–120. doi:10.1038/nchem.2159
5. Sil, D.; Rath, S. P. *Dalton Trans.* **2015,** *44,* 16195–16211. doi:10.1039/C5DT00947B

6. Fan, S.; Lu, X.; Sun, H.; Zhou, G.; Chanq, Y. J.; Wang, Z.-S. *Phys. Chem. Chem. Phys.* **2016,** *18,* 932–938. doi:10.1039/C5CP05986K
7. Hieringer, W.; Flechtner, K.; Kretschmann, A.; Seufert, K.; Auwärter, W.; Barth, J. V.; Görling, A.; Steinrück, H.-P.; Gottfried, J. M. *J. Am. Chem. Soc.* **2011,** *133,* 6206–6222. doi:10.1021/ja1093502
8. Smets, Y.; Stark, C. B.; Lach, S.; Schmitt, F.; Wright, C. A.; Wanke, M.; Ley, L.; Ziegler, C.; Pakes, C. I. *J. Chem. Phys.* **2013,** *139,* 044703. doi:10.1063/1.4815978
9. Picone, A.; Riva, M.; Brambilla, A.; Calloni, A.; Bussetti, G.; Finazzi, M.; Ciccacci, F.; Duò, L. *Surf. Sci. Rep.* **2016,** *71,* 32–76. doi:10.1016/j.surfrep.2016.01.003
10. Bussetti, G.; Calloni, A.; Celeri, M.; Yivlialin, R.; Finazzi, M.; Bottegoni, F.; Duò, L.; Ciccacci, F. *Appl. Surf. Sci.* **2016,** *390,* 856–862. doi:10.1016/j.apsusc.2016.08.137
11. Castellarin-Cudia, C.; Borghetti, P.; Di Santo, G.; Fanetti, M.; Larciprete, R.; Cepek, C.; Vilmercati, P.; Sangaletti, L.; Verdini, A.; Cossaro, A.; Floreano, L.; Morgante, A.; Goldoni, A. *ChemPhysChem* **2010,** *11,* 2248–2255. doi:10.1002/cphc.201000017
12. Calloni, A.; Berti, G.; Brambilla, A.; Riva, M.; Picone, A.; Bussetti, G.; Finazzi, M.; Ciccacci, F.; Duò, L. *J. Phys.: Condens. Matter* **2014,** *26,* 445001. doi:10.1088/0953-8984/26/44/445001
13. Cattoni, A.; Petti, D.; Brivio, S.; Cantoni, M.; Bertacco, R.; Ciccacci, F. *Phys. Rev. B* **2009,** *80,* 104437. doi:10.1103/PhysRevB.80.104437
14. Gao, W.; Kahn, A. *Org. Electron.* **2002,** *3,* 53–63. doi:10.1016/S1566-1199(02)00033-2
15. Ishii, H.; Seki, K. *IEEE Trans. Electron Devices* **1997,** *44,* 1295–1301. doi:10.1109/16.605471
16. Hill, I. G.; Rajagopal, A.; Kahn, A.; Hu, Y. *Appl. Phys. Lett.* **1998,** *73,* 662–664. doi:10.1063/1.121940
17. Hill, I. G.; Rajagopal, A.; Kahn, A. *J. Appl. Phys.* **1998,** *84,* 3236–3241. doi:10.1063/1.368477
18. Crispin, X.; Geskin, V.; Crispin, A.; Cornil, J.; Lazzaroni, R.; Salaneck, W. R.; Brédas, J.-L. *J. Am. Chem. Soc.* **2002,** *124,* 8131–8141. doi:10.1021/ja025673r
19. Berti, G.; Calloni, A.; Brambilla, A.; Bussetti, G.; Duò, L.; Ciccacci, F. *Rev. Sci. Instrum.* **2014,** *85,* 073901. doi:10.1063/1.4885447
20. Picone, A.; Brambilla, A.; Calloni, A.; Duò, L.; Finazzi, M.; Ciccacci, F. *Phys. Rev. B* **2011,** *83,* 235402. doi:10.1103/PhysRevB.83.235402
21. Bertacco, R.; Ciccacci, F. *Phys. Rev. B* **1999,** *59,* 4207–4210. doi:10.1103/PhysRevB.59.4207
22. Pierce, D. T.; Celotta, R. J.; Wang, G.-C.; Unertl, W. N.; Galejs, A.; Kuyatt, C. E.; Mielczarek, S. R. *Rev. Sci. Instrum.* **1980,** *51,* 478–499. doi:10.1063/1.1136250
23. Ciccacci, F.; Chiaia, G. *J. Vac. Sci. Technol., A* **1991,** *9,* 2991–2995. doi:10.1116/1.577161
24. Ciccacci, F.; Vescovo, E.; Chiaia, G.; De Rossi, S.; Tosca, M. *Rev. Sci. Instrum.* **1992,** *63,* 3333–3338. doi:10.1063/1.1142549
25. Finazzi, M.; Bastianon, A.; Chiaia, G.; Ciccacci, F. *Meas. Sci. Technol.* **1993,** *4,* 234–236. doi:10.1088/0957-0233/4/2/017
26. Chiaia, G.; De Rossi, S.; Mazzolari, L.; Ciccacci, F. *Phys. Rev. B* **1993,** *48,* 11298. doi:10.1103/PhysRevB.48.11298

License and Terms

The definitive version of this article is the electronic one which can be found at:
doi:10.3762/bjnano.7.146

BEILSTEIN JOURNAL OF NANOTECHNOLOGY

Hydrophilic silver nanoparticles with tunable optical properties: application for the detection of heavy metals in water

Paolo Prosposito*[1], Federico Mochi[1], Erica Ciotta[1], Mauro Casalboni[1], Fabio De Matteis[1], Iole Venditti*[2], Laura Fontana[2], Giovanna Testa[2] and Ilaria Fratoddi[2]

Full Research Paper

Open Access

Address:
[1]Department of Industrial Engineering, INSTM and CIMeR, University of Rome Tor Vergata, Rome, V. del Politecnico 1, 00133, Italy and [2]Department of Chemistry, University of Rome Sapienza, Rome, P.le A. Moro 5, 00187, Italy

Email:
Paolo Prosposito* - paolo.prosposito@uniroma2.it;
Iole Venditti* - iole.venditti@uniroma1.it

* Corresponding author

Keywords:
heavy metal sensor; nickel (II); optical materials; optical sensors; silver nanoparticles

Beilstein J. Nanotechnol. **2016,** *7,* 1654–1661.
doi:10.3762/bjnano.7.157

Received: 18 July 2016
Accepted: 17 October 2016
Published: 09 November 2016

This article is part of the Thematic Series "Self-assembly of nanostructures and nanomaterials II".

Guest Editor: I. Berbezier

Abstract

Due their excellent chemo-physical properties and ability to exhibit surface plasmon resonance, silver nanoparticles (AgNPs) have become a material of choice in various applications, such as nanosensors, electronic devices, nanobiotechnology and nanomedicine. In particular, from the environmental monitoring perspective, sensors based on silver nanoparticles are in great demand because of their antibacterial and inexpensive synthetic method. In the present study, we synthesized AgNPs in water phase using silver nitrate as precursor molecules, hydrophilic thiol (3-mercapto-1-propanesulfonic acid sodium salt, 3MPS) and sodium borohydride as capping and reducing agents, respectively. The AgNPs were characterized using techniques such as surface plasmon resonance (SPR) spectroscopy, dynamic light scattering (DLS), zeta potential (ζ-potential) measurements and scanning tunneling microscopy (STM). Further, to demonstrate the environmental application of our AgNPs, we also applied them for heavy metal sensing by detecting visible color modification due to SPR spectral changes. We found that these negatively charged AgNPs show good response to nickel (II) and presented good sensibility properties for the detection of low amount of ions in water in the working range of 1.0–0.1 ppm.

Introduction

Nanomaterials have become very popular in the last years in many fields because of their unique electronic, optical, magnetic and photocatalytic properties and for their large surface-to-volume ratio, which allows very good interaction with the external environment [1-6]. These properties can be exploited in the field of sensors for specific analytes [7-10]. In particular,

given their flexible and easy preparation, large specific surface area, and surface plasmon resonance (SPR) properties, metal nanoparticles are excellent candidates for a wide variety of applications ranging from catalysis [11,12], energy [13-15], optoelectronics [16,17] and biomedicine [18] to sensors [19,20]. A very promising field of application is chemical sensing, which includes gas detection, safety and environmental monitoring [21-25].

Moreover, the need for developing highly sensitive and selective sensors for the detection of very low amounts of heavy metal ions from biological and environmental samples has greatly increased [26]. The metal-ion toxicity depends on their physical state, chemical form as well as the oxidation state. Many groups have studied fluorescent chemosensors with fluorescence enhancement and quenching for the detection of metal ions [27-32].

The most studied nanoparticles are those based on gold, however many studies have revealed that a suitable functionalization of silver nanoparticles can significantly improve their sensing performance [17-22]. The presence of specific functionality on the particle surface can increase the adsorption of the analytes, resulting in an enhancement of sensitivity or selectivity. An interesting application of functionalized AgNPs is reported by Contino et al. [33] where synthesized AgNPs were capped by tyrosine and the heavy metal sensing performance was measured by observing the shift of SPR band. In this case the low detection limit for Cu(II) is attributed to the high quality of the AgNPs.

From the perspective of optimizing the properties of metal nanoparticles, research groups have focused on the control of the size and shape of nanoparticles [34,35], which is crucial in tuning their physical, chemical and optical properties [36-38].

Electrochemical, photochemical, sonochemical and chemical reduction methods can be used for the synthesis of metal nanoparticles [39-43]. On the other hand, the wet reduction is the most common synthetic technique for the fabrication of metal nanoparticles, using sodium borohydride as a reducing agent and thiols as a capping agent to prevent nanoparticles aggregation [44-46].

In the present article, we report the fabrication and characterization of AgNPs stabilized by sodium 3-mercaptopropane sulfonate (AgNP-3MPS). A new preparation was optimized to improve the optical sensing performances based on SPR spectral changes. The AgNP-3MPS nanoparticles have been tested as optical sensors in water solution towards different metal ions at concentration of 1 ppm at room temperature. Our system showed sensibility mainly to nickel (II) ions. For this type of ion, we tested the sensitivity as a function of the ion concentration in the range 1.0–0.1 ppm and we estimated a limit of detection (LOD) of 0.3 ppm.

Results and Discussion

Silver nanoparticle synthesis

AgNPs were synthesized by wet reduction, using sodium borohydride as a reducing agent and 3-mercapto-1-propanesulfonic acid sodium salt as a capping agent. The water solubility of the thiol induces a strongly hydrophilic character with respect to the nanoparticles, which present the sulfonate groups on the surface [47]. The presence of these negatively charged groups also guarantees the stability of the colloids over time, as was confirmed by the ζ-potential measurements [48,49]. Moreover, to improve the monodispersity of the AgNPs two different synthetic approaches were used. In the first one (synthesis a) the procedure was developed in analogy with previous work [22] and is reported in Scheme 1. This step leads to the hydrophilic character of silver nanoparticles.

At the end of the synthesis and purification, the reaction product was analyzed by UV–vis spectroscopy to confirm the presence of AgNPs by means of the measurement of the SPR spectra with a peak at 425 nm in the absorption spectrum, as shown in Figure 1a. The full with at half maximum (FWHM) was found to be about 170 nm. The DLS data are reported in Figure 1b,c. They show the diameter and ζ-potential of Ag-3MPS NPs obtained after the purification of the crude reaction by centrifugation in H_2O. Here we obtained well-dispersed AgNPs with an average diameter ($<2R_H>$) of 8 ± 2 nm and a ζ-potential of −34 ± 5 mV.

The nanoparticle diameter measured in water solution and in dry conditions are statistically different because in the water dispersion the hydrodynamic diameter is is measured and includes solvent layers. This therefore creates a potential on the surface of the particles (the ζ-potential) that induces negative charges on AgNPs surface due to sulfonate groups.

The sensitivity of the AgNPs to heavy metal ions was tested in water solution by monitoring the optical absorption changes in the presence of metal ions. A weak dependence of the peak wavelength as a function of the ion concentration was found. However, the large broadening of the SPR band and the high background of the absorption hindered the observation of a net effect of the presence of the ion. In this regard, since our main goal was the exploitation of the possible changes of the SPR band as a function of the external environment, a sharp and narrow absorption band was mandatory. For these reasons, we tuned and optimized a second, modified procedure (synthesis b)

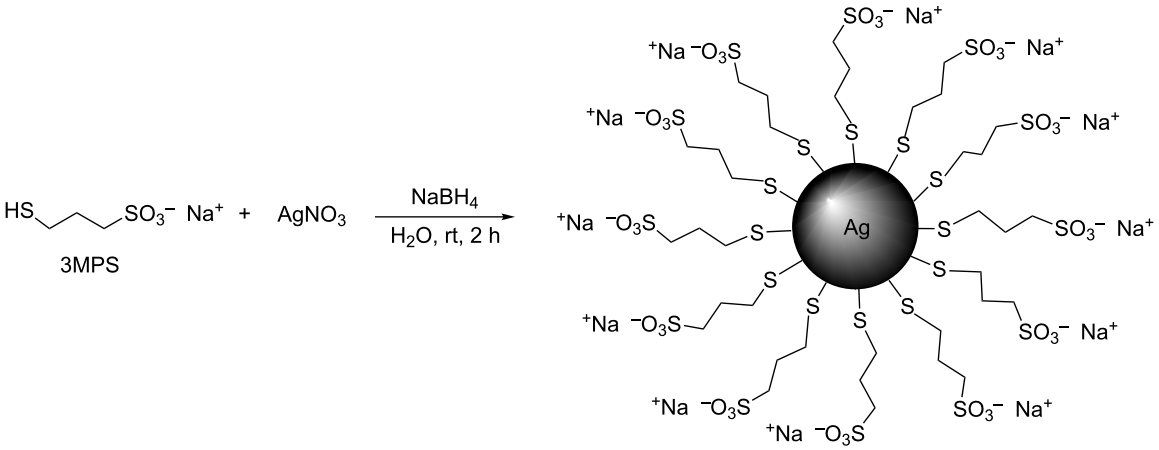

Scheme 1: Synthetic scheme of AgNP-3MPS nanoparticles (synthesis a).

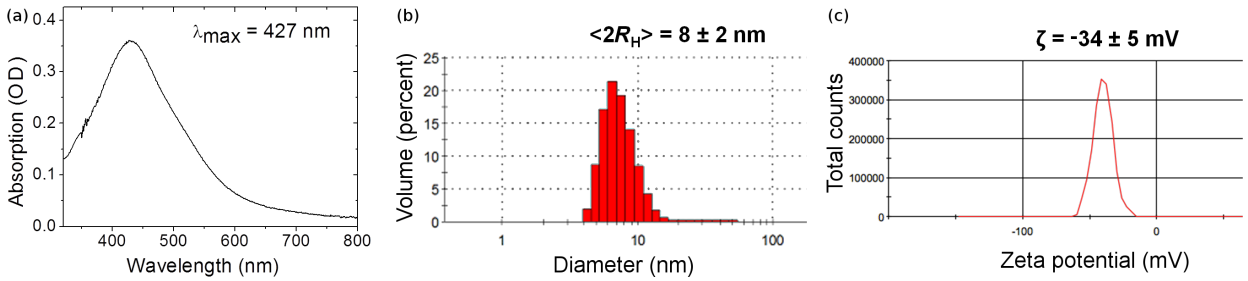

Figure 1: Characterization of AgNP-3MPS nanoparticles in H_2O (synthesis a): (a) UV–vis spectrum; (b) DLS measurements: $<2R_H> = 8 \pm 2$ nm; (c) ζ-potential measurements: $\zeta = -34 \pm 5$ mV.

for the synthesis of the AgNPs. In this case, the molar ratio between silver nitrate, sodium borohydride and 3-MPS was varied. The reaction was conducted at 3 °C and the final purification was avoided in order to prevent possible aggregation with a consequent broadening of the SPR band. For these reasons, we worked with very dilute AgNP solutions to minimize the residual unreacted chemical products. In particular, the concentration of the 3MPS was optimized to the ratio $AgNO_3$/3MPS 1:0.1 to ensure good coverage of the particles with 3MPS molecules, and thus increase the sensitivity of the sensor as much as possible.

Figure 2 shows the absorption spectra of the AgNP-3MPS solution. It shows a sharp peak at 404 nm. Its FWHM is 92 nm instead of 170 nm as obtained by the first synthetic method (synthesis a). It should be noted that the FWHM of the AgNP solution without capping agent (not reported) was about 60 nm. The broadening of about 30 nm can be ascribed to the surface functionalization of the AgNPs with 3MPS.

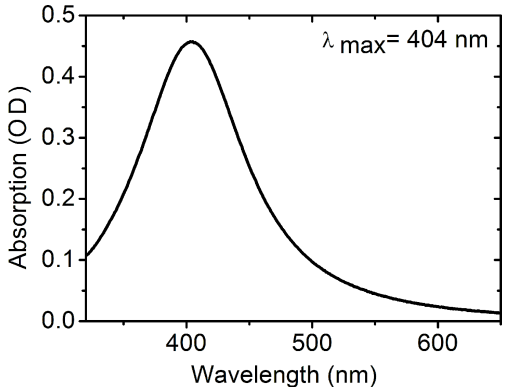

Figure 2: Absorption spectrum of AgNP-3MPS nanoparticles (synthesis b). The SPR exhibits a sharp peak at 404 nm with a FWHM of 92 nm.

We characterized the AgNP-3MPS nanoparticles via STM spectroscopy. Figure 3a,b shows the morphology and the profile of the nanoparticles, respectively. We estimated the average diam-

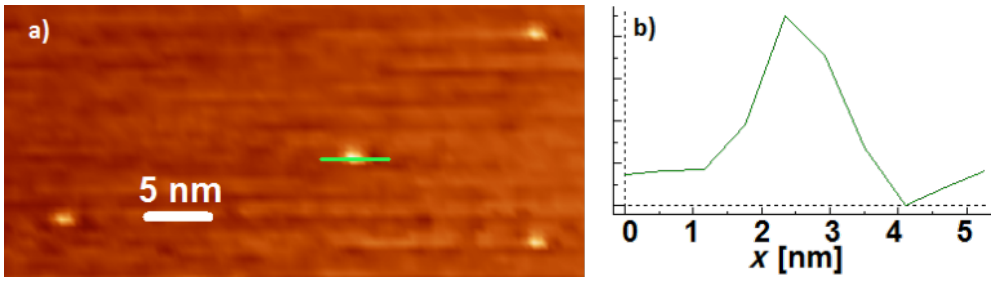

Figure 3: a) STM morphology measurements of AgNP-3MPS (synthesis b) and b) the height profile of one nanoparticle.

eter using about thirty nanoparticles with a resulting value of 2.5 ± 0.3 nm.

Figure 4 shows the results from the dynamic light scattering (DLS) measurement on the AgNP-3MPS material (synthesis b). The distribution indicates good monodispersity of the NPs and an average diameter of $<2R_H> = 5 \pm 2$ nm, in good agreement with the STM analysis.

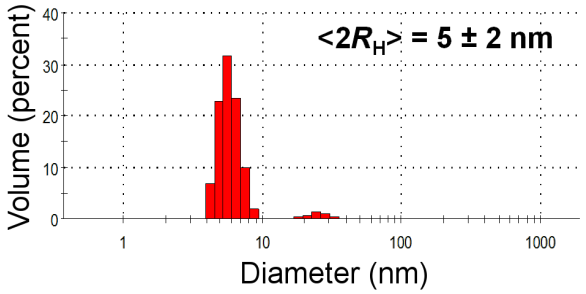

Figure 4: DLS of the AgNP-3MPS solution (synthesis b). The hydrodynamic diameter was $<2R_H> = 5 \pm 2$ nm.

The SPR absorption was monitored as a function of the time in order to check the long term stability of the NPs. As shown in Figure 5, the solution presents the same optical spectra 15 days after the preparation, indicating that no aggregation of the nanoparticles occurred.

Metal ion detection

We investigated the optical sensing properties of the AgNP-3MPS material via absorption spectroscopy. Each solution of AgNP-3MPS/ion was prepared in spectroscopic cuvettes that were carefully cleaned to avoid contamination. To a specific amount of AgNPs contained in a fixed volume of water, a fixed volume of water was added containing the ions with the specific final concentration. After the mixing, we waited for five minutes before measuring the absorption spectra in order to allow for the complete interaction with the NPs.

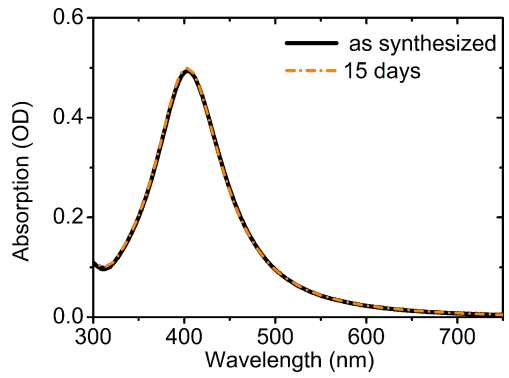

Figure 5: SPR absorption spectroscopy of the AgNP-3MPS solution (synthesis b) taken immediately after the synthesis and after 15 days, indicating good long term stability.

The sensitivity of the AgNPs-3MPS system was tested with different metal ions: Ni^{2+}, Cr^{3+}, Nd^{3+}, Cu^{2+} and Ca^{2+}. We found different behavior for the various ions. In Figure 6 the SPR bands are reported relative to all the tested ions for a fixed value of the concentration (1 ppm).

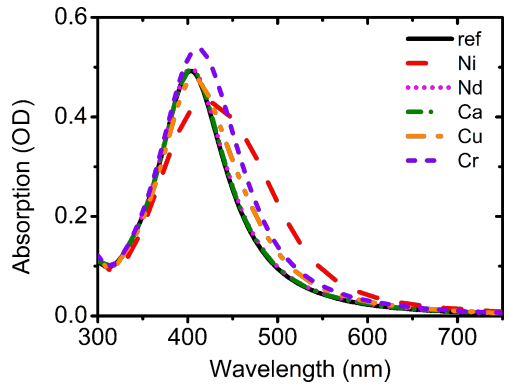

Figure 6: Absorption spectra of the AgNP-3MPS (synthesis b) solution with 1 ppm ion concentration.

The system shows a good response to Ni^{2+} since the absorption spectrum is strongly different with respect to that obtained from the solution without ions (reference). With the Cr^{3+} ions, only a small shift in the peak wavelength and an increase in the intensity is observed, while for the Ni^{2+} ions, a larger shift, a broadening and a reduction of the maximal value were detected in the plasmonic feature. The presence of Cu^{2+}, Nd^{3+} and Ca^{2+} on the contrary does not produce any substantial modifications in the plasmonic absorption neither in the intensity nor in the position and shape.

To quantitatively test the properties of the NPs we performed absorption measurements as a function of concentration of nickel ions. Figure 7a shows the optical absorption spectrum of the AgNP-3MPS solution with nickel for different ion concentrations in the range 1.0–0.1 ppm. Figure 7b presents the maximum wavelength of the absorption peak as a function of the concentration of metal ions.

In Figure 8 we report the normalized intensity, the peak wavelength and the FWHM of the absorption spectra obtained with different nickel ion concentrations (from 0–1 ppm). The reduction of intensity with the increase of the ion concentration can be ascribed to the reduction of the apparent number of NPs due to aggregation induced by the Ni^{2+} ions. The red shift and broadening of the SPR peak is a clear indication of the increase of the average size of the NPs and their size distribution and is fully compatible with the aggregation hypothesis.

At high ion concentrations (higher than 1 ppm), the shape of the SPR is sharper than that of the 1 ppm concentration and does not present sensitivity to different ion concentrations. This is probably due to the ratio between the number of ions and the number of silver nanoparticles. In the ion concentration range from 1 to 25 ppm, the number of ions exceeds the number of

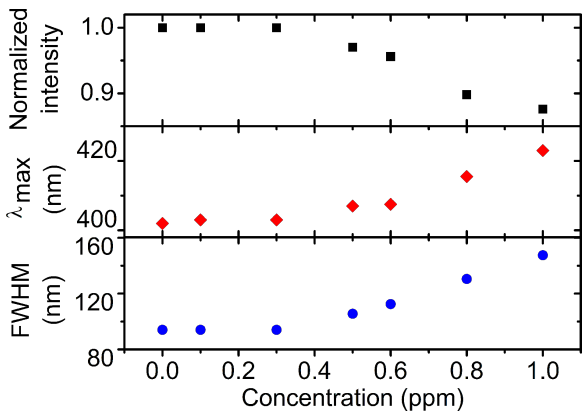

Figure 8: Normalized intensity, absorption maximum (λ_{max}) and FWHM as a function of the nickel ion concentration.

nanoparticles at least by a factor of 1000. Under these conditions, small changes of the number of ions do not affect the SPR band since all the external thiols present on the NP surface are saturated. On the other hand, for lower ion concentrations in the range 0.1–1 ppm the number of ions for each NP is on the order of a few tens and therefore a decrease in their number can strongly affect the optical properties of the solution. We can thus conclude that for high ion concentrations, the NPs are completely screened and a positive stabilization of the colloidal suspension occurs. In the intermediate region (0.3 to 1 ppm) the number of ions is comparable with the number of thiols surrounding the metal NPs and aggregation between NPs can easily occur. Finally, in the region below 0.3 ppm, the ions do not cause aggregation, but only a slight shift of the position of the surface plasmon.

On the basis of these considerations, we propose a simple model to explain the observed behavior reported in Figure 9. We estimated the concentration of the AgNP-3MPS solution,

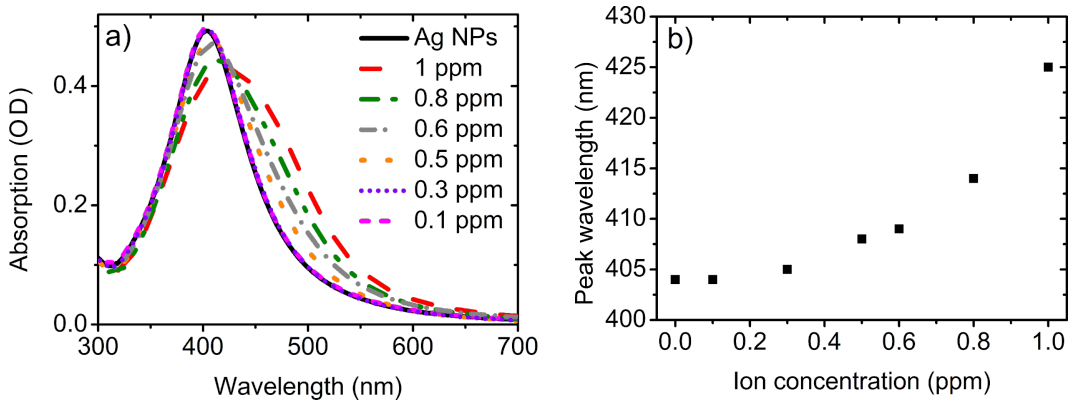

Figure 7: a) Absorption spectra of the AgNP-3MPS system (synthesis b) as a function of the Ni^{2+} concentration. b) Peak absorption wavelength as a function of the ion concentration.

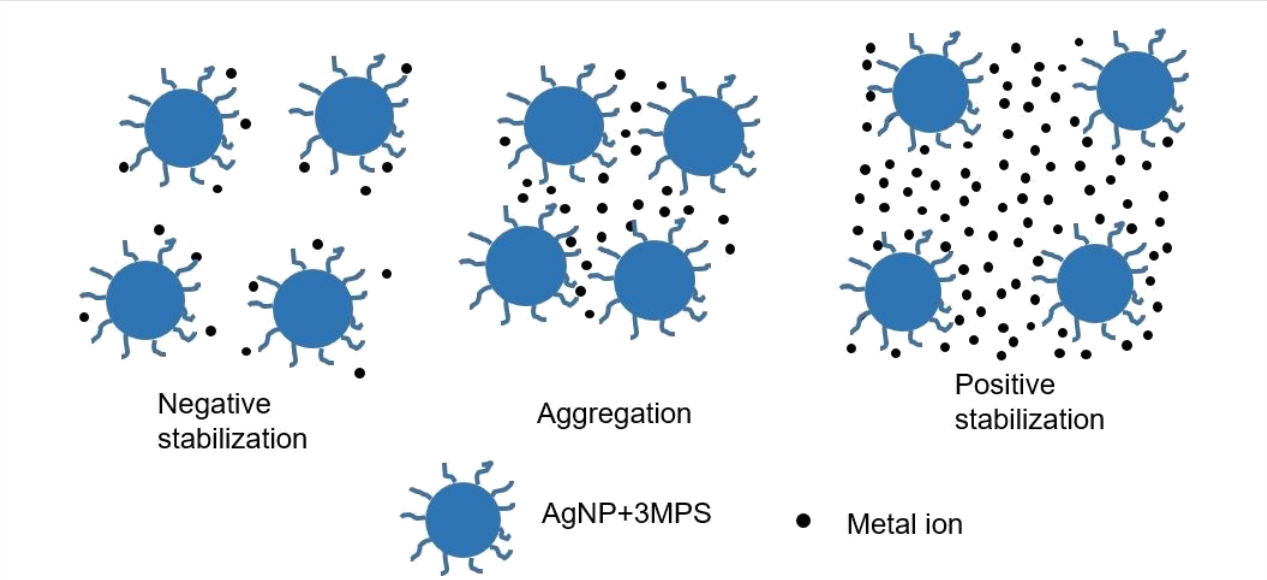

Figure 9: Model of the interaction of AgNP-3MPS and metal ions.

the average number of surface thiols present for each NP, and the number of nickel ions for each concentration. For a concentration greater than 2 ppm, the value of the ratio (number of ions/number of NPs) is in the range 100–200. In this case, the metal ions are able to totally screen the NP signal, since the sulfonate groups of the 3MPS on a single nanoparticle are on the order of a few tens. Under this condition, a positive stabilization occurs. When the number of metal ions decreases to a few tens (and is therefore is comparable with the number of available surface thiols) the positive shell is not dense enough to totally screen the nanoparticle and aggregation occurs since the ions themselves can act as bridges between adjacent AgNPs. Finally, when the number of metal ions is lower than the number of surface thiols, the metal ions do not cause aggregation, but the only effect is a slight shift of the SPR peak wavelength position.

Conclusion

In this work AgNP-3MPS nanoparticles with an average diameter of 2.5 ± 0.3 nm were synthetized with a narrow distribution range and negative charge on the surface. These particles were fully characterized by means of different techniques, such as STM, DLS and UV–vis spectroscopy. The SPR signal of the AgNP-3MPS sample in water solution demonstrated a spectral response to the presence of metal ions. This showed a sensitivity and selectivity to Ni^{2+} ions with a sensitivity as low as 0.3 ppm. A quantitative determination of these species in the concentration range of 0.3–1.0 ppm was provided. This approach seems very promising for the development of an analytical sensor system based on optical methods to detect metal ions in actual water samples.

Experimental

Materials and sample preparation

Silver nitrate ($AgNO_3$, Sigma-Aldrich, 99.5%), sodium borohydride ($NaBH_4$, Sigma-Aldrich, 98%) and 3-mercapto-1-propanesulfonic acid sodium salt ($C_3H_7S_2O_3Na$, 3MPS, Sigma-Aldrich, 98%) were used as received. Deionized water (electrical conductivity less than 1 μΩ/cm at room temperature) was obtained from a Millipore Milli-Q water purification system.

Synthesis a: silver NPs (AgNPs) were prepared at room temperature in a single phase system, following a procedure reported elsewhere [22,47,50]. AgNP-3MPS nanoparticles were prepared using a Ag/3MPS molar ratio of 0.25:1. In a typical synthesis, 0.100 g of $AgNO_3$ were dissolved in 10 mL of deionized water and a solution of 3MPS in deionized water (0.840 g in 10 mL) was added; the mixture was maintained under argon flux for deoxygenating the reactions and vigorous stirring for 10 min at room temperature. Finally, $NaBH_4$ solution in deionized water (0.223 g in 10 mL) was added dropwise. The reaction mixture was allowed to react for 2 h and the obtained suspension was centrifuged with deionized water several times (10 min, 15 000 rpm).

Synthesis b: sodium borohydride and silver nitrate solution (in deionized water) was mixed with concentration ratio $NaBH_4/AgNO_3$ 2:1. The $NaBH_4$ solution was cooled to 3 °C under vigorous stirring, then the $AgNO_3$ solution was added dropwise at approximately one drop per second. The volume ratio of the two solutions was $NaBH_4/AgNO_3$ 15:1. When all of the $AgNO_3$ solution was added, the stirring was stopped. Then the 3MPS was added to reach the final ratio of $AgNO_3$/3MPS

1:0.1. While adding the 3MPS, the solution was stirred for few seconds, then the AgNP-3MPS solution was stored at 4 °C.

For samples obtained with both synthesis methods, UV–vis spectra were run with a Varian Cary 100 Scan UV–visible spectrophotometer and Perkin-Elmer Lambda 19 from water suspensions. A Malvern Zetasizer Nanoseries instrument (Malvern, UK) equipped with a 10 mW HeNe laser at a 632.8 nm wavelength was used to obtain the DLS measurements on the AgNP aqueous suspensions (0.2 mg/mL) at $T = 25.0 \pm 0.2$ °C. The correlation functions were collected at 90° relative to the incident beam, and delay times from 0.8 μs to 10 s were explored. Non-negative least-squares (NNLSs) [51] or CONTIN [52] algorithms, supplied with the instrument software, were used to fit the correlation data. The average hydrodynamic radius of the diffusing objects was calculated, as reported in previous studies [53,54]. The ζ-potential was calculated from the measured electrophoretic mobility by means of the Smolukovsky equation [55]. The scanning tunneling microscope (Tops System, WA Technology) consists of a UHV attachment with an antivibration stacking and a piezoelectric tube with 2 mm maximum scanning area for the tip movement. The lateral resolution of the microscope is ±1 Å and the accuracy in the lateral displacement is ±0.05 Å. Tungsten tips were chemically etched in a solution of NaOH and glycerol.

Acknowledgements

This work was funded by Ateneo Sapienza with grants 2015/C26A15H5J9 and 2015/C26A15LRMA and by the University of Rome Tor Vergata from the "Uncovering Excellence 2014" PHANTOM project. We gratefully acknowledge the valuable assistance of Prof. Anna Sgarlata and Prof. G. Paradossi for the STM and DLS characterization, respectively.

References

1. Wang, L.; Nemoto, Y.; Yamauchi, Y. *J. Am. Chem. Soc.* **2011,** *133,* 9674–9677. doi:10.1021/ja202655j
2. Ataee-Esfahani, H.; Wang, L.; Nemoto, Y.; Yamauchi, Y. *Chem. Mater.* **2010,** *22,* 6310–6318. doi:10.1021/cm102074w
3. Li, C.; Yamauchi, Y. *Phys. Chem. Chem. Phys.* **2013,** *15,* 3490–3496. doi:10.1039/C3CP44313B
4. Venditti, I.; Fratoddi, I.; Palazzesi, C.; Prosposito, P.; Casalboni, M.; Cametti, C.; Battocchio, C.; Polzonetti, G.; Russo, M. V. *J. Colloid Interface Sci.* **2010,** *48,* 424–430. doi:10.1016/j.jcis.2010.04.061
5. De Angelis, R.; D'Amico, L.; Casalboni, M.; Hatami, F.; Masselink, W. T.; Prosposito, P. *Sens. Actuators, B* **2013,** *189,* 113–117. doi:10.1016/j.snb.2013.01.057
6. Fratoddi, I.; Venditti, I.; Cametti, C.; Russo, M. V. *Sens. Actuators, B* **2015,** *220,* 534–548. doi:10.1016/j.snb.2015.05.107
7. Bogue, R. *Sens. Rev.* **2008,** *28,* 12–17. doi:10.1108/02602280810849965
8. Barettin, D.; De Angelis, R.; Prosposito, P.; Auf der Maur, M.; Casalboni, M.; Pecchia, A. *Nanotechnology* **2014,** *25,* 195201. doi:10.1088/0957-4484/25/19/195201
9. De Angelis, R.; Casalboni, M.; Hatami, F.; Ugur, A.; Masselink, W. T.; Prosposito, P. *Sens. Actuators, B* **2012,** *162,* 149–152. doi:10.1016/j.snb.2011.12.052
10. Choi, I.; Choi, Y. *IEEE J. Sel. Top. Quantum Electron.* **2011,** *18,* 1110–1121. doi:10.1109/JSTQE.2011.2163386
11. Xia, Y.; Yang, H.; Campbell, C. T. *Acc. Chem. Res.* **2013,** *46,* 1671–1672. doi:10.1021/ar400148q
12. Burrows, N. D.; Vartanian, A. M.; Abadeer, N. S.; Grzincic, E. M.; Jacob, L. M.; Lin, W.; Li, J.; Dennison, J. M.; Hinman, J. G.; Murphy, C. J. *J. Phys. Chem. Lett.* **2016,** *7,* 632–641. doi:10.1021/acs.jpclett.5b02205
13. Venditti, I.; Barbero, N.; Russo, M. V.; Di Carlo, A.; Decker, F.; Fratoddi, I.; Barolo, C.; Dini, D. *Mater. Res. Express* **2014,** *1,* 015040. doi:10.1088/2053-1591/1/1/015040
14. Prosposito, P.; D'Amico, L.; Casalboni, M.; Motta, N. Periodic arrangement of mono-dispersed gold nanoparticles for high performance polymeric solar cells. In *Nanotechnology (IEEE-NANO) , 2015 IEEE 15th International Conference on,* July 27–30, 2015; IEEE, 2015; pp 378–380. doi:10.1109/NANO.2015.7389005
15. Graetzel, M.; Janssen, R. A. J.; Mitzi, D. B.; Sargent, E. H. *Nature* **2012,** *488,* 304–312. doi:10.1038/nature11476
16. Quintiliani, M.; Bassetti, M.; Pasquini, C.; Battocchio, C.; Rossi, M.; Mura, F.; Matassa, R.; Fontana, L.; Russo, M. V.; Fratoddi, I. *J. Mater. Chem. C* **2014,** *2,* 2517–2527. doi:10.1039/c3tc32567a
17. Tanabe, K. *Mater. Lett.* **2007,** *61,* 4573–4575. doi:10.1016/j.matlet.2007.02.053
18. Boisselier, E.; Astruc, D. *Chem. Soc. Rev.* **2009,** *38,* 1759–1782. doi:10.1039/b806051g
19. Fratoddi, I.; Macagnano, A.; Battocchio, C.; Zampetti, E.; Venditti, I.; Russo, M. V.; Bearzotti, A. *Nanoscale* **2014,** *6,* 9177–9184. doi:10.1039/c4nr01400f
20. Chen, S.; Yuan, R.; Chai, Y.; Hu, F. *Microchim. Acta* **2013,** *180,* 15–32. doi:10.1007/s00604-012-0904-4
21. Su, S.; Wu, W.; Gao, J.; Lu, J.; Fan, C. *J. Mater. Chem.* **2012,** *22,* 18101–18110. doi:10.1039/C2JM33284A
22. Venditti, I.; Fratoddi, I.; Russo, M. V.; Bearzotti, A. *Nanotechnology* **2013,** *24,* 155503. doi:10.1088/0957-4484/24/15/155503
23. Fratoddi, I.; Altamura, P.; Bearzotti, A.; Furlani, A.; Russo, M. V. *Thin Solid Films* **2004,** *458,* 292–298. doi:10.1016/j.tsf.2003.12.065
24. Huang, D.; Niu, C.; Ruan, M.; Wang, X.; Zeng, G.; Deng, C. *Environ. Sci. Technol.* **2013,** *7,* 4392–4398. doi:10.1021/es302967n
25. Li, Z.; Wang, Y.; Ni, Y.; Kokot, S. *Sens. Actuators, B* **2014,** *193,* 205–211. doi:10.1016/j.snb.2013.11.096
26. Ban, D. K.; Pratihar, S. K.; Paul, S. *RSC Adv.* **2015,** *5,* 81554–81564. doi:10.1039/C5RA16473G
27. Kim, H. N.; Ren, W. X.; Kim, J. S.; Yoon, J. *Chem. Soc. Rev.* **2012,** *41,* 3210–3244. doi:10.1039/C1CS15245A
28. Wang, A.-J.; Guo, H.; Zhang, M.; Zhou, D.-L.; Wang, R.-Z.; Feng, J.-J. *Microchim. Acta* **2013,** *180,* 1051–1057. doi:10.1007/s00604-013-1030-7
29. Yin, J.; Wu, T.; Song, J.; Zhang, Q.; Liu, S.; Xu, R.; Duan, H. *Chem. Mater.* **2011,** *23,* 4756–4764. doi:10.1021/cm201791r
30. Zhang, M.; Liu, Y.-Q.; Ye, B.-C. *Analyst* **2012,** *137,* 601–607. doi:10.1039/C1AN15909G
31. Makwana, B. A.; Vyas, D. J.; Bhatt, K. D.; Darji, S.; Jain, V. K. *Appl. Nanosci.* **2016,** *6,* 555. doi:10.1007/s13204-015-0459-x

32. Makwana, B. A.; Vyas, D. J.; Bhatt, K. D.; Jain, V. K.; Agrawal, Y. K. *Spectrochim. Acta, Part A* **2015,** *134,* 73–80. doi:10.1016/j.saa.2014.05.044
33. Contino, A.; Maccarrone, G.; Zimbone, M.; Reitano, R.; Musumeci, P.; Calcagno, L.; Oliveri, I. V. *J. Colloid Interface Sci.* **2016,** *462,* 216–222. doi:10.1016/j.jcis.2015.10.008
34. An, K.; Somorjai, G. A. *ChemCatChem* **2012,** *4,* 1512–1524. doi:10.1002/cctc.201200229
35. Zeng, J.; Zheng, Y.; Rycenga, M.; Tao, J.; Li, Z.-Y.; Zhang, Q.; Zhu, Y.; Xia, Y. *J. Am. Chem. Soc.* **2010,** *132,* 8552–8553. doi:10.1021/ja103655f
36. Rahim, E. H.; Kamounah, F. S.; Frederiksen, J.; Christensen, J. B. *Nano Lett.* **2001,** *1,* 499–501. doi:10.1021/nl015574w
37. Raveendran, P.; Fu, J.; Wallen, S. L. *J. Am. Chem. Soc.* **2003,** *125,* 13940–13941. doi:10.1021/ja029267j
38. Chen, M.; Feng, Y.-G.; Wang, X.; Li, T.-C.; Zhang, J.-Y.; Qian, D.-J. *Langmuir* **2007,** *23,* 5296–5304. doi:10.1021/la700553d
39. Mavani, K.; Shah, M. *Int. J. Eng. Technol.* **2013,** *2* (3), 1–5.
40. Reetz, M. T.; Helbig, W. *J. Am. Chem. Soc.* **1994,** *116,* 7401–7402. doi:10.1021/ja00095a051
41. Henglein, A. *J. Phys. Chem.* **1993,** *97,* 5457–5471. doi:10.1021/j100123a004
42. Fujimoto, T.; Terauchi, S.; Umehara, H.; Kojima, I.; Henderson, W. *Chem. Mater.* **2001,** *13,* 1057–1060. doi:10.1021/cm000910f
43. Ritchie, C. M.; Johnsen, K. R.; Kiser, J. R.; Antoku, Y.; Dickson, R. M.; Petty, J. T. *J. Phys. Chem. C* **2007,** *111,* 175–181. doi:10.1021/jp0648487
44. Kumar, C. M. K.; Yugandhar, P.; Suhrulatha, D.; Savithramma, N. *J. Pharm. Sci. Res.* **2015,** *7,* 76–82.
45. Jeyapriya, M.; Meenarathi, B.; Anbarasan, R. *J. Appl. Polym. Sci.* **2016,** *133,* 43804. doi:10.1002/app.43804
46. Jeong, M. H.; Hong, J. Y.; Park, J. S.; Kim, Y. *Bull. Korean Chem. Soc.* **2016,** *37,* 736–739. doi:10.1002/bkcs.10733
47. Cametti, C.; Fratoddi, I.; Venditti, I.; Russo, M. V. *Langmuir* **2011,** *27,* 7084–7090. doi:10.1021/la2007827
48. Zhang, Y.; Chen, Y.; Westerhoff, P.; Hristovski, K.; Crittenden, J. C. *Water Res.* **2008,** *42,* 2204–2212. doi:10.1016/j.watres.2007.11.036
49. Prathna, T. C.; Chandrasekaran, N.; Raichur, A. M.; Mukherjee, A. *Colloids Surf., B* **2011,** *82,* 152–159. doi:10.1016/j.colsurfb.2010.08.036
50. Fratoddi, I.; Venditti, I.; Battocchio, C.; Polzonetti, G.; Cametti, C.; Russo, M. V. *Nanoscale Res. Lett.* **2011,** *6,* 98–106. doi:10.1186/1556-276X-6-98
51. Lawson, C. L.; Morrison, I. D. *Solving least squares problems. A FORTRAN program and subroutines called NNLS;* Prentice-Hall: Englewood Cliffs, NJ, 1974.
52. Provencher, S. W. *Comput. Phys. Commun.* **1982,** *27,* 213–227. doi:10.1016/0010-4655(82)90173-4
53. D'Amato, R.; Medei, L.; Venditti, I.; Russo, M. V.; Falconieri, M. *Mater. Sci. Eng., C* **2003,** *23,* 861–865. doi:10.1016/j.msec.2003.09.104
54. D'Amato, R.; Venditti, I.; Russo, M. V.; Falconieri, M. *J. Appl. Polym. Sci.* **2006,** *102,* 4493–4499. doi:10.1002/app.24823
55. Venditti, I.; D'Amato, R.; Russo, M. V.; Falconieri, M. *Sens. Actuators, B* **2007,** *126,* 35–40. doi:10.1016/j.snb.2006.10.036

License and Terms

The definitive version of this article is the electronic one which can be found at:
doi:10.3762/bjnano.7.157

BEILSTEIN JOURNAL OF NANOTECHNOLOGY

Functionalized platinum nanoparticles with surface charge trigged by pH: synthesis, characterization and stability studies

Giovanna Testa, Laura Fontana, Iole Venditti and Ilaria Fratoddi*

Full Research Paper

Open Access

Address:
Department of Chemistry, University Sapienza of Rome, p.le Aldo Moro 5, 00185 Rome, Italy

Email:
Ilaria Fratoddi* - ilaria.fratoddi@uniroma1.it

* Corresponding author

Keywords:
functionalized platinum nanoparticles; pH responsive materials; synthesis of metal nanoparticles; thiol functionalization

Beilstein J. Nanotechnol. **2016,** *7,* 1822–1828.
doi:10.3762/bjnano.7.175

Received: 18 July 2016
Accepted: 10 November 2016
Published: 24 November 2016

This article is part of the Thematic Series "Self-assembly of nanostructures and nanomaterials II".

Guest Editor: I. Berbezier

Abstract

In this work, the synthesis and characterization of functionalized platinum nanoparticles (PtNPs) have been investigated. PtNPs were obtained by a wet redox procedure using 2-diethylaminoethanethiol hydrochloride (DEA) as capping agent. By varying the Pt/thiol molar ratio, monodispersed and stable particles with diameters in the range of 3–40 nm were isolated. The amino functionality allows neutral particles to be obtained in basic water solution and positive charged nanoparticles in neutral or acidic water solution (pH 7–2), as confirmed by DLS and ζ-potential measurements. FTIR spectroscopy, FE-SEM, DLS and ζ-potential measurements confirmed the size and showed long term water stability (up to three months) of the colloidal system.

Introduction

Metal nanoparticles (MNPs), in particular, platinum nanoparticles (PtNPs) offer a wide range of chemico-physical properties that can be of interest for many technological applications [1,2]. For example PtNPs are of interest due to their catalytic activity [3,4], electrochemical applications [5], chemical sensing [6-9] and optical features related to surface plasmon resonance (SPR) that occurs in the ultraviolet range of electromagnetic spectrum. It has been observed that the SPR band of PtNPs generally occurs at about 220 nm and exhibits a broad peak [10]. Moreover, the presence of high atomic number atoms makes MNPs likely candidates as innovative radiosensitizers for treatment in radiotherapy [11,12]. The role of the functionalizing layer around MNPs is of primary relevance; in fact, not only solubility but also optical properties and reactivity are strongly dependent on the external layer surrounding the MNPs [13]. The functionalization of MNPs determines their interaction with the external environment and affects their colloidal stability; hydrophobic or hydrophilic thiol-based ligands have been deeply

exploited [14,15]. Among others, 2-diethylaminoethanethiol hydrochloride (DEA) has been used as a stabilizing thiol for gold nanoparticles used for the immobilization of lipase [16].

Among others, hydrothermal and solvothermal techniques are well favored for the synthesis of PtNPs, together with sol–gel methods [17]. They give rise to colloidal suspensions although a fine control of the size, dispersity and the surface functionalization is quite difficult to reach. Poly(*N*-vinyl-2-pyrrolidone) (PVP) has been used as a stabilizer to protect the platinum nanoparticles [18]. However, an efficient separation of the colloid from solution could be difficult to reach [19]. Among the synthetic approaches, wet chemical synthesis offers the opportunity to introduce a selected functionalization onto the NP surface and generally give rise to monodisperse nanoparticles [20,21].

PtNPs are generally obtained from reduction of Pt(II) or Pt(IV) ions, starting from $[PtCl_4]^{2-}$ or $[PtCl_6]^{2-}$ precursors, in the presence of a strong reducing agent, to obtain the chemical reduction to Pt(0) atoms that starts the nucleation process. If a ligand, such as an organic thiol, is present in solution, it gives rise to a passivation layer that hinders the coalescence and precipitation, allowing the colloidal suspension to remain stable [22]. Among reducing agents, hydrazine and sodium borohydride are the most commonly used but also natural-origin reducing agents such as nanocrystalline cellulose from cotton or bacterial cellulose matrixes are currently being studied [23,24].

Thiol ligands have been thoroughly investigated [25-27] and particular attention has been devoted to hydrophilic ligands that confer to the PtNP stability in water suspensions and the potential applications in biotechnology, for example, in the case of mercaptosuccinic acid [28] and ammonium bearing thiols, such as trimethyl(11-mercaptoundecyl)ammonium [29]. Pt nanoparticles stabilized with 11-mercaptoundecanoic acid were developed for the detection of volatile organic compounds (VOCs) [30].

In this study, the synthesis and characterization of functionalized platinum nanoparticles has been investigated. PtNPs were obtained by a wet redox procedure, using 2-diethylaminoethanethiol hydrochloride (DEA) as a capping agent. By varying the Pt/thiol molar ratio, stable, monodisperse nanoparticles with diameters in the range of 3–40 nm were isolated. The amino functionality allows acid–base equilibria [31], and with this system, it is possible to obtain neutral particles in basic water solution and positive charged nanoparticles in acidic water solution.

Results and Discussion

PtNP synthesis and characterization

The procedure used for the synthesis of PtNPs stabilized with DEA is reported herein. It was based on a wet reduction with water as a solvent [32] at room temperature. The formation process of thiol-protected Pt nanoparticles (Pt-DEA) synthesized in water solution is herein presented as a representative example, and the reaction scheme is reported in Scheme 1. Different Pt/DEA molar ratios have been used and the reduction products were analyzed in order to study the effect of this parameter on the nanoparticle diameter.

The Pt(II) starting complex solution is pale yellow before mixing and shows a peak at 220 nm in the UV–vis spectrum

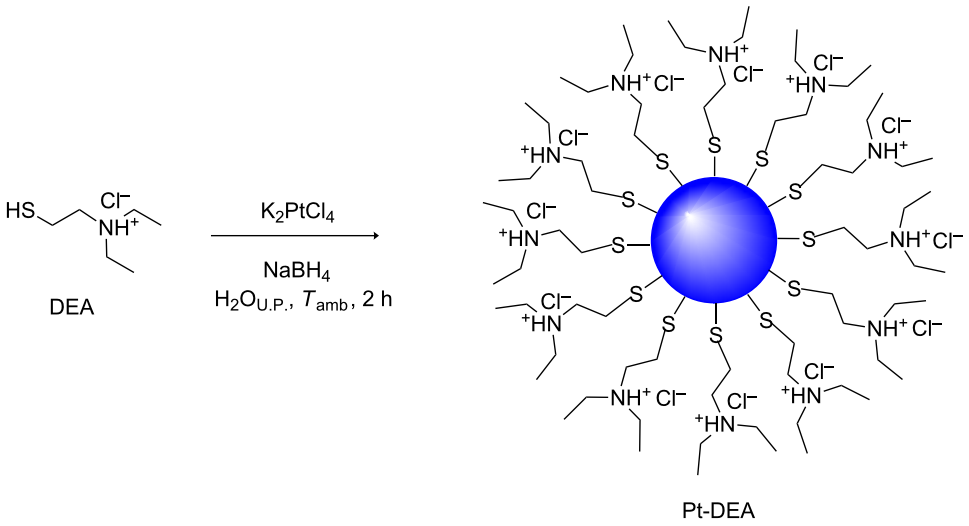

Scheme 1: Reaction scheme for Pt-DEA nanoparticles.

due to the ligand-to-metal charge-transfer transition of the $[PtCl_4]^{2-}$ ions [33]. This is shown in Figure 1 together with the absorption features of DEA thiol.

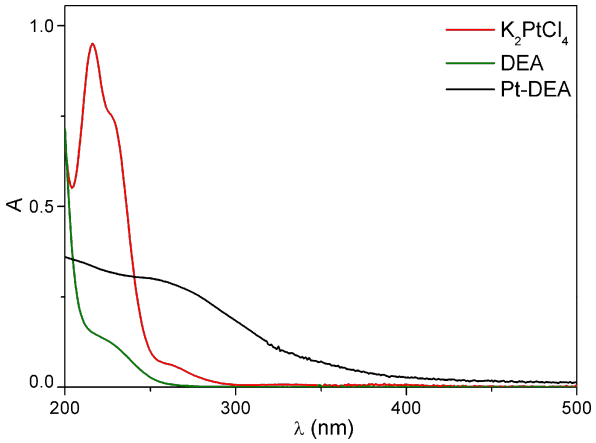

Figure 1: 1 UV–vis spectra in H_2O of: K_2PtCl_4 (red); DEA (green); Pt-DEA (black).

As the $NaBH_4$ reducing agent is added, the peak at 220 nm decreases and disappears within 30 min, indicating that the $[PtCl_4]^{2-}$ ions are completely reduced in 30 min according to Equation 1.

$$2NaBH_4 + K_2PtCl_4 + 3H_2O \longrightarrow Pt(0) + 2BO_3^{3-} + 7H_2 + 2Na^+ + 2K^+ + 4Cl^- \quad (1)$$

The color of the solution rapidly turns from yellow into dark brown, and the absorption of the mixture in the visible region increases, until a broad tailing peak appears at about 264 nm (see Figure 1), suggesting that the band structure of the Pt nanoparticles is formed [34].

After careful purification by centrifugation, the colloidal product was characterized by DLS, UV–vis spectroscopy, FTIR, and ζ-potential measurements. A FESEM study was carried out on selected samples.

In Figure 2, the trend of the DLS hydrodynamic diameter $<2R_H>$ as a function of the Pt/DEA molar ratio used during the synthesis is reported, where a fixed Pt/$NaBH_4$ molar ratio of 1:5 was maintained. It can be observed that a general decrease of the DLS-measured diameter is observed, from 40 ± 4 nm to 11 ± 2 nm ranging from 1:1 to 1:0.25 Pt/DEA molar ratio. The influence of the metal/ligand molar ratio has been thoroughly investigated in the literature for Au and Ag NPs [35] and is herein reported for the first time for Pt in the presence of the DEA ligand. Here, a complex effect can be envisaged, deriving from the presence of the thiol functionality and the ammonium end group [36] that undergoes to acidic–base equilibrium in aqueous solution.

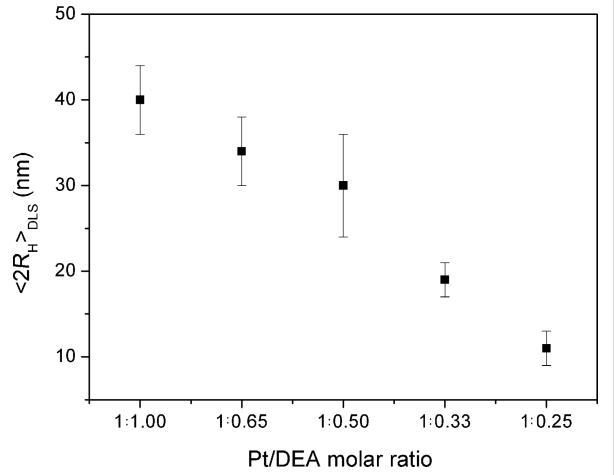

Figure 2: 2 Influence of Pt/DEA molar ratio: DLS results in water.

The role of the reducing agent has been studied and the effect of the widely used $NaBH_4$ has been compared with ammonium formiate ($HCOONH_4$) [37,38]. With this aim, maintaining the Pt/DEA ratio fixed at 1:0.5, the molar ratio between metal and reducing agent has been varied as follows: Pt/$NaBH_4$ 1:5, 1:10, 1:20, 1:30, 1:40 and the results were compared with the effect of $HCOONH_4$. From results reported in Figure 3, it can be observed that a similar behavior has been obtained for the used reducing systems, and as a general trend, the DLS-measured diameter increases, increasing the amount of reducing agents.

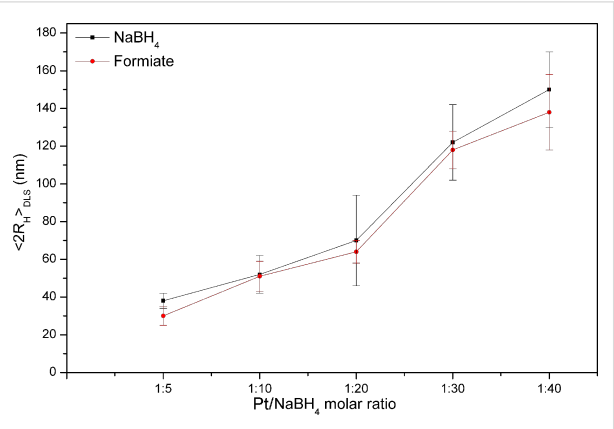

Figure 3: 3 Influence of Pt/reducing agent molar ration in the formation of Pt-DEA nanoparticles: DLS results in water.

The ζ-potential of Pt-DEA has been studied and values denoting a stable colloidal suspension of nanoparticles was found (±30 mV, indicating a stable colloid [39]). As observed in the

literature, the role of the stable negative counter-ion is underlined from the negative values observed [40]. Measurements carried out up to three months confirmed the long-term stability of the colloidal suspension for all the samples.

The FTIR spectrum of Pt-DEA nanoparticles (Pt/DEA 1:1) is reported in Figure 4, where the intense peaks at 2927 and 2854 cm^{-1} can be attributed to the symmetric and antisymmetric stretching of $–CH_2$ and $–CH_3$ groups of the DEA ligand, and the peak at 3346 cm^{-1} arises from the ammonium group of DEA. The absence of the S–H stretching mode of free thiol at about 2500 cm^{-1} can be due to the absence of free unreacted thiols. In the far infrared spectrum, as reported in Figure 5, the presence of the Pt–S stretching bands at about 330 cm^{-1} confirms the functionalization on the Pt surface with DEA thiol [41,42].

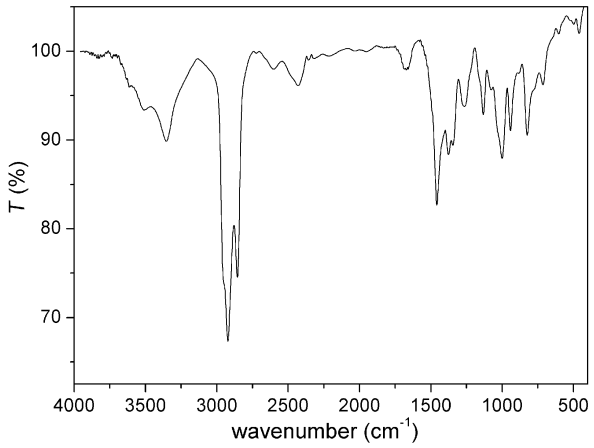

Figure 4: FTIR spectrum of Pt-DEA (Pt/DEA 1:1) nanoparticles (film).

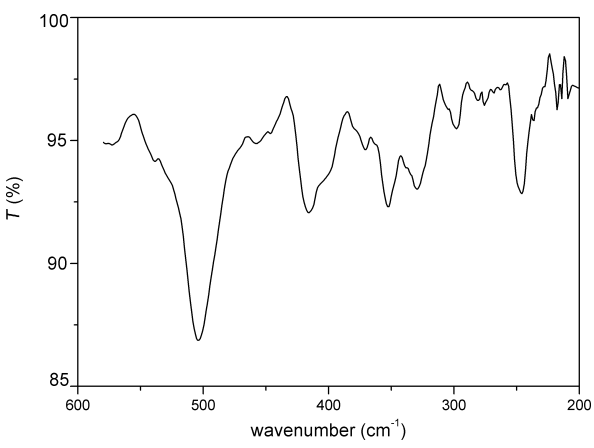

Figure 5: Far-IR spectrum of Pt-DEA (Pt/DEA 1:1) nanoparticles (Nujol).

FESEM images of Pt-DEA nanoparticles (reported in Figure 6 for different regions of the Pt/DEA 1:0.25 sample) evidenced the presence of small and uniform PtNPs, with diameter ≈5 nm, having a smaller diameter with respect to the DLS data, as already observed for similar compounds [43]. In fact, the hydrodynamic diameters given by DLS are usually larger than the number average diameter of the particles, and DLS overestimates the average particle sizes [44]. While FESEM is a solid state technique, in this case carried out on dried samples, DLS results take into account the dynamic equilibrium in a solution of nanoparticles [45].

Role of pH on aggregation

The role of pH on aggregation phenomena has been investigated for Pt-DEA nanoparticles with a Pt/DEA 1:0.33 molar ratio. In particular, at pH 7, the nanoparticles are more aggregated (18 ± 2 nm) than pH 2 (3 ± 1 nm). A chemical sketch of the aggregation phenomenon together with the DLS data are reported in Figure 7. The role of the ammonium end group could be a critical attributor to this behavior. In fact, at low pH values, the end group becomes positively charged and tends to disaggregate vicinal nanoparticles, whereas at higher pH values, the amine group becomes predominant in the acidic–base equilibrium and aggregation occurs.

Conclusion

In this work stable, monodisperse PtNPs with small diameter have been obtained. Among the various Pt/DEA molar ratios, the 1:0.25 sample was studied in detail. The FTIR and far IR measurements confirmed the formation of the Pt–S bond on the PtNP surface. The DLS characterization demonstrated the long-term stability of the colloidal system up to three months and the possibility to tune the aggregation phenomenon of the PtNPs by varying the pH due to modulation of the metal surface charge.

Experimental

Instrumentation

UV–vis spectroscopy was performed in H_2O solutions using quartz cells with a Varian Cary 100 Scan UV–vis spectrophotometer. The diameter and the diameter distribution of MNPs in H_2O solution were investigated at 25 ± 0.2 °C (pH 7 and pH 2) by means of dynamic light scattering (DLS) technique by using a Malvern Nano ZS90 scattering apparatus (Malvern Instruments Ltd., Worcestershire, UK). The correlation functions were collected at $\vartheta = 90°$ relative to the incident beam, and delay times from 0.8 μs to 10 s were explored [46,47]. Non-negative least-squares (NNLSs) [48] or CONTIN [49] algorithms, supplied with the instrument software, were used to fit correlation data. The ζ-potential was calculated from the measured electrophoretic mobility by means of the Smolukovsky equation [50]. FTIR and far IR spectra were re-

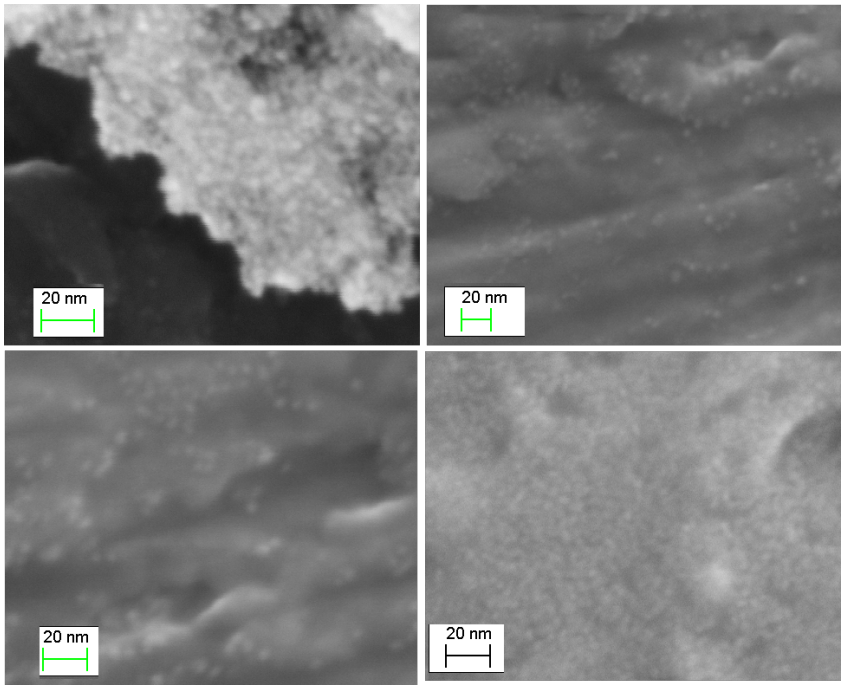

Figure 6: FESEM images of Pt-DEA nanoparticles (Pt/DEA 1:0.25).

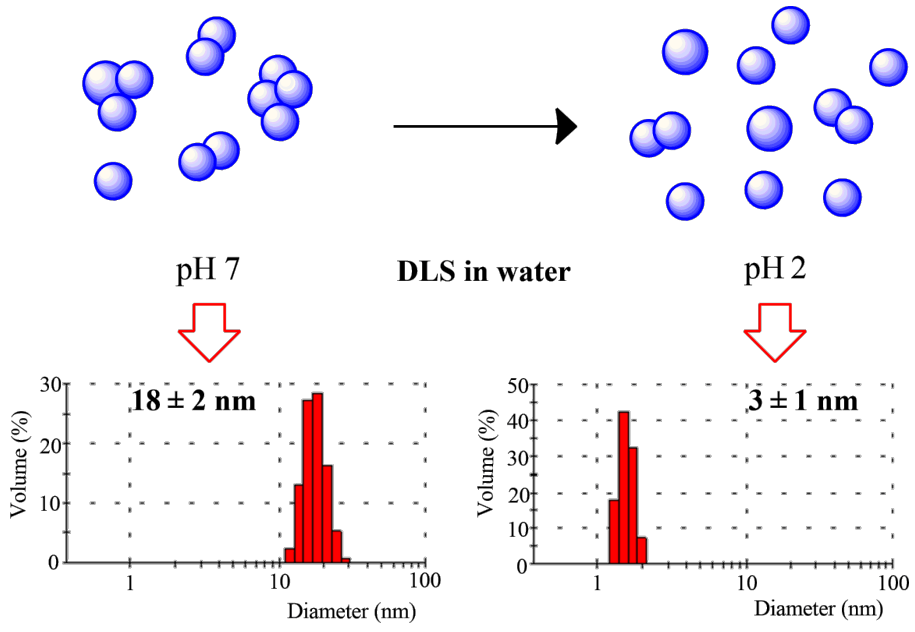

Figure 7: Sketch of the aggregation phenomenon together with DLS data of Pt-DEA nanoparticles (Pt/DEA 1:0.33) at different pH.

corded on cast-deposited films from Nujol using KRS-5 cells with a Bruker Vertex 70 spectrophotometer. Field emission scanning electron microscopy (FE-SEM) images and energy dispersion spectroscopy (EDS) were acquired with the Auriga Zeiss instrument (resolution 1 nm, applied voltage 6–12 kV) on freshly prepared films drop-cast from H_2O solution on a metallic sample holder. A MiniSpin (Eppendorf) centrifuge was used for purification of PtNP samples (13000 rpm, 20 min, 15 times with deionized water). Deionized water was obtained from Zeener Power I Scholar-UV (18.2 MΩ).

Materials

Potassium tetrachloroplatinate (K_2PtCl_4 98.5%, Sigma-Aldrich), 2-diethylaminoethanethiol hydrochloride ($HS(CH_2)_2N(CH_2CH_3)_2$·HCl, 98% Sigma-Aldrich, DEA), sodium borohydride ($NaBH_4$, 99% Sigma-Aldrich) were used as received.

PtNPs were prepared at room temperature in a single-phase system by modifying previous literature reports [51]. In particular, PtNPs-DEA were prepared with Pt/DEA molar ratios ranging from 1:1 to 1:0.25. In a typical procedure, 0.200 g of K_2PtCl_4 (4.8×10^{-4} mol) were dissolved in 10 mL of deionized water at pH 2 and mixed with a solution of DEA in deionized water (0.0815 g, 4.8×10^{-4} mol in 10 mL for the 1:1 Pt/DEA molar ratio). After stirring the mixture under argon for 10 min at room temperature, a $NaBH_4$ solution in deionized water (0.177 g, 4.8×10^{-3} mol in 10 mL) was added dropwise. The reaction mixture was allowed to react for 20 h and the obtained suspension was centrifuged with deionized water ten times (10 min, 15000 rpm), recovering the black solid from the supernatant (48 wt % yield).

The following are the experimental data for the various PtNPs-DEA samples:

- PtNPs-DEA 1 (Pt/DEA 1:1): DLS ($2R_H$ [nm], H_2O): 40 ± 4; IR (ν [cm^{-1}], Nujol): 3346, 1006, 948 (Et_3N^*–H), 325, 350 (Pt–S); ζ-potential ([mV], H_2O): −27.
- PtNPs-DEA 2 (Pt/DEA 1:0.65): DLS ($2R_H$ [nm], H_2O): 34 ± 4; IR (ν [cm^{-1}], Nujol): 3345, 1008, 950, 323, 350 (Pt–S); ζ-potential ([mV], H_2O): −25.
- PtNPs-DEA 3 (Pt/DEA 1:0.5): DLS ($2R_H$ [nm], H_2O): 30 ± 6; IR (ν [cm^{-1}], Nujol): 3342, 1006, 950; ζ-potential ([mV], H_2O): −27.
- PtNPs-DEA 4 (Pt/DEA 1:0.33): DLS ($2R_H$ [nm], H_2O): 18 ± 2; IR (ν [cm^{-1}], Nujol): 3344, 1008, 948; ζ-potential ([mV], H_2O): −25.
- PtNPs-DEA 5 (Pt/DEA 1:0.25): DLS ($2R_H$ [nm], H_2O): 11 ± 2; IR (ν [cm^{-1}], Nujol): 3342, 1007, 948; ζ-potential ([mV], H_2O): −27.

Acknowledgements

This work was funded by Ateneo Sapienza 2015/C26A15H5J9 and Ateneo Sapienza 2015/C26A15LRMA projects.

References

1. Stepanov, A. L.; Golubev, A. N.; Nikitin, S. I.; Osin, Y. N. *Rev. Adv. Mater. Sci.* **2014,** *38,* 160–175.
2. Venditti, I.; Fratoddi, I.; Russo, M. V.; Bearzotti, A. *Nanotechnology* **2013,** *24,* 155503. doi:10.1088/0957-4484/24/15/155503
3. Tang, Z.; Geng, D.; Lu, G. *Mater. Lett.* **2005,** *59,* 1567–1570. doi:10.1016/j.matlet.2005.01.024
4. Tan, T. L.; Wang, L.-L.; Zhang, J.; Johnson, D. D.; Bai, K. *ACS Catal.* **2015,** *5,* 2376–2383. doi:10.1021/cs501840c
5. Escobar Morales, B.; Gamboa, S. A.; Pal, U.; Guardián, R.; Acosta, D.; Magaña, C.; Mathew, X. *Int. J. Hydrogen Energy* **2010,** *35,* 4215–4221. doi:10.1016/j.ijhydene.2010.01.040
6. Fratoddi, I.; Macagnano, A.; Battocchio, C.; Zampetti, E.; Venditti, I.; Russo, M. V.; Bearzotti, A. *Nanoscale* **2014,** *6,* 9177–9184. doi:10.1039/C4NR01400F
7. Fratoddi, I.; Altamura, P.; Bearzotti, A.; Furlani, A.; Russo, M. V. *Thin Solid Films* **2004,** *458,* 292–298. doi:10.1016/j.tsf.2003.12.065
8. Zhang, Y.; Xu, J.; Xu, P.; Zhu, Y.; Chen, X.; Yu, W. *Nanotechnology* **2010,** *21,* 285501. doi:10.1088/0957-4484/21/28/285501
9. Verma, M. K.; Gupta, V. *Sens. Lett.* **2012,** *10,* 775–782.
10. Creighton, J. A.; Eadon, D. G. *J. Chem. Soc., Faraday Trans.* **1991,** *87,* 3881–3891. doi:10.1039/FT9918703881
11. Jain, S.; Hirst, D. G.; O'Sullivan, J. M. *Br. J. Radiol.* **2012,** *85,* 101–113. doi:10.1259/bjr/59448833
12. Porcaro, F.; Battocchio, C.; Antoccia, A.; Fratoddi, I.; Venditti, I.; Fracassi, A.; Luisetto, I.; Russo, M. V.; Polzonetti, G. *Colloids Surf., B* **2016,** *142,* 408–416. doi:10.1016/j.colsurfb.2016.03.016
13. Fontana, L.; Fratoddi, I.; Venditti, I.; Ksenzov, D.; Russo, M. V.; Grigorian, S. *Appl. Surf. Sci.* **2016,** *369,* 115–119. doi:10.1016/j.apsusc.2016.02.029
14. Venditti, I.; Fontana, L.; Fratoddi, I.; Battocchio, C.; Cametti, C.; Sennato, S.; Mura, F.; Sciubba, F.; Delfini, M.; Russo, M. V. *J. Colloid Interface Sci.* **2014,** *418,* 52–60. doi:10.1016/j.jcis.2013.11.063
15. Quintiliani, M.; Bassetti, M.; Pasquini, C.; Battocchio, C.; Rossi, M.; Mura, F.; Matassa, R.; Fontana, L.; Russo, M. V.; Fratoddi, I. *J. Mater. Chem. C* **2014,** *2,* 2517–2527. doi:10.1039/c3tc32567a
16. Venditti, I.; Palocci, C.; Chronopoulou, L.; Fratoddi, I.; Fontana, L.; Diociaiuti, M.; Russo, M. V. *Colloids Surf., B* **2015,** *131,* 93–101. doi:10.1016/j.colsurfb.2015.04.046
17. Chen, A.; Holt-Hindle, P. *Chem. Rev.* **2010,** *110,* 3767–3804. doi:10.1021/cr9003902
18. Bonet, F.; Tekaia-Elhsissen, K.; Sarathy, K. V. *Bull. Mater. Sci.* **2000,** *23,* 165–168. doi:10.1007/BF02719903
19. Wang, X.; Liang, M.; Zhang, J.; Wang, Y. *Curr. Org. Chem.* **2007,** *11,* 299–314. doi:10.2174/138527207779940856
20. Castro, E. G.; Salvatierra, R. V.; Schreiner, W. H.; Oliveira, M. M.; Zarbin, A. J. G. *Chem. Mater.* **2010,** *22,* 360–370. doi:10.1021/cm902748k
21. Brust, M.; Walker, M.; Bethell, D.; Schiffrin, D. J.; Whyman, R. *J. Chem. Soc., Chem. Commun.* **1994,** 801–802. doi:10.1039/C39940000801
22. Yee, C.; Scotti, M.; Ulman, A.; White, H.; Rafailovich, M.; Sokolov, J. *Langmuir* **1999,** *15,* 4314–4316. doi:10.1021/la9814283
23. Benaissi, K.; Johnson, L.; Walsh, D. A.; Thielemans, W. *Green Chem.* **2010,** *12,* 220–222. doi:10.1039/B913218J
24. Aritonang, H. F.; Onggo, D.; Ciptati, C.; Radiman, C. L. *J. Nanopart.* **2014,** 285954. doi:10.1155/2014/285954
25. Bakhmutsky, K.; Wieder, N. L.; Cargnello, M.; Galloway, B.; Fornasiero, P.; Gorte, R. J. *ChemSusChem* **2012,** *5,* 140–148. doi:10.1002/cssc.201100491
26. Dablemont, C.; Lang, P.; Mangeney, C.; Piquemal, J.-Y.; Petkov, V.; Herbst, F.; Viau, G. *Langmuir* **2008,** *24,* 5832–5841. doi:10.1021/la7028643

27. Vitaliano, R.; Fratoddi, I.; Venditti, I.; Roviello, G.; Battocchio, C.; Polzonetti, G.; Russo, M. V. *J. Phys. Chem. A* **2009,** *113,* 14730–14740. doi:10.1021/jp904865k
28. Chen, S.; Kimura, K. *J. Phys. Chem. B* **2001,** *105,* 5397–5403. doi:10.1021/jp0037798
29. Eklund, S. E.; Cliffel, D. E. *Langmuir* **2004,** *20,* 6012–6018. doi:10.1021/la049787n
30. Hosseini, M. R. M.; Jamalabadi, H.; Najafi, M. *Meas.* **2013,** *46,* 3328–3332. doi:10.1016/j.measurement.2013.04.070
31. Stewart, A.; Murray, S.; Bell, S. E. J. *Analyst* **2015,** *140,* 2988–2994. doi:10.1039/c4an02305f
32. Vitale, F.; Mirenghi, L.; Piscopiello, E.; Pellegrini, G.; Trave, E.; Mattei, G.; Fratoddi, I.; Russo, M. V.; Tapfer, L.; Mazzoldi, P. *Mat. Sci. Eng. C* **2007,** *27,* 1300–1304. doi:10.1016/j.msec.2006.06.041
33. Battocchio, C.; Fratoddi, I.; Russo, M. V.; Polzonetti, G. *Chem. Phys. Lett.* **2004,** *400,* 290–295. doi:10.1016/j.cplett.2004.10.126
34. Gharibshahi, E.; Saion, E. *Int. J. Mol. Sci.* **2012,** *13,* 14723–14741. doi:10.3390/ijms131114723
35. Zabetakis, K.; Ghann, W. E.; Kumar, S.; Daniel, M.-C. *Gold Bull.* **2012,** *45,* 203–211. doi:10.1007/s13404-012-0069-2
36. Venditti, I.; Hassanein, T. F.; Fratoddi, i.; Fontana, L.; Battocchio, C.; Rinaldi, F.; Carafa, I.; Marianecci, C.; Diociaiuti, M.; Agostinelli, E.; Cametti, C.; Russo, M. V. *Colloids Surf., B* **2015,** *134,* 314–321. doi:10.1016/j.colsurfb.2015.06.052
37. Mason, C. W.; Kannan, A. M. *ISRN Nanotechnol.* **2011,** 708045. doi:10.5402/2011/708045
38. Mehta, S. K.; Kumar, S.; Gradzielski, M. *J. Colloid Interface Sci.* **2011,** *360,* 497–507. doi:10.1016/j.jcis.2011.04.079
39. Uskoković, V. *Rev. J. Chem.* **2013,** *3,* 271–303. doi:10.1134/S2079978013040031
40. Guo, J. J.; Lewis, J. A. *J. Am. Ceram. Soc.* **2000,** *83,* 266–272. doi:10.1111/j.1151-2916.2000.tb01183.x
41. Risberg, E. D.; Mink, J.; Abbasi, A.; Skripkin, M. Yu.; Hajba, L.; Lindqvist-Reis, P.; Bencze, É.; Sandström, M. *Dalton Trans.* **2009,** 1328–1338. doi:10.1039/b814252a
42. Kennedy, B. P.; Lever, A. B. P. *Can. J. Chem.* **1972,** *50,* 3488–3507. doi:10.1139/v72-563
43. Bessar, H.; Venditti, I.; Benassi, L.; Vaschieri, C.; Azzoni, P.; Pellacani, G.; Magnoni, C.; Botti, E.; Casagrande, V.; Federici, M.; Costanzo, A.; Fontana, L.; Testa, G.; Mostafa, F. F.; Ibrahim, S. A.; Russo, M. V.; Fratoddi, I. *Colloids Surf., B* **2016,** *141,* 141–147. doi:10.1016/j.colsurfb.2016.01.021
44. Domingos, R. F.; Baalousha, M. A.; Ju-Nam, Y.; Reid, M. M.; Tufenkji, N.; Lead, J. R.; Leppard, G. G.; Wilkinson, K. J. *Environ. Sci. Technol.* **2009,** *43,* 7277–7284. doi:10.1021/es900249m
45. Fissan, H.; Ristig, S.; Kaminski, H.; Asbach, C.; Epple, M. *Anal. Methods* **2014,** *6,* 7324–7334. doi:10.1039/C4AY01203H
46. Cametti, C.; Fratoddi, I.; Venditti, I.; Russo, M. V. *Langmuir* **2011,** *27,* 7084–7090. doi:10.1021/la2007827
47. Venditti, I.; Fratoddi, I.; Battocchio, C.; Polzonetti, G.; Cametti, C.; Russo, M. V. *Polym. Int.* **2011,** *60,* 1222–1229. doi:10.1002/pi.3066
48. Lawson, C. L.; Morrison, I. D. *Solving least squares problems. A FORTRAN program and subroutines called NNLS;* Prentice-Hall: Englewood Cliffs, NJ, 1974; pp 48 ff.
49. Provencher, S. W. *Comput. Phys. Commun.* **1982,** *27,* 213–227. doi:10.1016/0010-4655(82)90173-4
50. Venditti, I.; Fratoddi, I.; Palazzesi, C.; Prosposito, P.; Casalboni, M.; Cametti, C.; Battocchio, C.; Polzonetti, G.; Russo, M. V. *J. Colloid Interface Sci.* **2010,** *348,* 424–430. doi:10.1016/j.jcis.2010.04.061
51. Fratoddi, I.; Venditti, I.; Battocchio, C.; Polzonetti, G.; Cametti, C.; Russo, M. V. *Nanoscale Res. Lett.* **2011,** *6,* 98. doi:10.1186/1556-276X-6-98

License and Terms

BEILSTEIN JOURNAL OF NANOTECHNOLOGY

Cubic chemically ordered FeRh and FeCo nanomagnets prepared by mass-selected low-energy cluster-beam deposition: a comparative study

Veronique Dupuis[*1], Anthony Robert[1], Arnaud Hillion[2], Ghassan Khadra[3], Nils Blanc[4,5], Damien Le Roy[1], Florent Tournus[1], Clement Albin[1], Olivier Boisron[1] and Alexandre Tamion[1]

Full Research Paper

Open Access

Address:
[1]Institut Lumière Matière, UMR5306 Université Lyon 1-CNRS, Université de Lyon F-69622 Villeurbanne cedex, France, [2]Institut Jean Lamour, UMR7198, Université H. Poincarré-CNRS, F-5406 Vandoeuvre les Nancy, France, [3]Interfaces, Confinement, Matériaux et Nanostructures, UMR7374 Université d'Orléans-CNRS, F-45071 Orléans cedex, France, [4]Université Grenoble Alpes, Inst NEEL, F-38000 Grenoble, France and [5]CNRS, Inst NEEL, F-38000 Grenoble, France

Email:
Veronique Dupuis[*] - Veronique.Dupuis@univ-lyon1.fr

* Corresponding author

Keywords:
bimetallic nanoparticles; magnetic moment and anisotropy; metamagnetic transition

Beilstein J. Nanotechnol. **2016,** *7,* 1850–1860.
doi:10.3762/bjnano.7.177

Received: 28 July 2016
Accepted: 10 November 2016
Published: 28 November 2016

This article is part of the Thematic Series "Self-assembly of nanostructures and nanomaterials II".

Guest Editor: I. Berbezier

Abstract

Near the point of equiatomic composition, both FeRh and FeCo bulk alloys exhibit a CsCl-type (B2) chemically ordered phase that is related to specific magnetic properties, namely a metamagnetic anti-ferromagnetic/ferromagnetic transition near room temperature for FeRh and a huge magnetic moment for the FeCo soft alloy. In this paper, we present the magnetic and structural properties of nanoparticles of less than 5 nm diameter embedded in an inert carbon matrix prepared by mass-selected low-energy cluster-beam deposition technique. We obtained a CsCl-type (B2) chemically ordered phase for annealed nanoalloys. Using different experimental measurements, we show how decreasing the size affects the magnetic properties. FeRh nanoparticles keep the ferromagnetic order at low temperature due to surface relaxation affecting the cell parameter. In the case of FeCo clusters, the environment drastically affects the intrinsic properties of this system by reducing the magnetization in comparison to the bulk.

Introduction

Magnetic bimetallic nanoparticles (NPs) are very attractive systems not only from a fundamental point of view but also because of their various areas of use [1,2]. In particular, the binary phase diagrams of bulk materials of iron and transition metals show a wide range of different properties, in particular magnetic properties [3].

Interestingly, near the point of equiatomic composition, both FeRh and FeCo bulk alloys present a CsCl-type (B2) chemically ordered phase at room temperature (Figure 1) with the competition between several magnetic orderings for FeRh and a huge magnetic moment for soft FeCo according to the Slater–Pauling graph.

It is interesting to examine the chemical and magnetic ordering at the nanoscale in both FeRh and FeCo alloys for their potential applications in heat-assisted magnetic recording and spintronics [5,6]. Several routes have been developed to produce such bimetallic nanoparticles during which annealing is generally necessary to give the nanoalloy enough energy to reach its thermodynamic equilibrium [1]. Considering chemical syntheses, Jia et al. [7] have shown that the coalescence of initially 4–5 nm FeRh NPs to structures of 20 nm in diameter after annealing is necessary to observe AF–FM transition in chemically ordered NPs. Recently, a strong correlation between morphology and magnetism has also been predicted from theoretical density functional theory calculations in agreement with experiments on FeRh nanoparticles prepared by co-sputtering [8]. In addition, for FeCo nanoparticles generated in the gas phase by means of an arc cluster ion source, a wide distribution of magnetic energy barriers has been obtained in a mass-filtered ensemble of particles with a mean diameter of 12 nm and size distribution lower than 15% [9].

In this paper, we present a comparative study performed on FeRh and FeCo nanocrystal assemblies prepared by mass-selected low-energy cluster-beam deposition (MS-LECBD) embedded in a carbon matrix. Notice that most of this work is based on the results of the PhD theses of A. Hillion [10] and G. Khadra [11] at Lyon, France. The structural and magnetic properties of as-prepared and annealed nanoalloys were investigated using various experimental techniques [4]. Here, we focus on anomalous X-rays diffraction (AXD) and X-ray magnetic circular dichroism (XMCD) performed by using well-adapted synchrotron radiation beamlines. We show how the competition between the stable bimetallic NPs structure and their chemical affinity with the environment affects their intrinsic magnetic properties compared to their bulk counterparts.

Results

Synthesis and structure

The clusters are synthetized in the gas phase in the low-energy cluster-beam deposition (LECBD) regime. Briefly, a pulsed laser beam is focused on a mixed equiatomic target while a continuous flow of helium allows the formation of the cluster beam. After isentropic expansion in vacuum, ionized species can be size-selected thanks to a quadupolar electrostatic deviator [4].Then, the mass-selected clusters are simultaneously co-deposited in an ultra-high vacuum (UHV) deposition chamber, with an independent atomic carbon beam. Notice that the strong asset of this experimental technique is the possibility to prepare nearly identical clusters in any matrix, with the possibility to vary the volume concentration of the magnetic phase.

According to the Wulff construction [12], we have been able to systematically show that our clusters are nanocrystallized and well-faceted (Figure 2).

In order to avoid magnetic interactions among the NPs, the samples are prepared with a cluster concentration of less than 1 vol %. Notice that the amorphous carbon matrix is chosen to protect the sample from oxidation but also to allow vacuum high-temperature annealing and so to reach the equilibrium phase without coalescence of the NPs.

To characterise the structure of the clusters by transmission electron microscopy (TEM), we prepared discontinuous thin

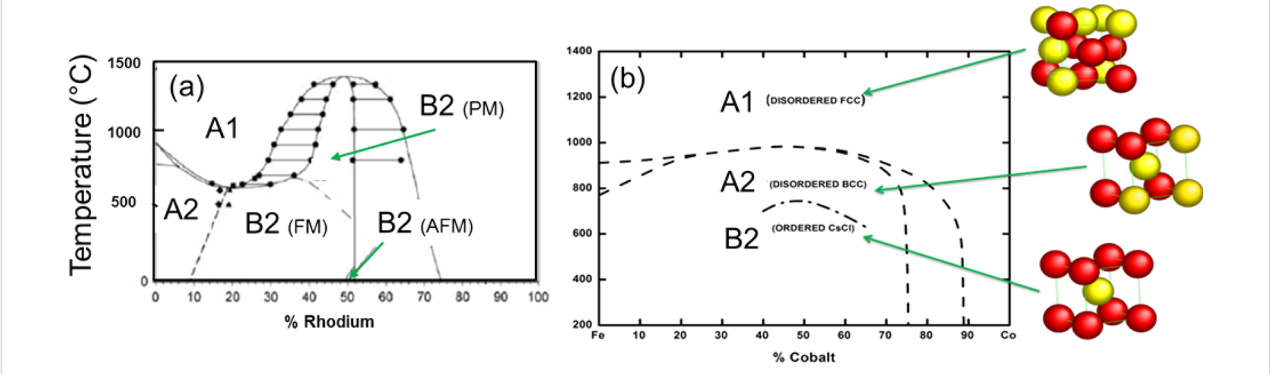

Figure 1: (a) Bulk magnetic FeRh phase diagram. Notice that metamagnetic transitions in bulk B2 FeRh are expected from the anti-ferromagnetic (AFM) to the ferromagnetic (FM) state at 96 °C and to the paramagnetic (PM) state at 380 °C. (b) Bulk FeCo phase diagram showing the different chemical and crystallographic orders for equiatomic concentration (adapted from [4]).

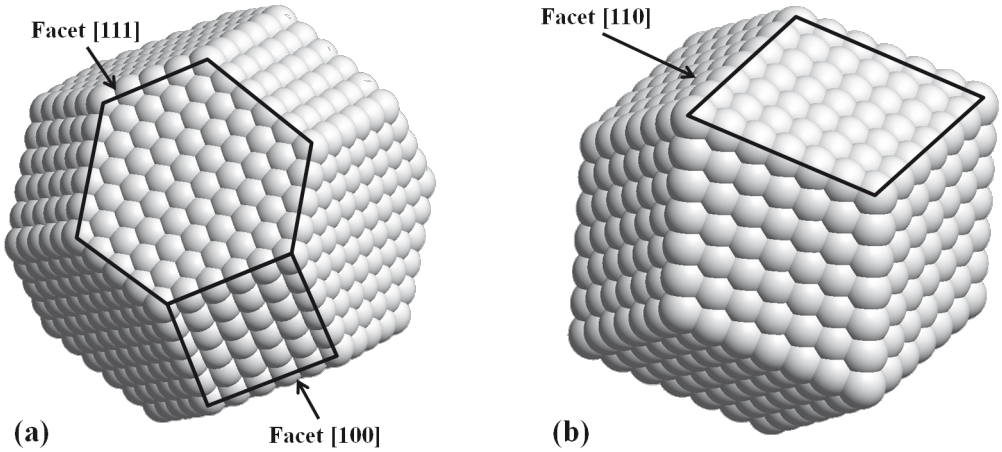

Figure 2: Stable shape for a face-centred cubic (fcc) truncated octahedron (a) and a body-centred cubic (bcc) rhombic dodecahedron (b) [11].

layers of NPs deposited on an carbon-coated grid and then capped it with a thin carbon film. We obtained nanoparticles with selected diameters from 2 to 5 nm, a Gaussian size distribution and a relative dispersion of around 0.15 (Figure 3).

In addition, several nanoparticles were analyzed using EDX (energy dispersive X-ray analysis) as shown in Figure 3c. In all cases, the EDX analysis showed no sign of oxidation of the nanoparticles and a roughly equiatomic composition

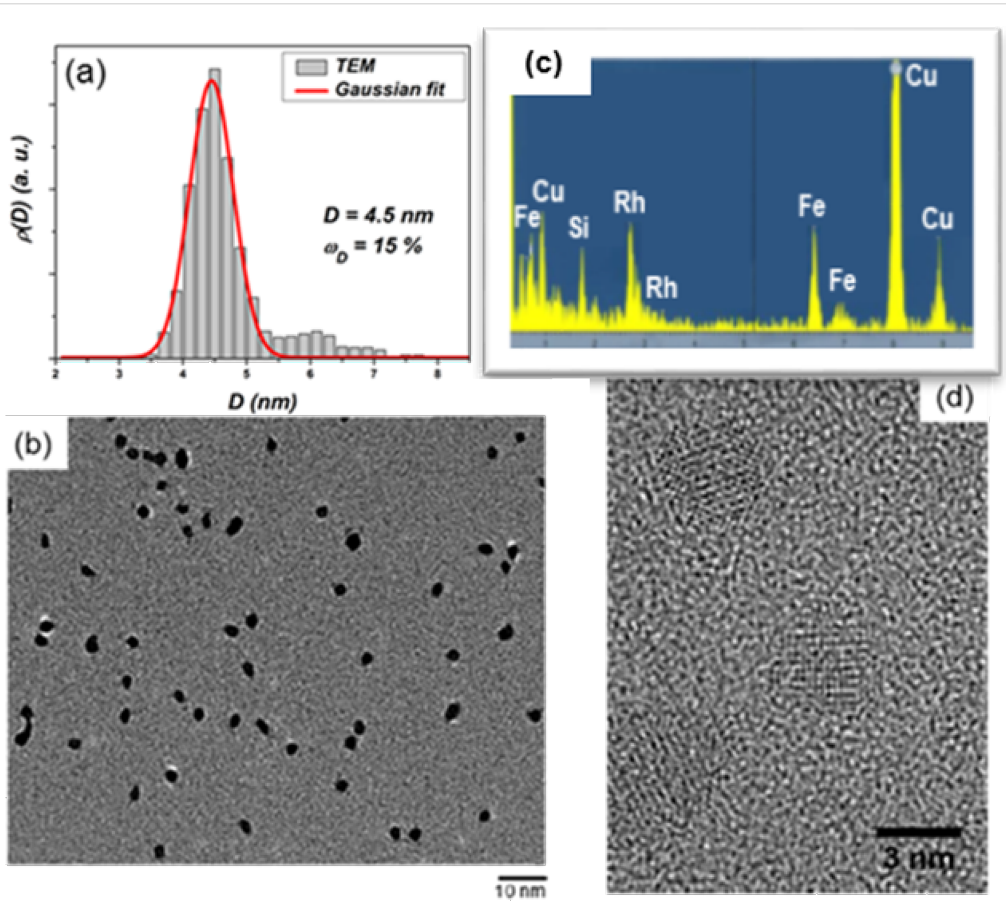

Figure 3: Size histogram (a), TEM observations (b) and corresponding EDX analysis (c) of annealed mass-selected FeRh nanoparticles with an average diameter of 4.5 nm. HRTEM images for annealed FeRh nanoparticles with 2 nm in diameter (d).

for both FeRh and FeCo cluster samples conserved after 2 h annealing at 500 °C under ultra-high vacuum (UHV) conditions [10,11].

High-resolution TEM (HRTEM) observations on as-prepared FeRh samples revealed a clear fcc (A1) structure with no sign of chemical ordering (Figure 4a). In the Figure 3d and Figure 4b, chemically ordered CsCl-type (B2) nanomagnets have been clearly evidenced on annealed FeRh NPs as small as 2 nm in diameter.

Even though the CsCl (B2) structure is the equilibrium bulk structure for equimolar FeCo alloys, it was not possible to distinguish a chemical ordering by HRTEM for annealed NPs because the electron density contrast between iron and cobalt is too low.

Generally, conventional diffraction measurements are used to determine the degree of chemical ordering in the B2 phase for equiatomic AB alloys. The B2 structure can be seen as the imbrication of two simple cubic sub-lattices, each occupied by either A or B atoms (with A = Fe and B = Rh/Co for FeRh/FeCo). Indeed, the structure factor is expected to present two maxima at $f_A + f_B$ (main reflection, with even $h + k + l$ value for the sum of Miller indices, as in bcc structures) and at $f_A - f_B$ (secondary or superlattice reflection, only for B2 structures with odd $h + k + l$ values related to the atomic number difference ΔZ_{AB} for X-rays and electrons). The supplementary reflections (100) and (012) are clearly visible on the FFT of Figure 4b for annealed FeRh ($\Delta Z_{FeRh} = 19$). While in the case of FeCo alloy, the secondary minima are negligible due to the small value of the atomic contrast ($\Delta Z_{FeCo} = 1$). Because the nuclear scattering factors for iron and cobalt differ considerably, neutron diffraction is generally preferred over X-ray diffraction to determine the degree of long-range order in FeCo alloy [14]. However, neutron diffraction is not applicable for the low quantities of matter in our samples.

Moreover, at finite size we also have to take into account the shape factor that enlarges the Bragg–Dirac peak distribution expected only for infinite crystals. So for both systems, a the CsCl-type (B2) structure was assumed for the simulations by using the Debye formula as previously developed on mass-selected $L1_0$ CoPt nanoparticles with truncated-octahedron shape, as shown in Figure 2a [15]. Figure 5 shows the simulated curves expected for the FeRh and FeCo assemblies of perfect rhombic dodecahedrons (as in Figure 2b) with different sizes governed by the number of atoms per edge m ($m = 12$ corresponds to nanoparticles with a size of around 5 nm) [11].

In the case of FeRh nanoparticles ($\Delta Z_{FeRh} = 19$), the CsCl-type (B2) phase signature, in red in Figure 5a, should be identifiable in our range size for FeRh nanoparticles but progressively vanishes as the size decreases. While in the case of FeCo, it should be impossible to extract the superlattice reflection peaks for small nanoparticles up to $m = 12$, our largest size.

To go a step further in the investigation of the chemical ordering in FeCo, we used anomalous X-ray diffraction (AXD) in order to experimentally overcome the low "Z-contrast" between Fe and Co. This was achieved by changing the X-ray wavelength (or photon energy) by using synchrotron radiation techniques, allowing for chemical selectivity and high photon flux. Indeed, for X-ray diffraction, the atomic scattering factor f is a complex number and can be written as follows: $f = f_0 + f'(\lambda) + if''(\lambda)$, where $f_0 \sim Z$ while f' and f'' are wavelength-dependent especially around the absorption edge for heavy atoms [16]. From Figure 6, we found that a photon

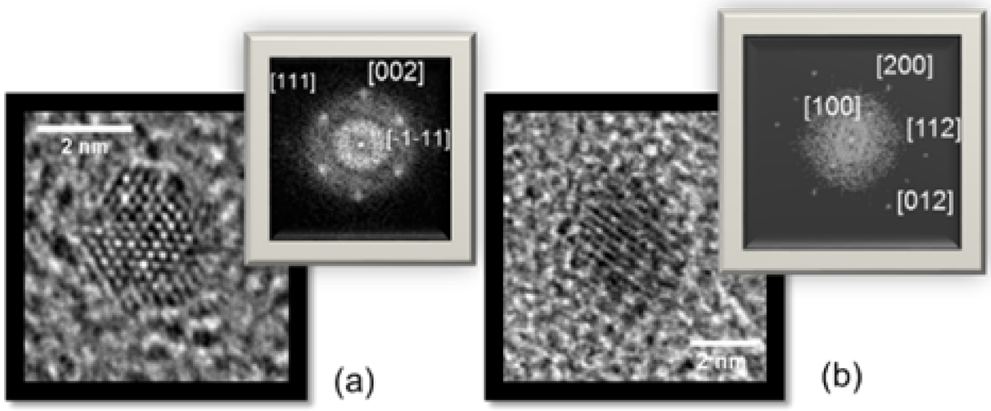

Figure 4: HRTEM images for as-prepared (a) and annealed (b) FeRh nanoparticles with their respective FFT corresponding to fcc (A1) (a) and CsCl-type (B2) phase (b). Figure 4a is a slightly changed reproduction from [13], copyright 2013 American Physical Society.

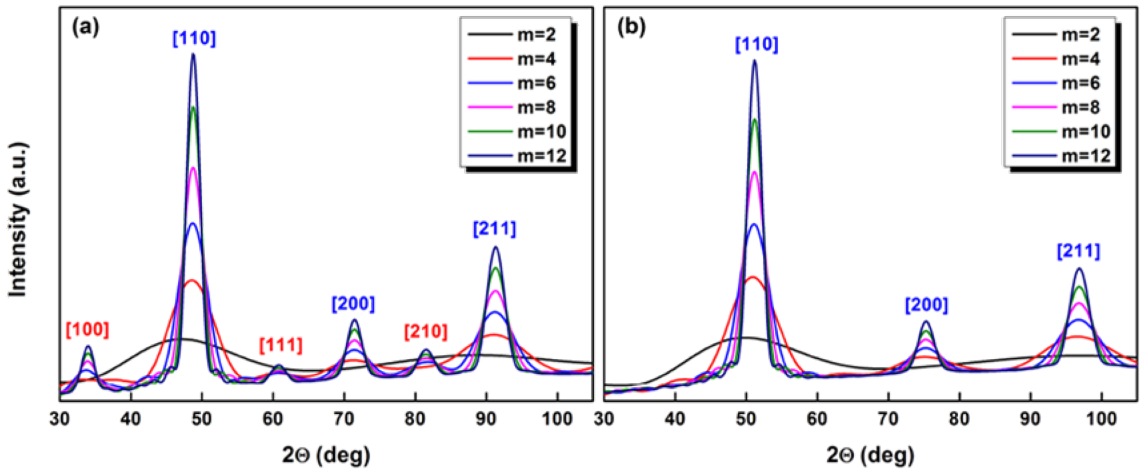

Figure 5: Simulated X-ray scattering curves for CsCl-type (B2) phase (a) FeRh and (b) FeCo nanoparticles with different sizes [11].

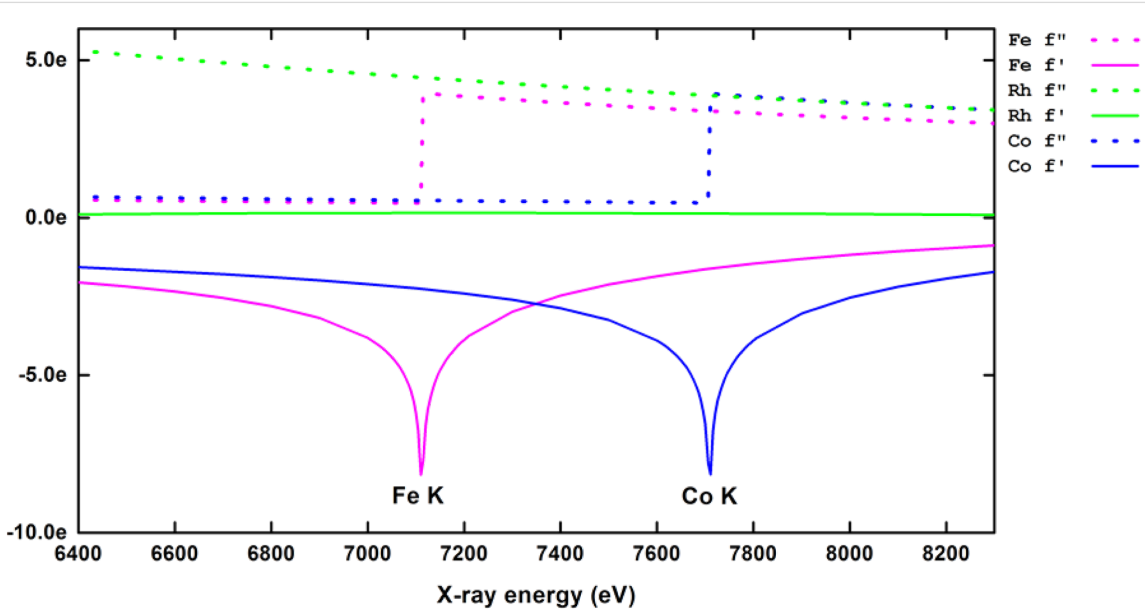

Figure 6: Anomalous scattering *f'* and *f"* coefficients as a function of photon energy for Fe, Co and Rh elements in the range of Fe and Co K edges.

energy of 7.108 keV just before the Fe K absorption edge gave a maximum of anomalous contrast for the atomic scattering factor equal to nine for FeCo, larger than the atomic contrast ($\Delta Z_{FeCo} = 1$).

Thus, mass-selected 5 nm-FeCo nanoparticles were measured with AXD after annealing at 500 °C for 2 h. The measurements were performed on the BM02-D2am French CGR beamline at the ESRF (Grenoble, France) at an X-ray energy fixed at 7.108 keV. The incidence angle was optimized after calibrations so as to have a good compromise between low signal from the Si substrate and maximum intensity of the Bragg (110) peak. The Figure 7 shows the measured X-ray scattering where we can see three peaks which correspond to the main Bragg peaks common to the B2 and bcc structures.

These three peaks, showing the very good crystallinity of the annealed FeCo nanoparticles embedded in the carbon matrix, were isolated and fitted with a Lorentz-type function. Using the Debye–Scherrer equation [17], the size of the nanoparticles is estimated based on the width of the scattered peaks:

$$D = \frac{K}{\beta \cos \theta},$$

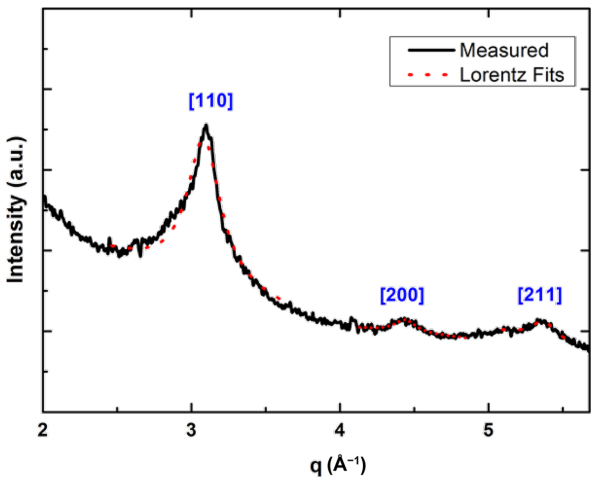

Figure 7: Measured X-ray scattering at 7.108 keV on annealed FeCo nanoparticles with 5 nm in diameter.

where D is the diameter of the nanoparticle, K is a dimensionless shape factor (approximated as $K \approx 0.9$), λ is the X-ray wavelength, β is the full width at half maximum (FWHM) of the peak and θ is the Bragg angle. The corresponding values obtained for both the Lorentz fit and the obtained estimated diameters are presented in Table 1.

Table 1: Values obtained for the Scherrer diameter ($D_{Scherrer}$) as well as the peak position and width for the X-ray scattering spectrum on annealed FeCo nanoparticles with 5 nm in diameter [11].

peak	2θ (°)	FWHM (°)	$D_{Scherrer}$ (nm)
(110)	50.7	4.83	4.13
(200)	76.1	3.46	6.60
(211)	96.5	5.36	5.04

Averaging the diameter values obtained from the three peaks we obtain $D_{Scherrer}$ = 5.25 nm, which is consistent with the results obtained from TEM microscopy for our mass-selected annealed FeCo nanoparticles. But again it was not possible to find evidence of any superstructure B2 peaks in our largest FeCo nanoparticles from AXD.

Therefore, we have performed a series of extended X-ray absorption fine structure (EXAFS) measurements on FeCo samples, at both Fe and Co K edges, to describe local order at each atomic site for different cluster sizes. We have had to develop a specific strategy, more complex than for our previous analysis in bimetallic clusters [18]. As shown in [11], the B2 phase is confirmed for the larger FeCo NPs while a detailed study will be published elsewhere. As a conclusion, the stable B2 chemical ordering is mainly conserved in both FeRh and FeCo nanoalloys. In the next section, we report on the magnetic behaviour of our nanoalloys.

Magnetic characterization

First, the magnetic properties of Fe-based clusters embedded in a carbon matrix have been studied by superconducting quantum interference device (SQUID) magnetometry experiments and simulations [4,19-21].

As illustrated in Figure 8a, the zero-field-cooling (ZFC) and field-cooling (FC) susceptibility curves show a transition from the superparamagnetic to the blocked regime for the as-prepared NPs with a maximum ZFC temperature (T_{max}). T_{max} is connected to the energy barrier ($\Delta E = K_{eff}V$, with K_{eff} the effective anisotropy constant and V the magnetic volume) that a macrospin has to overcome to switch from one stable state to another one. We use our recently developed accurate "triple fit" method, where the ZFC/FC susceptibility curves and a high-temperature magnetization curve are fitted entirely simultaneously (Figure 8a). This simultaneous-fit protocol allows us to determine with good accuracy the parameters of our samples. Indeed, ZFC, FC and $m(H)$ at high temperature can be expressed in a system of equations with common parameters, which are the total number of NPs, the magnetic diameter, the diameter dispersion, and the effective magnetic anisotropy constant. As demonstrated [21], only one set of parameters can fit the three curves at the same time. This "triple fit" method thus reduced the solution range of the different parameters and the uncertainty on their values. Alternating-current magnetic-susceptibility and ferromagnetic resonance measurements have not been used in our case because they are incompatible with the low quantities of matter in our samples. Then, we verified that the magnetic interactions are negligible in all our 1%-diluted samples. Based on the Wohlfarth relation [22], we can define the "well-known" parameter δm [23-25] as follows:

$$\delta m = DcD(H) - \left(m_r - 2IRM(H)\right),$$

where $DcD(H)$ is the direct-current demagnetization, m_r is the remanent magnetization and $IRM(H)$ is the isothermal remanent demagnetization.

If there are dipolar interactions in the sample, the Henkel plot will not be a straight line as provided through the Stoner–Wohlfarth model. Thus, this deviation in the Henkel plot is related to the interaction between NPs. We verified this parameter for our samples and found it to be equal to 0 regardless of the applied magnetic field (see Figure 8b,c). The magnetization loop and the IRM curves at 2 K have been simulated with a modified

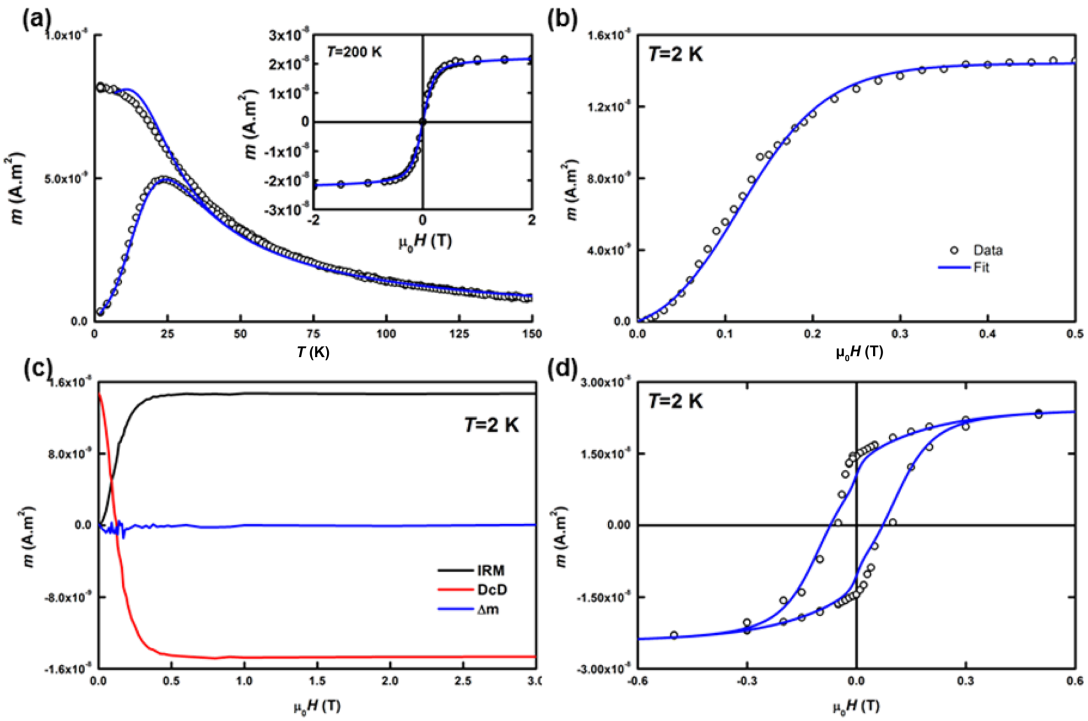

Figure 8: (a) ZFC/FC and $m(H)$ experimental data for mass-selected as-prepared FeCo clusters with 4.3 nm in diameter along with their best fits; (b) IRM experimental data at 2 K with the corresponding biaxial contribution simulation; (c) IRM/DcD and δm curves; (d) hysteresis loop at 2 K along with the corresponding simulation.

Stoner–Wohlfarth model combined with the geometrical approach of the coherent rotation of magnetization [26]. We introduced a bi-axial contribution to completely describe the effective magnetic anisotropy energy (MAE) [27]. For all samples, we have reached a reliable determination of all the magnetic characteristic parameters such as the magnetic particle diameter D_m identical to that of the TEM distribution and the normal evolution of the K_{eff} distribution upon annealing.

In order to obtain the atomic magnetic moments and to correlate them to the finite-size effect in nanoalloys, we use XMCD spectroscopy experiments at each specific Fe and Rh M edge (respectively the Co L edge), at the "X-Treme" beamline at the Swiss Light Source for the FeRh sample and at the "DEIMOS" beamline at the SOLEIL synchrotron for FeCo for various nanocluster sizes (Figure 9); before and after annealing of the same sample at both edges (Figure 10 and Figure 11).

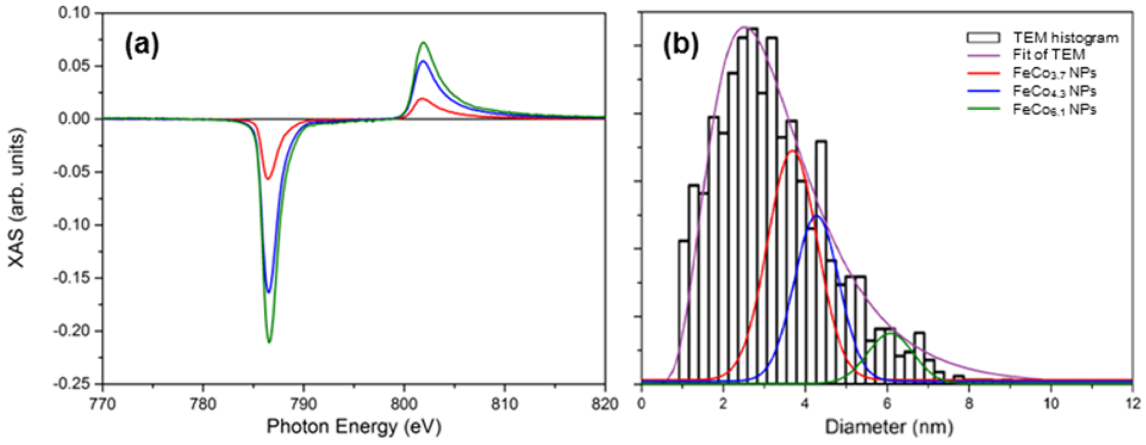

Figure 9: XMCD signal of as-prepared mass-selected FeCo samples at Co $L_{2,3}$ edge (a) with their corresponding nominal diameter histogram compared to the whole TEM dispersion without selection (b).

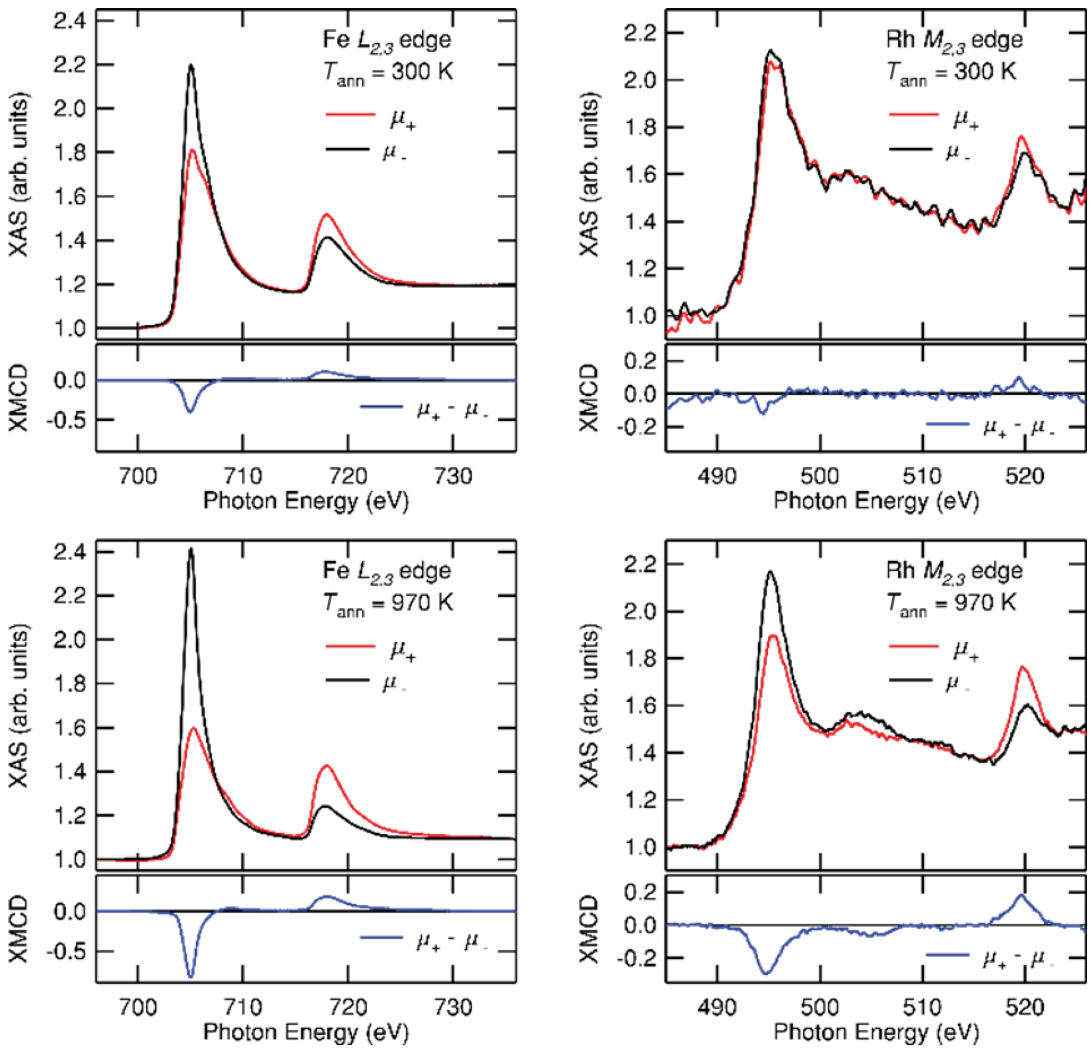

Figure 10: XMCD signals at Fe $L_{2,3}$ edge (left) and at Rh $M_{2,3}$ edge (right) measured at 3 K under 5 T before (top) and after annealing (bottom) on FeRh sample with 2 nm in diameter.

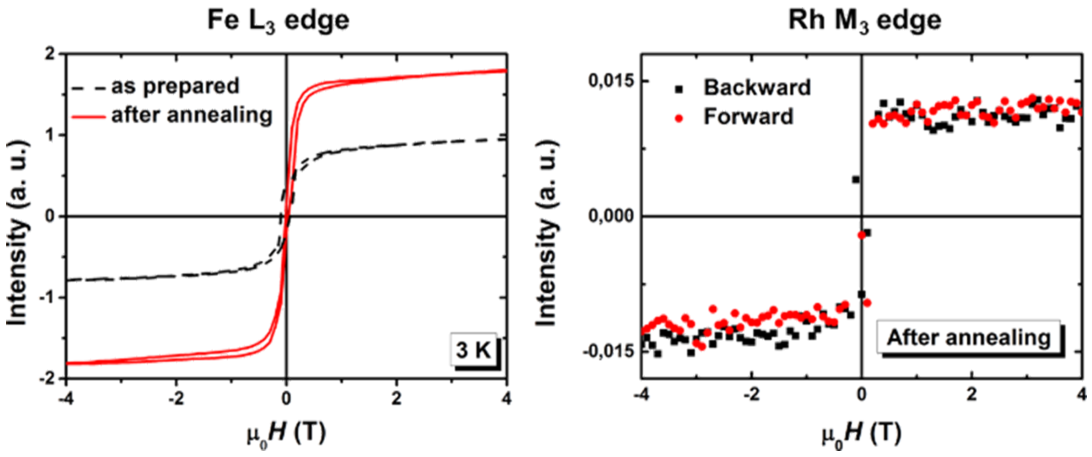

Figure 11: Magnetization curves obtained from XMCD signals measured at 3 K as a function of the applied magnetic field on as-prepared and annealed FeRh sample with 2 nm in diameter at Fe L_3 edge (left) and only after annealing at Rh M_3 edge (right).

In the following section, we discuss the main results concerning the magnetic behaviour of the different samples. Notice that the MAE is mainly determined by semi-analytical models of all the SQUID magnetizations curves and that the spin and angular magnetic moments measured from XMCD are reached by using the sum rules [28,29].

Discussion

At first, it is to notice that FeRh and FeCo samples are all ferromagnetic at low temperatures. In contrast to the anti-ferromagnetic order expected for the B2 phase in the bulk FeRh phase diagram (Figure 1a), we obtained the experimental persistence of high ferromagnetic magnetization down to 3 K for size-selected chemically ordered B2-like FeRh nanocrystals up to 5 nm in diameter. In particular, magnetic measurements on annealed 3.3 nm FeRh samples, have demonstrated ferromagnetic alignment of Fe and Rh at low temperatures with respective values of $3\mu_B$ and $1\mu_B$ [13]. The ferromagnetic order increases slightly for smaller nanoparticles as confirmed from XMCD measurements on annealed 2 nm FeRh (see Figure 10). It should be noted that the total magnetic moment of Rh which is expected to be non-magnetic in bulk, increases up to $1.5\mu_B$ in 2 nm FeRh sample (see Figure 11). While it has long been known that the bcc FeRh unit cell volume expands upon transforming to the FM order [30], we use EXAFS experiments to determine the local iron environment before and after annealing. From a quantitative FEFFIT analysis at the Fe K edge on FeRh nanoparticle, we confirmed the systematic transition upon annealing from the chemically disordered fcc (A1) phase to the ordered CsCl-type (B2) structure for 3 nm FeRh clusters assemblies embedded in a carbon matrix [13]. In the latter case, the unit cell size has been found compatible with those of B2 FeRh bulk material with a Debye–Waller (DW) factor decreasing with chemical ordering. However, possibly due to relaxation effects at the nanoscale (as already observed in CoPt nanoalloys [31]), the DW parameter is still large upon annealing. This does not allow a perfect crystal with a homogeneous B2 structure, which would be expected to exhibit AFM magnetic order as in the bulk phase.

For FeCo, T_{max} is in the range of 10–50 K for as-prepared FeCo samples and increases upon annealing especially for larger magnetic diameters ($D > 4$ nm) in relation with a slight enhancement of K_{eff} [11]. For smaller sizes, MAE is rather constant (with $K_{eff} \approx 130$ kJ/m^3 as in FeRh NPs [10]). This is in agreement with the fact that MAE in NPs is dominated by the effect of additional facets with a large ω_K dispersion increasing with the number of possible chemical arrangements [32].

Contrary to what is expected for free 3D transition metal clusters [33] the magnetic signal of FeCo clusters increases with size for as-prepared and annealed FeCo clusters embedded in a carbon matrix. Moreover, the reduced magnetic moments in the FeCo nanoparticles, which could be due to the formation of a non-collinear structure at the interface with the matrix [34] remains below the threshold of 50% of the bulk average magnetic moment per atom. From a qualitative overview of the measured data on the annealed samples, we generally observed an enhancement of the spin and orbital moments at the Co L edge for the FeCo systems as expected for chemically ordered phase and metastable interface carbon demixing as observed in pure Co clusters [18]. Contrarily, at the Fe-L edge, especially for small size, the reduction of magnetic moment is probably related to a progression of non-magnetic stable iron carbide upon annealing. Further systematic analysis will be published in a near future on collected data on FeCo as well as both Fe and Co reference samples prepared by MS-LECBD [11].

Conclusion

As a conclusion, we have obtained completely opposite thermal evolutions for the magnetic moments in CsCl-type (B2) chemically ordered FeRh and FeCo nanocrystal assemblies prepared by MS-LECBD. We have previously calculated that a Fe-based nanoparticle ranging from 2 to 5 nm in diameter (a few 100 to 6000 atoms per cluster) count, respectively, from 60% to 25% of the atoms at the interface between metallic atom cluster and carbon matrix atoms [10,11].

So on the one hand, because of the low chemical affinity of FeRh for carbon in the surrounding matrix, we have a strong proportion of relaxed first-neighbour distances at the surface of clusters in favour of FM order at low temperatures with uncompensated spins in the small FeRh nanoalloy, incompatible with AFM order at finite size. We are now preparing by the same MS LECBD technique, CsCl-type (B2) chemically ordered FeRh nanoparticles larger than 5 nm in diameter embedded in such inert carbon matrix, in order to determine the transition size for the temperature-dependent transition between FM to bulk-like AFM order.

On the other hand, even if some theoretical papers [35] predict that bulk FeCo alloys doped by carbon can lead to an enhanced magnetocrystalline anisotropy energy of up to 0.75 MJ/m^3 by conserving 70% of the FeCo average magnetic moment per atom, we have shown that for FeCo nanoalloys in carbon environment especially for sizes smaller than 4 nm in diameter, the drawback of carbide formation is in competition with the benefit of tetragonal distortion expected for improving their magnetic properties. In this case, we have shown that the chemical reactivity of FeCo clusters with their environment can profoundly affects their structure and magnetic properties in complete contradiction with thermodynamic predictions [36].

More generally, the binary phase diagram and Néel/Curie temperature interplay, observed in bulk materials, still complicate the predictions of the size-dependent phase diagrams and magnetic behaviour in nanoalloys.

Acknowledgements

The authors are grateful to S. Rusponi and H. Brune from EPFL for stimulating discussions, J. Dreiser, C. Piamonteze and F. Nolting from the Swiss Light Source on the X-Treme beamline and E. Otero and P. Ohresser from the french Synchrotron SOLEIL on the DEIMOS beamline for their respective investment in FeRh and FeCo XMCD measurements. Support is acknowledged from both GDR CNRS 3182 and COST-STSM-MP0903 on Nanoalloys. All cluster samples were prepared in the PLYRA platform while SQUID measurements were performed at the CML platform at Lyon.

References

1. Pierron-Bohne, V.; Tamion, A.; Tournus, F.; Dupuis, V. Magnetism of Low-Dimension Alloys. In *Nanoalloys – Synthesis, Structure and Properties;* Alloyeau, D.; Mottet, C.; Ricolleau, C., Eds.; Springer, 2012; pp 287–330. doi:10.1007/978-1-4471-4014-6_9
2. Calvo, F., Ed. *Nanoalloys – From Fundamentals to Emergent Applications;* Elsevier, 2013.
3. Massalski, T. B., Ed. *Binary Alloy Phase Diagrams;* ASM: OH, USA, 1996.
4. Dupuis, V.; Khadra, G.; Hillion, A.; Tamion, A.; Tuaillon-Combes, J.; Bardotti, L.; Tournus, F. *Phys. Chem. Chem. Phys.* **2015,** *17,* 27996–28004. doi:10.1039/C5CP00943J
5. Thiele, J.-U.; Maat, S.; Fullerton, E. E. *Appl. Phys. Lett.* **2003,** *82,* 2859. doi:10.1063/1.1571232
6. Jia, Z.; Seetala, N.; Misra, R. D. K. *Physica B* **2010,** *405,* 2189–2193. doi:10.1016/j.physb.2010.02.005
7. Jia, Z.; Harrell, J. W.; Misra, R. D. K. *Appl. Phys. Lett.* **2008,** *93,* 022504. doi:10.1063/1.2952956
8. Castiella, M. Elaboration et caractérisation de nanostructures de FeRh structure, ordre chimique et transition magnétique. Ph.D. Thesis, Université Toulouse 3 Paul Sabatier, Toulouse, France, 2015.
9. Kleibert, A.; Balan, A.; Fraile Rodríguez, A.; Nolting, F. *J. Phys.: Conf. Ser.* **2014,** *521,* 012003. doi:10.1088/1742-6596/521/1/012003
10. Hillion, A. Étude des propriétés magnétiques d'assemblées de nanoparticules de Co, FeRh et FeAu. Ph.D. Thesis, Université Claude Bernard Lyon 1, Lyon, France, 2012.
11. Khadra, G. Magnetic and structural properties of size-selected FeCo nanoparticle assemblies. Ph.D. Thesis, Université Claude Bernard Lyon 1, Lyon, France, 2015.
12. Van Hardeveld, R.; Hartog, F. *Surf. Sci.* **1969,** *15,* 189–230. doi:10.1016/0039-6028(69)90148-4
13. Hillion, A.; Cavallin, A.; Vlaic, S.; Tamion, A.; Tournus, F.; Khadra, G.; Dreiser, J.; Piamonteze, C.; Nolting, F.; Rusponi, S.; Sato, K.; Konno, T. J.; Proux, O.; Dupuis, V.; Brune, H. *Phys. Rev. Lett.* **2013,** *110,* 087207. doi:10.1103/PhysRevLett.110.087207
14. Smith, A. W.; Rawlings, R. D. *Phys. Status Solidi A* **1976,** *34,* 117–123. doi:10.1002/pssa.2210340109
15. Blanc, N. Caractérisation structurale et magnétique de nanoparticules de CoPt: mise en évidence de la transition de phase A1 vers $L1_0$. Ph.D. Thesis, Université Claude Bernard Lyon 1, Lyon, France, 2009.
16. Brennan, S.; Cowan, P. L. *Rev. Sci. Instrum.* **1992,** *63,* 850–853. doi:10.1063/1.1142625
17. Patterson, A. L. *Phys. Rev.* **1939,** *56,* 978–982. doi:10.1103/PhysRev.56.978
18. Blanc, N.; Díaz-Sánchez, L. E.; Ramos, A. Y.; Tournus, F.; Tolentino, H. C. N.; De Santis, M.; Proux, O.; Tamion, A.; Tuaillon-Combes, J.; Bardotti, L.; Boisron, O.; Pastor, G. M.; Dupuis, V. *Phys. Rev. B* **2013,** *87,* 155412. doi:10.1103/PhysRevB.87.155412
19. Tamion, A.; Hillenkamp, M.; Hillion, A.; Tournus, F.; Tuaillon-Combes, J.; Boisron, O.; Zafeiratos, S.; Dupuis, V. *J. Appl. Phys.* **2011,** *110,* 063904. doi:10.1063/1.3638035
20. Tamion, A.; Bonet, E.; Tournus, T.; Raufast, C.; Hillion, A.; Gaier, O.; Dupuis, V. *Phys. Rev. B* **2012,** *85,* 134430. doi:10.1103/PhysRevB.85.134430
21. Tamion, A.; Hillenkamp, M.; Tournus, F.; Bonet, E.; Dupuis, V. *Appl. Phys. Lett.* **2009,** *95,* 062503. doi:10.1063/1.3200950
22. Wohlfarth, E. P. *J. Appl. Phys.* **1958,** *29,* 595. doi:10.1063/1.1723232
23. García-Otero, J.; Porto, M.; Rivas, J. *J. Appl. Phys.* **2000,** *87,* 7376. doi:10.1063/1.372996
24. Martinez Huerta, J. M.; De La Torre Medina, J.; Piraux, L.; Encinas, A. *J. Appl. Phys.* **2012,** *111,* 083914. doi:10.1063/1.4704397
25. Kelly, P. E.; O'Grady, K.; Mayo, P. I.; Chantrell, R. W. *IEEE Trans. Magn.* **1989,** *25,* 3881–3883. doi:10.1109/20.42466
26. Thiaville, A. *Phys. Rev. B* **2000,** *61,* 12221. doi:10.1103/PhysRevB.61.12221
27. Hillion, A.; Tamion, A.; Tournus, F.; Gaier, O.; Bonet, E.; Albin, C.; Dupuis, V. *Phys. Rev. B* **2013,** *88,* 094419. doi:10.1103/PhysRevB.88.094419
28. Thole, B. T.; Carra, P.; Sette, F.; van der Laan, G. *Phys. Rev. Lett.* **1992,** *68,* 1943. doi:10.1103/PhysRevLett.68.1943
29. Carra, P.; Thole, B. T.; Altarelli, M.; Wang, X. *Phys. Rev. Lett.* **1993,** *70,* 694. doi:10.1103/PhysRevLett.70.694
30. De Bergevin, F.; Muldawer, L. *C. R. Hebd. Seances Acad. Sci.* **1961,** *252,* 1347.
31. Dupuis, V.; Blanc, N.; Díaz-Sánchez, L. E.; Hillion, A.; Tamion, A.; Tournus, F.; Pastor, G. M. *Eur. Phys. J. B* **2013,** *86,* 83. doi:10.1140/epjb/e2013-30644-0
32. Tournus, F.; Blanc, N.; Tamion, A.; Hillenkamp, M.; Dupuis, V. *Phys. Rev. B* **2010,** *81,* 220405(R). doi:10.1103/PhysRevB.81.220405
33. Billas, I. M. L.; Châtelain, A.; de Heer, W. A. *J. Magn. Magn. Mater.* **1997,** *168,* 64–84. doi:10.1016/S0304-8853(96)00694-4
34. Kleibert, A.; Rosellen, W.; Getzlaff, M.; Bansmann, J. *Beilstein J. Nanotechnol.* **2011,** *2,* 47–56. doi:10.3762/bjnano.2.6
35. Delczeg-Czirjak, E. K.; Edström, A.; Werwiński, M.; Rusz, J.; Skorodumova, N. V.; Vitos, L.; Eriksson, O. *Phys. Rev. B* **2014,** *89,* 144403. doi:10.1103/PhysRevB.89.144403
36. Doh, W. H.; Papaefthimiou, V.; Dintzer, T.; Dupuis, V.; Zafeiratos, S. *J. Phys. Chem. C* **2014,** *118,* 26621–26628. doi:10.1021/jp508895u

BEILSTEIN JOURNAL OF NANOTECHNOLOGY

Evolution of the graphite surface in phosphoric acid: an AFM and Raman study

Rossella Yivlialin*[1], Luigi Brambilla[2], Gianlorenzo Bussetti[1], Matteo Tommasini[2], Andrea Li Bassi[3], Carlo Spartaco Casari[3], Matteo Passoni[3], Franco Ciccacci[1], Lamberto Duò[1] and Chiara Castiglioni[2]

Full Research Paper

Open Access

Address:
[1]Department of Physics, Politecnico di Milano, p.za Leonardo da Vinci 32, I-20133 Milano, Italy, [2]Department of Chemistry, Materials and Chemical Engineering "Giulio Natta", Politecnico di Milano, p.za Leonardo da Vinci 32, I-20133 Milano, Italy and [3]Department of Energy, Politecnico di Milano, via Ponzio 34/3, I-20133 Milano, Italy

Email:
Rossella Yivlialin* - rossella.yivlialin@polimi.it

* Corresponding author

Keywords:
atomic force microscopy (AFM); electrochemical atomic force microscopy (EC-AFM); electrochemical delamination of graphite; graphene; phosphoric acid; Raman spectroscopy

Beilstein J. Nanotechnol. **2016,** *7,* 1878–1884.
doi:10.3762/bjnano.7.180

Received: 14 July 2016
Accepted: 09 November 2016
Published: 30 November 2016

This article is part of the Thematic Series "Self-assembly of nanostructures and nanomaterials II".

Guest Editor: I. Berbezier

Abstract

Phosphoric acid is an inorganic acid used for producing graphene sheets by delaminating graphite in (electro-)chemical baths. The observed phenomenology during the electrochemical treatment in phosphoric acid solution is partially different from other acidic solutions, such as sulfuric and perchloric acid solutions, where the graphite surface mainly forms blisters. In fact, the graphite surface is covered by a thin layer of modified (oxidized) material that can be observed when an electrochemical potential is swept in the anodic current regime. We characterize this particular surface evolution by means of a combined electrochemical, atomic force microscopy and Raman spectroscopy investigation.

Introduction

Sulfuric (H_2SO_4), perchloric ($HClO_4$) and phosphoric (H_3PO_4) acid in aqueous solutions have been used traditionally for the intercalation of anions in graphite in order to produce graphene [1]. At a given electrochemical potential, suitably defined for a given acid, the layer–layer interaction in the graphene crystal is reduced, facilitating a delamination. In general, after the electrochemical (EC) treatment, graphite is carefully ultrasonicated to ease the exfoliation process. After that single- or multi-layer graphene sheets with a size of about 1 μm can be retrieved from the electrochemical bath. The electronic and mechanical properties of the graphene sheets [1-6] and the main characteristics of the graphite crystals subjected to EC delamination [6,7] have been studied extensively. This allows one to shed light on the correlation between the modifications induced on the graphite

crystal and the structure of the exfoliated graphene sheets. H_2SO_4 produces blisters at the micrometer scale, i.e., local swellings of the surface caused by the production of gases (O_2, CO and/or CO_2) due to the oxidation processes occurring at high anodic potentials [7]. At the nanometer scale, protrusions have been observed together with an increase of the surface roughness caused by graphite oxidation [7,8]. $HClO_4$ solutions show a similar phenomenology during intercalation of anions [7]. In particular, the evolution of blisters as a function of time has been analyzed in the past [9,10], supporting the theoretical model proposed by Murray [11]. H_3PO_4 is another solvent that allows for successful graphite exfoliation, as reported quite recently [12,13]. However, a detailed analysis of the surface modification of a graphite crystal subjected to EC processes in phosphoric acid solution is still missing. In a recent work [7], we have shown that the EC characterization of the system, i.e., the cyclic-voltammetry (CV) curve, presents a single feature during the first EC potential sweep, but it disappears during the second scan. On the other hand, EC atomic force microscopy (EC-AFM) measurements, performed in situ in the EC cell, reveal a significant increase of the surface roughness. This result suggests that, despite of the good graphite delamination yield, the microscopic processes occurring at the solid–liquid interface could be different from those described in the case of H_2SO_4 and $HClO_4$ solutions.

In this paper, we focus our investigation on the processes occurring at the graphite surface during EC treatment in H_3PO_4, by using both (EC-)AFM (ex situ and in situ) and Raman spectroscopy (ex situ). A correlation between the observed morphology and spectroscopic properties of the surface helps to clarify the effects of phosphoric acid on graphite.

Results and Discussion

Graphite acts as working electrode (WE) in the EC cell (see Experimental section for further information). The EC potential is initially fixed at about +0.3 V with respect to the Pt reference electrode (RE). At this potential, the current flowing through the WE is negligible and EC processes do not occur. When the EC potential is swept towards more positive values, the anodic current increases and a clear feature in the cyclic voltammetry (CV) curve is observed at about +1.48 V (Figure 1a), indicating that a charge transfer process is activated at the graphite electrode.

Interestingly, no CV peaks are observed during the second anodic sweep, despite the fact that an enhancement of the oxidation current is always measured. A similar behavior is observed when the CV is confined in the negative EC potential range (see Figure 1b). If the CV is extended from negative to positive EC potentials, both the anodic (in the positive potential range) and cathodic (in the negative potential range) peaks are visible, suggesting that these two EC processes are coupled. The positions of the anodic (at 1.48 V in panel a) and cathodic peak (at −1.25 V in panel b) change when the CV is acquired on the whole range from negative to positive EC potentials. In this

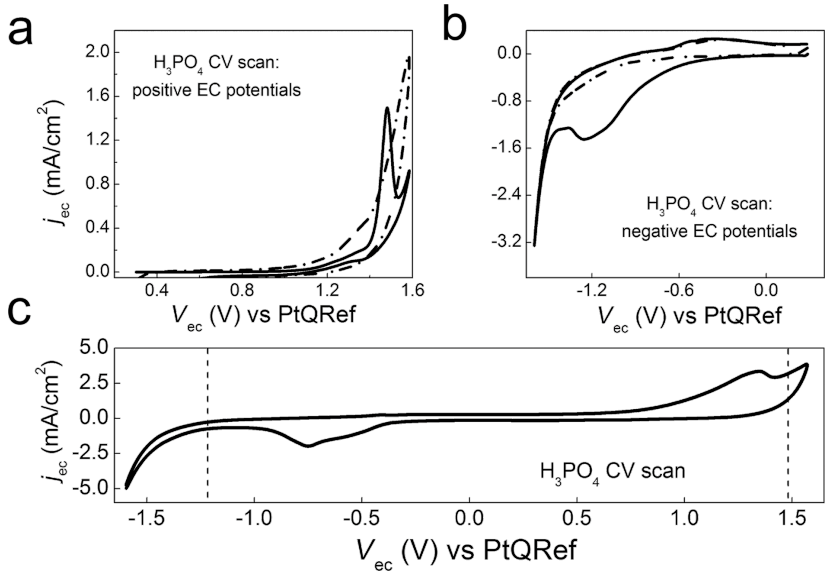

Figure 1: CV in H_3PO_4 at different EC potential ranges (scan rate = 150 mV/s). a) First (continuous line) and second (dash-dotted line) scan from 0.3 V to 1.6 V. b) First (continuous line) and second (dash-dotted line) scan from 0.3 V to −1.6 V. c) extended CV from −1.6 V to 1.6 V; the dashed lines mark the original position of the anodic and cathodic peaks.

case, see panel c, the anodic feature is placed at about 1.40 V, while the cathodic peak is at −0.75 V suggesting that the processes require a lower activation energy.

Aiming at a first investigation of the sample by optical microscopy, we confined the CV in the positive EC energy range (from 0.3 V to 1.6 V), where oxidation phenomena occur (in close comparison with the case of sulfuric and perchloric solutions [7]). We also cycled graphite fifteen times to enhance the peculiar surface changes induced by the phosphoric acid solution. Optical microscopy reveals an irregular surface, where three main regions can be identified (Figure 2). The majority of the surface is covered by an apparently thick brown film (label A in Figure 2).

Between these A-areas, we observe characteristic interference fringes (B-regions), which suggests that a thinner film is grown there with respect to the darker A-regions. Considering that (1) the EC process induces an oxidation of the graphite surface (anodic currents), (2) the refractive index of graphene oxide is about 1.85 [14,15] and that (3) the light used to acquire the image reported in Figure 2 is in the visible range, it is possible to roughly estimate that the film thickness in the B-areas is of the order of hundreds of nanometers. From this initial optical analysis of the sample, areas labeled as C seem not to be affected by any surface modification.

A deeper morphological analysis has been conducted on the same regions by ex situ AFM experiments. Figure 3a shows that the A-area, where the modified film is unquestionably present, is characterized by a high surface roughness (R_q = 0.3 nm from AFM analysis, which is about five times higher than characteristic mean square root values measured on pristine graphite), conversely to what is observed when sulfuric and perchloric acids are used in the electrolytic solutions. In the latter cases, (nano-)protrusion and blisters characterize the graphite surface after the EC intercalation [7].

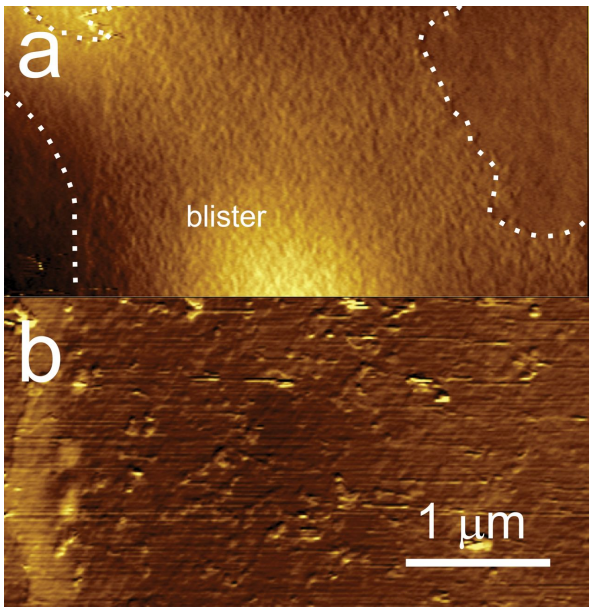

Figure 3: AFM topography images of the HOPG surface after the activation of the electrochemical process in H_3PO_4 described in the text. a) Characteristic topography image acquired over the A-region (see text for details), after positioning the AFM tip with the help of a CCD camera. The dotted line highlights the area covered by a rough film. At the bottom of the image, part of a blister is visible; b) characteristic topography image acquired over the C-region (see text for details).

Nevertheless, some blisters, randomly distributed on the surface, also occur after the treatment with H_3PO_4 acid, as shown in Figure 3a. No differences are observed between A- and

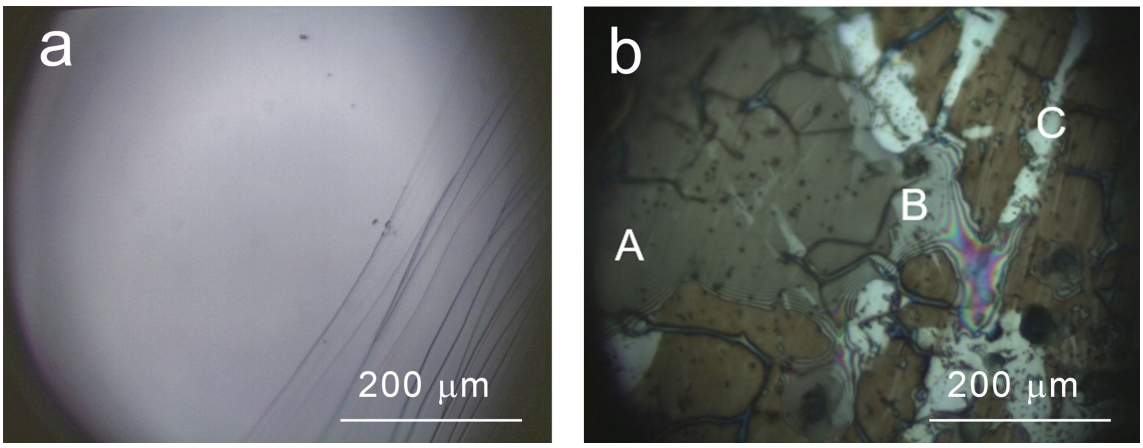

Figure 2: Optical microscopy image (magnification 50×) acquired ex situ on a) pristine graphite and b) graphite after 15 CVs from 0.3 to 1.6 V. Three different areas are observed: a) a thick brown film is recognized, b) a thinner region of the film where interference fringes are clearly visible, C) areas where no modifications can be observed.

B-areas by AFM. C-areas (see panel b) seem to be not affected by the presence of a surface film, but the surface is far from being clean, appearing seriously damaged and dusty.

To get further insight, we succeeded in following in situ the graphite degradation in these regions during the EC treatment by means of an EC-AFM. Figure 4 compares the surface topography before (panel a) and after (panel b) a single EC potential sweep in the positive potential range. The graphite steps are eroded during the EC process as well as the terraces, suggesting the occurrence of graphite dissolution at these high EC potentials.

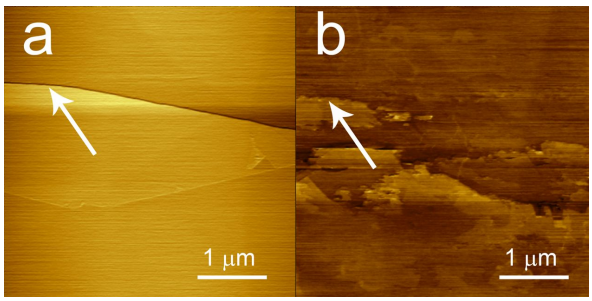

Figure 4: AFM topography images of the HOPG surface a) before EC treatment in phosphoric acid and b) after a single EC potential sweep in the positive energy range. The surface is damaged and eroded because of the EC process. The arrows help to recognize the original graphite step.

Turning back to the A- and B-areas, a chemical/structural analysis of the film surface requires a spectroscopic characterization carried out by Raman. Hence, we recorded ex situ several micro-Raman spectra with different excitation wavelengths to get information about the different regions of the sample. We analyzed the HOPG sample after fifteen CV cycles in the positive potentials range (see Figure 1a), focusing the 457.9 nm laser at the A, B and C regions. The four spectra compared in Figure 5 are representative of the pristine HOPG and of the A-, B-, C-regions displayed in Figure 2.

Similar observations can be made, independently on the excitation energy adopted. Indeed, spectra recorded with 632.8 nm and 784.5 nm excitations show a qualitative behavior similar to that observed with 457.9 nm excitation and are not reported in Figure 5. The three different analyzed regions display the typical spectral pattern of graphitic materials characterized by structural disorder [16-18], showing Raman features in the G-band region (1570–1650 cm^{-1}), in the D-band region (1250–1400 cm^{-1}) and several features belonging to the second-order Raman spectrum. However, the intensity pattern and/or band shapes are different in the three regions analyzed, in particular:

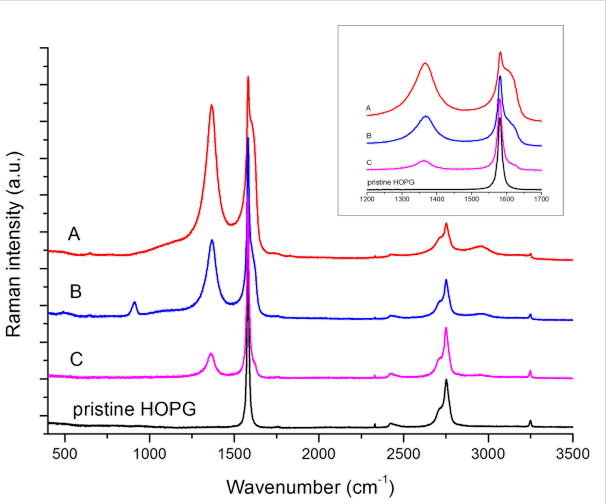

Figure 5: Raman spectra (excitation wavelength of 457.9 nm) of the HOPG sample subjected to 15 CV cycles in the range from +0.3 V to +1.6 V (see Figure 1a). From the top: spectrum of region A (red line); region B (blue line); region C (magenta line). The Raman spectrum drawn with the black line has been taken from a region of the sample not affected by the EC process and it can be considered as a representative reference spectrum of the pristine material (HOPG).

- In the spectra of the A-region the D band dominates and, close to the sharp G line at 1582 cm^{-1} typical of HOPG, a rather strong and broad new component appears (hereafter referred as G* band) at higher Raman shifts.
- Similar features can be observed in the B-region. However, in this case both the D line and the G* components are less pronounced than in the A-region. Moreover, an additional new line is observed at 913 cm^{-1}. In analogy to the experimental findings reported in [19], this line may be tentatively assigned to Raman modes characteristic of a hydrogen bonded network involving phosphoric acid, its anions and water molecules adsorbed on the graphite surface.
- The C-region, which displays an optically smooth surface, has a remarkably different spectrum, with a strong G line and weak D and G* bands.

The above observations clearly indicate that the signals observed in the spectra originate: i) from a complex disordered material made by several components, differently modified by the EC process and ii) from coexisting pristine HOPG. Hence, the results from Raman experiments can be better discussed by subtracting the spectrum of pristine HOPG from the spectra of the A-, B-, and C-regions (Figure 6). This was done by means of the standard procedure for spectral subtraction. The difference spectra have been obtained by suitably weighting the spectrum of the pristine HOPG, in such a way that the sharp G line assigned to the HOPG phase disappears (optimal compensation).

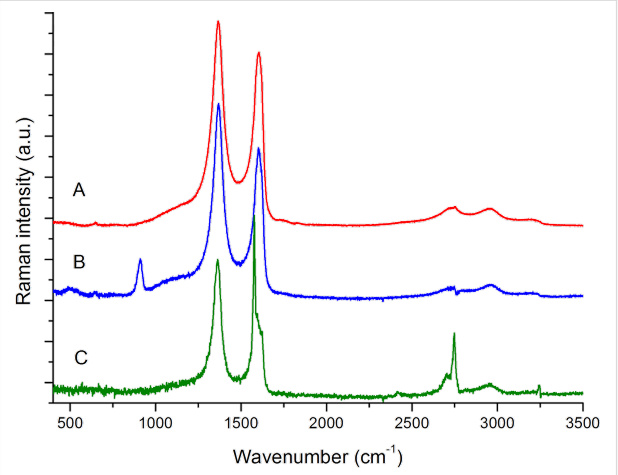

Figure 6: Spectral subtraction of the spectrum of the pristine HOPG from the Raman spectra of: A-region (red line), B-region (blue line) and C-region (green line) (see also Figure 5). Excitation at 457.9 nm.

The difference Raman spectra of regions A and B (Figure 6) are characterized by a very strong D feature at 1366 cm^{-1} and by the broad G* feature with a maximum at 1604 cm^{-1}. This is blue-shifted by 22 cm^{-1} with respect to the G line of HOPG. Moreover, also the sharp 2D feature at 2750 cm^{-1} typical of HOPG turns out to be fully compensated by the subtraction procedure. However, after subtraction we still observe other second-order features, which are commonly found in disordered carbon materials or graphene molecules [20]. The Raman features of the disordered phase show remarkable analogies to the Raman spectra of samples of graphene oxides subjected to chemical reduction [21]. This analogy suggests that the material formed at the graphite surface is the result of the EC oxidation of graphene sheets, possibly followed by partial reduction. Interestingly, the difference Raman spectrum of the B-region is practically superimposable to that of the A-region, with the only exception of the sharp feature at 913 cm^{-1}.

We report in Figure 7 the difference Raman spectra of the A-region obtained with the same procedure described above but at different excitation wavelengths. It is evident that modified graphitic species contribute to the spectra of Figure 7, independently of the chosen excitation wavelength. The position of the D line progressively red-shifts with increasing the laser wavelength, as usual in graphitic materials [16,22]. The observed behavior is often interpreted in the framework of the double resonance theory [23], firstly developed for the interpretation of the frequency dispersion observed in multi-wavelength Raman spectra of microcrystalline graphite [22]. However, the sample under investigation contains chemically modified material, probably consisting in a mixture of different, variously defected sp^2-hybridized layers. In this case the observed frequency dispersion of the D line should be rationalized as the consequence of the Raman response of graphitic domains of different size/perfection, which is selectively intensified by resonance effects [18,24,25].

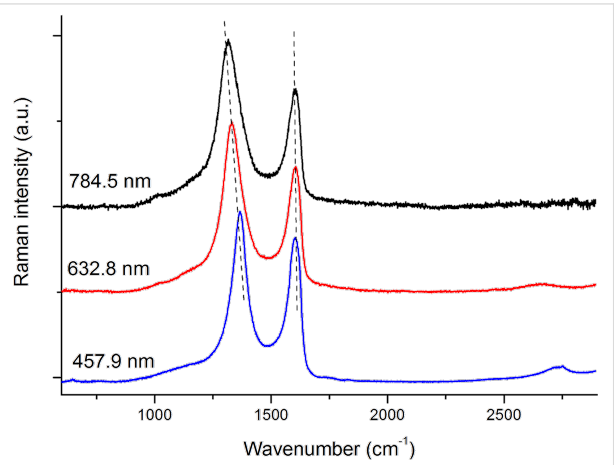

Figure 7: Spectral subtraction of the spectrum of the pristine graphite from the Raman spectra of the A region. From top to bottom: Raman excitation at 784.5 nm (black line), 632.8 nm (red line) and 457.9 nm (blue line). The D peak shows a dispersion of 44 cm^{-1}/eV, similar to that observed in microcrystalline graphite [19,22].

We may thus conclude that the A- and B-regions consist of a strongly modified graphitic component, which forms the highly rough surface measured with AFM. This film is grown on the HOPG surface, which is simultaneously probed by Raman spectroscopy. Notice that the difference spectra reported in Figure 6 are normalized, while comparing A with B in Figure 5 shows that the contribution of the disordered phase is lower in B. The last observation supports the idea that the modified film is thinner in the B-region, also in agreement with the interference fringes observed in optical microscopy (Figure 2).

A completely different result is obtained by subtracting the reference pristine HOPG spectrum from the Raman spectrum recorded over the optically smooth C-region (Figure 6). In this case a very sharp component of the G line persists, close to the characteristic line of HOPG, but red-shifted by 4 cm^{-1}. On the high frequency wing of this G line a rather complex G* feature appears, which does not correspond to the G* band observed over the regions A and B. This feature could be ascribed to some ion intercalation process, by analogy with Raman spectra reported in the literature [26,27]. However, HOPG samples affected by ions intercalation usually show very sharp characteristic lines in the G band region, whose peak position can be correlated to the intercalation stage [26,27], while in this case we observe a broad and structured feature with a peak at about 1622 cm^{-1}. Alternatively, we may interpret this spectral feature as partially exfoliated graphene sheets, characterized by structural defects as edges and/or holes. These two hypotheses

should be carefully validated by further experiments carried out in different CV regimes and cycling.

Conclusion

The effect of phosphoric acid solution (2 M) on the surface of HOPG submerged in an EC bath has been studied by conventional cyclic voltammetry (CV). The EC characterization reveals the presence of both anodic and cathodic peaks at 1.48 V and −1.25 V, respectively. The crystal oxidation process, generally exploited for graphite delamination, occurs in the positive potential range (anodic). Optical microscopy investigation reveals the presence of a thick layer deposited on the surface. The topographic analysis of this film has been performed ex situ by means of AFM, while the changes induced by phosphoric acid on the surface of graphite, during the very first stages of the EC treatment, have been monitored in situ by an EC-AFM, which reveals a clear erosion of the surface as a consequence of the high anodic potentials used in the cycle.

A detailed ex situ Raman analysis with three different excitation energies has been carried out on a HOPG sample after fifteen CV cycles in the anodic region. The Raman results corroborate the conclusions derived from the inspection of the sample with optical microscopy and AFM topography. A- and B-regions consist of pristine HOPG material co-existing with a surface layer of highly modified and disordered graphitic phase. The Raman spectra suggest that the disordered component is less abundant over the B-region, where optical microscopy indicates a thinner modified surface layer. The C-region is compatible with incipient anion intercalation and/or exfoliation of small graphene sheets. However, a wider EC-AFM/Raman analysis on samples subjected to different CV treatments is required in order to definitely assess the ability of phosphoric acid to give HOPG intercalation, especially in relation with the exfoliation mechanism.

Experimental

Sample and electrochemistry

As working electrode (WE) Z-grade highly oriented pyrolytic graphite (HOPG, 10 × 10 mm^2, Optigraph©) crystal is used inside a three-electrode electrochemical cell. The graphite is exfoliated by an adhesive tape along an edge of the sample. The 2 M H_3PO_4 solution has been purified by bubbling Ar gas (5.0 grade pure) inside a separator funnel for several days. A Pt wire is used both as counter electrode (CE) and reference electrode (RE). Further information on Pt electrodes is reported in [7].

After the electrochemical treatment, the sample is dried under pure nitrogen (N_2 5.5 grade) for several seconds. The nitrogen flux is directed perpendicularly to the sample surface. The N_2 vessel outlet is set to 0.25 bar above the atmospheric pressure. Following this procedure, we always recognize three morphological regions (labeled as A, B and C) on the HOPG surface by optical microscopy.

Optical microscopy analysis

An Olympus© BX41 optical microscope is used to characterize different areas of the sample after the intercalation process. The sample was removed from the EC cell, dried with nitrogen and placed below the microscope.

Electrochemical atomic force microscopy (EC-AFM)

A commercial (Keysight© 5500 apparatus) AFM is used in these experiments in air and in the electrochemical cell (EC-AFM). The EC-cell is placed on the WE, where a Viton O-ring ensures the seal of the acid solution. The EC-cell and the AFM can be placed inside a protected Ar environment to avoid a progressive degradation of the solution. AFM images are collected in contact mode.

Raman spectroscopy

Raman spectra were recorded with a Jobin Yvon Labram HR800 Raman spectrometer coupled with an Olympus BX41 microscope. Spectra were acquired in backscattering geometry using a 50× objective with different excitation lines (457.9 nm Ar^+ laser, 632.8 nm He–Ne laser, 784.5 nm diode laser).

References

1. Niu, L.; Coleman, J. N.; Zhang, H.; Shin, H.; Chhowalla, M.; Zheng, Z. *Small* **2016,** *12,* 272–293. doi:10.1002/smll.201502207
2. Geim, A. K. *Science* **2009,** *324,* 1530–1534. doi:10.1126/science.1158877
3. Rao, C. N. R.; Ramakrishna Matte, H. S. S.; Maitra, U. *Angew. Chem., Int. Ed.* **2013,** *52,* 13162–13185. doi:10.1002/anie.201301548
4. Nicolosi, V.; Chhowalla, M.; Kanatzidis, M. G.; Strano, M. S.; Coleman, J. N. *Science* **2013,** *340,* 1226419. doi:10.1126/science.1226419
5. Feng, H.; Hu, Z.; Liu, X. *Chem. Commun.* **2015,** *51,* 10961–10964. doi:10.1039/C5CC02625C
6. Xia, Z. Y.; Pezzini, S.; Treossi, E.; Giambastiani, G.; Corticelli, F.; Morandi, V.; Zanelli, A.; Bellani, V.; Palermo, V. *Adv. Funct. Mater.* **2013,** *23,* 4684–4693. doi:10.1002/adfm.201203686
7. Bussetti, G.; Yivlialin, R.; Alliata, D.; Li Bassi, A.; Castiglioni, C.; Tommasini, M.; Casari, C. S.; Passoni, M.; Biagioni, P.; Ciccacci, F.; Duò, L. *J. Phys. Chem. C* **2016,** *120,* 6088–6093. doi:10.1021/acs.jpcc.6b00407
8. Zhang, B.; Wang, E. *Electrochim. Acta* **1995,** *40,* 2627–2633. doi:10.1016/0013-4686(95)00111-Q
9. Alliata, D.; Kötz, R.; Haas, O.; Siegenthaler, H. *Langmuir* **1999,** *15,* 8483–8489. doi:10.1021/la990402o
10. Alliata, D.; Häring, P.; Haas, O.; Kötz, R.; Siegenthaler, H. *Electrochem. Commun.* **1999,** *1,* 5–9. doi:10.1016/S1388-2481(98)00005-8

11. Goss, C. A.; Brumfield, J. C.; Irene, E. A.; Murray, R. W. *Anal. Chem.* **1993,** *65,* 1378–1389. doi:10.1021/ac00058a014
12. Liu, J.; Yang, H.; Zhen, S. G.; Poh, C. K.; Chaurasia, A.; Luo, J.; Wu, X.; Yeow, E. K. L.; Sahoo, N. G.; Lin, J.; Shen, Z. *RSC Adv.* **2013,** *3,* 11745–11750. doi:10.1039/c3ra41366g
13. Parvez, K.; Yang, S.; Feng, X.; Müllen, K. *Synth. Met.* **2015,** *210,* 123–132. doi:10.1016/j.synthmet.2015.07.014
14. Ni, Z. H.; Wang, H. M.; Kasim, J.; Fan, H. M.; Yu, T.; Wu, Y. H.; Feng, Y. P.; Shen, Z. X. *Nano Lett.* **2007,** *7,* 2758–2763. doi:10.1021/nl071254m
15. Jung, I.; Vaupel, M.; Pelton, M.; Piner, R.; Dikin, D.; Stankovich, S.; An, J.; Ruoff, R. S. *J. Phys. Chem. C* **2008,** *112,* 8499–8506. doi:10.1021/jp802173m
16. Ferrari, A. C.; Basko, D. M. *Nat. Nanotechnol.* **2013,** *8,* 235–246. doi:10.1038/nnano.2013.46
17. Jorio, A.; Saito, R.; Dresselhaus, G.; Dresselhaus, M. S. *Raman Spectroscopy in Graphene Related Systems;* Wiley-VCH: Weinheim, Germany, 2011. doi:10.1002/9783527632695
18. Castiglioni, C.; Tommasini, M.; Zerbi, G. *Philos. Trans. R. Soc. London, Ser. A* **2004,** *362,* 2425–2459. doi:10.1098/rsta.2004.1448
19. Li, J.; Zhang, C.; Deng, M.; Luo, J. *Friction* **2014,** *2,* 164–172. doi:10.1007/s40544-014-0050-6
20. Maghsoumi, A.; Brambilla, L.; Castiglioni, C.; Müllen, K.; Tommasini, M. *J. Raman Spectrosc.* **2015,** *46,* 757–764. doi:10.1002/jrs.4717
21. King, A. A. K.; Davies, B. R.; Noorbehesht, N.; Newman, P.; Church, T. L.; Harris, A. T.; Razal, J. M.; Minett, A. I. *Sci. Rep.* **2016,** *6,* 19491. doi:10.1038/srep19491
22. Pocsic, I.; Hundhausen, M.; Kóos, M.; Ley, L. *J. Non-Cryst. Solids* **1998,** *227–230,* 1083–1086.
23. Thomsen, C.; Reich, S. *Phys. Rev. Lett.* **2000,** *85,* 5214–5217. doi:10.1103/PhysRevLett.85.5214
24. Castiglioni, C.; Negri, F.; Rigolio, M.; Zerbi, G. *J. Chem. Phys.* **2001,** *115,* 3769–3778. doi:10.1063/1.1381529
25. Negri, F.; di Donato, E.; Tommasini, M.; Castiglioni, C.; Zerbi, G.; Müllen, K. *J. Chem. Phys.* **2004,** *120,* 11889–11900. doi:10.1063/1.1710853
26. Alsmeyer, D. C.; McCreery, R. L. *Anal. Chem.* **1992,** *64,* 1528–1533. doi:10.1021/ac00038a006
27. Dresselhaus, M. S.; Dresselhaus, G. *Adv. Phys.* **2002,** *51,* 1–186. doi:10.1080/00018730110113644
And references cited therein.

License and Terms

BEILSTEIN JOURNAL OF NANOTECHNOLOGY

Graphene–polymer coating for the realization of strain sensors

Carmela Bonavolontà[1,2], Carla Aramo[2], Massimo Valentino*[1,3], Giampiero Pepe[1,3], Sergio De Nicola[1,3], Gianfranco Carotenuto[4], Angela Longo[4], Mariano Palomba[4], Simone Boccardi[5] and Carosena Meola[5]

Full Research Paper

Open Access

Address:
[1]Dipartimento Scienze Fisiche, University of Naples "Federico II", Via Cintia, 80134 Napoli, Italy, [2]INFN - Istituto Nazionale di Fisica Nucleare, sezione di Napoli, Napoli, Italy, [3]CNR-SPIN Institute for Superconductors, Oxides and other Innovative materials and Devices, Via Cintia, 80134 Napoli, Italy, [4]CNR-IPCB, Institute for Polymers, Composites and Biomaterials, Viale Kennedy, 54 - Mostra d'Oltremare Pad. 20, 80125 Napoli, Italy, and [5]Department of Industrial Engineering, University of Naples Federico II, Naples, Via Claudio 21, 80125 Napoli, Italy

Email:
Massimo Valentino* - massimo.valentino@spin.cnr.it

* Corresponding author

Keywords:
graphene; graphite; IR thermography; micro-Raman spectroscopy; strain sensor

Beilstein J. Nanotechnol. **2017,** *8,* 21–27.
doi:10.3762/bjnano.8.3

Received: 14 July 2016
Accepted: 16 December 2016
Published: 03 January 2017

This article is part of the Thematic Series "Self-assembly of nanostructures and nanomaterials II".

Guest Editor: I. Berbezier

Abstract

In this work we present a novel route to produce a graphene-based film on a polymer substrate. A transparent graphite colloidal suspension was applied to a slat of poly(methyl methacrylate) (PMMA). The good adhesion to the PMMA surface, combined with the shear stress, allows a uniform and continuous spreading of the graphite nanocrystals, resulting in a very uniform graphene multilayer coating on the substrate surface. The fabrication process is simple and yields thin coatings characterized by high optical transparency and large electrical piezoresitivity. Such properties envisage potential applications of this polymer-supported coating for use in strain sensing. The electrical and mechanical properties of these PMMA/graphene coatings were characterized by bending tests. The electrical transport was investigated as a function of the applied stress. The structural and strain properties of the polymer composite material were studied under stress by infrared thermography and micro-Raman spectroscopy.

Introduction

Many materials have been proposed for strain sensing applications including metals, silicon, carbon nanotubes and graphene. The unique thermal, mechanical and electrical properties of graphene [1] have inspired new and appealing applications in different fields. Its exceptional mechanical robustness and ability to withstand elastic strain (up to 25% for tensile in-plane

stretching) make this material interesting for use in advanced technological systems subjected to critical stresses and operating in harsh environments. The large piezoresitivity of graphene is attributed to the charge tunneling mechanism occurring between neighboring platelets, and it critically depends on the composition, density and interconnection properties of the graphene components [2]. Polymers have been used as substrates to support strips of strain sensing components to make a flexible strain gauge. These compounds have received significant interest not only for their high sensibility and tunability, but also for the potential for gauging strain that they offer in several biological systems. A highly stretchable and sensitive strain sensor based on reduced graphene oxide or graphene on polymer were also recently reported [3].

In this work we describe a simple and direct fabrication process based on a new micrographite colloidal suspension to produce thin coatings with large electrical piezoresitivity. When applied to a slat of poly(methyl methacrylate) (PMMA), the adhesion to the PMMA surface, combined with the shear stress, allowed for the uniform and continuous spreading of the graphite nanocrystals on the substrate surface with formation of a very uniform graphene multilayer coating.

The electrical response to the mechanical deformation of a strain sensor is generally quantified by the gauge factor (GF), that is, the ratio of the relative change in electrical resistance, R, to the mechanical strain, ε, namely the GF is given as $\Delta R/(\varepsilon R_0)$, where R_0 is the unstrained resistance. The values of GF for graphene range from 1.9–2.4 [2,3]. The GF has been considerably improved by using instead of single graphene layers, self-assembled arrays of nanostructures based on graphene, such as carbon nanotubes [4,5] or graphene nanoplatelets [6-8]. The values of GF on the order of 100 or larger can be obtained in these systems, approaching and in some cases exceeding the value 200, which constitutes the maximum achievable performance of silicon-based sensors.

The electrical resistance and mechanical properties of the graphene-coated PMMA slat were investigated by current–voltage (I–V) measurements and micro-Raman spectroscopy (μ-RS) during bending tests. Moreover, infrared thermographic technique (IRT) was used to assess the sensitivity of the PMMA/graphene slats to bending deformation.

Experimental

The graphite used for this strain sensor was prepared according to [9,10] as follows. Expandable graphite flakes (Faima S.r.l., Milano, Italy) were subjected to a thermal shock at 750 °C for 3 min in a muffle furnace to produce expanded graphite. The expanded graphite filaments were converted to nanostructured graphite by ultrasonic treatment in acetone, using a horn sonicator (Bandelin Sonopuls, model UW2200, 20 kHz, 200 W, Berlin, Germany). The suspension (800 mL) was sonicated for 30 min in a glass cylindrical beaker at room temperature (the beaker was placed in a refrigeration bath). The final product was a concentrated colloidal suspension (the nanostructured graphite concentration in this paste was ≈33 g/dm^3), which was dried in air at room temperature to give the nanostructured graphite powder. Then a concentrated nanostructured graphite colloid was prepared by accurately dispersing the graphite in ethanol (Sigma-Aldrich, 99.9%) under sonication. The nanostructured graphite colloid was gently rubbed on the surface of a slat of PMMA, by hand, using a low-density polyethylene (LDPE) film to achieve a very uniform coating of the substrate surface. The adhesion to the PMMA surface, combined with the applied shear stress, allowed a uniform and continuous spreading of the graphite nanocrystals on the substrate surface with formation of a very uniform graphene multilayer coating. The obtained PMMA slats coated by this very thin and optically transparent layer of graphene were rinsed in acetone and dried in air at room temperature.

The graphene compound layer on the top of the PMMA surface is clearly visible in the images of Figure 1, obtained by scanning electron microscopy (SEM) of the slat section. A 0.5 μm thick layer drapes over the PMMA surface (Figure 1a). At high magnification, the granular nature of the coating is evinced from the waviness of the slat surface at the neighboring fracture edge (Figure 1b).

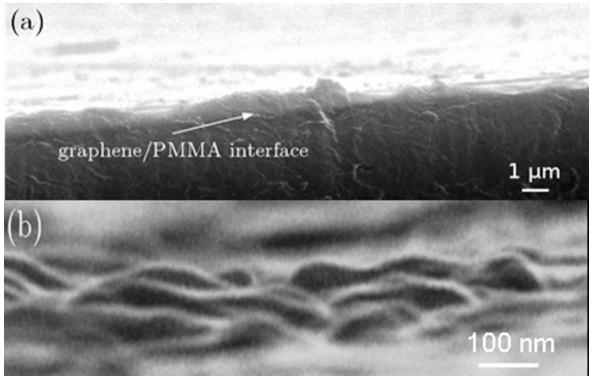

Figure 1: (a) SEM images of the slat section of the graphene/PMMA interface; (b) SEM image of the graphene surface at high magnification.

The bending stress was applied to the sample by tuning a screw located on one side of the specimen as reported in Figure 2. In this way the quasi-static loading was applied perpendicular to the sample surface as a function of bending. A sketch of the sample under test is reported in Figure 2a.

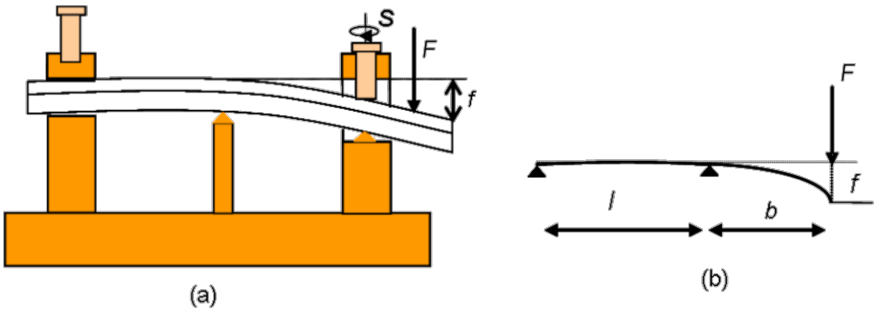

Figure 2: (a) Sketch of the setup used for bending tests; *F* represents the force produced by the screw *S* used to apply the bending stress and *f* is the vertical displacement of the sample surface from the horizontal position. (b) Schematic view of the geometry of the sample under test. The sample dimensions are: 150 × 20 × 3 mm.

An estimate of the applied load during the bending test can been obtained by using the follow relation [11]:

$$F = 3\frac{EI_{cs}}{(b+l)b^2}f, \quad (1)$$

where f is the displacement induced by the applied force F. E is the Young modulus and I_{cs} the moment of inertia of the cross section. The lengths l and b are defined in Figure 2.

In our case a force of 6 N is enough to induce a slat deflection f = 10 mm, that corresponds to the maximum bending of the slat during the experiment. The force F was estimated by assuming E = 3.8 GPa for the Young's modulus value of PMMA [12], and a moment of inertia $I_{cs} = wh^3/12$, where w = 0.02 m and $h = 3 \times 10^{-3}$ m are the width and thickness of PMMA/graphene sample, respectively, and $l = b$ = 75 mm.

The upside surface of the PMMA/graphene material was monitored with an infrared camera (Flir ThermaCam, SC6000), equipped with a quantum well infrared photon detector working in the 8–9 μm infrared band cooled at 70 K by a Stirling cooler, a noise equivalent differential temperature <35 mK, spatial resolution of 640 × 512 pixels (full frame) with pixel size 25 × 25 μm. In the present application, thermal images in time sequence at 60 Hz were collected and after were subjected to postprocessing procedures [13].

Firstly, to account for thermal changes with respect to the ambient temperature, the first image (t = 0) of the sequence (i.e., the temperature of the unloaded specimen surface) was subtracted from each subsequent image in order to determine a map of temperature variations:

$$\Delta T(i,j,t) = T(i,j,t) - T(i,j,0) \quad (2)$$

where i and j are the pixel indices ($1 \le i \le 240$; $1 \le j \le 320$). Therefore, a time sequence of $\Delta T(i,j,t)$ images are created. These images are further analyzed to bring out information on the temperature variations along the specimen surface and to provide structural analysis of the material under investigation. Infrared thermographic tests (IRT) were carried out on the PMMA/graphene coatings and compared to the IRT measurements performed on the various composite polymer-based systems. A sketch of the setup for the thermographic measurements is shown in Figure 3.

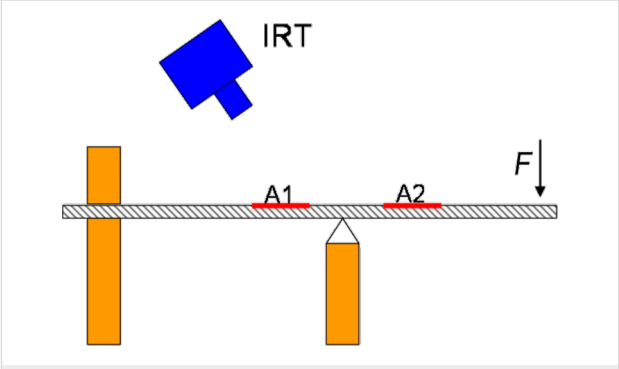

Figure 3: Sketch of the setup used for the thermographic analysis of the PMMA/nanocomposite sample.

The composites under test include: glass-reinforced plastic (GRP), nanocomposites, and PMMA. The nanocomposite sample is made using an epoxy resin EC01 and filled with multi-walled carbon nanotubes (MWCNT) provided by Nanocyl with a purity grade >95% with an average diameter ≈10 nm and an average length of 1.5 μm. Further details on the nanocomposite fabrication are reported elsewhere [14,15]. The electric transport measurements have been carried out under unload and maximum load conditions. For this purpose a two-probe configuration based on a picoammeter (Keithley, 6487) has been used to measure the current−voltage (I–V) curves between the electrodes located on A1 and A2 areas, as shown in Figure 4.

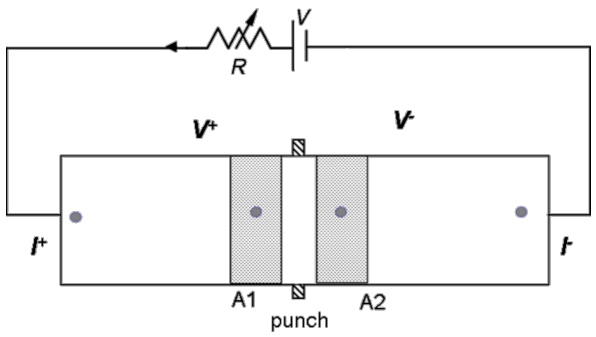

Figure 4: Sketch of the top view of the sample; A1, A2 are the (10 × 10 mm) areas on the sample monitored by the infrared camera during the bending tests. The positions of the voltage (V^+, V^-) and current (I^+, I^-) probes are indicated.

The same setup was used to monitor time changes of the current for $F = 0$ and $F = 6.9$ N. Structural deformation of graphene induced by bending the PMMA slat has been investigated by means of micro-Raman Spectroscopy (μ-RS). The μ-RS measurements were performed by using a Jobin-Yvon system from Horiba ISA, with a TriAx 180 monochromater, equipped with a liquid nitrogen-cooled charge-coupled detector. The grating with 1800 grooves/mm allows for a final spectral resolution of 4 cm^{-1}. The spectra were recorded in air at room temperature using a 17 mW He–Ne ($\lambda = 632.8$ nm) laser source. The laser light was focused to a 10 μm spot size on the samples through an Olympus confocal microscope with a 50× optical objective.

Results and Discussion

During the bending stress cycles between unload and maximum load conditions, the temperature variation on the sample surface is measured by the IRT technique over a surface area of (10 × 10 mm) as illustrated by A1 and A2 in Figure 3. It can be seen that the maximum change in temperature occurs for the area A1 at the edge of the slat where the force is applied. As already observed in previous work [14], the temperature variation correlates well with strain modifications: the increase or decrease in ΔT depends on the sign of strain.

Indeed, using the thermoelastic effect [16,17] under reversible and adiabatic conditions (i.e., in the elastic regime and neglecting heat transfer within the body and to the environment), for isotropic materials, it is possible to relate the temperature change ΔT to the amplitude variation of mean applied stress $\Delta\sigma$ (pressure) by the simple relation $\Delta T = -\Gamma T_\alpha \sigma$ where T is the absolute temperature of the sample, Γ is the material thermoelastic constant, given by $\Gamma = \alpha/\rho c_p$ where α is the thermal expansion coefficient, ρ the density and c_p the specific heat at constant pressure. For graphene we obtain $\Gamma T_\alpha = 0.19$ GPa^{-1} at room temperature ($T_\alpha = 300$ K) using the thermal expansion coefficient $\alpha = -3 \times 10^{-6}$ K^{-1} [18], $\rho = 2.25 \times 10^3$ Kg m^{-3} and $c_p = 2.125 \times 10^3$ $J{\cdot}kg^{-1}{\cdot}K^{-1}$ [19]. The negative sign of the thermal expansion coefficient implies that subjecting the graphene slat to positive dilatation (traction) results in heating whereas a compression gives rise to cooling of the sample. The maximum value of temperature change observed ($\Delta T \approx 0.1$ °C) corresponds to a maximum value of applied stress $\Delta\sigma$ of about 0.53 GPa. Accordingly, we obtain $\Delta\varepsilon/\Delta\sigma \approx 0.28\%$ GPa^{-1} which turns out to be about 0.1% higher than the value reported in [18], probably because of the softening of the PMMA/graphene compound with respect to pure graphene.

In the Figure 5 the maximum temperature variation ΔT for several composites is reported. Here, the different thermal behavior of the new material measured by the IRT technique is shown. The carbon nanotubes (CNTs) can be used as a filler in the polymer composite system to obtain ultralight structural materials (nanocomposites) with enhanced electrical, thermal and optical characteristics. Glass-reinforced plastic (GRP) is used for the realization of the components for use in the automotive and aerospace industry.

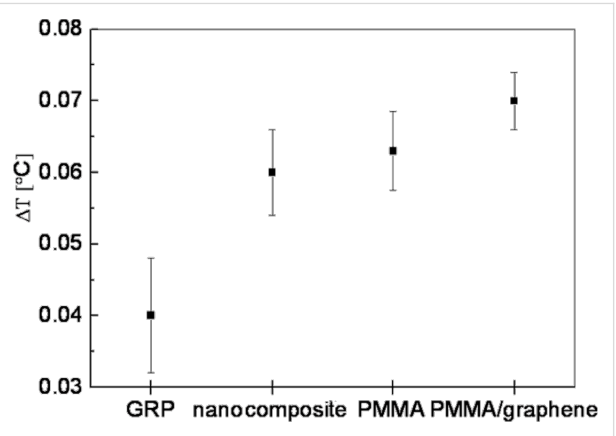

Figure 5: Comparison of the IRT temperature changes. The measurements were performed on various composite materials.

Thermographic measurements were carried out across the area A1 (see Figure 3) in the same experimental conditions as those of PMMA/graphene composite. Noticeably, the change in temperature of the graphene/PMMA sample is higher than that of the other considered functional materials, indicating a larger sensitivity of the graphene-based composite in terms of temperature response to external stimulus. In particular, the graphene-coated PMMA substrate exhibits higher temperature changes compared to that of PMMA substrate alone, and a lower thermal noise, as shown in the Figure 5. It is interesting to stress here that this result is obtained on a graphene/PMMA sample

where the graphene layer is about 1 μm thick. This behavior can be ascribed to the high thermal conductivity of graphene compared to the other materials reported in Figure 5.

The effect of the bending on the electrical properties of the PMMA/graphene compound were investigated by measuring the current–voltage (I–V) using the electrical connection shown Figure 4. The measurement was performed in presence of a voltage of 5 V. Figure 6 reports the results of the current–voltage measurements of the PMMA/graphene sample with and without tensile stress.

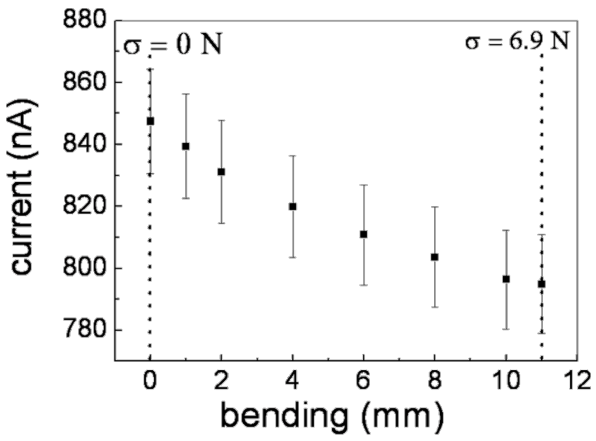

Figure 6: Electrical current variation due to the mechanical stress as measured on a PMMA/graphene sample.

Noteworthy, the graphene/PMMA sample exhibits a good Ohmic behavior with a linear increase in electrical resistance to value of about 0.3 MΩ upon application of load up to F = 6.9 N. The time dependence of the electrical resistance of the PMMA/graphene sample during loading cycles for a fixed voltage bias V = 5 V is shown in Figure 7. The cycle was performed between unload (F = 0) and maximum load (F = 6.9 N) conditions. Even after several cycles between the unload and loaded state, the electrical resistance value show no hysteretic effect, i.e., the PMMA/graphene does not store stress and the maximum load implemented can be considered as a reversible stress condition.

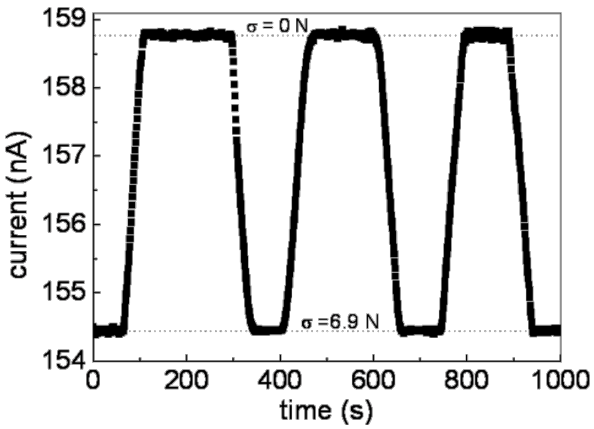

Figure 7: Time dependence of the electrical current for PMMA/graphene. A constant voltage bias V = 5 V is applied to the sample while the applied force varies cyclically between unload (F = 0 N) and load (F = 6.9 N).

In order to evaluate the microscopic effect of applied stress on sample micro-Raman spectroscopy (μ-RS) has been performed in the region A2 (see Figure 4) during the bending test. The Raman spectrum of the PMMA/graphene structure at rest (i.e., without applied force) is displayed in Figure 8. The Raman spectrum exhibits many peaks, mainly due to the presence of

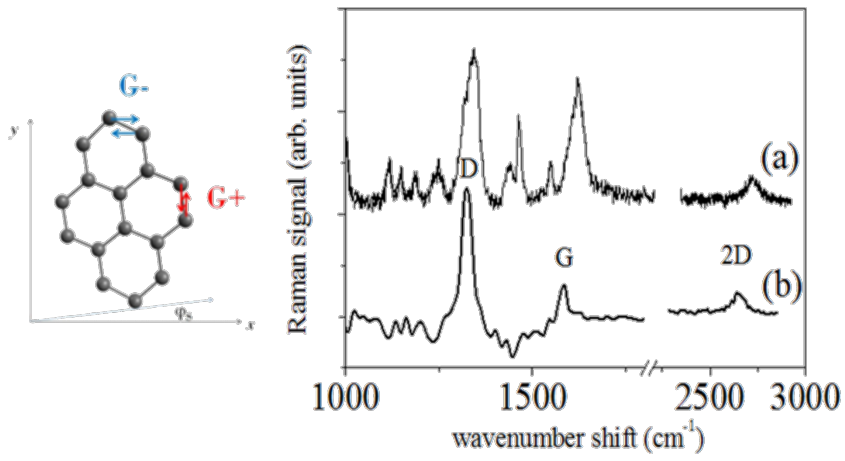

Figure 8: Schematic view of strain induced degenerate vibrational modes E_{2g} shown on the left. The uniaxial strain is directed along the x axis. The graphene lattice is turned with respect to the x axis at angle φ_S. On the right, the Raman spectrum of the PMMA/graphene sample is shown as measured (a) and after subtraction of PMMA Raman components (b).

the polymer substrate. The Raman components due to polymer are removed (Figure 8b) by comparing the data with the spectrum acquired on the bare substrate using a numerical data treatment based on a wavelets algorithm and linear regression [19].

The relative variation of electrical resistance $\Delta R/R_0$ is plotted as a function of the applied strain ε (Figure 9), where the data refer to two sets of bending tests. The strain values measured by μ-RS are consistent with those obtained by the IRT analysis, as their variation range is of the order of 0.15%. Noticeable in Figure 9 is that a significant strain, on the order of 0.45%, affects the graphene lattice for the equilibrium position of the slat (no bending) due to intramolecular forces occurring between graphene and PMMA substrate. The GF results were on the order of 40– 50. Note that this value is too high to account for the observed resistance change solely in terms of electronic modifications of the graphene itself [3].

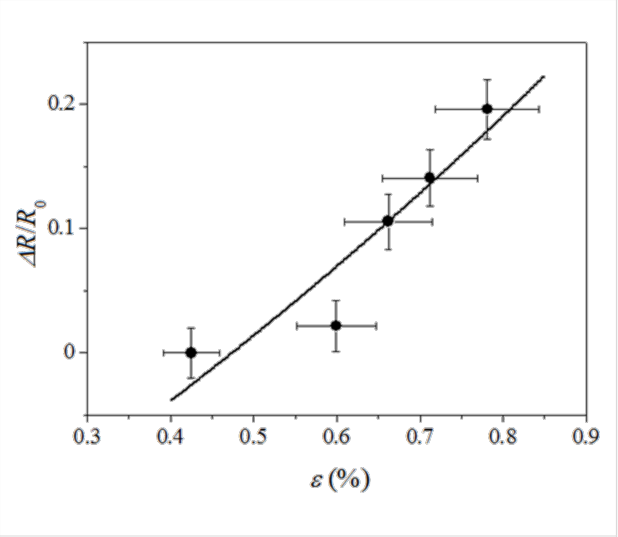

Figure 9: Dependence of the normalized electric resistance variation $\Delta R/R_0$ on strain ε. The bars indicate the relative measurement error estimated at 1% and 8% for ε and $\Delta R/R_0$, respectively. The solid line shows the best fit to the experimental data as calculated from the theoretical prediction given by Equation 3 with τ = 53 ± 11.

An intergrain electrical transport mechanism should be taken into account, yielding a dependence of the conductivity on the configuration of overlap area and contact resistance of the platelets. The graphene-based layer can be considered as a granular system consisting of metal grains embedded in an insulating matrix and its electrical conduction properties can be described assuming a simple electron hopping mechanism [20]. In this case the dependence of the electrical resistance on the strain can be expressed by the simple relation:

$$\frac{\Delta R}{R_0} = \frac{1-\tau\varepsilon_0+\varepsilon}{1-\tau\varepsilon_0}\left(\mathrm{e}^{\tau(\varepsilon-\varepsilon_0)}-1\right), \tag{3}$$

where τ is a parameter proportional to the tunnel barrier depth, d, between graphene platelets, R_0 is the value of the electric resistance in unstrained conditions and ε_0 is the residual strain occurring in the unload sample when resistivity value R_0 is measured.

The data reported in Figure 9 have been fit with Equation 3 using τ as the fit parameter, resulting in τ = 53 ± 11. The parameter τ is proportional to the square root of the actual energy barrier E_c between grains, which can be approximated by the energy of an electron transfer between a charged platelet to a neutral one as:

$$\tau = 2\pi\frac{(2mE_c)^{1/2}}{\hbar}d, \tag{4}$$

where $\hbar$ is the Plank constant and the energy barrier E_c is given by

$$E_c = \frac{\mathrm{e}^2}{\varepsilon(d+s)}, \tag{5}$$

where the average grain size is s and ε is the effective relative dielectric constant of the layer. The value of τ found by the fitting procedure implies that for $E_c \approx 100$ meV, an intergrain distance d of few nanometers is found, consistently with the adopted model.

From Equation 3, and taking into account the definition of gauge factor, it can be easily see that the GF is approximately 50. Due to this value of the GF, we can conclude that in a microscopic level, a large value of the intergrain separation distance results in improving the sensitivity of the polymer/graphene supported strain sensor.

Conclusion

In this work we have described a simple fabrication process to produce a low-cost graphene film on a PMMA substrate. The process makes use of the direct application of a nanostructured graphite colloidal suspension to a PMMA slat. Bending tests have been performed on this structure in order to study its piezoelectric response. Electrical, infrared thermography and micro-Raman spectroscopy have been carried out in order to investigate the behavior of the composite system as a local strain sensor. The experiments demonstrated the high piezoresitivity of the system. The electrical resistance changes with applied stress with a gauge factor on the order of 50. The electrical features are consistent with an intergrain electrical transport mechanism among graphene platelets undergoing strain solicitations.

The tensile strain of the PMMA/graphene structure during the bending test was confirmed by IRT and μ-RS measurements. The strain magnitude was evaluated by the wavenumber split of the Raman G-mode. The system was modelled as a granular system consisting of metal grains (nanoplatelets) embedded in an insulating matrix and its electrical conduction properties were analyzed within the framework of a simple electron hopping mechanism. The high sensitivity in addition to high stability of the graphene/PMMA structure and the high thermal sensitivity in the infrared wavelength region are interesting aspects that enable us to propose this polymer/graphene supported coating as a new kind of stress sensor useful for applications in different fields from civil, to automotive and aerospace engineering.

Acknowledgements

The work presented in this article was supported by the Project Campus SIHM Control and Health Monitoring and Management CUP B27112000080007.

References

1. Geim, A. K.; Novoselov, K. S. *Nat. Mater.* **2007,** *6,* 183–191. doi:10.1038/nmat1849
2. Zhao, J.; He, C.; Yang, R.; Shi, Z.; Cheng, M.; Yang, W.; Xie, G.; Wang, D.; Shi, D.; Zhang, G. *Appl. Phys. Lett.* **2012,** *101,* 063112. doi:10.1063/1.4742331
3. Tang, Y.; Zhao, Z.; Hu, H.; Liu, Y.; Wang, X.; Zhou, S.; Qiu, J. *ACS Appl. Mater. Interfaces* **2015,** *7,* 27432–27439. doi:10.1021/acsami.5b09314
4. Bonavolontà, C.; Valentino, M.; Meola, C.; Carlomagno, G. M. *Int. J. Appl. Electromagn. Mech.* **2012,** *39,* 363–368. doi:10.3233/JAE-2012-1483
5. Grow, R. J.; Wang, Q.; Cao, J.; Wang, D.; Dai, H. *Appl. Phys. Lett.* **2005,** *86,* 093104. doi:10.1063/1.1872221
6. Li, X.; Zhang, R.; Yu, W.; Wang, K.; Wei, J.; Wu, D.; Cao, A.; Li, Z.; Cheng, Y.; Zheng, Q.; Ruoff, R. S.; Zhu, H. *Sci. Rep.* **2012,** *2,* 870. doi:10.1038/srep00870
7. Raju, A. P. A.; Lewis, A.; Derby, B.; Young, R. J.; Kinloch, I. A.; Zan, R.; Novoselov, K. S. *Adv. Funct. Mater.* **2014,** *24,* 2865–2874. doi:10.1002/adfm.201302869
8. Carotenuto, G.; Nicolais, L. Graphene-Polymer Composite. In *Wiley Encyclopedia of Composites;* Nicolais, L.; Borzacchiello, A.; Lee, S. M., Eds.; John Wiley and Sons, 2012; Vol. 2, p 1232. doi:10.1002/9781118097298.weoc103
9. Palomba, M.; Salvatore, M.; Carotenuto, G.; Coscia, U.; Ambrosone, G.; De Nicola, S. Polymer-supported graphene obtained by a micromechanical tecnique based on shear-stress. In *Proceedings of the 15th IEEE International Conference on Nanotechnology,* IEEE-NANO 2015, Rome, Italy, July 27–30, 2015; pp 485–488. doi:10.1109/nano.2015.7388644
10. Carotenuto, G.; Longo, A.; De Nicola, S.; Camerlingo, C.; Nicolais, L. *Nanoscale Res. Lett.* **2013,** *8,* 403. doi:10.1186/1556-276X-8-403
11. Meola, C.; Carlomagno, G. M.; Bonavolontà, C.; Valentino, M. *Adv. Opt. Technol.* **2012,** 720813. doi:10.1155/2012/720813
12. Salamone, J. C., Ed. *Polymeric Materials Encyclopedia;* CRC Press, Inc.: Boca Raton, FL, USA, 1996; Vol. 12.
13. Boccardi, S.; Carlomagno, G. M.; Bonavolontà, C.; Valentino, M.; Meola, C. Infrared thermography to monitor Glare under cyclic bending tests with correction of camera noise. In *Proceedings of QIRT 2014,* Bordeaux, France, July 7–11, 2014; pp 215 ff.
14. Bonavolontà, C.; Valentino, M.; Meola, C.; Carlomagno, G. M.; Volponi, R.; Rosca, I. D. *Supercond. Sci. Technol.* **2009,** *22,* 095001. doi:10.1088/0953-2048/22/9/095001
15. Bonavolontà, C.; Valentino, M.; Pepe, G. P. *Supercond. Sci. Technol.* **2007,** *20,* 51. doi:10.1088/0953-2048/20/1/009
16. Thomson, W. *Philos. Mag. (1798-1977)* **1878,** *5,* 4–27.
17. Biot, M. A. *J. Appl. Phys.* **1956,** *27,* 240–253. doi:10.1063/1.1722351
18. Shao, T.; Wen, B.; Melnik, R.; Yao, S.; Kawazoe, Y.; Tian, Y. *J. Chem. Phys.* **2012,** *137,* 194901. doi:10.1063/1.4766203
19. Pop, E.; Varshney, V.; Roy, A. K. *MRS Bull.* **2012,** *37,* 1273–1281. doi:10.1557/mrs.2012.203
20. Németh, R.; Mühlschlegel, B. *Z. Phys. B: Condens. Matter* **1988,** *70,* 159–162. doi:10.1007/BF01318293

License and Terms

BEILSTEIN JOURNAL OF NANOTECHNOLOGY

Surface-enhanced Raman scattering of self-assembled thiol monolayers and supported lipid membranes on thin anodic porous alumina

Marco Salerno*[1], Amirreza Shayganpour[1,2], Barbara Salis[1,2] and Silvia Dante[1]

Full Research Paper

Open Access

Address:
[1]Department of Nanophysics, Istituto Italiano di Tecnologia, via Morego 30, I-16163 Genova, Italy and [2]Department of Bioengineering and Robotics, University of Genova, viale Causa 13, I-16145 Genova, Italy

Email:
Marco Salerno* - marco.salerno@iit.it

* Corresponding author

Keywords:
anodic porous alumina; SERS; nanopores; supported lipid bilayers; thiols

Beilstein J. Nanotechnol. **2017,** *8,* 74–81.
doi:10.3762/bjnano.8.8

Received: 15 July 2016
Accepted: 12 December 2016
Published: 09 January 2017

This article is part of the Thematic Series "Self-assembly of nanostructures and nanomaterials II".

Guest Editor: I. Berbezier

Abstract

Thin anodic porous alumina (tAPA) was fabricated from a 500 nm thick aluminum (Al) layer coated on silicon wafers, through single-step anodization performed in a Teflon electrochemical cell in 0.4 M aqueous phosphoric acid at 110 V. Post-fabrication etching in the same acid allowed obtaining tAPA surfaces with ≈160 nm pore diameter and ≈80 nm corresponding wall thickness to be prepared. The tAPA surfaces were made SERS-active by coating with a thin (≈25 nm) gold (Au) layer. The as obtained tAPA–Au substrates were incubated first with different thiols, namely mercaptobenzoic acid (MbA) and aminothiol (AT), and then with phospholipid vesicles of different composition to form a supported lipid bilayer (SLB). At each step, the SERS substrate functionality was assessed, demonstrating acceptable enhancement (≥100×). The chemisorption of thiols during the first step and the formation of SLB from the vesicles during the second step, were independently monitored by using a quartz crystal microbalance with dissipation monitoring (QCM-D) technique. The SLB membranes represent a simplified model system of the living cells membranes, which makes the successful observation of SERS on these films promising in view of the use of tAPA–Au substrates as a platform for the development of surface-enhanced Raman spectroscopy (SERS) biosensors on living cells. In the future, these tAPA–Au-SLB substrates will be investigated also for drug delivery of bioactive agents from the APA pores.

Introduction

Anodic porous alumina (APA) is a layered material usually obtained in thick form (≈10 µm thickness scale) from electrochemical anodization in the acidic aqueous electrolyte of aluminum (Al) foils [1]. In APA, the control of pore size, pore density and porosity is achieved by changing the anodization voltage during the fabrication and the etching parameters during the post-fabrication treatment [2]. It is widely recognized that the APA surface is biocompatible with practically all cell types and

provides a means of controlling the surface roughness [3,4], the latter of which can play an important role in the adhesion and proliferation of cells [5-7]. The self-ordered nano-structured APA, also demonstrated recently as a possible nanolithographic mask [8,9] and for chemical sensors and biosensors [10], after coating with noble metals can be used for plasmonics-based enhanced spectroscopy such as in surface-enhanced Raman spectroscopy (SERS) [11-14].

In recent years, the thin form of APA (tAPA), resulting from anodization of Al films of less than 1 μm thickness, has been increasingly used because it can be better integrated into applications involving optical microscopy inspection, which requires flat planar substrates. Moreover, it allows to move toward a more robust engineering of APA surfaces by exploiting the standard microtechnology of photolithography, thereby paving the way to large scale fabrication in possible future devices.

The enhancement factor in APA-based SERS can be as high as 1000, which means that the technique may detect molecules [15]. Additionally, the pores in tAPA can potentially serve as nano-wells for localized drug delivery [16,17]. In fact, while lower in loading capacity with respect to thick APA [18], 500 nm tAPA can still allocate a significant amount of bioactive compounds, representing a trade-off between the former case of maximized loading and the case of ultra-thin APA showing the highest SERS enhancement [19]. Finally, the controlled roughness of APA could also improve the physisorption of coating layers of functional materials [20,21].

The main component of the biological membrane that separates and protects the interior of all living cells from the outside environment is a phospholipid bilayer. For this reason, as well as for the complexity of real samples of living cells, we decided to test the tAPA–Au SERS-active substrates on SLBs in phosphate-buffered saline (PBS) buffer solution, which provide an excellent model system to mimic the native cellular membranes [22].

In the present work, the fabrication and modification of tAPA aiming at its exploitation as a functional substrate for biosensing based on SERS effect are presented. In particular, it is reported on SERS effect on SLBs obtained from spontaneous lipid vesicle fusion and representing a simplified model of living cells membrane. Since the vesicle fusion is not trivial to achieve on Au surfaces, we first functionalized the Au with self-assembled monolayers (SAM) of thiols, to provide the appropriate surface condition to allow SLB formation. SERS effect was tested and proved for each fabrication step of the system.

Experimental

tAPA fabrication and modification to achieve SERS-activity

An ≈500 nm thick Al layer was first coated on a silicon wafer by an electron-beam evaporation system PVD75 (Kurt J. Lesker Ltd., UK) working at a base pressure of 10^{-6} Torr with a deposition rate of 0.5–1 Å/s. tAPA was fabricated in a single-step (≈15 min) anodization performed at 110 V in 0.4 M phosphoric acid electrolyte at a bath temperature of ≈15 °C. Post-fabrication etching in the same electrolyte for 20 min at room temperature (RT) plus 15 min at 35 °C allowed to obtain tAPA with ≈160 nm pore size and ≈80 nm wall thickness. After thoroughly rinsing with de-ionized water, blowing dry with nitrogen and dehydrating on a hotplate set at 100 °C for 15 min, the tAPA was overcoated by the same electron-beam evaporation system with a ≈25 nm thick Au layer to make it SERS-active. More details on similar fabrication procedure can be found in references [12,13].

The characteristic size of tAPA pores was obtained by scanning electron microscope (SEM) imaging with a JSM-7500F (Jeol, Japan) and subsequent grain analysis carried out with Igor 6.22 (Wavemetrics, OR, USA).

Incubation of thiols and fabrication of lipid vesicles

Different thiols were used in combination with the different lipids to be coated onto them by electrostatically-driven physisorption. We used two thiols, namely 4-mercaptobenzoic acid (MbA) and 11-amino-1-undecanethiol hydrochloride (AT), from Sigma (Milan, Italy), and three lipids, namely 1-palmitoyl-2-oleoyl-*sn*-glycero-3-phosphocholine (POPC), 1-palmitoyl-2-oleoyl-*sn*-glycero-3-phospho-L-serine (POPS) and, 1,2-dioleoyl-3-trimethylammoniumpropane (DOTAP), from Avanti Polar Lipids (Alabaster, Alabama, US). All solvents were purchased from Sigma-Aldrich.

First, the substrates were incubated at rt for 2 h with a 1 mM aqueous solution of the thiol molecule, either MbA or AT, to let the sulfur of the –SH group bind covalently to the Au surface (chemisorption). The substrates were then gently washed with their aqueous solutions and dried under nitrogen flow.

All the lipids were dissolved in chloroform/methanol 2:1 vol/vol, dried under a gentle nitrogen flux in a test tube, and put under a mild vacuum overnight to remove all solvent traces. POPC/POPS in a 9:1 mol/mol ratio and DOTAP were then re-suspended in PBS at a 5 g/L concentration, let to swell for 30 min, and extruded 11 times through a polycarbonate filter (Whatman, USA) with 100 nm pore diameter to form unilamellar vesicles.

Preparation of the Raman target analytes: SLBs

The lipid vesicles were diluted to 0.5 g/L in the PBS buffer and vortexed immediately before use. The thiol SAM was incubated overnight with the lipid vesicle dispersion, to allow vesicle physisorption and fusion onto the substrate. The following day the samples were carefully washed with PBS three times to remove the exceeding vesicles.

For the cationic lipids (namely DOTAP), we used a thiolated molecule that presents a positively charged group at its end. This is MbA, whose COOH group is protonated in PBS buffer to COO^-. For the anionic lipid mixture (namely POPC/POPS) AT was used, which becomes positive in aqueous solution because of the terminal amino group.

SERS measurements

SERS measurements were performed with a micro-Raman spectrometer inVia (Renishaw, UK) equipped with the software program WiRE 3.2. We used for excitation a laser with 785 nm wavelength and 100 mW power, equipped for dispersion with a grating with 1200 grooves/mm. For detection microscope objectives with a magnification of 50× (NA: 0.75) and 60× (water immersion, NA: 1.0) were used. The spectra were collected in the 300–3200 cm^{-1} spectral range.

The SERS enhancement factor G achieved by employing tAPA–Au with respect to the flat Au on silicon substrate can be estimated by using a simple formula:

$$G = \frac{P_{\mathrm{Ref}}\ t_{\mathrm{Ref}}}{P_{\mathrm{SERS}}\ t_{\mathrm{SERS}}} \times \frac{A_{\mathrm{Ref}}}{A_{\mathrm{SERS}}} \times \frac{I_{\mathrm{SERS}}}{I_{\mathrm{Ref}}}. \qquad (1)$$

where P, t, A and I are laser power, accumulation time, active area for molecule adsorption and Raman intensity of the specific band, respectively [13]. The subscripts, SERS and Ref, indicate SERS and Raman measurements on tAPA–Au and on flat Au substrates, respectively.

QCM-D characterization of adsorption

A quartz microbalance Z500 (KSV Instruments, Finland) was used for the QCM-D experiments. Au coated AT-cut quartz crystals (QSense, Sweden) with a 5 MHz fundamental resonance frequency were used. Before each experiment, the quartz sensor was first cleaned in a UV/Ozone ProCleaner (BioForce Nanoscience, US) for 10 min, then washed with milli-Q (18.2 MΩ·cm resistivity) water, dried under nitrogen flux and cleaned again for 10 min in the ozone cleaner.

The sensor was then mounted in the measurement chamber. The chamber was filled with proper buffer (aqueous solution for thiols, PBS for DOTAP vesicles and milli-Q water for POPC/POPS vesicles), and left to reach an equilibrium (≈30 min) before injecting the solution of interest. 3 mL of solution (1 mM thiols in aqueous solution, and a concentration of 0.25 g/L for both DOTAP in PBS and POPC/POPS in milli-Q) where then injected in the measurement chamber and left until the adsorption process reached an end (overnight measurement for thiols, 2 h for vesicles). The sensor was then rinsed with the proper buffer solution. If not stated otherwise, changes in frequency and dissipation of the seventh overtone (35 MHz) are shown; all experiments were carried out at a temperature of 22 °C.

Results and Discussion

SERS-active tAPA–Au substrates

The control of the geometrical features of nanostructured substrates is of critical importance in SERS [23]. The SEM images reported in Figure 1 show the good control achieved in both mean pore size and its dispersion and prove the long range uniformity of the surfaces with the Au coating to make it plasmonic-active.

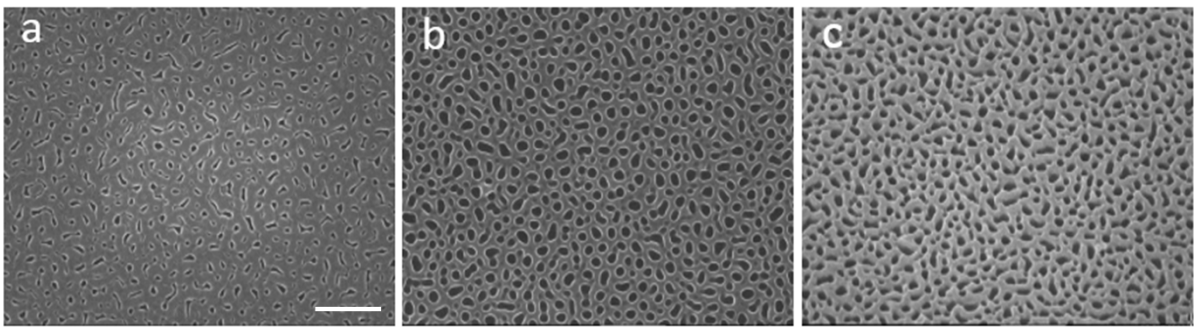

Figure 1: SEM images (20,000× magnification, scale bar 1 μm) of tAPA substrates (thickness ≈500 nm), a) as-prepared, b) after pore widening, and c) after 25 nm Au coating.

tAPA–Au substrates could possibly be used as a carrier layer for local drug delivery [24], as a substrate for living cell cultures thanks to its controlled porosity [3-7], and for SERS [25]. However, since SERS is a surface-only effect, this sensitive detection will be limited to the top of the tAPA–Au substrates, i.e., to the bottom of the living cells, where they would adhere to the nanoporous substrate.

SERS enhancement due to tAPA–Au on thiols, lipids, and thiol–lipid systems

The Raman measurements were performed first on the thiol molecules. We started from the raw materials, in powder form, to obtain reference spectra for future comparison and best identification of the typical bands. Then, we measured the Raman scattering of the thiols adsorbed to flat Au substrates. For technical reasons of SLBs assembly, the two thiols selected, MbA and AT, in ethanol and PBS solutions have a negatively or positively charged group, respectively.

The spectra of the thiols powder on flat Au, along with the respective molecular structures, are shown in Figure 2a. In Figure 2b the spectra of the SAM of the same thiols obtained after incubation on flat Au from 1 mM water solution for 2 h at RT are shown. The subsequent step was the deposition of the thiol molecules for the formation of SAM onto tAPA–Au and the observation of the respective spectra. The nanopores in the oxide under the Au, which are replicated by the top Au surface thanks to the low Au thickness of ≈25 nm, allowed for SERS effect. In Figure 2c we report the typical Raman spectra obtained on tAPA–Au for both MbA and AT.

The spectra of each thiol in all forms (pristine powder and film adsorbed onto the flat Au and tAPA–Au substrate) look similar. MbA present two major peaks at ≈1593 and ≈1076 cm^{-1}, which can be ascribed to aromatic ring vibrations, and also at ≈1181 and at ≈1290 cm^{-1}, which belong to C–H mode [26-28]. AT presents the major peaks at ≈1434 and ≈1477 cm^{-1} assigned to the C–H and at ≈1074 cm^{-1} assigned to the N–H, while the peak at ≈1074 cm^{-1} belongs to the C–C stretching.

In Supporting Information File 1, Figure S1 again the Raman spectra of both thiol SAMs, coupled according to the same thiol

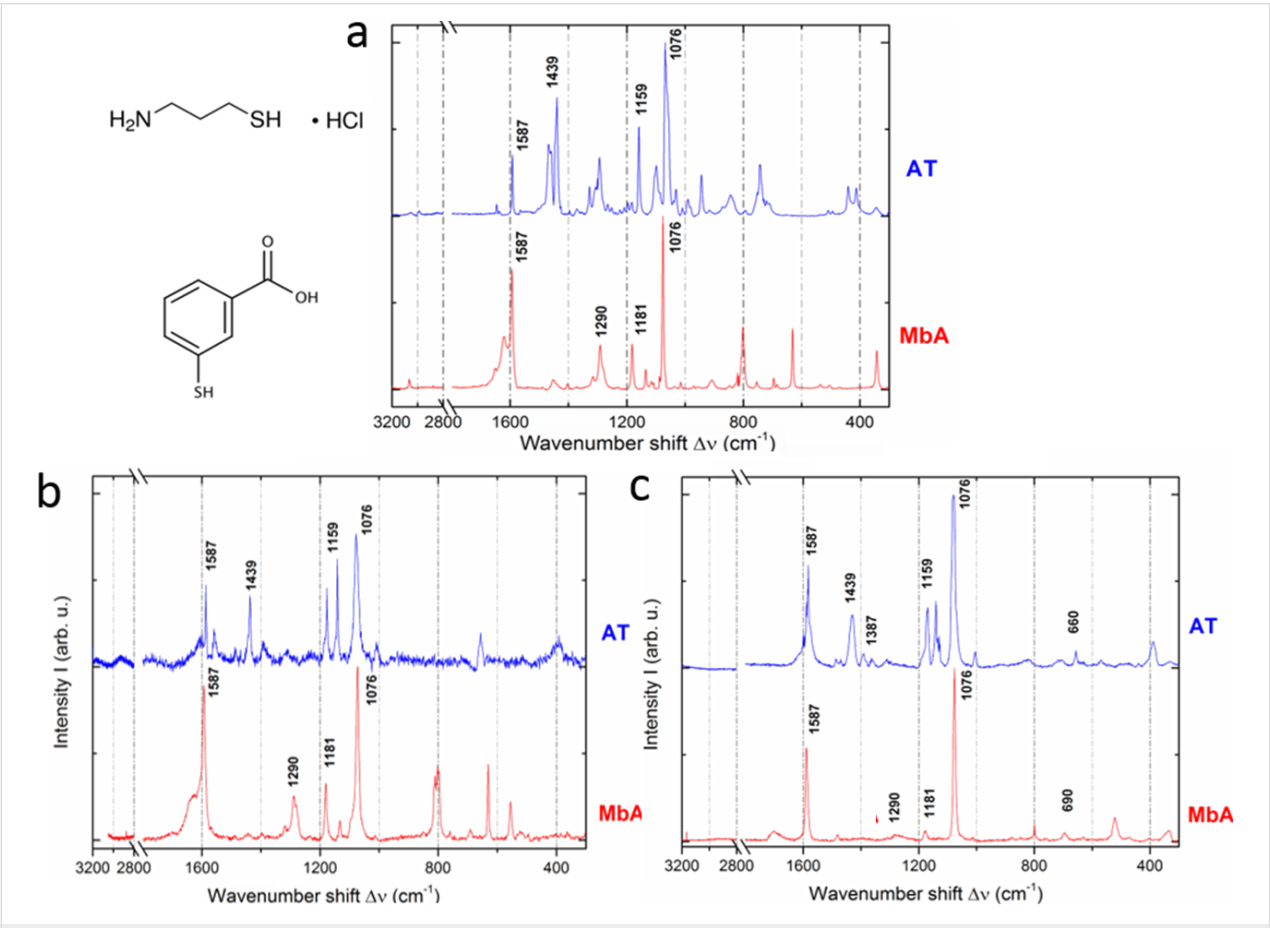

Figure 2: Raman spectra of thiols a) in powder form (with their molecular structures); b) in flat film form, after adsorption to the flat Au substrates from water solution; c) in film form on tAPA–Au.

deposited on the different substrates of flat Au and tAPA–Au, are presented, for easier visualization of the substrate effect. It appears clearly that on tAPA–Au the major characteristic peaks of both MbA and AT are highly enhanced. Taking into account the measurement parameters (i.e., t_{Ref} and t_{SERS} both 10 s, while P_{Ref} and P_{SERS} are 100 and 1, respectively), a G factor of approximately 600 and 1000 was calculated for MbA and AT, respectively. The SERS effect of the nanophotonic tAPA structure, after coating with Au and thus thanks to the localized surface plasmon resonances of this thin film, emerges. The same effect may also be used on the SLBs, at the later stage of the model system fabrication.

For the selected lipids, we first tested the Raman spectra of the powders and then of the SLB form, on both the flat Au and nanoporous tAPA–Au. The molecular structure and Raman spectra of lipids in powder form are shown in Figure 3.

The molecules of choice, i.e., POPC and POPS, are two glycerophospholipids largely present in real cellular membranes. In particular, we prepared a mixture of POPC and POPS suspended in PBS with the molar ratio of 8:2, in order to resemble the plasma membrane composition both for charge and acyl chain length and unsaturation grade. However, the reason for the choice of DOTAP is technical, associated with the fabrication of artificial bilayer membranes [29,30].

The lipids are larger molecules than the thiols and present richer spectra, at least in the powder form. The main features in their Raman spectra depend on the hydrocarbon chain, and can be ascribed to scissoring and twisting of CH_2 and CH_3 and to stretching of C–C and C–H. More precisely, the bands identified in the higher wavenumber region appear at 3007 cm^{-1} (unsaturated =CH stretching), 2882 cm^{-1} (CH_2 Fermi resonance) and 2847 cm^{-1} (CH_2 symmetric stretching). The middle wavenumber region presents bands at 1737 cm^{-1} (C=O ester stretching), 1657 cm^{-1} (C=C stretching), 1442 cm^{-1} (CH_2 scissoring), 1300 cm^{-1} (CH_2 twisting) and 1267 cm^{-1} (=C–H in-plane deformation). In the lower wavenumber region, the C–C stretching emerges as a broad band around 1090 cm^{-1}. In particular, two contributions at 1065 and 1089 cm^{-1} appear with a shoulder at 1125 cm^{-1}. Additional bands appear at 719 and 876 cm^{-1} that are ascribed to the symmetric and asymmetric stretching of choline $N^+(CH_3)_3$, respectively [31,32].

The lipids were further investigated on tAPA–Au substrates, for the possible occurrence of SERS. Figure 4 shows Raman spectra for three mixtures of lipids in SLBs form, on both flat Au and tAPA–Au.

From the comparison of the spectra of lipids in SLBs form versus those in powder form, the most interesting difference observed is that in the films several peaks disappear or are weaker. Whereas some form of quenching can't be excluded, this is probably due to light polarization constraints in the ordered geometry of the molecular film, where not all modes of chemical groups may be excited, as it can be instead in the assembly of randomly oriented microcrystals of the powders [33].

It appears that on tAPA–Au as compared to flat Au the characteristic thiol peaks are still present and enhanced. As a consequence, for MbA the major peaks at ≈1590 and ≈1080 cm^{-1}, ascribed to aromatic ring vibrations, and ≈1181 cm^{-1}, ascribed to C–H deformation, appear. Also AT presents the major peaks

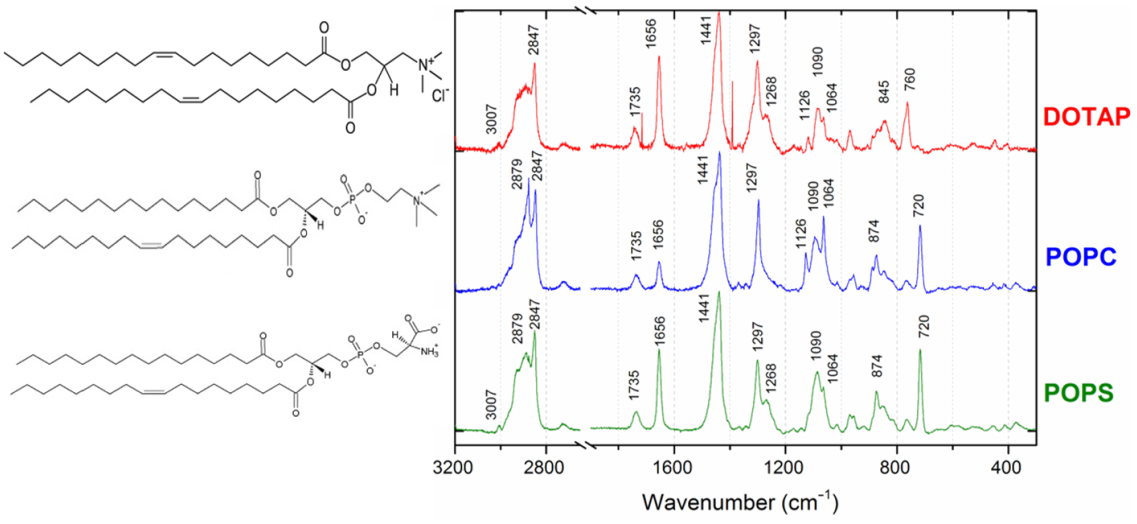

Figure 3: Raman spectra of lipids in powder form on flat Au substrates, with their molecular structures.

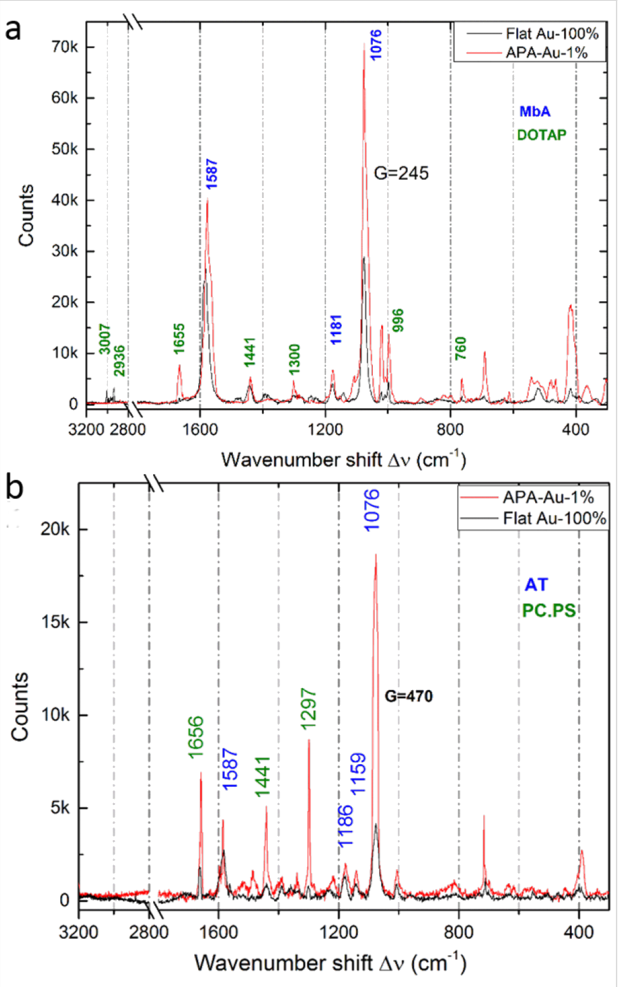

Figure 4: Raman spectra of the thiol-SLB systems on both flat Au and tAPA–Au: a) MbA and DOTAP, b) AT and POPC/POPS blend.

at ≈1580, ≈1159 and ≈1074 cm^{-1}, due to C–NH, N–H wagging and C–C stretching mode, respectively.

Additionally, in Figure 4 we have bands from the lipids, namely ≈1656 cm^{-1} (C=C stretching), ≈1440 cm^{-1} (CH_2 scissoring), ≈1300 cm^{-1} (CH_2 twisting), ≈1267 cm^{-1} (=C–H in-plane deformation), and ≈719 cm^{-1} (choline) [34].

The values of enhancement G due to the tAPA–Au nanostructured substrates have been calculated according to Equation 1. Since the peaks on tAPA–Au are 2–4 times higher in the presence of 100 times lower laser power, a G of ≈250 at ≈1076 cm^{-1} and 500 at ≈1076 cm^{-1} is obtained for the thiol–lipid system of MbA–DOTAP and AT–POPC/POPS, respectively.

QCM-D measurements

The lipid adsorption process on Au was independently monitored by QCM-D technique. This method allows the quantification of the adsorbed mass onto the surface of a vibrating Au-coated quartz electrode through the measurement of the mass-induced frequency shift. Additionally, the measurement of the dissipation gives indication about the viscoelastic properties of the adsorbed layer. The quartz–Au substrate was thus used as a control for success of the incubation of the tAPA–Au substrates in the lipid dispersion. In a preliminary step (data not shown) we have monitored the chemisorption of thiols onto the Au-coated QCM-D sensors; the functionalized sensors where then exposed to the lipid vesicles and the process of adsorption was monitored.

The QCM-D time-evolution profiles presented in Figure 5a,b show that the lipids successfully adsorbed to the Au surface of quartz in both cases. However, the two lipid systems behave differently. For DOTAP on MbA (Figure 5a) one can observe a big shift in frequency ($\Delta f \approx -1135$ Hz) and a high value of dissipation ($D \approx 40 \times 10^{-6}$), indicating the adsorption on the sensor's surface of a viscoelastic structure [35]. DOTAP vesicles do not fuse on Au functionalized with MbA, rather entire vesicles are adsorbed instead. On the contrary, for POPC/POPS on AT (Figure 5b) the frequency shift is low ($\Delta f \approx -157$ Hz for the reported 7th harmonic) and the value of dissipation is close to zero, indicating the adsorption of a smaller mass with more rigid structure on the surface. The reason may be that the POPC/POPS vesicles rupture in contact with the AT-functionalized Au and an SLB forms on the surface [36,37]. Table 1 shows the thickness values of SAM and adsorbed layers obtained with the QCM software. The values have been retrieved by using the Sauerbrey model of rigid layers for the SLBs and the Voigt model of viscoelastic layers for the adsorbed vesicles, assuming for the material densities the following values: $\rho_{AT} = 0.9$ g/cm^3 for AT, $\rho_{MbA} = 1.34$ g/cm^3 for MbA, and $\rho_v = 1$ g/cm^3 for vesicles (made mostly of water), according to references [38,39]. The data confirm that DOTAP vesicles adsorb on the sensor without rupturing, with a thickness of the adsorbed layer of ≈90 nm. POPC/POPS vesicles create an SLB on the sensor with a thickness of ≈4 nm. When the formation of an SLB occurs, the fingerprint region is not visible. As already pointed out in Figure 4, we ascribe this effect to the orientation of the molecules and the polarization of the incoming beam. When vesicles are adsorbed on the surface, all the characteristic peaks of the lipid molecules are expected from the Raman spectra, since the vesicles contain all molecular orientations. In accordance to this, the Raman spectra of DOTAP collected from QCM sensor show a signal in the lipid fingerprint region which is different from the spectra collected on the Au–tAPA surface that are flat in the 2800–3000 cm^{-1} region. This indicates that the porosity of the substrate may influence the vesicle fusion process. This finding is still under further investigation.

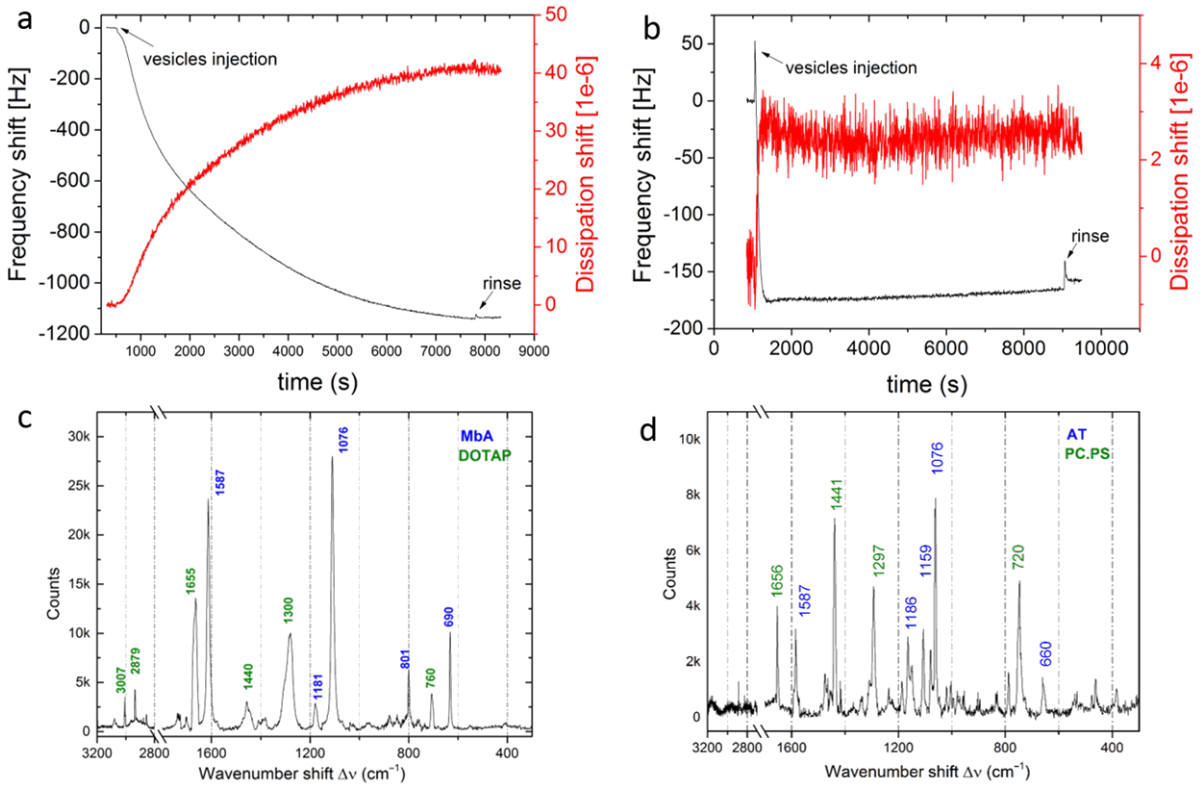

Figure 5: a,b) QCM-D measurements of shift in frequency and dissipation of a) DOTAP on MbA substrate, and b) POPC/POPS on AT substrate; c,d) respective Raman spectra on QCM sensors coated with c) MbA and DOTAP, and d) AT and POPC/POPS blend.

Table 1: Shift in frequency Δ*f* and shift in dissipation *D* and relative standard deviations of the layers adsorbed on the QCM sensor's surface. Every experiment was repeated three times.

Solution	*d* [nm]	std dev [nm]	Δ*f* [Hz]	std dev [Hz]	*D* [10^{-6}]	std dev [10^{-6}]
POPC/POPS (milli-Q) AT	3.9	0.1	−92	14	1.5	0.4
DOTAP (PBS) MbA	96	3.5	−1054	19.4	41.5	0.2

In Supporting Information File, Figure S1 the spectra of both lipids are presented again, grouped according to the different types of substrates, which makes it possible to compare the effect of the substrate on the resulting spectra.

Conclusion

We successfully fabricated tAPA substrates on silicon wafer through anodization of ≈500 nm thickness and post-production etching, resulting in oxide films with pores of ≈160 nm size and ≈80 nm wall thickness. After coating with a ≈25 nm Au layer covering the tAPA features, our substrates become SERS-active and allow for an investigation of the chemical vibrations of molecules, as demonstrated by sensitive Raman measurements on bare thiols and on their combinations with lipid membranes, namely MbA with DOTAP and AT with POPC/POPS. The enhancement factor was estimated to be 500 to 1000 on tAPA–Au with respect to the flat Au surface and to the silicon substrate. The chemisorption of thiols and lipids was confirmed on quartz-Au by QCM-D technique. The present results point to the possible future use of the tAPA–Au surfaces as disposable substrates for assessing the cell functionality in biosensors/bioassays.

Supporting Information

Supporting Information File 1

Additional figures.
[http://www.beilstein-journals.org/bjnano/content/supplementary/2190-4286-8-8-S1.pdf]

References

1. Diggle, J. W.; Downie, T. C.; Goulding, C. W. *Chem. Rev.* **1969,** *69,* 365–405. doi:10.1021/cr60259a005
2. Sulka, G. D. *Nanostructured Materials in Electrochemistry;* Wiley-VCH: Hoboken, NJ, U.S.A., 2008; pp 1–116.
3. Karlsson, M.; Johansson, A.; Tang, L.; Boman, M. *Microsc. Res. Tech.* **2004,** *63,* 259–265. doi:10.1002/jemt.20040
4. Salerno, M.; Caneva-Soumetz, F.; Pastorino, L.; Patra, N.; Diaspro, A.; Ruggiero, C. *IEEE Trans. NanoBioscience* **2013,** *12,* 106–111. doi:10.1109/TNB.2013.2257835
5. Gentile, F.; Tirinato, L.; Battista, E.; Causa, F.; Liberale, C.; di Fabrizio, E. M.; Decuzzi, P. *Biomaterials* **2010,** *31,* 7205–7212. doi:10.1016/j.biomaterials.2010.06.016
6. Ross, A. M.; Jiang, Z.; Bastmeyer, M.; Lahann, J. *Small* **2012,** *8,* 336–355. doi:10.1002/smll.201100934
7. Rahmany, M. B.; Van Dyke, M. *Acta Biomater.* **2013,** *9,* 5431–5437. doi:10.1016/j.actbio.2012.11.019
8. Yanagishita, T.; Masuda, H. *AIP Adv.* **2016,** 6.
9. Yanagishita, T.; Masuda, H. *Electrochim. Acta* **2015,** *184,* 80–85. doi:10.1016/j.electacta.2015.10.019
10. Santos, A.; Kumeria, T.; Losic, D. *TrAC, Trends Anal. Chem.* **2013,** *44,* 25–38. doi:10.1016/j.trac.2012.11.007
11. Chung, A. J.; Huh, Y. S.; Erickson, D. *Nanoscale* **2011,** *3,* 2903–2908. doi:10.1039/c1nr10265f
12. Toccafondi, C.; Thorat, S.; La Rocca, R.; Scarpellini, A.; Salerno, M.; Dante, S.; Das, G. *J. Mater. Sci.: Mater. Med.* **2014,** *25,* 2411–2420. doi:10.1007/s10856-014-5178-4
13. Toccafondi, C.; La Rocca, R.; Scarpellini, A.; Salerno, M.; Das, G.; Dante, S. *Appl. Surf. Sci.* **2015,** *351,* 738–745. doi:10.1016/j.apsusc.2015.05.169
14. Kneipp, K.; Kneipp, H.; Kneipp, J. *Acc. Chem. Res.* **2006,** *39,* 443–450. doi:10.1021/ar050107x
15. Nie, S.; Emory, S. E. *Science* **1997,** *275,* 1102–1106. doi:10.1126/science.275.5303.1102
16. Salerno, M.; Thorat, S. *13th Ceram. Cells Tissues. Regen. nanomedicine, tissue Genet. Eng. role Ceram.* **2011**, 171.
17. Gultepe, E.; Nagesha, D.; Sridhar, S.; Amiji, M. *Adv. Drug Delivery Rev.* **2010,** *62,* 305–315. doi:10.1016/j.addr.2009.11.003
18. Aw, M. S.; Bariana, M.; Losic, D. Nanoporous Anodic Alumina for Drug Delivery and Biomedical Applications. In *Nanoporous Alumina: Fabrication, Structure, Properties and Applications;* Losic, D.; Santos, A., Eds.; Springer Series in Materials Science, Vol. 219; Springer: Berlin, Germany, 2015; pp 319–354. doi:10.1007/978-3-319-20334-8_11
19. Toccafondi, C.; Zaccaria, R. P.; Dante, S.; Salerno, M. *Materials* **2016,** *9,* 403–414. doi:10.3390/ma9060403
20. Swan, E. E. L.; Popat, K. C.; Desai, T. A. *Biomaterials* **2005,** *26,* 1969–1976. doi:10.1016/j.biomaterials.2004.07.001
21. Chang, P.-C.; Liu, B.-Y.; Liu, C.-M.; Chou, H.-H.; Ho, M.-H.; Liu, H.-C.; Wang, D.-M.; Hou, L.-T. *J. Biomed. Mater. Res., Part A* **2007,** *81,* 771–780. doi:10.1002/jbm.a.31031
22. Tamm, L. K.; McConnell, H. M. *Biophys. J.* **1985,** *47,* 105–113. doi:10.1016/S0006-3495(85)83882-0
23. Das, G.; Patra, N.; Gopalakrishnan, A.; Zaccaria, R. P.; Toma, A.; Thorat, S.; Di Fabrizio, E.; Diaspro, A.; Salerno, M. *Analyst* **2012,** *137,* 1785. doi:10.1039/c2an16022f
24. Thorat, S.; Diaspro, A.; Scarpellini, A.; Povia, M.; Salerno, M. *Materials* **2013,** *6,* 206–216. doi:10.3390/ma6010206
25. Das, G.; Patra, N.; Gopalakrishanan, A.; Proietti Zaccaria, R.; Toma, A.; Thorat, S.; Di Fabrizio, E.; Diaspro, A.; Salerno, M. *Microelectron. Eng.* **2012,** *97,* 383–386. doi:10.1016/j.mee.2012.02.037
26. Zheng, J.; Zhou, Y.; Li, X.; Ji, Y.; Lu, T.; Gu, R. *Langmuir* **2003,** *19,* 632–636. doi:10.1021/la011706p
27. Mayo, D. W.; Miller, F. A.; Hannah, R. W. In *Course Notes on the Interpretation of Infrared and Raman Spectra;* Mayo, D. W.; Miller, F. A.; Hannah, R. W., Eds.; Wiley: Hoboken, NJ, U.S.A., 2004; i–xxvi. doi:10.1002/0471690082.fmatter
28. Velleman, L.; Bruneel, J.-L.; Guillaume, F.; Losic, D.; Shapter, J. G. *Phys. Chem. Chem. Phys.* **2011,** *13,* 19587–19593. doi:10.1039/c1cp21765h
29. An, H. H.; Han, W. B.; Kim, Y.; Kim, H.-S.; Oh, Y.; Yoon, C. S. *J. Raman Spectrosc.* **2014,** *45,* 292–298. doi:10.1002/jrs.4461
30. Taylor, R. W.; Benz, F.; Sigle, D. O.; Bowman, R. W.; Bao, P.; Roth, J. S.; Heath, G. R.; Evans, S. D.; Baumberg, J. J. *Sci. Rep.* **2014,** *4,* 5940. doi:10.1038/srep05940
31. Schulz, H.; Baranska, M. *Vib. Spectrosc.* **2007,** *43,* 13–25. doi:10.1016/j.vibspec.2006.06.001
32. Köhler, M.; MacHill, S.; Salzer, R.; Krafft, C. *Anal. Bioanal. Chem.* **2009,** *393,* 1513–1520. doi:10.1007/s00216-008-2592-9
33. Zumbusch, A.; Langbein, W.; Borri, P. *Prog. Lipid Res.* **2013,** *52,* 615–632. doi:10.1016/j.plipres.2013.07.003
34. Czamara, K.; Majzner, K.; Pacia, M. Z.; Kochan, K.; Kaczor, A.; Baranska, M. *J. Raman Spectrosc.* **2015,** *46,* 4–20. doi:10.1002/jrs.4607
35. Richter, R. P.; Bérat, R.; Brisson, A. R. *Langmuir* **2006,** *22,* 3497–3505. doi:10.1021/la052687c
36. Reimhult, E.; Höök, F.; Kasemo, B. *Langmuir* **2003,** *19,* 1681–1691. doi:10.1021/la0263920
37. Peng, P.-Y.; Chiang, P.-C.; Chao, L. *Langmuir* **2015,** *31,* 3904–3911. doi:10.1021/la504532a
38. Campiña, J. M.; Martins, A.; Silva, F. *J. Phys. Chem. C* **2007,** *111,* 5351–5362. doi:10.1021/jp0662146
39. Hewas, A. M. Analysis of metal ions in water using SAM-modified EQCM electrodes. Ph.D. Thesis, Department of Chemistry, University of Leicester, 2013.

License and Terms

BEILSTEIN JOURNAL OF NANOTECHNOLOGY

Tunable plasmons in regular planar arrays of graphene nanoribbons with armchair and zigzag-shaped edges

Cristian Vacacela Gomez[1,2], Michele Pisarra[1,3], Mario Gravina[1,2] and Antonello Sindona[*1,2]

Full Research Paper

Open Access

Address:
[1]Dipartimento di Fisica, Università della Calabria, Via P. Bucci, Cubo 30C, 87036 Rende (CS), Italy, [2]INFN, sezione LNF, Gruppo collegato di Cosenza, Via P. Bucci, Cubo 31C, 87036 Rende (CS), Italy and [3]Departamento de Química, Universidad Autónoma de Madrid, Calle Francisco Tomás y Valiente 7 (Módulo 13), 28049, Madrid, Spain

Email:
Antonello Sindona[*] - antonello.sindona@fis.unical.it

* Corresponding author

Keywords:
graphene nanoribbons; plasmonics; time-dependent density functional theory

Beilstein J. Nanotechnol. **2017,** *8,* 172–182.
doi:10.3762/bjnano.8.18

Received: 15 July 2016
Accepted: 03 January 2017
Published: 17 January 2017

This article is part of the Thematic Series "Self-assembly of nanostructures and nanomaterials II".

Guest Editor: I. Berbezier

Abstract

Recent experimental evidence for and the theoretical confirmation of tunable edge plasmons and surface plasmons in graphene nanoribbons have opened up new opportunities to scrutinize the main geometric and conformation factors, which can be used to modulate these collective modes in the infrared-to-terahertz frequency band. Here, we show how the extrinsic plasmon structure of regular planar arrays of graphene nanoribbons, with perfectly symmetric edges, is influenced by the width, chirality and unit-cell length of each ribbon, as well as the in-plane vacuum distance between two contiguous ribbons. Our predictions, based on time-dependent density functional theory, in the random phase approximation, are expected to be of immediate help for measurements of plasmonic features in nanoscale architectures of nanoribbon devices.

Introduction

Quantized, coherent and collective density fluctuations of the valence electrons in low-dimensional nanostructures, better known as plasmons, have been attracting significant interest, due their capability to couple with light and other charged particles, thus paving the way to novel applications in a wide range of technologies, as diverse as biosensing, light harvesting or quantum information [1-5]. On more fundamental grounds, plasmon-like modes are the “true” low-energy excitations of low-dimensional systems [6,7], while charged and spinful modes are realized as coherent states, with their own peculiar dynamics [8,9], both in normal superconducting phases [10-14]. Graphene has first emerged as an extraordinary platform for

controlling the propagation of surface-plasmon waves [15], because of its unique electronic and optical properties [16]. In particular, the extrinsic plasmons of this one-atom-thick hexagonal lattice of sp-bonded carbon atoms have shown much stronger confinement, larger tunablity and lower losses with respect to more conventional plasmonic nanoparticles, such as, for example, silver and gold [17]. With the rise of low-dimensional materials, a number of theoretical and experimental studies have been oriented to launch, control, manipulate and detect plasmons in graphene-related and beyond-graphene structures [18-21], which are expected to be embedded in next-generation nano-devices that may operate from infrared (IR) to terahertz (THz) frequencies [22-25]. As a noteworthy example, graphene nanoribbons (GNRs) preserve most of the exceptional features of graphene, with the additional property that they are semiconductors and their band gap is geometrically controllable.

A clear picture of confined edge (interband) and surface (intraband) plasmons in GNRs, as wide as 100–500 nm, has been achieved by infrared imaging measurements on the nanoscale [26]. On the theoretical side, some nearest-neighbor tight-binding [27,28] and semiclassical electromagnetic [29,30] approaches have been able to characterize the intraband mode, being generally excited by a THz electromagnetic field pulse. Very recently, an ab initio analysis has elucidated the role of both intraband and interband plasmons in narrow GNRs below ca. 1 nm in width [31].

In this work, we extend the results of [31], to include some GNRs up to 2.2 nm wide, and demonstrate how the extrinsic plasmons of these systems can be finely tuned by changing a small number of simple parameters, such as the unit-cell length, width and chirality of each GNR, or the in-plane distance between contiguous GNRs. Our study is carried out using time-dependent (TD) density functional theory (DFT), within the random phase approximation (RPA). The computations are performed at room temperature (T = 300 K), including both intrinsic and extrinsic conditions. Different zigzag (Z) and armchair (A) configurations are examined, with the GNR-ends being passivated by hydrogen atoms, which mimics an ideal setup of long ribbons, with perfectly symmetric edges, suspended or grown on inert substrates. A specific focus is made on the 5AGNR, 11AGNR and 4ZGNR, 10ZGNR geometries that are, respectively, characterized by 4,10 zigzag-chains and 5,11 dimer-lines across the width of the GNRs. The dielectric properties of these systems are calculated in response to probe electrons or photons with incident energies, ω, smaller than 20 eV, and in-plane incident momentum **q** below 0.8 Å^{-1}. For comparison purposes, the well-known intrinsic plasmonics of graphene are also reported.

In the following, we briefly account for the theoretical tools that we have used to explore the electronic structure and dielectric properties of 5AGNR, 11AGNR and 4ZGNR, 10ZGNR and graphene (Results and Discussion, chapter 'Theoretical framework'). Next, we will present a detailed analysis of the changes induced by the above mentioned parameters to the peak position, intensity, and dispersion of the GNR-plasmons (Results and Discussion, chapter 'Tunable plasmons in GNR arrays').

Results and Discussion

Theoretical framework

Our TDDFT approach is divided into two steps. First, the (ground-state) electronic properties of the different GNRs (and graphene) are obtained by DFT. Second, the basic equation of linear-response theory in the RPA is employed, with a corrected electron–electron interaction, to calculate the dielectric properties, and hence the plasmon structure, of the systems.

DFT method

Density-functional calculations are performed using the plane-wave (PW) basis-set [32], i.e., the normalized space functions $\mathbf{PW}_{\mathbf{k}+\mathbf{G}}(\mathbf{r}) = \Omega_0^{-1/2} e^{i(\mathbf{k}+\mathbf{G})\cdot\mathbf{r}}$, which depend on the wave-vectors **k** of the first Brillouin zone (1st BZ), and the reciprocal lattice vectors **G** associated to the three-dimensional (3D) crystal of unit-cell volume Ω_0. The ground-state electronic properties of the different GNRs (as well as graphene) are computed within the local density approximation (LDA), being defined by the Perdew–Zunger parameterization of the uniform-gas correlation energy [33]. Norm-conserving pseudopotentials of the Troullier–Martins type are adopted to eliminate the core electrons [34]. A cut-off energy of ca. 680 eV on the number of PWs is sufficient to obtain well-converged electronic structures with ca. 10^5 PWs.

In the GNR arrays, the C–C length is allowed to range from 1.414 to 1.426 Å, while the C–H bond length is fixed to 1.09 Å, with a bond-angle of 120 °(as shown in [31] relaxation effects play a minor role in 4ZGNR and 5AGNR). The 3D periodicity required by PW-DFT is generated by using an in-plane vacuum distance of 5–20 Å, and an out-of-plane lattice constant of 15 Å. The self-consistent run is carried out using an unshifted (and Γ-centered) Monkhorst–Pack (MP) grid, made of 60 × 60 × 1 **k**-points [35], which results in a uniform sampling of the irreducible 1st BZ on the ΓX-segment (shown in Figure 1). The converged electron densities are subsequently used to compute the Kohn–Sham (KS) electronic structure on a denser MP-mesh of 180 × 1 × 1 **k**-points, including up to 120 bands, which is enough to explore the dielectric properties of the GNRs at probing energies below ≈20 eV. The IR to THz region is further scrutinized with a finer MP mesh of 2000 × 1 × 1 **k**-points, including up to 30 bands.

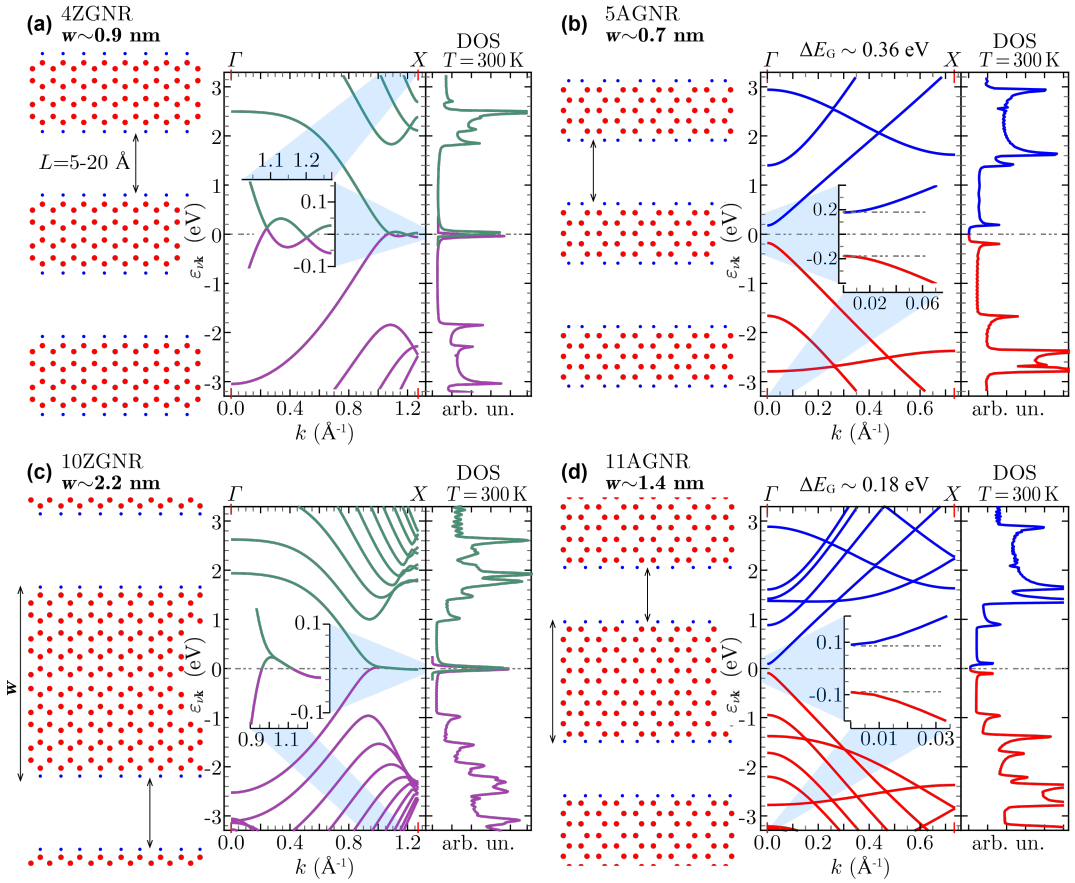

Figure 1: Geometry, LDA band-structure and DOS of the different (zigzag and armchair) GNR arrays reported in the present study, namely 4ZGNR (a), 5AGNR (b), 10ZGNR (c), and 11AGNR (d). In the LDA, the ZGNRs are gapless, while the AGNRs have a band gap ΔE_G, which decreases with increasing the ribbon width w, as attested by the insets in the band plots. The ground-state features of the systems are strongly sensitive to the value of the C–C bond-length (here fixed to 1.42 Å) and the ribbon width, while they are practically unaffected by in-plane vacuum distances L (here fixed to 15 Å). Figure 1a and Figure 1b are adapted from Figure 1 of [31].

The main results of our DFT computations are summarized in the plots of Figure 1, which show the different geometry, band structure and density of states (DOS) of the GNR arrays. 4ZGNR and 10ZGNR behave as semimetals, with barely touching valence and conduction bands (Figure 1a,c). 5AGNR and 11AGNR are small-gap semiconductors (Figure 1b,d), contrary to nearest-neighbor TB approaches in which all AGNRs appear gapless [27].

Indeed, several DFT studies have carefully characterized the band gaps of ZGNRs and AGNRs [36-39]. In particular, local spin-density calculations suggest the opening of a band gap larger than 0.1 eV in ZGNRs [36,37]. However, the LDA analysis of a virtually gapless GNR, i.e., 4ZGNR or 10ZGNR, in comparison with 5AGNR and 11AGNR, is particularly instructive to emphasize the different role played by doping in separating the extrinsic plasmon modes, which will be detailed in chapter 'Tunable plasmons in GNR arrays'.

The simulations at hand explore ranges of different geometrical and conformation parameters, which will be used to characterize the tunability of the GNR plasmons. In particular, (i) GNR widths (w) of around 0.7–2.2 nm are sorted out; (ii) zigzag and armchair edges are considered, to elucidate the role played by chirality; (iii) in-plane vacuum distances from 5 to 20 Å are tested; and (iv) different unit-cell extensions are simulated by changing the C–C bond length by about 0.5%, to account for stretching effects. As for intrinsic graphene, the C–C bond length and out-of-plane lattice constant are fixed to 1.42 Å and 15 Å, respectively. The self-consistent run is performed on a 60 × 60 × 1 MP-grid, and the KS electronic properties are then computed on a 180 × 180 × 1 MP-grid, including up to 80 bands.

TDDFT approach

The KS eigenvalues $\varepsilon_{\nu\mathbf{k}}$ (see Figure 1) and corresponding eigenfunctions $\langle \mathbf{r}|\nu\mathbf{k}\rangle = N^{-1/2}\sum_{\mathbf{G}} c_{\nu\mathbf{k}+\mathbf{G}} \mathrm{PW}_{\mathbf{k}+\mathbf{G}}(\mathbf{r})$ are the

main outputs of the DFT computations, with N being the total number of **k**-points in the 1st BZ, and ν being the band index. The KS eigensystem $\{\varepsilon_{\nu\mathbf{k}}, |\nu\mathbf{k}\rangle\}$ gives access to the unperturbed density–density response function, of the non-interacting valence electrons, to a probe particle of energy ω and momentum **q**. The latter is provided by the Alder–Wiser formula [40,41]:

$$\chi^0_{\mathbf{GG}'} = \frac{2}{N\cdot\Omega_0}\sum_{\mathbf{k},\nu,\nu'}\frac{\left(f_{\nu\mathbf{k}} - f_{\nu'\mathbf{k}+\mathbf{q}}\right)\rho^{\mathbf{kq}}_{\nu\nu'}(\mathbf{G})\rho^{\mathbf{kq}}_{\nu\nu'}(G')^*}{\omega+\varepsilon_{\nu\mathbf{k}}-\varepsilon_{\nu'\mathbf{k}+\mathbf{q}}+i\eta}. \quad (1)$$

Indeed, plasmons in solid-state materials are typically triggered by electron-beam radiation, photo-currents, and even charged ions, with incident kinetic energies of the order of 0.1–1 keV [42,43]. In the present context, the probe particle is an electron or a photon that weakly perturbs the system.

In Equation 1 (expressed in Hartree atomic units), the factor of two takes into account the electron spin, η indicates an infinitesimal (positive) broadening parameter (set to 0.02 eV), $f_{\nu\mathbf{k}}$ is the Fermi–Dirac distribution, and

$$\begin{aligned}\rho^{\mathbf{kq}}_{\nu\nu'}(\mathbf{G}) &= \left\langle \nu\mathbf{k}\left| e^{-i(\mathbf{q}+\mathbf{G})\cdot\mathbf{r}}\right|\nu'\mathbf{k}+\mathbf{q}\right\rangle \\ &= \sum_{\mathbf{G}'} c_{\nu\mathbf{k}-\mathbf{G}+\mathbf{G}'}\, c_{\nu'\mathbf{k}+\mathbf{q}+\mathbf{G}'}\end{aligned} \quad (2)$$

labels the density–density correlation matrix elements, which depend on the number of PWs included in the DFT simulations.

The full susceptibility or interacting density–density response function is determined by the central equation of linear-response TDDFT [44,45]

$$\chi_{\mathbf{GG}'} = \chi^0_{\mathbf{GG}'} + \left(\chi^0 \upsilon\chi\right)_{\mathbf{GG}'}, \quad (3)$$

where, in the RPA, the $\upsilon_{\mathbf{GG}'}$ terms are approximated to the bare Coulomb coefficients:

$$\upsilon^0_{\mathbf{GG}'} = \frac{4\pi\delta_{\mathbf{GG}'}}{|\mathbf{q}+\mathbf{G}|^2}. \quad (4)$$

However, the long-range character of the Coulomb potential yields non-negligible interactions between replicas along out-of-plane direction z. To erase this unphysical phenomenon, a two-dimensional (2D) cut-off, say, a truncated Coulomb potential is used [46-49] to replace the $\upsilon_{\mathbf{GG}'}$ terms by the truncated Fourier integral:

$$\upsilon_{\mathbf{GG}'} = \frac{2\pi}{|\mathbf{q}+\mathbf{g}|}\int_{-L/2}^{L/2} dz \int_{-L/2}^{L/2} dz' e^{iG_z z - iG'_z z' - |\mathbf{q}+\mathbf{g}||z-z'|}. \quad (5)$$

Here, **g** and G_z denote the in-plane and out-of-plane components of **G**, respectively.

With this 2D correction in mind, we can introduce the inverse dielectric matrix:

$$\left(\epsilon^{-1}\right)_{\mathbf{GG}'} = \delta_{\mathbf{GG}'} + \upsilon_{\mathbf{GG}'}\chi_{\mathbf{GG}'}. \quad (6)$$

The zeros in the real part of the macroscopic dielectric function (permittivity) provide the condition for a plasmon resonance to occur, stated as:

$$\mathrm{Re}\left(\epsilon^{\mathrm{M}}\right) = \mathrm{Re}\left[\frac{1}{\left(\epsilon^{-1}\right)_{00}}\right] = 0. \quad (7)$$

The imaginary part of the inverse permittivity is proportional to so-called energy loss (EL) function, which provides the plasmon structure:

$$E_{\mathrm{LOSS}} = -\mathrm{Im}\left[\left(\epsilon^{-1}\right)_{00}\right]. \quad (8)$$

Non-local field effects [50] are included in E_{LOSS} through Equation 3. We have verified that ca. 120 **G** vectors for all GNRs (and ca. 51 **G** vectors for graphene), sorted in length and being of the form $(0,0,G_z)$, give well-resolved and converged results in the sampled energy–momentum region, delimited by $\omega < 20$ eV and $q < 0.8$ Å^{-1}.

Tunable plasmons in GNR arrays

We proceed by clarifying the role played by the geometric and conformation parameters introduced above in the different GNRs, whose intrinsic response is shown in Figure 2 together with that of graphene. In the following, we will also evaluate several extrinsic conditions associated to Fermi energy shifts ΔE_{F} in the range of −0.2 to 0.2 eV.

Ribbon width and chirality

Independently on the width and chirality of the ribbons, all GNRs are characterized by two interband plasmons at excitation energies above about 2 eV. These excitations, shown in Figure 2b–e, are analogous to the well-known π and π–σ plasmons of graphene [51,52], as displayed in Figure 2a. Similar features occur in bilayer graphene [51], multilayer graphene

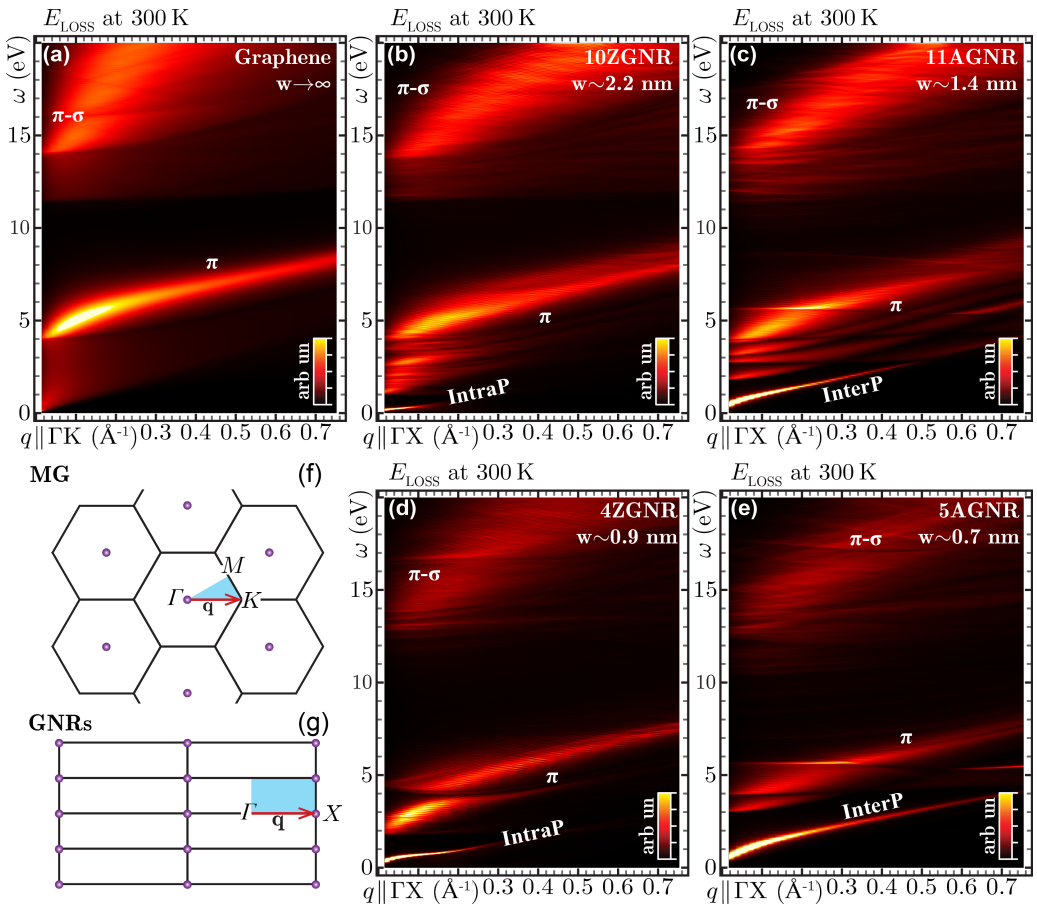

Figure 2: Loss properties of intrinsic graphene (a), i.e., an example of infinite-width GNR, and the undoped GNR arrays of Figure 1 (b–e), computed at room temperature from the TDDFT-RPA machinery summarized by Equations 1–8 of the main text. The EL function of Equation 8 is represented as a density-color plot vs incident energy ω (in eV) and momentum q (in Å^{-1}). The latter is sampled along the ΓK path of the 1st BZ of graphene (f), and the ΓX path of the 1st BZ of the different GNRs (g). Besides the π and π–σ plasmons, the ZGNRs present a low-energy intraband mode (IntraP), whereas the AGNRs have a low-energy interband mode (InterP). The intensity scale in (a–d) is cut at 80% of the π peak maximum, to ease comparison between the different density-color plots.

[52], graphene–metal interfaces [53-59] and graphite [52]. In our calculations, the intensity of the π and π–σ modes increases with increasing the GNR width, reaching its maximum brightness in graphene, which may be seen as a GNR of infinite width.

The energy window displayed in Figure 2 does not show the complete energy–momentum dispersion of the π–σ plasmon, however, the latter seems to be quadratic in graphene and linear in the GNRs. At long wavelengths, in the $q\to0$ region, the π plasmon of all systems has a $\sqrt{q}$-like dispersion, while at $q > 0.2$ Å^{-1} it exhibits linear behavior. The intrinsic plasmons of 10ZGNR and 11AGNR appear in the same energy region as those of graphene, i.e., at ω ≈ 4–5 eV and ω ≈ 14–15 eV. On the other hand, they are red-shifted in 4ZGNR and 5AGNR, with the π plasmon having a peak at ω ≈ 2–3 eV and the π–σ plasmon lying at ω ≈ 13–14 eV. Furthermore, the π and π–σ plasmons detected in 4ZGNRs (w ≈ 0.9 nm) and 5AGNR (w ≈ 0.7 nm) exhibit markedly discontinuous dispersions, being split into more branches [31]. This is a consequence of the narrow widths of the two systems that generate several, distinct one-dimensional bands of π- and σ-character (Figure 1c,d).

By increasing the GNR width (w > 1 nm), the number of bands increases, and less disjoint plasmon dispersions appear, which clearly tend to the continuous patterns of graphene ($w\to\infty$). Thus, semiconducting and semimetallic GNRs have plasmon resonances in the visible (VIS) to ultraviolet (UV) regime that may be controlled by the GNR width. This tunability feature is evidently absent in graphene.

Quantum confinement and chirality are key factors for plasmon resonances at frequencies smaller than 2 eV. We see that zigzag systems exhibit an intraband plasmon, while armchair systems

present an interband plasmon. These two modes correspond to the surface and edge plasmons detected in large-width, extrinsic GNR arrays fabricated on Al_2O_3 [26]. The surface plasmon of ZGNRs is originated by the large DOS peak observed at the Fermi level E_F (Figure 1a,c). This mode shows a $\sqrt{q}$-like dispersion [31] and seems to be analogous to the conventional 2D plasmons of extrinsic graphene [19,51]. The edge plasmon of AGNRs appears as an effect of collective excitations generated close to E_F [31], associated to single-particle excitations that connect the two DOS peaks around E_F (Figure 1b,d). The characteristics of this interband mode are similar to those of the π plasmon of intrinsic graphene, i.e., at long wavelengths the interband plasmon shows a $\sqrt{q}$-like dispersion, while at $q > 0.1$ Å^{-1} it displays a linear dispersion.

Both the intraband and interband modes have been proved to be genuine plasmons in intrinsic 4ZGNR and 5AGNR [31], as they are strictly associated to the zeroes of the real permittivity, satisfying the condition given by Equation 7. It has been further demonstrated that extrinsic 4ZGNR presents only an intraband plasmon structure, independently on the positive doping level used (below ca. 1 eV), while both intraband and interband plasmons coexist in 5AGNR [31].

To support this result, we report in Figure 3 the macroscopic dielectric function and the EL function of the different GNR arrays for a selected momentum value ($q = 0.011$ Å^{-1}) and a negative doping level ($\Delta E_F = -0.1$ eV). We see that 10ZGNR and 4ZGNR present similar plasmonic features, with the intraband plasmon resonance being blue-shifted by increasing the GNR width (Figure 3a,c). In 11AGNR and 5AGNR, not only the peak position but also the interplay of the interband and intraband plasmon is strongly dictated by the doping level and the GNR width (Figure 3b,d).

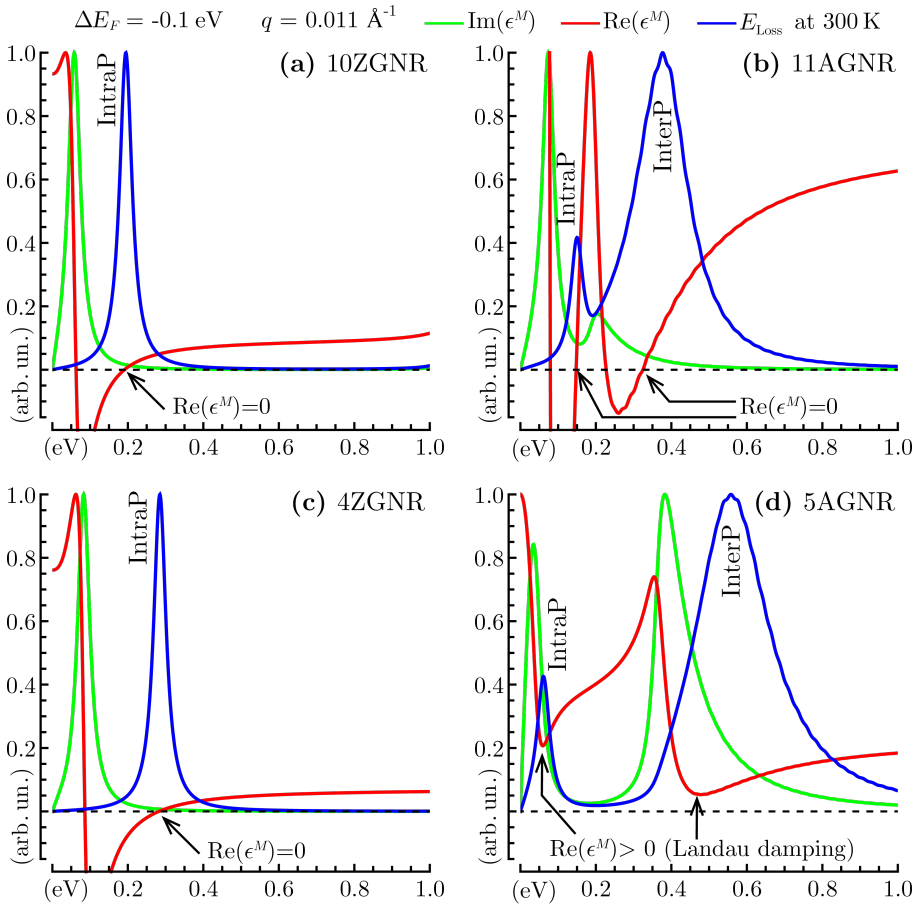

Figure 3: Macroscopic permittivity (ϵ^M, Equation 6) and EL function (E_{LOSS}, Equation 8) at room temperature for the GNR arrays of Figure 1 and Figure 2, i.e., 10ZGNR (a), 11AGNR (b), 4ZGNR (c) and 5AGNR (d). The energy region ω ≤ 1 eV is explored at a fixed incident momentum $q = 0.011$ Å^{-1} parallel to ΓX (Figure 2g), with a negative doping level ΔE_F of −0.1 eV. The black arrows mark the positions where the real permittivity has a zero value (a–c) or a minimum (d), which reflects a Landau damping mechanism due to single-particle excitation processes. The intraband and interband plasmons are denoted IntraP and InterP, as in Figure 2.

In 5AGNR, the two modes are well resolved in energy, with the zeroes of the real permittivity being hidden by the Landau damping mechanism, associated to single-particle excitation processes [25,46-48]. In 11AGNR the same modes strongly interfere and largely dominate with respect to single-particle excitations. A similar interplay was observed in extrinsic 5AGNR subject to a positive doping of about 0.3 eV [31]. These outcomes are basically due to the different band-gap values of the two AGNRs, which according to our predictions are ca. 0.18 eV for 11AGNR, and ca. 0.36 eV for 5AGNR. Accordingly, less energy requirements are needed to produce a well-defined intraband collective electronic excitation in 11AGNR. On the other hand, a positive doping larger than 0.2 eV yields a well-defined intraband plasmon in 5AGNR [31]. Interestingly enough, some GNRs with band-gap values of the same order of 11AGNR and 5AGNR have been recently synthetized on Au(111) [60]. Then, our ab initio analysis can be of help in interpreting plasmon measurements on currently synthetized GNR-structures.

Chirality seems to be a major point for the design of GNR-based plasmonic devices. One or two plasmon modes can be exploited, depending on the shape of the GNR edges. In this respect, negative or positive doping acts as a modulating factor of the plasmon modes.

In Figure 4 we see that a change in doping sign, from −0.1 to 0.1 eV, produces a slight red shift in the intraband plasmon of 10ZGNR and the interband plasmon of 11AGNR (Figure 4a,b). More significant variations are observed in the intraband plasmon of 11AGNR, which is markedly blue-shifted and doubled in intensity by the same change of extrinsic conditions (Figure 4b). Therefore, an asymmetric response is observed in the intraband plasmon of semiconducting GNRs (Figure 4b). Moreover, as the GNR width decreases an appreciable blue/red shift is detected in the plasmon peaks of both ZGNRs and AGNRs (Figure 4c,d). Thus, a tunable energy response may be more strongly influenced by the ribbon width than the doping level.

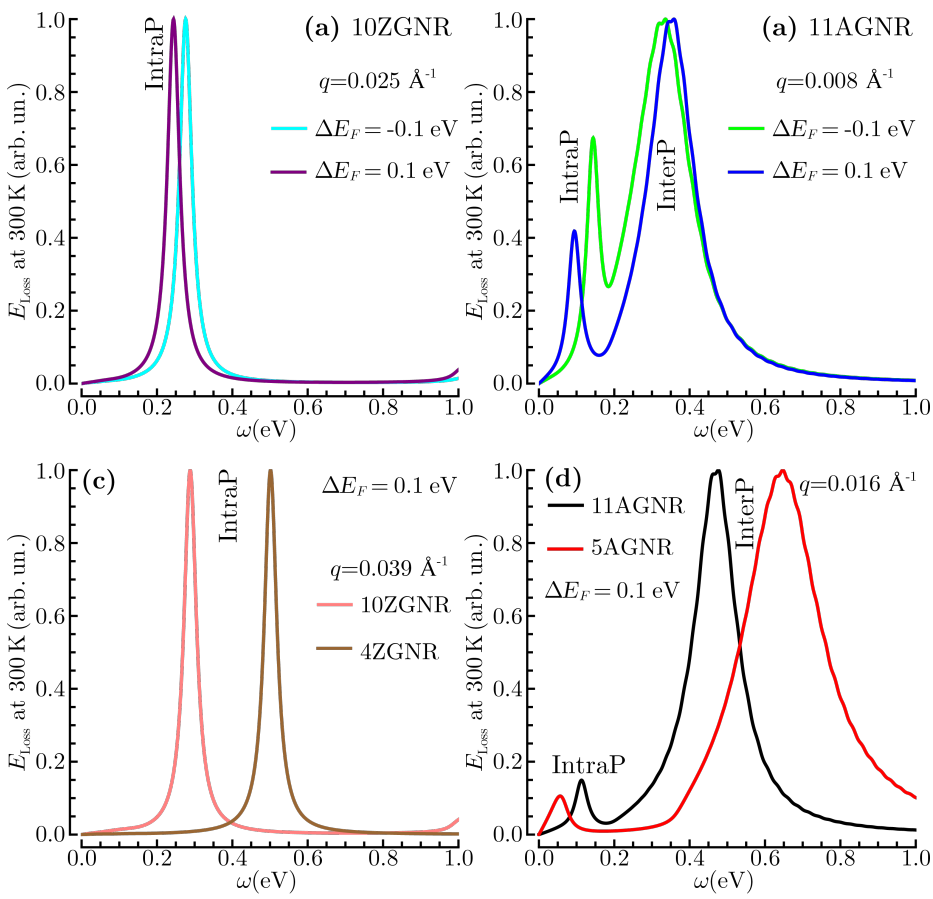

Figure 4: EL function of Equation 8 at room temperature for the GNR-arrays considered in the main text, e.g., 10ZGNR (a), 11AGNR (b), 4ZGNR (c) and 5AGNR (d), being subject to doping levels ΔE_F of ±0.1 eV. E_{LOSS} is plotted in the energy range ω ≤ 1 eV at some fixed transferred momentum values, q = 0.025 Å^{-1} (a), 0.008 Å^{-1} (b), 0.039 Å^{-1} (c), 0.016 Å^{-1} (d), parallel to ΓX (Figure 2g). The intraband and interband plasmons are denoted as IntraP and InterP, as in Figure 2 and Figure 3.

Mechanical deformations

Let us now see how the fascinating plasmonic features of semiconducting GNRs are affected by changes of the in-plane separation. With reference to the case of 5AGNR, we take a positive doping value of 0.2 eV and consider vacuum distances L, between continuous arrays, in the range of 5 to 20 Å (Figure 5).

As a first result, we see that both intraband and interband plasmon modes exist in 5AGNR, no matter how far apart the arrays are. The intraband plasmon is, however, affected in intensity, while the interband plasmon is blue-shifted as the vacuum distance decreases down to 5 Å. This effect is clearly visible at q = 0.025 Å^{-1} in Figure 5d, where a broad interband plasmon peak is detected at ω ≈ 0.6–1 eV. Both the large blue shift of the interband plasmon, and the intensity decrease of the intraband plasmon, are consistent with the idea that as the GNR arrays get closer a large graphene area is created.

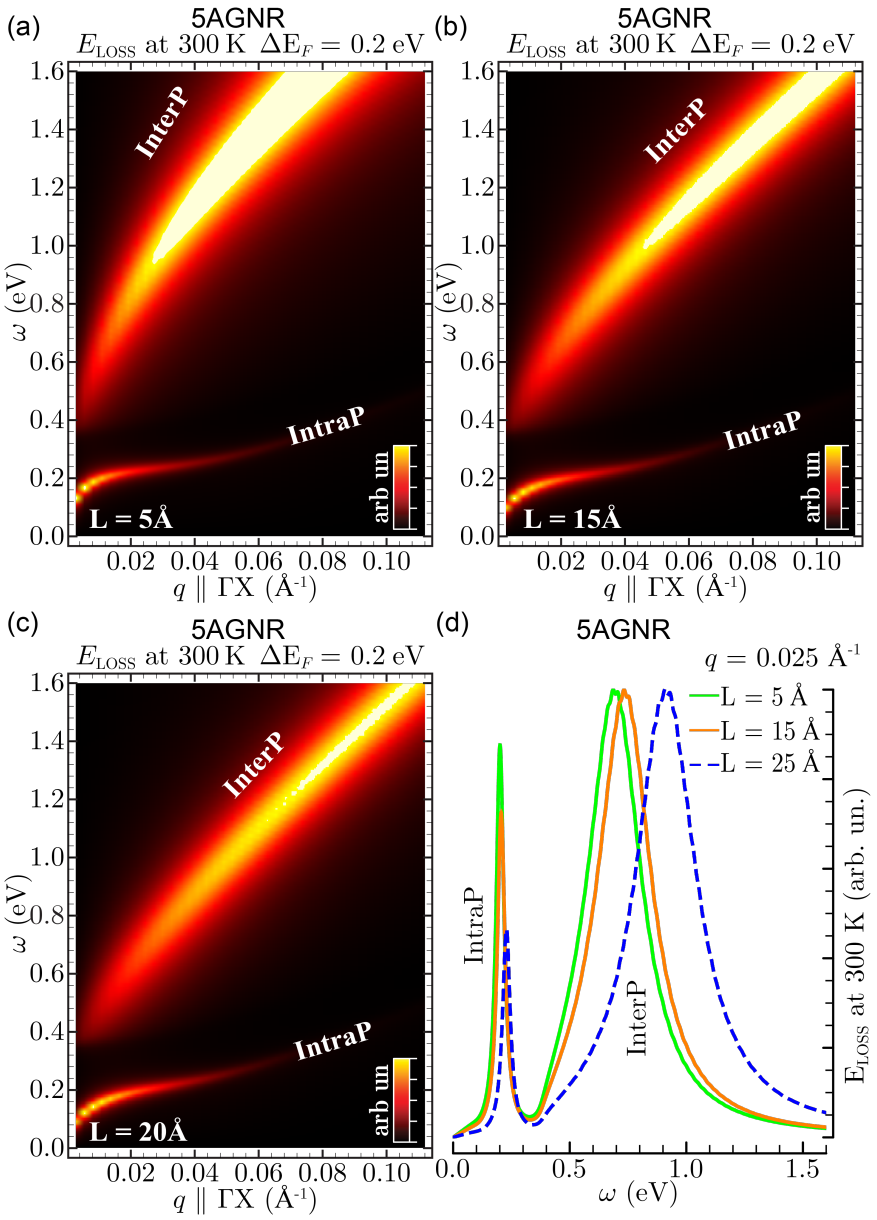

Figure 5: EL function of three positively doped 5AGNRs (ΔE_F = 0.2 eV) separated by an in-plane vacuum distance L of 5 Å (a), 15 Å (b), and 20 Å (c). In (a–c) the energy–momentum region ω ≤ 1.6 eV and $q \parallel \Gamma X \leq 0.1$ Å^{-1} is explored, showing how the parameter L modifies the relative position between the intraband and interband plasmons, denoted IntraP and InterP as in Figures 2–4. The intensity scale is cut at 95% of the IntraP peak. The effect of changing the in-plane vacuum distance is even more evident in (d), where the different EL functions of (a–c) are compared at a fixed momentum value of q = 0.025 Å^{-1} parallel to ΓX.

When the vacuum distance becomes negligibly small, the interband plasmon detected in AGNRs enters the region where the π plasmon of graphene are found, while the intraband plasmon decreases in intensity to a small contribution, reported in room temperature calculations of slightly doped graphene [19,31].

Finally, we show how the intraband and interband plasmons of 5AGNR are affected by stretching/shrinking the unit cell of the system by about 0.5%, with respect to its nominal value associated to a C–C bond length, a, of 1.42 Å. In this application, the in-plane vacuum distance is fixed to 15 Å is and a negative doping level of −0.2 eV is considered. As shown in Figure 6,

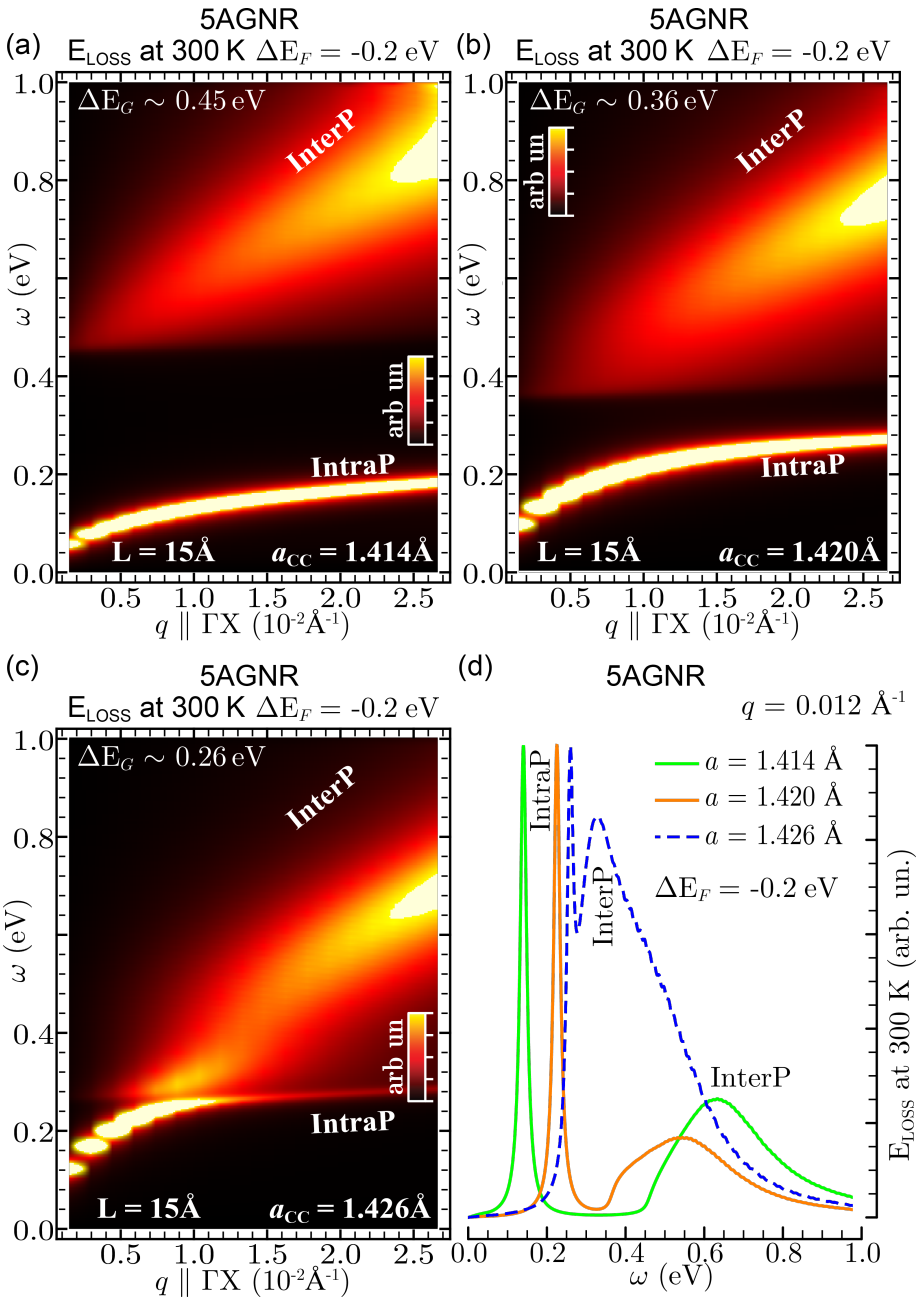

Figure 6: EL function of three negatively doped 5AGNR (ΔE_F = −0.2 eV), characterized by a C–C bond length a_{cc} of 1.411 Å (a), 1.420 Å (b), and 1.426 Å (c), which correspond, respectively, to the band gap values ΔE_G = 0.45 eV (a), 0.36 eV (b), 0.26 eV (c). In (a–c), the energy–momentum region ω ≤ 1 eV and q || ΓX ≤ 0.03 Å^{-1} is explored, showing that a_{cc} (or the lattice constant $3a_{cc}$) is a major factor in modulating the intraband and interband plasmons, denoted IntraP and InterP as in Figures 2–5. The intensity scale is cut at 40% of the IntraP peak. The effect of stretching the 5AGNR structure is even more evident in (d), where the different EL functions of (a–c) are compared at a fixed momentum value of q = 0.025 Å^{-1} parallel to ΓX.

the band gap decreases with increasingly stretching the unit cell from a = 1.414 to a = 1.426 Å. Accordingly, the interference between the intraband and interband plasmons strongly increases. A similar interference has been reported in undeformed 5AGNR-arrays doped by positive Fermi energy shifts larger than 0.4 eV [31]. However, such doping values seem to be impractical for current GNR applications.

Conclusion

We have presented a full ab initio modeling, based on ground-state local density calculations, followed by linear response theory, within the RPA, to explore the tunability properties of plasmon excitations in (infinitely periodic) semiconducting (armchair) and semimetallic (zigzag) arrays of GNRs, with ideal symmetric edges, passivated by hydrogen atoms.

All the tested structures are characterized by two interband plasmons at energies larger than 2 eV, which are analogous to the π and π–σ plasmons of graphene. Their peak positions and dispersions are mostly influenced by the GNR width.

At energies smaller than 2 eV, two more intriguing collective excitations appear, which correspond to recently reported edge and surface plasmons [26]. These modes are strongly sensitive not only to the extrinsic conditions, but also to a bunch of geometrical or conformation parameters, such as the width, chirality and unit-cell extension of each GNR, as well as the in-plane vacuum distance between two contiguous GNRs. In ZGNs the absence of a proper LDA band gap, prevents low energy interband excitation from producing a well-defined edge-plasmon structure.

It is worth mentioning that some recent tight-binding models have investigated the role of edge roughness due to asymmetric defects [61,62], which is at present impractical by TDDFT. These studies suggest the edge-plasmon resonances of narrow GNRs are shifted to lower wavelengths and the corresponding plasmon propagation suffers from higher losses with respect to the ideal case, presented here.

We expect that our findings, combined with non-ab initio approaches suitable for the device scale, may open new strategies to construct materials with plasmonic resonances that will be tunable to a specific demand in both the UV–vis and THz regimes, by altering the chemical doping, electronic gating, and also by means of a careful choice of the geometry.

Acknowledgements

C.V.G. acknowledges the financial support of the “Secretaria Nacional de Educación Superior, Ciencia, Tecnología e Innovación” (SENESCYT-ECUADOR).

References

1. Bao, Q.; Loh, K. P. *ACS Nano* **2012,** *6,* 3677–3694. doi:10.1021/nn300989g
2. Zia, R.; Schuller, J. A.; Chandran, A.; Brongersma, M. L. *Mater. Today* **2006,** *9,* 20–27. doi:10.1016/S1369-7021(06)71572-3
3. Tsargorodska, A.; Cartron, M. L.; Vasilev, C.; Kodali, G.; Mass, O. A.; Baumberg, J. J.; Dutton, P. L.; Hunter, C. N.; Törmä, P.; Leggett, G. J. *Nano Lett.* **2016,** *16,* 6850–6856. doi:10.1021/acs.nanolett.6b02661
4. Anker, J. N.; Hall, W. P.; Lyandres, O.; Shah, N. C.; Zhao, J.; Van Duyne, R. P. *Nat. Mater.* **2008,** *7,* 442–453. doi:10.1038/nmat2162
5. Fan, W.; Lawrie, B. J.; Pooser, R. C. *Phys. Rev. A* **2015,** *92,* 053812. doi:10.1103/PhysRevA.92.053812
6. Haldane, F. D. M. *Phys. Rev. Lett.* **1988,** *60,* 635. doi:10.1103/PhysRevLett.60.635
7. Haldane, F. D. M. *Phys. Rev. Lett.* **1991,** *66,* 1529. doi:10.1103/PhysRevLett.66.1529
8. Bernevig, B. A.; Giuliano, D.; Laughlin, R. B. *Phys. Rev. Lett.* **2001,** *86,* 3392. doi:10.1103/PhysRevLett.86.3392
9. Bernevig, B. A.; Giuliano, D.; Laughlin, R. B. *Phys. Rev. Lett.* **2001,** *87,* 177206. doi:10.1103/PhysRevLett.87.177206
10. Mooij, J. E.; Schön, G. *Phys. Rev. Lett.* **1985,** *55,* 114. doi:10.1103/PhysRevLett.55.114
11. Giuliano, D.; Sodano, P. *Nucl. Phys. B* **2007,** *770,* 332–370. doi:10.1016/j.nuclphysb.2007.02.015
12. Giuliano, D.; Sodano, P. *Nucl. Phys. B* **2010,** *837,* 153–185. doi:10.1016/j.nuclphysb.2010.04.022
13. Giuliano, D.; Sindona, A.; Falcone, G.; Plastina, F.; Amico, L. *New J. Phys.* **2010,** *12,* 025022. doi:10.1088/1367-2630/12/2/025022
14. Sindona, A.; Plastina, F.; Cupolillo, A.; Giallombardo, C.; Falcone, G.; Papagno, L. *Surf. Sci.* **2007,** *601,* 2805–2809. doi:10.1016/j.susc.2006.12.055
15. Koppens, F. H. L.; Chang, D. E.; García de Abajo, F. J. *Nano Lett.* **2011,** *11,* 3370–3377. doi:10.1021/nl201771h
16. Castro Neto, A. H.; Guinea, F.; Peres, N. M. R.; Novoselov, K. S.; Geim, A. K. *Rev. Mod. Phys.* **2009,** *81,* 109. doi:10.1103/RevModPhys.81.109
17. Christensen, J.; Manjavacas, A.; Thongrattanasiri, S.; Koppens, F. H. L.; Garcia de Abajo, F. J. *ACS Nano* **2011,** *6,* 431–440. doi:10.1021/nn2037626
18. Garcia de Abajo, F. J. *ACS Photonics* **2014,** *1,* 135–152. doi:10.1021/ph400147y
19. Sindona, A.; Pisarra, M.; Mencarelli, D.; Pierantoni, L.; Bellucci, S. Plasmon Modes in Extrinsic Graphene: Ab initio Simulations vs Semi-classical Models. In *Fundamental and Applied Nano-Electromagnetics;* Maffucci, A.; Maksimenko, S. A., Eds.; Springer, 2016; pp 125–144. doi:10.1007/978-94-017-7478-9_7
20. Woessner, A.; Lundeberg, M. B.; Gao, Y.; Principi, A.; Alonso-González, P.; Carrega, M.; Watanabe, K.; Taniguchi, T.; Vignale, G.; Polini, H. J.; Hillenbrand, R.; Koppens, F. H. L. *Nat. Mater.* **2015,** *14,* 421–425. doi:10.1038/nmat4169
21. Tong, J.; Muthee, M.; Chen, S.-Y.; Yngvesson, S. K.; Yan, J. *Nano Lett.* **2015,** *15,* 5295–5301. doi:10.1021/acs.nanolett.5b01635
22. Sensale-Rodriguez, B.; Yan, R.; Kelly, M. M.; Fang, T.; Tahy, K.; Hwang, W. S.; Jena, D.; Liu, L.; Xing, H. G. *Nat. Commun.* **2012,** *3,* 780. doi:10.1038/ncomms1787
23. Mencarelli, D.; Bellucci, S.; Sindona, A.; Pierantoni, L. *J. Phys. D: Appl. Phys.* **2015,** *48,* 465104. doi:10.1088/0022-3727/48/46/465104

24. Tao, L.; Cinquanta, E.; Chiappe, D.; Grazianetti, C.; Fanciulli, M.; Dubey, M.; Molle, A.; Akinwande, D. *Nat. Nanotechnol.* **2015,** *10,* 227–231. doi:10.1038/nnano.2014.325
25. Vacacela Gomez, C.; Pisarra, M.; Gravina, M.; Riccardi, P.; Sindona, A. *arXiv* **2016,** No. 1610.
26. Fei, Z.; Goldflam, M. D.; Wu, J.-S.; Dai, S.; Wagner, M.; McLeod, A. S.; Liu, M. K.; Post, K. W.; Zhu, S.; Janssen, G. C. A. M.; Fogler, M. M. *Nano Lett.* **2016,** *15,* 8271–8276. doi:10.1021/acs.nanolett.5b03834
27. Andersen, D. R.; Raza, H. *Phys. Rev. B* **2012,** *85,* 075425. doi:10.1103/PhysRevB.85.075425
28. Thongrattanasiri, S.; Manjavacas, A.; García de Abajo, F. J. *ACS Nano* **2012,** *6,* 1766–1775. doi:10.1021/nn204780e
29. Popov, V. V.; Bagaeva, T. Yu.; Otsuji, T.; Ryzhii, V. *Phys. Rev. B* **2010,** *81,* 073404. doi:10.1103/PhysRevB.81.073404
30. Wang, W.; Apell, P.; Kinaret, J. *Phys. Rev. B* **2011,** *84,* 085423. doi:10.1103/PhysRevB.84.085423
31. Vacacela Gomez, C.; Pisarra, M.; Gravina, M.; Pitarke, J. M.; Sindona, A. *Phys. Rev. Lett.* **2016,** *177,* 116801. doi:10.1103/PhysRevLett.117.116801
32. Gonze, X.; Amadon, B.; Anglade, P.-M.; Beuken, J.-M.; Bottin, F.; Boulanger, P.; Bruneval, F.; Caliste, D.; Caracas, R.; Côté, M.; Deutsch, T.; Genovese, L.; Ghosez, P.; Giantomassi, M.; Goedecker, S.; Hamann, D. R.; Hermet, P.; Jollet, F.; Jomard, G.; Leroux, S.; Mancini, M.; Mazevet, S.; Oliveira, M. J. T.; Onida, G.; Pouillon, Y.; Rangel, T.; Rignanese, G.-M.; Sangalli, D.; Shaltaf, R.; Torrent, M.; Verstraete, M. J.; Zerah, G.; Zwanziger, J. W. *Comput. Phys. Commun.* **2009,** *180,* 2582–2615. doi:10.1016/j.cpc.2009.07.007
33. Perdew, J. P.; Zunger, A. *Phys. Rev. B* **1981,** *23,* 5048. doi:10.1103/PhysRevB.23.5048
34. Troullier, N.; Martins, J. L. *Phys. Rev. B* **1991,** *43,* 1993. doi:10.1103/PhysRevB.43.1993
35. Monkhorst, H. J.; Pack, J. D. *Phys. Rev. B* **1976,** *13,* 5188. doi:10.1103/PhysRevB.13.5188
36. Son, Y.-W.; Cohen, M. L.; Louie, S. G. *Phys. Rev. Lett.* **2006,** *97,* 216803. doi:10.1103/PhysRevLett.97.216803
37. Yang, L.; Park, C.-H.; Son, Y.-W.; Cohen, M. L.; Louie, S. G. *Phys. Rev. Lett.* **2007,** *99,* 186801. doi:10.1103/PhysRevLett.99.186801
38. Raza, H.; Kan, E. C. *Phys. Rev. B* **2008,** *77,* 245434. doi:10.1103/PhysRevB.77.245434
39. Dubois, S. M.-M.; Zanolli, Z.; Declerck, X.; Charlier, J.-C. *Eur. Phys. J. B* **2009,** *72,* 1–24. doi:10.1140/epjb/e2009-00327-8
40. Adler, S. L. *Phys. Rev.* **1962,** *126,* 413. doi:10.1103/PhysRev.126.413
41. Wiser, N. *Phys. Rev.* **1963,** *129,* 62. doi:10.1103/PhysRev.129.62
42. Riccardi, P.; Sindona, A.; Barone, P.; Bonanno, A.; Oliva, A.; Baragiola, R. A. *Nucl. Instrum. Methods Phys. Res., Sect. B* **2003,** *212,* 339–345. doi:10.1016/S0168-583X(03)01424-1
43. Riccardi, P.; Pisarra, M.; Cupolillo, A.; Commisso, M.; Sindona, A.; Baragiola, R. A.; Dukes, C. A. *J. Phys.: Condens. Matter* **2010,** *22,* 305004. doi:10.1088/0953-8984/22/30/305004
44. Petersilka, M.; Gossmann, U. J.; Gross, E. K. U. *Phys. Rev. Lett.* **1996,** *76,* 1212. doi:10.1103/PhysRevLett.76.1212
45. Onida, G.; Reining, L.; Rubio, A. *Rev. Mod. Phys.* **2002,** *74,* 601. doi:10.1103/RevModPhys.74.601
46. Despoja, V.; Dekanić, K.; Šunjić, M.; Marušić, L. *Phys. Rev. B* **2012,** *86,* 165419. doi:10.1103/PhysRevB.86.165419
47. Despoja, V.; Novko, D.; Dekanić, K.; Šunjić, M.; Marušić, L. *Phys. Rev. B* **2013,** *87,* 075447. doi:10.1103/PhysRevB.87.075447
48. Novko, D.; Despoja, V.; Šunjić, M. *Phys. Rev. B* **2015,** *91,* 195407. doi:10.1103/PhysRevB.91.195407
49. Pisarra, M.; Sindona, A.; Gravina, M.; Silkin, V. M.; Pitarke, J. M. *Phys. Rev. B* **2016,** *93,* 035440. doi:10.1103/PhysRevB.93.035440
50. Kramberger, C.; Hambach, R.; Giorgetti, C.; Rümmeli, M. H.; Knupfer, M.; Fink, J.; Büchner, B.; Reining, L.; Einarsson, E.; Maruyama, S.; Sottile, F.; Hannewald, K.; Olevano, V.; Marinopoulos, A. G.; Pichler, T. *Phys. Rev. Lett.* **2008,** *100,* 196803. doi:10.1103/PhysRevLett.100.196803
51. Pisarra, M.; Sindona, A.; Riccardi, P.; Silkin, V. M.; Pitarke, J. M. *New J. Phys.* **2014,** *16,* 083003. doi:10.1088/1367-2630/16/8/083003
52. Eberlein, T.; Bangert, U.; Nair, R. R.; Jones, R.; Gass, M.; Bleloch, A. L.; Novoselov, K. S.; Geim, A.; Briddon, P. R. *Phys. Rev. B* **2008,** *77,* 233406. doi:10.1103/PhysRevB.77.233406
53. Ligato, N.; Cupolillo, A.; Sindona, A.; Riccardi, P.; Pisarra, M.; Caputi, L. S. *Surf. Sci.* **2014,** *626,* 40–43. doi:10.1016/j.susc.2014.03.005
54. Pisarra, M.; Riccardi, P.; Sindona, A.; Cupolillo, A.; Ligato, N.; Giallombardo, C.; Caputi, L. *Carbon* **2014,** *77,* 796–802. doi:10.1016/j.carbon.2014.05.084
55. Riccardi, P.; Cupolillo, A.; Pisarra, M.; Sindona, A.; Caputi, L. S. *Appl. Phys. Lett.* **2012,** *101,* 183102. doi:10.1063/1.4765053
56. Pisarra, M.; Riccardi, P.; Cupolillo, A.; Sindona, A.; Caputi, L. S. *Nanosci. Nanotechnol. Lett.* **2012,** *4,* 1100–1103. doi:10.1166/nnl.2012.1465
57. Cupolillo, A.; Pisarra, M.; Sindona, A.; Commisso, M.; Riccardi, P. *Vacuum* **2010,** *84,* 1029–1032. doi:10.1016/j.vacuum.2009.11.013
58. Generalov, A. V.; Dedkov, Yu. S. *Carbon* **2012,** *50,* 183–191. doi:10.1016/j.carbon.2011.08.018
59. Cupolillo, A.; Ligato, N.; Caputi, L. S. *Carbon* **2012,** *50,* 2588–2591. doi:10.1016/j.carbon.2012.02.017
60. Tao, C.; Jiao, L.; Yazyev, O. V.; Chen, Y.-C.; Feng, J.; Zhang, X.; Capaz, R. B.; Tour, J. M.; Zettl, A.; Louie, S. G.; Dai, H. *Nat. Phys.* **2011,** *7,* 616–620. doi:10.1038/nphys1991
61. Hou, H.; Teng, J.; Palacios, T.; Chua, S. *Opt. Commun.* **2016,** *370,* 226–230. doi:10.1016/j.optcom.2016.03.023
62. Li, J.; Li, Z.; Zhou, G.; Liu, Z.; Wu, J.; Gu, B.-L.; Ihm, J.; Duan, W. *Phys. Rev. B* **2010,** *82,* 115410. doi:10.1103/PhysRevB.82.115410

License and Terms

BEILSTEIN JOURNAL OF NANOTECHNOLOGY

Influence of hydrofluoric acid treatment on electroless deposition of Au clusters

Rachela G. Milazzo*[1], Antonio M. Mio[1], Giuseppe D'Arrigo[1], Emanuele Smecca[1], Alessandra Alberti[1], Gabriele Fisichella[1], Filippo Giannazzo[1], Corrado Spinella[1] and Emanuele Rimini[1,2]

Full Research Paper

Open Access

Address:
[1]CNR-IMM Institute for the Microelectronics and Microsystems, Z. I. VIII Strada 4, Catania, I-95121, Italy and [2]Department of Physics and Astronomy, v. S. Sofia 64, I-95123, Catania, Italy

Email:
Rachela G. Milazzo* - gabriella.milazzo@imm.cnr.it

* Corresponding author

Keywords:
electroless deposition; galvanic deposition; gold nanoparticles; HF acid treatment; HF-propelled motion; hydrogen termination; silicon surfaces

Beilstein J. Nanotechnol. **2017,** *8,* 183–189.
doi:10.3762/bjnano.8.19

Received: 07 August 2016
Accepted: 28 December 2016
Published: 18 January 2017

This article is part of the Thematic Series "Self-assembly of nanostructures and nanomaterials II".

Guest Editor: I. Berbezier

Abstract

The morphology of gold nanoparticles (AuNPs) deposited on a (100) silicon wafer by simple immersion in a solution containing a metal salt and hydrofluoric acid (HF) is altered by HF treatment both before and after deposition. The gold clusters are characterized by the presence of flat regions and quasispherical particles consistent with the layer-by-layer or island growth modes, respectively. The cleaning procedure, including HF immersion prior to deposition, affects the predominantly occurring gold structures. Flat regions, which are of a few tens of nanometers long, are present after immersion for 10 s. The three-dimensional (3D) clusters are formed after a cleaning procedure of 4 min, which results in a large amount of spherical particles with a diameter of ≈15 nm and in a small percentage of residual square layers of a few nanometers in length. The samples were also treated with HF after the deposition and we found out a general thickening of flat regions, as revealed by TEM and AFM analysis. This result is in contrast to the coalescence observed in similar experiments performed with Ag. It is suggested that the HF dissolves the silicon oxide layer formed on top of the thin flat clusters and promotes the partial atomic rearrangement of the layered gold atoms, driven by a reduction of the surface energy. The X-ray diffraction investigation indicated changes in the crystalline orientation of the flat regions, which partially lose their initially heteroepitaxial relationship with the substrate. A postdeposition HF treatment for almost 70 s has nearly the same effect of long duration, high temperature annealing. The process presented herein could be beneficial to change the spectral response of nanoparticle arrays and to improve the conversion efficiency of hybrid photovoltaic devices.

Introduction

Gold nanoparticles on silicon substrates have shown quite interesting applications in the fields of Si nanowire (SiNW) catalysis [1-3], metal-assisted etching (MAE) [4] or even as electrical contacts in standard miniaturized devices [5]. Their ability to display enhanced surface plasmon resonance (SPR) at optical frequencies makes them excellent at scattering and absorbing visible light [6-8]. For these reasons, they have found an interesting application in the field of metal–semiconductor hybrid structures for solar energy conversion [9,10]. Among the different adopted methods to deposit Au nanoclusters on a substrate, electroless deposition based on galvanic displacement reactions is an efficient and versatile technique. It consists of manually dipping samples in a plating bath for few seconds without the need for application of an external current or potential [11-15]. Details about the reaction between Au^+ and Si atoms involved in the deposition are described elsewhere [16]. The morphology of gold by electroless deposition is quite complex and a number of basic questions remain to be clarified, such as the nature of the interface with silicon in the presence of hydrofluoric acid (HF). It has been reported in some studies that silicides are formed due to the strong interaction of Au atoms with Si [17]. On this topic, several contrasting reports are found in the literature but it is generally accepted that at a critical thickness (in the range of 2 to 5 ML) the gold seems inert and unable to mix with silicon. For gold deposited on silicon via galvanic displacement (GD), both Volmer–Weber and Stranski–Krastanov modes of growth have been suggested to be involved. It has been found that Si atoms diffuse outwards through the deposited gold layers during the growth process with the subsequent formation of Si oxide on their surface. The process stops after a certain thickness of oxide is formed and on top of it gold atoms agglomerate as solid clusters [18-21]. The optical properties of these gold clusters depend on their shape and morphology. It is reported in literature that the local field enhancement factor of gold nanoparticles depends on their geometry and it is higher for well-shaped spherical particles than for flat islands [22]. Generally, an additional postdeposition annealing step is usually required to improve the spectral response. In our previous study on the GD of Au^+ ions onto silicon substrates, we found that metal nanoparticles nucleate instantaneously and their subsequent growth is governed by diffusion in the solution [23]. In detail, we showed that by immersion of a Si(100) substrate for a few seconds in a solution containing 1 mM $KAuCl_4$ and 4.8 M HF, AuNPs with a mean radius of less than 10 nm and a density higher than 10^{10} cm^{-2} are formed. In the present work, we show that with proper HF treatments, the 3D Au clusters prevail over the flat regions obtained by layer-by-layer growth. Such a beneficial alteration requires only a manual immersion for a few seconds in a diluted hydrofluoric acid solution (DHF) with 6% HF without the need for annealing or high power light irradiation [24].

Results and Discussion

The morphology of the samples was investigated with transmission electron microscopy (TEM). It has been reported in previous papers that the specimen preparation could alter the original and structural characteristics of the Au particles [25]. Therefore, we prepared the samples for TEM analysis using two different thinning procedures. One sample was obtained after a conventional TEM preparation technique, including mechanical and high energy ion thinning (Ar^+ ions at 5 keV). The other one was prepared instead with the so-called "gentle milling" procedure using low energy (0.1–1 keV) Ar^+ ions (see details in the Experimental section). The results are compared in Figure 1 that shows a plan view TEM of the silicon substrate after the same gold deposition process but prepared following the standard (Figure 1a) and the gentle milling (Figure 1b) procedures, respectively. The morphology is drastically modified by the high energy Ar^+ ion thinning, where the mean particle size is about 20% larger and the density increases by about 30% with respect to the low energy Ar^+ beam thinning procedure. The particles in Figure 1a are more spherical in shape with light grey areas of irregular shape, while in Figure 1b, the clusters are elongated and we observe square light gray regions. Clearly, gold atom rearrangement occurs in the sample during the standard thinning process that probably results from the heating of the sample due to the higher Ar^+ ion energy. In order to avoid artifacts, we therefore adopted the gentle milling procedure for all the samples to be analyzed by TEM. We tested the reliability of the mechanical thinning procedure by repeating both the HF pretreatments and the deposition step on a Si sample already thinned and then ready for TEM analysis. The Au cluster morphology was quite similar (see Supporting Information File 1, Figure S1) to that obtained by deposition on bulk substrates. As a result, we used standard wafers for deposition, and the samples were mechanically thinned and gently milled for TEM observations.

HF treatment before Au deposition

The Si(100) substrates were cleaned following the procedure described in the experimental section. Some of them were subsequently immersed in DHF (diluted HF, 6% HF) for 10 s and some others for 240 s. The electroless gold deposition takes place then by immersion in the plating solution for 3 s. The TEM images of the corresponding samples are reported in Figure 2a,b, respectively. The gold morphology clearly varies with the time of the DHF pretreatment. After 10 s in DHF (see Figure 2a), Au atoms uniformly assemble on the Si substrate with elongated and wide structures of a few tens of nanometers

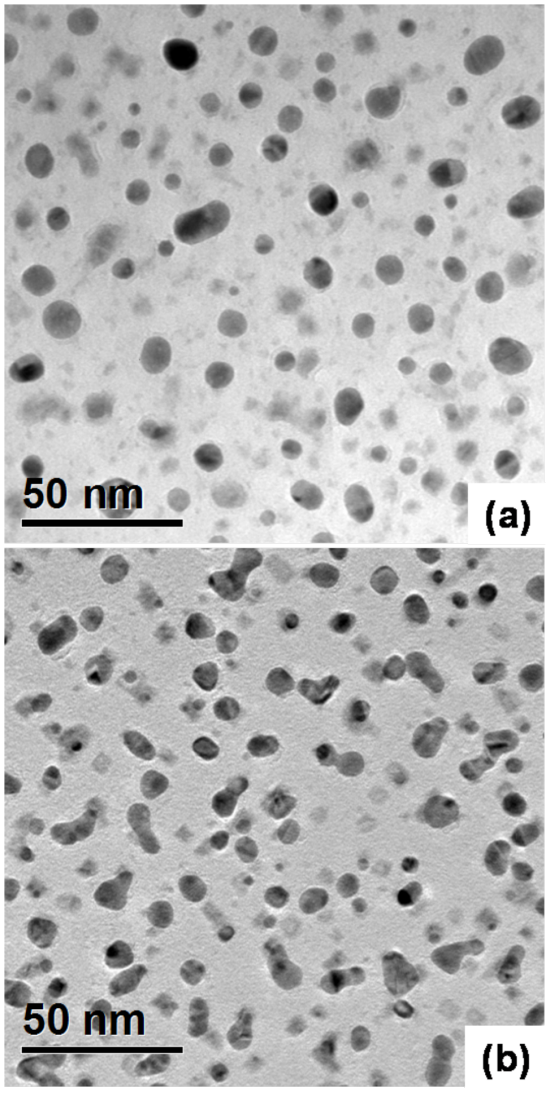

Figure 1: Plan view TEM micrographs of AuNPs electroless deposited on a Si substrate by immersion for 3 s in the solution after a DHF pretreatment of 240 s; sample preparation (a) standard high energy and (b) gentle milling procedure.

long. After 4 min in DHF (Figure 2b), they arrange as small particles of spherical shape with a radius of less than 10 nm. Although the images were taken in bright field mode, a huge mass contrast between light gray, thin regions of square shape (labeled 1 in Figure 2b) and the dark, thick round particles (labeled 2 in Figure 2b) is clearly shown.

The two samples were also analyzed by Rutherford backscattering (RBS) measurements with 2 MeV He^+ ions in order to obtain the areal density of the deposited gold atoms, which was found to be 4.24×10^{15} atoms cm^{-2} for sample (a) and to 4.73×10^{15} atoms cm^{-2} for sample (b). By comparing these results with the fractional covered area measured by the TEM micrographs we estimated an equivalent mean thickness of 3 nm and 10 nm, respectively. So, in other words, in the first case the layer-by-layer growth prevails while a 3D arrangement is promoted by the DHF pretreatment of 240 s. It is well known that HF strongly modifies the silicon surface roughness [26-29] and wetting properties [30]. The surface-free energy of gold is 1410×10^{-3} J/m^{-2}, while that of Si and SiO_2 are 1240×10^{-3} J/m^2 and 400×10^{-3} J/m^2, respectively [31]. The native SiO_2 is completely etched after 10 s (etch rate 500 Å/min) so nucleation occurs on the hydrogenated silicon surface [32]. The roughness of the Si surface after a pretreatment of 4 min in DHF was measured by AFM, and the obtained root mean square (RMS) was 3 nm, which is about one order of magnitude higher than a typical Si wafer (Figure 2c). Consequently, the surface-free energy increases [33] for a rougher surface and promotes 3D cluster formation by offering preferential sites for nucleation as apex or surface discontinuities.

HF postdeposition treatment

So far we have shown the influence of a DHF pretreatment on the subsequent Au deposition regarding the shape and morphology of the nanoclusters. We now consider what happens if the

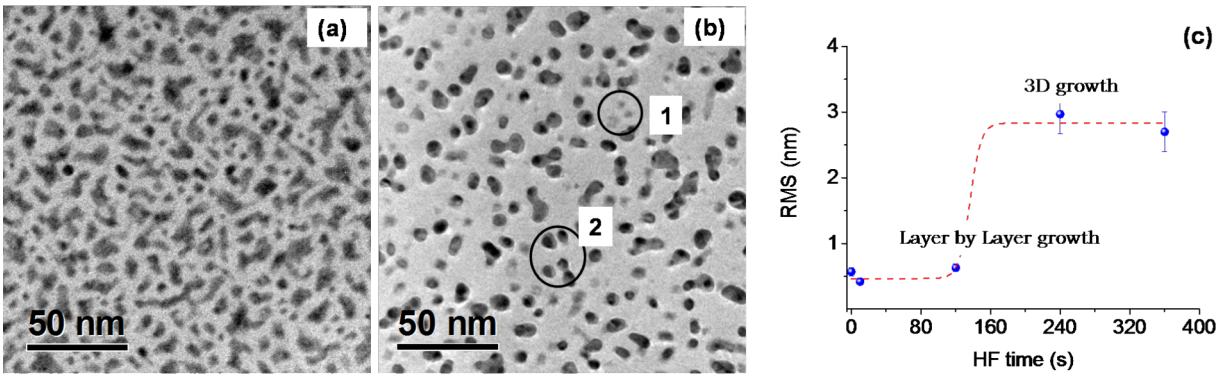

Figure 2: Gold electroless deposition on Si(100) after an DHF pretreatment of 10 s (a) and 240 s (b); root mean squared (RMS) for the corresponding Si substrates (c) measured with AFM.

DHF treatment is performed after the gold deposition. There are many papers dealing with dynamic coalescence of metal nanoparticles in liquids [34-36]. In a previous work, we found that silver nanoparticles are subjected to Smoluchowski [37] ripening in DHF solutions by increasing their size and decreasing their surface density. For the case of gold nanoparticles on Si, we expect a more complex scenario due to the stronger interaction between gold and silicon with the formation of quasi-heteroepitaxial layers. Figure 3 reports the morphologies observed by AFM (in tapping mode with a silicon tip of 10–15 nm curvature radius) of Si samples with AuNPs before (Figure 3a) and after (Figure 3b) an HF postdeposition treatment of 70 s.

The postdeposition treatment clearly results in a much flatter surface morphology than in the untreated sample. This effect can be quantified by calculating the root mean square (RMS) roughness from the two 1 × 1 µm scans in Figure 3, showing a decrease in the RMS value from 2.53 nm for the untreated sample to 1.16 nm after the HF treatment. This indicates a more uniform height distribution of clusters with respect to the substrate after the postdeposition treatment. To better illustrate this aspect, the histograms of the z values (in terms of deviation from the mean height) extracted from the two AFM images are also reported in Figure 3c, showing a broad distribution in the as-deposited sample, with an asymmetric tail extending toward lower z values, whereas a much narrower distribution is observed after the HF treatment.

The corresponding plan view TEM micrographs of the two samples are also reported in the inserts of Figure 3a and Figure 3b, respectively. The selected area electron diffraction (SAED), shown in Supporting Information File 1, Figure S2, of the AuNPs presents a bright spot in the (200)Au ring along the (400)Si directions indicating a heteroepitaxial arrangement of the deposited Au atoms, as also previously reported [21]. The intensity of this spot is reduced after HF treatment so one could envisage that the flat gray regions are heteroepitaxial with the substrate orientation. The 3D arrangement of the Au atoms after the HF solution treatment indicates that the heteroepitaxial relationship with the substrate is partially lost.

Moreover, the amount of Au on the sample, as measured using RBS, does not change even after an HF treatment of 70 s, indicating that the atomic arrangement is not associated to dissolution of the deposited gold atoms (see Supporting Information File 1, Figure S3).

For a better understanding of the process taking place under immersion in HF we prepared a sample with large, flat regions, obtained after a short HF pretreatment followed by an immersion for 20 s in the plating solution. The morphology of gold

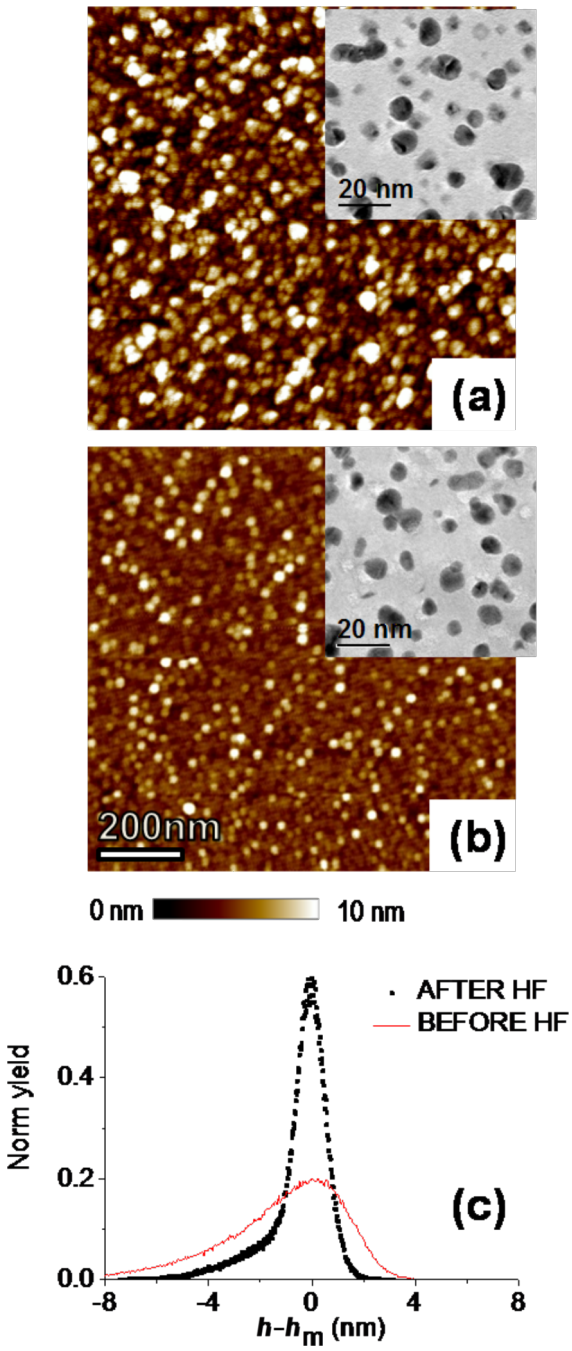

Figure 3: AFM z-scan of Si sample with AuNPs before (a) and after (b) a postdeposition bake in HF for 70 s, with the corresponding TEM images in the upper right hand part. (c) Height distribution relative to the mean value, as calculated from AFM images.

was examined with plan view TEM and scanning transmission electron microscopy (STEM) in high-angle annular dark-field imaging (HAADF) Z-contrast (atomic number) imaging mode, while the crystalline structure was analyzed in detail with X-ray diffraction. Figure 4a and Figure 4b are the plan view TEM of the samples before and after the HF postdeposition treatment

for 70 s. The more discernible effect is a pronounced change in the fractional covered area that varies by about 15%. By using a STEM detector with a large inner radius (a HAADF detector) electrons are collected which are not Bragg scattered. As such HAADF images show little or no diffraction effects, and their intensity is approximately proportional to Z^2. The HF postdeposition treatment levels off the intensity distribution of the corresponding STEM micrograph, indicating a more uniform thickness for the gold particles as clearly seen by comparing Figure 4c and Figure 4d, respectively.

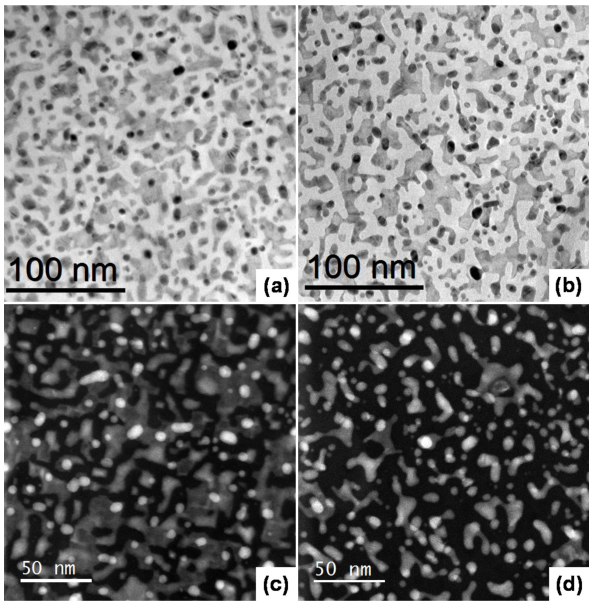

Figure 4: Plan view TEM of Si sample with Au islands obtained with 20 s immersion in the plating solution (a); the same sample after a HF postdeposition treatment of 70 s (b) and (c) and (d) STEM image of (a) and (b), respectively.

The samples were also inspected with X-ray diffraction (Figure 5). Two different configurations were adopted. In the Bragg–Brentano geometry we observed a significant (200) Au peak at 2θ = 44.3°. Although the (111) peak at 38.2° was expected to be the most dominant (the bars represented the computed intensities for a powder sample), the dominant peak at 2θ = 44.3° indicates the occurrence of texturing in the Au cluster orientation. The (111) Au peak at 2θ = 38.2°, measured with grazing incidence X-ray diffraction, showed the presence of randomly oriented Au clusters coexisting with the heteroepitaxial regions on the Si substrate.

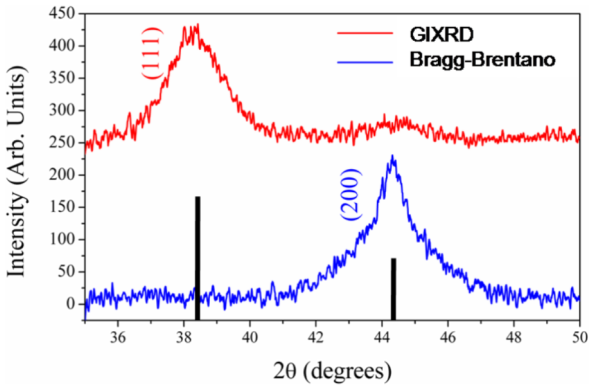

Figure 5: Diffraction profile of sample with AuNPs from a 20 s deposition for the grazing incidence (red, upper) and for the Bragg–Brentano (blue, lower). The bars represent the computed intensities for a random Au powder in the Bragg–Brentano geometry.

Moreover, the shape of the (200) diffraction peak indicates that two families of grains, both exhibiting texturing in the [001] crystallographic direction, are present. The deconvolution of the signal is reported in Figure 6a and the size of the corresponding crystals is determined by the Scherrer formula [38].

We observe a broad peak, with a FWHM of 2.6°, associated with large regions about 3 nm thick. They coexist with small 3D clusters that are about 15 nm high and whose contribution to the

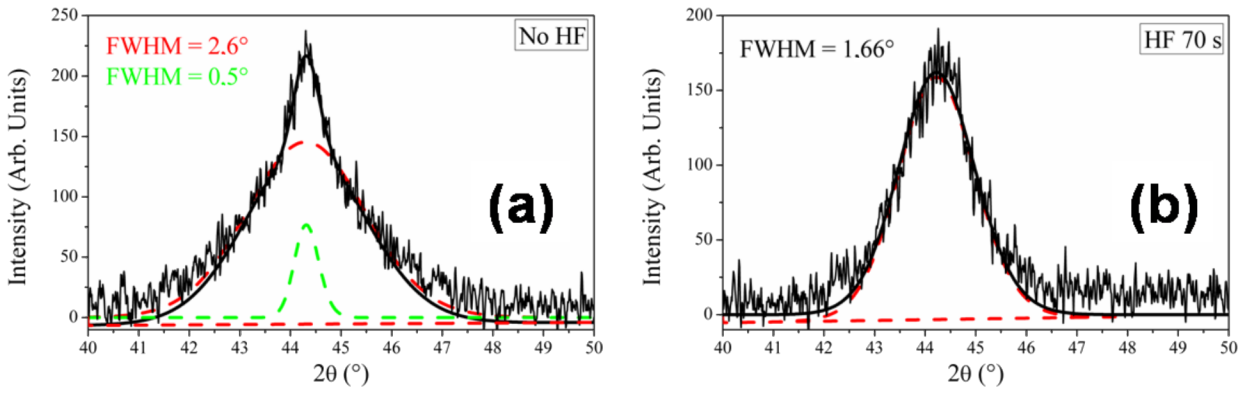

Figure 6: Au (200) peak as measured by XRD in Bragg–Brentano geometry of (a) as-deposited sample and (b) the same sample but after an HF treatment for 70 s.

diffraction profile is represented by the Gaussian shape with a FWHM of 0.5°. The same analysis was repeated after immersion of the sample in HF for 70 s, and the diffractogram is shown in Figure 6b. The FWHM for the XRD profile decreases with increasing time in HF and is 2.26° after 40 s and 1.66° after 70 s, indicating a thickening of the islands along the growth axis (3.8 nm and 5 nm, respectively). The results are in agreement with the TEM images that predicted an "in-plan" shrinkage plus "in-height" increase for gold structures. We probed the modification in the crystalline orientation, as found by SAED, by comparing the "heteroepitaxial ratio", defined as:

$$R_{\text{h.e.}} = \frac{\left(A_{200}/A_{111}\right)_{\text{as-dep}}}{\left(A_{200}/A_{111}\right)_{\text{post\_HF}}} \quad (1)$$

where A is the area under the corresponding peak. $R_{\text{h.e.}}$ is a parameter related to the degree of texturing exhibited by the Au particles as a function of the HF treatment. The ratio amounts to 1.17 after 40 s and to 1.75 after 70 s, indicating a reduction of the textured component with immersion time in the HF solution.

Conclusion

In this work we investigate the morphology of gold aggregates on silicon (100) substrates obtained by galvanic displacement using XRD, AFM and TEM (with a proper low-energy ion milling procedure). It was shown that Au atoms assemble in thin regions and are irregularly shaped and also form in 3D spherical clusters. The 3D spherical clusters form according to the layer-by-layer and island growth modes but it is possible to select between the two by varying the immersion time in DHF solution during the cleaning procedure. Specifically, after a quick immersion time of about 10 s and a deposition time of 3 s, we obtained a discontinuous gold film of a few monolayers thick. When the HF pretreatment is extended up to 4 min, for the same plating time, we observed mostly spherical clusters, while the thin regions were reduced to small squares of a few nanometers long, which were aligned with the [001] direction of the substrate. With a 10 s HF pretreatment and longer deposition times (about 20 s), both structures coexist, corroborating the layer-by-layer plus island growth modes for gold on silicon. The SAED and the XRD measurements showed a pronounced heteroepitaxial component but also a polycrystalline phase for Au on Si(100) obtained by galvanic displacement. The layered gold regions could be altered by means of postdeposition HF treatments. TEM observations and XRD analysis showed that they thicken and rearrange their own crystalline structure. HF is known to etch SiO_2, changing the surface chemical composition and also the free energy of Si. As a result, the layered gold is freed and the outlying atoms move toward inner regions to reduce their surface free energy. The process is very fast and bears similarities with the HF self-propelled motion of liquid droplets on solid surfaces [39]. The results are comparable to those obtained after high temperature and/or time consuming annealing procedures.

Experimental

Pretreatment of silicon substrate and metal deposition. The starting substrate was a Si(100) n-type substrate with ρ = 3–5 Ω cm. Prior to plating, each sample was cut into squares of 1.5 × 1.5 cm and degreased in acetone at 60 °C and then placed in an ultrasonic bath for 6 min. This was followed by immersion in DHF (6% HF) for 10 s or 240 s. The substrates were then thoroughly washed with deionized water and blow-dried in air. Gold deposition was carried out by manually soaking each sample in a solution containing 1 mM $KAuCl_4$ (99.995% trace metal, Sigma-Aldrich) and 10% HF (diluted HF, GPR RECTAPUR 40%, VWR) at room temperature, under ambient light conditions and without stirring. Then the samples were rinsed in water to remove all surfactants and products. They received an additional cleaning in acetone and were dried in air.

TEM sample preparation. For plan view, the samples were mechanically thinned from the backside to less than a micrometer. Then they were milled with a Gatan PIPS II device, according to a low-energy procedure. Gentle milling was performed at low temperature (less than −100 °C with LN_2 cooling) at a 6° milling angle and with beam energy of 1 keV and current of 30 μA at the beginning and of 0.1 keV and 25 μA for final polishing.

Supporting Information

We provide images for further understanding of the influence of the TEM thinning procedures and we give evidence of the random rearrangement of gold atoms by electron diffraction on a selected area. We also show the Rutherford backscattering spectra of the samples before and after the HF postdeposition treatments to demonstrate that the amount of gold atoms does not change.

Supporting Information File 1

Additional experimental data.
[http://www.beilstein-journals.org/bjnano/content/supplementary/2190-4286-8-19-S1.pdf]

Acknowledgements

The authors are grateful to Dr. F. Ruffino for his precious AFM analysis.

References

1. Kolasinski, K. W. *Curr. Opin. Solid State Mater. Sci.* **2006,** *10,* 182–191. doi:10.1016/j.cossms.2007.03.002
2. Schimdt, V.; Senz, S.; Gösele, U. *Nano Lett.* **2010,** *5,* 931–935. doi:10.1021/nl050462g
3. Garozzo, C.; La Magna, A.; Mannino, G.; Scalese, S.; Sberna, P. M.; Simone, F.; Puglisi, R. A. *J. Appl. Phys.* **2013,** *113,* 214313. doi:10.1063/1.4809557
4. Han, H.; Huang, Z.; Lee, W. *Nano Today* **2014,** *9,* 271–304. doi:10.1016/j.nantod.2014.04.013
5. Schmid, G.; Simon, U. *Chem. Commun.* **2005,** 697–710. doi:10.1039/B411696H
6. Noguez, C. *J. Phys. Chem. C* **2007,** *111,* 3806–3819. doi:10.1021/jp066539m
7. Ammari, H.; Deng, Y.; Millien, P. *Arch. Ration. Mech. Anal.* **2016,** *220,* 109–153. doi:10.1007/s00205-015-0928-0
8. Jeong, S.-H.; Choi, H.; Kim, J. Y.; Lee, T.-W. *Part. Part. Syst. Charact.* **2015,** *32,* 164–175. doi:10.1002/ppsc.201400117
9. Stratakis, E.; Kymakis, E. *Mater. Today* **2013,** *16,* 133–146. doi:10.1016/j.mattod.2013.04.006
10. Lu, R.; Xu, L.; Ge, Z.; Li, R.; Xu, J.; Yu, L.; Chen, K. *Nanoscale Res. Lett.* **2016,** *11,* 160. doi:10.1186/s11671-016-1374-0
11. Song, Y.-Y.; Gao, Z.-D.; Kelly, J. J.; Xia, X.-H. *Electrochem. Solid-State Lett.* **2005,** *8,* C148–C150. doi:10.1149/1.2033616
12. Qiu, T.; Chu, P. K. *Mater. Sci. Eng., R* **2008,** *61,* 59–77. doi:10.1016/j.mser.2008.03.001
13. Yae, S.; Nasu, N.; Matsumoto, K.; Hagihara, T.; Fukumuro, N.; Matsuda, H. *Electrochim. Acta* **2007,** *53,* 35–41. doi:10.1016/j.electacta.2007.04.058
14. Soejima, T.; Katayama, Y.; Fuji, S. *CrystEngComm* **2016,** *18,* 6683–6688. doi:10.1039/C6CE01199C
15. Wang, T.; Hu, F.; Ikhile, E.; Liao, F.; Li, Y.; Shao, M. *J. Mater. Chem. C* **2015,** *3,* 559–563. doi:10.1039/C4TC02310B
16. Zhao, L.; Siu, A. C.-L.; Petrus, J. A.; He, Z.; Leung, K. T. *J. Am. Chem. Soc.* **2007,** *129,* 5730–5734. doi:10.1021/ja070441j
17. Ruffino, F.; Grimaldi, M. G. *J. Appl. Phys.* **2010,** *107,* 104321. doi:10.1063/1.3428467
18. Andersson, T. G. *Gold Bull.* **1982,** *15,* 7–18. doi:10.1007/BF03216565
19. Okuno, K.; Ito, T.; Iwami, M.; Hiraki, A. *Solid State Commun.* **1980,** *34,* 493–497. doi:10.1016/0038-1098(80)90659-6
20. Hiraki, A.; Iwami, M. *Jpn. J. Appl. Phys.* **1974,** *13,* 749. doi:10.7567/JJAPS.2S2.749
21. Sayed, S. Y.; Wang, F.; Malac, M.; Meldrum, A.; Egerton, R. F.; Buriak, J. M. *ACS Nano* **2009,** *3,* 2809–2817. doi:10.1021/nn900685a
22. Li, B.; Huang, L.; Zhou, M.; Fan, X.; Ma, M. *J. Wuhan Univ. Technol., Mater. Sci. Ed.* **2012,** *29,* 651–655. doi:10.1007/s11595-014-0973-9
23. Milazzo, R. G.; Mio, A. M.; D'Arrigo, G.; Spinella, C.; Grimaldi, M. G.; Rimini, E. *IEEE Nanotechnol. Mater. Devices Conf.* **2014,** 37–40. doi:10.1109/NMDC.2014.6997416
24. Imama, H.; Elsayed, K.; Ahmed, M. A.; Ramdan, R. *Opt. Photonics J.* **2012,** *2,* 73–84. doi:10.4236/opj.2012.22011
25. Garozzo, C.; Filetti, A.; Bongiorno, C.; La Magna, A.; Simone, F.; Puglisi, R. A. *Gold Bull.* **2014,** *47,* 185–193. doi:10.1007/s13404-014-0142-0
26. Trucks, G. W.; Raghvachari, K.; Higashi, G. S.; Chabal, Y. J. *Phys. Rev. Lett.* **1990,** *65,* 504. doi:10.1103/PhysRevLett.65.504
27. Takahagi, T.; Nagai, I.; Ishitani, A.; Kuroda, H.; Nagasawa, Y. *J. Appl. Phys.* **1998,** *64,* 3516–3521. doi:10.1063/1.341489
28. Ubara, H.; Imura, T.; Hiraki, A. *Solid State Commun.* **1984,** *50,* 673–675. doi:10.1016/0038-1098(84)90156-X
29. Higashi, G. S.; Chabal, Y. J.; Trucks, G. W.; Raghavachari, K. *Appl. Phys. Lett.* **1990,** *56,* 656–658. doi:10.1063/1.102728
30. Kumar, V.; Bhat, K. N.; Sharma, N. N. *J. Adhes. Sci. Technol.* **2015,** *29,* 308–318. doi:10.1080/01694243.2014.986835
31. Tu, K. N.; Mayer, W. J.; Feldman, L. C. *Electronic thin film science for electrical engineering and material scientist;* Macmillan, 1992.
32. Monk, D. J.; Soane, D. S.; Howe, R. T. *Thin Solid Films* **1993,** *232,* 1–12. doi:10.1016/0040-6090(93)90752-B
33. Kubiak, K. J.; Wilson, M. C. T.; Mathia, T. G.; Carval, P. *Wear* **2011,** *271,* 523–528. doi:10.1016/j.wear.2010.03.029
34. Stoldt, C. R.; Jenks, C. J.; Thiel, P. A.; Cadilhe, A. M.; Evans, J. W. *J. Chem. Phys.* **1999,** *111,* 5157–5166. doi:10.1063/1.479770
35. Gerber, T.; Knudesn, J.; Feilbelman, P. J.; Grånäs, E.; Stratmann, P.; Schulte, K.; Andersen, J. N.; Michely, T. *ACS Nano* **2013,** *7,* 2020–2031. doi:10.1021/nn400082w
36. Polte, J. *CrystEngComm* **2015,** *17,* 6809–6830. doi:10.1039/C5CE01014D
37. Milazzo, R. G.; Mio, A. M.; D'Arrigo, G.; Grimaldi, M. G.; Spinella, C.; Rimini, E. *J. Chem. Phys.* **2015,** *143,* 024306. doi:10.1063/1.4926530
38. Scherrer, P. *Nachr. Ges. Wiss. Göttingen* **1918,** *1918,* 98–100.
39. Yao, X.; Bai, H.; Ju, J.; Zhou, D.; Li, J.; Zhang, H.; Yang, B.; Jiang, L. *Soft Matter* **2012,** *8,* 5988–5991. doi:10.1039/c2sm25153a

BEILSTEIN JOURNAL OF NANOTECHNOLOGY

Optical and photocatalytic properties of TiO_2 nanoplumes

Viviana Scuderi[1], Massimo Zimbone[*1], Maria Miritello[1], Giuseppe Nicotra[2], Giuliana Impellizzeri[1] and Vittorio Privitera[1]

Full Research Paper

Open Access

Address:
[1]CNR-IMM, Via S. Sofia 64, 95123 Catania, Italy and [2]CNR-IMM, Z.I. VIII Strada 5, 95121 Catania, Italy

Email:
Massimo Zimbone[*] - massimo.zimbone@ct.infn.it

* Corresponding author

Keywords:
black titania; nanostructures; photocatalysis; titanium dioxide (TiO_2)

Beilstein J. Nanotechnol. **2017,** *8,* 190–195.
doi:10.3762/bjnano.8.20

Received: 13 July 2016
Accepted: 06 January 2017
Published: 18 January 2017

This article is part of the Thematic Series "Self-assembly of nanostructures and nanomaterials II".

Guest Editor: I. Berbezier

Abstract

Here we report the photocatalytic efficiency of hydrogenated TiO_2 nanoplumes studied by measuring dye degradation in water. Nanoplumes were synthesized by peroxide etching of Ti films with different thicknesses. Structural characterization was carried out by scanning electron microscopy and transmission electron microscopy. We investigated in detail the optical properties of the synthesized material and related them to the efficiency of UV photodegradation of methylene blue dye. The obtained results show that TiO_2 nanoplumes act as an effective antireflective layer increasing the UV photocatalytic yield of the film.

Introduction

Today water, energy, and food are the most urgent problems of humanity. Since the seminal work of Honda and Fujishima in 1972 where photo-induced decomposition of water was discovered [1], semiconductor photocatalysis has shown great potential not only for renewable energy generation but also in sustainable technology to remove dangerous contaminants from water [2-6]. In this context, TiO_2 is one of the most extensively studied materials. However, TiO_2 is characterized by a wide band gap (ca. 3 eV) resulting in a poor absorption of light in the visible region [7]. Different approaches were proposed to overcome this limit: the inhibition of the recombination of photogenerated electrons and holes [8,9], the increase of the exposed surface area [10-12], and the decrease of the band-gap energy [13,14].

Recently, Chen et al. were able to synthesize black TiO_2 with a large optical absorption in the visible and infrared region [15-18]. The amorphous shell on a crystalline nanoparticle core, causes the formation of intragap states [19], which are responsible for the high absorption of visible light (and consequently of

the black color). Unfortunately, the synthesis of this remarkable material requires high pressures of H_2 (up to 20 bar) and long annealing treatments (up to 5 days).

Our group investigated the possibility to synthesize black TiO_2 by an easier method [20]. In 2016 we employed, for the first time [21], hydrogen peroxide etching of Ti films as an easy, rapid, and low-cost method to synthesize hydrogenated TiO_2 nanoplumes with significant photocatalytic properties under UV and visible light irradiation.

Here we report the optical properties of the TiO_2 nanoplumes and their correlation with the efficiency of UV photodegradation of methylene blue (MB). The obtained results show that TiO_2 nanoplumes act as effective antireflective layer increasing the UV photocatalytic yield.

Results and Discussion

In order to observe the morphology of the films we analyzed the Ti samples after different etching times by SEM in plan view. Two Ti film thicknesses, 70 nm and 430 nm, were used. Hereafter, we will call the samples Ti (70-x_i) and Ti (430-x_i), where x_i is the time of etching. The images are reported in Figure 1. Figure 1a and Figure 1b show a Ti film of 70 nm after etching for 60 and 150 s, respectively. After 60 s of etching there is no observable change in the surface of the film, compared with the as-deposited Ti film (inset of Figure 1a). After 150 s of etching, instead, the Ti (70-150) sample shows a rough surface. Figure 1c and Figure 1d show a Ti film of 430 nm after etching for 150 and 190 s, respectively. A statistical analysis showed that he roughness of the surface and the porosity of the structure increase with the etching time.

In Figure 2a, a cross-sectional view STEM image of Ti (430-190) is reported. The sample shows the presence of a nanostructured material. The etching clearly expands from the surface of the Ti film to the bulk of the material, generating a nanostructured film with high porosity and roughness, that we called nanoplumes [21]. Nanoplumes (ca. 300 nm in thickness) show the presence of a residual Ti layer at the bottom (ca. 70 nm in thickness). Energy dispersive X-ray analyses reported in [21] indicated that the nanoplumes are made of TiO_2. In addition, an accurate characterization of the nanoplumes performed by X-ray diffraction (XRD) measurements, X-ray Fourier transform infrared spectroscopy (FTIR), and photoelectron spectroscopy (XPS), revealed that after the etching the samples are

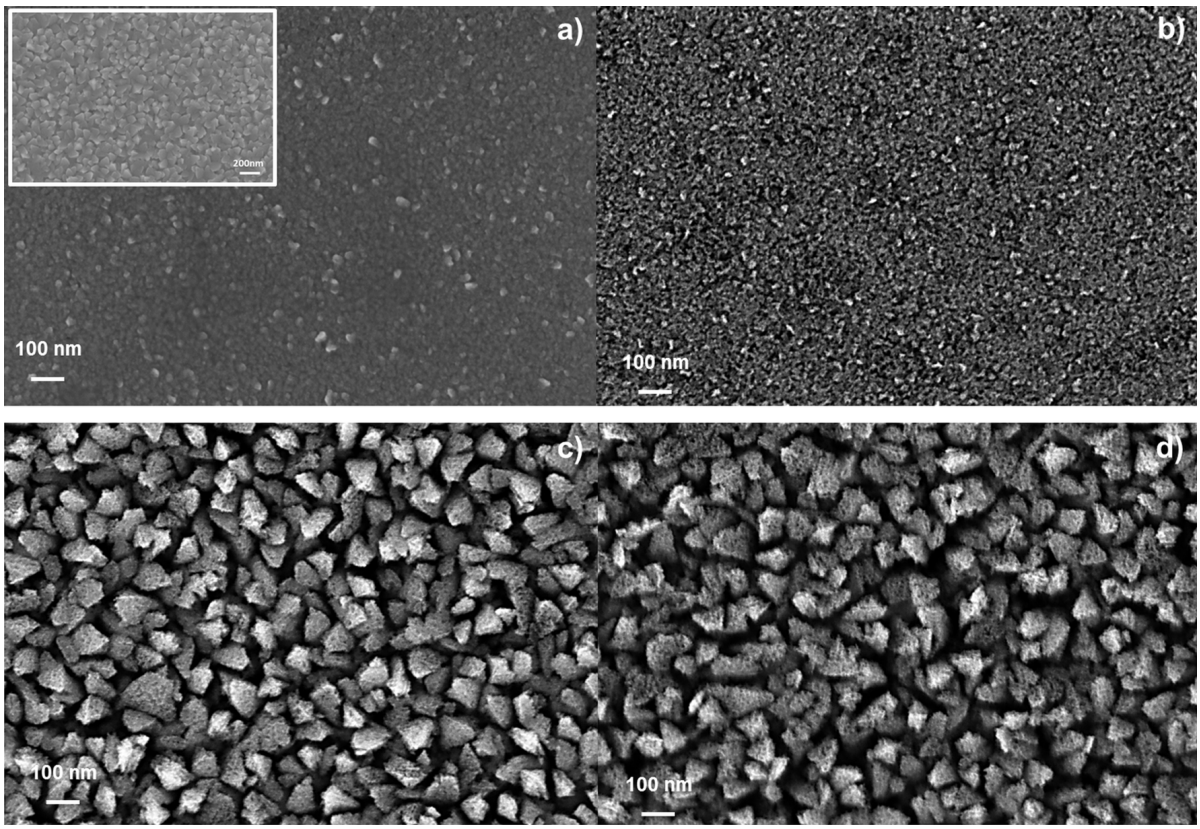

Figure 1: SEM images of a Ti film (70 nm thick) after etching for (a) 60 and (b) 150 s. Images of a Ti film (430 nm thick) after etching for (c) 150 and (d) 190 s. Inset of panel (a): Ti film before the etching.

amorphous and composed of titanium and oxygen [21]. An abundance of –OH groups was revealed on the surface of the samples.

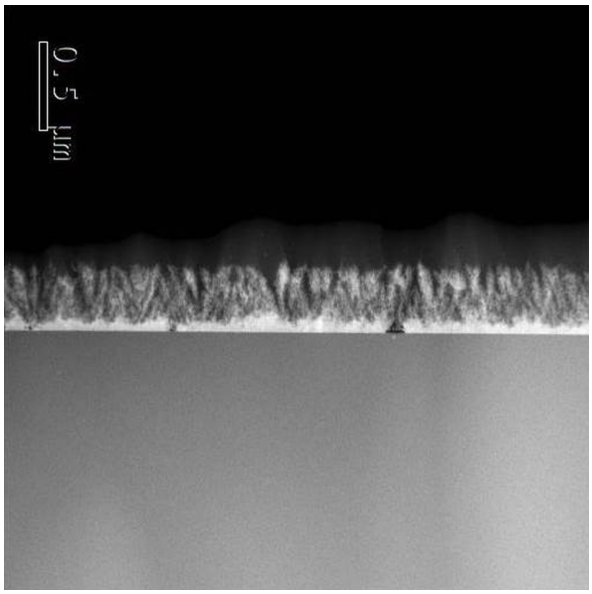

Figure 2: Cross-view TEM image of Ti (430-190).

Figure 3 shows the logarithmic residual concentration of MB as a function of the time under UV irradiation. C is the measured concentration of MB during irradiation, and C_0 is the starting concentration of MB. A pseudo-first order photocatalytic rate constant, k [3], was extracted and the values are reported in Figure 3 for all the analyzed samples. The surfaces were previously saturated with MB molecules. The samples were kept immersed in the MB solution in dark for 12 h. So the surfaces reached a steady-state of adsorption [21]. No photobleaching of the MB molecules on the control solution was detected, therefore the decay in the MB concentration is only related to the degradation of the reactant through a photocatalytic reaction with the surface. Ti (430-190) samples exhibit the best photocatalytic activity in degrading the MB dye under UV irradiation. In order to analyze the obtained photocatalytic results, it is necessary to take into account different factors that influence the reaction. Although the macroscopic surface is the same, the active surface areas for the photocatalytic reaction is different for each type of sample. Moreover the dynamic mechanisms of liquid circulation around [22] and inside nanostructures are not obvious [23]. However, the possible enhancement in the light trapping efficiency could provide additional photogenerated carriers, and as a consequence could favor the photocatalytic activity.

In order to gain more insight into the realized structure, we performed transmittance (T) and reflectance (R) measurements in

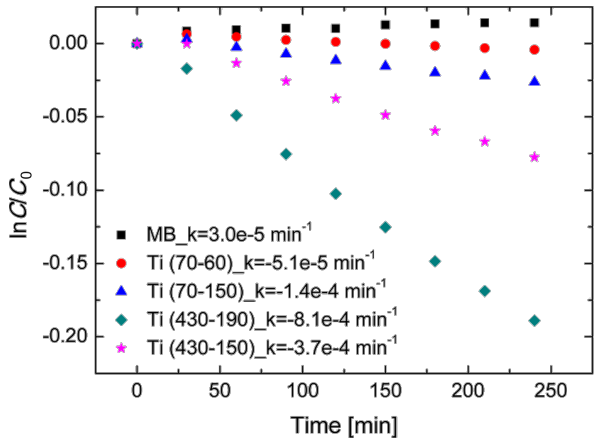

Figure 3: MB degradation under UV light irradiation for five samples: MB (black squares), MB with Ti (70-60) (red circles), MB with Ti (70-150) (blue triangles), MB with Ti (430-150) (pink stars), MB with Ti (430-190) (green diamonds).

the range of 200–800 nm. The optical spectra are reported in Figure 4. The transmittance spectra (Figure 4a) show that the transmitted light by the samples is closely related to the thickness of the residual Ti layer and, consequently, to the etching time. In fact, for a fixed Ti starting thickness we observed a more efficient transmittance after longer etching times (compare the dashed-dotted with the dotted line, and the dashed with the continuous line).

The reflectance measurements are reported in Figure 4b. The total reflectance spectra of Ti (70-60) and Ti (70-150) present a shift in the reflectance peak, from 302 to 314 nm. This shift may be related to the variation on the sample thickness, due to the different chemical etching time. Although the measured spectra include wavelengths from 200 to 800 nm we will focus on the UV region, since the light source of photocatalytic experiments emits in this range (dashed vertical line). In this region the absolute values of reflectance for Ti (70-60) and Ti (70-150) are about 10%. The total reflectance of Ti (430-150) and Ti (430-190) exhibits an almost completely suppression, below 5% in the UV range, and a 50% decrease between 410 and 700 nm compared to the previous two samples. The oscillations of the spectra are due to optical interference. Ti (430-190) exhibits a high exposed surface area due to the longer chemical etching and the lowest reflectivity in the UV-A region. Both parameters affect the photocatalytic properties of the sample making it particularly active in the presence of MB.

As shown before [21], the defects introduced in the material by the chemical etching (in particular, Ti^{3+} and OH groups) are responsible for a blurring of the valence and conduction bands. Consequently, a reduction of the optical gap was reported.

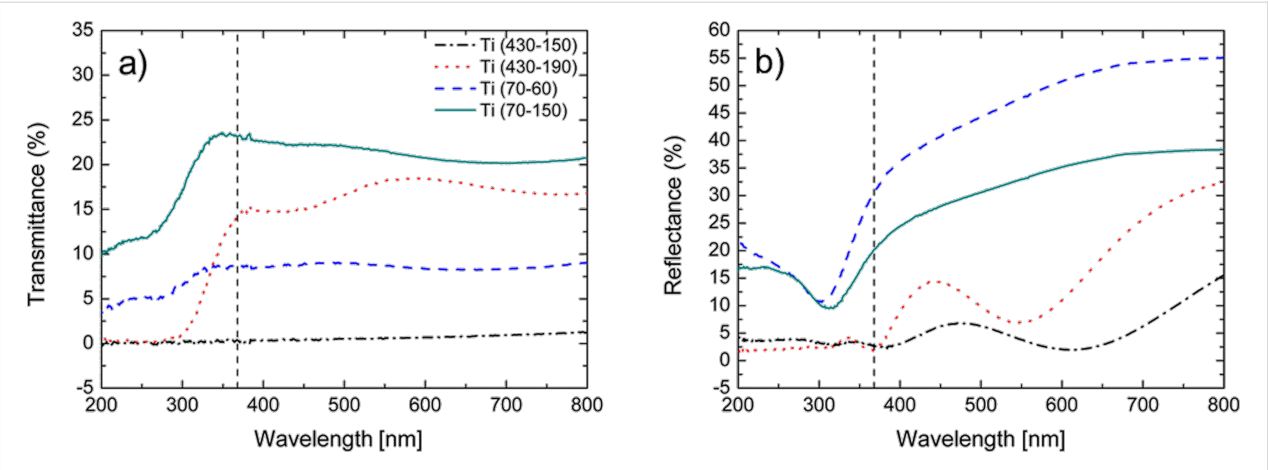

Figure 4: Transmittance (a) and reflectance (b) measurements in the range of 200–800 nm. The vertical lines mark the wavelength of the UV-A light source used for the photocatalytic experiments.

Ascertained of the high photocatalytic activity of the Ti (430-190) sample due to its structural and optical properties, we interpreted the *R* and *T* measurements in terms of the Fresnel formulae [24], regardless of the effects of depolarization due to the roughness and non-uniformity of the surface. We assumed that the sample is constituted by two layers on a quartz substrate, namely a titanium oxide layer and a metallic titanium layer (from the top to the bottom). A schematic view is shown as inset in Figure 5. The refractive indexes of the three layers (TiO_2/Ti/quartz) were calculated separately. For the quartz substrate it was assumed to be 1.5 [25]. The refractive index of the metallic film was extracted by fitting the reflectance spectrum of the titanium layer before the chemical etching. We assumed that the functional form for the dielectric constant of the metallic film is given by the "Drude free carrier" expression [26]:

$$\varepsilon(\omega)=\varepsilon_{\infty}\left(1-\frac{\omega_{\mathrm{P}}^2}{\left(\omega^2+i\,\omega\gamma\right)}\right), \tag{1}$$

where ω, ω_P, γ and ε_∞ are, respectively, the light frequency, the plasma frequency, the damping constant, and the low-frequency dielectric constant tabulated for titanium. The refractive index of titanium is calculated by the square root of Equation 1 [26]:

$$n(\omega)=\sqrt{\varepsilon(\omega)}. \tag{2}$$

The refractive index of the TiO_2 film was extracted by fitting both the reflectance and transmittance spectra of the Ti (430-190) sample, by using a Forouhi–Bloomer (FB) functional form for amorphous samples [27-29]:

$$n(\omega)=n_{\infty}+A\frac{B\left(\omega-\omega_0\right)+C+i\Theta\left(\omega-\omega_{\mathrm{g}}\right)\left(\omega-\omega_{\mathrm{g}}\right)^2}{\left(\omega-\omega_0\right)^2+\Gamma^2}, \tag{3}$$

where

$$B=\frac{\Gamma^2-\left(\omega_0-\omega_{\mathrm{g}}\right)^2}{\Gamma}, \tag{4}$$

$$C=2\Gamma\left(\omega_0-\omega_{\mathrm{g}}\right) \tag{5}$$

and $\Theta(\omega-\omega_g)$ is a step function, ω_g is the energy gap of the amorphous material, n_∞, A, ω_0, Γ are the "low-frequency" refractive index, the amplitude, the position, and the damping constant of the FB oscillator, respectively. The transmittance spectra reported in Figure 4a clearly indicate that the transmittance strongly depends on the thickness of the metallic film (d_m), whereas the reflectance spectra are mostly influenced by the TiO_2 layer parameters n_∞, ω_g, A, ω_0, Γ, and d_0 (thickness of titanium oxide layer). To start the fitting, we fixed d_0 and d_m to be 300 and 70 nm, respectively, as obtained by TEM analysis, and we assumed values of ω_g and ω_0 of 3.0 eV and 4.3 eV, respectively, in agreement with the values reported for TiO_2 [30]. The other parameters n_∞, A, and Γ were extracted by fitting both transmittance and reflectance. The simulated reflectance and transmittance spectra by the Fresnel formulae [24] are shown in Figure 5 by the dashed and the continuous line, respectively.

We wish to underline that the position of the maxima and minima in the measured reflectance and transmittance spectra do not coincide as expected. For example, the Ti (430-190) sample shows a minimum of reflectance at 547 nm, which is

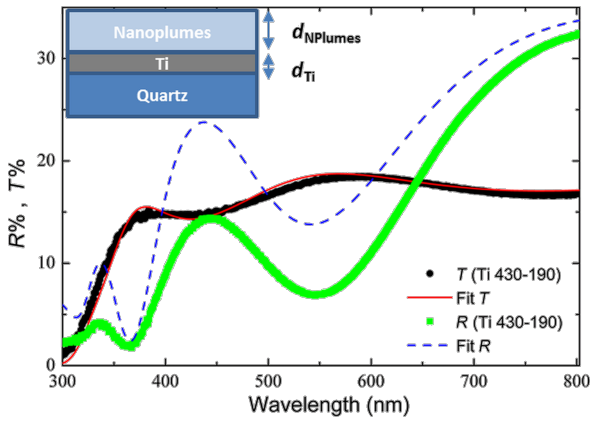

Figure 5: Fitting of the transmittance and reflectance spectra of Ti (430-190).

shifted by about 40 nm with respect to the maximum of the transmittance (at 592 nm). This effect is related to the intrinsic inhomogeneity of the etching process. Although the shape of both *T* and *R* spectra can be reproduced by the fitting process, some minor discrepancies between the experimental and calculated spectra need to be addressed. The fitted transmittance is in perfect agreement with the experimental spectrum (Figure 5). Indeed, the fit mainly depends on the thickness [27-29] of the metallic Ti film and this value was established by the TEM analyses. On the other hand, the fit of the reflectance is less accurate at shorter wavelengths and in particular in the UV range. This discrepancy can be explained by considering the scattering effects from a rough surface. The light reflected by the titanium layer undergoes multiple scattering in the nanoplume layer and it is partially re-absorbed. This effect is due to the high roughness and porosity of the material. Therefore, the measured spectrum shows a lower reflectivity value compared to the fitted spectrum in which the scattering effects were not considered.

It is worth noting that the refractive index of the nanoplumes, albeit it depends on the wavelength, does not exceed the value of 1.4. In particular, it is 1.2 at 800 nm, and 1.3 at 300 nm. TiO_2 is known to be a high refractive index material (n = 2.5–2.7) [31], whereas the nanoplumes show a very low refractive index. This result can be correlated to the high porosity and the high content of air into the nanoplumes, so that the refractive index can be considered as an average value of those of air and TiO_2.

The model used to fit the experimental *R* and *T* curves shows that the metal Ti layer acts as an efficient reflective layer, whereas the nanoplume layer acts as an antireflective coating. We found an ideal combination of 70 nm of highly reflective metallic Ti under 300 nm of TiO_2 with low refractive index. Moreover, scattering effects improve the light adsorption by the nanoplumes, increasing the generation of electron–hole pairs and, therefore, enhancing the photocatalytic performance.

Conclusion

In summary, TiO_2 nanoplumes were synthesized by a straightforward method, involving rapid chemical etching of Ti films in a H_2O_2 solution. The present results reveal that the most important optical effect of the synthesized nanoplumes is the suppression of reflectance, particularly in the UV range of the spectra. The suppression of the reflectance is due to scattering effects of the nanoplumes, which lead to the absorption of additional photons reflected from titanium layer. The generation of electron–hole pairs is subsequently increased, and leads to the significant photocatalytic activity of the TiO_2 nanoplumes.

Experimental

The samples were synthesized by chemical etching of titanium films as reported in [21]. Briefly, titanium films with a thickness of about 70 and 430 nm, were sputtered on quartz substrates by ultra-high vacuum magnetron sputtering from a Ti target of 99.99% purity. The Ti samples (1 cm × 1 cm in size) were put into 3 mL H_2O_2 (30%) solution at 60 °C for different etching times. Afterwards, the samples were rinsed with de-ionized water and dried in air.

SEM analyses in plan view were performed by a field emission Zeiss Supra 25 microscope. TEM analyses were performed in cross-sectional view with a JEOL JEM ARM200CF in scanning mode (STEM) at 60 kV of beam acceleration voltage using the microscope installed at the Beyond-Nano laboratory in Catania (Italy). The optical characterization was obtained by extracting both the total transmittance (*T*) and the total reflectance (*R*) spectra in the 200–800 nm wavelength range, by using a spectrophotometer Perkin-Elmer Lambda 35 equipped with an integrating sphere (RSA-PE-20, Perking-Elmer).

The photocatalytic properties of the synthesized material were evaluated by the degradation of methylene blue (MB) dye, a chemical compound commonly used to evaluate the photocatalytic efficiency of a material. The experimental setup was in agreement with the ISO 10678:2010 international standard. The samples were immersed in a solution (2 mL) containing MB and de-ionized water (starting concentration: 1.3×10^{-5} M). The mixture was irradiated by an 8 W UV lamp (350–400 nm wavelength range) with a irradiance of 1 mW/cm^2, for a total time of 3 h. Every 30 min of irradiation the solutions were measured with an UV–vis spectrophotometer (Perkin-Elmer Lambda 45) in the 500–800 nm wavelength range. The degradation of MB was evaluated by the absorbance peak at 664 nm, according to the Lambert–Beer law. The decomposition of the

dye in absence of any material was also measured as a reference. Before each measurement, the samples were irradiated by the UV lamp for 50 min in order to remove the hydrocarbons localized on the sample surface [32].

Acknowledgements

This research was supported by the FP7 European Project-WATER (Grant Agreement No. 316082).

References

1. Fujishima, A.; Honda, K. *Nature* **1972,** *238,* 37–38. doi:10.1038/238037a0
2. Malato, S.; Fernández-Ibañez, P.; Maldonado, M. I.; Blanco, J.; Gernjak, W. *Catal. Today* **2009,** *147,* 1–59. doi:10.1016/j.cattod.2009.06.018
3. Chong, M. N.; Jin, B.; Chow, C. W. K.; Saint, C. *Water Res.* **2010,** *44,* 2997–3027. doi:10.1016/j.watres.2010.02.039
4. Zuo, F.; Wang, L.; Wu, T.; Zhang, Z.; Borchardt, D.; Feng, P. *J. Am. Chem. Soc.* **2010,** *132,* 11856–11857. doi:10.1021/ja103843d
5. Gallo, A.; Marelli, M.; Psaro, R.; Gombac, V.; Montini, T.; Fornasiero, P.; Pievo, R.; Dal Santo, V. *Green Chem.* **2012,** *14,* 330–333. doi:10.1039/C2GC16112E
6. Gallo, A.; Montini, T.; Marelli, M.; Minguzzi, A.; Gombac, V.; Psaro, R.; Fornasiero, P.; Dal Santo, V. *ChemSusChem* **2012,** *5,* 1800–1811. doi:10.1002/cssc.201200085
7. Bendavid, A.; Martin, P. J.; Jamting, A.; Takikawa, H. *Thin Solid Films* **1999,** *355–356,* 6–11. doi:10.1016/S0040-6090(99)00436-8
8. Scuderi, V.; Impellizzeri, G.; Romano, L.; Scuderi, M.; Brundo, M. V.; Bergum, K.; Zimbone, M.; Sanz, R.; Buccheri, M. A.; Simone, F.; Nicotra, G.; Svensson, B. G.; Grimaldi, M. G.; Privitera, V. *Nanoscale* **2014,** *6,* 11189–11195. doi:10.1039/C4NR02820A
9. Di Mauro, A.; Zimbone, M.; Scuderi, M.; Nicotra, G.; Fragalà, M. E.; Impellizzeri, G. *Nanoscale Res. Lett.* **2015,** *10,* 484. doi:10.1186/s11671-015-1126-6
10. Scuderi, V.; Impellizzeri, G.; Romano, L.; Scuderi, M.; Nicotra, G.; Bergum, K.; Irrera, A.; Svensson, B. G.; Privitera, V. *Nanoscale Res. Lett.* **2014,** *9,* 458. doi:10.1186/1556-276X-9-458
11. Scalese, S.; Scuderi, V.; D'Angelo, D.; Buscema, M. M. G.; Libertino, S.; Puglisi, R. A.; Miritello, M.; Privitera, V. *Mater. Sci. Semicond. Process.* **2016,** *42,* 45–49. doi:10.1016/j.mssp.2015.09.004
12. Scuderi, V.; Amiard, G.; Boninelli, S.; Scalese, S.; Miritello, M.; Sberna, P. M.; Impellizzeri, G.; Privitera, V. *Mater. Sci. Semicond. Process.* **2016,** *42,* 89–93. doi:10.1016/j.mssp.2015.08.008
13. Impellizzeri, G.; Scuderi, V.; Romano, L.; Napolitani, E.; Sanz, R.; Carles, R.; Privitera, V. *J. Appl. Phys.* **2015,** *117,* 105308. doi:10.1063/1.4915111
14. Cantarella, M.; Sanz, R.; Buccheri, M. A.; Ruffino, F.; Rappazzo, G.; Scalese, S.; Impellizzeri, G.; Romano, L.; Privitera, V. *J. Photochem. Photobiol., A: Chem.* **2016,** *321,* 1–11. doi:10.1016/j.jphotochem.2016.01.020
15. Chen, X.; Liu, L.; Yu, P. Y.; Mao, S. S. *Science* **2011,** *331,* 746–750. doi:10.1126/science.1200448
16. Wang, G.; Wang, H.; Ling, Y.; Tang, Y.; Yang, X.; Fitzmorris, R. C.; Wang, C.; Zhang, J. Z.; Li, Y. *Nano Lett.* **2011,** *11,* 3026–3033. doi:10.1021/nl201766h
17. Zhang, Z.-K.; Bai, M.-L.; Guo, D.-Z.; Hou, S.-M.; Zhang, G.-M. *Chem. Commun.* **2011,** *47,* 8439–8441. doi:10.1039/c1cc12669e
18. Liu, N.; Schneider, C.; Freitag, D.; Hartmann, M.; Venkatesan, U.; Müller, J.; Spiecker, E.; Schmuki, P. *Nano Lett.* **2014,** *14,* 3309–3313. doi:10.1021/nl500710j
19. Naldoni, A.; Allieta, M.; Santangelo, S.; Marelli, M.; Fabbri, F.; Cappelli, S.; Bianchi, C. L.; Psaro, R.; Dal Santo, V. *J. Am. Chem. Soc.* **2012,** *134,* 7600–7603. doi:10.1021/ja3012676
20. Zimbone, M.; Cacciato, G.; Sanz, R.; Carles, R.; Gulino, A.; Privitera, V.; Grimaldi, M. G. *Catal. Commun.* **2016,** *84,* 11–15. doi:10.1016/j.catcom.2016.05.024
21. Scuderi, V.; Impellizzeri, G.; Zimbone, M.; Sanz, R.; Di Mauro, A.; Buccheri, M. A.; Miritello, M.; Terrasi, A.; Rappazzo, G.; Nicotra, G.; Privitera, V. *Appl. Catal., B* **2016,** *183,* 328–334. doi:10.1016/j.apcatb.2015.10.055
22. Sendner, C.; Horinek, D.; Bocquet, L.; Netz, R. R. *Langmuir* **2009,** *25,* 10768–10781. doi:10.1021/la901314b
23. Liu, B.; Nakata, K.; Liu, S.; Sakai, M.; Ochiai, T.; Murakami, T.; Takagi, K.; Fujishima, A. *J. Phys. Chem. C* **2012,** *116,* 7471–7479. doi:10.1021/jp300481a
24. Born, M.; Wolf, E. *Principles of Optics,* 4th ed.; Pergamon Press, 1970.
25. Liu, J.; Chen, Y.; Cai, H.; Chen, X.; Li, C.; Yang, C.-F. *Materials* **2015,** *8,* 2688–2699. doi:10.3390/ma8052688
26. Yu, P. Y.; Cardona, M. *Fundamentals of Semiconductors;* Springer: Berlin, Heidelberg, 2010. doi:10.1007/978-3-642-00710-1
27. Forouhi, A. R.; Bloomer, I. *Phys. Rev. B* **1986,** *34,* 7018–7026. doi:10.1103/PhysRevB.34.7018
28. Forouhi, A. R.; Bloomer, I. *Phys. Rev. B* **1988,** *38,* 1865–1874. doi:10.1103/PhysRevB.38.1865
29. Jellison, G. E., Jr.; Modine, F. A. *Appl. Phys. Lett.* **1996,** *69,* 371–373. doi:10.1063/1.118064
30. DeVore, J. R. *J. Opt. Soc. Am.* **1951,** *41,* 416–419. doi:10.1364/JOSA.41.000416
31. Tao, P.; Li, Y.; Rungta, A.; Viswanath, A.; Gao, J.; Benicewicz, B. C.; Siegela, R. W.; Schadler, L. S. *J. Mater. Chem.* **2011,** *21,* 18623–18629. doi:10.1039/c1jm13093e
32. Wang, R.; Hashimoto, K.; Fujishima, A.; Chikuni, M.; Kojima, E.; Kitamura, A.; Shimohigoshi, M.; Watanabe, T. *Nature* **1997,** *388,* 431–432. doi:10.1038/41233

License and Terms

BEILSTEIN JOURNAL OF NANOTECHNOLOGY

Laser irradiation in water for the novel, scalable synthesis of black TiO_x photocatalyst for environmental remediation

Massimo Zimbone[1], Giuseppe Cacciato[*1], Mohamed Boutinguiza[2], Vittorio Privitera[1] and Maria Grazia Grimaldi[1,3]

Full Research Paper

Open Access

Address:
[1]CNR-IMM, via S. Sofia 64, 95123 Catania, Italy, [2]Grupo de Aplicaciones Industriales de los Láseres, Departamento de Física Aplicada, E.T.S. Ingenieros Industriales de Vigo, Rúa Maxwell, s/n, Campus Universitario, 36310 Vigo, Spain and [3]Dipartimento di Fisica e Astronomia, Università di Catania, via S. Sofia 64, 95123 Catania, Italy

Email:
Giuseppe Cacciato[*] - giuseppe.cacciato@ct.infn.it

* Corresponding author

Keywords:
black titania; laser irradiation in water; photocatalysis; TiO_x; water treatment

Beilstein J. Nanotechnol. **2017,** *8,* 196–202.
doi:10.3762/bjnano.8.21

Received: 18 August 2016
Accepted: 23 December 2016
Published: 19 January 2017

This article is part of the Thematic Series "Self-assembly of nanostructures and nanomaterials II".

Guest Editor: I. Berbezier

Abstract

Since 1970, TiO_2 photocatalysis has been considered a possible alternative for sustainable water treatment. This is due to its material stability, abundance, nontoxicity and high activity. Unfortunately, its wide band gap (≈3.2 eV) in the UV portion of the spectrum makes it inefficient under solar illumination. Recently, so-called "black TiO_2" has been proposed as a candidate to overcome this issue. However, typical synthesis routes require high hydrogen pressure and long annealing treatments. In this work, we present an industrially scalable synthesis of TiO_2-based material based on laser irradiation. The resulting black TiO_x shows a high activity and adsorbs visible radiation, overcoming the main concerns related to the use of TiO_2 under solar irradiation. We employed a commercial high repetition rate green laser in order to synthesize a black TiO_x layer and we demonstrate the scalability of the present methodology. The photocatalyst is composed of a nanostructured titanate film (TiO_x) synthetized on a titanium foil, directly back-contacted to a layer of Pt nanoparticles (PtNps) deposited on the rear side of the same foil. The result is a monolithic photochemical diode with a stacked, layered structure (TiO_x/Ti/PtNps). The resulting high photo-efficiency is ascribed to both the scavenging of electrons by Pt nanoparticles and the presence of trap surface states for holes in an amorphous hydrogenated TiO_x layer.

Introduction

The interest in titanium dioxide dates back in 1972, thanks to the pioneering work of Honda and Fujishima [1]. TiO_2 has been widely used for both water splitting and mineralization of organic contaminants in solution [2]. The applications range from third generation solar cells [3] to material for air or water purification [4] to antifogging and self-cleaning surfaces [5,6]. The main advantage of this material is its high inertness (even in a corrosive environment), stability, abundance and nontoxi-

city. Nevertheless, its exploitation in environmental remediation, and in particular in water purification, is relatively limited due to its wide band gap (≈3.2 eV). This means that only 5% of the incoming solar radiation can be readily employed for water decontamination. In order to enhance the photocatalytic performance of TiO_2 under visible (solar) irradiation, many efforts have been made in the last years, ranging from doping with N, C and transition metals [7-9], to coupling with narrow band gap semiconductor quantum dots [10], to the use of metal grafting [11-14] or plasmonic metal nanostructures [15-19] and the preparation of oxygen-deficient and/or hydrogen-rich TiO_x [20-22]. We are interested, in particular, in this last approach.

Hydrogenated black TiO_2 has attracted attention due to its low band gap and large optical absorption [20,21] in the visible and IR spectral range. This material has also encouraged theoretical studies due to its peculiarities related to the hydrogen insertion. In the case of TiO_2 nanoparticles, hydrogen induces the amorphization of a layer at the surface and the creation of acceptor states. These states are responsible for the visibly dark coloration and, consequently, for sunlight absorption [23]. Unfortunately, this material is not suitable for industrial implementation since it requires up to 20 bar of hydrogen pressure and up to 15 days of annealing treatment, according to the most common synthesis techniques [21]. Recently, we proposed laser ablation in water as a synthesis route for efficient TiO_2-based catalysts by using a high energy 1064 nm wavelength laser [22,24,25].

In the present work, we focus our attention on the synthesis of a nanostructured, black TiO_x film on a Ti foil (TiO_x/Ti) by using a high repetition rate green laser commonly used in industry and metallurgy. This laser has a shorter wavelength (532 nm vs 1064 nm) and a fluence (2 J/cm^2 vs 20 J/cm^2) and pulse energy (10 mJ/pulse vs 1 J/pulse) of an order of magnitude lower than our previously presented methodology [22]. We demonstrate the scalability of the reported methodology and open up the possible further exploitation of such a technology. In fact, several differences arose with respect to our previous work, mainly regarding the morphology and crystallinity of the obtained film. However, variations were not observed in the composition (stoichiometry) or the optical and catalytic properties of the material. In the present work, we are working near the threshold for the formation of the black layer of TiO_x. This means that the laser supplies enough energy to induce melting and oxidation on the metallic titanium surface and, at the same time, the process is fast enough to allow the formation of sub-stoichiometric oxides. We have demonstrated that the proposed methodology allows for the successful synthesis of a black TiO_x material suitable for water purification applications. The morphological, structural and optical properties of the film surface were investigated. Moreover, we fabricated a photochemical diode with remarkable activity for the degradation of pollutants in water. The device is created by depositing a layer of Pt nanoparticles (PtNps) on the rear side of the TiO_x/Ti substrate, producing a monolithic electrochemical cell [22]. The device consists of a stacked, layered structure: TiO_x/Ti/PtNps. The photo-activity of the material is related to the trapping and scavenging of holes due to the amorphous black layer and to the scavenging of electrons caused by the presence of the PtNp layer.

Experimental

Preparation

The synthesis of the TiO_x film was performed by irradiating a titanium metal foil (Goodfellow, purity 99.9%, as rolled) by a diode-pumped Nd:YVO_4 laser operating at wavelength of 532 nm, a repetition rate of 20 kHz, and a pulse duration of 15 ns to give a fluence of 2.0 J/cm^2. The scanning speed was kept at 100 mm/s. The laser was focused using a lens (focal length of 20 cm), on the bottom of a vessel filled with 9 mm of deionized Milli-Q water (resistivity 18 MΩ·cm) above the sample. The sample was irradiated at a fluence of 2 J/cm^2. A schematic representation of the sample preparation procedure is shown in Figure 1. During laser irradiation, TiO_2 nanoparticles were obtained in solution, as also reported in a previous publication [24,26], and a thin black layer of TiO_x was formed on the top of the Ti foil (Figure 1a). The samples have a surface area of 0.7 cm^2.

The synthesis of platinum nanoparticles (PtNps) was performed by pulsed laser ablation in liquid by irradiating a Pt metal foil (Sigma Aldrich, purity 99%) with a Nd:YAG laser (Giant G790-30) at 1064 nm (10 ns pulse duration, 10 Hz repetition rate). The laser was focused using a lens (focal length of 20 cm) on the bottom of a Teflon vessel filled with 5 mL of deionized Milli-Q water (resistivity 18 MΩ·cm). The sample was irradiated at a fluence of 20 J/cm^2. Pt nanoparticles, dispersed in water, are stable for some months. The synthesis of Pt nanoparticles is represented in Figure 1b.

Samples for photo-degradation tests were realized by depositing some drops (about 2 mL) of the PtNps solution on the rear side of the titanium foil at 90 °C and waiting for evaporation of the water. A continuous layer of platinum nanoparticles adhered to the substrate is formed, leading to the black-TiO_x/Ti/PtNp multilayer structure depicted in Figure 1c.

Methods

SEM images were acquired by using a field emission SEM (Gemini Zeiss SUPRATM25) at a working distance of 5–6 mm, using an electron beam of 5 keV and SE detector.

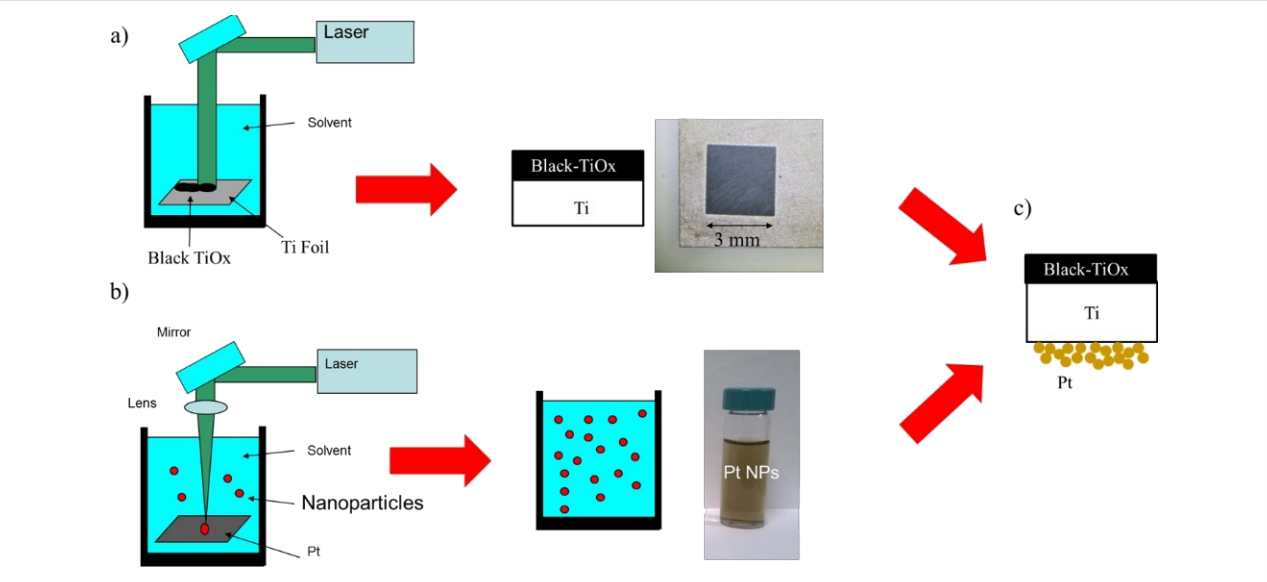

Figure 1: Schematic representation of the sample preparation steps: (a) laser irradiation of the Ti foil in order to form the black TiO_x layer; (b) synthesis of Pt nanoparticles via laser ablation in water; (c) schematic representation of the black TiO_x/Ti/PtNp multilayer structure after the deposition of the Pt nanoparticles on the rear side of the irradiated Ti foil.

The UV–vis spectrum was collected using a Perkin-Elmer Lambda40 spectrometer in the wavelength range 350–900 nm with an integrating sphere (Labsphere 20). The IR spectra were collected using an FTIR spectrometer (Perkin-Elmer Spectrum 1000) in the range 350–7000 cm^{-1}. The absorbance was calculated with the formula: $A = 100 - R$ where R is the reflectivity as percentage.

The crystalline structure of the Ti and TiO_x/Ti samples was determined by grazing angle (0.5°) X-ray diffraction by using a Bruker D-9000 instrument (Cu Kα) and Bruker diffraction suite software for the diffraction analysis.

Rutherford backscattering spectrometry (RBS) measurements were run using a 2 MeV He^+ beam with a scattering angle of 165° in normal incidence. The RUMP software was employed for the analysis of the RBS spectra.

In order to evaluate the photocatalytic activity of the TiO_x nanostructured film, the methylene blue (MB) discoloration test was performed [24]. The apparent photon efficiency in the UV range was calculated according to ISO10678:2010 [27]. The quantum efficiency (QE) was calculated as the ratio between the apparent photon efficiency and the measured absorbance in the wavelength range of the light source. QE represents the ratio between the number of molecules degraded for unit of time (and area) and the number of photons adsorbed by the sample per unit of time (and area). The UV light source (TL 8W BLB 1FM, Philips) spectrum was centred at 368 nm with a FWHM of less than 10 nm, the measured irradiance was about 1.5 mW/cm^2.

Results and Discussion

When a high energy, nanosecond laser pulse is focused on a Ti foil, a hot plasma plume forms on the metal surface. The plasma is characterized by high temperature and pressure (≈4700 °C and $\approx 10^7$ Pa, respectively) [28]. The plume expansion is slowed down by the presence of liquid. As a consequence, inside the plasma, high temperature and pressure are maintained for several µs. Water dissociates and reacts with titanium atoms ejected from the target, realizing H–Ti–O_x. In addition, a cavitation bubble appears, expands, shrinks and collapses in the timescale of hundreds of µs. The collapse is a complex phenomenon that terminates by depositing a layer of titanium oxides on the Ti target [24,28,29]. The redeposited material is black in colour. The effect of the laser irradiation on the titanium foil is reported in Figure 2. In the left side of Figure 2, the irradiated zone is the black square of the sample. The surface morphology, as reported by SEM, reveals that after irradiation, the black surface is uniformly covered by small structures (Figure 2 centre). A high magnification image (Figure 2 right) shows that they consist of cavities and grain boundaries. It is worth noting that the nanostructure of the film appears similar to the case of irradiation under 1064 nm wavelength [22]. However, in the present condition, the holes on the surface of the irradiated sample appear to be concentrated at the grain boundaries generated on the surface by the laser annealing.

RBS spectra clearly show the presence of oxygen in the irradiated zone, as indicated in Figure 3. The spectra of the black TiO_x film and the Ti target are reported together with the simulation of their profiles. Close to the surface of the irradiated

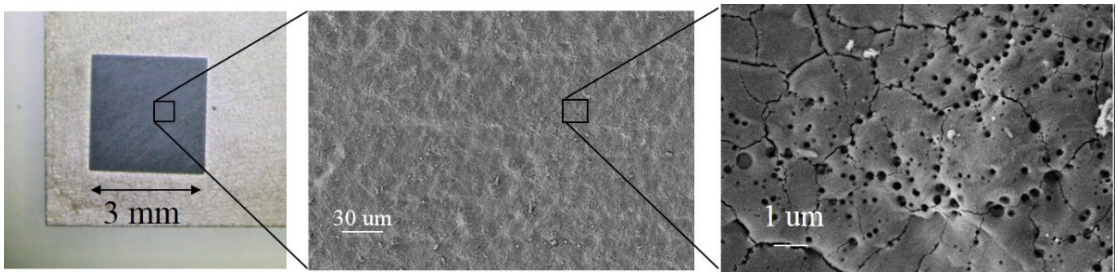

Figure 2: Left: Photograph of the irradiated sample. Middle: low-magnification SEM image of the surface after laser irradiation. Right: High-magnification image of the surface of black TiO_x.

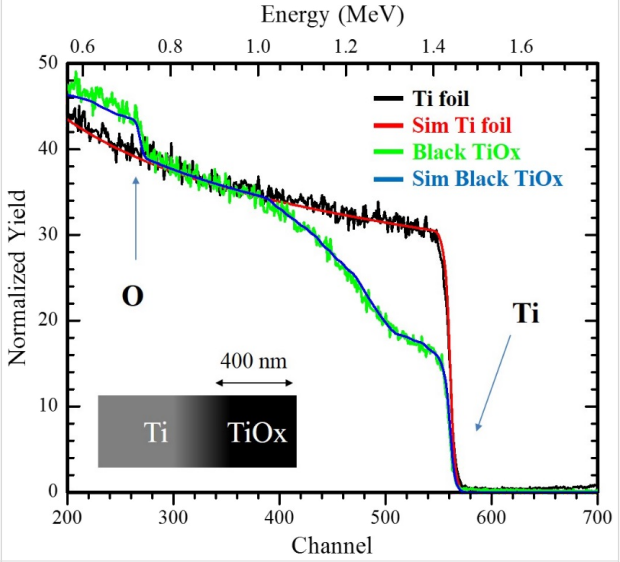

Figure 3: RBS spectra of the TiO_x film and the Ti target. Arrows indicate signals coming from titanium and oxygen, respectively. Simulations of the spectra are also reported. Left lower side: a schematic representation of the irradiated sample is reported.

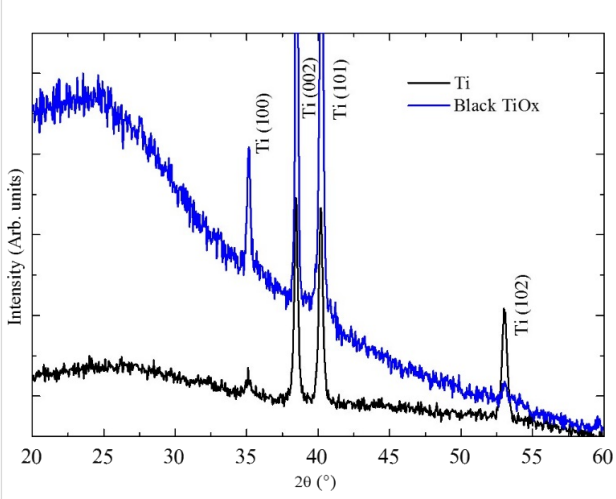

Figure 4: XRD spectra of the TiO_x/Ti film and the Ti foil (before irradiation). The main characteristic peaks of titanium are indicated. The main feature of the black TiO_x sample is the pronounced amorphous signal observed at low scattering angles.

sample, substoichiometric titanium oxides (such as TiO and Ti_2O_3) are revealed by the RUMP simulation [30]. It is observed that the oxygen content decreases to negligible values going from the surface to the inner part of the sample. The RBS profile implies a change in stoichiometry from TiO_2 on the surface to bulk Ti. The oxidation profile cannot steadily be extracted from the simulation (owing to the complex morphology of the sample). Nevertheless, the average layer thickness can be estimated to be roughly 400 nm.

In Figure 4, the XRD spectra of the TiO_x film is shown. In the same figure the spectra of the Ti substrate is shown for comparison. The peaks at about 35°, 38°, 40°, and 53° are apparent in both spectra and they are related to the metallic Ti substrate. The presence of an amorphous phase is clearly recognizable in the spectrum in the low angle range. We ascribe such signal to an amorphous titanium oxide layer.

The absorbance spectra ($1 - R$ %) of the black TiO_x film is reported in Figure 5. The measured absorbance is higher than 90% in the range from 0.35 to 5 eV (from 3.5 to 0.25 μm in wavelength). The high absorption and black coloration is ascribed to reduced oxidation states of Ti (electrons in the Ti 3d states) and to the presence of H in association with an oxygen vacancy [23]. It is worth noting the obtained black TiO_x has very high absorbance in the full range of solar radiation: in particular, solar radiation spans from 0.5 eV (2.5 μm) to 5 eV (250 nm).

Although it depends on other concomitant surface processes, photocatalytic activity benefits from the high absorption in UV–vis and IR ranges. Indeed, the presence of hydrogen (either interstitial, in TiH or in OH complexes) can effectively enhance the photocatalytic performance of the film [2,6,20-22,24,25]. Furthermore, H-rich zones on the surface can enhance electron scavenging, preventing recombination [2].

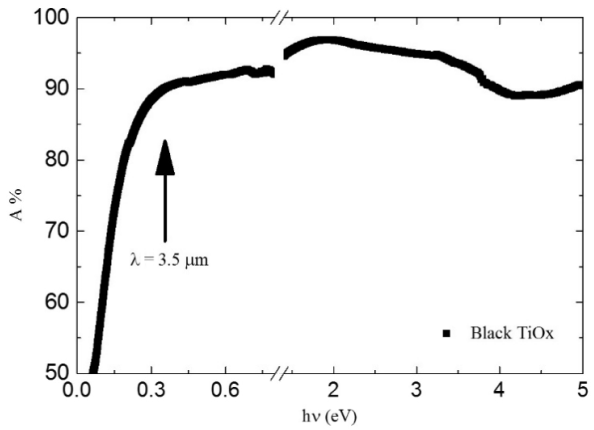

Figure 5: Absorbance spectra of the TiO_x/Ti film in the IR, visible and UV spectral range.

In the present work, the photocatalytic activity is measured by using the methylene blue (MB) discoloration method [27]. Samples for discolouration measurements were prepared by sandwiching the Ti substrate between a TiO_x layer (irradiated surface) and a Pt nanoparticle layer, thus realizing a TiO_x/Ti/PtNp monolithic chemical diode. The Pt nanoparticles were 20 nm in diameter [29,31] as measured by dynamic light scattering. They were deposited on the rear side of the sample as shown in Figure 1b and discussed in the experimental section. In Figure 6, the concentration of MB under UV irradiation in the presence of black TiO_x material (black) and without the photocatalyst (green) are reported. The MB concentration follows a pseudo first-order kinetic law in the first 10 hours of irradiation. The discoloration rate constant k is measured by fitting the curve in Figure 6 with the following formula: $C/C_0 = e^{-kt}$. A discoloration rate k of 0.22 ± 0.01 and 0.01 ± 0.01 $h^{-1} \cdot cm^{-2}$ was measured for TiO_x/Ti/PtNps and MB, respectively. By using the

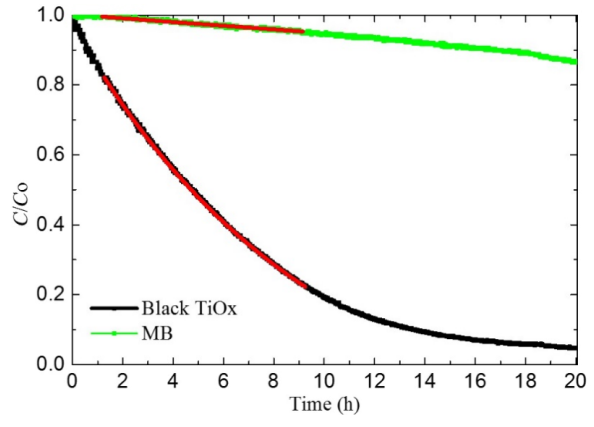

Figure 6: UV discoloration of methylene blue (MB) dye in the presence of TiO_x/Ti/Pt foil. The discoloration of a MB solution without photocatalyst is also reported for comparison purposes.

above result, a quantum efficiency of 0.041% is calculated for the decolouration of methylene blue in water. It is worth noting that the UV quantum efficiency for the TiO_x/Ti/PtNp sample is higher than that reported for standard commercial photocatalytic glass (0.025%) [32].

The photo-activity is mainly due to oxidation of MB molecules adhered to the surface of the TiO_x [12]. This reaction is mainly mediated by holes. In a photocatalytic process driven by titania, electrons have to be transferred (contemporaneously to holes) to the solution in order to maintain charge neutrality in solution. An accumulation of electrons in the material causes an increase of the Fermi level and an increase of the recombination rate of *e*–*h* couples, with a consequent decrease of the photo-activity. Despite some controversial debates in the literature in the past years (mainly regarding the potential activity of the amorphous phase), it has been recently reported that both the presence of an amorphous phase or different crystalline phases (i.e., anatase and rutile, as in the case of the Evonik Aeroxide P25®, the former Degussa-P25® powder) can be beneficial in terms of photocatalytic activity [20,24]. In the material presented in this work, the crystalline content is highly reduced (if not absent) with respect our previous work [22]. Regardless, the catalytic performance is remarkable, thus indicating that the role of electron scavenging is the key to prevent recombination and boost the photochemical reactions occurring at the surface. We realized a platinum nanoparticle layer in order to favour the scavenging of electrons due to the high affinity of Pt with oxygen [33] and the high surface/mass ratio of the nanoparticle layer. We observed the presence of a series of substoichiometric oxides (as reported by RBS analysis) that allows for good electrical contact between the black TiO_x surface and the Pt nanoparticle layer on the rear side of the film through the metallic titanium substrate. A higher photo-activity is achieved when holes interact with adhered molecules on the surface by means of surface trap states. In amorphous TiO_x, free holes interact with Ti^{+4} cation surface trap states [12], superficial Ti interstitials [34,35], or hydrogen complexes (realised during the synthesis of the material). These defects on the surface favour the trapping of holes in specific superficial sites and facilitate the interaction with adhered molecules.

Conclusion

In conclusion, we have proposed a new, simple, scalable and environmentally friendly methodology for synthesizing black TiO_x by using laser irradiation in liquid. We used a commercial, industrial laser with a high repetition rate in order to synthetize black TiO_x. We also noted that this methodology has important advantages with respect to the commonly used synthesis techniques. The obtained material has an extremely high absorbance in the IR, visible and UV spectral range. Although it is

composed of amorphous titanium oxide, it is able to degrade pollutants (methylene blue) dissolved in solution at a high rate (QE = 0.041%). This high activity is ascribed to the presence of trap states for holes in the illuminated surface and the a stacked, layered structure (TiO_x/Ti/PtNps) in which the Pt nanoparticle layer (on the rear side of the sample) permits the scavenging of electrons.

Acknowledgements

This research has been supported by the FP7 European Project WATER (Grant Agreement n. 316082). The Government of Spain is acknowledged for the Mobility Grant of Senior Professors and Researchers (MAT2015-71459-C2-P, Grant PRX15/00088).

References

1. Fujishima, A.; Honda, K. *Nature* **1972,** *238,* 37–38. doi:10.1038/238037a0
2. Fujishima, A.; Zhang, X.; Tryk, D. A. *Surf. Sci. Rep.* **2008,** *63,* 515–582. doi:10.1016/j.surfrep.2008.10.001
3. Grätzel, M. *J. Photochem. Photobiol., C* **2003,** *4,* 145–153. doi:10.1016/S1389-5567(03)00026-1
4. Miyauchi, M.; Irie, H.; Liu, M.; Qiu, X.; Yu, H.; Sunada, K.; Hashimoto, K. *J. Phys. Chem. Lett.* **2016,** *7,* 75–84. doi:10.1021/acs.jpclett.5b02041
5. Guldin, S.; Kohn, P.; Stefik, M.; Song, J.; Divitini, G.; Ecarla, F.; Ducati, C.; Wiesner, U.; Steiner, U. *Nano Lett.* **2013,** *13,* 5329–5335. doi:10.1021/nl402832u
6. Hashimoto, K.; Irie, H.; Fujishima, A. *Jpn. J. Appl. Phys., Part 1* **2005,** *44,* 8269. doi:10.1143/JJAP.44.8269
7. Asahi, R.; Morikawa, T.; Ohwaki, T.; Aoki, K.; Taga, Y. *Science* **2001,** *293,* 269. doi:10.1126/science.1061051
8. Litter, M. I. *Appl. Catal., B* **1999,** *23,* 89–114. doi:10.1016/S0926-3373(99)00069-7
9. Khan, S. U. M.; Al-Shahry, M.; Ingler, W. B., Jr. *Science* **2002,** *297,* 2243. doi:10.1126/science.1075035
10. Robel, I.; Subramanian, V.; Kuno, M.; Kamat, P. V. *J. Am. Chem. Soc.* **2006,** *128,* 2385–2393. doi:10.1021/ja056494n
11. Yu, H.; Irie, H.; Hashimoto, K. *J. Am. Chem. Soc.* **2010,** *132,* 6898–6899. doi:10.1021/ja101714s
12. Liu, M.; Inde, R.; Nishikawa, M.; Qiu, X.; Atarashi, D.; Sakai, E.; Nosaka, Y.; Hashimoto, K.; Miyauchi, M. *ACS Nano* **2014,** *8,* 7229–7238. doi:10.1021/nn502247x
13. Dette, C.; Pérez-Osorio, M. A.; Kley, C. S.; Punke, P.; Patrick, C. E.; Jacobson, P.; Giustino, F.; Jung, S. J.; Kern, K. *Nano Lett.* **2014,** *14,* 6533–6538. doi:10.1021/nl503131s
14. Beranek, R.; Kisch, H. *Photochem. Photobiol. Sci.* **2008,** *7,* 40–48. doi:10.1039/B711658F
15. Linic, S.; Christopher, P.; Ingram, D. B. *Nat. Mater.* **2011,** *10,* 911–921. doi:10.1038/nmat3151
16. Hou, W.; Cronin, S. B. *Adv. Funct. Mater.* **2013,** *23,* 1612–1619. doi:10.1002/adfm.201202148
17. Cacciato, G.; Ruffino, F.; Zimbone, M.; Reitano, R.; Privitera, V.; Grimaldi, M. G. *Mater. Sci. Semicond. Process.* **2016,** *42,* 40–44. doi:10.1016/j.mssp.2015.07.074
18. Cacciato, G.; Bayle, M.; Pugliara, A.; Bonafos, C.; Zimbone, M.; Privitera, V.; Grimaldi, M. G.; Carles, R. *Nanoscale* **2015,** *7,* 13468–13476. doi:10.1039/C5NR02406D
19. Scuderi, V.; Impellizzeri, G.; Romano, L.; Scuderi, M.; Brundo, M. V.; Bergum, K.; Zimbone, M.; Sanz, R.; Buccheri, M. A.; Simone, F.; Nicotra, G.; Svensson, B. G.; Grimaldi, M. G.; Privitera, V. *Nanoscale* **2014,** *6,* 11189–11195. doi:10.1039/C4NR02820A
20. Chen, X.; Liu, L.; Yu, P. Y.; Mao, S. S. *Science* **2011,** *331,* 746. doi:10.1126/science.1200448
21. Chen, X.; Liu, L.; Huang, F. *Chem. Soc. Rev.* **2015,** *44,* 1861. doi:10.1039/C4CS00330F
22. Zimbone, M.; Cacciato, G.; Sanz, R.; Carles, R.; Gulino, A.; Privitera, V.; Grimaldi, M. G. *Catal. Commun.* **2016,** *84,* 11–15. doi:10.1016/j.catcom.2016.05.024
23. Mo, L.-B.; Wang, Y.; Bai, Y.; Xiang, Q.-Y.; Li, Q.; Yao, W.-Q.; Wang, J.-O.; Ibrahim, K.; Wang, H.-H.; Wan, C.-H.; Cao, J.-L. *Sci. Rep.* **2015,** *5,* 17634. doi:10.1038/srep17634
24. Zimbone, M.; Buccheri, M. A.; Cacciato, G.; Sanz, R.; Rappazzo, G.; Boninelli, S.; Reitano, R.; Romano, L.; Privitera, V.; Grimaldi, M. G. *Appl. Catal., B: Environ.* **2015,** *165,* 487. doi:10.1016/j.apcatb.2014.10.031
25. Zimbone, M.; Cacciato, G.; Buccheri, M. A.; Sanz, R.; Piluso, N.; Reitano, R.; La Via, F.; Grimaldi, M. G.; Privitera, V. *Mater. Sci. Semicond. Process.* **2016,** *42,* 28–31. doi:10.1016/j.mssp.2015.09.012
26. Zimbone, M.; Musumeci, P.; Baeri, P.; Messina, E.; Boninelli, S.; Compagnini, G.; Calcagno, L. *J. Nanopart. Res.* **2012,** *14,* 1308. doi:10.1007/s11051-012-1308-4
27. ISO:10678 "*Determination of photocatalytic activity of surfaces in an aqueous medium by degradation methylene blue*".
28. Sasaki, K. Dynamics of Liquid-Phase Laser Ablation. In *Laser ablation in liquids: principles and applications in the preparation of nanomaterials;* Yang, G., Ed.; CRC Press: Boca Raton, FL, U.S.A., 2009; pp 269–295.
29. Di Mauro, A.; Zimbone, M.; Scuderi, M.; Nicotra, G.; Fragalà, M. E.; Impellizzeri, G. *Nanoscale Res. Lett.* **2015,** *10,* 484. doi:10.1186/s11671-015-1126-6
30. Doolittle, L. R. *Nucl. Instrum. Methods Phys. Res., Sect. B* **1986,** *15,* 227–231. doi:10.1016/0168-583x(86)90291-0
31. Messina, E.; Donato, M. G.; Zimbone, M.; Saija, R.; Iatì, M. A.; Calcagno, L.; Fragalà, M. E.; Compagnini, G.; D'Andrea, C.; Foti, A.; Gucciardi, P. G.; Maragò, O. M. *Opt. Express* **2015,** *23,* 8720–8730. doi:10.1364/OE.23.008720
32. Fateh, R.; Dillert, R.; Bahnemann, D. *ACS Appl. Mater. Interfaces* **2014,** *6,* 2270–2278. doi:10.1021/am4051876
33. Young Park, J.; Renzas, J. R.; Contreras, A. M.; Somorjai, G. A. *Top. Catal.* **2007,** *46,* 217–222. doi:10.1007/s11244-007-0331-7
34. Gopal, N. O.; Lo, H.-H.; Sheu, S.-C.; Ke, S.-C. *J. Am. Chem. Soc.* **2010,** *132,* 10982–10983. doi:10.1021/ja909901f
35. Wendt, S.; Sprunger, P. T.; Lira, E.; Madsen, G. K. H.; Li, Z.; Hansen, J. Ø.; Matthiesen, J.; Blekinge-Rasmussen, A.; Lægsgaard, E.; Hammer, B.; Besenbacher, F. *Science* **2008,** *320,* 1755–1759. doi:10.1126/science.1159846

BEILSTEIN JOURNAL OF NANOTECHNOLOGY

Impact of contact resistance on the electrical properties of MoS_2 transistors at practical operating temperatures

Filippo Giannazzo*[1], Gabriele Fisichella[1], Aurora Piazza[1,2,3], Salvatore Di Franco[1], Giuseppe Greco[1], Simonpietro Agnello[2] and Fabrizio Roccaforte[1]

Full Research Paper

Open Access

Address:
[1]Consiglio Nazionale delle Ricerche – Istituto per la Microelettronica e Microsistemi, Strada VIII, n 5, 95121 Catania, Italy, [2]Department of Physics and Chemistry, University of Palermo, Via Archirafi 36, 90143 Palermo, Italy and [3]Department of Physics and Astronomy, University of Catania, Via Santa Sofia, 64, 95123 Catania, Italy

Email:
Filippo Giannazzo* - filippo.giannazzo@imm.cnr.it

* Corresponding author

Keywords:
contact resistance; mobility; MoS_2; temperature dependence; threshold voltage

Beilstein J. Nanotechnol. **2017,** *8,* 254–263.
doi:10.3762/bjnano.8.28

Received: 14 September 2016
Accepted: 03 January 2017
Published: 25 January 2017

This article is part of the Thematic Series "Self-assembly of nanostructures and nanomaterials II".

Guest Editor: I. Berbezier

Abstract

Molybdenum disulphide (MoS_2) is currently regarded as a promising material for the next generation of electronic and optoelectronic devices. However, several issues need to be addressed to fully exploit its potential for field effect transistor (FET) applications. In this context, the contact resistance, R_C, associated with the Schottky barrier between source/drain metals and MoS_2 currently represents one of the main limiting factors for suitable device performance. Furthermore, to gain a deeper understanding of MoS_2 FETs under practical operating conditions, it is necessary to investigate the temperature dependence of the main electrical parameters, such as the field effect mobility (μ) and the threshold voltage (V_{th}). This paper reports a detailed electrical characterization of back-gated multilayer MoS_2 transistors with Ni source/drain contacts at temperatures from T = 298 to 373 K, i.e., the expected range for transistor operation in circuits/systems, considering heating effects due to inefficient power dissipation. From the analysis of the transfer characteristics (I_D–V_G) in the subthreshold regime, the Schottky barrier height ($\Phi_B \approx 0.18$ eV) associated with the Ni/MoS_2 contact was evaluated. The resulting contact resistance in the on-state (electron accumulation in the channel) was also determined and it was found to increase with T as R_C proportional to $T^{3.1}$. The contribution of R_C to the extraction of μ and V_{th} was evaluated, showing a more than 10% underestimation of μ when the effect of R_C is neglected, whereas the effect on V_{th} is less significant. The temperature dependence of μ and V_{th} was also investigated. A decrease of μ proportional to $1/T^{\alpha}$ with $\alpha = 1.4 \pm 0.3$ was found, indicating scattering by optical phonons as the main limiting mechanism for mobility above room temperature. The value of V_{th} showed a large negative shift (about 6 V) increasing the temperature from 298 to 373 K, which was explained in terms of electron trapping at MoS_2/SiO_2 interface states.

Introduction

Transition metal dichalcogenides (TMDs) are compound materials formed by the Van der Waals stacking of MX_2 layers (where M = Mo, W, etc., i.e., a transition metal, and X = S, Se, Te, i.e., a chalcogen atom). Among the large number of existing layered materials [1], TMDs are currently attracting increasing scientific interest due to some distinct properties, such as the presence of a sizable bandgap in their band structure. As an example, MoS_2 (the most studied among TMDs due to its high abundance in nature and relatively high stability under ambient conditions) exhibits an indirect bandgap of ≈1.3 eV in the case of few layers and bulk material and a direct bandgap of ≈1.8 eV in the case of a single layer. These properties make MoS_2 an interesting material for the next generation of electronics and optoelectronics devices [2]. As an example, field effect transistors with very interesting performance in terms of the on/off current ratio (10^6–10^8) and low subthreshold swing (≈70 meV/decade) have been demonstrated using single [3] and multilayers of MoS_2 [4].

MoS_2 thin films, obtained either by cleavage from the bulk material or by chemical vapor deposition, are typically unintentionally n-type doped. Since well-assessed methods for doping enrichment of MoS_2 under source/drain contacts are still lacking, MoS_2 transistors are mostly fabricated by deposition of metals directly on the unintentionally doped material, resulting in the formation of Schottky contacts. Experimental investigations showed that both low work function (e.g., Sc, Ti) and high work function (e.g., Ni, Pt) metals mostly exhibit a Fermi level pinning close to the conduction band of MoS_2 [5], resulting in a Schottky barrier height (SBH) for electrons typically ranging from 0.1 to 0.3 eV. The origin of this Fermi level pinning is currently a matter of investigation and a crucial role seems to be played by nanoscale defects/inhomogeneities at the metal/MoS_2 interface [6,7].

The presence of this small but not negligible Schottky barrier at source/drain contacts certainly has a strong impact on the electrical characteristics of MoS_2 transistors in the subthreshold regime [5]. In addition, the resulting source/drain contact resistance, R_C, can also have a significant influence on the electrical properties of the device in the on-state, i.e., above the threshold voltage (V_{th}). In particular, R_C is expected to affect, to some extent, the values of V_{th} and of the field effect mobility μ extracted from the transfer characteristics (drain current, I_D, vs gate bias, V_G) of the device and of the on-resistance (R_{on}) extracted from the output characteristics (drain current, I_D, vs drain bias, V_{DS}). Clearly, all these parameters (V_{th}, μ, and R_{on}) have their own dependence on the temperature, and their combination results in the device electrical characteristics at a fixed measurement condition. Hence, to gain a deeper understanding of the behavior of MoS_2 transistors for real applications, a temperature-dependent characterization of the main electrical parameters under practical operating conditions is mandatory. A temperature range from room temperature to 400 K is a realistic range for device operation in circuits/systems, taking into account the heating effect they undergo due to inefficient heat dissipation. However, to date, only a limited number of papers have focused on the high temperature behavior of MoS_2 transistors [8,9].

In this paper, we report a detailed temperature dependent investigation of multilayer MoS_2 transistors with Ni source/drain contacts, focusing on the role played by the contact both in the subthreshold regime and above the threshold voltage. In contrast to other literature works, mainly focused on the use of low work function contacts (such as Sc or Ti) to minimize the effect of contact resistance in n-type MoS_2 FETs [5], we focused on a high work function metal such as Ni in this paper in order to evaluate the impact of Ni/MoS_2 contact resistance on the device field effect mobility μ and threshold voltage V_{th}. The interest on Ni was also motivated by the recently demonstrated possibility to achieve MoS_2 FETs with ambipolar behavior by performing a temperature-bias annealing processes on as-deposited Ni contacts [10]. In the following, the temperature dependence of μ, V_{th} and R_C in the range from 298 to 373 K was determined and the physical mechanisms of these dependences were discussed.

Results and Discussion

Back-gated transistors have been fabricated using multilayer MoS_2 flakes (with thickness ranging from ≈40 to ≈50 nm) exfoliated from bulk molybdenite crystals onto a highly doped Si substrate covered with 380 nm thick, thermally grown SiO_2. Such relatively thick MoS_2 samples have been chosen since it has been reported that the electrical properties (μ, V_{th}) of simple back-gated transistors fabricated with multilayer MoS_2 are much less affected by the effect of the external environment (water/oxygen) [9] with respect to single or few layer devices [11], for which encapsulation is instead required to achieve good electrical performance [3].

Furthermore, as reported in the literature, carrier mobility is only slightly dependent on MoS_2 thickness for transistors fabricated on ≈20 to ≈70 nm thick flakes, whereas stronger variations are observed for thinner flakes, with the largest mobility values obtained for thicknesses ranging from 6 to 12 nm [5].

The experiments discussed in this paper have been carried out on a set of ten FETs fabricated on the same substrate. For consistency, the reported temperature-dependent analysis has

been carried out on one of the transistors from this set of devices. Figure 1a shows a schematic representation including an optical image of a MoS_2 transistor with the SiO_2/Si backgate and Ni/Au source and drain contacts. An atomic force microscopy image (Figure 1b) and the corresponding height linescan (Figure 1c) of the MoS_2 flake on the SiO_2 substrate are also reported, showing ≈40 nm flake thickness.

The transfer characteristics (I_D–V_G) measured at a low fixed drain bias (V_{DS} = 0.1 V) on this device at different temperatures from 298 to 373 K are reported in Figure 2 both on a semilogarithmic scale (Figure 2a) and on a linear scale (Figure 2b). Clearly, the linear scale plot allows the current transport above the threshold voltage (V_{th}) to be studied, whereas the semilog scale plot allows for a better visualization of transport in the subthreshold regime. In the following two sections, a detailed analysis of the characteristics in the subthreshold and above-threshold regime will be reported and the device electrical parameters will be extracted. In particular, the Ni/MoS_2 Schottky barrier height and the flat band voltage (V_{FB}) will be evaluated from the temperature-dependent analysis of the subthreshold I_D–V_G curves, whereas the temperature behavior of V_{th} and μ will be obtained from the curves above the threshold.

Subthreshold behavior

The semilog scale I_D–V_G characteristics (Figure 2a) measured at 298 K exhibit a current variation of more than six orders of magnitude in the bias range from V_G = −55 V to 0 V. This current variation is significantly reduced with increasing the temperature from 298 to 373 K, especially due to the strong increase of current with the temperature at large negative bias.

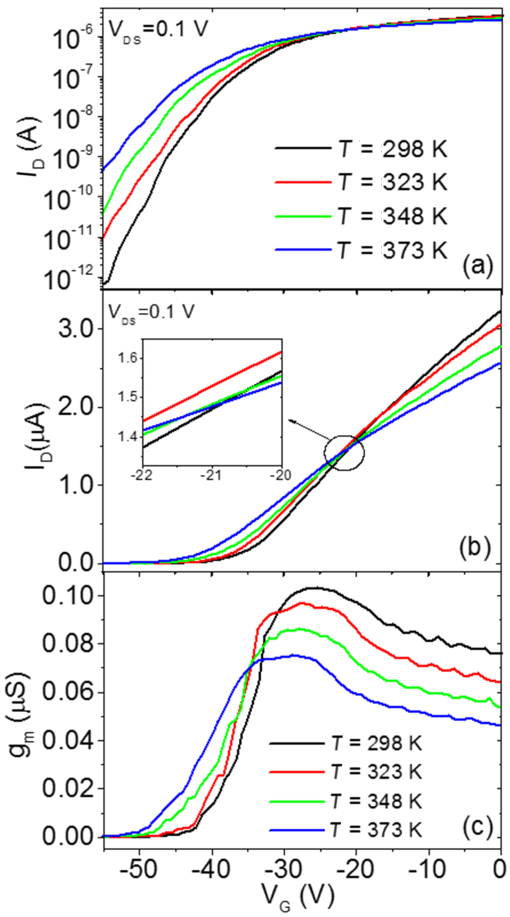

Figure 2: Semilog scale plot (a) and linear scale plot (b) of the transfer characteristics (I_D–V_G) measured at a fixed drain bias (V_{DS} = 0.1 V) and at different temperatures ranging from 298 to 373 K. (c) Transconductance (g_m = dI_D/dV_G) vs V_G curves at different temperatures calculated from the I_D–V_G characteristics in (b).

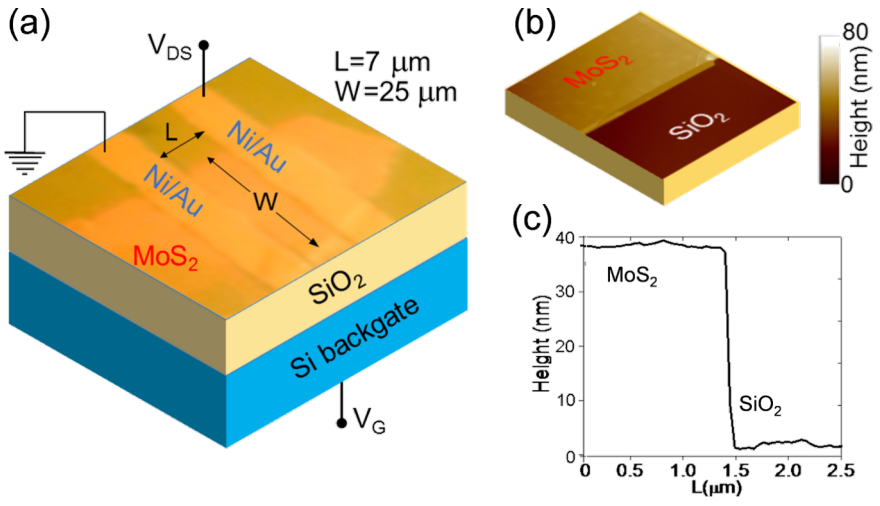

Figure 1: (a) Schematic including an optical image of a MoS_2 transistor with the SiO_2/Si backgate and Ni/Au source and drain contacts. (b) Atomic force microscopy image and (c) the corresponding height linescan of the MoS_2 flake on the SiO_2 substrate.

This is better highlighted in Figure 3a, where the I_D−V_G characteristics in the gate bias range from −55 to −35 V and at different temperatures from 298 to 373 K have been reported. Such strong dependence of I_D on T suggests that current transport in the subthreshold regime is dominated by thermionic current injection through the reverse biased source/MoS_2 Schottky contact, according to the relation $I_D \propto T^2 \exp\left[-q\Phi_B(V_G)/k_BT\right]$ [5], where $\Phi_B(V_G)$ is the effective Schottky barrier height (SBH), modulated by the gate bias V_G. To verify this, for each V_G an Arrhenius plot of I_D/T^2 vs $1000/T$ is reported in Figure 3b. A nice linear dependence was observed for all the V_G in the considered bias range. The effective SBH values Φ_B, obtained from the slope of the linear fit of the Arrhenius plot in Figure 3b are reported in Figure 3c as a function of V_G. The schematic band diagrams corresponding to the different transistor operation regimes, i.e., depletion (i), flat band (ii) and accumulation (iii), are also illustrated in the inserts of Figure 3c.

In the depletion regime (Figure 3c (i)), the applied gate bias induces an upward band bending, ψ, in MoS_2 at the interface with the SiO_2 gate insulator. The experimentally evaluated SBH is found to depend linearly on V_G. This dependence can be fitted with the relation $\Phi_B = \Phi_B(V_{FB}) - \gamma(V_G - V_{FB})$, where $\Phi_B(V_{FB})$ is the effective SBH at the flat band voltage and the term $\psi = \gamma(V_G - V_{FB})$ is the upward band bending. The slope γ indicates the modulation efficiency of Φ_B by the gate bias. It depends on the SiO_2 layer capacitance, $C_{ox} = \varepsilon_0\varepsilon_{ox}/t_{ox} \approx 9.1 \times 10^{-5}$ F/m^2 (ε_0 is the vacuum dielectric constant, $\varepsilon_{ox} = 3.9$, $t_{ox} = 380$ nm, the permittivity and the thickness of the SiO_2 film, respectively), on the capacitance of the MoS_2 depletion region, C_s, as well as on the capacitance associated with MoS_2/SiO_2 interface traps, C_{it} [5]. In the depletion regime, the current transport in the transistor is ruled by thermionic emission (TE) of electrons from the source contact to the channel.

The effective SBH Φ_B and, hence, the band bending $\psi = \Phi_B(V_G) - \Phi_B(V_{FB})$ is found to decrease linearly moving toward positive V_G values. The flat band voltage V_{FB} corresponds to the gate bias for which $\psi = 0$ (see (ii) in Figure 3b), whereas for $V_G > V_{FB}$ the band bending $\psi < 0$ (see (iii) in Figure 3b), i.e., the channel starts to accumulate electrons. In the accumulation regime, current injection in the channel is ruled by thermionic field emission (TFE) through the source triangular barrier. The TFE mechanism yields a reduced effective SBH with respect to the constant Φ_B value (red dashed line in Figure 3c) that would be expected if only TE over the barrier would occur. As a guide

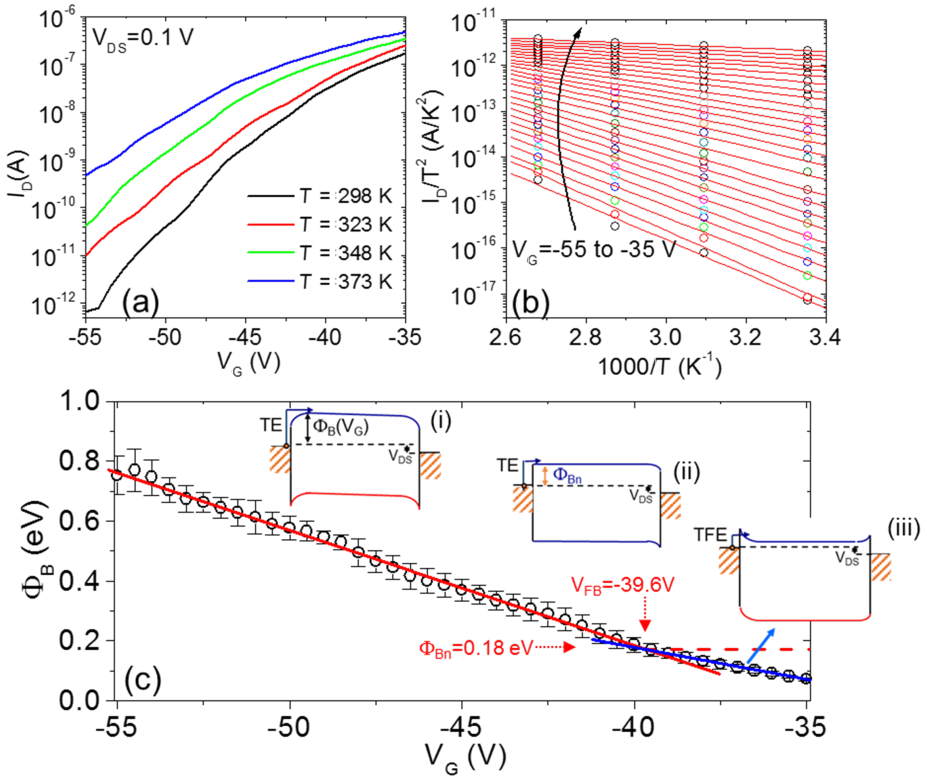

Figure 3: (a) Semilog scale plot of the transfer characteristics (I_D−V_G) in the subthreshold regime at different temperatures ranging from 298 to 373 K. (b) Arrhenius plot of I_D/T^2 vs $1000/T$ for each gate bias. (c) Effective SBH Φ_B as a function of V_G. In the inserts, schematic band diagrams are given for the transistor operation in different regimes: depletion (i), flat band voltage (ii) and accumulation (iii).

for the eye, the SBH dependence on V_G in the accumulation regime has been fitted with a blue line in Figure 3c. Hence, V_{FB} = −39.6 V can be experimentally determined as the bias corresponding to the intercept between the two linear fits [5]. The corresponding SBH value $\Phi_B(V_{FB})$ = 0.18 eV represents the "real" (i.e., gate bias independent) value of the Ni/MoS_2 Schottky barrier.

The experimental V_{FB} for the MoS_2 transistor exhibits a large negative value, as reported in other literature works [12]. Such a result has been ascribed to donor-like interface trap states (positively charged when empty) between the SiO_2 and MoS_2 [13,14]. In order to evaluate the amount of this positive charge at the interface, it is worth comparing the experimental value with the one deduced from theoretical expression of the flat band voltage ($V_{FB,id}$) of an ideal metal-oxide-semiconductor field effect transistor (i.e., without fixed or interface charges). $V_{FB,id}$ is expressed as [15]:

$$V_{FB,id} = W_M - \left[\chi + E_G/2 - kT/q \ln\left(N_D/n_i\right)\right], \quad (1)$$

where W_M is the work function of the gate material (4.05 eV for the n^+-doped Si back gate in our transistor), χ is the semiconductor electron affinity (4.2 eV for MoS_2), N_D is the semiconductor doping concentration (on the order of 10^{16} cm^{-3} in unintentionally doped MoS_2) and n_i is the intrinsic carrier concentration (for MoS_2, $n_i \approx 6\times10^{15}T^{3/2}\exp\left(-E_G/2kT\right)$ cm^{-3}). According to this expression a low value of $V_{FB,id}$ slightly varying with the T (from −0.35 V at 298 K to −0.42 V at 273 K) would be expected for our device. The negative shift of the experimental V_{FB} with respect to $V_{FB,id}$ can be accounted for by the presence of a net positive charge density at the interface with SiO_2 that can be evaluated as $C_{ox}(V_{FB}-V_{FB,id})/q \approx 2.2 \times 10^{12}$ cm^{-2}.

In the following section, the device transfer characteristics above the threshold will be analyzed to extract the threshold voltage and mobility.

Transfer characteristics above threshold

The linear scale transfer characteristics (Figure 2b) show very low current below a threshold voltage (V_{th}) and a nearly linear increase of I_D vs V_G above V_{th}. Two effects can be observed from the comparison of the I_D–V_G curves at increasing temperatures, i.e., (i) a negative shift of the threshold voltage and (ii) a decrease of the I_D–V_G curve slope in the linear region above V_{th}. The origin of these two effects will be discussed more in detail later on. Interestingly, as a result of these two competing effects, the I_D–V_G characteristics tend to cross nearly at the same gate bias V_G = −21 V (see details in the insert of Figure 2b). This bias condition can be interesting for some applications where it is desirable that the device performance does not depend significantly on the temperature ($dI_D/dT \approx 0$).

Figure 2c shows the transconductance g_m vs V_G curves calculated by differentiation ($g_m = dI_D/dV_G$) of the I_D–V_G characteristics in Figure 2b. In the considered bias range, all the curves exhibit an increase of g_m with V_G up to a maximum value, followed by a decrease of g_m. The maximum transconductance value ($g_{m,max}$) is found to decrease with increasing temperature. Furthermore, a rigid shift of the g_m–V_G curves toward negative gate bias values is observed with increasing T.

From the linear scale transfer characteristics and the transconductance, two key electrical parameters for transistor operation, i.e., the threshold voltage (V_{th}) and the field effect mobility (μ), are typically evaluated. Figure 4a shows a linear scale plot of I_D (left axis) and of the transconductance g_m (right axis) at V_{DS} = 0.1 V and T = 298 K. The field effect mobility in the linear region, μ_{lin}, of the transfer characteristics is typically extracted from the transconductance using the following formula $\mu_{lin} = g_m L/(WC_{ox}V_{DS})$, where L and W are the channel length and width, respectively, and C_{ox} the SiO_2 gate capacitance. For our device with L/W = 7 μm/25 μm and $C_{ox} \approx 9.1 \times 10^{-5}$ F/m^2, the evaluated mobility from the maximum transconductance value $g_{m,max}$ was μ_{lin} = 31.75 $cm^2V^{-1}s^{-1}$, as indicated in Figure 4a. A method for evaluating V_{th} consists of drawing the tangent line to the I_D–V_G curve at the bias ($V_{G,max}$) corresponding to $g_{m,max}$ and taking the intercept with the I_D = 0 baseline [16], as shown in Figure 4a.

This procedure can be explained by simple geometrical considerations. In the linear region of the transfer characteristics, I_D can be expressed as [14]:

$$I_D = \frac{W}{L}\mu C_{ox} V_{DS}\left(V_G - V_{th}\right). \quad (2)$$

Hence, it results that $I_{D,max} = g_{m,max}(V_{G,max}-V_{th})$ and the threshold voltage can be calculated as

$$V_{th,lin} = -I_{D,max}/g_{m,max} + V_{G,max} \approx -35.39\,V.$$

As a matter of fact, for the evaluation of $V_{th,lin}$ and μ_{lin} based on Equation 2 the contribution of the contact resistance is assumed to be zero. However, as deduced from the analysis of the subthreshold characteristics, a Schottky barrier is associated to the source/drain contacts with MoS_2, which is also expected to result in a non-negligible contact resistance, R_C. The value of the contact resistance above the threshold and its temperature dependence will be estimated in the last section of this paper from the analysis of the on-resistance (R_{on}) extracted from the

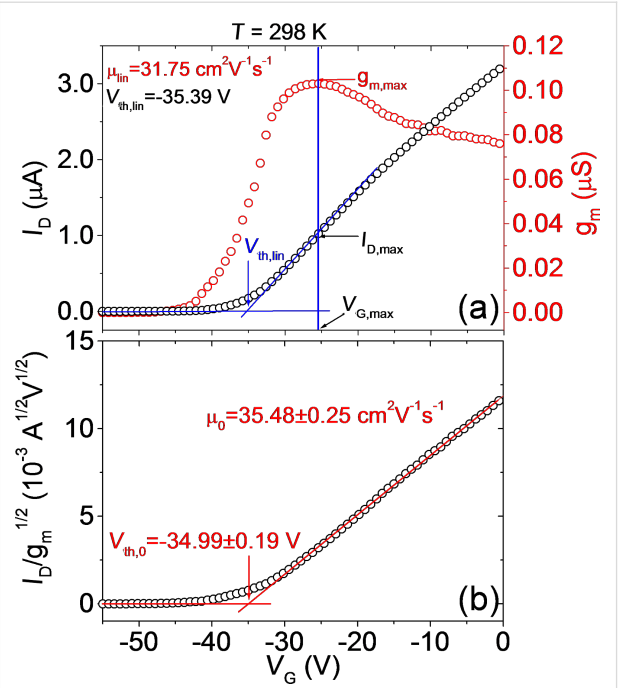

Figure 4: (a) Linear scale plot of I_D (left axis) and of the transconductance g_m (right axis) at V_{DS} = 0.1 V and T = 298 K. The extraction of the field effect mobility (μ_{lin}) from the maximum of g_m and of V_{th} by the linear extrapolation method ($V_{th,lin}$) is illustrated. (b) Plot of $I_D/g_m^{1/2}$ vs V_G with illustration of extraction of the mobility (μ_0) and threshold voltage value ($V_{th,0}$) corrected by the effect of the contact resistance (R_C).

device output characteristics (I_D–V_{DS}) at low V_{DS}. Here, we want to discuss how R_C can influence the evaluation of μ and V_{th} from the transfer characteristics.

In order to take into account the role of R_C, V_{DS} can be replaced by V_{DS}–I_DR_C in Equation 2, and solving by I_D, the following expression for I_D is obtained:

$$I_D = \frac{\frac{W}{L}\mu_0 C_{ox} V_{DS}\left(V_G - V_{th,0}\right)}{1+\frac{W}{L}\mu_0 C_{ox} R_c\left(V_G - V_{th,0}\right)}, \quad (3)$$

where μ_0 and $V_{th,0}$ represent the values of the mobility and threshold voltage corrected by the effect of R_C. As a consequence, the transconductance $g_m = dI_D/dV_G$ can be expressed as:

$$g_m = \frac{\frac{W}{L}\mu_0 C_{ox} V_{DS}}{\left[1+\frac{W}{L}\mu_0 C_{ox} R_c\left(V_G - V_{th,0}\right)\right]^2}. \quad (4)$$

Noteworthy, the ratio $I_D/\sqrt{g_m} = \sqrt{W/L\,\mu_0 C_{ox} V_{DS}}\left(V_G - V_{th,0}\right)$ is independent of R_C. A plot of $I_D/g_m^{1/2}$ vs V_G is reported in Figure 4b. The corrected value of the field effect mobility ($\mu_0 = 35.48 \pm 0.25$ cm^{2}V^{-1}s^{-1}) can be calculated from the slope of the linear fit of these data, whereas the threshold voltage ($V_{th,0} = -34.99 \pm 0.19$ V) can be obtained from the intercept with the x axis. It is worth noting that the mobility value μ_0 after correction for the contact resistance is more than 10% higher than the value estimated without any correction, whereas the threshold voltage $V_{th,0}$ after correction is only 1% higher than the value estimated without accounting for R_C. This indicates that the underestimation of the mobility neglecting the contact resistance effect can be quite relevant, whereas the threshold voltage is less affected by R_C. By repeating this procedure for all the measured characteristics reported in Figure 2b,c, the temperature dependence of the mobility (μ_{lin} and μ_0), threshold voltage (V_{th} and $V_{th,0}$) in the considered temperature range has been evaluated, as illustrated in Figure 5a,b, respectively.

Both μ_{lin} and μ_0 were found to decrease as a function of T with a similar dependence $1/T^{\alpha}$, with $\alpha = 1.5 \pm 0.2$ in the case of μ_{lin} and $\alpha = 1.4 \pm 0.3$ in the case of μ_0. Such a dependence of $\mu \approx 1/T^{\alpha}$ with $\alpha > 1$ indicates that the main mechanism limiting the mobility of electrons in the multilayer MoS_2 channel in this temperature range is scattering by optical phonons, as reported by other experimental and theoretical investigations [4]. Instead, electron mobility was found to be limited by Coulomb scattering by charged impurities only at lower temperatures (<100 K) [4]. Noteworthy, scattering by charged impurities at the interface with the substrate results in the dominant mechanism for another well-studied 2D material, graphene, even at room temperature and higher temperatures [17,18].

In Figure 5b, the threshold voltage V_{th} exhibits a negative shift of about 6 V with increasing the temperature from 298 to 273 K. For convenience, the difference V_{th}–V_{FB} is also reported in Figure 5b, right scale. It is useful to compare the experimental temperature dependence of V_{th} with the expected theoretical variation with temperature, in order to understand which are the relevant physical parameters ruling this behavior.

For an ideal transistor (without interface states) operating under accumulation conditions, the shift between the threshold voltage $V_{th,id}$ and the flat band voltage $V_{FB,id}$ can be expressed as:

$$V_{th,id} - V_{FB,id} = \psi_{th} + \frac{qN_s\left(\psi_{th}\right)}{C_{ox}} \quad (5)$$

where ψ_{th} is the downward (negative) band bending at the threshold (as illustrated in the band diagram (iii) of Figure 3c,

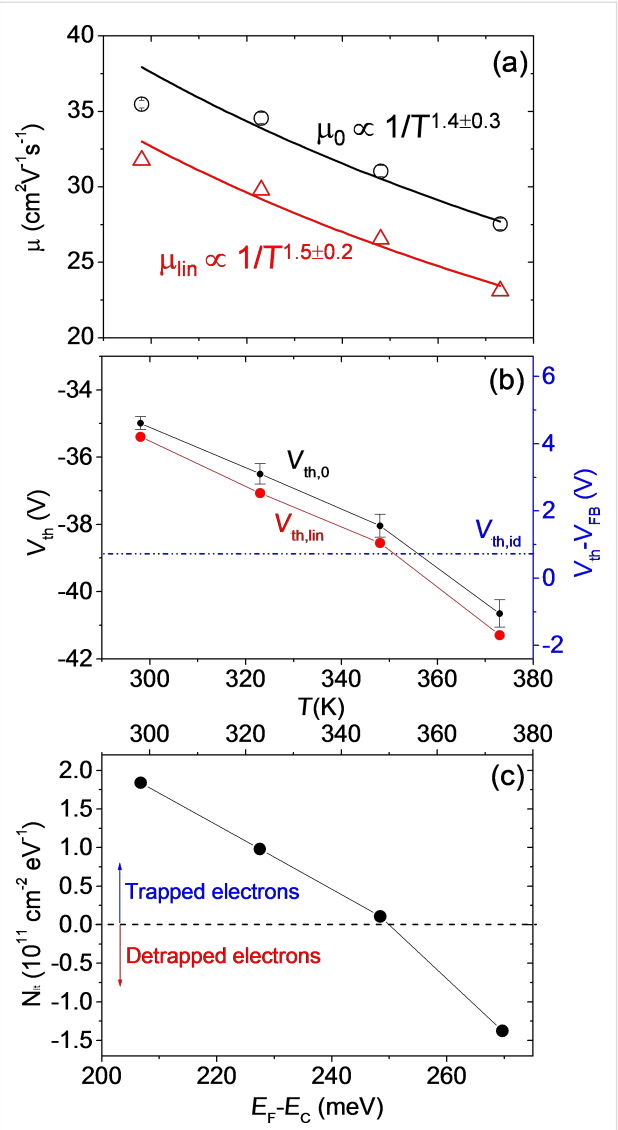

Figure 5: (a) Temperature dependence of the field effect mobility extracted from the linear region of the I_D–V_G characteristics without (μ_{lin}) and with (μ_0) the correction for the effect of the contact resistance R_C. Experimental data have been fitted with a temperature dependence $1/T^{\alpha}$. (b) Temperature dependence of the threshold voltage evaluated without ($V_{th,lin}$) and with ($V_{th,0}$) the correction for the effect of the contact resistance R_C. (c) Density of trapped/detrapped electrons at MoS_2/SiO_2 as a function of T (upper scale) and the corresponding position of the Fermi level with respect to the conduction band (E_F–E_C).

and $N_s(\psi_{th})$ is the electron density in the channel at ψ_{th}

$$N_s(\psi_{th}) = \frac{\sqrt{2}\varepsilon_0\varepsilon_s}{kTL_D}\sqrt{\left[\exp\left(-\frac{\psi_{th}}{kT}\right)+\frac{\psi_{th}}{kT}-1\right]}, \quad (6)$$

where $L_D = \sqrt{\varepsilon_0\varepsilon_s kT/q^2N_D}$ is the Debye length. The band bending ψ_{th} can be evaluated assuming that the electron density in the channel at the threshold corresponds to $N_s(\psi_{th}) = tN_D$, where N_D is the uniform doping concentration in the MoS_2 thin film and t its thickness. Assuming $N_D = 10^{16}$ cm^{-3} for our unintentionally doped MoS_2, we obtain $N_s \approx 4 \times 10^{10}$ cm^{-2}. Furthermore, a value of ψ_{th} ranging from approximately −34 meV (at T = 298 K) to −39 meV (at T = 373 K) can be estimated from the dependence of N_s on ψ_{th} in Equation 6. Under these assumptions, $V_{th,id}$–$V_{FB,id} \approx 0.7$ eV (nearly independent of T) can be estimated, as indicated in Figure 5b (blue dashed line).

In order to account for the large change of V_{th} with temperature, the role of interface states at SiO_2/MoS_2 interface must be considered. The difference between the experimental V_{th}–V_{FB} and theoretical $V_{th,id}$–$V_{FB,id}$ can be described by a term $\Delta V_{it} = qN_{it}/C_{ox}$, where N_{it} is the density of trapped/detrapped electrons by SiO_2 interface traps. These interface traps exhibit a donor like behavior, i.e., they are positively charged above the Fermi level (when they are empty) and neutral below the Fermi level (when they are filled by electrons) [13]. Hence, electron trapping results in a neutralization of the interface states, resulting in a positive shift of V_{th} with respect to V_{FB} (i.e. $\Delta V_{it} > 0$). On the contrary, detrapping of electrons from these states results in an increase of the positive charge and, hence, in $\Delta V_{it} < 0$.

From the experimental data in Figure 5b, trapped electron densities $N_{it} = 2 \times 10^{11}$, 1×10^{11}, and 2×10^{10} cm^{-2} are estimated at 298, 323, and 348 K, respectively, whereas a detrapped electron density $N_{it} = 1.3 \times 10^{11}$ cm^{-2} is obtained at 373 K (see Figure 5c). Electron trapping and detrapping at MoS_2/SiO_2 interface have been shown to be thermally activated processes [13]. Hence, for a given interface trap distribution D_{it} close to the MoS_2 conduction band, N_{it} can be expressed as

$$N_{it} = \left[P_{tr}(T) - P_{det}(T)\right]\int_{E_F-E_C+\psi}^{E_F-E_C} D_{it}\,d\phi \quad (7)$$

where $P_{tr}(T)$ and $P_{det}(T)$ are the trapping and detrapping probabilities, respectively [13]. The experimentally found temperature dependence of N_{it} can be explained as follows. As T increases, the shift of the Fermi energy E_F with respect to E_C increases as

$$E_F - E_C = \frac{E_G}{2} - \frac{kT}{q}\ln\left[\frac{N_D}{n_i(T)}\right]$$

resulting in a change of the integration range in Equation 7. Furthermore, the difference $P_{tr}(T)$–$P_{det}(T)$ can change with T. The dependence of N_{it} on E_F is also illustrated in Figure 5c. It is consistent with a decrease of D_{it} with increasing E_F–E_C.

Furthermore, at 373 K, it can be argued that the P_{det} becomes higher than P_{tr}, resulting in a negative value of N_{it}.

Output characteristics

Figure 6 shows the output characteristics I_D–V_{DS} for different gate bias values ranging from V_G = −56 to 0 V (with steps ΔV = 4 V) measured at different temperatures, i.e., (a) 298 K, (b) 323 K, (c) 348 K and (d) 373 K. For all the V_G values, I_D exhibits a linear increase with V_{DS} at low drain bias ($V_{DS} << V_G - V_{th}$), whereas it deviates from the linear behavior at larger V_{DS}. In particular, current saturation is achieved whenever the condition $V_{DS} > V_G - V_{th}$ is reached. By comparing the output characteristics measured at the different temperatures with the same V_G values, it is evident that both the slope of the I_D–V_{DS} curves in the linear region and the saturation current value decreases with increasing T.

The reciprocal of the I_D–V_{DS} curves slope in the linear region at low V_{DS} is the device on-resistance R_{on}, which can be expressed as:

$$R_{on} = 2R_C + \frac{L}{W}R_{ch} = 2R_C + \frac{L}{W}\frac{1}{q\mu(V_G - V_{th})}, \quad (8)$$

where R_C is the source and drain contact resistance and R_{ch} the channel sheet resistance, which depends inversely on (V_G–V_{th}), according to Equation 2.

Figure 7a reports the plots of R_{on} vs $1/(V_G - V_{th,lin})$ extracted from the I_D–V_{DS} characteristics in Figure 6 at the different temperatures. The linear fit of the data was performed for the four temperatures and, from the intercept with the vertical axis, the value of the contact resistance R_C was estimated. The behavior of R_C vs T is reported in Figure 7b, indicating an increase of $R_C \propto T^{\alpha}$, with $\alpha = 3.1 \pm 0.3$.

Finally, the behavior of the output characteristics at high V_{DS} is discussed. Figure 8a shows the I_D–V_{DS} characteristics measured at T = 298 K. The V_G–V_{th} value for each curve is indicated. It can be observed that the current saturation regime (i.e., I_{DS} in-

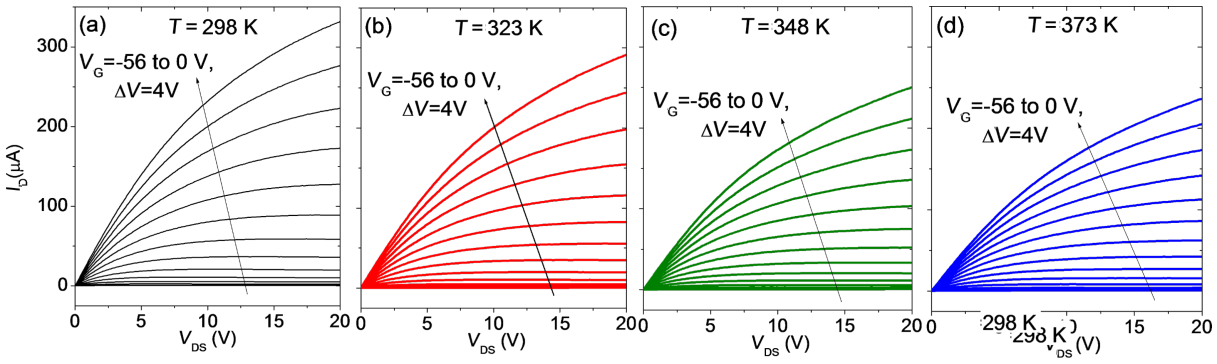

Figure 6: Output characteristics I_D–V_{DS} for different gate bias values from −56 to 0 V at different temperatures: (a) T = 298 K, (b) T = 323 K, (c) T = 348 K and (d) T = 373 K.

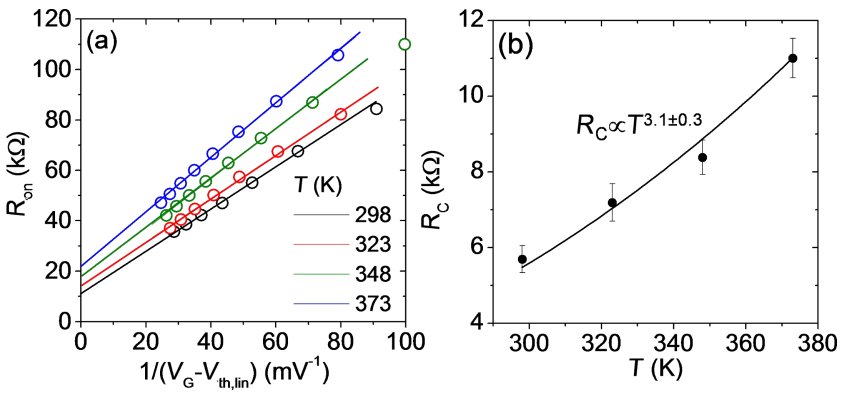

Figure 7: (a) On-resistance R_{on} vs $1/(V_G - V_{th,lin})$ at different temperatures. (b) Temperature dependence of R_C.

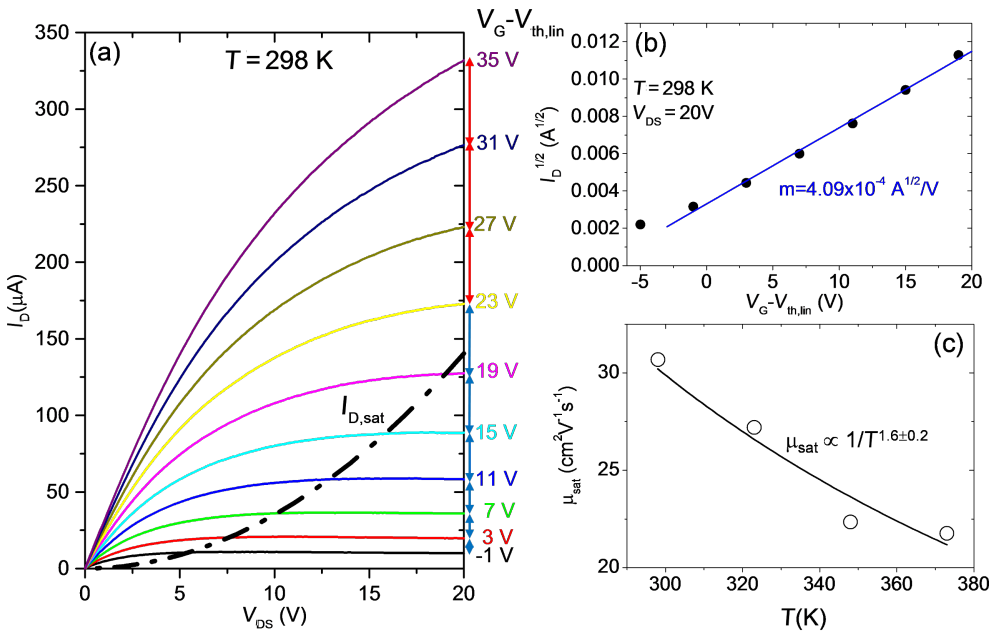

Figure 8: (a) Output characteristics (I_D–V_{DS}) for different gate bias values from −56 to 0 V at T = 298 K. (b) Plot of $I_D^{1/2}$ vs V_G–$V_{th,lin}$ for V_{DS} = 20 V and linear fit of the data. (c) Saturation mobility μ_{sat} vs temperature.

dependent of V_{DS}) is reached only for V_G–V_{th} < 20 V, corresponding to an accumulated electron density in the channel $N_s < 1.1 \times 10^{12}$ cm^{-2}. For V_G–V_{th} > 20 V, saturation is not reached.

In the saturation condition, I_D is only a quadratic function of V_G–V_{th} [14]:

$$I_{D,sat} = \frac{W}{2BL}\mu_{sat}C_{ox}\left(V_G - V_{th}\right)^2, \qquad (9)$$

where μ_{sat} is the mobility value under saturation conditions and the term B is the so-called body coefficient, which depends on the gate oxide capacitance, on the doping concentration in the film and on the temperature:

$$B = 1 + \frac{1}{2C_{ox}}\sqrt{\frac{\varepsilon_0\varepsilon_s q^2 N_D}{kT\ln\left[N_D/n_i(T)\right]}}.$$

For thin gate dielectrics and low doping in the film, B can be approximated to 1, but for thick dielectrics and high doping its value can be significantly higher. In the case of our device with C_{ox} = 9.1 × 10^{-5} F/m and assuming a MoS_2 doping $N_D \approx 1 \times 10^{16}$ cm^{-3}, B can range from ≈2.97 to ≈3.12 in the considered temperature range. In Figure 8b, $I_D^{1/2}$ at V_{DS} = 20 V is reported as a function of V_G–V_{th}, showing a linear behavior. According to Equation 9, the mobility under saturation condition can be evaluated from the slope m of the fit, as $\mu_{sat} = 2BLm^2/WC_{ox}$. By repeating this procedure for all the output characteristics measured at the different temperatures, the behavior of μ_{sat} as a function of T can be obtained. The main error source in the estimation of μ_{sat} is related to the fact that the doping concentration N_D and, hence, the coefficient B is not exactly known. Noteworthy, the values of μ_{sat} in Figure 8c, estimated assuming $N_D \approx 1 \times 10^{16}$ cm^{-3}, are very close to those evaluated from the linear region of the transfer characteristics (see Figure 5a) and exhibit a similar temperature dependence. This also confirms that the assumption for the doping concentration is correct.

Conclusion

In conclusion, a temperature dependent investigation of back-gated multilayer MoS_2 transistors with Ni source/drain contacts in the range from T = 298 to 373 K has been performed. The SBH $\Phi_B \approx 0.18$ eV of the Ni/MoS_2 contact was evaluated from the analysis of the transfer characteristics I_D–V_G in the subthreshold regime. The resulting R_C associated with the SBH was determined by fitting the R_{on} dependence on $1/(V_G–V_{th})$ extracted from the device output characteristics I_D–V_{DS} at low V_{DS}. An increase of $R_C \propto T^{3.1}$ was demonstrated. The impact of R_C on the values of μ and V_{th} values was determined, showing an underestimation of μ by more than 10% if the effect of R_C is neglected, whereas the influence of R_C on the estimated value of V_{th} is only 1%. Furthermore, the temperature dependence of μ and V_{th} was investigated, showing a decrease of

$\mu \approx 1/T^{\alpha}$ with $\alpha = 1.4 \pm 0.3$ (indicating scattering by optical phonons as the limiting mechanism), and a negative shift of V_{th} by about 6 V with increasing T. The role played by electron trapping at the MoS_2/SiO_2 interface to explain such a large V_{th} shift was discussed.

Experimental

Back-gated transistors were fabricated using MoS_2 flakes exfoliated from molybdenite bulk crystals (supplier SPI [19]) with thicknesses ranging from ≈40 to ≈50 nm and transferred onto a highly doped n-type Si substrate covered with 380 nm of thermally grown SiO_2. An accurate sample preparation protocol has been adopted for controlled quality of the MoS_2/SiO_2 interface, as this is crucial to achieve reproducible electrical behavior of the devices. In particular, thermo-compression printing using a Karl-Suss nanoimprint device with fixed temperature and pressure conditions [20,21] has been employed to transfer the exfoliated MoS_2 flakes onto the SiO_2 surface that was previously cleaned using solvents and a soft O_2 plasma treatment. Finally, source and drain contacts were obtained by deposition and lift-off of a Ni(50 nm)/Au(100 nm) bilayer.

The temperature-dependent electrical characterization in the range from 298 to 373 K was performed using a Cascade Microtech probe station with an Agilent 4156b parameter analyzer. All the measurements were carried out in dark conditions and under nitrogen flux.

Acknowledgements

P. Fiorenza, I. Deretzis, A. La Magna, C. Bongiorno and G. Nicotra from CNR-IMM are acknowledged for helpful discussions. This work has been supported, in part, by MIUR in the framework of the FlagERA project “GraNitE: Graphene heterostructures with Nitrides for high frequency Electronics” (Grant number 0001411).

References

1. Geim, A. K.; Grigorieva, I. V. *Nature* **2013,** *499,* 419–425. doi:10.1038/nature12385
2. Wang, Q. H.; Kalantar-Zadeh, K.; Kis, A.; Coleman, J. N.; Strano, M. S. *Nat. Nanotechnol.* **2012,** *7,* 699–712. doi:10.1038/nnano.2012.193
3. Radisavljevic, B.; Radenovic, A.; Brivio, J.; Giacometti, V.; Kis, A. *Nat. Nanotechnol.* **2011,** *6,* 147–150. doi:10.1038/nnano.2010.279
4. Kim, S.; Konar, A.; Hwang, W.-S.; Lee, J. H.; Lee, J.; Yang, J.; Jung, C.; Kim, H.; Yoo, J.-B.; Choi, J.-Y.; Jin, Y. W.; Lee, S. Y.; Jena, D.; Choi, W.; Kim, K. *Nat. Commun.* **2012,** *3,* No. 1011. doi:10.1038/ncomms2018
5. Das, S.; Chen, H.-Y.; Penumatcha, A. V.; Appenzeller, J. *Nano Lett.* **2013,** *13,* 100–105. doi:10.1021/nl303583v
6. Giannazzo, F.; Fisichella, G.; Piazza, A.; Agnello, S.; Roccaforte, F. *Phys. Rev. B* **2015,** *92,* 081307. doi:10.1103/PhysRevB.92.081307
7. McDonnell, S.; Addou, R.; Buie, C.; Wallace, R. M.; Hinkle, C. L. *ACS Nano* **2014,** *8,* 2880–2888. doi:10.1021/nn500044q
8. Jiang, C.; Rumyantsev, S. L.; Samnakay, R.; Shur, M. S.; Balandin, A. A. *J. Appl. Phys.* **2015,** *117,* 064301. doi:10.1063/1.4906496
9. Kwon, H.-J.; Jang, J.; Kim, S.; Subramanian, V.; Grigoropoulos, C. P. *Appl. Phys. Lett.* **2014,** *105,* 152105. doi:10.1063/1.4898584
10. Giannazzo, F.; Fisichella, G.; Piazza, A.; Di Franco, S.; Greco, G.; Agnello, S.; Roccaforte, F. *Phys. Status Solidi RRL* **2016,** *10,* 797–801. doi:10.1002/pssr.201600209
11. Late, D. J.; Liu, B.; Ramakrishna Matte, H. S. S.; Dravid, V. P.; Rao, C. N. R. *ACS Nano* **2012,** *6,* 5635–5641. doi:10.1021/nn301572c
12. Choi, K.; Raza, S. R. A.; Lee, H. S.; Jeon, P. J.; Pezeshki, A.; Min, S.-W.; Kim, J. S.; Yoon, W.; Ju, S.-Y.; Lee, K.; Im, S. *Nanoscale* **2015,** *7,* 5617–5623. doi:10.1039/C4NR06707J
13. Guo, Y.; Wei, X.; Shu, J.; Liu, B.; Yin, J.; Guan, C.; Han, Y.; Gao, S.; Chen, Q. *Appl. Phys. Lett.* **2015,** *106,* 103109. doi:10.1063/1.4914968
14. Park, Y.; Baac, H. W.; Heo, J.; Yoo, G. *Appl. Phys. Lett.* **2016,** *108,* 083102. doi:10.1063/1.4942406
15. Sze, S. M.; Ng, K. K. *Physics of Semiconductor Devices,* 3rd ed.; Wiley: New York, 2007.
16. Schroder, D. K. *Semiconductor Material and Device Characterization,* 3rd ed.; Wiley: Hoboken, NJ, 2006.
17. Giannazzo, F.; Sonde, S.; Lo Nigro, R.; Rimini, E.; Raineri, V. *Nano Lett.* **2011,** *11,* 4612–4618. doi:10.1021/nl2020922
18. Sonde, S.; Giannazzo, F.; Vecchio, C.; Yakimova, R.; Rimini, E.; Raineri, V. *Appl. Phys. Lett.* **2010,** *97,* 132101. doi:10.1063/1.3489942
19. SPI Supplies. http://www.2spi.com (accessed Dec 30, 2016).
20. Giannazzo, F.; Fisichella, G.; Piazza, A.; Di Franco, S.; Oliveri, I. P.; Agnello, S.; Roccaforte, F. *Mater. Sci. Semicond. Process.* **2016,** *42,* 174–178. doi:10.1016/j.mssp.2015.07.062
21. Fisichella, G.; Di Franco, S.; Roccaforte, F.; Ravesi, S.; Giannazzo, F. *Appl. Phys. Lett.* **2014,** *104,* 233105. doi:10.1063/1.4882165

License and Terms

BEILSTEIN JOURNAL OF NANOTECHNOLOGY

Performance of natural-dye-sensitized solar cells by ZnO nanorod and nanowall enhanced photoelectrodes

Saif Saadaoui[1], Mohamed Aziz Ben Youssef[1], Moufida Ben Karoui[1,2], Rached Gharbi[*1], Emanuele Smecca[3], Vincenzina Strano[4], Salvo Mirabella[4], Alessandra Alberti[3] and Rosaria A. Puglisi[3]

Full Research Paper

Open Access

Address:
[1]Laboratoire des Semi-conducteurs et Dispositifs Electroniques, LISIER, University of Tunis, Ecole Nationale Supérieure d'Ingénieurs de Tunis, 05 Av. Taha Hussein 1008 Montfleury, Tunis, Tunisia, [2]Laboratoire de Photovoltaïque, centre de Recherche et des Technologies de l'énergie, Technopole de Borej-Cedria, BP 95, Hammam-Lif, Tunis 2050, Tunisia, [3]CNR-IMM, Zona Industriale Strada VIII, N°. 5, 95121 Catania, Italy and [4]MATIS CNR-IMM and Dipartimento di Fisica e Astronomia, Università di Catania, via S. Sofia 64, Catania, Italy

Email:
Rached Gharbi[*] - rached.gharbi@esstt.rnu.tn

* Corresponding author

Keywords:
DSSCs; *I–V* measurement; nanorods; nanowalls; natural dye; ZnO

Beilstein J. Nanotechnol. **2017,** *8,* 287–295.
doi:10.3762/bjnano.8.31

Received: 16 August 2016
Accepted: 29 December 2016
Published: 30 January 2017

This article is part of the Thematic Series "Self-assembly of nanostructures and nanomaterials II".

Guest Editor: I. Berbezier

Abstract

In this work, two natural dyes extracted from henna and mallow plants with a maximum absorbance at 665 nm were studied and used as sensitizers in the fabrication of dye-sensitized solar cells (DSSCs). Fourier transform infrared (FTIR) spectra of the extract revealed the presence of anchoring groups and coloring constituents. Two different structures were prepared by chemical bath deposition (CBD) using zinc oxide (ZnO) layers to obtain ZnO nanowall (NW) or nanorod (NR) layers employed as a thin film at the photoanode side of the DSSC. The ZnO layers were annealed at different temperatures under various gas sources. Indeed, the forming gas (FG) (N_2/H_2 95:5) was found to enhance the conductivity by a factor of 10^3 compared to nitrogen (N_2) or oxygen (O_2) annealing gas. The NR width varied between 40 and 100 nm and the length from 500 to 1000 nm, depending on the growth time. The obtained NWs had a length of 850 nm. The properties of the developed ZnO NW and NR layers with different thicknesses and their effect on the photovoltaic parameters were studied. An internal coverage of the ZnO NWs was also applied by the deposition of a thin TiO_2 layer by reactive sputtering to improve the cell performance. The application of this layer increased the overall short circuit current J_{sc} by seven times from 2.45×10^{-3} mA/cm^2 to 1.70×10^{-2} mA /cm^2.

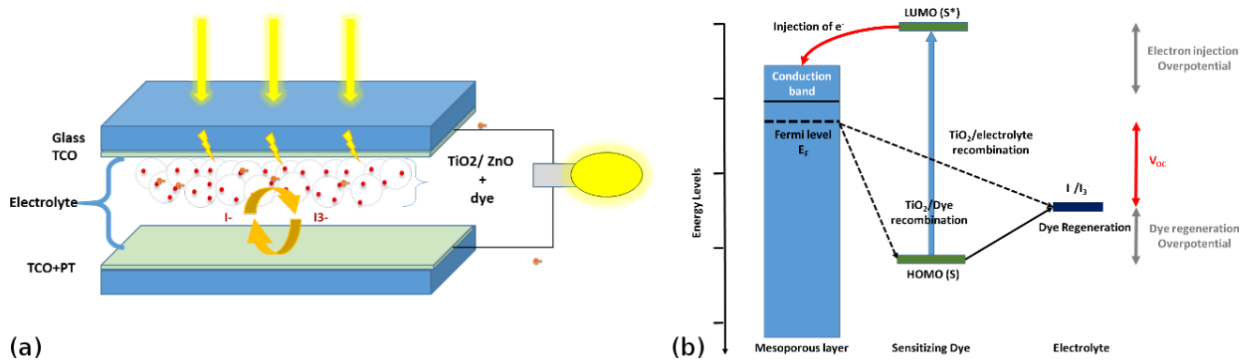

Figure 1: (a) Principle of operation and (b) energy level diagram of a typical DSSC.

Introduction

Energy demand has increased rapidly during the last forty years to reach a growth rate of 1.8% per year [1]. To satisfy this growing need, it is necessary to find new sources of renewable energy. For instance, photovoltaic (PV) technologies offer a promising green industry for the future power demand. Among these technological resources, dye-sensitized solar cells (DSSCs) have shown good performance since their first demonstration by O'Regan and Grätzel in 1991 [2]. Figure 1a shows the standard structure of DSSC: The first part of this structure represents the photoelectrode, composed of a wide band gap semiconductor thin layer coated on transparent conducting oxide (TCO) films. A mesoporous film layer is used as a semiconductor in the photoelectrode. Because of its stability and easy synthesis, titanium dioxide (TiO_2) is mostly used as the semiconductor in DSSCs [2-5]. Besides, the TiO_2 offers high electronic mobility for photogenerated electron collection, a suitable band gap, which adapts to the injection of the electrons of most studied dyes, and high surface area to enhance the dye loading by anchoring the dye [6,7].

Zinc oxide (ZnO) has been studied as a mesoporous wide band gap semiconductor for use in DSSCs. It presents itself in the form of different morphological nanostructures, such as nanorods, nanocrystals, nanowires, nanotubes and nanowalls that can be exploited to optimize the dye loading [6-9]. The main purpose of the photoelectrode is to collect the injected electrons from the excited dye absorbed by the semiconductor layer and to transport the electrons to the external load. The second main part of the structure is the counter electrode formed by a thin layer of platinum coated on TCO to accelerate the redox reaction with the electrolyte solution, which constitutes the third main part of the cell [3].

The internal process starts with the excitation of the sensitizer (S) through the absorption of a photon to obtain an excited sensitizer (S^*). The latter injects an electron into the conduction band of the semiconductor. Then, it stays in the oxidized state (S^+), as mentioned in Figure 1b. The injected electron reaches the external load through the semiconductor and the TCO layers. When arriving at the counter electrode, the electron reduces the redox solution and regenerates the sensitizer to complete the reaction [2,10]. Different high-raked commercial dyes, such as N719 or N3, have been widely studied in the literature and their performance has been proven. Because these organometallic dyes contain environmental pollutants, such as heavy metals [6], recent studies have focused on finding a metal-free organic dye with high performance [8,11-13]. Indeed, several studies were carried out using natural dyes, such as spinach and red turnip as a sensitizer. However, their efficiency is lower than that of commercial organometallic dyes. In this work, we investigate two different natural dyes extracted from henna and mallow plants. We discuss also their application to different semiconductor structures.

The photoelectrode is regarded as an important part in the DSSC where it represents the electron generator of the cell. Solar cell parameters, such as open-circuit voltage (V_{oc}), short-circuit current density (J_{sc}) and fill factor (FF), are the most significant parameters used to evaluate the enhancement of the power conversion efficiency (PCE) of solar cells [10]. The short circuit current density, J_{sc}, depends essentially on dye adsorption, the collection efficiency in the semiconductor thin layer film and the efficiency of the collected dye molecules [3,14,15]. The adsorption of the dye can be improved by various means, such as increasing the thickness and/or the porosity of the photoelectrode or by using organized structures, such as nanowalls or nanorods. The V_{oc} can be improved by modifying the energy difference between the Fermi level (E_F) of the semiconductor potential and redox potential (E_{redox}) of the electrolyte [10].

Results and Discussion

Dye analysis

In order to understand the structure of natural dye molecules and to determine the main elements responsible for absorbing light, we used FTIR spectroscopy techniques and ultraviolet–visible spectrophotometry (UV–vis) to characterize dyes extracted from henna and mallow powder as shown in Figure 2.

The scopoletin molecule, shown in Figure 3b [15-17], is the major component in the mallow dye. From the FTIR spectrum of the mallow dye (Figure 3a), it is clear that mallow has a primary O–H bond associated with the peak at 3372 cm^{-1}. We notice also the existence of aliphatic groups, CH_2 and CH_3 (2904 cm^{-1}, 2949 cm^{-1}, 2990 cm^{-1}), an ether function (ν_{C-O}) at 1055 cm^{-1}, and a regular deformation band δC_{sp2-H} at 668 cm^{-1}.

2-Hydroxy-1,4-napthaquinone ($C_{10}H_6O_3$), frequently called lawsone [15,18], is one of the constituents of the natural dye henna in addition to other compounds, such as gallic acid, sterols, resin, tannin and coumarins [19]. Lawsone (Figure 4b), the main component of henna extract, has been used as a dye in the cosmetics industry. The most significant feature of the lawsone molecule is its ability to absorb visible light between 400 and 600 nm.

The FTIR spectrum of henna extract, presented in Figure 4a, shows the existence of three valence bands associated with C=C aromatics at 1338 cm^{-1}, 1421 cm^{-1} and 1458 cm^{-1}, and also a stretching absorption band at 3368 cm^{-1} corresponding to the vibration of the associated O–H bond.

The UV–vis measurements of the extracted dyes of henna and mallow powders diluted in ethanol are given in Figure 5. Both of the studied dyes show two remarkable peaks: the first around 470 nm (blue light), and the second at 665 nm (red light). Both peaks correspond to the mixture of chlorophyll [20]. In the region from 525 nm to 625 nm, the mallow dye spectrum reveals two small peaks at 536 nm and 608 nm. These peaks could serve to increase the charge-transfer reaction under sun illumination in the final DSSC [21].

Figure 2: Photograph of mallow and henna powders.

Morphological results of the layers

In order to estimate the capacity of the dye loading, scanning electron microscopy (SEM) analysis was carried out to study the porosity and the morphology of the layers prepared by the CBD technique [8,22].

Figure 6a gives the SEM images illustrating the morphology of the ZnO NRs annealed in forming gas (FG) (N_2/H_2, 95:5). From this figure, we observe that nanorods cover the entire surface of the fluorine-doped tin oxide (FTO) conductive glass and

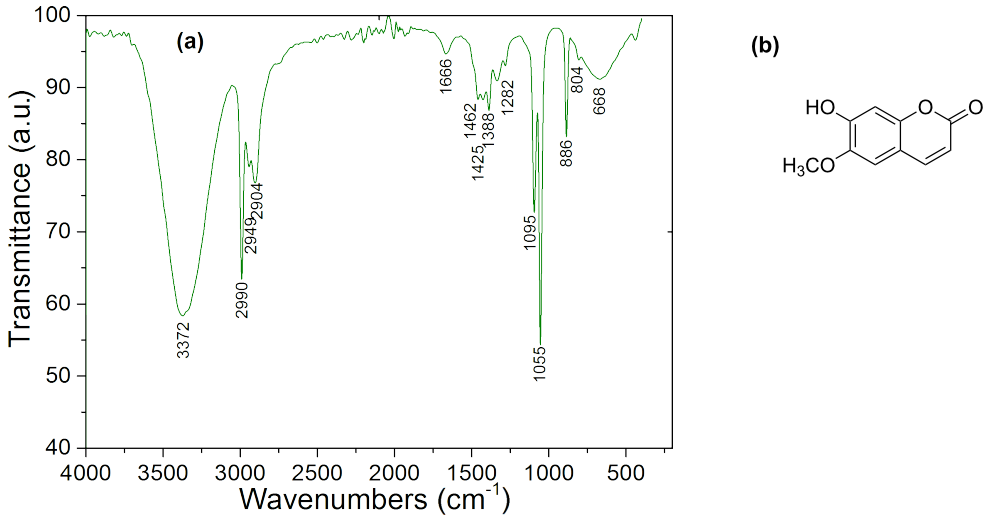

Figure 3: (a) FTIR spectrum of mallow. (b) Scopoletin molecule.

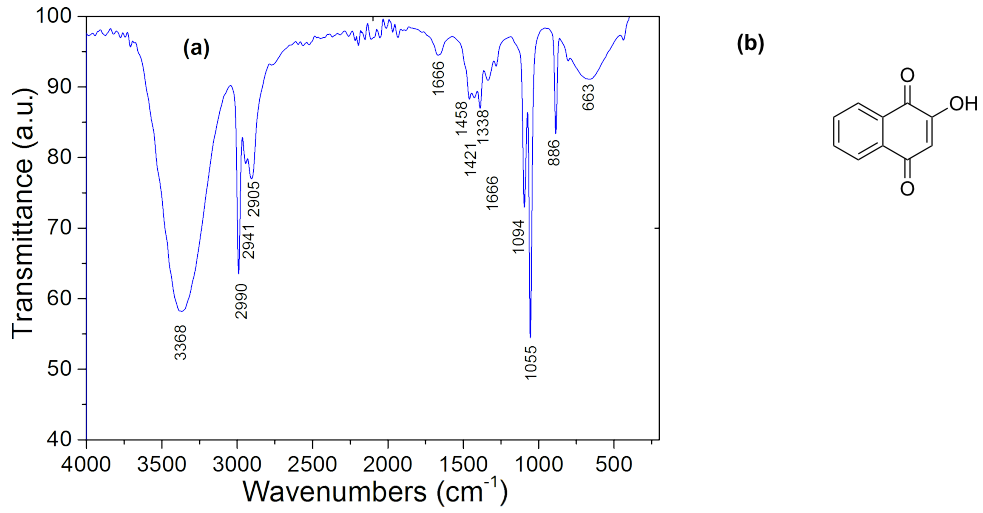

Figure 4: (a) FTIR spectrum of henna. (b) Lawsone molecule.

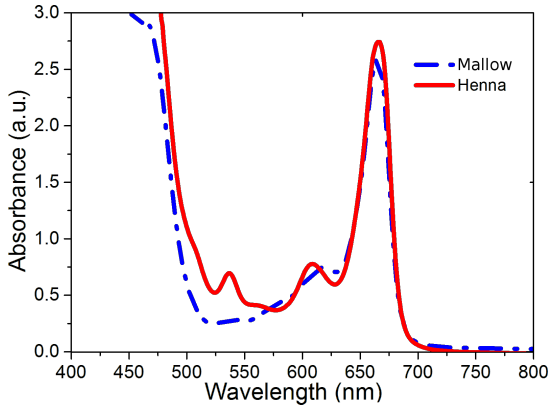

Figure 5: UV–vis measurements of henna and mallow dye solutions.

have a hexagonal shape with uniform size and length [23]. The width of the NRs varies between 40 and 100 nm, while their length ranges from 500 to 1000 nm, depending on growth time, as shown in Figure 6b and mentioned by Iwu et al. [8]. In Figure 6c and Figure 6d, we give the SEM images of the ZnO NR after being immersed in henna and mallow dye, respectively. The images show the formation of a thin layer between the NRs. This layering effect may be due to a reaction between the ZnO nanoparticles and the solvent in the dye solution. From these images, we notice that the number of individual hexagonal NRs is reduced and their shapes are no longer visible. This morphological change can be explained by aggregation of the dye and Zn^{2+} when the films were immersed in henna and mallow dye [24].

Figure 7a shows the morphology of the ZnO NWs annealed in FG. The NWs intersect at different angles, creating hollow spaces, acting to increase the porosity of the layer, which may improve the dye loading as observed by Polkoo et al. [25]. By analyzing the cross-section of the ZnO NWs, we obtained a NW vertical length of around 850 nm, as shown in Figure 7b. In Figure 7c, we give the images of the ZnO NWs after being immersed in mallow dye. We notice that dye molecules cover the NWs without affecting their overall shape, as compared to NRs. The formed layer does not appear clearly in the surface of the NWs. However, there is a small difference in the intersection angles between walls. After the immersion, Figure 7c shows less acute angles of wall intersections compared to those presented in Figure 7b. This variation in the angle sharpness shows that a thin layer is formed in the different intersections and not in the walls.

Figure 8a illustrates the magnified image of the ZnO NWs over which a TiO_2 layer was deposited by the sputtering technique. We observe that the nanowall vertical length is about 1000 nm. Besides, the shape is arranged in a more vertical orientation as compared to the nanowalls without the TiO_2 blocking layer. The main idea is to cover the ZnO NWs with a thin layer of TiO_2 (about 150 nm of thickness), which enhances the electron transport by exploiting the high mobility and diffusion rate of the ZnO. This covering layer also increases the efficient electron diffusion from the TiO_2 layer to the ZnO NWs. Using this structure, the electrons were quickly transported from the sensitizer to the ZnO through the TiO_2 to reach the FTO (Figure 8b). This solution created an energy barrier allowing the reduction of the charge recombination [26].

Optical characterization

Based on the SEM analysis, we conclude that the growth time can influence the layer thickness, which affects the light absorbance [9] and conductivity [27]. For these reasons, after the

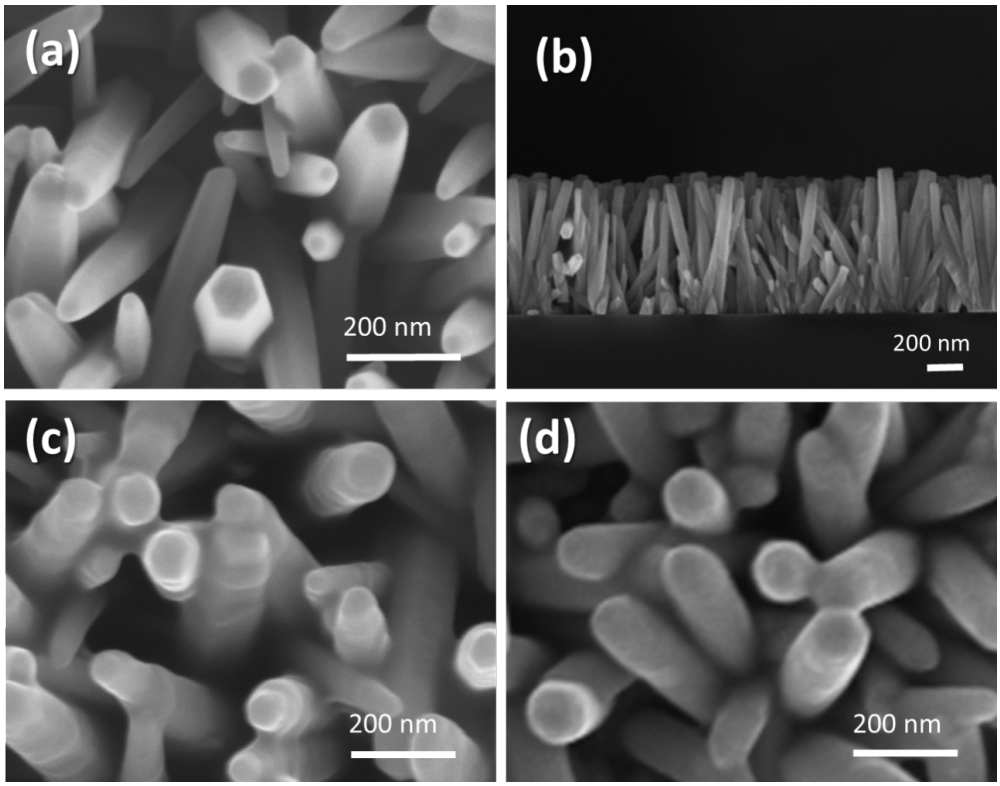

Figure 6: SEM images of ZnO NRs (a) before immersion in dye, (b) cross-section view of ZnO NRs, (c) after immersion in henna dye and (d) after immersion in mallow dye.

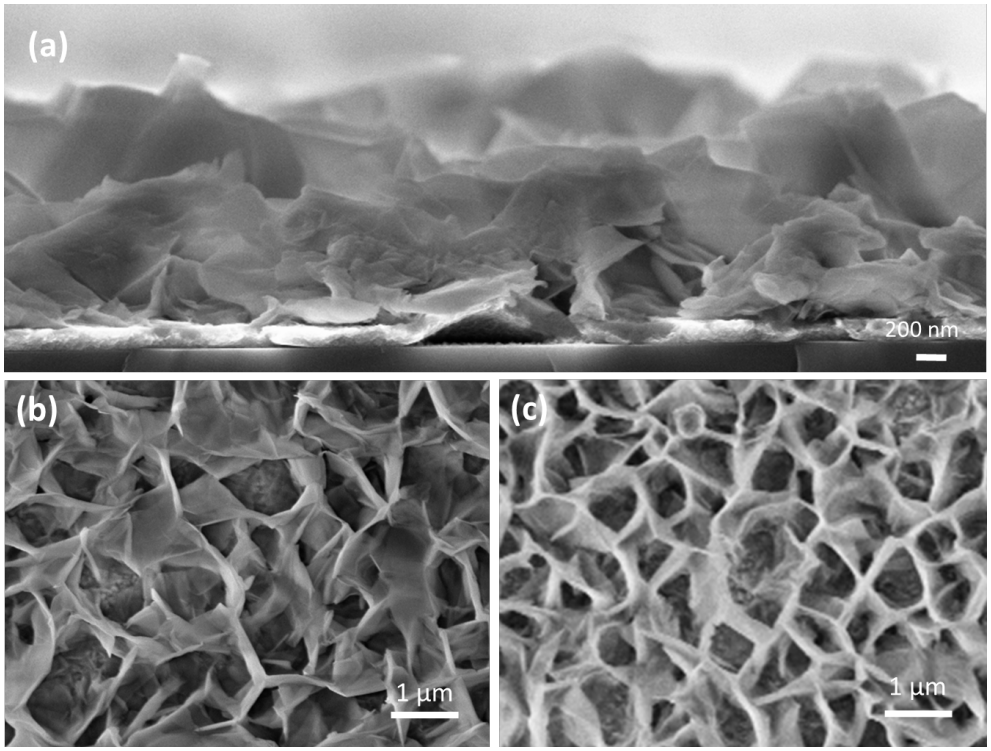

Figure 7: SEM images of ZnO NWs (a) cross-section view of ZnO NWs (b) before immersion in dye and (c) after immersion in mallow dye.

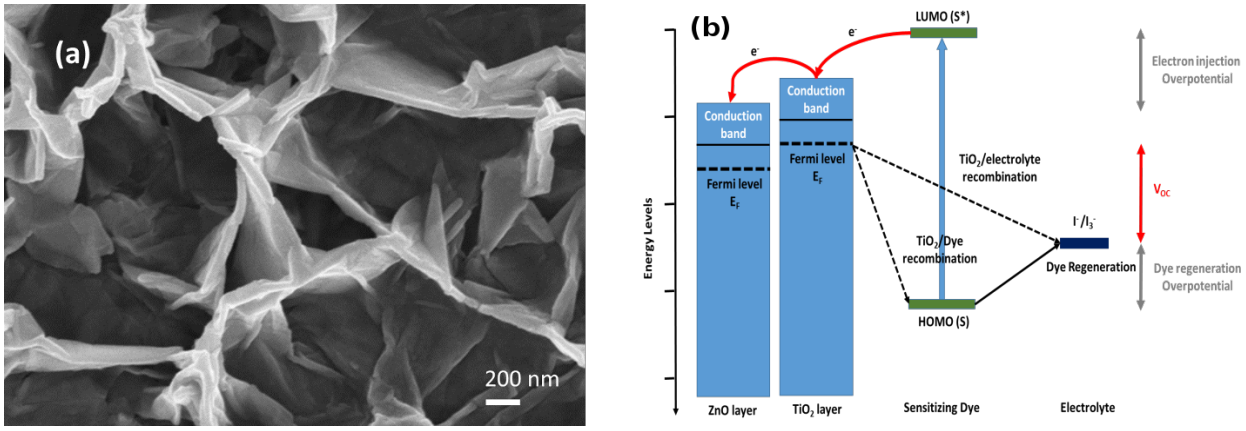

Figure 8: (a) SEM images of ZnO NWs after the deposition of the TiO_2 layer by sputtering. (b) Energy level diagram of a ZnO/TiO_2 DSSC.

growth of the ZnO NR layers on FTO, they were annealed in O_2, FG and N_2 gas at 300 °C.

As shown in Table 1, the sheet resistance of the ZnO NRs depends on the used annealing gas. By using O_2, we obtained the highest sheet resistance with a ratio of 10^3 compared to those prepared under N_2 or FG. The best sheet resistance was measured in the case of annealing in FG.

Figure 9 shows the ZnO NR layer absorbance in different conditions of the annealing gas and the growth time annealed at 200 °C. We see that the sample without annealing gas has the lowest absorbance, which implies the necessity of the annealing step. The sample, annealed in FG and grown for 45 minutes, has the highest absorbance in the region between 300 nm and 600 nm compared to those annealed in the same gas condition. However, the growth time influences the absorbance, which indicates that thin ZnO NR layers absorb more in this region.

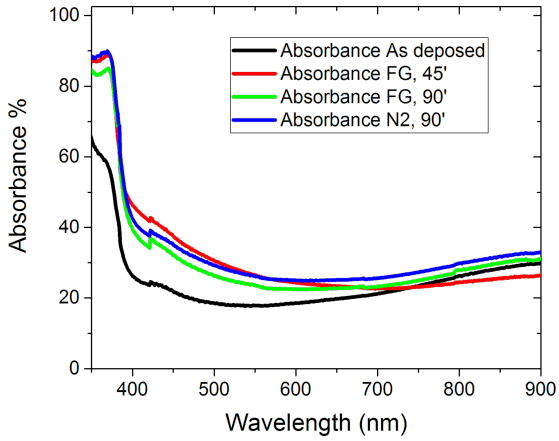

Figure 9: The ZnO NR absorbance measurements, as deposited in forming gas and in nitrogen for 45 minutes and 90 minutes growth time, annealed at 200 °C.

Table 1: Sheet resistance of ZnO layers for different ambient annealing gases and *J*–*V* measurement results of the assembled cells.

Cell N°	Dye	Photoanode layer	Annealing gas	Annealing temp. (°C)	Sheet resistance (Ω/sq)	Growth time (min)	J_{SC} (mA/cm^2)	V_{OC} (V)	FF (%)
1	henna	ZnO nanorods	FG	200	5.3×10^3	90	1.26×10^{-1}	0.370	27
2	mallow		FG			90	1.55×10^{-1}	0.425	27
3			FG			45	1.49×10^{-1}	0.428	29
4			N_2		90×10^3	90	5.35×10^{-2}	0.136	30
5			as deposited	–	600×10^3	90	4.24×10^{-2}	0.379	27
6			O_2	200	1.4×10^6	–	–	–	–
7		TiO_2 + ZnO nanowalls	FG	300	5.3×10^3	5	8.02×10^{-3}	0.426	34
8			FG	200			1.70×10^{-2}	0.380	26
9			as deposited	–	600×10^3		1.23×10^{-2}	0.413	29
10		ZnO nanowalls	FG	200	5.3×10^3		2.45×10^{-3}	0.169	29

The second UV–vis measurements were performed after the immersion of the ZnO NR layer in dye. Figure 10 demonstrates the absorbance spectra versus the variation in time and the concentration of mallow dye. The initial concentration is 3.25 g of mallow powder stirred in 40 mL of ethanol. By multiplying the concentration three times, we increase the loaded dye in the ZnO NR layer and we clearly observed the absorbance peak related to the collected dye in the photoanode side at 665 nm.

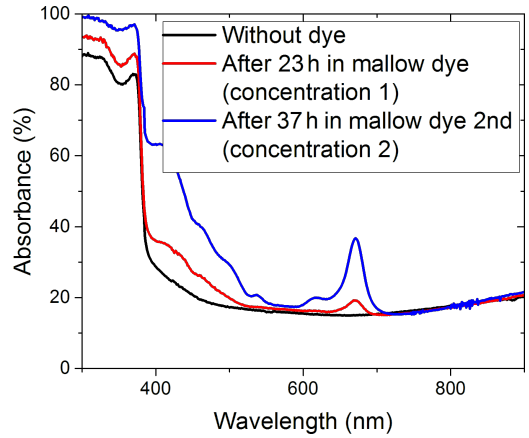

Figure 10: The ZnO NR absorbance measurements before and after immersion in dye for 23 h, in the first concentration, and after 37 h in the second concentration.

The prepared photoanode was assembled with a platinized counter electrode. The current–voltage (*I*–*V*) measurements were carried out using a Keithley 4200 device under AM1.5 conditions.

Figure 11a shows the *I*–*V* measurement response of the DSSC cells assembled with a ZnO NW layer on photoanodes annealed at different temperatures with two different structures formed by using only ZnO NWs in the photoanode and with applying a TiO_2 blocking layer deposited by sputtering (Table 1). The mallow dye was chosen because of its optimum absorbance in the visible region. The DSSC, based on NWs with a TiO_2 blocking layer annealed at 200 °C in FG, presents the highest V_{OC} compared to the NW cell without a blocking layer prepared under the same thermal conditions, where the V_{OC} increases from 0.169 to 0.380 V. This result verifies the main role of the blocking layer in decreasing the electron–hole recombination and the negative shift of the conduction band edge due to the increased electron density in TiO_2, as previously reported by Yao et al. [26].

We also noticed that the increase of the temperature treatment from 200 °C to 300 °C in FG maintains the same sheet resistance of the NW layer at 5.3 Ω/sq. However, the short circuit current density of the cell decreases from 1.70×10^{-2} mA/cm^2 to 8.02×10^{-3} mA/cm^2. This decrease can be explained by the fact that when increasing the annealing temperature, the stability of the ZnO nanoparticles was considerably affected, which resulted in higher reaction with the dye solution.

However, the DSSC assembled without an annealed photoanode side gave a slightly higher short circuit current and smaller variation of 5% in the FF as compared to the cell annealed at 300 °C using a TiO_2 blocking layer as shown in Figure 11. This increase can be explained by the high variation in the sheet resistance of the ZnO NWs in the photoanode side [28].

For the NR-based photoanode cells, we annealed using different gas sources. The forming gas provided the most conductive layers as compared to N_2 and O_2, as discussed above. More-

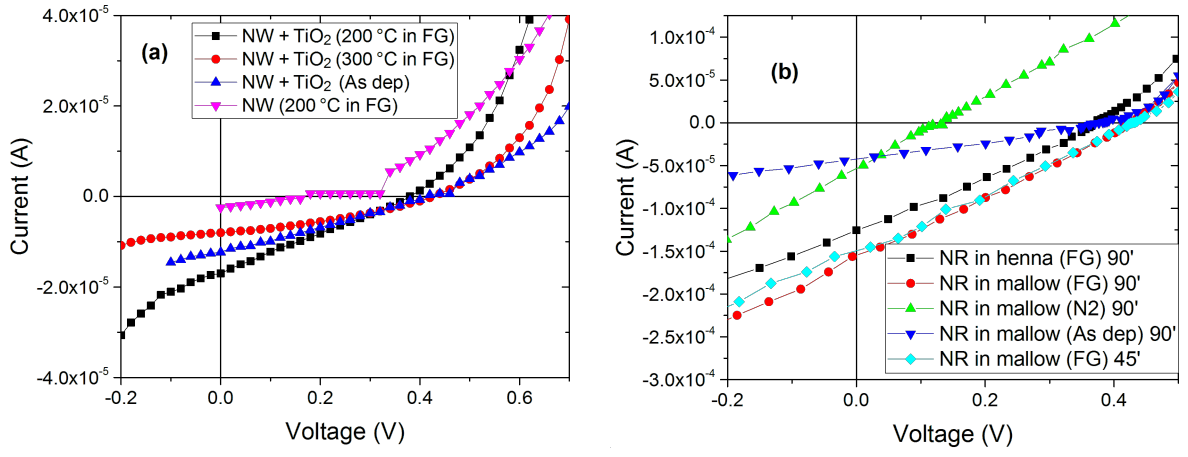

Figure 11: Current–voltage measurements (a) assembled cells with ZnO NWs as a layer in the photoanode side with and without a TiO_2 blocking layer annealed at 200 °C, 300 °C, and without annealing using different ambient gas conditions. (b) Assembled cells with NR layer grown in 90 minutes and 45 minutes, annealed in FG, N_2 and as deposited in 200 °C.

over, the sheet resistance increased from 5.3×10^3 Ω/sq, when annealing in FG, to 90×10^3 Ω/sq in N_2. It also increased considerably in O_2 to reach 1.4×10^3 Ω/sq due to the ZnO ionization, which decreased the volume of Zn interstitials, resulting in a decrease of the carrier concentration [29].

Therefore, by comparing the two used sensitizers, under the same thermal conditions (200 °C) and at the same growth time (90 minutes), we noticed that the electrical performance was almost identical and they have the same FF value equal to 27%. By changing the growth time from 90 to 45 minutes, the FF value rises slightly from 27% to 29%. This increase implies that the reduction in the length of NRs, caused by the decrease of growth time, augments the internal shunt resistance of the cell, resulting in a small decrease of the short circuit current, J_{sc}, from 0.155 mA/cm^2 to 0.149 mA/cm^2 and a small increase of V_{OC} from 0.425 to 0.428 V [30].

The efficiency of the ZnO NR- and NW-based DSSCs is lower than that of conventional DSSCs. The main reason for this difference in performance is related to the nature of the photosensitizer used in the present investigation.

Furthermore, the small thickness of the ZnO NRs and NWs can be a major reason for this degradation in the efficiency. However, the chemical reaction of the ZnO nanostructures when immersed in dye solution was carried out at the surface of the layer, resulting in Zn–dye complex aggregates affecting the electron injection efficiency [31].

Conclusion

In this work, we reported the fabrication and characterization of natural DSSCs with two different ZnO layer structures. We analyzed two natural dye sensitizers extracted from henna and mallow plants in different concentrations and at various immersion times. Furthermore, we analyzed the properties of the different used dyes and we reported the most anchoring-dominant molecules. By studying different gases used in the annealing process, we noted that the FG gave the most conductive layers compared to N_2 or O_2, which was confirmed in the photovoltaic parameters of the final cells. We also highlight the fact that the use of a TiO_2 blocking layer in the structure ZnO NW/TiO_2/dye increases the photovoltaic performance of the realized DSSC by enhancing the morphological and physical properties of the photoanode.

Experimental

Both ZnO NRs and NWs were grown on FTO substrates (1.5×1.5 cm^2) by CBD [8,22]. Before the ZnO NR preparation, a seed layer of ZnO crystallites was deposited by spin coating (1000 rpm, 60 s) using a solution of 5 mM zinc acetate dihydrate in ethanol, followed by 20 min annealing in air on a hot plate (at nominal 240 °C).

However, in the case of the ZnO NWs, the seed layer was replaced by an Al film (100 nm thick). The basic Al films were sonicated in soapy water, water, ethanol and acetone before being used. After the pre-layer deposition, we prepared the CBD bath [8,22] by mixing two solutions: a 100 mL solution of variable hexamethylenetetramine (HMTA) concentration in deionized (DI) water was well stirred and preheated at 90 °C. Then, it was added to a 100 mL solution of zinc nitrate hexahydrate in DI water.

The zinc nitrate concentration in the CBD bath was fixed at 25 mM both for ZnO NR and NW growth. The HMTA final concentration was set at 25 mM and 50 mM for three different growth times (45 min, 60 min and 90 min) in case of ZnO NRs. In the synthesis of NWs, the growth time was set to 5 min. The HMTA concentration was 25 mM. Moreover, 16 mM of ammonium hydroxide (NH_4F) was added to the synthetic solution since its presence enhanced the quality of the NWs [22].

The DSSC preparation started by covering an active area of 0.5×0.5 cm^2 TCO glass with a thin film ZnO layer (NRs, NWs, or TiO_2 on NWs). After the annealing step, the prepared film was submerged in a solution containing the natural dye. The used natural dyes were prepared using ethanol as the solvent. The electrode and the counter electrode were sealed with thermoplastic sealing film (Meltonix 1170-60PF from SOLARONIX), followed by injection of (Iodolyte AN-50) the electrolyte (SOLARONIX).

The used henna and mallow powders were prepared in-house by drying henna and mallow plants. Afterwards, the dried plants were milled and sieved to obtain the final powder.

Current–voltage characteristics and layer conductivity were measured using a computer-controlled Keithley 4200 instrument under standard conditions using a solar simulator based on a 150 W xenon lamp equipped with an ASTM-certified filter with a calibrated Si photodiode to produce the AM1.5 solar spectrum.

For the FTIR measurements, we used a Nicolet 560 FTIR spectrometer with a measurement region varying between 400 and 4000 cm^{-1} with suitable scan resolution of 2 cm^{-1}. The UV–vis measurements were studied by means of a UV–vis Lambda 40 spectrophotometer with an integrating sphere. The study of the structural properties of ZnO NWs and NRs was performed using scanning electron microscopy (Gemini field emission SEM, Carl Zeiss SUPRATM 25).

References

1. Nejat, P.; Jomehzadeh, F.; Taheri, M. M.; Gohari, M.; Majid, M. Z. A. *Renewable Sustainable Energy Rev.* **2015,** *43,* 843–862. doi:10.1016/j.rser.2014.11.066
2. O'Reagan, B.; Grätzel, M. A. *Nature* **1991,** *353,* 737–740. doi:10.1038/353737a0
3. Sutthana, S.; Wongratanaphisan, D.; Gardchareon, A.; Phadungdhitidhada, S.; Ruankham, P.; Choopun, S. *Energy Procedia* **2015,** *79,* 1021–1026. doi:10.1016/j.egypro.2015.11.603
4. Marimuthu, T.; Anandhan, N.; Thangamuthu, R.; Mummoorthi, M.; Ravi, G. *J. Alloys Compd.* **2016,** *677,* 211–218. doi:10.1016/j.jallcom.2016.03.219
5. Alberti, A.; Pellegrino, G.; Condorelli, G. G.; Bongiorno, C.; Morita, S.; La Magna, A.; Miyasaka, T. *J. Phys. Chem. C* **2014,** *118,* 6576–6585. doi:10.1021/jp411811q
6. Narayan, M. R. *Renewable Sustainable Energy Rev.* **2012,** *16,* 208–215. doi:10.1016/j.rser.2011.07.148
7. Shahzad, N.; Risplendi, F.; Pugliese, D.; Bianco, S.; Sacco, A.; Lamberti, A.; Gazia, R.; Tresso, E.; Cicero, E. *J. Phys. Chem. C* **2013,** *117,* 22778–22783. doi:10.1021/jp406824f
8. Iwu, K. O.; Strano, V.; Di Mauro, A.; Impellizzeri, G.; Mirabella, S. *Cryst. Growth Des.* **2015,** *15,* 4206–4212. doi:10.1021/acs.cgd.5b00216
9. Strano, V.; Smecca, E.; Depauw, V.; Trompoukis, C.; Alberti, A.; Reitano, R.; Crupi, I.; Gordon, I.; Mirabella, S. *Appl. Phys. Lett.* **2015,** *106,* 013901. doi:10.1063/1.4905389
10. Sutthana, S.; Wongratanaphisan, D.; Gardchareon, A.; Phadungdhitidhada, S.; Ruankham, P.; Choopun, S. *Energy Procedia* **2015,** *79,* 102–1026. doi:10.1016/j.egypro.2015.11.603
11. Choi, H.; Raabe, I.; Kim, D.; Teocoli, F.; Kim, C.; Song, K.; Yum, J.-H.; Ko, J.; Nazeeruddin, M. K.; Grätzel, M. *Chem. – Eur. J.* **2010,** *16,* 1193–1201. doi:10.1002/chem.200902197
12. Hunbae, I.; Sukwon, K.; Chanmoo, P.; Seok-Hoon, J.; Chang-Ju, K.; Kyungkon, K.; Nam-Gyu, P.; Chulhee, K. *Chem. Commun.* **2010,** *46,* 1335–1337. doi:10.1039/b917065k
13. Cai, N.; Moon, S.-J.; Cevey-Ha, L.; Moehl, T.; Humphry-Baker, R.; Wang, P.; Zakeeruddin, S. M.; Grätzel, M. *Nano Lett.* **2011,** *11,* 1452–1456. doi:10.1021/nl104034e
14. Barea, E. M.; Bisquert, J. *Langmuir* **2013,** *29,* 8773–8781. doi:10.1021/la401419n
15. Chang, W.-C.; Tang, B.-H.; Lu, Y.-W.; Yu, W.-C.; Lin, L.-Y.; Wu, R.-J. *J. Power Sources* **2016,** *319,* 131–138. doi:10.1016/j.jpowsour.2016.04.055
16. Torchani, A.; Saadaoui, S.; Gharbi, R.; Fathallah, M. *Curr. Appl. Phys.* **2015,** *15,* 307–312. doi:10.1016/j.cap.2015.01.003
17. Darmawan, A.; Kosela, S.; Kardono, L. B. S.; Syah, Y. M. *J. Appl. Pharm. Sci.* **2012,** *2,* 175–177.
18. Tanihaha, S. I.; Uranus, H. P.; Darma, J. Fabrication and Characterization of Dye-Sensitized Solar Cell Using Blackberry Dye and Titanium Dioxide Nanocrystals. In *Proceedings of the Second International Conference on Advances in Computing, Control and Telecommunication Technologies (ACT),* Dec 2–3, 2010; 2010; pp 60–63. doi:10.1109/ACT.2010.46
19. Hamdy, A.; El-Gendy, N. S. *Egypt. J. Pet.* **2013,** *22,* 17–25. doi:10.1016/j.ejpe.2012.06.002
20. Lichtenthaler, H. K.; Buschmann, C. Extraction of Phtosynthetic Tissues: Chlorophylls and Carotenoids. *Current Protocols in Food Analytical Chemistry;* 2001; UNIT F4.2. doi:10.1002/0471142913.faf0402s01
21. Chang, H.; Wu, H. M.; Chen, T. L.; Huang, K. D.; Jwo, C. S.; Lo, Y. J. *J. Alloys Compd.* **2010,** *495,* 606–610. doi:10.1016/j.jallcom.2009.10.057
22. Strano, V.; Urso, R. G.; Scuderi, M.; Iwu, K. O.; Simone, F.; Ciliberto, E.; Spinella, C.; Mirabella, S. *J. Phys. Chem. C* **2014,** *118,* 28189–28195. doi:10.1021/jp507496a
23. Chung, J.; Lee, J.; Lim, S. *Physica B* **2010,** *405,* 2593–2598. doi:10.1016/j.physb.2010.03.041
24. Tammy, P. C.; Qifeng, Z.; Guozhong, C. *J. Phys. Chem. C* **2007,** *111,* 18804–18811. doi:10.1021/jp076724f
25. Polkoo, S. S.; Saievar-Iranizad, E.; Bayatloo, E. *Appl. Phys. A* **2015,** *119,* 1269–1276. doi:10.1007/s00339-015-9091-6
26. Yao, J.; Lin, C.-M.; Yin, S.; Ruffin, P.; Brantley, C.; Edwards, E. *J. Photonics Energy* **2015,** *5,* 053088. doi:10.1117/1.JPE.5.053088
27. Kushwaha, A.; Aslam, M. *J. Appl. Phys.* **2012,** *112,* 054316. doi:10.1063/1.4749808
28. Guo, T.; Chen, Y.; Liu, L.; Cheng, Y.; Zhang, X.; Li, Q.; Wei, M.; Ma, B. *J. Power Sources* **2012,** *201,* 408–412. doi:10.1016/j.jpowsour.2011.10.114
29. Kang, H. S.; Kang, J. S.; Pang, S. S.; Shim, E. S.; Lee, S. Y. *Mater. Sci. Eng., B* **2003,** *102,* 313–316. doi:10.1016/S0921-5107(02)00730-4
30. Zi, M.; Zhu, M.; Chen, L.; Wei, H.; Yang, X.; Cao, B. *Ceram. Int.* **2014,** *40,* 7965–7970. doi:10.1016/j.ceramint.2013.12.146
31. Kim, J.-H.; Kim, K.-W.; Cho, K.-S.; Ryu, K.-K. *Mater. Technol. (Abingdon, U. K.)* **2012,** *27,* 18–20. doi:10.1179/175355511X13240279339527

License and Terms

BEILSTEIN JOURNAL OF NANOTECHNOLOGY

In-situ monitoring by Raman spectroscopy of the thermal doping of graphene and MoS_2 in O_2-controlled atmosphere

Aurora Piazza[1,2,3], Filippo Giannazzo[1], Gianpiero Buscarino[2], Gabriele Fisichella[1], Antonino La Magna[1], Fabrizio Roccaforte[1], Marco Cannas[2], Franco Mario Gelardi[2] and Simonpietro Agnello[*2,4]

Full Research Paper

Open Access

Address:
[1]CNR-IMM, Strada VIII, 5, Zona Industriale, 95123 Catania, Italy, [2]Department of Physics and Chemistry, University of Palermo, Via Archirafi 36 - Palermo, 90123, Italy, [3]Department of Physics and Astronomy, University of Catania, Via Santa Sofia 64 - Catania, 95123, Italy and [4]AteN Center, Universita'di Palermo, Viale delle Scienze, Ed.18 - Palermo, 90128, Italy

Email:
Simonpietro Agnello[*] - simonpietro.agnello@unipa.it

* Corresponding author

Keywords:
two-dimensional (2D) materials; graphene; MoS_2; Raman spectroscopy; thermal doping

Beilstein J. Nanotechnol. **2017,** *8,* 418–424.
doi:10.3762/bjnano.8.44

Received: 15 September 2016
Accepted: 24 January 2017
Published: 10 February 2017

This article is part of the Thematic Series "Self-assembly of nanostructures and nanomaterials II".

Guest Editor: I. Berbezier

Abstract

The effects of temperature and atmosphere (air and O_2) on the doping of monolayers of graphene (Gr) on SiO_2 and Si substrates, and on the doping of MoS_2 multilayer flakes transferred on the same substrates have been investigated. The investigations were carried out by in situ micro-Raman spectroscopy during thermal treatments up to 430 °C, and by atomic force microscopy (AFM). The spectral positions of the G and 2D Raman bands of Gr undergo only minor changes during treatment, while their amplitude and full width at half maximum (FWHM) vary as a function of the temperature and the used atmosphere. The thermal treatments in oxygen atmosphere show, in addition to a thermal effect, an effect attributable to a p-type doping through oxygen. The thermal broadening of the line shape, found during thermal treatments by in situ Raman measurements, can be related to thermal phonon effects. The absence of a band shift results from the balance between a red shift due to thermal effects and a blue shift induced by doping. This shows the potential of in situ measurements to follow the doping kinetics. The treatment of MoS_2 in O_2 has evidenced a progressive erosion of the flakes without relevant spectral changes in their central zone during in situ measurements. The formation of MoO_3 on the edges of the flakes is observed indicative of the oxygen-activated transformation.

Introduction

A wide interest for two-dimensional (2D) materials has grown in recent years [1]. Graphene (Gr) is a 2D carbon material with zero-energy band gap and turned out to be relevant because of its electrical, transport and optical properties. It is considered the lead example of the emerging 2D solids [2-4]. For example, optical transparency and bipolar charge carrier availability of Gr

paved the way for studies and applications in many fields of materials science and technology including optics, electronics, and photovoltaics [5,6]. In these contexts, different growth processes optimized to obtain large area-samples, comprising epitaxial growth on silicon carbide [7,8] and chemical vapor deposition (CVD) on catalytic metals [9,10] followed by the poly(methyl methacrylate) (PMMA) assisted transfer [11,12], enlarged the interest and perspectives for applications.

In particular in view of the realization of electronic devices and to obtain Gr-based field effect transistors, one demanding physical feature of Gr connected to the energy levels distribution is the removal of the zero energy gap between valence and conduction states to enable a more efficient current modulation in the devices on/off states [13]. Furthermore, the need to control the charge carrier density and the energy of the Fermi level evidenced that doping of graphene is an important aspect for electronic devices. The possibility to obtain stable p- or n-type doping in order to modulate the Gr sheet resistance for specific electronic and optoelectronic applications is mandatory for technical application such as thin flexible circuits and interconnecting transparent conductive electrodes for solar cells and/or touch screens [6]. Among the possible dopants for Gr, an easily accessible and promising one is oxygen. It acts as a p-type dopant and can also be activated by thermal treatments [13,14]. Nevertheless, thermal activation has the drawback that it could induce relevant changes to the Gr structure because of the high annealing temperatures or reactions with ambient gas molecules [13-19]. We have recently shown [19] that p-type doping of Gr can be induced by thermal treatment in oxygen at temperatures below 400 °C. It has also been shown that the effect of doping is sensitive to the ambient atmosphere. In particular, water molecules affect the doping stability [20,21].

Alongside Gr, the transition metal dichalcogenide MoS_2 is one of the stable 2D materials of interest [1]. Especially the possibility to produce van der Waals heterostructures combining Gr and MoS_2, is pushing the study of this subject [1]. Indeed, the non-zero band gap, good chemical sensitivity and photo response of MoS_2 pave the way for its application in optoelectronics, sensing and photovoltaic devices [22-24]. In this context, the possibility to tune the properties of MoS_2 and to evaluate the thermal effects in the case of heterostructures are of interest [25,26]. As recently shown, the possibility to obtain doping by treatment in controlled atmosphere, accurately studied through Raman spectroscopy, could be useful for a future application of this material [25,27,28]. In fact, the A_{1g} Raman mode band at about 403 cm^{-1} undergoes a red shift and line width widening after n-type doping, and a blue shift and a line width shrinking after p-type doping, allowing for a spectroscopic control of the doping level [25,27].

In this paper, in order to clarify the dynamics of doping and the role of atmosphere during thermal treatment as well as to check the material stability, we investigated the effects of temperature and atmosphere by in situ Raman measurements during thermal treatment in air or in O_2 gas on samples of Gr produced by CVD on copper foil and successively transferred on a SiO_2 substrate on Si. Analogous studies were carried out on MoS_2 transferred on the same substrate to evaluate the features and doping effectiveness of thermal processes similar to those used for Gr.

Results and Discussion

To evaluate the quality of the studied Gr samples AFM and micro-Raman measurements have been carried out. A typical result is reported in Figure 1 for the as-transferred Gr.

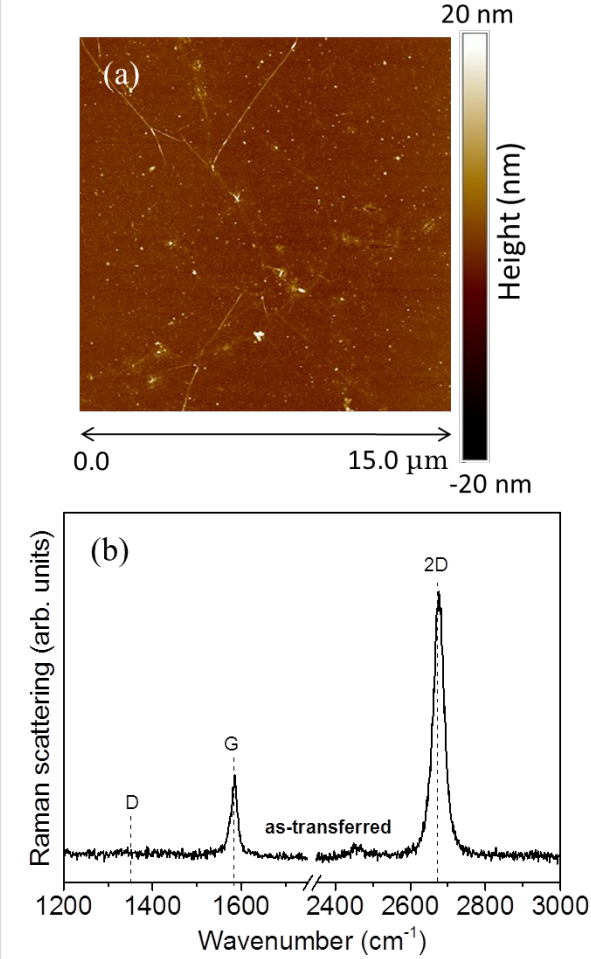

Figure 1: (a) AFM morphology image and (b) micro-Raman spectra of the as transferred graphene on SiO_2 substrate on Si.

The AFM measurements (Figure 1a) show that Gr features islands of dimensions larger than 10 µm without any superimposed particles from the transfer process. The micro-Raman measurements show the typical bands associated with Gr

centered at (2677 ± 1) cm^{-1} and at (1585 ± 1) cm^{-1} (Figure 1b). They are attributed to the 2D and G bands, respectively. No signal of the D band at about 1350 cm^{-1} is found. The amplitude ratio I_{2D}/I_G of the 2D and G bands is 3.2, and a full width at half maximum (FWHM) of the 2D band of (35 ± 1) cm^{-1} was determined. On the basis of AFM and the micro-Raman measurements it can be concluded that the studied samples are monolayer Gr with a low number of defects [29,30].

To evaluate the effects of temperature and to follow the changes in the Raman spectrum during thermal treatments, we made two experiments with in situ measurements. The first experiment, reported in Figure 2, was carried out in air varying the temperature from 100 to 300 °C in 50 °C steps and maintaining each single temperature for 30 min during which Raman measurements were made every 5 min.

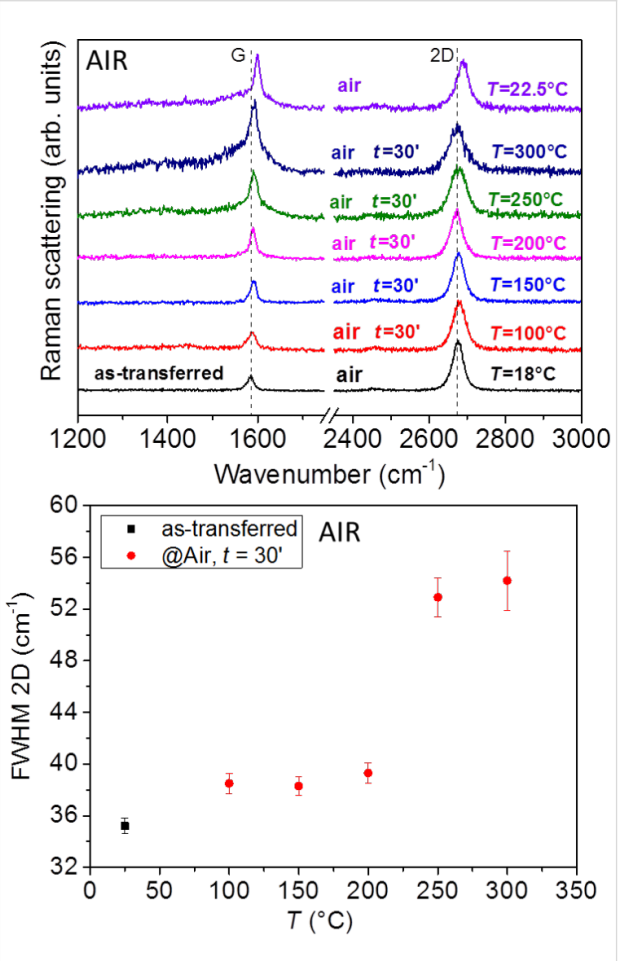

Figure 2: (Top) Comparison of the in situ Raman spectra of a Gr sample as transferred and subsequently treated in air, the temperature varies from 100 to 300 °C. The reported time is the elapsed time from the treatment beginning at the given temperature, the top spectrum is acquired after decreasing the temperature. Spectra have been arbitrarily vertically shifted for clearness. (Bottom) Measured FWHM of the 2D band as a function of the temperature.

In Figure 2 we can see a clear increase in the FWHM of the 2D band with increasing temperature, which is attributable to thermal effects [31]. In detail, the FWHM features a constant increased value between 100 and 200 °C, and a further increase at 250 °C. The value returns to that of the as-transferred sample after cooling to sample to room temperature. There is no evident shift of the 2D band peak position, and only a small blue shift of the G band. Furthermore, we found the appearance of a shoulder at low wavenumbers near the G band above 200 °C. In addition, beginning at 150 °C we observed a change in the amplitude ratio of the 2D and G bands, I_{2D}/I_G, with a tendency to decrease. After cooling the sample to room temperature (top spectrum in Figure 2) there is a permanent blue shift of the G (13 cm^{-1}) band and of the 2D (13 cm^{-1}) band, and a decrease of their ratio from 3.4 down to 1.4 (the latter value has been evaluated subtracting a linear tangent to the G band bottom to take into account the shoulder and background induced by thermal treatments above 200 °C). The observed blue shift can be attributed to the doping by molecular oxygen present in the air atmosphere [19,21].

The second experiment with in situ measurements was made by thermal treatment in 2 bar of oxygen atmosphere at 300 °C for up to one hour and, successively, at 350 °C for an additional hour. This choice was determined by the above reported temperature value inducing major observable spectral changes and by the previously reported study about the doping effects as a function of temperature in similar samples, showing a larger effectiveness of doping at these temperatures [19].

As shown in Figure 3, also in this case we see the thermal effect with a larger increase in the FWHM of the 2D band compared to that observed in the air, without a shift. Again a decrease of the I_{2D}/I_G bands amplitude ratio down to 1.1 is observed. Also in this case, after cooling the sample to room temperature (top spectrum in Figure 3) a blue shift of the G and 2D bands (of 20.5 and 18 cm^{-1}, respectively) is detected. The FWHM of the latter band returns to be like that recorded for the as-transferred sample. Compared to the sample treated in air, we note a greater shift of the G and 2D bands, indicating an additional doping effect induced by the exposure to pure oxygen [18,19].

These findings are compatible with those reported in our previous work [20], were a blue shift of both the G and 2D bands of 19 and 14 cm^{-1}, respectively, was found. The differences to the treatment carried out in air could be partially due to the presence of other molecules in the atmosphere as can be deduced by the experiments carried out previously in similar systems [20]. Furthermore, on returning to room temperature we observed an increase of the I_{2D}/I_G ratio probably caused by the high temperature that could induce the deterioration of

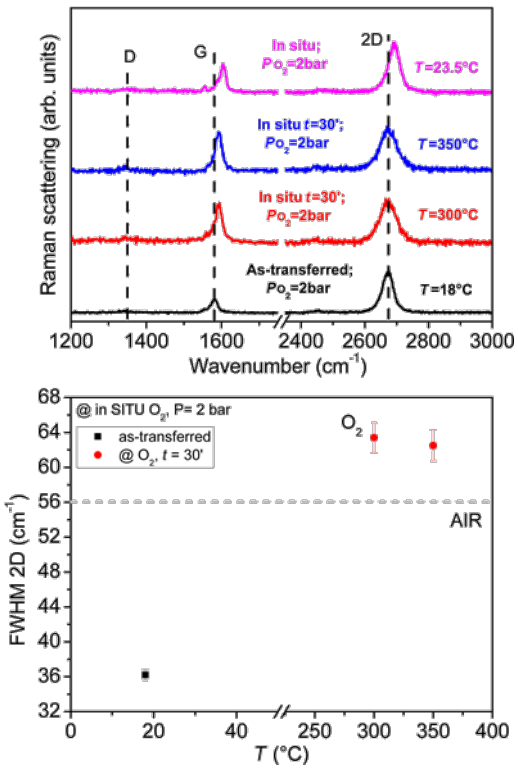

Figure 3: (Top) Comparison of the in situ Raman spectra of a Gr sample as transferred and subsequently treated in O_2, at a pressure of 2 bar and at temperatures of 300 and 350 °C. The reported time is the elapsed time from the treatment beginning at the given temperature. Spectra have been arbitrarily vertically shifted for clearness. (Bottom) Trend of the FWHM of the 2D band as a function of the temperature. The dashed line indicates the maximum value of the FWHM of the 2D band obtained by the treatment in air (see Figure 2).

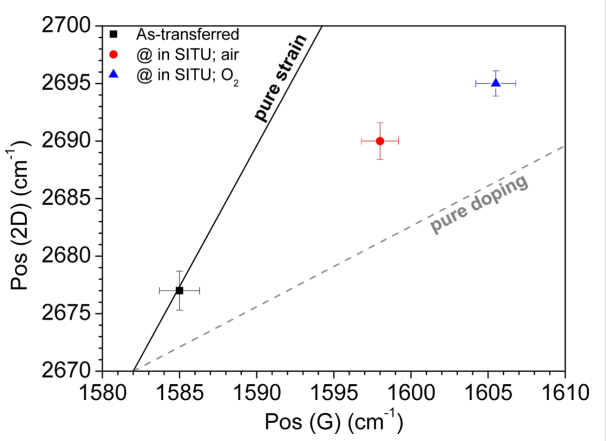

Figure 4: Correlation map of the 2D and G peak positions measured at room temperature in the Gr/SiO_2/Si samples as transferred and thermally treated selectively in air and in O_2. The full line marks the stress limit and the dashed line the doping limit as reported in [30].

graphene. In fact, in a previous work [19] it was shown that at 350 °C a removal of the edges of Gr flakes occurs, thereby suggesting that a strong structural change can be induced by this temperature.

Similarly to what is found in the literature [30], we report in Figure 4 a map of the 2D band position as a function of the G band position to evidence doping and stress effects. As shown in the figure, the sample that has undergone a treatment in oxygen is closer to the line of doping than to the strain line, obtained by a Raman spectrometer with 2.33 eV laser excitation. This supports the conclusion that p-type doping was obtained by treatment in O_2. Furthermore, a comparison with previous results [21] reporting the effects of thermal treatments in a similar temperature range evidence that the effectiveness of doping found in the present work can be mainly attributed to the presence of oxygen molecules in the treatment atmosphere. Indeed, using other gases (N_2, CO_2, vacuum) gives points in a map analogous to the one in Figure 4 more confined to the "pure strain" line.

It has been recently reported that a temperature increase induces a red shift both of G and 2D bands as well as line broadening and the appearance of a shoulder in the G band due to thermal strain [31]. These features are compatible to the results reported here. In particular, the absence of a blue shift during in situ measurements and exposure to oxygen can be interpreted as a competition between a temperature-induced red shift and a doping-induced blue shift. This effect needs to be further investigated to be fully clarified and to disentangle mechanical and doping effects, for example by changing the gas composition during thermal treatments.

To investigate the effects of a similar oxygen treatment on MoS_2, a sample has been treated in O_2 atmosphere at 2 bar in the temperature range of 300–430 °C in a Linkam cell. In this temperature range doping should be effective for few layers as recently reported in literature [25]. An increase of temperature in steps of 10 °C was applied from 300 up to 390 °C and, at each step, the sample was maintained at the selected temperature for 10 min and Raman measurements were collected every minute. Afterward the sample temperature was increased up to 400 °C for 30 min, collecting Raman spectra. As reported in Figure 5, the Raman spectrum of the native sample features the typical bands of bulk MoS_2 associated to the E^1_{2g} and A_{1g} modes at 383 and 409 cm^{-1}, respectively. This shows that the applied exfoliation process produced multilayer flakes. For all the investigated temperatures, the treatments give no detectable changes in the Raman band features. In particular we did not observe the appearance of the bands at 158, 285 and 820 cm^{-1} associated to MoO_3, which is expected as side product of the oxygen thermally induced doping of MoS_2 [25]. Nevertheless, during these treatments, we observed by microscope a gradual

size reduction of the flakes. A further increase of temperature up to 430 °C had the same effects as lower temperatures.

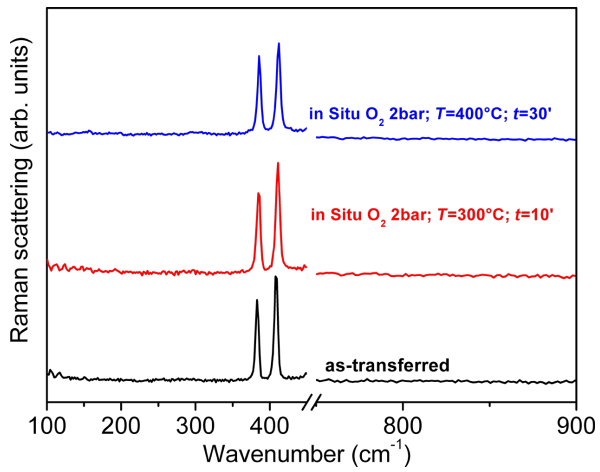

Figure 5: In situ Raman spectra of MoS_2 before thermal treatments (bottom), after thermal treatment in O_2 at 300 °C (middle) and 400 °C (top). Spectra are vertically shifted for the sake of comparison.

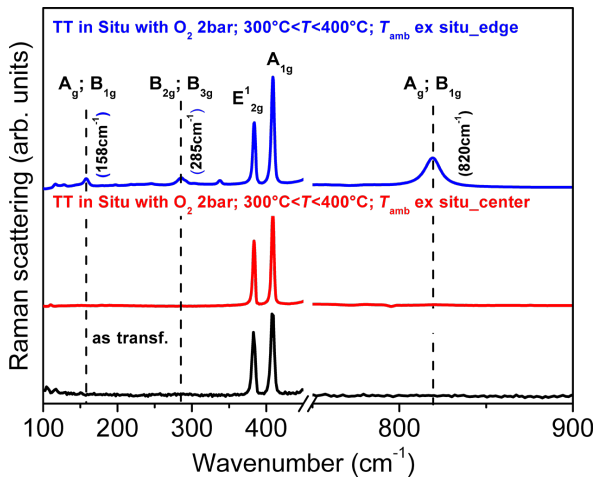

Figure 7: Ex situ Raman spectra of MoS_2 before thermal treatment (bottom line), after thermal treatment in O_2 at T < 430°C in the center of a flake (middle) and on the edge of a flake (top). Spectra are vertically shifted for the sake of comparison.

As shown in Figure 6, we noticed a decrease of optical contrast in optical microscope measurements between the center of the MoS_2 flakes and their edges, the latter appearing darker. To go deeper into this aspect we carried out AFM measurements and, as shown in Figure 6, we found that the edges of the flakes are thinner, suggesting the presence of a smaller number of layers.

By carrying out Raman measurements ex situ (Figure 7), we found that the edges of the flakes have a different spectrum. In particular, the bands attributed to MoO_3 at the spectral positions 158, 285 and 820 cm^{-1} are now clearly seen. This finding suggests that the observed erosion of the flakes is driven by the formation of oxidized regions at the borders of the MoS_2 flakes that gradually convert them to MoO_3, before completely destroying them. Similar effects have been suggested for other transition metal dichalcogenides and show that the thermal processes could be driven by analogous reactions [32]. In particular, these effects are of relevance for the application of 2D materials in ambient environments where the temperature could be increased during their use. Finally, the possibility that doping of central parts of the flakes occurred during the treatments cannot be excluded. But in order to obtain more information further in situ measurements with higher spectral resolution, which are able to detect shift or broadening of MoS_2 Raman bands, are necessary.

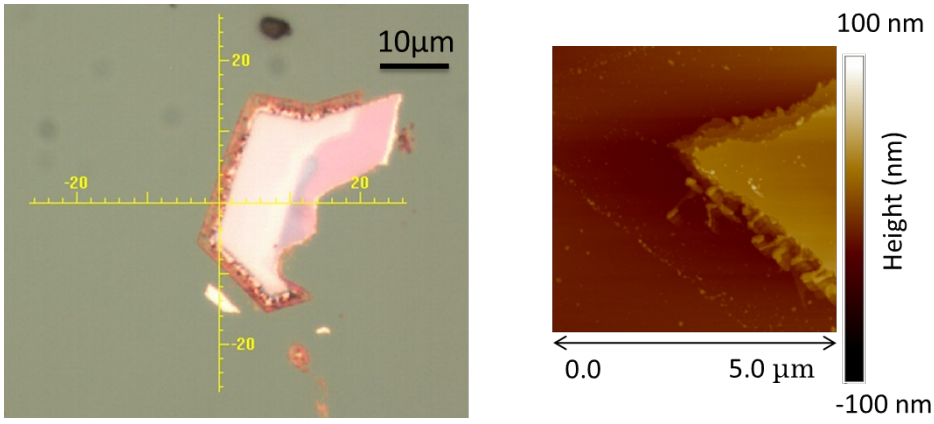

Figure 6: MoS_2 flake after the thermal treatment up to 430 °C in O_2; optical microscopy (left) and AFM (right) images.

Conclusion

The experiments here reported on Gr samples transferred on SiO_2 substrates have shown the possibility to monitor by in situ Raman measurements the effects of temperature and doping during thermal treatment in controlled atmosphere (air and oxygen). This study evidenced the competition in the Raman spectral changes between the thermal and the doping effects. In particular, the temperature increase induces a clear line broadening of the 2D band and masks the doping-induced shift of the G and 2D bands. At variance, doping effects can be monitored online through the change in the amplitude ratio of the G and 2D bands. Similar in situ measurements carried out to monitor O_2-doping of MoS_2 on SiO_2 substrates have shown that the flakes produced by exfoliation are progressively destroyed at $T > 300$ °C through the generation of MoO_3 on their edges, while mainly unchanged MoS_2 remains in the central part.

Experimental

The used samples are monolayer Gr and mechanically exfoliated MoS_2 deposited on SiO_2. The Gr samples were produced by chemical vapor deposition process on a Cu foil [11,19]. After Gr growth the foils were covered by PMMA and Cu was removed in a $FeCl_3$ bath. Successively, a transfer process on a 300 nm thick SiO_2 layer on Si following a well-established procedure has been carried out [11,19]. Micro-Raman measurements were carried out with a Horiba LabRam HR-Evolution spectrometer equipped with a 532 nm excitation laser. Raman measurements were carried out in situ, i.e., during thermal treatment, with the sample inserted inside a Linkam THMS600PS cell with temperature and pressure control, at a nominal laser output power of 25 mW and spectrometer spectral resolution of 7 cm^{-1} (600 lines per mm) to speed up acquisition time, after verifying that these parameters do not affect the Gr Raman signal. During the measurements the temperature was fixed up to 350 °C and the pressure up to 2 bar, when oxygen was used. The cell was purged twice at higher pressure to remove ambient atmosphere before sealing it and increasing the temperature. A heating ramp of 100 °C/min was selected, whereas cooling to room temperature was obtained within 25 min. Heating and cooling were executed in controlled atmosphere.

MoS_2 samples were obtained by mechanical exfoliation of bulk natural molybdenite crystals, obtained from SPI (http://www.2spi.com). The exfoliation was based on thermal release tape and thermocompression printing on a SiO_2 (300 nm) layer on Si substrate of the same kind used for Gr [11]. Flakes of lateral size larger than 10 μm, and thickness ranging from 10 to 100 nm were typically obtained by this procedure. In situ Raman measurements and thermal treatment up to 430 °C were carried out with the same equipment used for Gr. Furthermore, additional ex situ Raman measurements were carried out only on MoS_2 with a Bruker Senterra micro-Raman spectrometer, with excitation at 532 nm, 5 mW output power and 9 cm^{-1} maximum spectral resolution (400 lines per mm).

Atomic force microscopy (AFM) measurements in air were executed by a Veeco DI3100 atomic force microscope with Nanoscope V controller working in tapping mode and employing a commercial silicon probe with spring constants of $k = 20–80$ $N \cdot m^{-1}$ and oscillation frequencies from 332 to 375 kHz.

Acknowledgements

The authors would like to thank people of the LAMP group (http://www.unipa.it/lamp/) at the Department of Physics and Chemistry of University of Palermo, and P. Fiorenza and R. Lo Nigro of CNR-IMM, Catania, for useful discussions and comments. The Raman spectroscopy CHAB laboratories at ATeN Center are acknowledged for the Linkam equipment use (http://www.chab.center/home, Med-CHHAB, PONa3_00273, University of Palermo).

References

1. Geim, A. K.; Grigorieva, I. V. *Nature* **2013,** *499,* 419–425. doi:10.1038/nature12385
2. Nair, R. R.; Blake, P.; Grigorenko, A. N.; Novoselov, K. S.; Booth, T. J.; Stauber, T.; Peres, N. M. R.; Geim, A. K. *Science* **2008,** *320,* 1308. doi:10.1126/science.1156965
3. Bao, Q.; Zhang, H.; Wang, Y.; Ni, Z.; Yan, Y.; Shen, Z. X.; Loh, K. P.; Tang, D. Y. *Adv. Funct. Mater.* **2009,** *19,* 3077–3083. doi:10.1002/adfm.200901007
4. Xing, G.; Guo, H.; Zhang, X.; Sum, T. C.; Huan, C. H. A. *Opt. Express* **2010,** *18,* 4564–4573. doi:10.1364/OE.18.004564
5. Bae, S.; Kim, H.; Lee, Y.; Xu, X.; Park, J.-S.; Zheng, Y.; Balakrishnan, J.; Lei, T.; Kim, H. R.; Song, Y., II; Kim, Y.-J.; Kim, K. S.; Özyilmaz, B.; Ahn, J.-H.; Hong, B. H.; Iijima, S. *Nat. Nanotechnol.* **2010,** *5,* 574–578. doi:10.1038/nnano.2010.132
6. Casaluci, S.; Gemmi, M.; Pellegrini, V.; Di Carlo, A.; Bonaccorso, F. *Nanoscale* **2016,** *8,* 5368–5378. doi:10.1039/C5NR07971C
7. Berger, C.; Song, Z.; Li, X.; Wu, X.; Brown, N.; Naud, C.; Mayou, D.; Li, T.; Hass, J.; Marchenkov, A. N.; Conrad, E. H.; First, P. N.; de Heer, W. A. *Science* **2006,** *312,* 1191–1196. doi:10.1126/science.1125925
8. Sonde, S.; Giannazzo, F.; Vecchio, C.; Yakimova, R.; Rimini, E.; Raineri, V. *Appl. Phys. Lett.* **2010,** *97,* 132101. doi:10.1063/1.3489942
9. Reina, A.; Jia, X.; Ho, J.; Nezich, D.; Son, H.; Bulovic, V.; Dresselhaus, M. S.; Kong, J. *Nano Lett.* **2009,** *9,* 30–35. doi:10.1021/nl801827v
10. Li, X.; Cai, W.; An, J.; Kim, S.; Nah, J.; Yang, D.; Piner, R.; Velamakanni, A.; Jung, I.; Tutuc, E.; Banerjee, S. K.; Colombo, L.; Ruoff, R. S. *Science* **2009,** *324,* 1312–1314. doi:10.1126/science.1171245
11. Fisichella, G.; Di Franco, S.; Roccaforte, F.; Ravesi, S.; Giannazzo, F. *Appl. Phys. Lett.* **2014,** *104,* 233105. doi:10.1063/1.4882165
12. Pirkle, A.; Chan, J.; Venugopal, A.; Hinojos, D.; Magnuson, C. W.; McDonnell, S.; Colombo, L.; Vogel, E. M.; Ru-off, R. S.; Wallace, R. M. *Appl. Phys. Lett.* **2011,** *99,* 122108. doi:10.1063/1.3643444

13. Liu, H.; Liu, Y.; Zhu, D. *J. Mater. Chem.* **2011,** *21,* 3335–3345. doi:10.1039/C0JM02922J
14. Ryu, S.; Liu, L.; Berciaud, S.; Yu, Y.-J.; Liu, H.; Kim, P.; Flynn, G. W.; Brus, L. E. *Nano Lett.* **2010,** *10,* 4944–4951. doi:10.1021/nl1029607
15. Yamada, Y.; Murota, K.; Fujita, R.; Kim, J.; Watanabe, A.; Nakamura, M.; Sato, S.; Hata, K.; Ercius, P.; Ciston, J.; Song, C. Y.; Kim, K.; Regan, W.; Gannett, W.; Zettl, A. *J. Am. Chem. Soc.* **2014,** *136,* 2232–2235. doi:10.1021/ja4117268
16. Mehmood, F.; Pachter, R.; Lu, W.; Boeckl, J. J. *J. Phys. Chem. C* **2013,** *117,* 10366–10374. doi:10.1021/jp312159v
17. Liu, L.; Ryu, S.; Tomasik, M. R.; Stolyarova, E.; Jung, N.; Hybertsen, M. S.; Steigerwald, M. L.; Brus, L. E.; Flynn, G. W. *Nano Lett.* **2008,** *8,* 1965–1970. doi:10.1021/nl0808684
18. Das, A.; Pisana, S.; Chakraborty, B.; Piscanec, S.; Saha, S. K.; Waghmare, U. V.; Novoselov, K. S.; Krishnamurthy, H. R.; Geim, A. K.; Ferrari, A. C.; Sood, A. K. *Nat. Nanotechnol.* **2008,** *3,* 210–215. doi:10.1038/nnano.2008.67
19. Piazza, A.; Giannazzo, F.; Buscarino, G.; Fisichella, G.; La Magna, A.; Roccaforte, F.; Cannas, M.; Gelardi, F. M.; Agnello, S. *J. Phys. Chem. C* **2015,** *119,* 22718–22723. doi:10.1021/acs.jpcc.5b07301
20. Piazza, A.; Giannazzo, F.; Buscarino, G.; Fisichella, G.; La Magna, A.; Roccaforte, F.; Cannas, M.; Gelardi, F. M.; Agnello, S. *Phys. Status Solidi A* **2016,** *213,* 2341–2344. doi:10.1002/pssa.201532909
21. Piazza, A.; Giannazzo, F.; Buscarino, G.; Fisichella, G.; La Magna, A.; Roccaforte, F.; Cannas, M.; Gelardi, F. M.; Pignataro, B.; Scopelliti, M.; Agnello, S. *Carbon* **2016,** *107,* 696–704. doi:10.1016/j.carbon.2016.06.077
22. Matte, H. S. S. R.; Gomathi, A.; Manna, A. K.; Late, D. J.; Datta, R.; Pati, S. K.; Rao, C. N. R. *Angew. Chem.* **2010,** *122,* 4153–4156. doi:10.1002/ange.201000009
23. Radisavljevic, B.; Radenovic, A.; Brivio, J.; Giacometti, V.; Kis, A. *Nat. Nanotechnol.* **2011,** *6,* 147–150. doi:10.1038/nnano.2010.279
24. Guo, Y.; Wei, X.; Shu, J.; Liu, B.; Yin, J.; Guan, C.; Han, Y.; Gao, S.; Chen, Q. *Appl. Phys. Lett.* **2015,** *106,* 103109. doi:10.1063/1.4914968
25. Yamamoto, M.; Einstein, T. L.; Fuhrer, M. S.; Cullen, W. G. *J. Phys. Chem. C* **2013,** *117,* 25643–25649. doi:10.1021/jp410893e
26. Zhou, H.; Yu, F.; Liu, Y.; Zou, X.; Cong, C.; Qiu, C.; Yu, T.; Yan, Z.; Shen, X.; Sun, L.; Yakobson, B. I.; Tour, J. M. *Nano Res.* **2013,** *6,* 703–711. doi:10.1007/s12274-013-0346-2
27. Chakraborty, B.; Bera, A.; Muthu, D. V. S.; Bhowmick, S.; Waghmare, U. V.; Sood, A. K. *Phys. Rev. B* **2012,** *85,* 161403(R). doi:10.1103/PhysRevB.85.161403
28. Islam, M. R.; Kang, N.; Bhanu, U.; Paudel, H. P.; Erementchouk, M.; Tetard, L.; Leuenberger, M. N.; Khondaker, S. I. *Nanoscale* **2014,** *6,* 10033–10039. doi:10.1039/C4NR02142H
29. Ferrari, A. C.; Meyer, J. C.; Scardaci, V.; Casiraghi, C.; Lazzeri, M.; Mauri, F.; Piscanec, S.; Jiang, D.; Novoselov, K. S.; Roth, S.; Geim, A. K. *Phys. Rev. Lett.* **2006,** *97,* 187401. doi:10.1103/PhysRevLett.97.187401
30. Verhagen, T. G. A.; Drogowska, K.; Kalbac, M.; Vejpravova, J. *Phys. Rev. B* **2015,** *92,* 125437. doi:10.1103/PhysRevB.92.125437
31. Tian, S.; Yang, Y.; Liu, Z.; Wang, C.; Pan, R.; Gu, C.; Li, J. *Carbon* **2016,** *104,* 27–32. doi:10.1016/j.carbon.2016.03.046
32. Liu, Y.; Tan, C.; Chou, H.; Nayak, A.; Wu, D.; Ghosh, R.; Chang, H.-Y.; Hao, Y.; Wang, X.; Kim, J.-S.; Piner, R.; Ruoff, R. S.; Akinwande, D.; Lai, K. *Nano Lett.* **2015,** *15,* 4979–4984. doi:10.1021/acs.nanolett.5b02069

License and Terms

BEILSTEIN JOURNAL OF NANOTECHNOLOGY

Fabrication of black-gold coatings by glancing angle deposition with sputtering

Alan Vitrey[1], Rafael Alvarez[2], Alberto Palmero[2], María Ujué González[1] and José Miguel García-Martín[*1]

Full Research Paper

Open Access

Address:
[1]IMM-Instituto de Microelectronica de Madrid (CNM-CSIC), Isaac Newton 8, Tres Cantos 28760, Madrid, Spain and [2]Instituto de Ciencia de Materiales de Sevilla (CSIC-US), Americo Vespucio 49, Seville 41092, Spain

Email:
José Miguel García-Martín[*] - josemiguel.garcia.martin@csic.es

* Corresponding author

Keywords:
black coatings; black metals; glancing angle deposition; light absorption; sputtering

Beilstein J. Nanotechnol. **2017,** *8,* 434–439.
doi:10.3762/bjnano.8.46

Received: 29 July 2016
Accepted: 25 January 2017
Published: 14 February 2017

This article is part of the Thematic Series "Self-assembly of nanostructures and nanomaterials II".

Guest Editor: I. Berbezier

Abstract

The fabrication of black-gold coatings using sputtering is reported here. Glancing angle deposition with a rotating substrate is needed to obtain vertical nanostructures. Enhanced light absorption is obtained in the samples prepared in the ballistic regime with high tilt angles. Under these conditions the diameter distribution of the nanostructures is centered at about 60 nm and the standard deviation is large enough to obtain black-metal behavior in the visible range.

Introduction

Black-metal coatings are metallic coatings that exhibit a high absorption in a certain region of the electromagnetic spectra. They are of interest in a wide range of applications [1-7] such as radiative heat exchangers, solar energy absorbers, electrodes of photovoltaic cells, separators to avoid cross effects in optical devices, thermal light emitters and electrodes of sensor or biosensors. In particular, gold is frequently used due to its high resistance to oxidation. As the spectrum of the solar radiation exhibits maximum irradiance in the visible range, finding a suitable method to produce black-metal coatings in the visible range is of the utmost importance for some of the abovementioned applications that require conducting behavior.

Physical vapor deposition (PVD) techniques are used to manufacture high-purity thin-film coatings in an environmentally friendly manner (no chemicals are involved, therefore no recycling problems are associated) onto any kind of substrates (e.g., conductor/isolator, flexible/rigid). By employing glancing angle deposition (GLAD), nanostructured coatings can be produced onto flat substrates, taking advantage of atomic shadowing effects. Although the nanostructures fabricated with evaporation methods (such as thermal evaporation or electron-beam evaporation) exhibit very well defined shapes and impressive homogeneity due to their almost punctual material sources, they cannot be scaled-up to mass production.

Consequently, from an industrial point of view, sputtering is the best choice.

From the pioneering work of GLAD sputtering [8], the importance of "low-pressure, long-throw" deposition was stated, i.e., a collimated flux of sputtered atoms was needed to obtain nanostructure formation. In the last few years, we have followed a systematic approach to study the growth regimes [9-11] and the deposition rate [12] of the nanostructured coatings prepared by GLAD sputtering, pinpointing the role of the ballistic atoms (i.e., those that preserve their directionality when they travel from the source to the substrate) to achieve such effect. In this new work, we report the fabrication of black-gold coatings in the visible range via GLAD sputtering by rotating the substrate during the deposition. It will be shown that we have achieved over 85% of absorption between 400 nm and 700 nm when silicon substrates are used.

Experimental

The fabrication of the nanostructured coatings has been carried out at room temperature in an UHV chamber (base pressure in the range of 10^{-9} mbar) using a magnetron source from AJA with a gold target (3.8 cm diameter). Argon was the sputter gas and the pressure during the deposition was 1.5×10^{-3} mbar, which was the lowest value that allowed for maintaining a stable plasma and for warranting that the deposition took place in the ballistic regime. The target-to-substrate distance was 19 cm, the substrate rotated at 3.6 rpm and the power and the deposition time were kept constant at 100 W and 1800 s, respectively. Two different monocrystalline substrates have been used: opaque Si(001) and transparent MgO(001). The tilt angle, σ, was varied from 75 to 87°. A scheme of the set-up is depicted in Figure 1. For the sake of comparison, continuous thin films were also fabricated using the standard configuration with the substrate being parallel to the target, i.e., σ = 0°, the same power (100 W) and the equivalent deposition time to get the same amount of material per area as in the GLAD configuration.

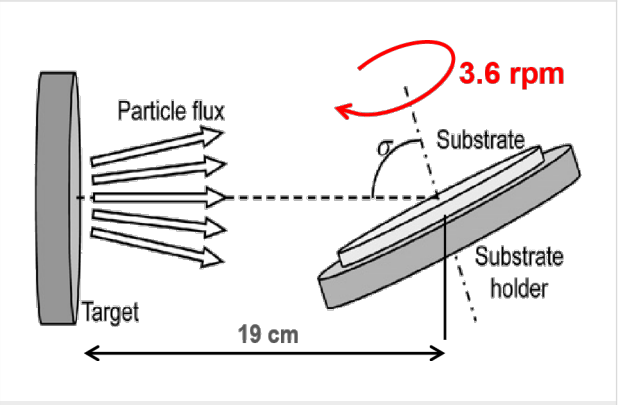

Figure 1: Scheme of the sputtering process with glancing angle deposition and rotating substrate.

The morphological characterization has been obtained by field emission scanning electron microscopy (FESEM), on a Hitachi equipment working at 5 kV, and atomic force microscopy (AFM), on a Dimension Icon microscope from Bruker with super-sharp tips (radius about 3 nm) to minimize the inherent convolution with the shape of the probe.

In order to study the optical behavior, spectral reflectance and transmittance measurements have been performed using unpolarized light with almost normal incidence in the VIS–nIR range and an Andor Shamrock spectrometer.

Results and Discussion

Figure 2a shows a photograph of two samples prepared onto Si(001) substrates with 1 cm^2 area: the one on the left was prepared with σ = 87° and exhibits black color, whereas that on the right was prepared with 75° tilt and shows golden color. These samples present different morphologies, as it is shown in Figure 2b and Figure 2c with AFM and FESEM images, respectively. As a result of the shadowing mechanism at the nanoscale induced by the ballistic regime (due to the low pressure used) and the high-tilt configuration (σ > 70°), instead of continuous thin films, nanostructures are formed. Due to the substrate rotation during the glancing angle deposition, these nanostructures display axial symmetry, with the axis in the vertical direction. It can be seen that, on average, the black 87° sample has shorter nanostructures than the golden 75° one: the highest nanostructures on the former sample are about 130 nm height, whilst those on the latter reach 260 nm. Moreover, with a careful inspection it can also be seen that the height distribution of the nanostructures obtained at σ = 87° is wider than the height distribution of those obtained at σ = 75°.

Furthermore, from the top-view SEM images the diameter size distribution can be obtained, and it is plotted in Figure 3a. The samples prepared with σ = 75° and σ = 80°, both exhibiting golden color, have wide distributions with a plateau shape and a significant number of nanostructures with diameters above 130 nm. On clear contrast, the samples prepared with σ = 85° and 87°, both black, have narrower distributions, with a well-defined peak corresponding to 70 nm and 60 nm diameter, respectively. Figure 3b shows the dependence of the areal density of nanostructures on the tilt angle, also deduced from the SEM images. When the tilt angle increases, the number of nanostructures per area also increases. Summarizing the information obtained from Figure 2 and Figure 3, high tilt angles produce more nanostructures, with narrower lateral size distribution and with a strongly non-uniform height distribution. On the contrary, low

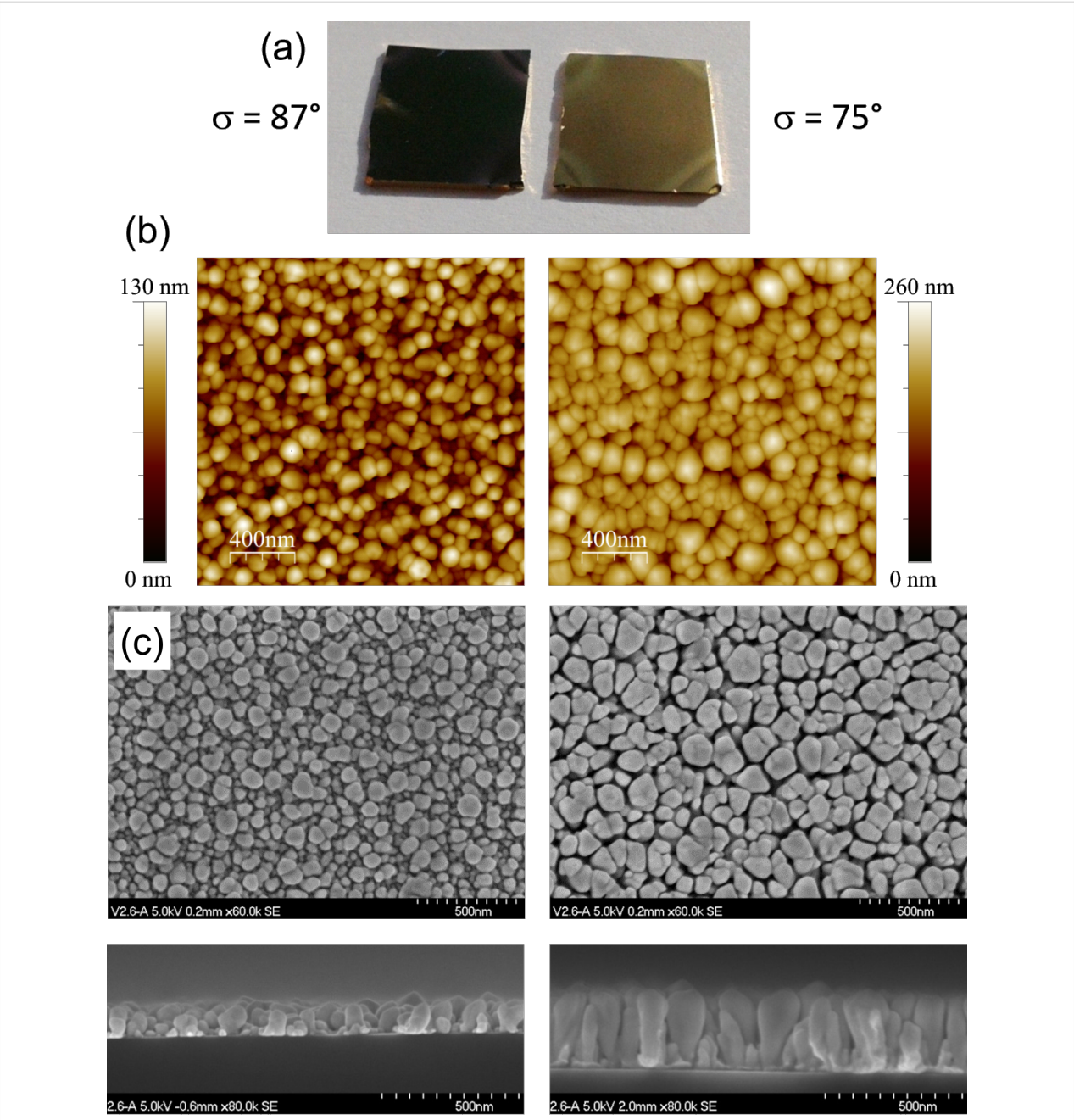

Figure 2: (a) Photograph, (b) AFM images, and (c) SEM images (upper row: top view, lower row: fracture cross section) of two Au samples prepared onto Si substrates with σ = 87° (left column) and σ = 75° (right column).

tilt angles generate less nanostructures, with wider lateral size distribution and more uniform in height.

These important differences in the morphology of the samples are responsible for their different appearance shown in Figure 2 and their distinctive spectral behavior presented in Figure 4, where the reflectance of the samples with black and golden color is plotted. For the sake of comparison, the calculated reflectance of a bare Si substrate and that of a sample with a continuous Au layer with 47 nm thickness (obtained with the deposition time that provides the equivalent material per area as in the case of GLAD deposition) are also included (the dielectric constants for Si and Au in the calculations were taken from [13] and [14], respectively). The most significant fact in Figure 4a is that the nanostructured samples deposited at high tilt angle exhibit low reflectance in the visible range (400–700 nm), less than 10% for the sample prepared with σ = 87° and less than 15% for that prepared with σ = 85°. Taking into account that the

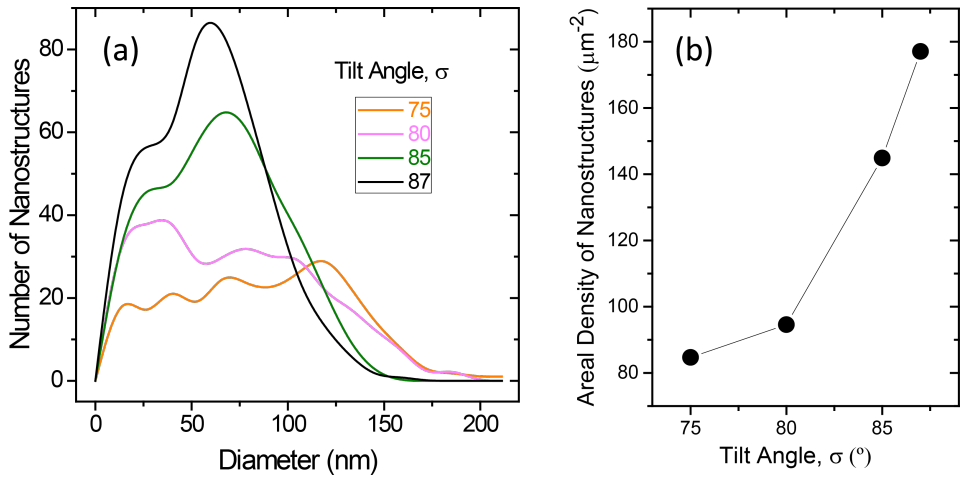

Figure 3: (a) Diameter distribution obtained from top-view SEM images for the Au samples prepared onto Si substrates with different tilt angles. (b) Areal density of nanostructures of the same samples.

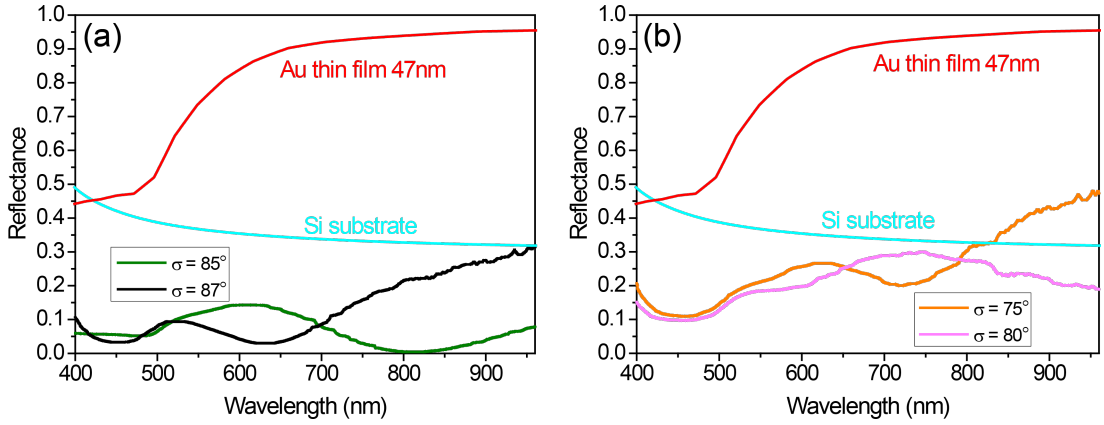

Figure 4: Reflectance spectra of nanostructured Au samples exhibiting black color (a) and golden color (b). For the sake of comparison, the calculated spectra of a bare Si substrate (cyan) and a continuous Au thin film (red) have been also included.

optical properties of gold nanostructures are dominated by the existence of localized surface plasmon resonances (LSPRs), and that these LSPRs induce enhanced scattering, it is reasonable to assume that such low reflectance is due to the combined effect of the LSPRs and the light trapping associated with multiple scattering that arises when those nanostructures are closely packed forming a non-periodic, non-uniformly sized array [15,16]. In particular, the high number of nanostructures and their broad height distribution favors multiple scattering processes, improving light trapping and increasing absorption, therefore resulting in a uniform low reflectivity and the black color appearance. On the other hand, the reduced number of nanostructures exhibited by the samples prepared with σ = 75° and 80°, together with their broader lateral size distribution and their height uniformity, do not provide such an efficient light trapping (Figure 4b). It can be seen that the reflectance values shown by these samples are not as low as those obtained in the samples prepared with 87° and 85° tilt angle. Finally, the only common feature for all the nanostructured samples and the continuous film is a decrease in the reflectance at wavelengths below 500 nm, which is due to an interband transition in gold [17] and it is responsible of the golden color of continuous and bulk gold. The values of this decrease are, however, quite different. The values are very small for the high tilt angle deposition samples, which therefore present a uniform low reflectivity in the visible range and look black. But they are more noticeable in the samples with σ = 75° and 80°, which then preserve the golden color, although dull because of the reduced reflectivity.

The black-metal behavior has been also obtained with transparent substrates. Having in mind a future scalability of the

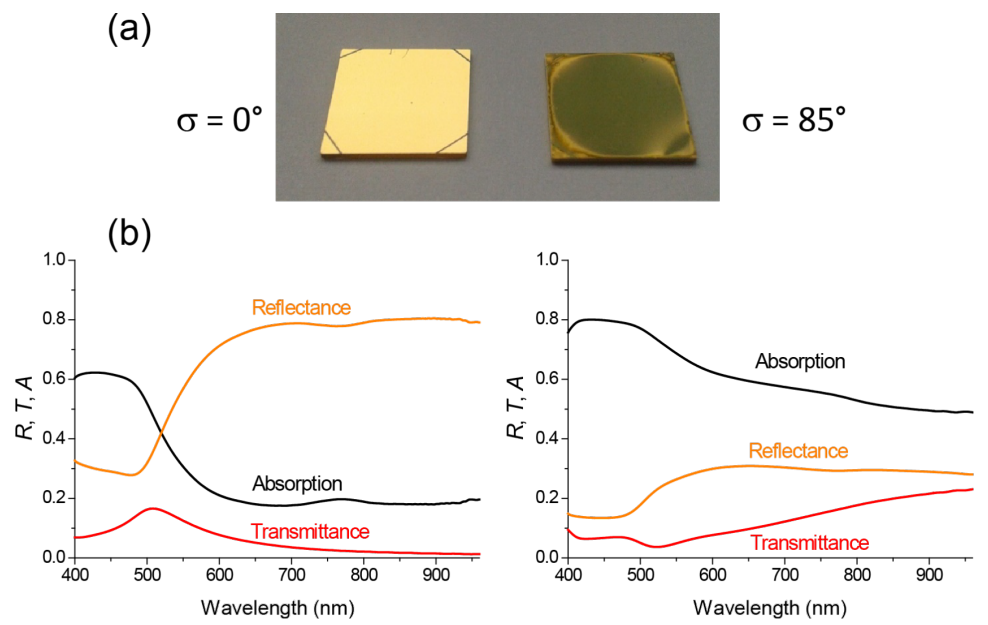

Figure 5: (a) Photograph of two samples prepared onto MgO substrates: a continuous Au thin film prepared with σ = 0° (left) and a nanostructured Au sample prepared with σ = 85° (right). (b) Transmittance, reflectance and absorption spectra of those samples.

process, from an industrial point of view it is better to use the smaller tilt angle that is able to give rise to black-metal samples. Hence, 85° has been our choice for this proof of concept. Figure 5a shows a photograph of two gold samples prepared onto MgO(001) substrates with 1 cm^2 area: The one on the left was prepared without tilt angle and as a consequence is a continuous thin film, whereas that on the right was prepared with σ = 85° and therefore is nanostructured. The continuous sample exhibits the characteristic golden color of the noble metal, whereas the nanostructured sample shows a much darker color. Their optical spectra are shown in Figure 5b. The transmittance (T) and the reflectance (R) have been measured directly, whereas the absorption (A) has been deduced taken into account that $T + R + A = 1$ (strictly speaking, in the nanostructured sample the magnitude A that we are deducing is extinction = absorption + scattering instead of merely absorption). As it was explained previously, both samples exhibit a decrease of the reflectance for wavelengths below 500 nm due to a characteristic interband transition in gold. Above 500 nm, the evolution is quite different. The continuous film shows the characteristic reflecting behavior of metallic films, related to the contribution of the free electrons (Drude) to the dielectric constant. The reflectance of this sample goes up to 80%. In the nanostructured sample, on the other hand, the same contribution of the free electrons to the dielectric constant is responsible for the appearance of LSPRs, which as discussed above induce enhanced multiple scattering and light-trapping effects for the particular size distribution and separation among nanostructures occurring in the nanostructured films obtained at high tilt angle. As a result, the nanostructured sample exhibits absorption above 60% over the whole visible-light range, slightly decreasing to 50% in the nIR region.

Conclusion

It has been shown that black-gold coatings in the visible range can be fabricated by means of sputtering using glancing angle deposition with substrate rotation. The coatings are made of columnar nanostructures that are produced due to shadowing effects in the ballistic regime of sputtering. In order to obtain enhanced light absorption in the visible range, high tilt angle is needed, which gives rise to a diameter distribution of the nanostructures centered at about 60 nm.

Acknowledgements

The authors thank MINECO (Projects MAT2014-59772-C2-1, MAT2015-69035-REDC) for financial support.

References

1. Numthuam, S.; Ginoza, T.; Zhu, M.; Suzuki, H.; Fukuda, J. *Analyst* **2011,** *136,* 456. doi:10.1039/c0an00619j
2. Hedayati, M. K.; Javaherirahim, M.; Mozooni, B.; Abdelaziz, R.; Tavassolizadeh, A.; Chakravadhanula, V. S. K.; Zaporojtchenko, V.; Strunkus, T.; Faupel, F.; Elbahri, M. *Adv. Mater.* **2011,** *23,* 5410. doi:10.1002/adma.201102646
3. Imamura, M.; Haruyama, T.; Kobatake, E.; Ikariyama, Y.; Aizawa, M. *Sens. Actuators, B* **1995,** *24–25,* 113. doi:10.1016/0925-4005(95)85024-4

4. Toyama, S.; Takei, O.; Tsuge, M.; Usami, R.; Horikoshi, K.; Kato, S. *Electrochem. Commun.* **2002,** *4,* 540. doi:10.1016/S1388-2481(02)00366-1
5. Kravets, V. G.; Schedin, F.; Grigorenko, A. N. *Phys. Rev. B* **2008,** *78,* 205405. doi:10.1103/PhysRevB.78.205405
6. Jeong, H.; Kim, J. *Electrochim. Acta* **2012,** *80,* 383. doi:10.1016/j.electacta.2012.07.040
7. Vorobyev, A. Y.; Guo, C. *J. Appl. Phys.* **2008,** *104,* 053516. doi:10.1063/1.2975989
8. Sit, J. C.; Vick, D.; Robbie, K.; Brett, M. J. *J. Mater. Res.* **1999,** *14,* 1197. doi:10.1557/JMR.1999.0162
9. García-Martín, J. M.; Alvarez, R.; Romero-Gómez, P.; Cebollada, A.; Palmero, A. *Appl. Phys. Lett.* **2010,** *97,* 173103. doi:10.1063/1.3506502
10. Alvarez, R.; García-Martín, J. M.; Macías-Montero, M.; González-García, L.; González, J. C.; Rico, V.; Perlich, J.; Cotrino, J.; González-Elipe, A. R.; Palmero, A. *Nanotechnology* **2013,** *24,* 045604. doi:10.1088/0957-4484/24/4/045604
11. Alvarez, R.; García-Martín, J. M.; Garcia-Valenzuela, A.; Macías-Montero, M.; Ferrer, F. J.; Santiso, J.; Rico, V.; Cotrino, J.; González-Elipe, A. R.; Palmero, A. *J. Phys. D: Appl. Phys.* **2016,** *49,* 045303. doi:10.1088/0022-3727/49/4/045303
12. Alvarez, R.; García-Martín, J. M.; Lopez-Santos, M. C.; Rico, V.; Ferrer, F. J.; Cotrino, J.; González-Elipe, A. R.; Palmero, A. *Plasma Processes Polym.* **2014,** *11,* 571. doi:10.1002/ppap.201300201
13. Herzinger, C. M.; Johs, B.; McGahan, W. A.; Woollam, J. A.; Paulson, W. *J. Appl. Phys.* **1998,** *83,* 3323. doi:10.1063/1.367101
14. Johnson, P. B.; Christy, R. W. *Phys. Rev. B* **1972,** *6,* 4370. doi:10.1103/PhysRevB.6.4370
15. Xu, Z.; Chen, Y.; Gartia, M. R.; Jiang, J.; Liu, G. L. *Appl. Phys. Lett.* **2011,** *98,* 241904. doi:10.1063/1.3599551
16. Abdulrahman, R. B.; Cansizoglu, H.; Cansizoglu, M. F.; Herzog, J. B.; Karabacak, T. *J. Vac. Sci. Technol., A* **2015,** *33,* 041501. doi:10.1116/1.4919737
17. Etchegoin, P. G.; Le Ru, E. C.; Meyer, M. *J. Chem. Phys.* **2006,** *125,* 164705. doi:10.1063/1.2360270

License and Terms

BEILSTEIN JOURNAL OF NANOTECHNOLOGY

Self-assembly of silicon nanowires studied by advanced transmission electron microscopy

Marta Agati[1,2,3], Guillaume Amiard[2,4], Vincent Le Borgne[3], Paola Castrucci[5], Richard Dolbec[6], Maurizio De Crescenzi[5], My Alì El Khakani[3] and Simona Boninelli[*2]

Full Research Paper

Open Access

Address:
[1]Dipartimento di Fisica e Astronomia, Università di Catania, Via S. Sofia 64, Catania 95123, Italy, [2]CNR IMM-MATIS, Via S. Sofia 64, Catania 95123, Italy, [3]Institut national de la recherche scientifique, Centre-Énergie, Matériaux et Télécommunications (INRS-EMT), 1650 Blvd. Lionel Boulet, Varennes QC-J3X 1S2, Canada, [4]Institut Pprime, UPR 3346, CNRS - Université de Poitiers, ISAE-ENSMA, 11 Boulevard Marie et Pierre Curie, 86962 Futuroscope-Chasseneuil, France, [5]Dipartimento di Fisica, Università di Roma "Tor Vergata", Via della Ricerca Scientifica 1, Roma 00133, Italy, and [6]Tekna Plasma Systems Inc., 2935 Industrial Blvd., Sherbrooke QC-J1L 2T9, Canada

Email:
Simona Boninelli[*] - simona.boninelli@ct.infn.it

* Corresponding author

Keywords:
silicon nanowires; transmission electron microscopy; vapor–liquid–solid growth

Beilstein J. Nanotechnol. **2017,** *8,* 440–445.
doi:10.3762/bjnano.8.47

Received: 30 September 2016
Accepted: 17 January 2017
Published: 15 February 2017

This article is part of the Thematic Series "Self-assembly of nanostructures and nanomaterials II".

Guest Editor: I. Berbezier

Abstract

Scanning transmission electron microscopy (STEM) was successfully applied to the analysis of silicon nanowires (SiNWs) that were self-assembled during an inductively coupled plasma (ICP) process. The ICP-synthesized SiNWs were found to present a Si–SiO_2 core–shell structure and length varying from ≈100 nm to 2–3 μm. The shorter SiNWs (maximum length ≈300 nm) were generally found to possess a nanoparticle at their tip. STEM energy dispersive X-ray (EDX) spectroscopy combined with electron tomography performed on these nanostructures revealed that they contain iron, clearly demonstrating that the short ICP-synthesized SiNWs grew via an iron-catalyzed vapor–liquid–solid (VLS) mechanism within the plasma reactor. Both the STEM tomography and STEM-EDX analysis contributed to gain further insight into the self-assembly process. In the long-term, this approach might be used to optimize the synthesis of VLS-grown SiNWs via ICP as a competitive technique to the well-established bottom-up approaches used for the production of thin SiNWs.

Introduction

As the scaling down of the feature size of devices proceeds [1], new synthesis routes are being explored to produce materials with ultra-low dimensionality to be used as building blocks to improve the functionality of next-generation devices [2]. So far, conventional manufacturing processes based on top-down methods have been employed in Si-based microelectronics.

These methods have encountered, among others, a non-trivial issue related to the cost of the sequential steps required to achieve the desired nanostructure and to the scaling up of such procedures. On the other hand, bottom-up approaches, founded on the aggregation of atoms or molecules as elementary components for the synthesis of nanomaterials, seem to be a good strategy to fabricate ultra-small structures. This concept encompasses the physics and the chemistry of nanostructure formation via a "self-assembly" route. Such ultra-low dimensional systems require appropriate characterization tools, which may lead to further insight in the comprehension of the dynamics of nanostructure formation. Transmission electron microscopy (TEM) has been the principal imaging and analytical technique for the characterization of materials at the nanoscale. Quite recently, subangstrom resolution has been reached in scanning TEM (STEM) mode, thanks also to the improvements in aberration correctors [3]. In order to access a more realistic three-dimensional vision of nanomaterial components, 3D characterization techniques are highly demanded. For this purpose, atom probe tomography (APT) [4] and X-ray tomography [5] have been used. Nevertheless, while X-ray tomography has a rather limited spatial resolution (≈2 μm), APT offers better resolution (up to the single atom detection) but has the disadvantages that a limited volume can be measured (no more than 100 nm^3) and the sample is destroyed during analysis. In this context, electron tomography (ET) together with TEM arises as a remarkable technique to study a larger range of volumes, while still offering reasonable spatial resolution from ≈1 nm^3 [6] down to atomic resolution in very recently developed microscopes [7,8]. Electron tomography is accomplished through the reconstruction of a sequence of projection images acquired by tilting the TEM sample holder. However, to achieve an accurate 3D reconstruction, all the images of the series should obey the "projection requirement", which states that the intensity of each micrograph must be a monotonic function of the physical property of the object [9]. It is well known that conventional bright field (BF) and dark field (DF) imaging are dominated by diffraction contrast. Thus in crystalline samples, the contrast changes abruptly as long as the beam axis intercepts the different crystalline zone axes. More recently, this issue has been overcome whereas the improvement of high angular annular dark field (HAADF) in STEM associated with ET has been confirmed as the most appropriate mode to image crystals, since it meets the projection requirement, associating the contrast to the atomic number [6]. By combining the HAADF and ET techniques along with energy dispersive X-ray (EDX) spectroscopy, it is possible to gather both imaging and analytical information at the same time.

In the present work, ET combined with STEM-EDX and energy-filtered TEM (EFTEM) enabled the structural characteristics of SiNWs spontaneously assembled during an inductively coupled plasma (ICP) process to be elucidated as finely as possible. The ICP technique has been conventionally exploited for the synthesis of micrometer-structured Si spheres [10]. In this regard, the formation of one-dimensional nanostructures such as SiNWs within the micrometer-sized spherical particles should be explained. In particular, we focus our study on ICP-produced SiNWs (less than 5% of the whole population) on which a peculiarity exists in the form of a high-contrast nanoparticle at the top. However, conventional 2D TEM imaging would not be able to definitively demonstrate whether the nanoparticle is embedded inside the SiNW or located at the tip. To unequivocally resolve this point, 3D STEM tomography characterization at the nanoscale was employed. Finally, the metallic composition of such nanoparticles was ascertained via the synergetic use of EFTEM and STEM-EDX. The ensemble of our results suggests that the vapor–liquid–solid (VLS) mechanism is the driving process for the growth of these SiNWs and could open the route for the production of SiNWs via the ICP technique.

Results and Discussion

Preliminary examinations of the ICP sample were performed by means of scanning electron microscopy (SEM). In the typical SEM image, as reported in Figure 1a, the presence of both nanospheres (NSs) and nanowires (NWs) can be observed. Statistical analyses conducted on hundreds of nanostructures allowed us to estimate that the diameter of the NSs range from 50 to 500 nm, while the NW length varies from ≈100 nm up to ≈2–3 μm. Energy-filtered TEM (EFTEM) images, acquired in correspondence to the Si plasmon loss (17 eV) and SiO_2 plasmon loss (23 eV), display a common core–shell Si–SiO_2 internal structure for both the NSs and the NWs (see Figure 1b and Figure 1c). Further EFTEM investigations conducted on hundreds of NWs revealed that their structural characteristics, in terms of length and diameter distribution, can be associated with two main families of SiNWs: longer SiNWs (2–3 μm) exhibiting an ultra-thin diameter (2–3 nm) and shorter SiNWs (maximum length of ≈300 nm) with a diameter of a few tens of nanometers. In this paper we focus our study on NWs belonging to the second family. In fact, the reason for our investigation stems from a peculiarity of these SiNWs, namely the presence of a high-contrast nanoparticle on the top (diameter ≈15 nm) corresponding to the SiNW core diameter, as shown in the EFTEM images in Figure 1b and Figure 1c.

Electron tomography and STEM-EDX analyses were conducted on these short SiNWs in order to better elucidate their structural and chemical characteristics. 3D tomography was performed on the nanostructures shown in Figure 2a–c, where three HAADF-STEM images of a SiNS with two SiNWs, acquired at

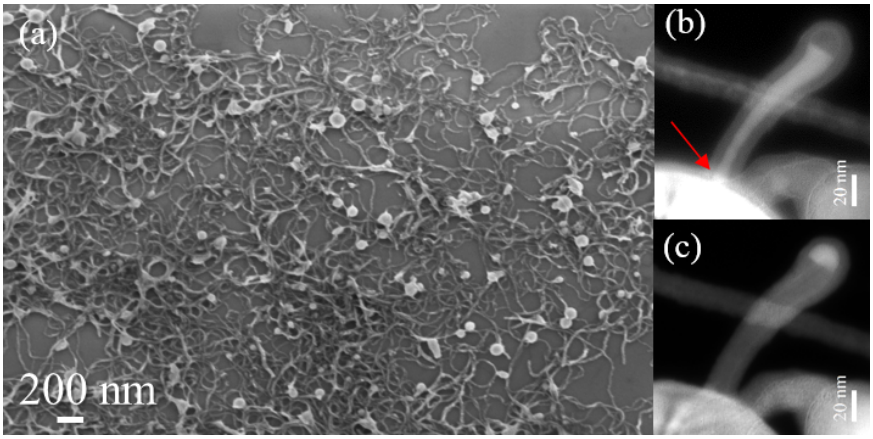

Figure 1: (a) Typical SEM image showing the morphology of the as-collected sample; EFTEM images obtained at (b) the Si plasmon loss (17 eV) and (c) the SiO_2 plasmon loss (23 eV), revealing the Si–SiO_2 core–shell structure and the structural continuity between the Si core of the SiNW and the SiNS, as indicated by the red arrow in (b).

tilting angles of 0°, 35° and 70°, are reported. The axis of rotation of the tomography measurement sample holder, depicted in Figure 2d and superimposed on the HAADF-STEM image in Figure 2a for a better understanding, was nearly aligned to the top right NW in Figure 2a. This allowed us to tilt the sample from −50° to +57° with a step of 2°, without any shadowing effect caused by the C networked structure of the TEM grid. Image shift compensation and focus were manually adjusted during acquisition. With this procedure, we acquired 55 images at different projections in about two hours.

Nevertheless, from the inspection of Figure 2a alone, it is not possible to discern the nature of another Si nanostructure, indicated by the red arrow in Figure 2a. The presence of a second SiNW appears when the nanostructure is tilted at 35° with respect to the rotation axis, which is better shown in Figure 2b. Moreover, the inspection of the projection at 70° cleary demonstrates that both SiNWs exhibit a nanoparticle on top. The chemical composition of this nanoparticle was investigated by STEM-EDX and will be discussed hereafter. The reconstructed 3D structure, comprised of the SiNWs connected with the SiNS, is represented in Figure 3. Additionally, a video showing the 3D reconstructed volume, from which the corresponding image in Figure 3 was extracted, is reported in Supporting Information File 1. The shape and the location of the nanoparticles can be clearly identified. In fact, the different elements of the reconstructed volume have been shown separately in Figure 3b–d.

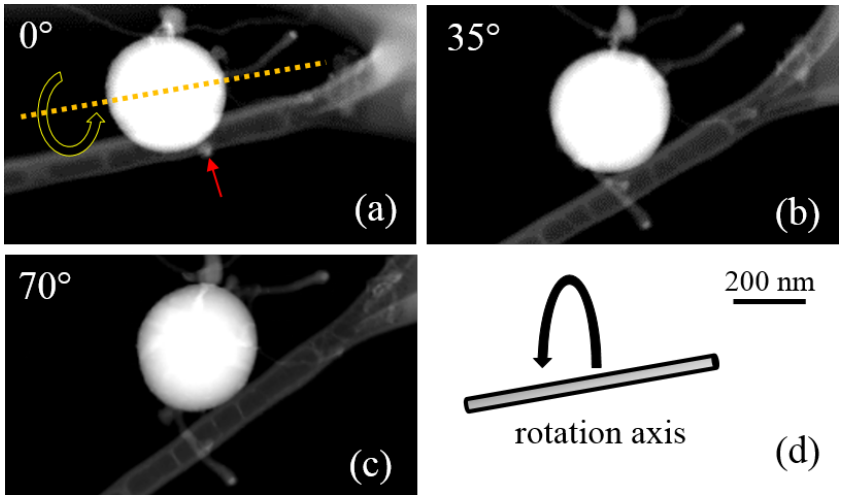

Figure 2: HAADF-STEM micrographs of a SiNS with two connected SiNWs, acquired at (a) 0°, (b) 35° and (c) 70° with respect to the rotation axis shown in (d), which corresponds to the axis of one of the two SiNWs, as indicated by the yellow dashed line in (a). The other SiNW, indicated by the red arrow in (a), is not visible at a rotation angle of 0°, but becomes evident after rotation of the sample (b and c).

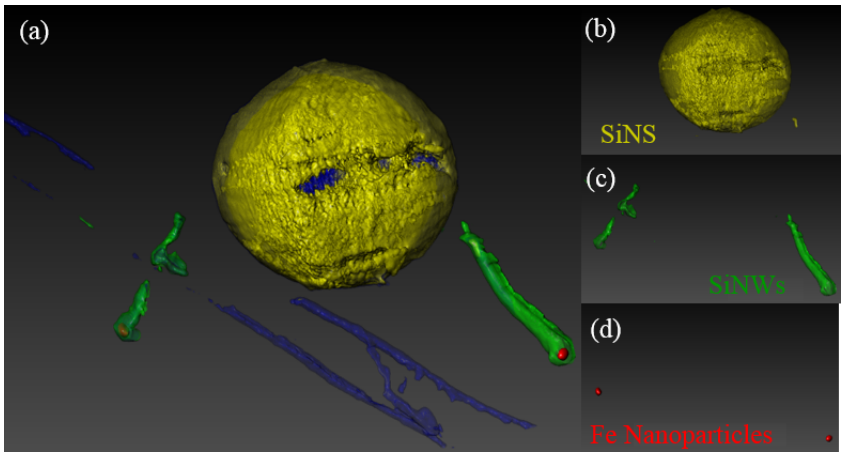

Figure 3: (a) Volume reconstruction of the system formed of (b) a SiNS and (c) two SiNWs having a Fe nanoparticle at the top, as illustrated in (d).

The identification of these elements was accomplished by performing the same reconstruction four times and separating the four different areas of interest. Thus, it is possible to distinguish the SiNS in yellow, the two SiNWs in green, the two nanoparticles in darkish red and the carbon support layer in blue in Figure 3. From this 3D reconstruction, we can conclude that the nanoparticles are located on the top of the SiNWs, and are not embedded inside of them, as it could be misleadingly inferred by a conventional 2D TEM image. On the other hand, due to the poor contrast at the base of the SiNWs, it was not possible to reconstruct the SiNW–SiNS interface. However, this issue is clarified by the EFTEM images, as depicted in Figure 1b, which demonstrate the structural continuity between the SiNW core and the SiNS (indicated by the arrow). This indicates the Si substrate on which the NWs grow before further oxidation occurs, which is induced by the oxygen present in the ICP chamber. Indeed, the oxygen derives from the native oxide of the Si powder feedstock, which is released during the spheroidization process in the ICP reactor.

Statistical STEM-EDX analyses were carried out using a subnanometer electron probe in order to corroborate the structural analysis with further chemical information. Typical EDX spectra were acquired in two different regions over the SiNWs, namely (i) at the dark particle (indicated by point A in the inset in Figure 4a), and (ii) along the SiNW (indicated by point B in Figure 4a). The spectra, reported in Figure 4a, clearly evidenced that only Si and O peaks are present along the SiNW, which is in agreement with the previous EFTEM analyses. The C peak comes from the underlying lacey carbon Cu TEM grid used as a supporting substrate for the analysis, representing a background for our study. More interestingly, the presence of Fe was detected in correspondence with the nanoparticle at the tip of the SiNW, while no iron signal was found along the

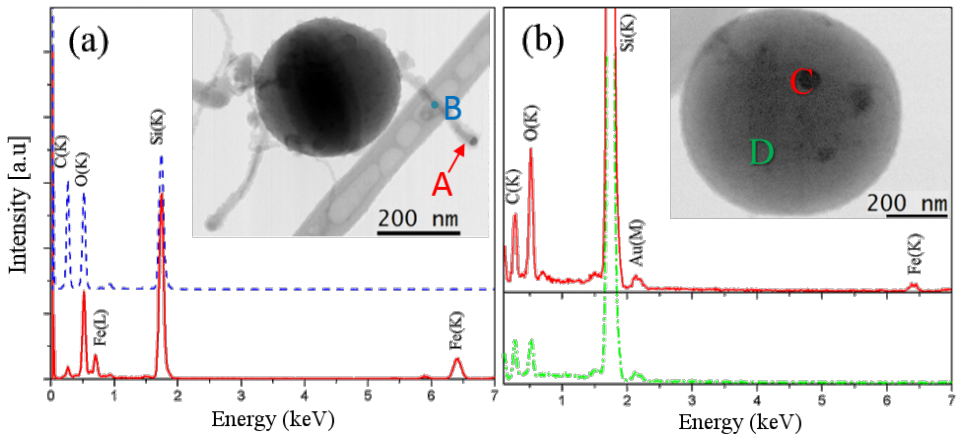

Figure 4: STEM-EDX spectra acquired at the points indicated in the BF STEM image in the insets: (a) SiNWs growing from the underling SiNS and (b) SiNS with Fe nanoparticles on the surface.

SiNW, within the sensitivity of our EDX measurements (i.e., less than 1 atom %).

Calculations based on the ZAF method [11] applied to our STEM-EDX analyses revealed that the nanoparticle at the tip was comprised of 7 atom % Fe and 14 atom % Si. Thus, we can infer that the nanoparticles are composed of a $FeSi_2$ alloy. This result is in agreement with that previously reported in [12], where we demonstrated using high-resolution TEM imaging that the interplanar distance in the nanoparticle is compatible with a $FeSi_2$ alloy. Such a composition corresponds to the most stable Fe–Si-based alloy at high temperature (≈10,000 K) under conditions of an abundance of Si content, as established by the Fe–Si binary phase diagram [13].

It is well known that metal-containing particles located at the top of SiNWs are a distinctive feature of VLS-grown SiNWs, which occurs on crystalline Si substrates [14,15]. Hence, we argue that the growth of short SiNWs via the above-described ICP process occurs through the VLS mechanism catalyzed by iron nanoparticles. The origin of the nanoparticles is the impurities present in the initial Si powder feedstock (containing 0.18 atom % Fe impurities), while the Si core of the NSs acted as the local substrate where the growth occurs. Indeed, the Fe nanoparticles are expected to form at the outer surface of the larger SiNSs formed during the spheroidization process. Once the Fe nanoparticles are present at the SiNS surface, the SiNW synthesis can occur via supersaturation of the Si vapor in the catalytic nanoparticle and precipitation of Si, which then crystallizes in the form of nanowire, as predicted by the VLS model [14]. Nevertheless, it should be noticed that some HAADF images revealed the presence of some nanoparticles on the SiNS surface (see point C in the inset of Figure 4b), from which no SiNW emerges. EDX spectra were acquired at regions exhibiting no contrast on the SiNSs (point D) and on the dark spots present on the SiNS surface (point C). It was observed that, while the peaks of Au and C come from the supporting lacey carbon Au grid, only Si and O signals are found at point D, whereas point C indicates the additional presence of iron corresponding to the nanoparticle. In the literature, it has been demonstrated that Fe-catalyzed VLS growth cannot take place under temperatures below 1150 °C [13]. It should be considered that a temperature gradient is generated inside the ICP chamber and temperatures lower than 1150 °C can be reached at the bottom [16]. It is noteworthy to recall that the ICP process was designed for the synthesis of spherical Si particles. This leads us to suppose that, while the synthesis of spherical Si takes place, the self-assembly of SiNWs via VLS does not occur on those SiNS formed at temperatures lower than 1150 °C, i.e., at the bottom of the ICP machine [16]. Instead, SiNWs assembled via the VLS mechanism grown from SiNSs formed closer to the center of the ICP reactor, where the temperature is much higher.

Conclusion

In conclusion, the combination of EFTEM, HAAD-STEM tomography and STEM-EDX spectroscopy was essential to confirm the growth mechanism of short SiNWs grown via the above-described ICP process. Indeed, by revealing the 3D structure of our ICP-produced Si nanostructures, it was possible to pinpoint the presence of small iron-containing nanoparticles at the top of the SiNWs. Moreover, EFTEM images revealed that the Si core of the SiNSs acted as a substrate from which the SiNWs grow. Metal-containing nanoparticles at the top of the SiNWs are an evident feature of VLS-grown SiNWs, where the growth is expected to start from the crystalline Si substrate. Hence, we conclude that the VLS mechanism is responsible for the growth of short SiNWs in the above-described ICP process, provided that a small amount of Fe is present during the spheroidization process. In this way, the ICP technique can be seen as a prospect for the synthesis of SiNWs via the VLS mechanism after suitable optimization of the process.

Experimental

The inductively coupled plasma process [10] is conventionally exploited to transform a rough Si powder feedstock (irregular particles with mean size of 115 μm and 99.5% purity) into spherical microspheres of equivalent diameter. To this aim, the Si feedstock is introduced via an Ar carrier gas in the ICP reactor, where an Ar/H_2 plasma is maintained at extremely high temperature (on the order of ≈10,000 K). The Si particles partially melt in-flight and, while being carried down in the first collector of the ICP machine, re-condensate as silicon spheres due to the surface-energy minimization principle. During the formation of the microspheres, a fraction of the Si feedstock sublimates and the molecules in the vapor phase aggregate in the form of lighter Si nanostructures. These are transported downstream in the reactor towards a second collector where they accumulate in the form of Si nanopowder. To perform our studies, this Si nanopowder was collected, dispersed into isopropyl alcohol, and sonicated for 5 min. By dropcasting this solution on Si substrates and on lacey carbon Cu or Au grids, both scanning electron microscope (SEM) imaging and TEM-based analyses were performed, respectively.

The SEM characterizations were carried out using a field emission gun (FEG) Zeiss Supra25. TEM analyses were performed with a JEOL JEM 2010F operating at 200 kV and with a spherical aberration probe corrected cold FEG ARM JEOL (0.27 eV energy spread) operating at 100 keV and equipped with a large area (100 mm^2) EDX silicon drift detector with an energy resolution of 127 eV. The former was used to realise the EFTEM

analysis on individual SiNWs, while the latter was used to accomplish the STEM-EDX analysis with a sub-nanometer probe and ET in STEM mode by using a HAADF detector. Electron tomography was conducted by using a single-tilt Fischione tomography sample holder (±60° range). Finally, the Composer Kai software was used for the reconstruction based on the filtered back projection (FBP) alghoritm, while the Visualiser Kai software was used for visualization.

Supporting Information

Supporting Information File 1

A video showing the 3D reconstructed volume of a SiNS and VLS-grown SiNWs with an Fe nanoparticle on top. The image presented in Figure 3 was extracted from this video.
[http://www.beilstein-journals.org/bjnano/content/supplementary/2190-4286-8-47-S1.mp4]

Acknowledgements

The authors would like to acknowledge the support from the Italian Ministry of Foreign Affairs and International Cooperation, Directorate General for the Promotion of the Country System. Most of this work was performed at Beyondnano CNR-IMM, which was supported by project Beyond-Nano (PON a3_00363). The authors would also like to acknowledge the financial support from the Natural Sciences and Engineering Research Council (NSERC) of Canada through the Discovery Grants Program, and the FRQNT (Le Fonds de Recherche du Québec-Nature et Technologies) through its strategic Network “Plasma-Québec”.

References

1. Hu, S.; Liu, H.; Wang, P.; Wang, X. *J. Am. Chem. Soc.* **2013,** *135,* 11115–11124. doi:10.1021/ja403471d
2. Cui, Y.; Lieber, C. M. *Science* **2001,** *291,* 851–853. doi:10.1126/science.291.5505.851
3. Nellist, P. D.; Chisholm, M. F.; Dellby, N.; Krivanek, O. L.; Murfitt, M. F.; Szilagyi, Z. S.; Lupini, A. R.; Borisevich, A.; Sides, W. H., Jr.; Pennycook, S. J. *Science* **2004,** *17,* 1741. doi:10.1126/science.1100965
4. Miller, M. K.; Kelly, T. F.; Rajan, K.; Ringer, S. P. *Mater. Today* **2012,** *15,* 158–165. doi:10.1016/S1369-7021(12)70069-X
5. Baruchel, J.; Buffiere, J. Y.; Maire, E. *X-ray tomography in material science;* Hermes science publications: Paris, France, 2000.
6. Midgley, P. A.; Weyland, M. *Ultramicroscopy* **2003,** *96,* 413–431. doi:10.1016/S0304-3991(03)00105-0
7. Van Aert, S.; Batenburg, K. J.; Rossell, M. D.; Erni, R.; Van Tendeloo, G. *Nature* **2011,** *470,* 374–377. doi:10.1038/nature09741
8. Scott, M. C.; Chen, C.-C.; Mecklenburg, M.; Zhu, C.; Xu, R.; Ercius, P.; Dahmen, U.; Regan, B. C.; Miao, J. *Nature* **2012,** *483,* 444–447. doi:10.1038/nature10934
9. Hawkes, P. W. The Electron Microscope as a Structure Projector. In *Electron Tomography: Methods Three-Dimensional Visualization of Structures in the Cell;* Frank, J., Ed.; Springer: Berlin, Germany, 2006; pp 83–111. doi:10.1007/978-0-387-69008-7_4
10. Guo, J. Y.; Gitzhofer, F.; Boulos, M. I. *J. Mater. Sci.* **1995,** *30,* 5589–5599. doi:10.1007/BF00356691
11. Williams, D. B.; Carter, C. B. *Transmission Electron Microscopy: A Textbook for Materials Science;* Springer: New York, NY, U.S.A., 2009.
12. Agati, M.; Amiard, G.; Le Borgne, V.; Castrucci, P.; Dolbec, R.; De Crescenzi, M.; El Khakani, M. A.; Boninelli, S. *Sci. Rep.* **2016,** *5,* 37598. doi:10.1038/srep37598
13. Morales, A. M.; Lieber, C. M. *Science* **1998,** *279,* 208–211. doi:10.1126/science.279.5348.208
14. Wang, N.; Cai, Y.; Zhang, R. Q. *Mater. Sci. Eng., R* **2008,** *60,* 1–51. doi:10.1016/j.mser.2008.01.001
15. Wagner, R. S.; Ellis, W. C. *Appl. Phys. Lett.* **1964,** *4,* 89–90. doi:10.1063/1.1753975
16. Jiayin, G.; Xiaobao, F.; Dolbec, R.; Siwen, X.; Jurewicz, J.; Boulos, M. *Plasma Sci. Technol. (Bristol, U. K.)* **2010,** *12,* 188–199. doi:10.1088/1009-0630/12/2/12

License and Terms

BEILSTEIN JOURNAL OF NANOTECHNOLOGY

Study of the surface properties of ZnO nanocolumns used for thin-film solar cells

Neda Neykova*[1], Jiri Stuchlik[1], Karel Hruska[1], Ales Poruba[1], Zdenek Remes[1] and Ognen Pop-Georgievski[2]

Full Research Paper

Open Access

Address:
[1]Institute of Physics AS CR v.v.i., Cukrovarnicka 10, 162 53 Prague, Czech Republic and [2]Institute of Macromolecular Chemistry AS CR v.v.i., Heyrovsky sq. 2, 162 06 Prague, Czech Republic

Email:
Neda Neykova* - neykova@fzu.cz

* Corresponding author

Keywords:
3-dimensional solar cells; hydrothermal growth; optical spectroscopy; photothermal deflection spectroscopy; plasma treatment; X-ray photoelectron spectroscopy; ZnO nanocolumns

Beilstein J. Nanotechnol. **2017,** *8,* 446–451.
doi:10.3762/bjnano.8.48

Received: 12 September 2016
Accepted: 26 January 2017
Published: 16 February 2017

This article is part of the Thematic Series "Self-assembly of nanostructures and nanomaterials II".

Guest Editor: I. Berbezier

Abstract

Densely packed ZnO nanocolumns (NCs), perpendicularly oriented to the fused-silica substrates were directly grown under hydrothermal conditions at 90 °C, with a growth rate of around 0.2 µm/h. The morphology of the nanostructures was visualized and analyzed by scanning electron microscopy (SEM). The surface properties of ZnO NCs and the binding state of present elements were investigated before and after different plasma treatments, typically used in plasma-enhanced CVD solar cell deposition processes, by X-ray photoelectron spectroscopy (XPS). Photothermal deflection spectroscopy (PDS) was used to investigate the optical and photoelectrical characteristics of the ZnO NCs, and the changes induced to the absorptance by the plasma treatments. A strong impact of hydrogen plasma treatment on the free-carrier and defect absorption of ZnO NCs has been directly detected in the PDS spectra. Although oxygen plasma treatment was proven to be more efficient in the surface activation of the ZnO NC, the PDS analysis showed that the plasma treatment left the optical and photoelectrical features of the ZnO NCs intact. Thus, it was proven that the selected oxygen plasma treatment can be of great benefit for the development of thin film solar cells based on ZnO NCs.

Introduction

The widely accepted design of thin-film silicon (TF-Si) solar cells, used for mass production, is composed of a transparent conductive oxide with roughness at the nanoscale on the front (TCO), e.g., tin oxide (SnO_2) or zinc oxide (ZnO), followed by p–i–n Si layers (amorphous and/or nanocrystalline) in the cell and a back reflector [1,2]. In such a layer arrangement, the light scattering and the consequent light trapping, caused by the interfaces with nano-scale roughness (front TCO–active layer and active layer–back reflector), increase the optical path inside in the thin silicon layer. These effects are observed in the weakly absorbing spectral region of silicon above approximately 650 nm, leading to efficiencies well above 13% at the

cell level and above 12% at the module level [3,4]. However, the photo-generated current, determined by light absorption, is limited by the drift of generated electrons and holes across the absorber layer. Thus, the highest performances are expected for solar cells having a sufficiently large "optical thickness" and a sufficiently short distance between the electrodes, the "electrical thickness". In common planar TF-Si solar cells, it is impossible to simultaneously fulfil these two conditions. Recently developed solar cells based on a three dimensional (3-D) design, in which periodically ordered zinc oxide nanocolumns (ZnO NCs) are used as a front electrode, have been of great interest, because they would exceed in the ultimate light trapping and provide excellent charge separation [5-7]. Due to the vertical geometry of these textures, the optical thickness is dictated by the height of the NCs, such that most of the light traversing the cell sees an absorber-layer thickness approximately equal to the NC height. In contrast, as the front and back TCO contacts are interpenetrating, the inter-electrode distance, given by the thickness of the Si layers on the walls of the NCs, is generally substantially thinner than that applied for state-of-the-art a-Si:H solar cells; the lateral carrier transport provided by this type of texture should thus ensure an optimal current collection. Therefore, it is envisaged that in comparison to thin-film planar cells with nano-scale roughness, the 3-D solar cells might lead to higher efficiency providing important assets such as minimal material consumption [8-10]. The proposed 3-D concept is not limited to thin-film silicon solar cells, but could be advantageously used for all other thin-film solar cells.

So far, a wide diversity of methods have been used for the preparation of ZnO nanocolumns such as metal organic chemical vapor deposition (MOCVD) [11], electrochemical deposition [12], sputtering [13], reactive ion etching [5] and the hydrothermal method [6,14,15]. The last mentioned is an attractive and preferable method for growing one-dimensional structures of ZnO, as it is simple, does not require expensive equipment, is safe and environmentally friendly since water is used as a solvent, and it is easy to scale-up for further mass production.

Solar cell deposition is a multistep process during which different plasma processes are being used. Oxygen plasma is applied for both, activation of the surface and stripping of the polymer mask used for fabrication of periodically ordered ZnO NCs, while hydrogen plasma is usually used immediately before the deposition of the active solar-cell layer for directly increasing the electrical conductivity. The employed plasma treatments could significantly influence the concentration of defects and free carriers, reflected in the defect and free-carrier adsorption, and consequently impact the efficiency of the solar cell. Therefore, the investigation of the effects of the different plasma treatments on the ZnO nanocolumns is of crucial importance. Herein, a low-temperature hydrothermal method is used to synthesize densely packed NCs on fused silica substrates covered with a ZnO seed layer, which were prepared before by DC reactive magnetron sputtering. The optical absorption of the pristine ZnO layers as well as that of the substrates bearing the dense ZnO NCs was investigated by photothermal deflection spectroscopy (PDS) [16,17]. Furthermore, we investigated the changes in the PDS spectrum of the dense NCs induced by hydrogen and oxygen plasma treatment under conditions typical for plasma processing of thin-film silicon solar cells. XPS was used to determine the changes in surface composition as a result of the different plasma treatments.

Results and Discussion

Figure 1 reports SEM images of densely packed ZnO nanocolumns grown at 90 °C for 180 min. As it can be seen from the SEM cross-sectional view, the ZnO nanocolumns are not interconnected and are well spaced with gaps of several nanometers. Notably, it is evident that each column has well defined boundaries (Figure 1a). The position of the individual nanocolumns is random with diameters varying from around 30 to 180 nm, as revealed by the top-view SEM image (Figure 1b).

An average nanocolumn length of 650 nm was measured from the cross section, as shown in the SEM image of Figure 1a. The thickness of the seed layer is about 150 nm. It should be noted, that after the hydrogen or oxygen surface plasma treatments the morphology of the nanocolumns does not change (see Figure S1 and Figure S2, Supporting Information File 1 for details).

The chemical bonding structure of the ZnO films prepared by hydrothermal growth from a seed layer on fused silica carriers was examined by XPS. Figure 2 reports typical XPS high-resolution Zn 2p and O 1s spectra of the ZnO nanocolumns before and after 25 min of treatment in H- and O-plasma. The pristine ZnO NCs are characterized by a characteristic spin-split doublet with a Zn $2p_{3/2}$ peak centered at 1021.6 eV and a Zn $2p_{1/2}$ peak (at 1044.7 eV) showing 23.1 eV separation from the main contribution. The O 1s spectrum of the as-prepared nanocolumns could be deconvoluted with three contributions arising from lattice oxygen (Zn–O–Zn), non-lattice oxygen (Zn–O–H, Zn–O^-) and O=C moieties, and C–O–H contributions centered at 530.4, 531.7 and 532.5 eV, respectively. The O=C and C–O–H contributions originate from organic contaminants adsorbed on the ZnO NCs surface during the transfer of the substrates to the XPS chamber.

The plasma treatments that are typically used in the solar cell fabrication processes, shift the position of the Zn 2p peaks by 0.3–0.4 eV toward higher binding energies and significantly broaden their width, irrespectively of the exposure time. While

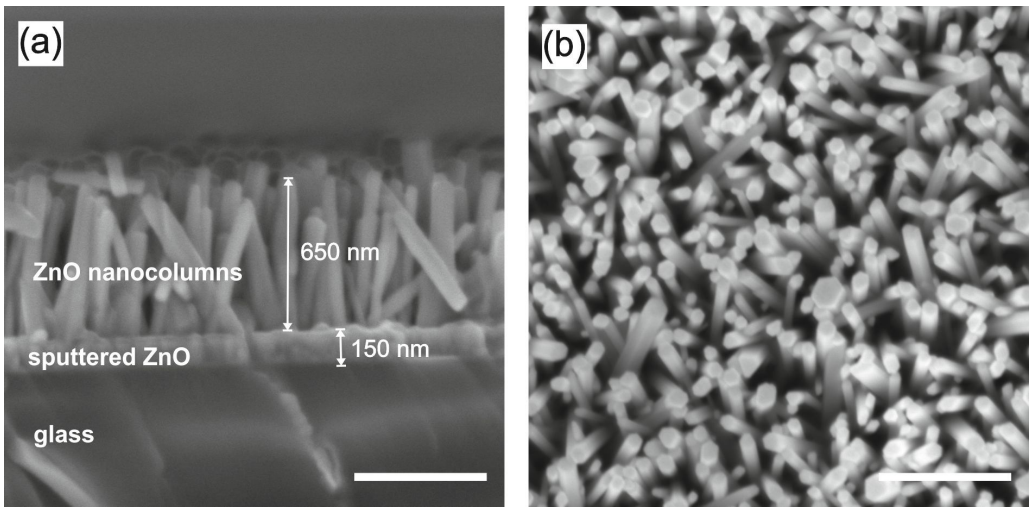

Figure 1: Cross-sectional (a) and top (b) view of densely packed ZnO NCs grown at 90 °C for 180 min (scale bar: 500 nm).

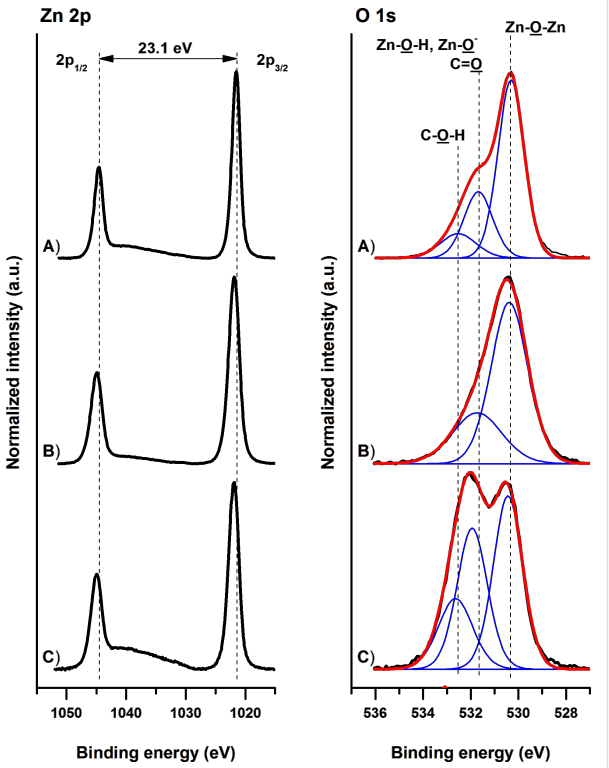

Figure 2: High-resolution core-level Zn 2p and O 1s XPS spectra of pristine (A) ZnO NCs and ZnO NCs after 25 min treatment in (B) H- and (C) O-plasmas. Measured spectra are presented with black lines, while their corresponding fitted envelopes are presented in red. The individual contributions of different functional groups present in the ZnO nanocolumns are represented with blue lines.

the full width at half maximum (FWHM) of the pristine nanocolumns is about 1.8 eV, the FWHM of H- and O-plasma treated ZnO structures increased to 2.3 and 2.0 eV, respectively. The observed changes in the high-resolution Zn 2p spectra indicate the enhanced presence of surface defects, i.e., the existence of Zn atoms in different chemical surroundings. Concomitantly, the plasma treatment introduces changes in the high-resolution O 1s spectra and a strong increase of the contributions at about 531.7 eV, mainly due to the rise of the plasma induced Zn–O–H and Zn–O$^-$ contributions [18]. Pristine nanocolumns are characterized by a ratio between the non-lattice oxygen (Zn–O–H, Zn–O$^-$) (excluding the O=C contaminants contributions) and the lattice Zn–O–Zn structures of 0.29. Upon the H- and O-plasma treatment this ratio rises to 0.43 and 0.60, respectively. The concomitant observations in the high-resolution Zn 2p and O 1s spectra were independent from the duration of the plasma treatment. The XPS data show an increase of defect density upon the plasma treatments in the surface area of the ZnO NCs, i.e., an increased presence of Zn–O–H and Zn–O$^-$ groups/species as a result of plasma seizure of the lattice Zn–O–Zn structures. The higher concentration of non-lattice oxygen (Zn–O–H and Zn–O$^-$) species in the case of O-plasma treatment evidences the more effective surface activation when this type of plasma is being used.

The changes induced to the synthesized ZnO NCs by the exposure to different plasma treatments was further probed by PDS. Figure 3 shows the optical absorptance spectra of as-grown ZnO nanocolumns and NCs treated in H-plasma for 1, 5, 10 and 25 min. The measured PDS absorptance spectra reflect the absorption edge, Urbach tail, absorption on defects and free-carrier absorption (proportional to the concentration of free carriers).

All optical absorptance spectra show the optical absorption edge at a photon energy of 3.3 eV and the free-carrier absorption in the red and the infrared part of the spectrum below photon ener-

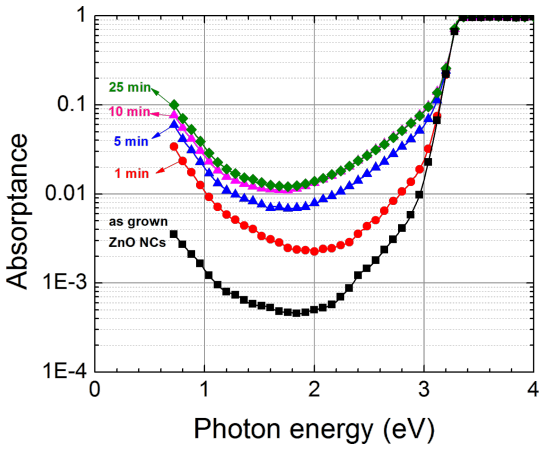

Figure 3: The optical absorptance spectra of as-grown ZnO nanocolumns and NCs treated in H-plasma for 1, 5, 10 and 25 min.

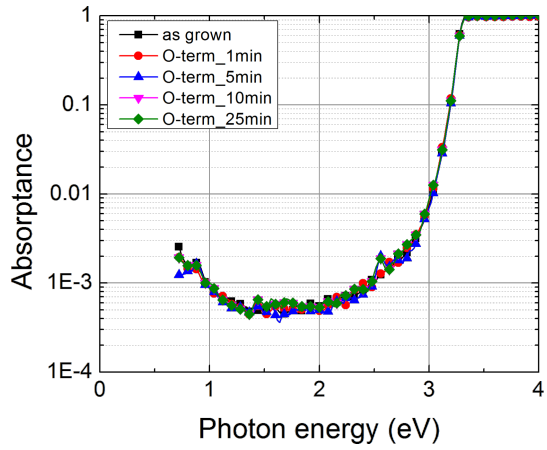

Figure 4: The optical absorptance spectra of as-grown ZnO nanocolumns and NCs treated in O-plasma for 1, 5, 10 and 25 min.

gies of 2 eV. The infrared optical absorption increases with hydrogen plasma treatment indicating the increase of the free-carrier concentration as described in the Drude model. The increase of the free-carrier concentration is reasonably expected to increase the electrical conductivity of the ZnO NCs. Nevertheless, precise measurement of electrical conductivity is a difficult task and we plan to approach it by direct measurement on individual ZnO nanocolumns. The major changes appear within several minutes of exposure to hydrogen plasma and the effect saturates after about 10 min. We suppose that hydrogen diffuses into ZnO creating shallow donors [19,20]. We note that the hydrogen doping does not shift the optical absorption edge [21], which means that the lattice as well as the occupancy of valence and conductive states does not change significantly (up to the degenerate conduction band) [22].

While the hydrogen plasma treatment induced significant changes in the optical absorptance spectra, notably, the PDS spectra show that there is no detectable change of the infrared optical absorptance (Figure 4). This observation strongly suggests that the O-plasma treatment does not have any detrimental effects on the free-carrier concentration in the ZnO NCs.

Conclusion

In this work, randomly arranged densely packed and preferentially perpendicularly oriented ZnO nanocolumn arrays were grown from seed layers on fused silica substrates. The surface composition of the ZnO NCs drastically changes upon the exposure to H- and O-plasma treatments. The plasma treatments increase the presence of non-lattice oxygen in the form of Zn–O–H and Zn–O^- contributions regardless of exposure time. The O-plasma treatment led to a more effective surface activation of the ZnO NCs as evidenced by the XPS analysis. The employed hydrogen-plasma treatment led to an increase of the free-carrier adsorption of up to two orders of magnitude, thus seriously affecting the optical and photoelectrical characteristics of the ZnO NCs. The oxygen-plasma treatment led to negligible changes in the PDS absorptance spectra. The concomitant increase in the presence of active surface species and only minor influence on the optical and photoelectrical features of the ZnO NCs absorptance spectra, make the O-plasma a preferred treatment for the preparation of thin-film solar cells based on ZnO NCs. The reported ZnO nanocolumns layer with a proper spacing could be used as a 3-D scaffold not only for amorphous silicon solar cells, but also for other absorbers with a short lifetime such as CuO, CuO_2, FeS_2, quantum dots or nanocrystalline Si.

Experimental

The growth of densely packed ZnO nanocolumns was performed on fused silica (Suprasil®) substrates that were covered with an undoped thin seed layer of ZnO by DC reactive magnetron sputtering. The parameters of magnetron sputtering were as follows: processing temperature of 400 °C at a target voltage of 400 V, ratio between gas species of Ar/O = 2/0.5 for 10 min.

The dimensions of all substrates were 10 × 10 mm^2. Before seed layer deposition, the substrates were cleaned in an ultrasonic bath with acetone for 10 min, then rinsed with deionized water and dried under nitrogen flow.

The hydrothermal growth of ZnO nanocolumns was performed from an equimolar aqueous solution of 25 mmol zinc nitrate hexahydrate ($Zn(NO_3)_2{\cdot}6H_2O$) and hexamethylenetetramine ($(CH_2)_6N_4$) in an aqueous bath at 90 °C for 3 h [15,23]. During the nanocolumns growth, the substrate was mounted upside-down on a sample holder. After termination the sample was thoroughly washed in deionized water and dried in nitrogen

flow. The surface morphology of the samples was characterized by SEM (MAIA3, TESCAN). The electron energies were 5 keV or 10 keV. An in-lens detector was used to image the investigated surfaces.

Plasma treatment

Half of the as-prepared substrates with densely packed ZnO NCs were treated in oxygen plasma at 100 W, 0.5 mbar for 1, 5, 10 and 25 min at room temperature (Femto, Diener electronic GmbH).

The other half of the substrates underwent hydrogen plasma treatment, it was done in a capacitively coupled radio frequency plasma reactor KIII [24] at 20 W, 1 mbar for 1, 5, 10 and 25 min at room temperature [25-27].

X-ray photoelectron spectroscopy (XPS)

XPS measurements were performed using a K-Alpha$^+$ XPS spectrometer (ThermoFisher Scientific, UK) operating at a base pressure of 1.0×10^{-7} Pa. The data acquisition and processing were performed using the Thermo Avantage software. All samples were analyzed using a microfocused, monochromated Al Kα X-ray radiation (400 μm spot size) with a pass energy of 150 eV for survey and 50 eV for high-resolution core level spectra. The X-ray angle of incidence was 30° and the emission angle was along the surface normal. The K-Alpha charge dual compensation system was employed during analysis, using electrons and low-energy argon ions to prevent any localized build-up of charge. The measured high-resolution spectra were fitted with Voigt profiles. The analyzer transmission function, Scofield sensitivity factors, and effective attenuation length for photoelectrons were applied for quantification. All spectra were referenced to the adventitious C 1s peak at a binding energy (BE) of 285.0 eV. The BE scale was controlled on standards of poly(ethylene terephthalate) and metallic Cu, Ag, and Au.

Photothermal deflection spectroscopy (PDS)

Measurements of optical absorption on bare sputtered ZnO substrates (not shown here) as well as on as-grown densely packed ZnO NCs and further plasma-treated nanocolumns were carried out through photothermal deflection spectroscopy (PDS), a technique for measuring weak optical absorption in thin films [14,28]. Unlike optical transmittance spectroscopy, PDS detects directly the amount of the absorbed light by measuring the heat generated by the optical absorption with the optical absorptance sensitivity down to 0.01%. PDS is based on measuring the deflection of the laser beam in the vicinity of the thin film immersed in a transparent liquid due to thermal changes of medium induced by heating of thin film by the absorption of the incident monochromatic light. A significant advantage of the PDS is the weak influence of the optical scattering, which is important in the case of ZnO nanocolumns for which the transmittance spectra are significantly deteriorated by optical scattering.

Supporting Information

Supporting Information File 1

Additional SEM pictures.
[http://www.beilstein-journals.org/bjnano/content/supplementary/2190-4286-8-48-S1.pdf]

Acknowledgements

This work was supported by the Czech Science Foundation under project 16-10429J. O.P.G. acknowledges the support from the European Regional Development Funds through the Operational Programme Prague - Competitiveness (Project number: CZ.2.16/3.1.00/21545).

References

1. Krishnakumar, V.; Han, J.; Klein, A.; Jaegermann, W. *Thin Solid Films* **2011,** *519,* 7138–7141. doi:10.1016/j.tsf.2010.12.118
2. Bosio, A.; Menossi, D.; Mazzamuto, S.; Romeo, N. *Thin Solid Films* **2011,** *519,* 7522–7525. doi:10.1016/j.tsf.2010.12.137
3. Shah, A.; Moulin, E.; Ballif, C. *Sol. Energy Mater. Sol. Cells* **2013,** *119,* 311–316. doi:10.1016/j.solmat.2013.09.001
4. Lin, J.; Cashmore, J.; Iwahashi, T.; Sakurai, J.; Losio, P.; Orhan, J. B.; Hoetzel, J.; Ristau, S.; Saito, Y.; Tsuji, A.; Roschek, T.; Meier, J.; Sinicco, I.; Zindel, A.; Hayashi, H.; Matsunaga, D. *Blazing New Paths to High Efficiency Amorphous Silicon Based Solar Modules.* Oral presentation at 40th IEEE Photovoltaics Specialist Conference, Denver, CO, USA, June 8–13, 2014. http://www.flip-programs.com/PVSC/PVSC-40-YB/
5. Vanecek, M.; Babchenko, O.; Purkrt, A.; Holovsky, J.; Neykova, N.; Poruba, A.; Remes, Z.; Meier, J.; Kroll, U. *Appl. Phys. Lett.* **2011,** *98,* 163503. doi:10.1063/1.3583377
6. Neykova, N.; Moulin, E.; Campa, A.; Hruska, K.; Poruba, A.; Stuckelberger, M.; Haug, F.-J.; Topic, M.; Ballif, C.; Vanecek, M. *Phys. Status Solidi A* **2015,** *212,* 1823–1829. doi:10.1002/pssa.201431869
7. Vanecek, M.; Neykova, N.; Hruska, K.; Poruba, A.; Remes, Z.; Holovsky, J.; Purkrt, A.; Babchenko, O.; Meier, J.; Kroll, U. Photovoltaic cell and methods for producing a photovoltaic cell. U.S. Patent US8772080B2, July 8, 2014.
8. Kim, J.; Battaglia, C.; Charrière, M.; Hong, A.; Jung, W.; Park, H.; Ballif, C.; Sadana, D. *Adv. Mater.* **2014,** *26,* 4082–4086. doi:10.1002/adma.201400186
9. Kuang, Y.; van der Werf, K. H. M.; Houweling, Z. S.; Schropp, R. E. I. *Appl. Phys. Lett.* **2011,** *98,* 113111. doi:10.1063/1.3567527
10. Ho, C.-I; Liang, W.-C.; Yeh, D.-J.; Su, V.-C.; Yang, P.-C.; Chen, S.-Y.; Yang, T.-T.; Lee, J.-H.; Kuan, C.-H.; Cheng, I-C.; Lee, S.-C. *J. Appl. Phys.* **2013,** *113,* 163106. doi:10.1063/1.4803045
11. Liu, X.-Y.; Shan, C.-X.; Wang, S.-P.; Zhao, H.-F.; Shen, D.-Z. *Nanoscale* **2013,** *5,* 7746. doi:10.1039/c3nr02263c
12. Elias, J.; Tena-Zaera, R.; Lévy-Clément, C. *J. Electroanal. Chem.* **2008,** *621,* 171–177. doi:10.1016/j.jelechem.2007.09.015

13. Mamat, M. H.; Malek, M. F.; Hafizah, N. N.; Asiah, M. N.; Suriani, A. B.; Mohamed, A.; Nafarizal, N.; Ahmad, M. K.; Rusop, M. *Ceram. Int.* **2016,** *42,* 4107–4119. doi:10.1016/j.ceramint.2015.11.083
14. Neykova, N.; Brož, A.; Remeš, Z.; Hruška, K.; Kalbáčová, M.; Kromka, A.; Vaněček, M. *Appl. Surf. Sci.* **2012,** *258,* 3485–3489. doi:10.1016/j.apsusc.2011.11.101
15. Neykova, N.; Hruska, K.; Holovsky, J.; Remes, Z.; Vanecek, M. *Thin Solid Films* **2013,** *543,* 110–113. doi:10.1016/j.tsf.2013.02.110
16. Jackson, W. B.; Amer, N. M.; Boccara, A. C.; Fournier, D. *Appl. Opt.* **1981,** *20,* 1333–1344. doi:10.1364/AO.20.001333
17. Granqvist, C. G.; Hultåker, A. *Thin Solid Films* **2002,** *411,* 1–5. doi:10.1016/S0040-6090(02)00163-3
18. Chen, C.; Lu, Y.; He, H.; Xiao, M.; Wang, Z.; Chen, L.; Ye, Z. *ACS Appl. Mater. Interfaces* **2013,** *5,* 10274–10279. doi:10.1021/am403133u
19. Cox, S. F. J.; Davis, E. A.; Cottrell, S. P.; King, P. J. C.; Lord, J. S.; Gil, J. M.; Alberto, H. V.; Vilão, R. C.; Piroto Duarte, J.; Ayres de Campos, N.; Weidinger, A.; Lichti, R. L.; Irvine, S. J. C. *Phys. Rev. Lett.* **2001,** *86,* 2601–2604. doi:10.1103/PhysRevLett.86.2601
20. Hofmann, D. M.; Hofstaetter, A.; Leiter, F.; Zhou, H.; Henecker, F.; Meyer, B. K.; Orlinskii, S. B.; Schmidt, J.; Baranov, P. G. *Phys. Rev. Lett.* **2002,** *88,* 045504. doi:10.1103/PhysRevLett.88.045504
21. Miloslavskii, V. K.; Pogrebniak, P. S. *Phys. Status Solidi B* **1972,** *51,* K99–K102. doi:10.1002/pssb.2220510252
22. Kim, Y. H.; Karazhanov, S. Zh.; Kim, W. M. *Phys. Status Solidi B* **2011,** *248,* 1702–1707. doi:10.1002/pssb.201046426
23. Greene, L. E.; Law, M.; Goldberger, J.; Kim, F.; Johnson, J. C.; Zhang, Y.; Saykally, R. J.; Yang, P. *Angew. Chem., Int. Ed.* **2003,** *42,* 3031–3034. doi:10.1002/anie.200351461
24. Stuchlik, J.; Stuchlikova, T. H.; Artemenko, A.; Remes, Z. *JJAP Conf. Proc.* **2015,** *3,* 011301. doi:10.7567/JJAPCP.3.011301
25. Neykova, N.; Kozak, H.; Ledinsky, M.; Kromka, A. *Vacuum* **2012,** *86,* 603–607. doi:10.1016/j.vacuum.2011.07.055
26. Pop-Georgievski, O.; Neykova, N.; Proks, V.; Houdkova, J.; Ukraintsev, E.; Zemek, J.; Kromka, A.; Rypaček, F. *Thin Solid Films* **2013,** *543,* 180–186. doi:10.1016/j.tsf.2012.11.128
27. Krátká, M.; Neykova, N.; Ukraintsev, E.; Kromka, A.; Rezek, B. *Int. J. Electrochem. Sci.* **2013,** *8,* 1598–1608.
28. Remes, Z.; Babchenko, O.; Varga, M.; Stuchlik, J.; Jirasek, V.; Prajzler, V.; Nekvindova, P.; Kromka, A. *Thin Solid Films* **2016,** *618,* 130–133. doi:10.1016/j.tsf.2016.04.026

License and Terms

The definitive version of this article is the electronic one which can be found at:
doi:10.3762/bjnano.8.48

BEILSTEIN JOURNAL OF NANOTECHNOLOGY

The longstanding challenge of the nanocrystallization of 1,3,5-trinitroperhydro-1,3,5-triazine (RDX)

Florent Pessina* and Denis Spitzer

Review

Open Access

Address:
NS3E, UMR 3208 ISL-CNRS-Unistra, Institut franco-allemand de recherches de Saint-Louis (ISL), 5 rue du Général Cassagnou, F-68301 St. Louis, France

Email:
Florent Pessina* - fpessina@unistra.fr

* Corresponding author

Keywords:
crystallization; nanoparticles; RDX; review; submicrometer; 1,3,5-trinitroperhydro-1,3,5-triazine

Beilstein J. Nanotechnol. **2017,** *8,* 452–466.
doi:10.3762/bjnano.8.49

Received: 14 September 2016
Accepted: 01 February 2017
Published: 17 February 2017

This article is part of the Thematic Series "Self-assembly of nanostructures and nanomaterials II".

Guest Editor: I. Berbezier

Abstract

Research efforts for realizing safer and higher performance energetic materials are continuing unabated all over the globe. While the thermites – pyrotechnic compositions of an oxide and a metal – have been finely tailored thanks to progress in other sectors, organic high explosives are still stagnating. The most symptomatic example is the longstanding challenge of the nanocrystallization of 1,3,5-trinitroperhydro-1,3,5-triazine (RDX). Recent advances in crystallization processes and milling technology mark the beginning of a new area which will hopefully lead the pyroelectric industry to finally embrace nanotechnology. This work reviews the previous and current techniques used to crystallize RDX at a submicrometer scale or smaller. Several key points are highlighted then discussed, such as the smallest particle size and its morphology, and the scale-up capacity and the versatility of the process.

Review

Introduction

While nanotechnology has spread to nearly all other sub-fields of material science, the pyrotechnic community has struggled to produce very fine particles of organic explosives. Beside the technical considerations, scientists are also striving to convince the quite conservative military industry of the added value of energetic nanomaterials. While the interest in nanoparticles has been recently highlighted, companies continue with process optimization [1] and observe the technological breakthroughs of the last decades with caution. As a consequence, the innovation has been mainly focused on the synthesis and prediction of new molecules such as 1,3,3-trinitroazetidine (TNAZ), 2,4,6,8,10,12-hexanitro-2,4,6,8,10,12-hexaazaisowurtzitane (CL-20), octanitrocubane (ONC), 1,1-diamino-2,2-dinitroethene (FOX7), ammonium dinitramide (ADN), and 5-nitro-1,2,4-triazol-3-one (NTO). These new materials aim to achieve higher density, to increase the processability and to attain insensitive munition (IM) characteristics; however, IM properties actually rely on the whole physics-chemistry of the system.

Therefore, the development of powders with controlled particle size and morphology and well-defined surface chemistry is largely unexplored for energetic materials at the sub-micrometer scale and smaller. The criteria that are advantageous for new energetic materials include the following:

- high decomposition temperature
- low sensitivity
- no phase transitions under compression or depression
- no autocatalytic decomposition
- no voids from solvents or gas
- mechanical behavior independent from temperature
- good availability/cost ratio
- easy processing

The compression of gaseous inclusions, cavities and voids, deformation, frictional heating, intercrystalline shearing and spark discharge (electrostatic discharge (ESD)) are initiation processes which can cause areas of an energetic material to heat up to several hundred Kelvin. These areas are called hot spots and are deflagration or detonation origins if they reach a critical temperature. Tarver [2] calculated the critical temperature for octahydro-1,3,5,7-tetranitro-1,3,5,7-tetrazocine (HMX) of different sized hot spots. For a 2 µm diameter hot spot he calculated a critical temperature of 985 K, whereas the critical temperature for a 0.2 µm hot spot already rises to 1162 K.

Risse [3] measured a noticeable desensitization towards initiation by friction and electrostatic discharge for nanostructured 1,3,5-trinitroperhydro-1,3,5-triazine (RDX) crystallized by spray flash evaporation (SFE), compared to the raw material (Table 1). The noticeably lower sensitivity towards friction can be based on the self-lubricating effect, as small particles will tend to occupy small interstices instead of breaking. Sensitivity measurements were also performed on hexolite, which showed a clear desensitization of the nanostructured explosive (Table 2).

Table 1: Sensitivity towards impact, friction and ESD of micrometer-sized and nanostructured RDX (n-RDX) [3].

RDX	Impact [J]	Friction [N]	ESD [mJ]
M5 (raw material)	>3.52	160	120
nanostructured RDX	>3.52	>360	270

Using a sonocrystallization process, Bayat and Zeynali [4] succeeded in the preparation of n-2,4,6,8,10,12-hexanitro-2,4,6,8,10,12-hexaazaisowurtzitane (n-CL-20), which was less sensitive towards friction, impact and electrostatic discharge (Table 3).

Table 2: Comparison of the sensitivity levels of micrometer-sized hexolite with those of a nanometer-sized hexolite (n-hexolite) [3].

Hexolite	Impact [J]	Friction [N]	ESD [mJ]
micrometer	6	54	353.6
nanometer	25.06	72	436.6

Table 3: Comparison of the sensitivity levels of micrometer and nanometer-sized CL-20 [4].

Particle size [µL]	Impact [cm]	Friction [kg]	ESD [J]
15	25	6.4	45
0.095	55	no reaction	60

Klapötke has often experienced the influence of particle size on ESD, when stating for example ”the finer the powder of a particular (note from authors: RDX) sample is, the higher the ESD sensitivity values are” [5]. However, this trend is not always observed. Crystallized from rapid expansion of supercritical solutions (RESS), several nanometer-scale RDX (n-RDX) lots have been tested by Stepanov et al. [6]; while both 500 nm and 200 nm diameter RDX are less sensitive toward impact than milled 4 µm RDX, the 200 nm diameter lot is substantially more sensitive than the 500 nm one. As it can be seen in Figure 1, the minimum sensitivity to impact is confirmed when coating the powders with a binder; however, that confirmation might reveal that the trend is more due to the intrinsic bulk properties of the particles instead of their surface. Klaumünzer et al. [7] investigated the sensitization of n-RDX against impact and strongly reaffirmed that the generalization of a direct

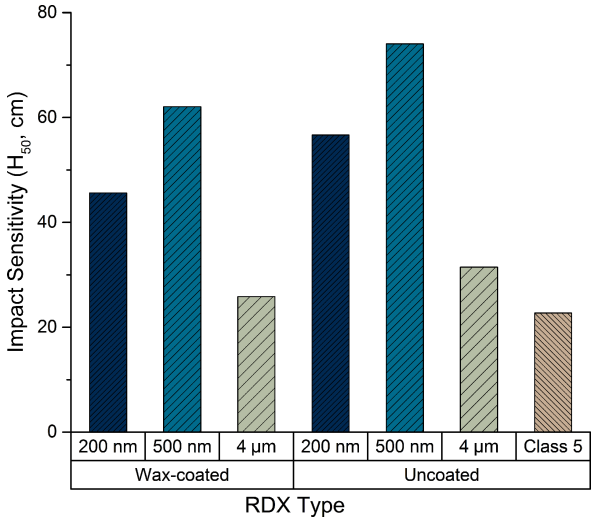

Figure 1: Impact sensitivity of RDX as a function of RDX type and particle diameter, adapted from [6].

link between smaller particle and lower impact sensitivity – as seen many times in the literature – should be more forcefully addressed.

Beside safety, other improvements can emerge from materials prepared on the nanoscale. The critical diameter, tunable detonation velocity, delay before the detonation steady state, etc. may be improved by the drastic grain size reduction. Energetic nanocomposites are also promising materials improved by a more intimate mixing. Liu et al. [8] showed that detonation velocities of PBX composition from their milled n-RDX and n-HMX materials are slightly better while being significantly safer. The burning rate of nitrocellulose was also improved by Zhang and Weeks [9] due to the formation of sub-micrometer spheres. Recently, Comet et al. [10] proved that energetic nanocomposites can easily replace the hazardous primary explosives to initiate a secondary explosive: 500 nm diameter n-RDX from SFE was mixed with a nanoscale thermite to initiate the detonation of PETN. The flame propagation velocity (FPV) of composites made of n-WO_3/n-Al/n-RDX can be tuned from 0.2 to 3.5 km/s through their explosive content. Under the same conditions, n-WO_3/n-Al with μ-RDX exhibit unstable regimes from 187 to 733 m/s, whereas the n-WO_3/n-Al/n-RDX composite deflagrates at a constant velocity of 2529 m/s. Those and other unpublished results from our laboratory confirm the drastic reduction of the critical diameter with the decrease of particle size.

1,3,5-Trinitroperhydro-1,3,5-triazine is also found under the following descriptors: cyclo-1,3,5-trimethylene-2,4,6-trinitramine, 1,3,5-trinitrohexahydro-s-triazine, cyclotrimethylenetrinitramine, hexahydro-1,3,5-trinitro-s-triazine, trimethylenetrinitramine, T4, cyclonite, hexogene and RDX. The most common and widely accepted one is the acronym RDX and is the one used in this present work. With nitro groups and a triazine cycle, it is chemically similar to many organic explosives and thus a good representative sample. Additionally, although it was created in the 1930s, RDX is still widely used for civilian and military applications, reinforcing its interest in industrial and scientific studies. Therefore, RDX has been used over the years as a reference for crystallization experiments, aiming to reduce the size of energetic organic crystals below a micrometer. Many crystallization processes inspired from other fields of chemistry, such as polymer crystallization, have been applied but only a few resulted in a significant size reduction.

The present review aims to fairly depict all the crystallization processes used on the same material, RDX, and the limitations encountered. The smallest particle size is of interest and will be offset against the maturity of the technology. The interest for a process can be also expressed according to its versatility and its ability to process continuously as per industrial standards. Such key points are further discussed in the conclusion. The classification suggested here is based on the final state of the particle formation. If a significant additional step is required to dry the particles, which is often because the crystallization occurs in a liquid that does not simultaneously evaporate or is not in a supercritical state, the technique is classified as a wet production method. There is only one notable exception, the aerosol solvent extraction system (ASES), sorted among the supercritical processes for a better understanding. Melting and milling processes for producing sub-micrometer energetic materials require one or more additional liquids, therefore these techniques are classified as wet methods.

Wet production methods

Crystallization from solution

Crystallization from solution has been studied but also used at the industrial scale for centuries. From solution, hydraulic processes can be easily monitored, controlled, and continuously operated. Therefore, substantial efforts have been made to scale the crystallization of energetic particles with existing technologies.

Depending on the creation of supersaturation, distinctions are made between cooling, evaporation, vacuum cooling, drowning-out and reaction crystallization. The study of the solubility of the compound is the key to determine which crystallization process can be used. For instance, if the solubility is not very temperature dependent, evaporation will be more effective than cooling. To our knowledge, no consistent study of the behavior of the solubility of RDX has been made. Fedoroff and Sheffield [11] indicate that the RDX solubility in acetone is reduced four times by cooling from 60 to 0 °C. Pant et al. [12] used all standard techniques available to recrystallize RDX into sub-micrometer crystals in a beaker. The smallest size was obtained when the antisolvent was added to a cooled, highly supersaturated solution, while applying ultrasonication and stirring. Achieving a high level of supersaturation results in a higher nucleation rate, but aggregation increases rapidly. For this solvent/compound system, they produced smaller particles and reduced the agglomeration by sonication and the particles were finally obtained by drying. This method may be suitable for industry, however, the minimum size obtained was only 850 nm under tough conditions, with a yield of 60%, resulting in rod-shaped crystals. Such morphology must be avoided due the well-established sensitization for materials with a high length-to-width ratio [13-15]. Increasing roughness due to surface defects also sensitizes the energetic materials.

Kumar et al. [16] succeeded in producing finer RDX particles by quickly injecting a very small volume (100 μL) of RDX dis-

solved in acetone into ultrapure water. The smallest mean particle size was 38 nm as determined by scanning electron microscopy (SEM) for the highest temperature (70 °C) and lowest concentration of RDX in acetone (5 mM). It is worth mentioning that dynamic light scattering (DLS) measurements were found to be not reliable when compared to SEM analysis, which can be explained by the lack of surfactant to stabilize the colloid. This technique was also applied on HMX [17] with a particle size around 30 nm and the same conclusions were drawn.

Bayat et al. [18], through an optimization of the microemulsion process, crystallized 80 nm plate-like β-CL-20 particles. The severe agglomeration and plate-like morphology could be due to the freeze drying and washing of the microemulsion. Gao et al. [19] recrystallized 1,1-diamino-2,2-dinitroethene (FOX7) in ethyl alcohol down to the sub-micrometer range. SEM pictures show an irregular plate-like morphology and therefore highlight the inconsistency of the unique mean particle size of 340 nm claimed. The particles also exhibit a certain degree of agglomeration which can be explained again by the pool of surfactant and the air-drying method used.

Luo et al. [20] reached an impressive mean diameter of 30 nm of RDX. They used an unusual technique where RDX is dispersed in bacterial cellulose. The smallest particle size was obtained with a 71% RDX/gelatine mixture. However, increasing the content of RDX leads to an increase in the particle size and the maximum RDX loading tested was 91% resulting in a mean particle diameter of 50 nm. The sensitivity of this composite towards impact and friction was reduced by two times, therefore questioning the reactivity. Nevertheless, further efforts were made to replace the bacterial cellulose with an energetic matrix.

Crystallization in solution allows the formation of large crystals by growth, thus allowing more parametric studies regarding the influence of solvents. For instance, one work [21] has studied the importance of temperature and supersaturation for the crystallization for HMX in γ-butyrolactone, revealing that low temperature and highly supersaturated solutions tend to increase the defects in HMX crystals.

Solvent substitution using reverse micelles

Dabin et al. [22] have developed an ingenious method to prepare nanometer-scale RDX using a simple technique. The crystallization is triggered by a solvent substitution, and the nanometer scale material is obtained by restricting the reactor volume using reverse micelles. NaAOT (sodium 1,4-bis(2-ethylhexoxy)-1,4-dioxobutane-2-sulfonate) with isooctane was used to form reverse micelles. Then RDX in dimethylformamide (DMF) is added to one solution containing these micelles, and water to another solution of micelles. Both are finally mixed together to form the n-RDX with a diameter of 70 to 100 nm. However, the nanoparticles produced from this elegant solution exhibit an undesired rod-like morphology.

Sol–gel

Energetic materials processed by the sol–gel method are desensitized by being embedded in a matrix, usually a silica one. Developed by Gash et al. [23] and Tillotson et al. [24,25], the silica explosive gels are prepared by dissolving the energetic compound, the silica precursor and a catalyst in a co-solvent. After the gelification, an antisolvent of the explosive is injected to replace the solvent in the pores and precipitate the explosives in the silica matrix. By drying with heating or at low pressure, a xerogel with higher density is obtained. If supercritical CO_2 is used to extract the solvent, an aerogel with low density is formed. Therefore, the nanostructured nature of the explosive comes from the porous matrix: cavities of mesoporous gels are 2 to 50 nm large and less than 2 nm for microporous gels. Macroporous materials have pore diameters greater than 50 nm [26].

An RDX/resorcinol formaldehyde (RF) nanocomposite has been synthesized [27] where 38 nm RDX crystallized in an RF aerogel matrix with a surface area of 551.5 m^2/g (measurement taken without RDX). Wuillaume et al. [28] trapped ammonium perchlorate (AP) and RDX in a mesoporous low-density energetic organogel. During the impact test, a negligible decrease of sensitivity was measured: 75 wt % RDX nanogels and macrogels had the same sensitivity and the 90 wt % nanogels are even more sensitive than their macroscopic counterparts. When compared to pure RDX, the 90 wt % nanogels are not desensitized. However, small scale gap tests (SSGTs) preformed on pressed gels (95% TMD) revealed an improvement of the sensitivity for the 90 wt % RDX nanoformulation. The nanogel exhibits an uncommon microstructure of sheets, with micrometer-sized particles potentially formed by primary nanoparticles. The lack of desensitization in the loose powder may be explained by the sensitization by the sheet-like shape counteracted by the presence of the gel coating each nanoparticle.

Li et al. [29] used a better energetic matrix, GAP, with a maximum of 40 wt % RDX. They noticed a lower sensitivity than the physical mix. However, the claimed nanometer diameter is only deduced from the porosity without RDX and from X-ray diffraction (XRD) patterns which only give the mean coherence length. They also created NC-RDX-AP nanocomposites using a technique similar to sol–gel [30]. The matrix is the NC itself solidified by micrometer-sized AP crystals and cross-linked with toluene diisocyanate (TDI) and dibutyltin dilaurate (DBTDL), whereas RDX is dissolved in acetone inside that

template. The gel and the crystallization of RDX is triggered by supercritical CO_2 drying. Even if the sensitivity and the density were not improved, the increase of the heat of explosion measured and the originality of the approach make the formation of a nanocomposite based entirely on energetic materials through chemical binding promising.

Melting

Many high energetic materials degrade very close to their melting point. Therefore, only a few such as 2,4,6-trinitrotoluene (TNT) or TNB can be used in the molten state since the melting temperature is at least 100 °C away from the exothermic decomposition. The melt–cast process of TNT-based compositions has been used for shaping charges or loading them into ammunitions since World War I. Crystallization from an emulsified molten explosive is an innovative technique used by Anniyappan et al. [31]. 2,4,6-triazido-1,3,5-triazine (or cyanuric triazide, CTA) has been processed at 95 °C to crystallize as micrometer-sized agglomerates. CTA is a promising primary explosive compliant with the new REACH legislation [32] forbidding the use of heavy-metal-based materials. Further investigation with surfactants might lead to smaller particles by counteracting the high viscosity of molten droplets.

Milling

Redner et al. [33] developed a batch wet-milling process, producing sub-micrometer RDX. A mixture of water, isobutanol, a dispersant and RDX was filled into an unspecified mill, resulting in a minimum mean particle size of 310 nm and a crystallite size of about 65 nm. Several milling issues were mentioned such as the yield of about 25% and the importance of the residence time and the drying step.

Liu et al. [34,35] studied the effect of drying n-RDX and HMX samples under various conditions. They first obtained n-RDX in solution from a mixture of water, ethanol, isopropanol and RDX. The suspension was put in a bidirectional rotation mill for 6 h. Just as Rednere experienced, the drying process is a critical step to obtain a nanogranular powder. They dried the RDX under different conditions: freeze drying and supercritical drying led to quite impressive results, with median diameters of 160 nm and 200 nm, respectively from a solution containing an average particle size of 64 nm. After RDX and HMX, CL-20 was successfully processed the same way resulting in a median diameter of 180 nm, as determined by SEM [8]. For the three compounds, the nanopowders were found to be less sensitize than their micrometer-sized counterparts.

Spray drying is a less energy intensive RDX drying method studied by Patel et al. [36]. RDX and CL-20 were bead milled from water with the addition of isobutanol and poly(vinyl alcohol) (PVOH) to stabilize the colloid by dispersion and coating. Then, an unknown polymeric binder was added just before drying the slurry by spray drying. Mean particle diameters down to 400 and 200 nm have been measured by DLS for RDX- and CL-20-based composites, respectively, after milling. However, no particle size distribution (PSD) curve was provided nor was the dispersion of the results indicated. It has been noticed that for 200 nm particles of CL-20 the α phase is obtained. From the same research group, nanoscale CL-20:HMX has been prepared by bead milling an aqueous suspension of ε-CL-20 and β-HMX in a 2:1 stoichiometric ratio [37]. The progressive conversion of raw materials into the co-crystal is achieved after one hour, resulting in a particle diameter of less than 200 nm. However, not much attention was paid to the drying effect of large-scale batches. SEM and XRD measurements were performed on a drop-dried material at room temperature, and it is likely that the drying of several grams of such molecular crystal will behave differently. Furthermore, the accuracy of the XRD technique does not allow one to conclude that a complete conversion into the co-crystal has occurred, but rather indicates that the percentage of ε-CL-20 and β-HMX is lower by approximately 10%. The full quantification by Rietveld or full pattern matching methods would have been useful to follow the conversion with time.

Dry production methods

Physical vapor deposition (PVD)

In 2002, Frolov and Pivkina first reported on a vacuum condensation process for high energetic materials [38-40]. The vacuum deposition of ammonium nitrate (AN), RDX and a composite AN–RDX was performed on a cooled quartz substrate. The mean particle diameter was directly measured from atomic force microscopy (AFM): a diameter of 50 nm was obtained for the three materials, even after processing the nanopowder (removal from the quartz substrate and pressing into tablets).

Mil'chenko et al. [41] delved further in the physical vapor deposition (PVD) process with the deposition of 2,4,6-triamino-1,3,5-trinitrobenzene (TATB), HMX, RDX, PETN and BTF as thin layers on several substrates such as plexiglas and copper while changing operative parameters. The critical thickness of the detonating layer is an order of magnitude lower; the sensitivity toward impact and friction is barely mentioned as being similar to the raw materials but the sensitivity to laser excitation has been substantially increased.

Therefore, the PVD technique is highly suitable for pyrotechnic integrated circuits or micro-electromechanical systems [42,43], whereas mass production of loose powder is not economically viable.

Electrospray

Radacsi et al. [44] crystallized sub-micrometer RDX using an electrospray technique. A solution of RDX/acetone is sprayed through a nozzle that is electrically charged to a grounded plate. This charges the droplet surface, increasing the surface energy and thus triggering the fission into smaller droplets. This Coulomb fission phenomenon and the evaporation of the solvent leads to crystallization and the deposition of nonagglomerated particles. By adjusting the nozzle parameters and the potential difference various morphologies of RDX particles resulted. For instance, micrometer-sized hollow spheres of agglomerated RDX were produced. The minimum mean size was 400 nm. This sub-micrometer RDX sample exhibited a clear insensitivity towards friction, but with the same impact sensitivity as conventional micrometer-sized RDX (Table 4).

Table 4: Comparison of the sensitivity levels of conventional and 400 nm diameter RDX.

RDX	Impact [J]	Friction [N]
conventional	7.5	120
sub-micrometer	10	>360

Reus et al. [45] then processed bicomponent systems: proteins and RDX/TNT. It is mentioned that the XRD patterns of the final products differ from that of the raw material, which seems to indicate either a strong degradation or cocrystallization. Infrared spectroscopy definitely demonstrated a critical partial decomposition of both RDX and TNT due to the electrospray technique and the same phenomenon has likely happened for Radacsi et al., too. Whatever was really obtained, Reus crystallized very small particles, estimated by us to be less than or approximately 100 nm for any initial ratio of TNT/RDX. AFM measurements could have provided much more information about the size and shape of such nanoparticles, especially since they are well dispersed on a substrate. The sensitivity tests have been performed on those degraded materials, which were found to be as insensitive as TNT.

The electrospray technique can be used to create a fine spray of micrometer-sized charged droplets repelling each other, which is ideal for crystallization. The high voltage needed is a major handicap for processing sensitive powders such as energetic materials containing nitro groups.

Plasma

During his Ph.D. project [46], Radacsi used an innovative and advanced technique to crystallize sub-micrometer RDX: a collison nebulizer that aerosolizes an RDX/acetone solution to a surface dielectric barrier discharge (SDBD) plate where a cold plasma disrupts the droplet by the Coulomb fission. Like the electrospray technique, each droplet should crystallize into a unique single crystal. The minimum mean diameter obtained was 500 nm, with a diameter distribution from 200 to 900 nm, and the particles had a prismatic or spherical shape. Again, like the sub-micrometer powder obtained from the electrospray technique, the 500 nm RDX was desensitized to friction but not to impact (Table 5).

Table 5: Comparison of the sensitivity levels of conventional and 500 nm diameter RDX [46].

RDX	Impact [J]	Friction [N]
conventional	5	144
sub-micrometer	5	>360

Supercritical/gas antisolvent precipitation

Supercritical antisolvent (SAS) precipitation uses the same principle as liquid crystallization, substituting the liquid antisolvent by a supercritical fluid. The very high diffusivity of supercritical fluids leads to a rapid supersaturation and thus to a sudden precipitation. Various approaches are used in SAS. One is the supercritical antisolvent (GAS) precipitation, where the liquid solution is first loaded into the vessel before the addition of the supercritical antisolvent. For RDX, CO_2 is an appropriate supercritical antisolvent. Gallagher et al. [47] first investigated the use of the GAS process for RDX in 1992. Supercritical CO_2 injected into an RDX/cyclohexanone solution at various injection times, injection quantities and temperatures. In this first use of GAS for RDX, various particle sizes and morphologies were obtained, but none under the micrometer scale. Since then, several process derived from the GAS process (which could be referred as SAS subprocesses) have been used to form particles on the sub-micrometer and nanoscale for energetic materials. However, since 1992, no GAS/SAS process has been reported to produce energetic materials with a diameter less than a micrometer [48-51], except for 5-nitro-1,2,4-triazol-3-one (NTO) by Lim et al. [52,53].

Aerosol solvent extraction system (ASES) process

The aerosol solvent extraction system (ASES) process involves precipitation through spraying the solution through an atomization nozzle into supercritical CO_2. Lee et al. [51] used GAS and ASES systems to crystallize β-HMX. However, undesirables shapes (needle-like, irregular and aggregated) were produced by ASES at all operating conditions, whereas GAS led to regular shapes with the desired β-phase. Dou et al. [54] sprayed RDX dissolved in DMF to obtain micrometer-sized particles of high polydispersity. However, sub-micrometer-sized polymers and biopolymers produced by ASES have been reported since the

1990s by Reverchon [55] and Dixon et al. [56]. Nevertheless, that technique can still be used on NC-based composites due to its polymer-like behavior.

Solution-enhanced dispersion by supercritical fluid (SEDS)

The solution-enhanced dispersion by supercritical fluid (SEDS) process was developed and patented by the Bradfort University to achieve a smaller droplet size compared to the previously described SAS methods. In the SEDS process, a solution with the solvated compound is sprayed into a supercritical antisolvent gas (CO_2 for RDX) through a nozzle with two coaxial passages. This technique can be seen as a specific implementation of the ASES process, where CO_2 is introduced through the nozzle simultaneously with the solution. Shang and Zhang [57] produced spherical RDX particles with a mean particle diameter of 770 nm using SEDS, which finally resulted in the reduction of the particle size under to less than a micrometer.

Particles from gas-saturated solutions (PGSS)

Two patents ([58,59]) first described a procedure that today is called particles from gas-saturated solutions (PGSS). The PGSS technique consists of dissolving a compressed gas into a solution of the substrate in a solvent, then passing it through a nozzle. The sudden decompression leads to crystallization and thus to the formation of solid particles. Although this method is widely used on a large scale with a wide range of products (from inorganic powder to pharmaceutical compounds [60]), nothing has been reported [49] concerning energetic materials processed by PGSS.

Rapid expansion of supercritical solutions (RESS)

The rapid expansion of supercritical solutions (RESS) concept was first described by Hannay and Hogart more than a century ago [61] but studied by Krukonis [62] and the Battelle Institute research team [63,64] in more detail. The RESS process consists of spraying a supercritical (sc) fluid containing the substrate through a nozzle in a low pressure chamber (0–60 bar). The sudden pressure decrease leads to rapid nucleation where small particles (from micrometer- to nanometer-sized) are finally collected. The use of a supercritical fluid like CO_2 allows the direct production of a dry, pure powder. Teipel et al. [48,65] first reported the use of RESS for energetic materials: 10 μm diameter TNT particles were crystallized in those preliminary experiments. In this work, parameters which strongly influence the crystallization in a RESS apparatus were discussed: pressure, temperature, geometry of the nozzle and mass flow. Stepanov, a member of the research group of Krasnoperov, succeeded in the fine tuning of the RESS process to prepare dried n-RDX [66-69]. The formed n-RDX particles had a mean particle diameter ranging from 110 to 220 nm and an irregular spherical morphology. He performed a scale-up of the RESS process in order to increase the production capacity of RDX to 6 g/h but with a CO_2 consumption of 35 kg/h. Through RESS, a slight sensitization to impact and shock stimuli of the 200 nm RDX occurred compared to 500 nm RDX [6].

CL-20 has also been processed by RESS from trifluoromethane (CHF_3) [53]. Supercritical CHF_3 has similar thermodynamic properties and is a better solvent of CL-20 than $scCO_2$. Only micrometer-sized particles could be produced and no article reporting the results could be found. Changing the solvent is an area of research followed by Lee et al. [70] using compressed liquid dimethyl ether (DME) for RDX. The parametric study points out the role of inlet pressure and temperature and the nozzle diameter. The increase of any of those three parameters increases the particle size. Therefore, the two minimal mean particle sizes of 370 and 360 nm were obtained for the lowest mass flow rate of 0.37 and 0.85 g/s of DME.

Rapid expansion of supercritical solutions into an aqueous solution (RESS-AS) (or RESOLV)

After the success of the RESS process, Essel et al. developed a new method based on that technique called RESS-AS, which as first reported in 2010 [71]. RESS-AS uses the versatility of the RESS process, while spraying into an aqueous solution containing a dispersant and/or growth inhibitor [72]. They reported [73] the synthesis of 30 nm RDX in a pH 7-stabilized solution. For such sizes and even at that pH, agglomeration and Ostwald ripening occur. Therefore, to avoid the degradation of the nanoparticles, a polymer coating (PEI or poly(vinylpyrrolidone) (PVP)) is necessary. It should be mentioned that no subsequent sensitivity tests have been reported, provoking the question about whether a nanopowder could have be obtained from those colloidal suspensions.

Laser ablation

For the first time, Gottfried et al. [74] successfully produced RDX nanoparticles using laser ablation. A near-infrared, nanosecond pulsed laser was focused on military-grade RDX pellets. The scanning mobility particle sizer (SMPS) and SEM analyses showed a particle size distribution around 64 nm for a 200 mJ pulse and a 75 mJ pulse. No further analysis has been reported, such as trace decomposition, crystalline quality, apparent density, sensitivity, etc.

Ultrasonic spray pyrolysis

Since the nineties, spray crystallization and synthesis has been performed using several atomizers, and among them piezoelectric transducers [75,76]. As a spray technique, the goal is to produce one particle per droplet, but here the crystallization is controlled by the drying step, an oven just after the atomization.

Spitzer et al. [77,78] and Kim et al. [79] both developed an apparatus to produce dried sub-micrometer RDX from an ultrasonic transducer. After the droplet generation, the solvent is evaporated by thermal gradient applied on the flux pulled by a pump. Highly agglomerated particles 200–500 nm were produced. Gao et al. [19,80] used the same experimental setup – while the previous works of Spitzer et al. and Kim et al. are never cited – with the exception of the furnace having here a gradient of temperature in order to produce 78 nm FOX7 particles and sub-micrometer-sized CL-20:HMX cocrystals. The claimed large-scale synthesis has not been fairly investigated. For instance increasing the number of piezoelectric transducers and scaling up the furnace would require excessive amounts of electrical power, thus making the cost-effectiveness of this method doubtful.

Spray drying

The development of spray drying [81,82] has been expanding over the years and has recently become a suitable commercial solution at both R&D and industry scales to produce dried particles from micrometers to nanometers. The pyrotechnic community quickly discerned the advantages of this simple technique to process energetic compounds as pure and composite materials.

The process sprays a solution containing a dissolved compound or particles in suspension into a hot gaseous stream (air or nitrogen) thus crystallizing into particles and/or drying the granules. van der Heijden et al. [83] showed that spray drying is able to crystallize finer RDX particles ("from 400 nm and larger") than their technique of precipitation into antisolvent (1 to 10 μm). Qiu et al. studied the crystallization of energetic compounds using spray drying with ultrasonic [84] or pneumatic [85] nozzles or with both type of nozzles [86]. All their experiments were done with the addition of poly(vinyl acetate) (PVAc) and resulted in micrometer-sized or sub-micrometer hollow spheres made of primary nanoparticles; the smallest of which were estimated at 20 nm for RDX/PVAc made from a pneumatic nozzle with a mean droplet size of around 7 μm. The versatility of the process allows the production of energetic composites (coating of TATB on micrometer-sized HMX, RDX or CL-20 by Ma et al. [87]), energetic/elastomer composites (micrometer-sized CL-20/EPDM by Ji et al. [88], micrometer-sized spheres of agglomerated HMX/Viton by Shi et al. [89]), and even co-crystals (micrometer-sized spheres of agglomerated HMX/TNT by Li et al. [90]).

Spray flash evaporation (SFE)

Risse and Spitzer developed an innovative process after experiencing the limitations of the ultrasonic spray pyrolysis method: beyond the inherent risk of using a high voltage electrostatic precipitator for energetic powders, the rate of evaporation of droplets was too low to avoid agglomeration and to crystallize sub-micrometer particles. Risse et al. [3,91] used the flash-evaporation behavior of droplets to dramatically reduce the lifetime and the size of droplets. The compound is dissolved in a volatile solvent and that solution is heated just before being sprayed into vacuum, where the crystallization is triggered by the sudden temperature depression and the solvent evaporation. Due to the recent advances in that technique and its versatility, the spray flash evaporation (SFE) process deserves the following review of the corresponding literature.

Theoretical insights on the SFE technology

Flash evaporation is the physical phenomenon occurring when the boiling point of a liquid is lower than its actual temperature due to a sudden drop of pressure and/or a quick increase of temperature. The excess heat is instantly converted into latent heat of vaporization, cooling both liquid and vapor down to the saturation temperature. Multistage flash (MSF) evaporators of static water have been used since the middle of the 20th century [92-94] with yield of around 100 m^3 per day, receiving interest mainly from the U.S. West Coast [95] and Japan (national research program "seawater desalting and by product recovery" launched in 1969, [96]). Current applications are extended from solution concentration such as in wine industry [97] to heat dissipation of electronic chips and laser devices [98].

Brown and York [99] found a critical temperature above which the liquid jet burst by rapid bubbling. They injected water up to 13 bar through simple single-hole nozzles with a minimal diameter of 500 μm into ambient pressure. The linear mean droplet size was found to follow a linear variation of temperature. Then, in 1981, Miyatake et al. were pioneers in the field of flash evaporation and published the first known articles about spray flash evaporation with superheating [100,101], after studying flash evaporation from water pool [102]. Many technical limitations restricted their studies for current issues: only straight-lined liquid jets were studied with basic optical techniques where the smallest drops and bubbles could not be indexed. However, Miyatake et al. [103] interestingly used electrolysis to generate more bubbles into a flashing water jet. Nowadays, not many laboratories still investigate flashing liquid jets. Guenther and Wirth [104] characterized flashing liquid jets with modern techniques and noticed the formation of bubbles inside a glass nozzle for high superheating. They also demonstrated that a simple acoustic measurement can be used to monitor the atomization of superheated liquids. The current application of flashing liquid jet is the improvement of MSF desalination processes of sea water [105,106], where a much higher evaporation rate is obtained in contrast to static flash evaporation where the rate is surface dependent.

We mentioned applicative publications for now, but specific studies on the flashing phenomenon of droplets are rare. Owen and Jalil [107] investigated that specific form of evaporation on isolated drops. A superheating of 0 to 5 °C triggers only surface evaporation, then boiling occurs at higher superheating. Flashing is triggered for superheating from 18 to 24 °C for a drop of 1–3 mm and larger drops flash more readily as illustrated in Figure 2. Since flash evaporation is closely related to cooling, many theoretical approaches start with a simplified model without superheating: Shin et al. [108] and Satoh et al. [109] thoroughly described the evaporation behavior of a water droplet in an abruptly evacuated atmosphere leading to its solidification. Sobac et al. [110] developed a comprehensive model of the evaporation of a liquid spherical drop that is not applicable to extremely small droplets as in flashing spray.

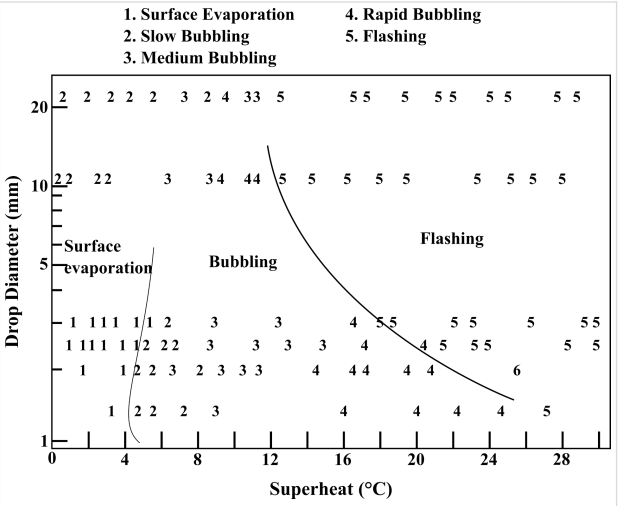

Figure 2: Empirical diagram of the evaporation of a water drop, adapted from [107]

Interesting studies close to the current SFE process came from Gebauer et al. [111-114]. In their system, a pressurized, superheated liquid is atomized through an hollow cone nozzle into a low pressure chamber and micrometer-sized particles are recovered. However, only a partial evaporation occurs and leads to further crystal growth during the flight time and is deposited in the sump collected in the bottom of the crystallizer.

Comprehensive description of SFE

Figure 3 describes a standard SFE apparatus, where two zones can be distinguished: a high pressure one is in red and the low pressure one in blue. One storage tank (**4**) is used for technical operation such as preheating, postcooling and cleaning and is filled with technical grade solvent. The compounds of interest are dissolved in solvent in an other tank (**1**). Both tanks are pressurized with a dry carrier gas up the pre-expansion pressure. the fluid is brought inside the atomization chamber at this pressure using standard industrial hydraulic tubes; there, the liquid is superheated within a jacket around a metallic heat conductor. A regulation is made within a thermocouple (type K, diameter 1.5 mm) plugged to a proportional/integral/derivative (PID) controller and inserted in the the tubing. Details can be seen in Figure 4: the tip of the thermocouple measures the temperature after the heating jacket and just before the nozzle mounted on a full flow quick coupling. The superheated fluid is then sprayed through a hollow cone nozzle (**3**) into a chamber at a vacuum below 10 mbar.

Figure 5 illustrates the recovery system of the solid particles from the gaseous flow coming from the evaporation. The cyclonic separators are made from the description of Chen and Tsai [115] who calculated a cut-off diameter of 21.7–49.8 nm. A glass flat flange reaction vessel allows one to gather the powder easily. One cyclone separates the aerosol, while the other unit can be isolated from the vacuum to recover the product. In this way the process operates continuously, spraying and separating the aerosol at any flow rate. At the end, the flow of gaseous solvent passes through a 35 m^3/h vacuum pump; a

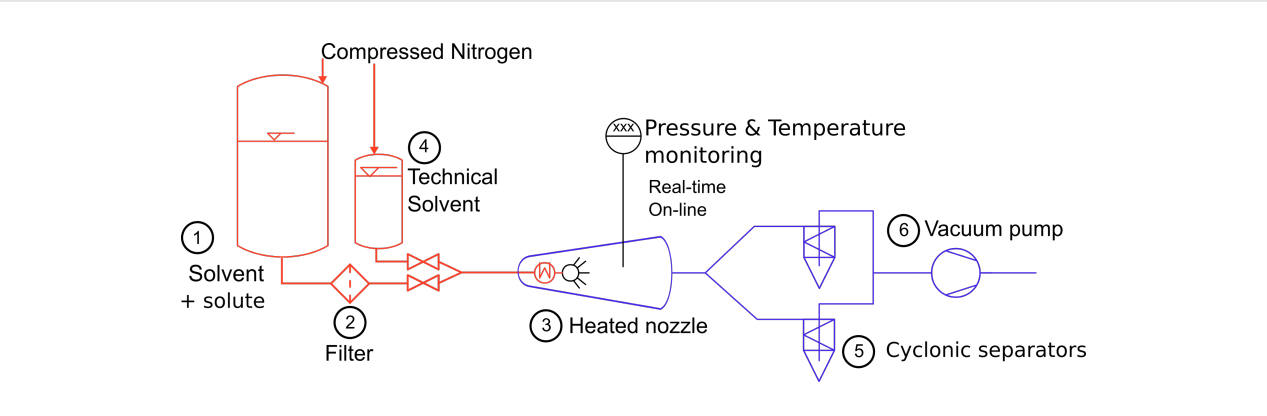

Figure 3: SFE installation as patented and used in this present work

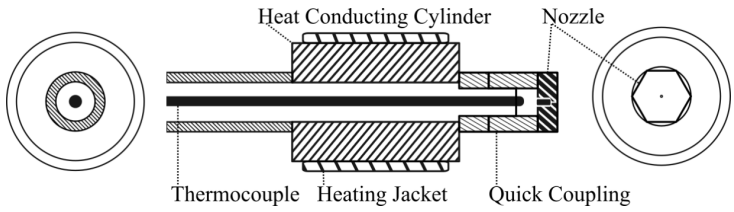

Figure 4: Schematic cross-sections of the nozzle and its heating system; from left to right, rear view, longitudinal cross-section and front view.

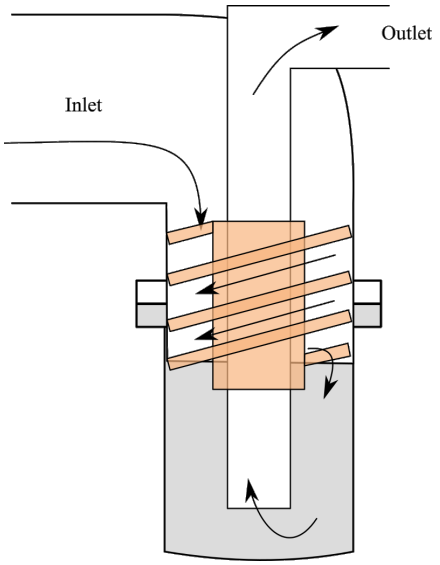

Figure 5: System for the product recovery: the cyclonic separator for vacuum (orange) and the interchangeable vessel (grey).

condenser after the pump can recover the solvent for industrial installations. The standard operating conditions are: 40 bar of inlet pressure, 160 °C at the hollow cone nozzle, and an orifice diameter of 60 µm.

Versatility of SFE

The following parameters of SFE can be adapted, according to the solute and the desired particle size range:

- Type of solvent: The most suitable solvents for SFE are those having a low boiling point in the range of 30–70 °C. A high molar heat capacity helps to stabilize the fluid in its superheated state.
- Superheating temperature: Higher superheating temperature increases the evaporation rate, as mentioned earlier. The superheating temperature depends on the mass flow, the heat exchanger (surface, geometry and residence time) and the fluid properties.
- Pre-expansion pressure: The pre-expansion pressure has to be above the vapor pressure of the superheated solvent. That pressure should also be compatible with nozzle diameter and type, with for instance an operating range from 30 to 150 bar for sub-millimeter nozzles. The droplet size is also known to decrease at higher pressures. However a higher pressure involves a higher flow rate, and a degradation of the superheating.
- Saturation pressure and temperature: The vacuum pump specifications mainly dictate the saturation pressure and temperature of the spray cone in the atomization chamber. The volume and geometry of the chamber and the ones of the whole vacuum piping system have only a minor influence when reaching high pumping flow rate.
- Nozzle diameter: For most nozzles types like hollow cone nozzles, full cone nozzles, or flat jet nozzles, a reduced orifice diameter decreases the droplet size; it also increases the preexpansion pressure needed to guarantee a fine spraying.

Besides the innovative applications of energetic nanomaterials, such as the synthesis of ultrafine nanodiamonds [116,117] and reactivity enhancement [10], the versatility of SFE allows the crystallization at a sub-micrometer or nanometer scales of a wide range of organic compounds. In particular, cocrystals of medical materials are of interest for drug enhancement and were successfully processed through SFE at the nanoscale [118]. Inorganic nanoparticles were also produced on the nanoscale through SFE by Klaumuenzer et al. [119]. ZnO was crystallized from the precursor zinc acetate dihydrate dissolved in ethanol with addition of water. From early experiments, primary nanoparticles of 20 nm were found to be agglomerated in sub-size structures, whereas the slightly larger nanoparticles were found much less agglomerated using the classical wet method. However, the SFE clearly demonstrated the feasibility of faster and quite efficient crystallization of inorganic particles from precursors. Le Brize and Spitzer [120] processed energetic composite materials by SFE: a sub-micrometer structure was evidenced from SEM pictures and an higher degree of chemical interaction was also found from IR and Raman spectra. The high versatility of the SFE permits the processing of

liquid (poly(ethylene glycol) (PEG) 400) and solid (PVP 40k) polymers to tune the RDX particle size distribution from the nanometer to the micrometer scale with controlled shapes [121]. The smallest particle diameter obtained was at 160 nm with a spherical morphology. Adding 0.05 wt % of PVP decreased the size of RDX by 34%, from around 500 nm to 320 nm, but also significantly improved the spheric shape. Additionally, all the synthesized RDX samples were less sensitive, especially toward electrostatic discharge.

Conclusion

As displayed in Table 6, the smallest diameter of RDX is either obtained from wet techniques or from small-scale approaches which cannot be transferred to industry (PVD and laser ablation). Even if PVD has been successfully used in the semiconductor sector for our everyday electronic devices for decades, PVD applied on energetic materials will never be able to reach a production of several hundred of grams per hour. However, PVD is suitable for the current trend to create ”pyrotechnic integrated circuits”. Femtosecond laser ablation is used for nanoparticle synthesis of metal in solution at the laboratory scale. The colloids produced are found to be extremely stable. Used in dried conditions, a deposit of nanoparticles on a substrate could be obtained from a gas flow, or a dried powder could be collected within a cyclonic separator. This laser-based technique has been used to cut high energetic material quite safely [122] but nanoparticle production would be severely limited to high-added-value industrial applications due to low production rate and high operation cost. Besides those two aspects, neither methods would process advanced composites, with a binder for instance, or would be able to do concomitant or co-crystallization.

The production of nanoparticles through wet techniques has become a common industrial chemical process. The European project, Sustainable Hydrothermal Manufacturing of Nanometerials (SHYMAN), aims to increase the production rate of a continuous hydrothermal process from 1–10 tons/year to 100 tons/year for inorganic nanomaterials [123]. Tsuzuki et al. [124] statistically studied which methods for inorganic nanosynthesis are mostly employed in industry: vapor (39% mainly chemical vapor deposition (CVD)) and liquid (45%) phase synthesis are the two main types of techniques. Since patents or brand marketing can restrain the choice of a technology, this distribution should not be interpreted as a way to estimate the robustness or versatility of the methods. Considering such wide adoption of wet techniques [125] and the knowledge from chemical engineering (homogenization in large reactor, processing of liquid flow, versatility, safety etc.), wet crystallization methods are a logical choice to process organic materials. However, unlike inorganic and metal nanoparticles, organic matter is very sensitive to drying as we previously saw for milling. Yet this delicate step is required since the reactivity of high energetic materials is fully exploited in the dried state. Freeze drying and supercritical drying seem to kinetically and partially prevent crystal growth from occurring. Only a complete growth inhibition will lead to the production of smaller nanoparticles under 100 nm from milling or antisolvent/cooling crystallization. From an industrial point of view, freeze or supercritical drying are batch-only processes. All current industrial drying process are not designed to tackle the fast growth of soft matter. Innovative techniques such as spin freezing [126] or spray drying enhance the processability, and potentially the performance, but the rigorous testing of their reliability is yet an open issue.

Table 6: Comparison and summary of the major techniques for the nanocrystallization of energetic materials with an industrial point of view.

Process	Working pressure(s)	Heating (°C)	Continuous	Scale-up	Limiting step(s)	Smallest size[a]
Sol–gel	atmospheric	no	no	−+	matrix, drying	100–150[b]
Antisolvent	atmospheric	70	could be	−	injection, drying	38
Milling	atmospheric	cooling	no	+	drying	160[c]
PVD	10^{-4} Pa[d]	100–200	no	−−	vacuum	50
Electrospray	atmospheric	no	could be	−	mass flow, electric field	400
ASES	12 MPa	yes and cooling	no	−−	$scCO_2$[e]	micrometers
SEDS	35 MPa[d]	yes	no	−−	$scCO_2$	micrometers
RESS	35 MPa → 0.1–5 MPa	yes and cooling	could be	−+	$scCO_2$	200
RESS-AS	35 MPa → atmospheric	25	could be	−+	$scCO_2$, drying	30[f]
Laser	atmospheric	no	no	−	mass flow	64
Ultrasonic	atmospheric	50–150	could be	−+	transducer	200–500
Spray drying	atmospheric	50–100	could be	++	evaporation ratio	400
SFE	5 MPa → 5 mbar	150	yes	++	vacuum	300

[a]Smallest pure RDX mean diameter reported in nm; [b]XRD measurement; [c]Freeze-dried from a 64 nm RDX slurry; [d]Not available in the references, so the value is based on usual operating conditions; [e]supercritical carbon dioxide; [f]From DLS, no report about dried state.

The ball milling techniques raise concerns about the purity of the product. It is well know that after such an extensive friction process, industrially milled ceramics cannot be used for high purity chemical processes [127]. Industry moved to other techniques such as vapor phase-based techniques to overcome that limitation in addition to others like the lake of control, local heating etc. Even with soft matter, similar issues can be expected; even small quantities of metallic impurities could catalyze the degradation of the explosive and/or sensitize it.

After 25 years of research and 10 years of process engineering, the supercritical fluid (SCF) technology has not convinced the industry and only marginal use for the specific commercial drug products have been reported [125]. First, the choice of the gas at industrial scales is returning to CO_2 due to safety and affordability criteria. For instance, gases such as nitrous oxide or ethane have low critical values, but explosive mixtures can be generated. Trifluoromethane is inert, nonflammable and is usually a better solvent, but is significantly more expensive than CO_2 and a potent greenhouse gas. Second, the main limitation, the solubility into $scCO_2$, can be overcome by the addition of an organic cosolvent. Such a modification alters the environmentally safe nature of $scCO_2$-based SCF and complicates the process by the need to remove any residual organic solvents. The aggregation phenomenon is commonly observed in SCF processes; further investigations on the role of different particle collection environments are needed, but RESS-AS processes greatly avoid the particle aggregation. The use of a liquid antisolvent with polymeric stabilizers has been found to be very effective. However, it compromises the recovery of a dry, pure powder, going back to square one with the drying issues previously discussed.

Spray techniques are commonly used in the industry, such as microencapsulation massively used for food [128,129], spray drying in pulmonary drug delivery for production of uniform and breathable size particles [130] or even thermal spray deposition of metallic material [131]. Spraying is a method which allows easy implementation of an installation and easy direct control over the injection. However, because of the low technological cost of atomizing nozzles and the low control over the spray itself, details and know-how are much more important than for other processes. Direct spray drying as a crystallization technique for RDX does not produce sub-micrometer-sized particles without the help of an additive and the SCF techniques are not suitable for industry. The need for an intermediate method in terms of pressure and temperature leads to the creation of the SFE technique, especially tailored for crystallization. SFE operates from 40–100 bar with an RDX solubility in acetone around 5 wt %, whereas $scCO_2$ is formed from 74–500 bar for a solubility from null to 0.025 wt %.

The SFE technology has proven its high level of versatility and reliability, and is now entering advanced stages of development. Scale-up studies are performed and advanced in situ characterization is under investigation. Preliminary results using phase Doppler interferometry (PDA) reveals that SFE produces micrometer sized droplets with high velocities, typical features of interest for metastable crystalline structures.

For a deeper understanding of the crystallization of energetic materials at the nanoscale, a better comprehension of the resulting powder is needed. Beyond the issue of the reliability of the sensitivity values of energetic materials at the nanoscale [132] and tested at the laboratory scale [133], the pyrotechnic community should actively discuss the repeatability, the agglomeration of particles and the particle size distribution with accurate peak fittings.

Supporting Information

Supporting Information File 1

CSV data on fine energetic materials.
[http://www.beilstein-journals.org/bjnano/content/supplementary/2190-4286-8-49-S1.csv]

References

1. Nouguez, B.; Eck, G. *Propellants, Explos., Pyrotech.* **2016,** *41,* 548–554. doi:10.1002/prep.201600031
2. Tarver, C. M.; Chidester, S. K.; Nichols, A. L., III. *J. Phys. Chem.* **1996,** *100,* 5794–5799. doi:10.1021/jp953123s
3. Risse, B. Continuous Crystallization of Ultra-Fine Energetic Particles by the Flash-Evaporation Process. Ph.D. Thesis, Université de Lorraine, France, 2012.
4. Bayat, Y.; Zeynali, V. *J. Energ. Mater.* **2011,** *29,* 281–291. doi:10.1080/07370652.2010.527897
5. Klapötke, T. M. *Chemistry of High-Energy Materials,* 3rd ed.; De Gruyter: Berlin, Germany, 2015.
6. Stepanov, V.; Anglade, V.; Balas Hummers, W. A.; Bezmelnitsyn, A. V.; Krasnoperov, L. N. *Propellants, Explos., Pyrotech.* **2011,** *36,* 240–246. doi:10.1002/prep.201000114
7. Klaumünzer, M.; Pessina, F.; Spitzer, D. *J. Energ. Mater.* **2016,** 1–10. doi:10.1080/07370652.2016.1199610
8. Liu, J.; Jiang, W.; Yang, Q.; Song, J.; Hao, G.-z.; Li, F.-s. *Def. Technol.* **2014,** *10,* 184–189. doi:10.1016/j.dt.2014.04.002
9. Zhang, X.; Weeks, B. L. *J. Hazard. Mater.* **2014,** *268,* 224–228. doi:10.1016/j.jhazmat.2014.01.019
10. Comet, M.; Martin, C.; Klaumünzer, M.; Schnell, F.; Spitzer, D. *Appl. Phys. Lett.* **2015,** *107,* 243108. doi:10.1063/1.4938139
11. Fedoroff, B. T.; Sheffield, O. E. *Encyclopedia of Explosives and Related Items;* Picatinny Arsenal Dover: Dover, NJ, U.S.A., 1966; Vol. 3.
12. Pant, A.; Nandi, A. K.; Newale, S. P.; Gajbhiye, V. P.; Prasanth, H.; Pandey, R. K. *Cent. Eur. J. Energ. Mater.* **2013,** *10,* 393–407.

13. Chen, H.; Li, L.; Jin, S.; Chen, S.; Jiao, Q. *Propellants, Explos., Pyrotech.* **2012,** *37,* 77–82. doi:10.1002/prep.201000014
14. Hudson, R. J.; Moniruzzaman, M.; Gill, P. P. *Propellants, Explos., Pyrotech.* **2015,** *40,* 233–237. doi:10.1002/prep.201400129
15. Hudson, R. J. *Investigating the Factors Influencing RDX Shock Sensitivity;* Cranfield University: Cranfield, United Kingdom, 2012.
16. Kumar, R.; Siril, P. F.; Soni, P. *Propellants, Explos., Pyrotech.* **2014,** *39,* 383–389. doi:10.1002/prep.201300104
17. Kumar, R.; Siril, P. F.; Soni, P. *J. Energ. Mater.* **2015,** *33,* 277–287. doi:10.1080/07370652.2014.988774
18. Bayat, Y.; Zarandi, M.; Khadiv-Parsi, P.; Beni, A. S. *Cent. Eur. J. Energ. Mater.* **2015,** *12,* 459–472.
19. Gao, B.; Wu, P.; Huang, B.; Wang, J.; Qiao, Z.; Yang, G.; Nie, F. *New J. Chem.* **2014,** *38,* 2334. doi:10.1039/c3nj01053h
20. Luo, Q.; Pei, C.; Liu, G.; Ma, Y.; Li, Z. *Nano* **2015,** *10,* 1550033. doi:10.1142/S1793292015500332
21. Li, W.; Liao, N.; Duan, X.; Pei, C.; Zhou, X. *Cryst. Res. Technol.* **2015,** *50,* 505–515. doi:10.1002/crat.201400425
22. Dabin, L.; Dong, X.; Baochang, Z. Preparation of Nanometer RDX In-situ by Solvent Substitution Effect in Reverse Micelles. *26th International Pyrotechnics Seminar;* 1999; pp 269–275.
23. Gash, A. E.; Simpson, R. L.; Tillotson, T. M.; Satcher, J. H.; Hrubesh, L. W. Making Nanostructured Pyrotechnics in a Beaker. *27th International Pyrotechnics Seminar;* Grand Junction, CO, U.S.A., 2000.
24. Tillotson, T. M.; Fox, G. L.; Hrubesh, L. B.; Simpson, R. L.; Lee, K. W.; Swansiger, K. W.; Simpson, L. R. Sol–Gel Processing of Energetic Materials. 1997.
25. Tillotson, T. M.; Gash, A. E.; Simpson, R. L.; Hrubesh, L. W.; Satcher, J. H., Jr.; Poco, J. F. *J. Non-Cryst. Solids* **2001,** *285,* 338–345.
26. Rouquerol, J.; Avnir, D.; Fairbridge, C. W.; Everett, D. H.; Haynes, J. M.; Pernicone, N.; Ramsay, J. D. F.; Sing, K. S. W.; Unger, K. K. *Pure Appl. Chem.* **1994,** *66,* 1739–1758. doi:10.1351/pac199466081739
27. Guo, Q.-X.; Nie, F.-D.; Yang, G.-C.; Li, J.-S.; Chu, S.-J. *Chin. J. Energ. Mater.* **2006,** *14,* 268–271.
28. Wuillaume, A.; Beaucamp, A.; David-Quillot, F.; Eradès, C. *Propellants, Explos., Pyrotech.* **2014,** *39,* 390–396. doi:10.1002/prep.201400021
29. Li, G.; Liu, M.; Zhang, R.; Shen, L.; Liu, Y.; Luo, Y. *Colloid Polym. Sci.* **2015,** *293,* 2269–2279. doi:10.1007/s00396-015-3620-x
30. Jin, M.; Wang, G.; Deng, J.; Li, G.; Huang, M.; Luo, Y. *J. Sol-Gel Sci. Technol.* **2015,** *76,* 58–65. doi:10.1007/s10971-015-3750-0
31. Anniyappan, M.; Sonawane, S. H.; Shee, S. K.; Sikder, A. K. *Cent. Eur. J. Energ. Mater.* **2015,** *12,* 785–797.
32. *Regulation (EC) No 1907/2006 of the European Parliament and of the Council*; Registration, Evaluation, Authorisation and Restriction of Chemicals (REACH), 18 December 2006. http://data.europa.eu/eli/reg/2006/1907/2014-04-10
33. Redner, P.; Kapoor, D.; Patel, R.; Chung, M.; Martin, D. *Production and Characterization of Nano-RDX;* DTIC Document, 2006.
34. Liu, J.; Jiang, W.; Zeng, J.-b.; Yang, Q.; Wang, Y.-j.; Li, F.-s. *Def. Technol.* **2014,** *10,* 9–16. doi:10.1016/j.dt.2013.12.006
35. Liu, J.; Jiang, W.; Li, F.; Wang, L.; Zeng, J.; Li, Q.; Wang, Y.; Yang, Q. *Propellants, Explos., Pyrotech.* **2014,** *39,* 30–39. doi:10.1002/prep.201300050
36. Patel, R. B.; Stepanov, V.; Swaszek, S.; Surapaneni, A.; Qiu, H. *Propellants, Explos., Pyrotech.* **2016,** *41,* 114–119. doi:10.1002/prep.201500130
37. Qiu, H.; Patel, R. B.; Damavarapu, R. S.; Stepanov, V. *CrystEngComm* **2015,** *17,* 4080–4083. doi:10.1039/C5CE00489F
38. Frolov, Y. V.; Pivkina, A. N.; Ul'yanova, P. A.; Zav'yalov, S. A. *Combust., Explos. Shock Waves (Engl. Transl.)* **2002,** *38,* 709–713.
39. Pivkina, A.; Ulyanova, P.; Frolov, Y.; Zavyalov, S.; Schoonman, J. *Propellants, Explos., Pyrotech.* **2004,** *29,* 39–48. doi:10.1002/prep.200400025
40. Frolov, Yu. V.; Pivkina, A. N.; Zav'yalov, S. A.; Murav'ev, N. V.; Skryleva, E. A.; Monogarov, K. A. *Russ. J. Phys. Chem. B* **2010,** *4,* 916–922. doi:10.1134/S1990793110060072
41. Mil'chenko, D. V.; Gubachev, V. A.; Andreevskikh, L. A.; Vakhmistrov, S. A.; Mikhailov, A. L.; Burnashov, V. A.; Khaldeev, E. V.; Pyatoikina, A. I.; Zhuravlev, S. S.; German, V. N. *Combust., Explos. Shock Waves (Engl. Transl.)* **2015,** *51,* 80–85.
42. Rossi, C.; Zhang, K.; Esteve, D.; Alphonse, P.; Tailhades, P.; Vahlas, C. *J. Microelectromech. Syst.* **2007,** *16,* 919–931. doi:10.1109/JMEMS.2007.893519
43. Piekiel, N. W.; Morris, C. J. *ACS Appl. Mater. Interfaces* **2015,** *7,* 9889–9897. doi:10.1021/acsami.5b01964
44. Radacsi, N.; Stankiewicz, A. I.; Creyghton, Y. L. M.; van der Heijden, A. E. D. M.; ter Horst, J. H. *Chem. Eng. Technol.* **2011,** *34,* 624–630. doi:10.1002/ceat.201000538
45. Reus, M. A.; Hoetmer, G.; van der Heijden, A. E. D. M.; ter Horst, J. H. *Chem. Eng. Process.* **2014,** *80,* 11–20. doi:10.1016/j.cep.2014.03.016
46. Radacsi, N. Process Intensification in Crystallization: Submicron Particle Generation Using Alternative Energy Forms. Ph.D. Thesis, Delft University of Technology, Delft, Netherlands, 2012.
47. Gallagher, P. M.; Coffey, M. P.; Krukonis, V. J.; Hillstrom, W. W. *J. Supercrit. Fluids* **1992,** *5,* 130–142. doi:10.1016/0896-8446(92)90030-N
48. Teipel, U.; Förter-Barth, U.; Gerber, P.; Krause, H. H. *Propellants, Explos., Pyrotech.* **1997,** *22,* 165–169. doi:10.1002/prep.19970220313
49. Jung, J.; Perrut, M. *J. Supercrit. Fluids* **2001,** *20,* 179–219. doi:10.1016/S0896-8446(01)00064-X
50. Lee, B.-M.; Jeong, J.-S.; Lee, Y.-H.; Lee, B.-C.; Kim, H.-S.; Kim, H.; Lee, Y.-W. *Ind. Eng. Chem. Res.* **2009,** *48,* 11162–11167. doi:10.1021/ie900448w
51. Lee, B.-M.; Kim, S.-J.; Lee, B.-C.; Kim, H.-S.; Kim, H.; Lee, Y.-W. *Ind. Eng. Chem. Res.* **2011,** *50,* 9107–9115. doi:10.1021/ie102593p
52. Lim, G. B.; Lee, S. Y.; Koo, K. K.; Park, B. S.; Kim, H. S. Gas Anti-Solvent Recrystallization of Molecular Explosives under Subcritical to Supercritical Conditions. *Proceedings of the 5th Meeting on Supercritical Fluids;* 1998.
53. Reverchon, E.; Kröber, H.; Teipel, U. Crystallization with Compressed Gases. *Energetic Materials;* Wiley-VCH: Weinheim, Germany, 2005; pp 159–182.
54. Dou, H.; Kim, K.-H.; Lee, B.-C.; Choe, J.; Kim, H.-S.; Lee, S. *Powder Technol.* **2013,** *235,* 814–822. doi:10.1016/j.powtec.2012.11.042
55. Reverchon, E. *J. Supercrit. Fluids* **1999,** *15,* 1–21. doi:10.1016/S0896-8446(98)00129-6
56. Dixon, D. J.; Johnston, K. P.; Bodmeier, R. A. *AIChE J.* **1993,** *39,* 127–139.
57. Shang, F.; Zhang, J. *J. Energ. Mater.* **2014,** *32,* S71–S82. doi:10.1080/07370652.2013.829133

58. Best, W.; Mueller, F.-J.; Schmieder, K.; Frank, R.; Paust, J. Finely dispersed carotenoid pigments prodn. - by dissolving carotenoid in a supercritical gas, pref. carbon di:oxide, and dispersing the soln. in an aq. colloidal matrix. German Patent DE2943267 A1, Oct 26, 1981.
59. Graser, F.; Wickenhaeuser, G. Conditioning of Finely Divided Crude Organic Pigments. U.S. Patent US4451654 A, May 29, 1984.
60. Pourmortazavi, S. M.; Hajimirsadeghi, S. S. *Ind. Eng. Chem. Res.* **2005,** *44,* 6523–6533. doi:10.1021/ie0503242
61. Hannay, J. B.; Hogarth, J. *Proc. R. Soc. London* **1879,** *30,* 178–188. doi:10.1098/rspl.1879.0104
62. Krukonis, V. Supercritical Fluid Nucleation of Difficultto-Comminute Solids. *Annual Meeting - American Institute of Chemical Engineers;* 1984.
63. Matson, D. W.; Petersen, R. C.; Smith, R. D. *J. Mater. Sci.* **1987,** *22,* 1919–1928. doi:10.1007/BF01132917
64. Matson, D.; Fulton, J.; Petersen, R.; Smith, R. *Ind. Eng. Chem. Res.* **1987,** *26,* 2298–2306.
65. Teipel, U.; Kröber, H.; Krause, H. H. *Propellants, Explos., Pyrotech.* **2001,** *26,* 168–173. doi:10.1002/1521-4087(200110)26:4<168::AID-PREP168>3.0.CO;2-X
66. Stepanov, V. Production of Nanocrystalline Nitramine Energetic Materials by Rapid Expansion of Supercritical Solutions. M.S. Thesis, New Jersey Institute of Technology, 2003.
67. Stepanov, V.; Krasnoperov, L. N.; Elkina, I. B.; Zhang, X. *Propellants, Explos., Pyrotech.* **2005,** *30,* 178–183. doi:10.1002/prep.200500002
68. Stepanov, V.; Anglade, V.; Bezmelnitsyn, A.; Krasnoperov, L. N. Production and Characterization of Nanocrystalline Explosive RDX. AIChE Annual Meeting, San Francisco, CA, U.S.A.; 2006.
69. Stepanov, V. Production of nanocrystalline RDX by RESS: development and material characterization. Ph.D. Thesis, New Jersey Institute of Technology, 2008.
70. Lee, B.-M.; Kim, D. S.; Lee, Y.-H.; Lee, B.-C.; Kim, H.-S.; Kim, H.; Lee, Y.-W. *J. Supercrit. Fluids* **2011,** *57,* 251–258. doi:10.1016/j.supflu.2011.03.008
71. Essel, J. T.; Cortopassi, A. C.; Kuo, K. K.; Adair, J. H.; Leh, C. G.; Klapoetke, T. M. *Synthesis of Energetic Materials by Rapid Expansion of a Supercritical Solution into Aqueous Solution (RESS-AS) Process;* DTIC Document, 2010.
72. Essel, J. Processing Energetic Materials with Supercritical Fluid Precipitation Techniques. Ph.D. Thesis, Pennsylvania State University, 2012.
73. Essel, J. T.; Cortopassi, A. C.; Kuo, K. K.; Leh, C. G.; Adair, J. H. *Propellants, Explos., Pyrotech.* **2012,** *37,* 699–706. doi:10.1002/prep.201100139
74. Gottfried, J. L.; De Lucia, F. C., Jr.; Piraino, S. M. *Characterization of the Morphology of RDX Particles Formed by Laser Ablation;* U.S. Army Research Lab, Aberdeen Proving Ground, MD, Weapons and Materials Research Directorate, 2012. http://www.dtic.mil/cgi-bin/GetTRDoc?Location=U2&doc=GetTRDoc.pdf&AD=ADA562280
75. Okuyama, K.; Wuled Lenggoro, I. *Chem. Eng. Sci.* **2003,** *58,* 537–547. doi:10.1016/S0009-2509(02)00578-X
76. Messing, G. L.; Zhang, S.-C.; Jayanthi, G. V. *J. Am. Ceram. Soc.* **1993,** *76,* 2707–2726. doi:10.1111/j.1151-2916.1993.tb04007.x
77. Spitzer, D.; Baras, C.; Schäfer, M. R.; Ciszek, F.; Siegert, B. *Propellants, Explos., Pyrotech.* **2011,** *36,* 65–74. doi:10.1002/prep.200900002
78. Spitzer, D.; Comet, M.; Baras, C.; Pichot, V.; Piazzon, N. *J. Phys. Chem. Solids* **2010,** *71,* 100–108. doi:10.1016/j.jpcs.2009.09.010
79. Kim, J.-W.; Shin, M.-S.; Kim, J.-K.; Kim, H.-S.; Koo, K.-K. *Ind. Eng. Chem. Res.* **2011,** *50,* 12186–12193. doi:10.1021/ie201314r
80. Gao, B.; Wang, D.; Zhang, J.; Hu, Y.; Shen, J.; Wang, J.; Huang, B.; Qiao, Z.; Huang, H.; Nie, F.; Yang, G. *J. Mater. Chem. A* **2014,** *2,* 19969–19974. doi:10.1039/C4TA04979A
81. Stein, W. A. *Chem. Ing. Tech.* **1973,** *45,* 906–907. doi:10.1002/cite.330451311
82. Broadhead, J.; Rouan, S. K. E.; Rhodes, C. T. *Drug Dev. Ind. Pharm.* **1992,** *18,* 1169–1206. doi:10.3109/03639049209046327
83. van der Heijden, A. E. D. M.; Creyghton, Y. L. M.; Marino, E.; Bouma, R. H. B.; Scholtes, G. J. H. G.; Duvalois, W.; Roelands, M. C. P. M. *Propellants, Explos., Pyrotech.* **2008,** *33,* 25–32. doi:10.1002/prep.200800204
84. Qiu, H.; Stepanov, V.; Di Stasio, A. R.; Chou, T.; Lee, W. Y. *J. Hazard. Mater.* **2011,** *185,* 489–493. doi:10.1016/j.jhazmat.2010.09.058
85. Qiu, H.; Stepanov, V.; Chou, T.; Surapaneni, A.; Di Stasio, A. R.; Lee, W. Y. *Powder Technol.* **2012,** *226,* 235–238. doi:10.1016/j.powtec.2012.04.053
86. Qiu, H.; Stepanov, V.; Di Stasio, A. R.; Surapaneni, A.; Lee, W. Y. *Powder Technol.* **2015,** *274,* 333–337. doi:10.1016/j.powtec.2015.01.032
87. Ma, Z.; Gao, B.; Wu, P.; Shi, J.; Qiao, Z.; Yang, Z.; Yang, G.; Huang, B.; Nie, F. *RSC Adv.* **2015,** *5,* 21042–21049. doi:10.1039/C4RA16527F
88. Ji, W.; Li, X.; Wang, J. *Cent. Eur. J. Energ. Mater.* **2015,** *12,* 831–840.
89. Shi, X.; Wang, C.; Wang, J.; Li, X.; An, C.; Wang, J.; Ji, W. *Cent. Eur. J. Energ. Mater.* **2015,** *12,* 487–495.
90. Li, H.; An, C.; Guo, W.; Geng, X.; Wang, J.; Xu, W. *Propellants, Explos., Pyrotech.* **2015,** *40,* 652–658. doi:10.1002/prep.201400175
91. Risse, B.; Spitzer, D.; Hassler, D.; Schnell, F.; Comet, M.; Pichot, V.; Muhr, H. *Chem. Eng. J.* **2012,** *203,* 158–165. doi:10.1016/j.cej.2012.07.032
92. Edwin, B. Flash-type distillation system. U.S. Pat. Appl. 2,908,618, Oct 13, 1959.
93. Porter, W. E.; Smith, B. F. Combined flash and vapor compression evaporator. U.S. Pat. Appl. 2,759,882, Aug 21, 1956.
94. Allen, E.; Hanson, K. Method of and apparatus for flash evaporation treatment. U.S. Pat. Appl. 2,803,589, Aug 20, 1957.
95. *Desalting - State of the Art, Bulletin No. 134-69;* Department of Water Resources, State of California, 1969.
96. Sawa, T.; Izumi, K.; Takahashi, S. *Desalination* **1976,** *19,* 369–380. doi:10.1016/S0011-9164(00)88045-5
97. Sebastian, P.; Nadeau, J. P. *Int. J. Therm. Sci.* **2002,** *41,* 269–280. doi:10.1016/S1290-0729(01)01315-1
98. Cheng, W.-L.; Zhang, W.-W.; Chen, H.; Hu, L. *Renewable Sustainable Energy Rev.* **2016,** *55,* 614–628. doi:10.1016/j.rser.2015.11.014
99. Brown, R.; York, J. L. *AIChE J.* **1962,** *8,* 149–153. doi:10.1002/aic.690080204
100. Miyatake, O.; Tomimura, T.; Ide, Y.; Fujii, T. *Desalination* **1981,** *36,* 113–128. doi:10.1016/S0011-9164(00)88635-X
101. Miyatake, O.; Tomimura, T.; Ide, Y.; Yuda, M.; Fujii, T. *Desalination* **1981,** *37,* 351–366. doi:10.1016/S0011-9164(00)88658-0

102. Miyatake, O.; Murakami, K.; Kawata, Y.; Fujii, T. *Bull. Soc. Sea Water Sci., Jpn.* **1972,** *26,* 189–198. doi:10.11457/swsj1965.26.189
103. Miyatake, O.; Tomimura, T.; Ide, Y. *J. Sol. Energy Eng.* **1985,** *107,* 176–182. doi:10.1115/1.3267673
104. Günther, A.; Wirth, K.-E. *Int. J. Heat Mass Transfer* **2013,** *64,* 952–965. doi:10.1016/j.ijheatmasstransfer.2013.05.034
105. Miyatake, O.; Koito, Y.; Tagawa, K.; Maruta, Y. *Desalination* **2001,** *137,* 157–166. doi:10.1016/S0011-9164(01)00214-4
106. Ikegami, Y.; Sasaki, H.; Gouda, T.; Uehara, H. *Desalination* **2006,** *194,* 81–89. doi:10.1016/j.desal.2005.10.026
107. Owen, I.; Jalil, J. M. *Int. J. Multiphase Flow* **1991,** *17,* 653–660. doi:10.1016/0301-9322(91)90030-7
108. Shin, H. T.; Lee, Y. P.; Jurng, J. *Appl. Therm. Eng.* **2000,** *20,* 439–454. doi:10.1016/S1359-4311(99)00035-6
109. Satoh, I.; Fushinobu, K.; Hashimoto, Y. *Int. J. Refrig.* **2002,** *25,* 226–234. doi:10.1016/S0140-7007(01)00083-4
110. Sobac, B.; Talbot, P.; Haut, B.; Rednikov, A.; Colinet, P. *J. Colloid Interface Sci.* **2015,** *438,* 306–317. doi:10.1016/j.jcis.2014.09.036
111. Gebauer, J.; Kaiser, R.; Kind, M. *Chem. Ing. Tech.* **2012,** *84,* 1901–1910. doi:10.1002/cite.201200021
112. Gebauer, J.; Kind, M. *Chem. Eng. Process.* **2015,** *91,* 130–140. doi:10.1016/j.cep.2015.03.012
113. Gebauer, J.; Kind, M. *Chem. Eng. Sci.* **2015,** *133,* 75–81. doi:10.1016/j.ces.2014.12.034
114. Gebauer, J.; Selzer, D.; Kind, M. *Chem. Ing. Tech.* **2016,** *88,* 881–889. doi:10.1002/cite.201500148
115. Chen, S.-C.; Tsai, C.-J. *J. Nanopart. Res.* **2007,** *9,* 71–83. doi:10.1007/s11051-006-9152-z
116. Pichot, V.; Risse, B.; Schnell, F.; Mory, J.; Spitzer, D. *Sci. Rep.* **2013,** *3,* 2159. doi:10.1038/srep02159
117. Pichot, V.; Comet, M.; Risse, B.; Spitzer, D. *Diamond Relat. Mater.* **2015,** *54,* 59–63. doi:10.1016/j.diamond.2014.09.013
118. Spitzer, D.; Risse, B.; Schnell, F.; Pichot, V.; Klaumünzer, M.; Schaefer, M. R. *Sci. Rep.* **2014,** *4,* 6575. doi:10.1038/srep06575
119. Klaumünzer, M.; Schlur, L.; Schnell, F.; Spitzer, D. *Chem. Eng. Technol.* **2015,** *38,* 1477–1484. doi:10.1002/ceat.201500053
120. Le Brize, A.; Spitzer, D. *Cent. Eur. J. Energ. Mater.* **2016,** *13,* 547–556. doi:10.22211/cejem/64956
121. Pessina, F.; Schnell, F.; Spitzer, D. *Chem. Eng. J.* **2016,** *291,* 12–19. doi:10.1016/j.cej.2016.01.083
122. Roeske, F.; Benterou, J.; Lee, R.; Roos, E. *Propellants, Explos., Pyrotech.* **2003,** *28,* 53–57. doi:10.1002/prep.200390008
123. Charitidis, C. A.; Georgiou, P.; Koklioti, M. A.; Trompeta, A.-F.; Markakis, V. *Manuf. Rev.* **2014,** *1,* 11. doi:10.1051/mfreview/2014009
124. Tsuzuki, T. *Nanotechnology Commercialization;* CRC Press: Boca Raton, FL, U.S.A., 2013.
125. Sheth, P.; Sandhu, H.; Singhal, D.; Malick, W.; Shah, N.; Serpil Kislalioglu, M. *Curr. Drug Delivery* **2012,** *9,* 269–284. doi:10.2174/156720112800389052
126. De Meyer, L.; Van Bockstal, P.-J.; Corver, J.; Vervaet, C.; Remon, J. P.; De Beer, T. *Int. J. Pharm.* **2015,** *496,* 75–85. doi:10.1016/j.ijpharm.2015.05.025
127. Carter, C. B.; Norton, M. G. *Ceramic Materials;* Springer: New York, NY, U.S.A., 2013.
128. Madene, A.; Jacquot, M.; Scher, J.; Desobry, S. *Int. J. Food Sci. Technol.* **2006,** *41,* 1–21. doi:10.1111/j.1365-2621.2005.00980.x
129. Gibbs, B. F.; Kermasha, S.; Alli, I.; Mulligana, C. N. *Int. J. Food Sci. Nutr.* **1999,** *50,* 213–224. doi:10.1080/096374899101256
130. Patel, B. B.; Patel, J. K.; Chakraborty, S. *Recent Pat. Drug Delivery Formulation* **2014,** *8,* 63–78. doi:10.2174/1872211308666140211122012
131. Lavernia, E. J.; Srivatsan, T. S. *J. Mater. Sci.* **2010,** *45,* 287–325. doi:10.1007/s10853-009-3995-5
132. Radacsi, N.; Bouma, R. H. B.; Krabbendam-la Haye, E. L. M.; ter Horst, J. H.; Stankiewicz, A. I.; van der Heijden, A. E. D. M. *Propellants, Explos., Pyrotech.* **2013,** *38,* 761–769. doi:10.1002/prep.201200189
133. Brown, G. W.; Sandstrom, M. M.; Preston, D. N.; Pollard, C. J.; Warner, K. F.; Sorensen, D. N.; Remmers, D. L.; Phillips, J. J.; Shelley, T. J.; Reyes, J. A.; Hsu, P. C.; Reynolds, J. G. *Propellants, Explos., Pyrotech.* **2015,** *40,* 221–232. doi:10.1002/prep.201400191

License and Terms

BEILSTEIN JOURNAL OF NANOTECHNOLOGY

Advances in the fabrication of graphene transistors on flexible substrates

Gabriele Fisichella[*1], Stella Lo Verso[2], Silvestra Di Marco[2], Vincenzo Vinciguerra[2], Emanuela Schilirò[1], Salvatore Di Franco[1], Raffaella Lo Nigro[1], Fabrizio Roccaforte[1], Amaia Zurutuza[3], Alba Centeno[3], Sebastiano Ravesi[2] and Filippo Giannazzo[1]

Full Research Paper

Open Access

Address:
[1]CNR-IMM, VIII Strada 5, 95121 Catania, Italy, [2]STMicroelectronics, Stradale Primosole 50, 95121 Catania, Italy and [3]Graphenea, Tolosa Hiribidea 76, Donostia-San Sebastian, Spain

Email:
Gabriele Fisichella[*] - Gabriele.fisichella@imm.cnr.it

* Corresponding author

Keywords:
atomic layer deposition; chemical sensing; field effect transistor; flexible electronics; graphene

Beilstein J. Nanotechnol. **2017,** *8,* 467–474.
doi:10.3762/bjnano.8.50

Received: 15 September 2016
Accepted: 24 January 2017
Published: 20 February 2017

This article is part of the Thematic Series "Self-assembly of nanostructures and nanomaterials II".

Guest Editor: I. Berbezier

Abstract

Graphene is an ideal candidate for next generation applications as a transparent electrode for electronics on plastic due to its flexibility and the conservation of electrical properties upon deformation. More importantly, its field-effect tunable carrier density, high mobility and saturation velocity make it an appealing choice as a channel material for field-effect transistors (FETs) for several potential applications. As an example, properly designed and scaled graphene FETs (Gr-FETs) can be used for flexible high frequency (RF) electronics or for high sensitivity chemical sensors. Miniaturized and flexible Gr-FET sensors would be highly advantageous for current sensors technology for in vivo and in situ applications. In this paper, we report a wafer-scale processing strategy to fabricate arrays of back-gated Gr-FETs on poly(ethylene naphthalate) (PEN) substrates. These devices present a large-area graphene channel fully exposed to the external environment, in order to be suitable for sensing applications, and the channel conductivity is efficiently modulated by a buried gate contact under a thin Al_2O_3 insulating film. In order to be compatible with the use of the PEN substrate, optimized deposition conditions of the Al_2O_3 film by plasma-enhanced atomic layer deposition (PE-ALD) at a low temperature (100 °C) have been developed without any relevant degradation of the final dielectric performance.

Introduction

One of the new challenges in the field of electronics is represented by flexible devices. The evolution of the processing technologies for soft substrates and the discovery of new materials suitable for bending, stretching or conformably shaping [1], such as in the case of many 2D materials [2], paved the way to a huge number of stretchable, foldable or form factor reconfigurable demonstrators. Such devices can be considered for various applications, from consumer devices [3] to biomedical

in vivo applications [4,5]. Among all the two-dimensional materials, graphene is one of the most appealing to be used as a flexible, conductive membrane, given its Young's modulus on the order of TPa and large spring constant (1–5 N/m) [6]. Besides its high charge mobility of up to thousands of $cm^2 \cdot V^{-1} \cdot s^{-1}$, even at room temperature for both electron and holes, graphene is characterized by exhibiting only a small variation in electrical performance under mechanical deformation [7,8]. These are essential characteristics for stable and reliable operation.

Thanks to these properties, graphene can be considered for high frequency FETs both on conventional substrates [9] and on flexible platforms [10]. In particular, remarkable cut-off frequency values (≈25 GHz) and robust performance under repeated bending (down to 0.7 mm bending radius) have been reported in graphene FETs (Gr-FETs) even with gradually scaled (≈0.5 μm) channel lengths fabricated on a flexible polyimide substrate and adopting a back-gate configuration and Al_2O_3 as a gate dielectric.

In addition, due to the low density of states (DOS) around the Dirac point, the carrier density of graphene is very sensitive to the adsorption of charged/polar species at or near its surface – a peculiarity particularly suitable for chemical/biological sensing. As an example, gas sensors with single molecule sensitivity have been initially demonstrated using high quality, exfoliated graphene from graphite [11]. Considering the scalable graphene production methods, epitaxial graphene grown on silicon carbide has also been demonstrated as an excellent material for sensing [12]. However, for many applications, flexible and disposable sensors are needed. For these applications graphene has to be easily transferred to the target substrate. In this sense, the use of graphene grown by chemical vapor deposition (CVD) on various metals (Ni [7], Cu [13]) and using various precursors [14] represents the most suitable choice.

Among the various device architectures, Gr-FET-based sensors can represent a great combination between a chemical-to-electrical signal converter and an electrical signal amplifier [15]. In particular, the first characteristic can be achieved by using a properly extended channel area able to effectively interact with the chemical target, while the second one can be obtained by maximizing the gate capacitance. For this last reason, from a purely research perspective, the best device configuration is the ion sensing FET (IS-FET) [16] constituted of a graphene channel covered by the target solution and a macroscopic reference electrode immersed in the solution itself as the gate contact. Beside the fabrication simplicity, this configuration exploits electric double layer capacitance at the gate/solution interface and at the channel/solution interface, which can reach tens of $\mu F/cm^2$ (depending on the ions concentration). However, for real applications, especially for a potential totally flexible device, there is a need of a reference electrode that is an external, rigid and macroscopic element, which represents a relevant drawback. The solid IS-FET [17] (where a local back-gate buried under a solid dielectric film replaces the reference electrode) represents a valid alternative for real applications. In this case the thickness and the dielectric constant of the insulating film have crucial importance in order to maintain a reasonably high gate capacitance of the final device. In particular, considering high κ-dielectrics such as HfO_2 or Al_2O_3 with film thickness in the order of 10 nm, the gate capacitance can reach hundreds or even thousands of nF/cm^2, which is still reasonably high for sensing applications. It is clear that the high quality and the scaled thickness of the dielectric film fabricated below the temperature limit of the plastic support is the key point for the final devices performance.

A low temperature (100 °C) deposition process to obtain a high quality dielectric film is essential in order to be compatible with common plastic substrates, such as poly(ethylene terephthalate) (PET) or poly(ethylene naphthalate) (PEN), which is also the case of our study.

Atomic layer deposition (ALD) represents an optimal method to fabricate a good quality Al_2O_3 dielectric film with a tight control on the deposited thickness and a high level of conformal coverage. While the thickness control allows easy fabrication of a tens of nanometer thick dielectric film (resulting in a beneficially high dielectric capacitance), the conformal coverage is essential to contain the potential local degradation of the dielectric performance. Otherwise, this degradation can take over due to the device topography and the high starting roughness of the plastic substrate.

ALD is essentially a low temperature process. It is possible to obtain a high quality Al_2O_3 film by depositing using a plasma-enhanced ALD process and exploiting trimethylaluminium (TMA) as the metalorganic chemical precursor and O_2 as the co-reagent at an optimal growth temperature of 250 °C. Nevertheless, such a temperature is still high in combination with a plastic substrate such as PEN, for which the glass transition temperature is ≈155 °C. Using ALD it is possible to grow at lower temperatures as reported in the case of plastic coating and gas diffusion barrier fabrication [18]. However, with reducing the temperature, the deposition conditions must be optimized in order to ensure the expected layer-by-layer ALD mechanism of the insulating film, instead of a massive CVD growth mechanism, which in turn can result in a degradation of the overall structural and electrical quality of the insulator. This aspect is particularly relevant for the fabrication of a FET where the properties of the gate dielectric (e.g., permittivity, leakage

current, critical breakdown field) are crucial for the device operation.

Results and Discussion

Low temperature gate dielectric

In our experiments we developed a 100 °C PE-ALD process using a PE ALD LL reactor by SENTECH Instruments GmbH, starting with trimethylaluminium (TMA) as a metal-organic chemical precursor and O_2 as the oxygen source for the Al_2O_3 synthesis. In particular, we explored the resulting properties obtained by modifying the deposition cycle and enlarging the purging periods between the precursor exposure in order to prevent the precursor mixing and a consequent CVD growth mechanism.

The developed low temperature (LT) and prolonged cycle process was analyzed on a silicon (100) reference wafer and compared to a standard temperature (ST) PE-ALD growth process. The morphology collected by tapping mode atomic force microscopy (tAFM) for the LT growth (Figure 1a left) is comparable to the morphology obtained by the ST growth (Figure 1a right). The dielectric thickness and the consequent growth per cycle was determined by spectroscopic ellipsometry measurements performed on an array of several positions on a wafer scale. A thickness of 28.9 ± 0.5 nm after 250 ALD cycles (0.12 nm/cycle growth rate) was revealed by the ST process, whereas after the same number of cycles, the LT process revealed a thickness of 40.9 ± 0.5 nm (0.16 nm/cycle growth rate).

The LT process thickness was also confirmed (43 ± 1 nm) by the local step height measure reported in Figure 1b for a patterned Al_2O_3. The dielectric patterning was obtained by depositing the oxide on a silicon wafer masked by a negative profile resist and then removing the resist by an ultrasonic hot chemical bath. This approach, namely the lift-off method, allows a structured layer to be defined without direct chemical/physical etching of the patterned layer. This completely avoids incomplete or over etching, resulting in a step profile which corresponds to the patterned layer thickness. It should be noted that this method is allowed only for the LT process if a standard resist for lift-off process is considered [19]. The 250 °C used in the ST process would totally degrade the resist.

Both LT and ST processes were repeated on an aluminum-coated silicon wafer, where a number of cycles was needed to produce a ≈30 nm dielectric thickness. The Al-coated Si wafer was prepared by depositing a 200 nm thick Al film by RF reactive sputtering with a surface roughness (measured by AFM, image not reported) of about 4.3 nm. The RMS roughness values obtained for both the LT Al_2O_3 (Figure 1c, left) and the ST Al_2O_3 (Figure 1c, right) were 4.20 nm and 4.49 nm, respectively, that is, very similar to the starting Al surface roughness.

The Al/Al_2O_3 stack was exploited for a mercury probe measurement of the dielectric capacitance. In particular, a metal–insulator–metal capacitor (MIM) is defined by the Al/Al_2O_3 stack from one side and from the reversibly contacted

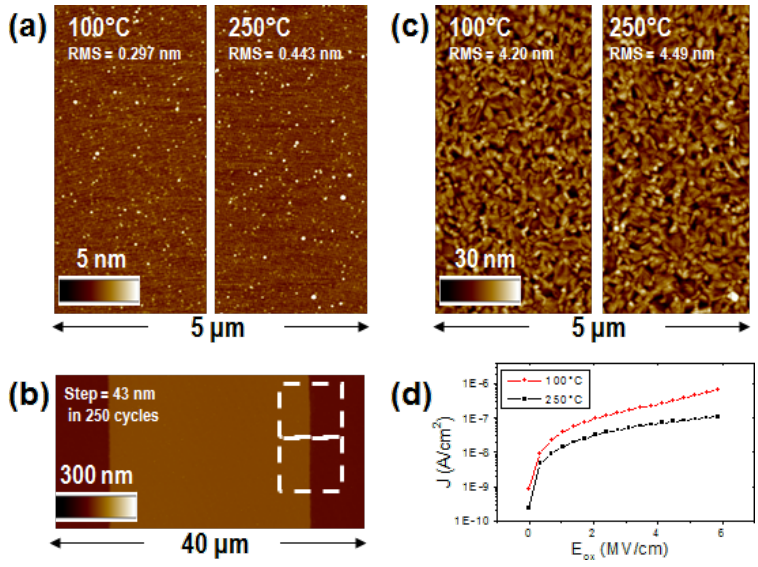

Figure 1: a) Comparison between tapping mode atomic force microscopy (tAFM) morphologies of low temperature (left) and standard temperature (right) dielectric materials deposited on a Si wafer; b) AFM local step height of the lift-off patterned low temperature dielectric; c) comparison between tAFM morphologies of low temperature (left) and standard temperature (right) dielectric material deposited on an Al coated Si wafer; and d) current density leakage through low temperature and standard temperature dielectric materials.

mercury probe on the other side. A wafer-scale matrix of sampled positions were collected on both the ST and the LT dielectric layers. Dielectric constants of 7.94 ± 0.05 and 7.91 ± 0.05 where extracted for ST and LT dielectrics, respectively, confirming a similar dielectric quality of the two films and an extremely good homogeneity of the result on the wafer scale (standard deviation below 1%). As reported in Figure 1d the leakage current through the dielectric was also extracted. In both cases, a negligible current on the order of hundreds of nA/cm^2 (see Table 1) was collected for electric fields up to 6 MV/cm, which is a reasonable operating range. It is possible to conclude that the LT film obtained by a proper modification of the deposition parameters reveals a dielectric quality close to that obtained by a ST film and is good enough to be exploited as a dielectric material for FETs on plastic.

Fabrication and electrical characterization of Gr-FETs on flexible substrates

We fabricated several arrays of independently back-gated Gr-FETs by adopting a specifically optimized process flow. In particular, we considered large area devices with channel widths and lengths on the order of ≈100 µm, suitable for solution sensing applications. This channel size poses a challenge considering that the larger the channel dimension, the higher the effect can be on the device performance due to the material defects (e.g., graphene cracks and grain boundaries, surface asperities, dielectric inhomogeneity).

We started with a thermally flattened PEN Teonex film purchased from Dupont Teiji Films. PEN is an analogous material to poly(ethylene terephthalate) (PET), with superior physical and thermal stability (up to 155 °C), which are advantageous properties for flexible technology.

The polymer film was reversibly bonded on a Si wafer by mechanical lamination, adopting a double face thermal release tape (Nitto Denko, 150 °C thermal release) and shaped by cutting along the wafer edges. This is essential for proper manageability of the substrate during fabrication and testing.

The polymer film, as reported in Figure 2a, was morphologically characterized by tAFM and a starting RMS of ≈7 nm was

Table 1: Comparison between the low temperature and standard temperature process properties extracted during the material characterization on the standard Si substrates.

	Low temperature (100 °C)	Standard temperature (250 °C)
Growth per Cycle:		
* Ellipsometry	0.16 nm/cycle	0.12 nm/cycle
* Local step height	0.168 nm/cycle	–
Relative permittivity	7.91	7.95
Leakage (6 MV/cm)	6.6 × 10^{-7} A/cm^2	1.1 × 10^{-7} A/cm^2
Roughness (RMS):		
* On Si wafer	0.297 nm	0.443 nm
* On sputtered Al	4.20 nm	4.49 nm

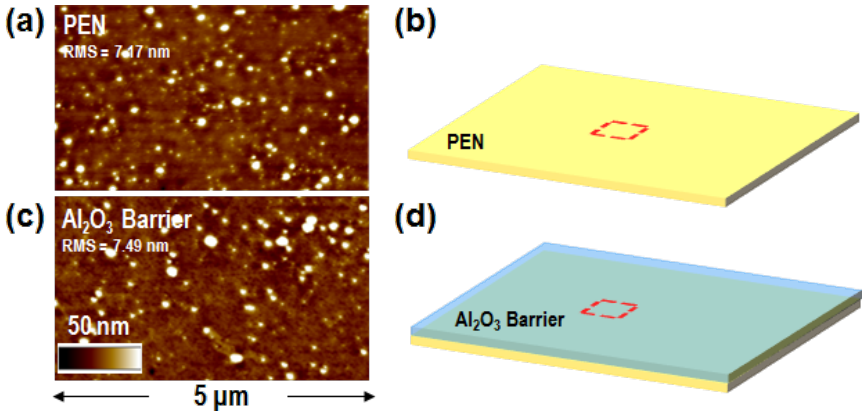

Figure 2: a) Tapping mode atomic force microscopy (tAFM) morphology of the PEN surface and b) a schematic representation of the PEN starting substrate. c) tAFM morphology of the PEN-coated surface by a 100 nm protective Al_2O_3 layer and d) a schematic representation of the Al_2O_3 barrier/PEN substrate.

found. It is worth noting that even if this is a reasonable roughness for a plastic substrate, it is 1–2 orders of magnitude higher than the RMS values of traditional rigid substrates for electronics, such as silicon dioxide on Si.

The polymer film surface was coated by a 100 nm protective Al_2O_3 layer, deposited by DC-pulsed RF reactive sputter, assisted by a cooling system able to maintain the sample below 100 °C. This is a relevant precaution in order to prevent polymer degradation which may occur due to the processing, in particular, where a plasma is involved. The tAFM morphology reported in Figure 2c shows an essentially unchanged morphology of the substrate surface after the protective coating deposition. This is an important indication of the absence of polymer degradation during the integration of the protective barrier. Figure 2d reports the schematic representation of the PEN substrate after the Al_2O_3 barrier integration.

200 nm thick aluminum back gate pads have been fabricated by metal sputtering, considering the same metal deposition process previously exploited on Si during the dielectric layer testing, and patterning by a lift-off approach. The metal morphology is reported in Figure 3a, revealing an RMS of ≈9.8 nm, consistent with the roughness of the underlying substrate. Figure 3b reports the schematic illustration of the patterned Al pads on the plastic substrate.

A ≈30 nm thick Al_2O_3 dielectric film was deposited by the previously analyzed LT ALD process. The surface tAFM morphology reported in Figure 3c shows a roughness of ≈7.6 nm, slightly lower than the underlying Al gate contact. The absence of substrate morphological degradation demonstrates that the previously discussed LT process is completely compatible with the final plastic substrate.

Graphene transistor channels were fabricated starting from a single layer graphene film grown by CVD on large area copper foils (provided by Graphenea). The graphene membrane was transferred to a large area (100 mm diameter) of the target substrate by a PMMA-assisted wet transfer procedure and patterned by soft O_2 plasma etching.

Figure 4a shows the tAFM morphology of graphene. The typical, wrinkled morphology of CVD-synthesized graphene [13] is less evident on PEN substrates compared with smoother substrates. However, it is still possible to identify wrinkles, as indicated by the dashed green circle in Figure 4a. A schematic illustration of the graphene channel fabricated over the FET gate contact is reported in Figure 4b.

After patterning the graphene channel, the source and drain contacts were fabricated by lift-off of a 30/120 nm thick Ni/Au double layer, which partially overlaps the edges of the graphene channel. A complete Gr-FET device is shown in the optical microscopy image in Figure 4c and schematically illustrated in Figure 4d. Furthermore, the resistance contributions which determine the total electrical resistance, R_{TOT}, between source and drain contacts are also illustrated in Figure 4d. Here, the gate-bias-dependent graphene channel resistance, $R_{ch}(V_g)$, the source and drain contact resistance, R_c, and the access resistance, R_{acc}, associated with the ungated graphene access regions between the channel and the source and drain contacts (L_{acc} = 20 µm length per access region) are shown.

The total resistance resulting from the series combination of these contributions can be expressed as:

$$R_{TOT}\left(V_g\right) = R_{ch}\left(V_g\right) + 2R_c + 2R_{acc}\,. \qquad (1)$$

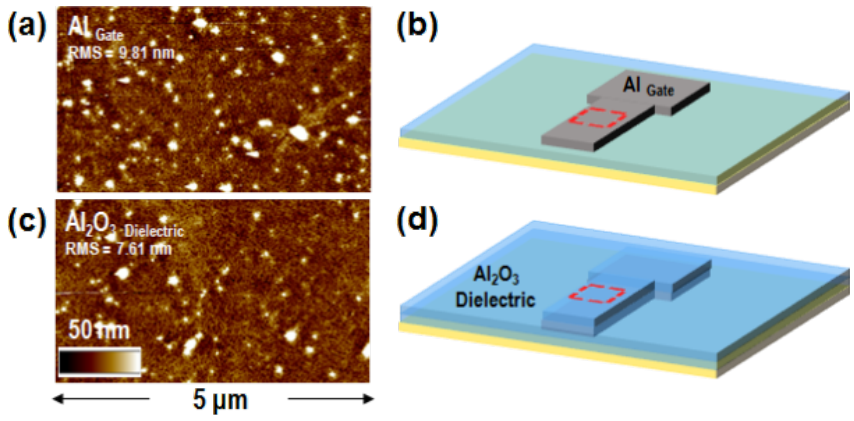

Figure 3: a) Tapping mode atomic force microscopy (tAFM) morphology and b) schematic illustration of the aluminum back-gate pad. c) tAFM morphology and d) related schematic illustration of the Al_2O_3 deposited by the low temperature ALD process.

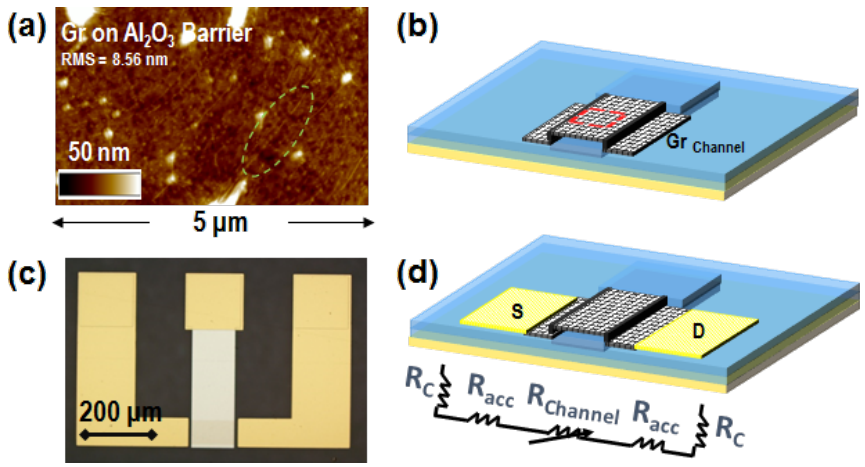

Figure 4: a) Tapping mode atomic force microscopy (tAFM) morphology and b) schematic illustration of the graphene channel. c) Optical microscopy and d) schematic illustration of the final back-gated device with the detail of the involved series resistance contributions from source to drain.

The capacitance of the Al_2O_3 dielectric deposited by ALD on the flexible substrate was characterized by metal–insulator–metal (MIM) test devices properly manufactured together with the Gr-FETs, into the same wafer. The resulting gate capacitance per unit area is $C_g = 2.05 \times 10^{-7}$ F/cm^2. The Al_2O_3 film thickness of 29.9 nm is known from the growth rate previously determined on the reference substrate. The resulting dielectric constant is 6.9, which is reasonably high considering the low temperature (100 °C) adopted for the dielectric growth and the high roughness of the substrate. As a way of comparison with silicon dioxide, the resulting equivalent oxide thickness (EOT) is 16.8 nm.

Several arrays of independently biased back-gated Gr-FETs with different channel geometries were fabricated on the wafer scale using the above described process flow. The electrical characterization of more than 50 devices revealed a significant number of early failures. The origin of these failures is out of the scope of this paper and will be the subject of further investigations. Interestingly, working devices showed quite reproducible electrical characteristics.

Figure 5a reports the output characteristics (drain current vs drain bias, I_d vs V_d) at incremental values of the back gate bias (V_g from 0 to 11 V) for a representative Gr-FET device with channel width W = 100 µm, channel length L = 190 µm (area = $W \times L = 19 \times 10^3$ µm^2) and an access region length L_{acc} = 20 µm, defined as the distance between source (drain) and the channel region. All the output characteristics exhibit a linear (ohmic) behavior, with a gradually decreasing slope (i.e., an increasing channel resistance) in the considered gate bias range.

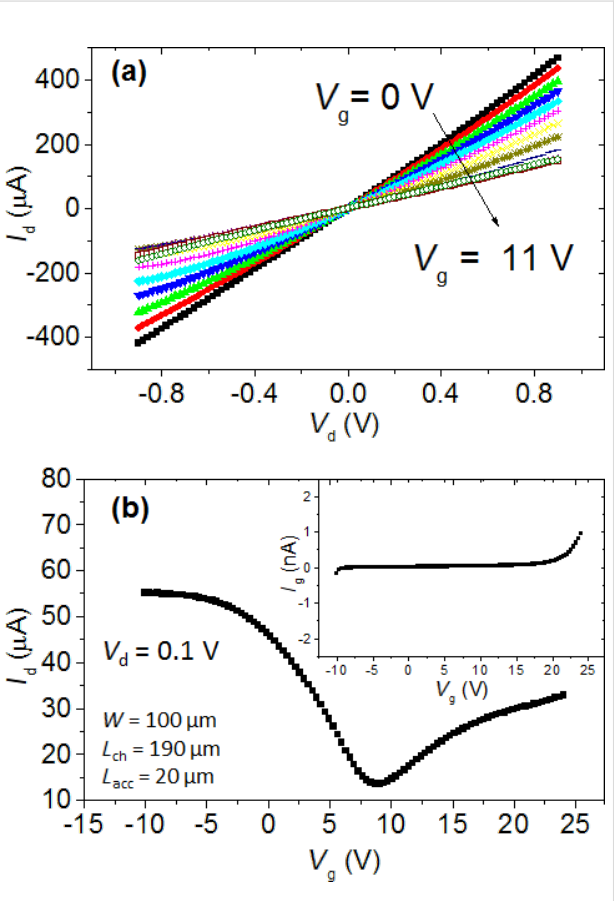

Figure 5: a) I_d–V_d characteristics at different back gate bias values and b) I_d–V_g transfer characteristic for a representative Gr-FET with channel width W = 100 µm, channel length L = 190 µm and access regions length L_{acc} = 20 µm. In the insert of b) the leakage current (I_g vs V_g) collected simultaneously to the transfer characteristic measurement is shown.

Figure 5b shows a representative transfer characteristic of the Gr-FET, i.e., I_d vs V_g for a fixed drain bias (V_d = 0.1 V). It shows the typical ambipolar behavior for a graphene channel with a current minimum at the neutrality (or Dirac) point (V_{NP}) at 9.0 V. The neutrality point is significantly shifted at high positive bias with respect to the expected ideal value calculated considering the difference between Al and neutral graphene workfunctions ($V_{NP,id} = W_{Al} - W_{Gr} \approx 4.1 - 4.5 = -0.4$ eV). This positive shift is a clear indication of graphene p-type doping, as estimated by $p = C_g(V_{NP} - V_{NP,id})/q \approx 1.2 \times 10^{13}$ cm^{-2} [20], where q is the electron charge. This doping can be ascribed to the effect of the chemical (PMMA) residues which normally persist after the graphene transfer. It is worth noting that due to the constrains imposed by the use of a PEN substrate, it is not possible to perform thermal annealing processes (in vacuum or Ar/H_2 ambient at temperatures from 300 to 400 °C) or stronger chemical treatments typically used to remove polymeric residues after graphene transfer on standard substrates. Furthermore, a certain doping can be attributed to the electrostatic effect of fixed or trapped charges in the gate oxide when deposited at low temperature.

The insert of Figure 5b shows the leakage current through the gate dielectric (I_g vs V_g) collected simultaneously to the transfer characteristic measurement, showing only a negligible current flow (less than nA) in the whole back gate bias range. The transfer conductance g_m of the Gr-FET reported in Figure 6 was obtained considering the I_d vs V_g characteristic by the formula:

$$g_m = dI_d / dV_g \,. \tag{2}$$

From the peak transfer conductance, we calculated the hole and electron field effect mobility, μ_h = 476 cm^2·V^{-1}·s^{-1} and μ_e = 204 cm^2·V^{-1}·s^{-1} using the formula:

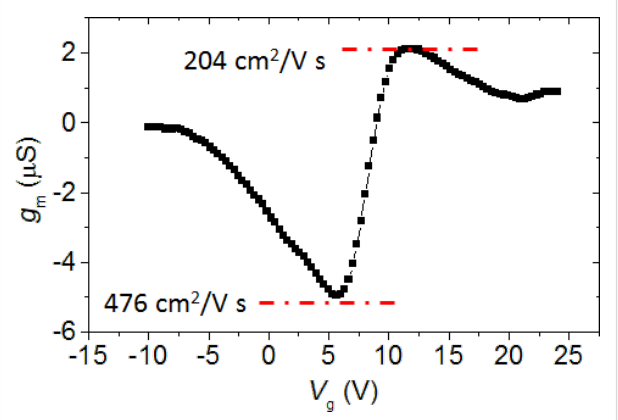

Figure 6: Transfer conductance, g_m, of the Gr-FET, calculated from the I_d vs V_g transfer characteristic.

$$\mu = g_m L / \left(WC_g V_d\right), \tag{3}$$

These field effect mobility values are reasonably high, considering the channel area (about 10^4 μm^2), the high roughness due to the plastic substrate and the unintentional doping of graphene. In particular, it is expected that the polycrystalline nature of CVD graphene has a direct effect on the current transport in a large area channel. In addition to these natural defects originating from CVD growth, the graphene membrane is subjected to significant strain if transferred to a rough surface while a certain amount of mechanical defects, such as cracks or folding is expected by the transfer procedure itself, especially onto a structured surface. Besides these macroscopic defects, nanoscale scattering mechanisms [21], such as charged impurities scattering and resonant scattering by defects/polymer contaminations, is expected to play a key role in reducing graphene mobility. Finally, it should also be noted that this is a calculation of the extrinsic field effect mobility, where the contribution of the series resistances (such as the contact resistance R_c and the access resistance R_{acc}) are still included. A more refined calculation of the graphene field effect mobility would include the elimination of the series resistance contributions in order to extract the intrinsic transfer conductance and the related mobility.

Significant improvements in the transfer conductance and mobility of large area Gr-FETs on flexible substrates will be expected by the use polymeric substrates with optimized lower roughness and by further improvements in the graphene transferring methods, e.g., adopting alternative transfer layers different than common PMMA, leaving a very limited amount of chemical residues on graphene [22].

The field effect modulation of the channel conductivity obtained so far using the thin Al_2O_3 back-gate dielectric make the fabricated Gr-FETs interesting as a platform for chemical sensing applications. In this sense, a key step will be proper functionalization of graphene channel to enhance the sensitivity to specific analytes.

Conclusion

In conclusion, we reported recent advances in the fabrication of Gr-FET with large channel areas (≈10^4 μm^2) and local back-gate on flexible PEN substrates. Particular attention was paid to the fabrication of a thin Al_2O_3 dielectric film at low temperature. In particular, a low temperature (100 °C) PE-ALD process was optimized and properly tested on a standard substrate (Si) in comparison with a standard PE-ALD deposition. This revealed a material with good morphology, reasonable growth per cycle and comparable dielectric performance. The opti-

mized dielectric material deposition was exploited in order to fabricate back-gated Gr-FETs directly on a PEN substrate, with a gate oxide thickness of 30 nm. Electrical characterization of the Gr-FET devices is reported in order to evaluate key electrical parameters such as the transfer conductance, graphene doping and electron and hole mobility. The fabricated devices will represent the platform for the implementation of solid IS-FETs that can be part of a fully flexible, integrated system for sensing and signal processing.

Acknowledgements

This work has been supported, in part, by European Union Seventh Framework Program under Grant Agreement No. 604391 Graphene Flagship and by MIUR in the framework of the FlagERA project GraNitE.

References

1. Cheng, I-C.; Wagner, S. Overview of Flexible Electronics Technology. In *Flexible Electronics;* Wong, W. S.; Salleo, A., Eds.; Electronic Materials: Science & Technology, Vol. 11; Springer: Berlin, Germany, 2009; pp 1–28. doi:10.1007/978-0-387-74363-9_1
2. Akinwande, D.; Petrone, N.; Hone, J. *Nat. Commun.* **2014,** *5,* 5678. doi:10.1038/ncomms6678
3. Kim, D.-H.; Ahn, J.-H.; Choi, W. M.; Kim, H.-S.; Kim, T.-H.; Song, J.; Huang, Y. Y.; Liu, Z.; Lu, C.; Rogers, J. A. *Science* **2008,** *320,* 507. doi:10.1126/science.1154367
4. Viventi, J.; Kim, D.-H.; Moss, J. D.; Kim, Y.-S.; Justin, J. A.; Annetta, N.; Hicks, A.; Xiao, J.; Huang, Y.; Callans, D. J.; Rogers, J. A.; Litt, B. *Sci. Transl. Med.* **2010,** *2,* 24. doi:10.1126/scitranslmed.3000738
5. Hwang, S.-W.; Tao, H.; Kim, D.-H.; Cheng, H.; Song, J.-K.; Rill, E.; Brenckle, M. A.; Panilaitis, B.; Won, S. M.; Kim, Y.-S.; Song, Y. M.; Yu, K. J.; Ameen, A.; Li, R.; Su, Y.; Yang, M.; Kaplan, D. L.; Zakin, M. R.; Slepian, M. J.; Huang, Y.; Omenetto, F. G.; Rogers, J. A. *Science* **2012,** *337,* 1640. doi:10.1126/science.1226325
6. Lee, C.; Wei, X.; Kysar, J. W.; Hone, J. *Science* **2008,** *321,* 385. doi:10.1126/science.1157996
7. Kim, K. S.; Zhao, Y.; Jang, H.; Lee, S. Y.; Kim, J. M.; Kim, K. S.; Ahn, J.-H.; Kim, P.; Choi, J.-Y.; Hong, B. H. *Nature* **2009,** *457,* 706. doi:10.1038/nature07719
8. Kwak, B. W.; Choi, Y. C.; Lee, B. S. *Phys. E (Amsterdam, Neth.)* **2015,** *68,* 33. doi:10.1016/j.physe.2014.12.017
9. Lin, Y.-M.; Dimitrakopoulos, C.; Jenkins, K. A.; Farmer, D. B.; Chiu, H.-Y.; Grill, A.; Avouris, P. *Science* **2010,** *327,* 662. doi:10.1126/science.1184289
10. Lee, J.; Ha, T.-J.; Li, H.; Parrish, K. N.; Holt, M.; Dodabalapur, A.; Ruoff, R. S.; Akinwande, D. *ACS Nano* **2013,** *7,* 7744. doi:10.1021/nn403487y
11. Schedin, F.; Geim, A. K.; Morozov, S. V.; Hill, E. W.; Blake, P.; Katsnelson, M. I.; Novoselov, K. S. *Nat. Mater.* **2007,** *6,* 652. doi:10.1038/nmat1967
12. Pearce, R.; Iakimov, T.; Andersson, M.; Hultman, L.; Lloyd Spetz, A.; Yakimova, R. *Sens. Actuators, B* **2011,** *155,* 451. doi:10.1016/j.snb.2010.12.046
13. Li, X.; Cai, W.; An, J.; Kim, S.; Nah, J.; Yang, D.; Piner, R.; Velamakanni, A.; Jung, I.; Tutuc, E.; Banerjee, S. K.; Colombo, L.; Ruoff, R. S. *Science* **2009,** *324,* 1312. doi:10.1126/science.1171245
14. Faggio, G.; Capasso, A.; Messina, G.; Santangelo, S.; Dikonimos, T.; Gagliardi, S.; Giorgi, R.; Morandi, V.; Ortolani, L.; Lisi, N. *J. Phys. Chem. C* **2013,** *117,* 21569. doi:10.1021/jp407013y
15. Yan, F.; Zhang, M.; Li, J. *Adv. Healthcare Mater.* **2014,** *3,* 313. doi:10.1002/adhm.201300221
16. Bergveld, P. *IEEE Trans. Biomed. Eng.* **1970,** *MBE–17,* 70. doi:10.1109/TBME.1970.4502688
17. Zhu, Y.; Wang, C.; Petrone, N.; Yu, J.; Nuckolls, C.; Hone, J.; Lin, Q. A solid-gated graphene fet sensor for PH measurements. In *2015 28th IEEE International Conference on Micro Electro Mechanical Systems (MEMS),* Estoril, Portugal, Jan 18–22, 2015; IEEE Publishing: Piscataway, NJ, U.S.A., 2015; pp 869 ff. doi:10.1109/memsys.2015.7051097
18. Groner, M. D.; Fabreguette, F. H.; Elam, J. W.; George, S. M. *Chem. Mater.* **2004,** *16,* 639. doi:10.1021/cm0304546
19. Blaho, M.; Gregušová, D.; Jurkovič, M.; Haščík, Š.; Fedor, J.; Kordoš, P.; Fröhlich, K.; Brunner, F.; Cho, M.; Hilt, O.; Würfl, J.; Kuzmík, J. *Microelectron. Eng.* **2013,** *112,* 204. doi:10.1016/j.mee.2013.03.120
20. Kim, S.; Nah, J.; Jo, I.; Shahrjerdi, D.; Colombo, L.; Yao, Z.; Tutuc, E.; Banerjee, S. K. *Appl. Phys. Lett.* **2009,** *94,* 062107. doi:10.1063/1.3077021
21. Giannazzo, F.; Sonde, S.; Lo Nigro, R.; Rimini, E.; Raineri, V. *Nano Lett.* **2011,** *11,* 4612. doi:10.1021/nl2020922
22. Van Ngoc, H.; Qian, Y.; Han, S. K.; Dae, J. K. *Sci. Rep.* **2016,** *6,* 33096. doi:10.1038/srep33096

License and Terms

BEILSTEIN JOURNAL OF NANOTECHNOLOGY

Anodization-based process for the fabrication of all niobium nitride Josephson junction structures

Massimiliano Lucci*[1], Ivano Ottaviani[1], Matteo Cirillo[1,2], Fabio De Matteis[3], Roberto Francini[3], Vittorio Merlo[1] and Ivan Davoli[1]

Full Research Paper

Open Access

Address:
[1]Dipartimento di Fisica and MINAS Lab, Università di Roma Tor Vergata, 00133 Roma, Italy, [2]CNR-SPIN Institute, Via Giovanni Paolo II, 84084 Fisciano (SA), Italy and [3]Dipartimento di Ingegneria Industriale, Università di Roma "Tor Vergata", Via del Politecnico, 00133 Roma, Italy

Email:
Massimiliano Lucci* - lucci@roma2.infn.it

* Corresponding author

Keywords:
Josephson effect; superconductors; thin films; tunneling

Beilstein J. Nanotechnol. **2017,** *8,* 539–546.
doi:10.3762/bjnano.8.58

Received: 05 October 2016
Accepted: 17 February 2017
Published: 02 March 2017

This article is part of the Thematic Series "Self-assembly of nanostructures and nanomaterials II".

Guest Editor: I. Berbezier

Abstract

We studied the growth and oxidation of niobium nitride (NbN) films that we used to fabricate superconductive tunnel junctions. The thin films were deposited by dc reactive magnetron sputtering using a mixture of argon and nitrogen. The process parameters were optimized by monitoring the plasma with an optical spectroscopy technique. This technique allowed us to obtain NbN as well as good quality AlN films and both were used to obtain NbN/AlN/NbN trilayers. Lift-off lithography and selective anodization of the NbN films were used, respectively, to define the main trilayer geometry and/or to separate electrically, different areas of the trilayers. The anodized films were characterized by using Auger spectroscopy to analyze compounds formed on the surface and by means of a nano-indenter in order to investigate its mechanical and adhesion properties. The transport properties of NbN/AlN/NbN Josephson junctions obtained as a result of the above described fabrication process were measured in liquid helium at 4.2 K.

Introduction

Niobium (Nb) is the most commonly used material in superconducting electronics [1-3], but several groups have been investigating the properties of metals and alloys that could represent an alternative to it. Niobium nitride (NbN), in particular, is a promising material in this respect given its relatively high critical temperature and energy gap of the order, respectively, of 16 K and 2.5 mV [4-8]. The transition temperature is appealing because of the progress achieved in closed-cycle refrigeration, while the value of the gap is stimulating for engineering devices in the terahertz range. Several papers have been dedicated in the past to the realization of all-NbN-based superconducting tunnel junctions [9-11], but a reliable technology generating samples with quality features similar to the ones of all-Nb samples [1,12] has not emerged yet.

We have undertaken a systematic study of the production of all-NbN films and all-NbN tunnel junctions. In a previous publication the authors of the present paper investigated the effect of

the substrate on the quality of the NbN films and the NbN/AlN interface [13] while preliminary lithographic attempts on NbN/AlN/NbN trilayers were presented in another publication [14]. In the present paper our effort toward the realization of high-quality all-NbN tunnel junctions continues. We have first set up the conditions for a highly reproducible and controllable growth of good-quality NbN monitoring the sputtering plasma by optical spectroscopy [15-17]. The same technique has been employed to obtain AlN thin films. At first, we have decided to concentrate on AlN as dielectric layer in NbN/AlN/NbN junctions because this material seems to be the most promising at present. Moreover, as a first step we considered reasonable to match our overall fabrication recipe with existing processes and literature. Along with the optimal and controlled film growth we also carried out an investigation of the anodization of these films since this technique is necessary for the most of the procedures leading to the patterning of tunnel junctions.

The processes for defining patterns on NbN thin films are typically based on ion etching and subsequent deposition of insulating layers [9-11]. We have tried to limit our fabrication recipe instead to minimal procedures, namely just lift-off lithography and selective anodization. By using lift-off lithography aggressive and high-energy etching processes such as ion milling and reactive ion etching (RIE) can be avoided. The use of anodization can reduce the number of mask and photolithography steps. In particular, it is not necessary to deposit further insulators to separate different metals in multilayers. In all of our investigations the substrates are commercially available silicon wafers coated with 1 μm artificial oxide. This choice was also dictated by the perspective of setting up a recipe that could well lend itself to be developed for "large-scale" commercial applications.

Experimental

Methods

One reliable process to deposit NbN and AlN films consists of using a reactive sputtering chamber [4-8]. When such a technique is employed, however, the quality of the films depends on several parameters: the purity of the deposition chamber, the reciprocal positions of source and substrate, the relative pressure of N_2, the magnetic field, the dc or the rf power used and the surface temperature of the substrate. The last condition is particularly critical because the increase of the kinetic energy of ions close to the substrate promotes the formation of nitrides, but deteriorates the vacuum conditions. Temperature control is particularly relevant when lithographic patterns impressed by photoresist (an organic polymeric compound melting above 120 °C) are present on the substrate because the degassing of the polymer pollutes the deposition chamber. For this reason the temperature of the substrate must be kept constantly below 120 °C. This often makes it necessary to alternate periods of sputtering with periods in which the sputtering is stopped.

Eye inspection of the plasma during the sputtering reveals that the color of the glow discharge changes from blue to red with increasing nitrogen concentration. A quantitative analysis of this effect can be obtained by relating the concentration of N_2 in the plasma to the intensities of the emission lines observed with the aid of a spectrometer [15-17]. This technique has enabled us to link the plasma composition and the final composition of the nitride films. To our knowledge, this is the first time this optical spectrometry technique is applied in the production of superconductive metallic films for optimizing the transition temperature and film quality. Since the deviation from a stoichiometric composition of the NbN affects (reducing it) the superconducting critical temperature, the pattern of the emission lines in the glow discharge provides direct information on the critical temperature of the deposited nitride films. For AlN the gas composition affects the resistivity of the film and, even in this case, the pattern of the emission lines in the glow discharge provides information on the final resistivity of the sputtered films.

The anodization of the NbN layer was obtained by means of a 1 mol solution of ammonium pentaborate in ethylene glycol. In order to oxidize NbN samples, we used a current-control technique, i.e., the current density has been set while the potential difference (V_s) between cathode and anode in the electrolytic cell has been monitored simultaneously. The samples were anodized using different current bias and voltage compliance (V_c) to scrutinize the effects on the growth of NbN oxide. The cell has a platinum electrode at fixed distance of 1 cm parallel to the sample surface.

A systematic study on different thicknesses (depending on V_s) was performed to obtain a compact layer without defects and cracks. The anodized films were also characterized by Auger spectroscopy to analyze compounds formed on the surface and their stoichiometry. A multilayer superconductor/insulator/superconductor was obtained by successive depositions and patterned by means of the proposed anodization technique to obtain a NbN/AlN/NbN Josephson junction the current–voltage characteristic of which was measured in a liquid helium bath at 4.2 K.

Equipment

The sputtering system used in our experiment is a commercial Leybold sputtering system equipped with two 4 inch dc and rf magnetron sources and one etching source. A flux meter controls the inlet for N_2 and Ar. Finally, a rotatable disk plate holds several substrates in the chamber; this plate is grounded to

allow for ion cleaning before the sputtering process. For the deposition of NbN, the dc mode was used with different gas mixtures of N_2/Ar flux, (total pressure 5×10^{-1} Pa), while AlN was deposited in rf mode (150 W) with a gas mixture of N_2 and 20 sccm of Ar, the base pressure in the chamber being 10^{-4} Pa. In these conditions, the deposition rates for NbN and AlN were 0.6 nm/s and 0.06 nm/s, respectively.

The calibration of the deposition rate was performed by measuring, ex situ, the thickness of the obtained film by means of a profilometer. All the samples described in this work were grown on Si(111) substrates covered by 1 µm of amorphous, artificially grown oxide. Following common recipes reported in literature the target–substrate distance is about 10 cm and the substrate temperature, measured by a thermocouple, is kept below 50 °C during the NbN film growth. Alternating flash deposition of 120 s with pauses of about 20 s was carried out. The thickness of the deposited films was 300 nm.

The critical temperature T_c of the NbN thin films has been determined by four-probe measurements of resistance as a function of the temperature with the samples secured to the cold finger of a Gifford–McMahon cryocooler. The characteristics of the films were measured as a function of two parameters of the deposition process: the dc power of the source (increasing or reducing the rate of the flash and pause during sputtering) and the concentration of N_2 in the gas mixture present during the sputtering process. Under these conditions, we obtained films with different superconducting transition temperatures (T_c) ranging from 9.0 to 15.5 K. The room-temperature sheet resistance (resistivity per unit thickness) of the AlN films was also measured by using the four-probe technique. Different AlN specimens have been prepared, keeping constant the rf power (150 W) and the argon flux (20 sccm), but varying the nitrogen concentration during the sputtering process.

The optical emission spectra of the plasma discharge were acquired with an Ocean Optics Spectrometer, model HR 4000, in the range of 300–1000 nm, connected to the vacuum chamber by means of an optical fibre pointing directly into the plasma. The measurements of hardness, reduced modulus and surface roughness have been performed by Nano Test Micro Materials Ltd., using a diamond Berkovich tip.

Results and Discussion

NbN films

In Figure 1 we show two optical emission spectra of the glow discharge in a selected wavelength range as detected during the preparation of the NbN deposition, just before opening the shutter. Both curves show the intensity of the light emission peaks as a function of the wavelength, detected during the glow discharge for a fixed power of 200 W. The data show the trend of the intensity of the N_2 and of Nb peaks, when the gas content of the chamber changes from a constant flux of Ar (91 sccm) to a mixture of N_2/Ar obtained by increasing the N_2 injection from 0 to 25 sccm in steps of 5 sccm. We note that the intensity of the N_2 peak (see the peak at 337 nm) increases to a value 2.5 times that of the background (600 a.u.), while the Nb peak (416 nm) decreases to about half of its maximum value. This happens because niobium reacts with N_2 to the nitride. The more N_2 is present the higher is the amount of nitride generated and the lower is the amount of Nb atoms emitting at a given spectral position. The relative height of the Nb and N_2 peaks is the parameter that we correlate to the transition temperatures (and quality) of our NbN films. In order to do so we always select the spectral lines exhibiting the largest variation as a

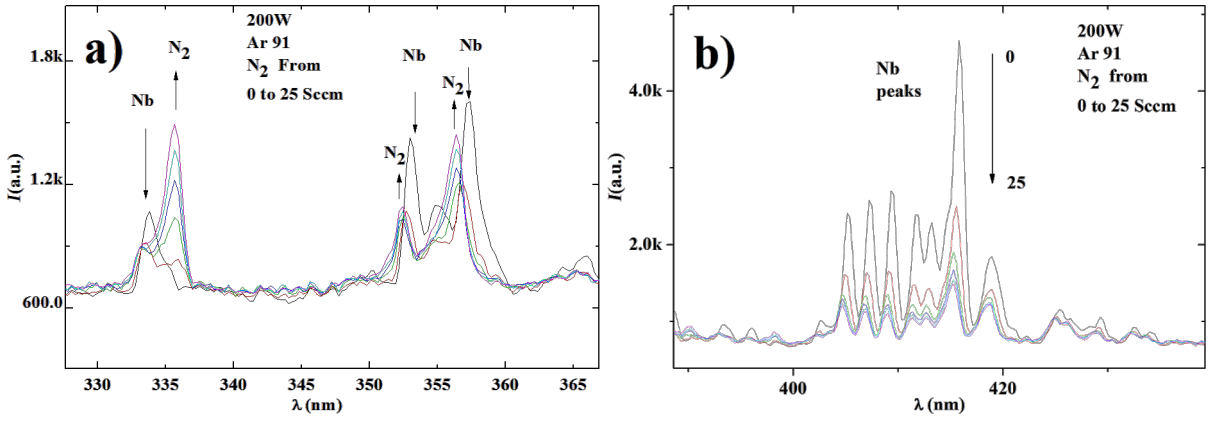

Figure 1: a) Glow-discharge peak intensity monitored in the region of 328–367 nm, an energy region in which we find both Nb and N_2 peaks. In the inset the power, the fixed Ar concentration and the range of the amount of N_2 are reported. The color of the six curves, obtained for increasing values of the N_2 flux, starting from 0 and going up to 25 sccm in steps of 5 sccm are as follows: black, red, green, dark blue, cyan, and magenta; b) Glow-discharge peak intensity in the region 388–438 nm, inset as in panel a.

function of the nitrogen inlet. In this specific case (Figure 1), we select the lines mentioned before, namely 337 nm for N_2 and 416 nm for Nb.

Figure 1 also shows how to quantify the color change visible by eye in the plasma and obtain a fine tuning of the composition of the plasma during the sputtering deposition. Each of the curves shown in Figure 1 corresponds to a different concentration of N_2 and to different colors, which are shown in Figure 2.

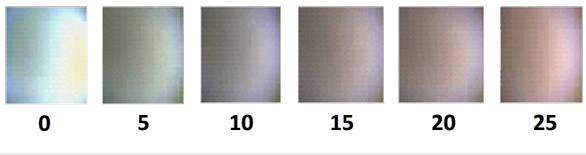

Figure 2: The color of the plasma corresponding to the six increasing values of the input flux described in Figure 1 (0 sccm is the leftmost, 25 sccm is the rightmost).

In Figure 3 we report a three-dimensional plot showing the values of critical temperature (T_c) of NbN films as a function of the dc power applied on the target and the N_2 flux inlet in the deposition chamber for 40 different recipes. T_c is the temperature for which the electrical resistance, measured with the four-point probe technique, drops to zero. We have fabricated more than 100 films with a thickness maintained constant at about 300 nm. Several points in the plot of Figure 3 were repeatedly measured with a variance of the values of the critical temperature within few tenths of a degree.

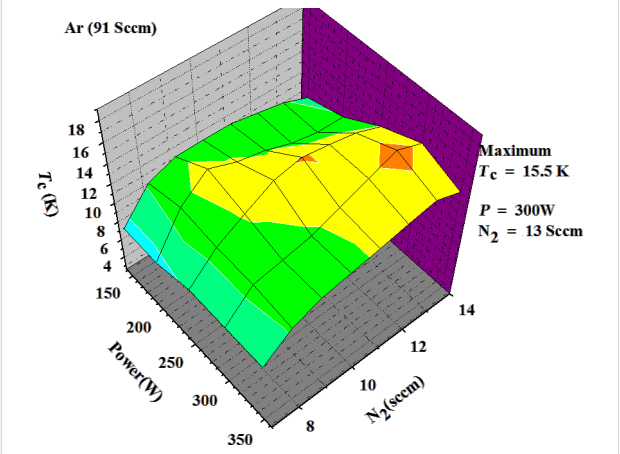

Figure 3: 3D plot constructed to optimize sputter deposition. Each point of the grid corresponds to a sample fabricated with the given set of parameters. We can see that in our apparatus with a basic pressure of 2 × 10^{-5} Pa the highest T_c (15.5 K) is obtained with 300 W and a gas mixture of 14% N_2 in Ar.

For each film, we have varied either the dc power or the concentration of N_2 in the chamber. We note that the film with the highest critical temperature (15.5 K) is obtained when the N_2 flux is 13 sccm and the dc power applied is 300 W. Unfortunately, high power on the target implies a high temperature on the substrate. Consequently, in order to deposit NbN films on a patterned mask, we must use a lower dc power, and find another concentration of N_2. Because the high temperature induced on the substrate softens the photoresist and pollutes the NbN films. In Figure 4 the section of the 3D-plot of Figure 3 corresponding to a dc power of 200 W is shown. We can see more clearly that a N_2 flux of 9 sccm gives NbN film with a T_c of 14 K. In addition from the top axis of Figure 4 we can trace the dependence of T_c upon the ratio between the height of the peaks on Nb and N_2. Thus, by monitoring the relative height of the spectrometric peaks, as mentioned above, we can follow the growth of NbN and estimate the expected transition temperature.

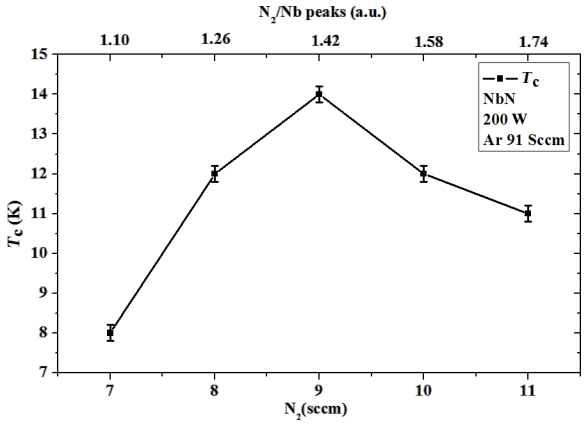

Figure 4: Critical temperature T_c of NbN as a function of the N_2 flux and of the of N_2/Nb peak ratio. In the inset the deposition parameters are given.

Equation 1 gives the fit of the measured T_c (the surface of Figure 3) as a function of the power (P) in watts and the nitrogen flux (F) in sccm. We observe a strong dependence of T_c on the nitrogen flux, a tendency opposite to the data obtained by Dawson-Elli et al. [5] who worked in a saturated regime of nitrogen flux.

$$T_c\,(\mathrm{K}) = -16.16 + 0.036P + 4.26F \\ -0.00012P^2 - 0.22F^2 + 0.0031PF \quad (1)$$

AlN films

In Figure 5 the relative intensities of the optical plasma emission obtained during the deposition of AlN films, are plotted in the wavelength range of 590–820 nm. The spectra are recorded for a constant rf power of 150 W, while the N_2/Ar mixture is varied by changing the N_2 flux from 0 to 100 sccm while

keeping the Ar flux constant at 20 sccm. With increasing N_2 flux the N_2 peaks increase and the Ar peaks decrease. Similarly to what we did for NbN (Figure 1), we correlated the relative height of two peaks (for N_2 and Ar) to the conductivity of the film.

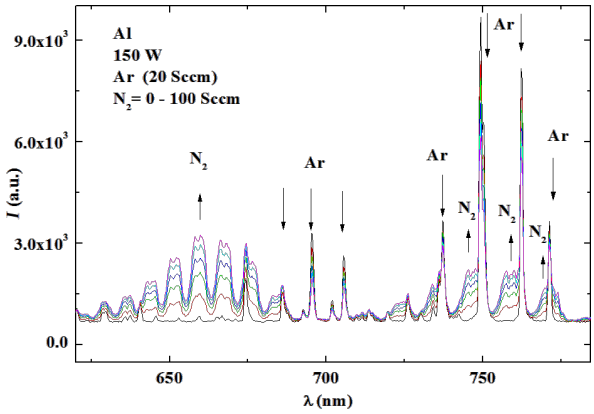

Figure 5: Spectrum of the emission lines. Details of AlN for different values of N_2 flux (starting from 0 and going up to 100 sccm in steps of 20 sccm, the colors are as follows: black, red, green, dark blue, cyan, and magenta) at fixed power (150 W) and an Ar flux of 20 sccm.

In Figure 6 we plot the sheet resistance of the deposited AlN films as a function of the composition of the N_2/Ar mixture and of the N_2/Ar peak ratio. We choose from Figure 5 the peaks with high intensity that were also very responsive to the gas variations of the gas flux (Ar and N_2 peaks at 750 nm and 660 nm, respectively). The spectral lines of Ar and N_2 should be close enough to be simultaneously visualized on the spectrometer display. It is impossible to measure the sheet resistance of a highly insulating film. However, we estimated that when the peak ratio of N_2/Ar is close to 2.63 the resistance is

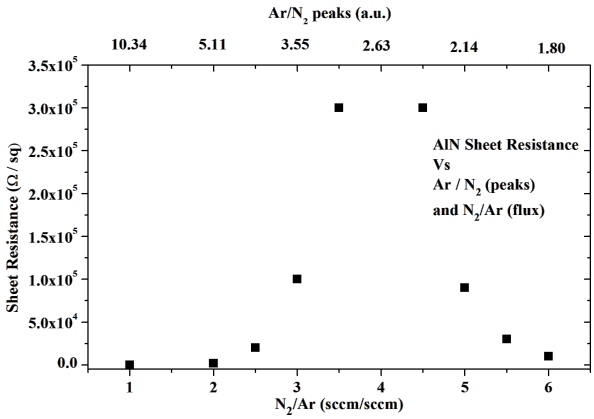

Figure 6: Resistivity of AlN film as a function of N_2/Ar gas flux and Ar/N_2 peak ratio. The rf power was fixed at 150 W.

higher than 4.53×10^6 Ω/sq. (10 MΩ is the maximum value that can be measured by our data-acquisition set-up.)

NbN anodization

For the anodization recipe we started selecting the parameters generally used to anodize niobium, namely current densities of {10; 1; 0.3; 0.1} mA/cm^2 at different compliance voltages. In Figure 7 we show the voltage difference between the NbN films and the counter electrode during the anodization process as a function of time. The inset indicates the anodization currents and voltages. We observed that a voltage noise is present at high current densities (curves 1,2,3) that reduces V_c from 150 to 90 V.

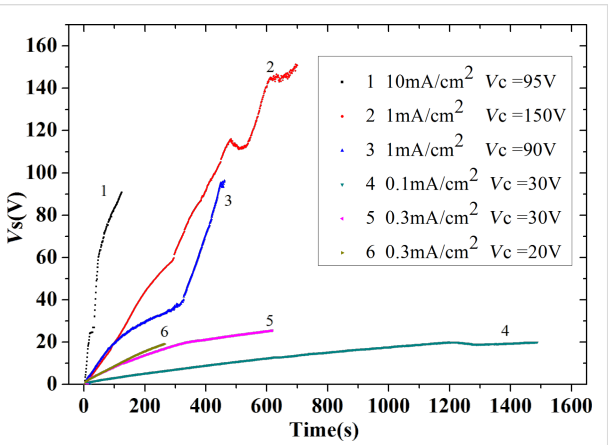

Figure 7: Film voltages as a function of the time obtained varying the current density and compliance voltages for different samples in our NbN anodization process. The number close to each curve is associated with the current and voltage parameters indicated in the inset.

Moreover, for these three samples (1,2,3) we clearly see changes in slope which is a signal of a non-uniform oxidation process, and of the fact that cracks and fractures are damaging the film. The existence of fractures and cracks is also confirmed from optical analysis of the surfaces. Indeed, after the oxidation the samples 1,2 and 3 the oxidized films were completely delaminated (Figure 8a). The visible contour separating the top from the bottom represents the separation between NbN (top) and the anodized Nb (bottom).

Reducing the current density (curves 4 and 5) and *Vc* to 30 V, the fluctuations of *Vs* were reduced and the adhesion of the films was improved although the sample corresponding to curve 4 and 5 were still conducting. A careful analysis of these two curves in Figure 7 reveals that a change in slope is still present around 20–25 V. Further reducing *Vc* to 18–20 V we obtained curve 6, a smooth curve without voltage noise and change in slope. From an optical and electric analysis, the film is uniform, shows good adhesion and is an electric insulator (sheet resis-

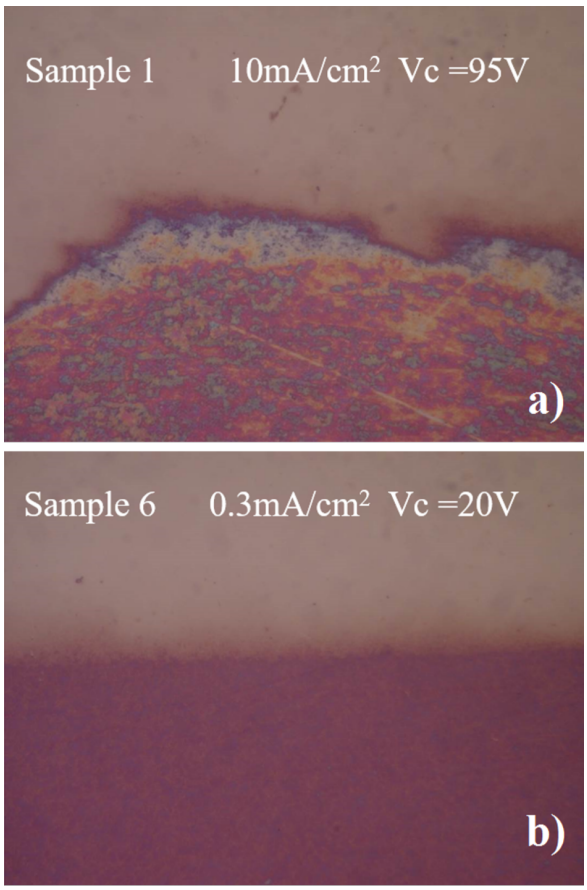

Figure 8: Optical microscopy images at 100× magnification of a) sample 1 in a) and b) sample 6. The upper part of the pictures is the NbN film, and the lower part is the oxided film after the anodization process.

tance larger than 10 MΩ/sq). In Figure 8b we can see that the surface of the oxidized Nb (bottom part) is rather smooth and exhibits good adhesion (we shall later comment more on the mechanical properties). The oxide film grown on the NbN has a different final thickness due to different lattice parameters (Figure 9). NbN has a cubic structure ($Fm\bar{3}m$, space group 255, a = 0.44 nm, corresponding to a cell volume of 0.0846 nm^3), whereas Nb_xO_y (the stable stoichiometry for an insulator should be Nb_2O_5) has an orthorhombic structure (a = 0.398 nm, b = 0.382 nm and c = 1.279 nm, cell volume of 0.194 nm^3).

From the measurement of the step thickness and assuming a one-directional oxide growth (free space) we extracted the following relationship, where T denotes the thickness (see Figure 9 for the symbols): $T_{INT}/(T_{EXT} + T_{INT}) \approx 0.0846/0.194$ and $T_{OX} \approx 1.8 \cdot T_{EXT}$.

It is possible to predict the thickness of the oxide layer measuring the height of the step. As a further relationship between the oxide thickness T and the voltage across the sample Vs we found $T \approx (2.8\ \text{nm})V_s$. This relationship could be the connection between the maximum voltage and the maximum thickness (ca. 60 nm) that we can grow before a crack or a fracture starts damaging the film. In the mechanical characterization, performed at 1 mN as maximum load, we observed continuous and smooth load-vs-depth graphs. The absence of cracks and delaminations during the measurements reveals good adhesion between the film and the substrate. When the composition of the layer changes from NbN to Nb_xO_y hardness and reduced modulus both decrease, respectively, from an average value of 5.9 GPa to 4.6 GPa and from 85 GPa to 78 GPa. The roughness of the oxidized surface was ±5 nm.

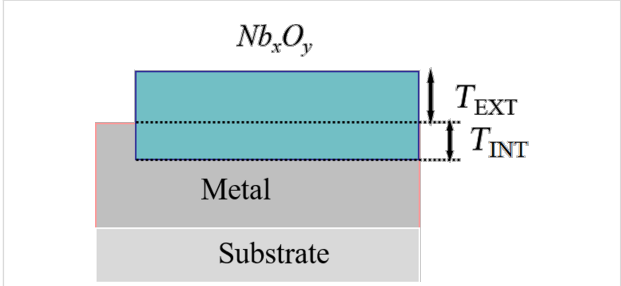

Figure 9: Scheme of the oxidized film grown on NbN. The total thickness of the oxide (T_{EXT} + T_{INT}) is higher than the initial thickness of NbN (T_{INT}).

To determine the chemical composition of the grown film we performed Auger electron spectroscopy (AES) and the spectra are shown in Figure 10. A complete nitrogen replacement with oxygen is observed from the measurements and a rough stoichiometry can be extrapolated compatible with Nb_2O_5.

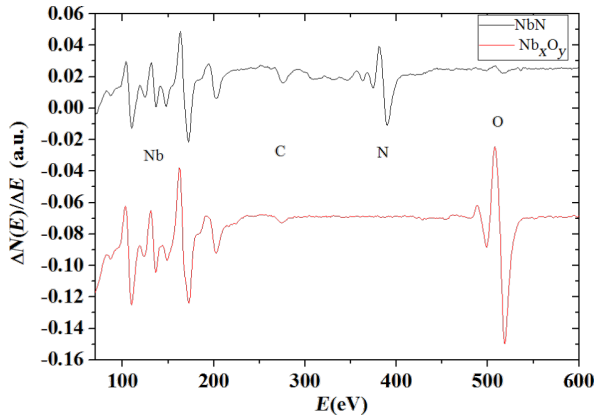

Figure 10: Auger electron spectroscopy of the initial NbN sample before and after anodization. A soft surface cleaning process by Ar ion etching was performed before the measurements. From the spectra is observed that only niobium and nitrogen are present before the process. After the oxidation process the nitrogen was completely replaced with oxygen.

Tunnel junctions

In Figure 11a we show the current–voltage characteristic of a Josephson-junction measured at 4.2 K. The three-layer junction (NbN/AlN/NbN) is formed by three films of different thickness, namely 175 nm, 2 nm and 360 nm. The choice of the thicknesses of the films was imposed by design requirements. The Josephson junctions (Figure 12) were realized using UV lithography and a lift-off process. The (10 × 10) μm^2 junction areas were defined anodizing the top layer following standard techniques [14]. The parameters of this junction are a representative result of our fabrication recipe: Josephson critical current density j_c = 14.2 A/cm^2, product of maximum critical current and normal resistance $I_c{\cdot}R_{NN}$ = 1.63 mV, R_{NN}/R_{SG} = 10, $V_m = I_C{\cdot}R_{SG}$ = 16.3 mV, gap sum voltage V_G = 3.6 mV. These parameters are sufficiently consistent with those reported by other research groups (10 A/cm^2 < j_c < 8 kA/cm^2, 1.7 mV < $I_c{\cdot}R_{NN}$ < 3.32 mV, 5 < (R_{NN}/R_{SG}) < 40, 13 mV < V_m < 100 mV, gap sum voltage 4.2 mV < V_G < 5.6 mV [9-11]) thereby confirming the apparent impression of an overall reasonable result of our fabrication process. This conclusion is especially encouraging if we consider that the fabrication processes of other groups were carried out on crystalline substrates brought to high temperatures during deposition.

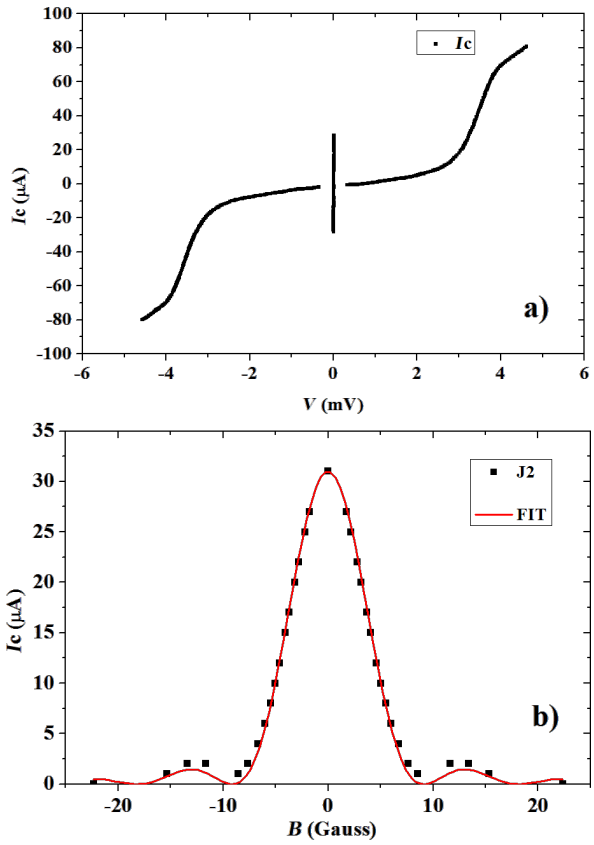

Figure 11: a) Current–voltage characteristic for NbN Josephson junction and b) diffraction pattern obtained measuring *Jc* as function of the applied magnetic field. The continuous line is a fit obtained imposing a Josephson current distribution "rounded" along the corners of the nominally square area.

From the magnetic field diffraction pattern of Figure 11b we can extract the London penetration depth of our NbN films of 500 ± 30 nm. This result is in good agreement with previous results obtained through NbN deposition on non-heated substrates [18,19]. The pattern shows a somewhat non-uniform Josephson current distribution [20], which we speculate to be due to a reshaping of the contour of the junctions during the anodization process. The continuous line in Figure 11b is a fit to the data obtained by a non-uniform Josephson current distribution in the junction, namely a profile rounded around the corners of the supposed rectangular shape.

It is known that the growth of NbN/AlN/NbN tunnel junctions on oxidized silicon substrates can give rise to a non-optimal barrier formation. In order to check the influence of the substrate on trilayers we plan to test our trilayer process on MgO substrates, which are known, for providing the highest quality of the tunneling barrier [13]. We are not sure, however, that the nature of the substrate is the only crucial factor in fabricating NbN-based tunnel junctions with excellent quality. We have shown indeed that an acceptable (in terms of results) NbN process can be obtained just by lift-off lithography and anodization of the superconductive films grown over "cold" amorphous silicon oxide. Improvements of this recipe could substantially enhance the ease of fabrication and lead to noticeable progress in the scientific and technical usefulness of all-NbN tunneling devices.

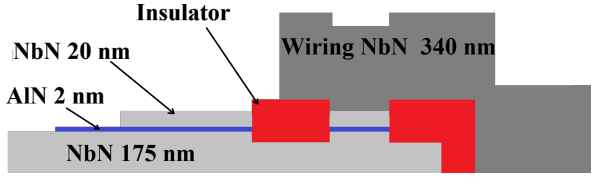

Figure 12: A section of our samples indicating the layers of the fabrication steps and their relative thicknesses.

Conclusion

A viable method to optically monitor and tune, in a timely fashion, the chemical composition of the plasma in a sputtering process has been applied to grow thin films of niobium nitride and aluminium nitride. The advantage of this optical spectroscopy technique is that the control of the chemical composition of the film is no longer system-dependent and provides objective advantages during the reactive sputtering deposition. We have shown that for the NbN superconducting films, this

method gives the possibility to increase or to reduce the flux of nitrogen and to obtain the best chemical composition within the constraints imposed by the other growth parameters. Similarly, it is possible to predict and obtain the conductive or insulating properties of AlN.

We have adapted the deposition process to the lithographic and technological needs for the realization of superconductor/insulator/superconductor and Josephson junctions devices. These techniques rely on three layers of NbN/AlN/NbN, and require, as a first step in the fabrication process the use of a photoresist-patterned substrate. This condition, in turn, limits the highest acceptable dc power to 200 W. For a reduced sputtering power, the plasma composition must be redefined, because only the right amount of N_2 in the plasma composition gives the highest critical temperature of the NbN film. The highest transition temperature was reached for a ratio N_2/Nb equal to 1.42 corresponding to a N_2 flux of 9 sccm.

We have presented the required values for current density and compliance voltage to obtain a controlled and stable oxidation of a NbN thin film. Auger electron spectroscopy and nanoindentation analysis has been employed to verify respectively the complete oxidation of the surface and the mechanical stability of the film. We have also found a relationship between the growth of the oxide film and the voltage during the anodization as a method to control its thickness up to few angstroms per second. The properties and the quality of Josephson junctions obtained using our patterning based on lift-off lithography on cold substrates and the anodization of NbN for defining the junction area are not far from those reported by other groups for high-temperature deposition of the films and reactive etching for geometry definition.

References

1. Murduck, J. M. *Thin Films* **2001,** *28,* 271–317. doi:10.1016/S1079-4050(01)80022-3
   Part of the Special Issue *Frontiers of Thin Film Technology* edited by Maurice H. Francombe.
2. Lucci, M.; Ren, J.; Sarwana, S.; Ottaviani, I.; Cirillo, M.; Badoni, D.; Salina, G. *IEEE Trans. Appl. Supercond.* **2016,** *26,* 1300905. doi:10.1109/TASC.2016.2535146
3. Lucci, M.; Badoni, D.; Merlo, V.; Ottaviani, I.; Salina, G.; Cirillo, M.; Ustinov, A. V.; Winkler, D. *Phys. Rev. Lett.* **2015,** *115,* 107002. doi:10.1103/PhysRevLett.115.107002
4. Nigro, A.; Nobile, G.; Palmieri, V.; Rubino, G.; Vaglio, R. *Phys. Scr.* **1988,** *38,* 483–485. doi:10.1088/0031-8949/38/3/027
5. Dawson-Elli, D. F.; Fung, C. A.; Nordman, J. E. *IEEE Trans. Magn.* **1991,** *27,* 1592. doi:10.1109/20.133489
6. Noat, Y.; Cherkez, V.; Brun, C.; Cren, T.; Carbillet, C.; Debontridder, F.; Ilin, K.; Siegel, M.; Semenov, A.; Hübers, H.-W.; Roditchev, D. *Phys. Rev. B* **2013,** *88,* 014503. doi:10.1103/PhysRevB.88.014503
7. Chaudhuri, S.; Nevala, M. R.; Maasilta, I. J. *Appl. Phys. Lett.* **2013,** *102,* 132601.
8. Hazra, D.; Tsavdaris, N.; Jebari, S.; Grimm, A.; Blanchet, F.; Mercier, F.; Blanquet, E.; Chapelier, C.; Hofheinz, M. *Supercond. Sci. Technol.* **2016,** *29,* 105011.
9. Nagai, Y.; Akaike, H.; Kanada, R.; Naito, N.; Fujimaki, A. *Supercond. Sci. Technol.* **2009,** *22,* 114015. doi:10.1088/0953-2048/22/11/114015
10. Wang, Z.; Terai, H.; Kawakami, A.; Uzawa, Y. *Supercond. Sci. Technol.* **1999,** *12,* 868. doi:10.1088/0953-2048/12/11/352
11. Meckbach, J. M. Superconducting Multilayer Technology for Josephson Devices. Ph.D. Thesis, University of Karlsruhe, Germany, 2013.
12. Gurvitch, M.; Washington, M. A.; Huggins, H. A. *Appl. Phys. Lett.* **1983,** *42,* 472. doi:10.1063/1.93974
13. Lucci, M.; Sanna, S.; Contini, G.; Zema, N.; Merlo, V.; Salvato, M.; Thanh, H. N.; Davoli, I. *Surf. Sci.* **2007,** *601,* 2647. doi:10.1016/j.susc.2006.11.078
14. Lucci, M.; Thanh, H. N.; Davoli, I. *Superlattices Microstruct.* **2008,** *43,* 518–523. doi:10.1016/j.spmi.2007.07.029
15. Zambrano, G.; Riascos, H.; Prieto, P.; Restrepo, E.; Devia, A.; Rincón, C. *Surf. Coat. Technol.* **2003,** *172,* 144. doi:10.1016/S0257-8972(03)00339-6
16. Henry, F.; Duluard, C. Y.; Batan, A.; Reniers, F. *Thin Solid Films* **2012,** *520,* 6386. doi:10.1016/j.tsf.2012.06.048
17. Pana, I.; Vitelaru, C.; Zoita, N. C.; Braic, M. *Plasma Processes Polym.* **2016,** *13,* 208. doi:10.1002/ppap.201400202
18. Weihnacht, M. *Phys. Status Solidi* **1969,** *32,* K169–K172. doi:10.1002/pssb.19690320259
19. Kubo, S.; Asahi, M.; Hikita, M.; Igarashi, M. *Appl. Phys. Lett.* **1984,** *44,* 258. doi:10.1063/1.94690
20. Barone, A.; Paternò, G. *Physics and Applications of the Josephson Effect;* John Wiley & Sons: New York, NY, U.S.A., 1982. See in particular section 4.4.

License and Terms

BEILSTEIN JOURNAL OF NANOTECHNOLOGY

Optical response of heterogeneous polymer layers containing silver nanostructures

Miriam Carlberg[1], Florent Pourcin[2], Olivier Margeat[2], Judikaël Le Rouzo[*1], Gérard Berginc[3], Rose-Marie Sauvage[4], Jörg Ackermann[2] and Ludovic Escoubas[1]

Full Research Paper

Open Access

Address:
[1]Aix Marseille Univ, Université de Toulon, CNRS, IM2NP, Marseille, France, [2]Aix Marseille Univ, CNRS, CINaM, Marseille, France, [3]Thales Optronics, Elancourt, France and [4]DGA/DS/MRIS, 75015 Paris, France

Email:
Judikaël Le Rouzo[*] - judikael.lerouzo@im2np.fr

* Corresponding author

Keywords:
nanoprisms; nanospheres; plasmonic nanoparticles; spectroscopic ellipsometry; thin film layers

Beilstein J. Nanotechnol. **2017,** *8,* 1065–1072.
doi:10.3762/bjnano.8.108

Received: 12 September 2016
Accepted: 21 April 2017
Published: 16 May 2017

This article is part of the Thematic Series "Self-assembly of nanostructures and nanomaterials II".

Guest Editor: I. Berbezier

Abstract

This work is focused on the study of the optical properties of silver nanostructures embedded in a polymer host matrix. The introduction of silver nanostructures in polymer thin films is assumed to result in layers having adaptable optical properties. Thin film layers with inclusions of differently shaped nanoparticles, such as nanospheres and nanoprisms, and of different sizes, are optically characterized. The nanoparticles are produced by a simple chemical synthesis at room temperature in water. The plasmonic resonance peaks of the different colloidal solutions range from 390 to 1300 nm. The non-absorbing, transparent polymer matrix poly(vinylpyrrolidone) (PVP) was chosen because of its suitable optical and chemical properties. The optical studies of the layers include spectrophotometry and spectroscopic ellipsometry measurements, which provide information about the reflection, transmission, absorption of the material as well as the complex optical indices, n and k. Finite difference time domain simulations of nanoparticles in thin film layers allow the visualization of the nanoparticle interactions or the electric field enhancement on and around the nanoparticles to complete the optical characterization. A simple analysis method is proposed to obtain the complex refractive index of nanospheres and nanoprisms in a polymer matrix.

Introduction

Noble metal nanoparticles (NPs) are of considerable interest in various domains, ranging from chemistry to medicine and light filtering [1-6]. Silver NPs are especially challenging because of the possibility to control the phenomenon of light–matter interaction in the visible wavelength range. The optical properties of these metallic NPs are induced by localized surface plasmon resonances, which are size, shape, material and environment dependent [7]. At the localized surface plasmon resonance wavelengths, the conduction electrons of the NPs oscillate coherently, which induces an electric field enhancement. The incom-

ing light is either absorbed or scattered by the NPs [8]. The absorption and scattering are commonly referred to as optical extinction. Single NPs are widely studied under different characterization techniques and computer modeling, such as Mie theory for spherical NPs. The absorption dominates the extinction for small radii and scattering dominates for larger radii. For silver, the threshold radius is 20 nm [9].

Given these properties, the optical properties of the thin films can be engineered by embedding specifically designed NPs. For example, by choosing silver NPs, the thin film layers will absorb in the visible wavelength range. This leads to applications of plasmonic thin film layers for photodetectors [10], photovoltaics [6,11] or nonreflective coatings [12-14].

In this works, silver NPs were chosen for their high electric field enhancement in the visible wavelength range [15]. Progress in the chemistry of NP synthesis allowed us to choose a chemical process adapted to our study that produces NPs of different shapes and sizes. Among different NP production methods, chemical synthesis is easy to implement and produces NPs at low cost. Standard physical vapor deposition methods require high energy sources, such as lasers [16], whereas chemical synthesis produces, among other shapes, nanospheres and nanoprisms of different sizes in water at room temperature. Taking advantage of the size and shape versatility of this chemical synthesis, we aim to control the absorption of thin film layers by embedding different NPs.

When included in polymer thin film layers (such as poly(vinylpyrrolidone) (PVP)), the plasmon resonance wavelengths of the NPs are red-shifted with respect to the resonance wavelengths in water. This environment dependence can easily be understood by considering the variation of the absorption cross-section, σ_{abs}, of a spherical NP according to the Mie theory:

$$\sigma_{abs} = 4\pi k r^3 \,\mathrm{Im}\left(\frac{\varepsilon - \varepsilon_m}{\varepsilon + 2\varepsilon_m}\right), \qquad (1)$$

where k is the wave vector, ε is the complex dielectric function of the NP and ε_m the complex dielectric function of the surrounding medium. Furthermore, collective resonances can alter the optical properties of these NPs and further redshift the absorption peaks.

In the following, we present studies of thin film layers with differently shaped and sized silver NP inclusions. The NPs are obtained by a facile water-based chemical synthesis at room temperature [17,18]. Depending on the chosen reagents, different shapes are achieved. To cover the whole visible wavelength range, we synthesized nanospheres and nanoprisms as their colloidal solutions absorb from 390 up to 1300 nm. The nature of the absorption peak was determined through spectrophotometer measurements coupled with computer simulations and transmission electron microscopy (TEM) imaging. Spectrophotometer and spectroscopic ellipsometry measurements of the PVP host matrix validated its non-absorbing and transparent properties. Spectroscopic ellipsometry measurements of the heterogeneous layers of nanospheres and nanoprisms embedded in the host matrix were fitted by the mathematical addition of the Cauchy law and the single Lorentz law centered at the dipolar resonance wavelength of the nanoparticles. Spectroscopic ellipsometry has been previously performed on nanoparticles embedded in dielectrics [19,20], but the NPs were primarily spherical or ellipsoidal. We propose here a simple analysis of nanoprisms based on the analysis of nanospheres in PVP.

Results and Discussion

Characterization of the colloidal nanoparticle solution

The NPs are synthesized as described below in the Experimental section. As synthesized, the nanospheres and nanoprisms were at first dispersed in water. The growth of the nanoprisms was fulfilled in two steps: first spherical seeds with specific crystallographic defects were produced, and second, the growth took place on these defects to form nanoprisms [18,21,22]. The absorption of the colloidal solutions of the first and second step, as seeds and prisms (Figure 1a), shows the characteristic plasmonic absorption peaks. The peaks 1 and 1’ were identified as the dipolar resonance of the nanoprisms and the nanospheres, respectively. The dipolar resonance of the nanoprisms induced absorption between 540–750 nm. The width of this absorption was not due to the distribution in size of the NPs, but rather to the random orientation of the NPs in the solution. The nanoprisms, as synthetized, are visualized in TEM images (Figure 1b). The residual seeds are removed by successive centrifugation steps. Furthermore, finite difference time domain (FDTD) simulations show that the maximum electric field enhancement (Figure 1c) for p- and s-polarized light does not occur at the same wavelength. For a single nanoprism (50 nm edge size and 10 nm thickness) in water, the maximum electric field enhancement for p-polarized light, corresponding to the dipolar resonance wavelength, occurs at 625 nm, whereas the maximum electric field enhancement for s-polarized light occurs at 619 nm.

This absorption peak can be tailored to any wavelength desired in the visible wavelength range by changing the size of the nanoprisms. This is simply done by changing the quantity of seeds added during the second step of the nanoprism synthesis. The spherical seeds absorbed light between 350–430 nm. The

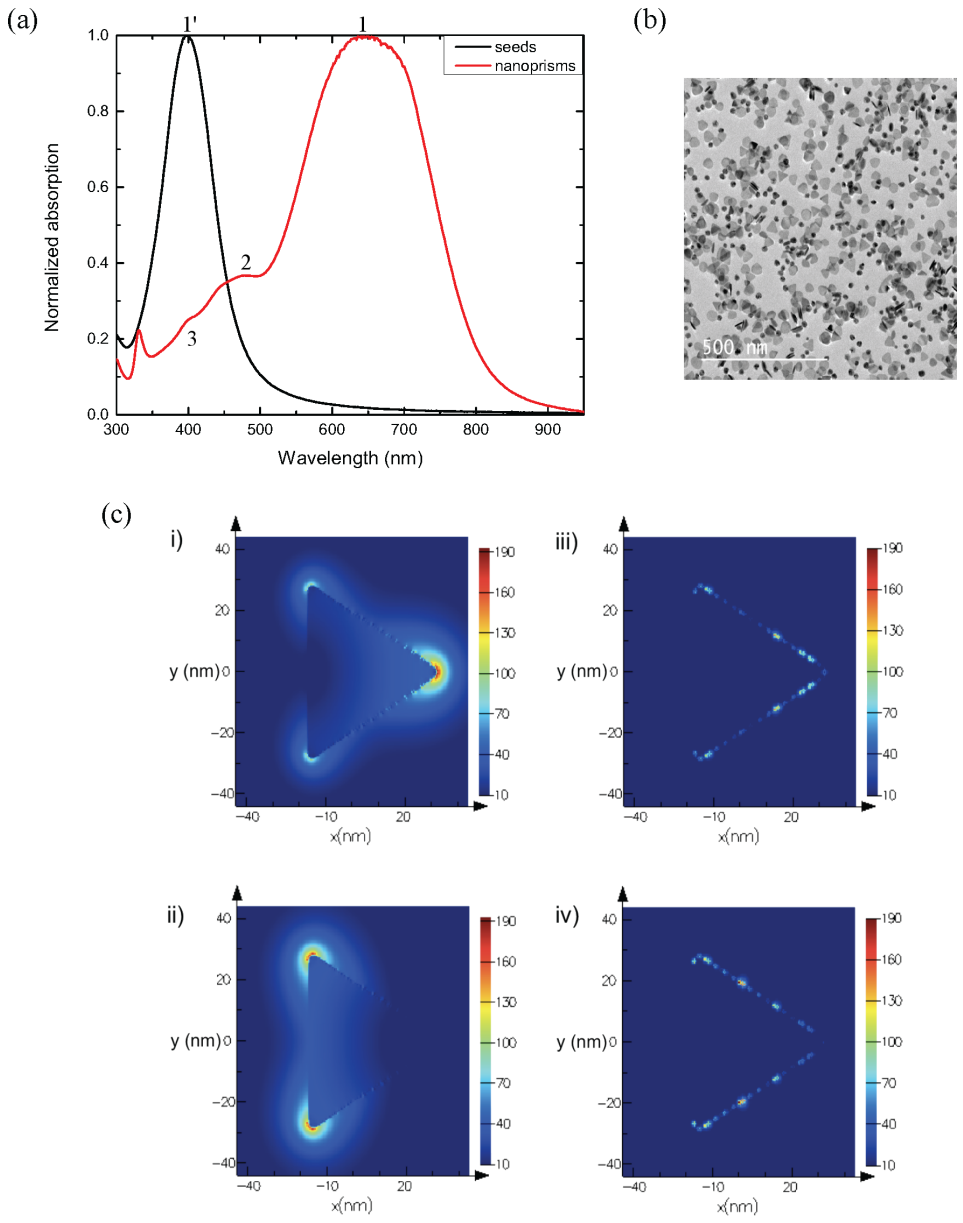

Figure 1: a) Normalized absorption of nanosphere and nanoprism solutions. b) TEM image of the synthetized nanoprisms before centrifugation and c) visualization of the electric field enhancement normalized to the incident electric field in the nanoprism for wavelength of peak 1 under *z*-oriented (i) p-polarized light and (ii) s-polarized light, and for the wavelength of peak 2 under (iii) p-polarized light and (iv) s-polarized light.

nature of the resonances was verified by computer calculations using the Mie theory for the spherical seeds and FDTD for the non-spherical particles. The maximum electric field enhancement for p- and s-polarized light for the dipolar and quadrupolar exaltations are pictured on Figure 1c. Peak 2 was identified as the quadrupolar resonance peak of the nanoprisms. The absorption peak 3 was assumed to be due to the dipolar resonance of the residual seeds in the nanoprism solution from the absorption spectrum. TEM images of the NPs in solution confirmed that residual spheres are present. These different plasmonic resonance peaks presented in the absorption spectrum of the NPs in solution resulted mathematically in the addition of Lorentz functions centered at the different energies.

In summary, silver NPs that absorb over the entire visible wavelength range were synthesized, and the nature of the absorption peak of the colloidal solution was determined. Additionally, the optical response in thin film layers was studied.

Spectroscopic ellipsometry

Spectroscopic ellipsometry is a powerful technique to determine the effective optical indices (real and imaginary parts) of

thin film layers or the thickness of known materials. Indeed, the thickness and the optical indices of the thin film layer are coupled parameters and cannot be controlled simultaneously. To obtain the real and imaginary part of the optical index of the thin films, variable angle spectroscopic ellipsometry (VASE) measurements were performed with a Semilab rotating compensator ellipsometer. The incident beam was focused on a micrometer sized spot diameter of the sample (about 100 µm). We measured the polarization change of light upon reflection on a sample in the visible wavelength range at which the silver NP absorb: 350–950 nm at incident angles of 65°, 70°, 71°, 72°, 73°, 74° and 75°. This polarization change depended on the amplitude and phase variations of the electric fields for p- and s-polarization. More details on spectroscopic ellipsometry can be found in textbooks [23,24].

For data analysis, the films were considered as an effective medium having properties including those both of the NPs and the polymer, as has been previously reported [19,20,25,26]. The optical modeling was developed using SEA (WinElli3) software. This software uses the Levenberg−Marquardt algorithm [27] to minimize the mean squared error (MSE) between the measured and calculated ellipsometric data, Ψ and Δ. To verify the validity of our mathematical model, transfer matrix method (TMM) calculations of the reflectance were compared with reflectance measurements carried out on a spectrophotometer (Lambda 950, PerkinElmer).

It should be noted that the complex refractive index $\tilde{n}$ is $\tilde{n} = n + ik$, where n is the frequency-dependent real refractive index, and k is the frequency-dependent extinction coefficient.

PVP host matrix

To maximize the influence of the nanospheres and nanoprisms on the light interaction, the NP host matrix must be a transparent, non-absorbing polymer in the visible wavelength range. Furthermore, the matrix should be a mild environment for the NPs and help the adherence of the NPs to the substrate [28]. Attempts to deposit the nanoparticles directly on the substrates did not succeed as the optical properties of the measured substrates did not show any nanoparticle optical signature. PVP is commonly used to stabilize silver NPs [29,30]. PVP is also a flexible polymer [31], thus the integration of plasmonic properties into this flexible matrix could be interesting for flexible devices.

First, the polymer alone was studied. To obtain a complete understanding of the host matrix, PVP of different molar weights, 40,000 g·mol^{-1} and 55,000 g·mol^{-1}, were deposited in thin film layers. In order to determine the optical indices of the films as a function of the molar weight, a dispersion model based on the Cauchy mathematical law was used for each sample:

$$n(\lambda) = n_\infty + \frac{B}{\lambda^2} + \frac{C}{\lambda^4}, \quad (2)$$

where n is the refractive index varying with the wavelength, n_∞ is the refractive index at infinite energy, and B and C are two constants. The extinction coefficient of the host matrix is zero in the visible wavelength range, i.e., the absorption of the heterogeneous thin films will be only due to plasmonic effects.

The parameters for the Cauchy law are listed in Table 1. The measured refractive indices (Figure 2) indicate a dependence on the molar weight. With increasing molar weight, the material fraction in the layer changes, leading to a higher refractive index. The choice of the molar weight therefore has importance when considering the optical properties of the thin film layers.

In the following, the PVP of molar weight of 55,000 g·mol^{-1} was be chosen for experimental reasons. Taken together, the host matrix was characterized by spectroscopic ellipsometry and fitted by a non-absorbing Cauchy law. The absorption of the thin film layer was derived from the presence of the silver NPs.

Heterogeneous thin film layers

By embedding NPs into the non-absorbing polymer host matrix, the absorption of light was induced at specific plasmonic wavelength resonances. In order to determine the optical indices of the films containing NPs, the thin film layer was visualized as

Table 1: Fitting parameters of spectroscopic ellipsometry measurements for different structures.

Sample	Laws	Cauchy parameters	Lorentz parameters
PVP 40,000 g·mol^{-1}	Cauchy	B = 0.0053 µm^2, C = 0 µm^4	
PVP 55,000 g·mol^{-1}	Cauchy	B = 0.00709 µm^2, C = 0 µm^4	
PVP 55,000 g·mol^{-1} + 20 nm nanospheres	Cauchy + 1 Lorentz	B = 0.00544 µm^2, C = 0 µm^4, n_∞ = 1.57	f = 0.005, E_0 = 3.09 eV, Γ = 0.41 eV, ε_∞ = 0.0002
PVP 55,000 g·mol^{-1} + 25 nm nanoprisms	Cauchy + 1 Lorentz	B = 0.00502 µm^2, C = 0 µm^4, n_∞ = 1.56	f = 0.003, E_0 = 1.9 eV, Γ = 0.32 eV, ε_∞ = 0.0066

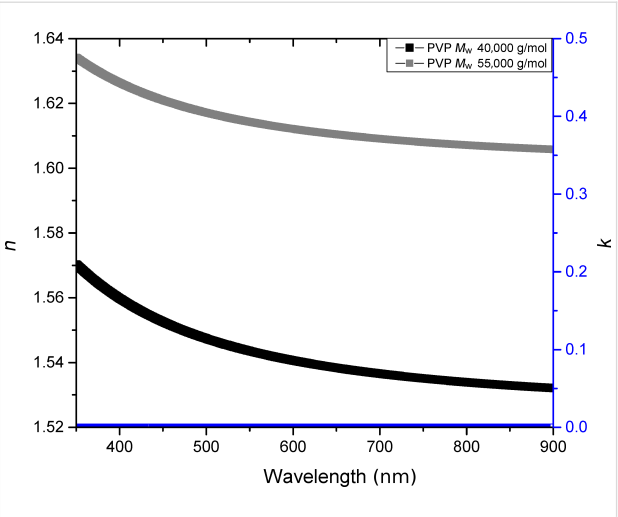

Figure 2: Real and imaginary optical indices of PVP of 40,000 and 55,000 g·mol^{-1} average molar weight, fitted by a non-absorbing Cauchy law.

an effective medium [32-36]. A dispersion model based on a non-absorbing Cauchy mathematical law and one or more Lorentz mathematical laws was used. The Lorentz oscillator model is derived from the classical theory of interaction between light and matter [27]. As it describes the dipolar frequency-dependent polarization due to bound charges, it represents well the plasmonic behavior of metal NPs. The Lorentz model influences both the real and imaginary part of the dielectric function as

$$\varepsilon_1(E) = \varepsilon_\infty + \frac{fE_0^2\left(E_0^2 - E^2\right)}{\left(E_0^2 - E^2\right)^2 + \Gamma^2 E^2}, \qquad \varepsilon_2(E) = \frac{fE_0^2\Gamma E}{\left(E_0^2 - E^2\right)^2 + \Gamma^2 E^2} \tag{3}$$

where f is the oscillator strength, E_0 (in eV) is the resonant energy of the oscillator, Γ (in eV) is the broadening of the oscillator and ε_∞ is the high energy dielectric constant.

We focused on the plasmonic properties of the silver NPs in the visible wavelength range. Therefore, the Lorentz model was sufficient to account for the optical properties of the NPs, and the electronic intraband transitions occurring in the UV [27] were not considered in this study. The resonant energy and the broadening width of the oscillator were deduced from the absorption energy of the NPs. The oscillator strength was the only parameter varied as function of the size and shape of the embedded NP.

By a mathematical addition of the Cauchy and the Lorentz laws, we noticed that the two constants (n_∞ from the Cauchy model and ε_∞ from the Lorentz model) are only contained in the real part of the dielectric constant and correspond to an offset.

Nanospheres of 10 nm diameter were included in a 55,000 g·mol^{-1} PVP layer on a silicon substrate. Spectrophotometric measurements indicated that these nanospheres in PVP absorbed at 405 nm, i.e., the oscillator in the Lorentz model was centered at an energy of 3.06 eV. The thickness of the thin film layer, determined by a mechanical stylus profilometer (Brucker Decktak XT), was 190 ± 5 nm. The fitting parameters are summarized in Table 1.

Nanoprisms of 25 nm edge size were deposited into a 55,000 g·mol^{-1} PVP layer. Their absorption in the PVP layer was centered at 650 nm or 1.9 eV. The thin film layer thickness was 230 ± 5 nm. To fit the data, the Cauchy parameter B was varied. The introduction of the silver NPs reduces the amount of PVP, therefore the value of B was affected in comparison with the fit parameters of the PVP layer alone. The parameters of the Lorentz law, E_0 and Γ, were fixed by the knowledge of the dipolar absorption peak wavelength of the corresponding NPs in PVP. The strength of the oscillator was varied in function of the NP density in the thin film layer.

Surprisingly, the nanoprisms were modeled with a single Lorentz law, accounting for the dipolar plasmonic resonance at 700 nm. Adding a second Lorentz law, accounting for quadrupolar resonances of the prisms, did not improve the fitting. The second law increases the number of variables from six to nine, but the RMSE did not decrease and the correlation coefficient R^2 did not increase. This leads to the question whether the shape has an influence on the optical indices of the heterogeneous layers or only the size. According to the above samples, only the size has an influence and a single Lorentz law models the plasmonics signature of the NPs.

The fit to the data for the nanospheres in PVP was optimized up to a R^2 = 99.45% and a RMSE = 2.1 and up to R^2 = 99.44% and RMSE = 1.9 for the nanoprisms in PVP. The obtained optical indices were then used to calculate the reflectance using a TMM calculation. The calculated reflectance was compared to the measured reflectance (Figure 3) in order to validate the mathematical laws used to model the thin film layer.

With the fit quality optimized, the comparison between the measured and calculated reflectance is necessary to verify the physical validity of the fit. The two curves follow the same tendency. The slight discrepancy in the reflectance spectra could be attributed to the measurement or to diffusion phenomena in-

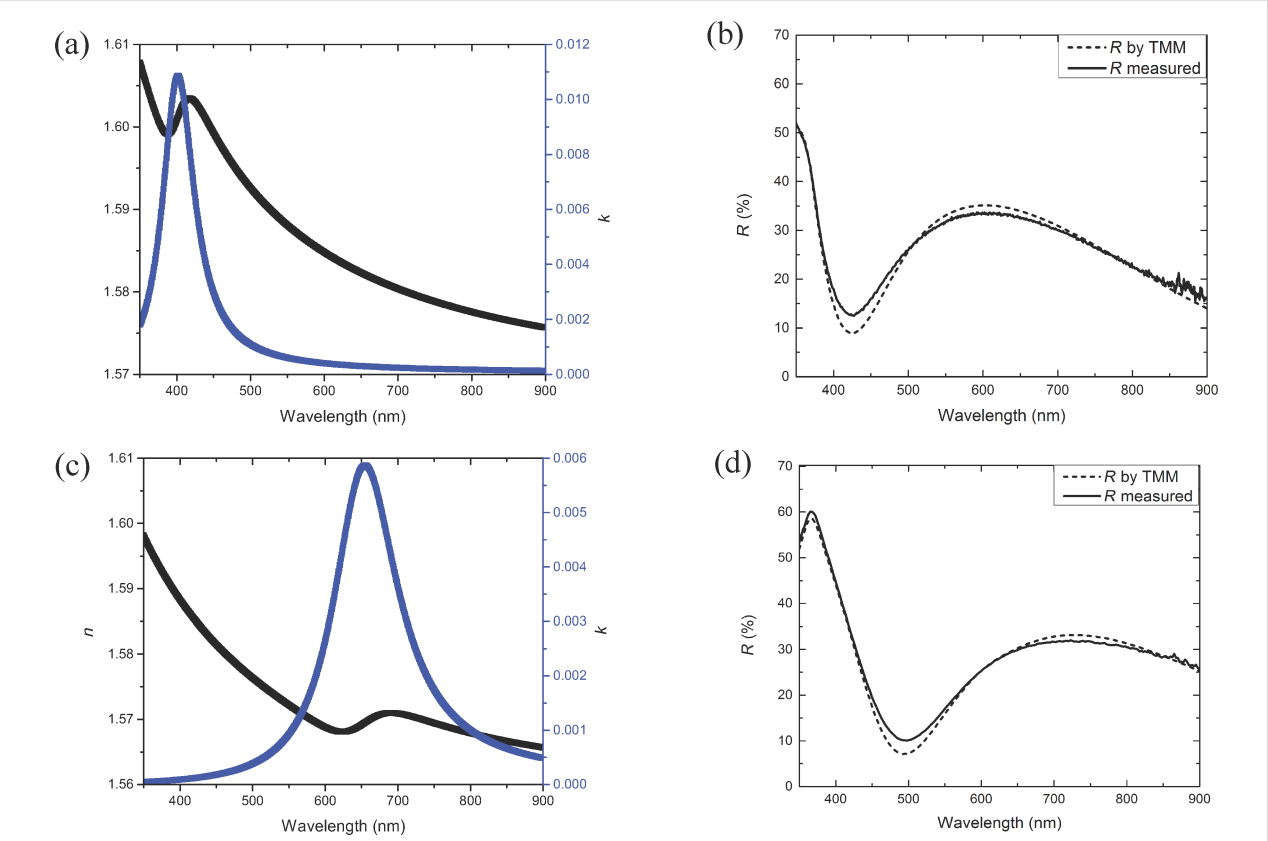

Figure 3: (a) Optical indices *n* and *k*, (b) reflectance measured and calculated by TMM for heterogeneous layers with nanospheres, (c) optical indices and (d) reflectance measured and calculated for heterogeneous layers with nanoprisms.

duced by the NPs, which is not taken into account in our ellipsometry model.

In summary, the complex optical index of silver nanospheres and nanoprisms embedded into a transparent, non-absorbing polymer layer were modeled by the mathematical addition of the Cauchy law, accounting for the optical properties of the polymer, and the Lorentz law, centered at the dipolar absorption wavelength of the embedded NPs. The addition of further Lorentz law accounting for higher order resonances or intraband transitions occurring in the UV did not improve the data fit for this specific density of nanoprisms. Further Lorentz laws might be necessary to account for other absorption peaks when the density of nanoparticles in the thin film layer is increased.

Conclusion

In conclusion, chemically synthesized nanospheres and nanoprisms were embedded in a transparent, non-absorbing PVP layer. Spectroscopic ellipsometry measurement results were fit in the scope of an effective medium theory with the mathematical addition of the Cauchy law and a single Lorentz law. This model is based on a multiple oscillator approach, where the effective dielectric function is the simple addition of the dielectric function of one or more Lorentz oscillators. Since the nanoparticles are randomly distributed in the layer, the effective dielectric constant accounts for the averaged optical response of the nanoprisms. A single Lorentz oscillator is required to fit the nanospheres and nanoprisms in PVP. This easy method allows us to obtain the optical indices of thin films with complex inclusions. The question arising from these results is whether the shape of the NP matters when embedded in a thin film layer. Further studies with additional shapes of NPs will be required to generalize our results, that is, the determination of whether only the size matters. The precise knowledge of the morphology of our structures, through AFM or TEM studies, may improve our optical models in the future.

Experimental

Synthesis of nanoparticles

The NPs were synthesized by the reduction of silver ions by sodium borohydride at room temperature in water. The nanospheres were synthesized in a one-step method [17]. The nanoprisms were created in a two-step seed-based method [18]. By depositing the nanospheres directly onto the substrate, their size was determined by atomic force microscopy (AFM, Figure 4).

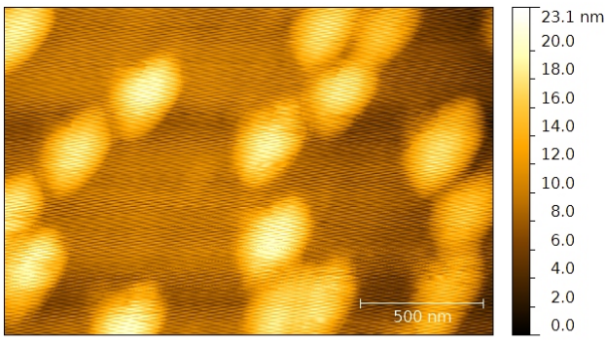

Figure 4: AFM topography of the nanospheres on a substrate.

The synthesized nanospheres have a diameter of 20 nm. The nanoprisms were equilateral and their edge size varied from 10 to 100 nm depending on the quantity of seed taken in the second step of the synthesis [18,37]. Their thickness was constant and found to be 10 nm. The NPs were stabilized by citrates and PVP. The colloidal solutions were washed by successive centrifugation steps and redispersed in ethanol.

Host matrix

PVP was chosen as the host matrix due to its transparent and non-absorbing properties in the visible range. Furthermore, the pyrridil group has strong affinity to metals, such as silver NPs [28]. A few microliters of a highly concentrated PVP solution (40 g/L) in ethanol, was added to the washed NPs.

Deposition of thin film layers

The substrates were chosen according to the measurements performed afterwards. Indeed, spectrophotometer measurements require a transparent substrate, therefore microscopic glass slides (VWR international) were used. Spectroscopic ellipsometry required a high optical index difference between the substrate and the thin film layer, thus a silicon wafer was chosen. The substrates were cleaned in an ultrasonic bath in acetone and ethanol, dried by nitrogen flow and an oxygen plasma. The latter step also increased the wettability of the substrate.

The deposition of the thin film layers was performed by spin coating. The spin coating speed was set to 500–1000 rpm, in order to obtain layers of a few hundred micrometers thickness. The deposition technique yields homogeneous thin film layers in the center of the sample where the optical measurements are performed. Nevertheless, every measurement was repeated at least twice on two different areas to avoid thickness-dependent artefacts. The thickness and homogeneity of the thin films were determined by a mechanical stylus profilometer (Brucker Decktak XT).

Acknowledgements

The research was supported by DGA-MRIS scholarship to Miriam Carlberg and Florent Pourcin.

References

1. Gentile, A.; Ruffino, F.; Grimaldi, M. G. *Nanomaterials* **2016,** *6,* 110. doi:10.3390/nano6060110
2. Daniel, M.-C.; Astruc, D. *Chem. Rev.* **2004,** *104,* 293–346. doi:10.1021/cr030698+
3. Wang, A. Z.; Langer, R.; Farokhzad, O. C. *Annu. Rev. Med.* **2012,** *63,* 185–198. doi:10.1146/annurev-med-040210-162544
4. Shenashen, M. A.; El-Safty, S. A.; Elshehy, E. A. *Part. Part. Syst. Charact.* **2014,** *31,* 293–316. doi:10.1002/ppsc.201300181
5. de Aberasturi, D. J.; Serrano-Montes, A. B.; Liz-Marzán, L. M. *Adv. Opt. Mater.* **2015,** *3,* 602–617. doi:10.1002/adom.201500053
6. Otanicar, T. P.; DeJarnette, D.; Hewakuruppu, Y.; Taylor, R. A. *Adv. Opt. Photonics* **2016,** *8,* 541–585. doi:10.1364/AOP.8.000541
7. García, M. A. *J. Phys. D: Appl. Phys.* **2011,** *44,* 283001. doi:10.1088/0022-3727/44/28/283001
8. Jones, A. R. *Prog. Energy Combust. Sci.* **1999,** *25,* 1–53. doi:10.1016/S0360-1285(98)00017-3
9. Khlebtsov, N. G. *Quantum Electron.* **2008,** *38,* 504. doi:10.1070/QE2008v038n06ABEH013829
10. Schuller, J. A.; Barnard, E. S.; Cai, W.; Jun, Y. C.; White, J. S.; Brongersma, M. L. *Nat. Mater.* **2010,** *9,* 193–204. doi:10.1038/nmat2630
11. Cushing, S. K.; Wu, N. *J. Phys. Chem. Lett.* **2016,** *7,* 666–675. doi:10.1021/acs.jpclett.5b02393
12. Akselrod, G. M.; Huang, J.; Hoang, T. B.; Bowen, P. T.; Su, L.; Smith, D. R.; Mikkelsen, M. H. *Adv. Mater.* **2015,** *27,* 8028–8034. doi:10.1002/adma.201503281
13. Hu, C.; Liu, L.; Zhao, Z.; Chen, X.; Luo, X. *Opt. Express* **2009,** *17,* 16745–16749. doi:10.1364/OE.17.016745
14. Liu, N.; Mesch, M.; Weiss, T.; Hentschel, M.; Giessen, H. *Nano Lett.* **2010,** *10,* 2342–2348. doi:10.1021/nl9041033
15. Hao, E.; Schatz, G. C. *J. Chem. Phys.* **2004,** *120,* 357–366. doi:10.1063/1.1629280
16. Arakelyan, S. M.; Veiko, V. P.; Kutrovskaya, S. V.; Kucherik, A. O.; Osipov, A. V.; Vartanyan, T. A.; Itina, T. E. *J. Nanopart. Res.* **2016,** *18,* 155. doi:10.1007/s11051-016-3468-0
17. Mulfinger, L.; Solomon, S. D.; Bahadory, M.; Jeyarajasingam, A. V.; Rutkowsky, S. A.; Boritz, C. *J. Chem. Educ.* **2007,** *84,* 322. doi:10.1021/ed084p322
18. Aherne, D.; Ledwith, D. M.; Gara, M.; Kelly, J. M. *Adv. Funct. Mater.* **2008,** *18,* 2005–2016. doi:10.1002/adfm.200800233
19. Voué, M.; Dahmouchène, N.; De Coninck, J. *Thin Solid Films* **2011,** *519,* 2963–2967. doi:10.1016/j.tsf.2010.12.109
20. Kravets, V. G.; Neubeck, S.; Grigorenko, A. N.; Kravets, A. F. *Phys. Rev. B* **2010,** *81,* 165401. doi:10.1103/PhysRevB.81.165401
21. Sau, T. K.; Rogach, A. L. *Adv. Mater.* **2010,** *22,* 1781–1804. doi:10.1002/adma.200901271
22. Zhang, J.; Langille, M. R.; Mirkin, C. A. *Nano Lett.* **2011,** *11,* 2495–2498. doi:10.1021/nl2009789

23. Fujiwara, H. *Spectroscopic ellipsometry: principles and applications;* John Wiley & Sons: New York, NY, U.S.A., 2007. doi:10.1002/9780470060193 https://books.google.de/books?lr=&id=tTMn0NKcpjsC&oi=fnd&pg=PR7&ots=NqWTnrQXvO&sig=iOqpHLDoiH15wSgP_-o51jUWF5Y&redir_esc=y#v=onepage&q&f=false
24. Tompkins, H.; Irene, E. A. *Handbook of ellipsometry;* William Andrew Publishing: Norwich, NY, U.S.A., 2005. doi:10.1007/3-540-27488-X https://books.google.de/books?lr=&id=6PQf1fSzHHEC&oi=fnd&pg=PP1&sig=L_HM89eQKp5BDxrnzupygyL5Wfw&redir_esc=y#v=onepage&q&f=false
25. Baron, A.; Iazzolino, A.; Ehrhardt, K.; Salmon, J.-B.; Aradian, A.; Kravets, V.; Grigorenko, A. N.; Leng, J.; Le Beulze, A.; Tréguer-Delapierre, M.; Correa-Duarte, M. A.; Barois, P. *Opt. Mater. Express* **2013,** *3,* 1792–1797. doi:10.1364/OME.3.001792
26. Zhang, H.-L.; Evans, S. D.; Henderson, J. R. *Adv. Mater.* **2003,** *15,* 531–534. doi:10.1002/adma.200390124
27. Oates, T. W. H.; Wormeester, H.; Arwin, H. *Prog. Surf. Sci.* **2011,** *86,* 328–376. doi:10.1016/j.progsurf.2011.08.004
28. Malynych, S.; Luzinov, I.; Chumanov, G. *J. Phys. Chem. B* **2002,** *106,* 1280–1285. doi:10.1021/jp013236d
29. Wang, H.; Qiao, X.; Chen, J.; Wang, X.; Ding, S. *Mater. Chem. Phys.* **2005,** *94,* 449–453. doi:10.1016/j.matchemphys.2005.05.005
30. Shin, H. S.; Yang, H. J.; Kim, S. B.; Lee, M. S. *J. Colloid Interface Sci.* **2004,** *274,* 89–94. doi:10.1016/j.jcis.2004.02.084
31. Seurin, M. J.; Gilli, J. M.; Sixou, P. *Eur. Polym. J.* **1983,** *19,* 683–690. doi:10.1016/0014-3057(83)90083-6
32. Moiseev, S. G. *Phys. B (Amsterdam, Neth.)* **2010,** *405,* 3042–3045. doi:10.1016/j.physb.2010.01.045
33. Levy, O.; Stroud, D. *Phys. Rev. B* **1997,** *56,* 8035. doi:10.1103/PhysRevB.56.8035
34. Skryabin, I. L.; Radchik, A. V.; Moses, P.; Smith, G. B. *Appl. Phys. Lett.* **1997,** *70,* 2221–2223. doi:10.1063/1.118821
35. Weiglhofer, W. S.; Lakhtakia, A.; Michel, B. *Microwave Opt. Technol. Lett.* **1997,** *15,* 263–266. doi:10.1002/(SICI)1098-2760(199707)15:4<263::AID-MOP19>3.0.CO;2-8
36. Stroud, D. *Phys. Rev. B* **1975,** *12,* 3368. doi:10.1103/PhysRevB.12.3368
37. Carlberg, M.; Pourcin, F.; Margeat, O.; Le Rouzo, J.; Berginc, G.; Sauvage, R.-M.; Ackermann, J.; Escoubaset, L. *J. Nanophotonics* **2017,** *11,* 43504. doi:10.1117/1.JNP.11.043504

License and Terms

The definitive version of this article is the electronic one which can be found at: doi:10.3762/bjnano.8.108

BEILSTEIN JOURNAL OF NANOTECHNOLOGY

Uptake and intracellular accumulation of diamond nanoparticles – a metabolic and cytotoxic study

Antonín Brož[1], Lucie Bačáková[1], Pavla Štenclová[2], Alexander Kromka[2] and Štěpán Potocký[*2]

Full Research Paper

Open Access

Address:
[1]Institute of Physiology of the Czech Academy of Sciences, v.v.i., Vídeňská 1083, 142 20, Praha 4, Czech Republic and [2]Institute of Physics of the Czech Academy of Sciences, v.v.i., Cukrovarnická 10, 162 00 Praha 6, Czech Republic

Email:
Štěpán Potocký[*] - potocky@fzu.cz

* Corresponding author

Keywords:
cell viability; FTIR; live-cell imaging; MTS; nanodiamond; SAOS-2 cells

Beilstein J. Nanotechnol. **2017,** *8,* 1649–1657.
doi:10.3762/bjnano.8.165

Received: 15 July 2016
Accepted: 17 July 2017
Published: 10 August 2017

This article is part of the Thematic Series "Self-assembly of nanostructures and nanomaterials II".

Guest Editor: I. Berbezier

Abstract

Diamond nanoparticles, known as nanodiamonds (NDs), possess several medically significant properties. Having a tailorable and easily accessible surface gives them great potential for use in sensing and imaging applications and as a component of cell growth scaffolds. In this work we investigate in vitro interactions of human osteoblast-like SAOS-2 cells with four different groups of NDs, namely high-pressure high-temperature (HPHT) NDs (diameter 18–210 nm, oxygen-terminated), photoluminescent HPHT NDs (diameter 40 nm, oxygen-terminated), detonation NDs (diameter 5 nm, H-terminated), and the same detonation NDs further oxidized by annealing at 450 °C. The influence of the NDs on cell viability and cell count was measured by the mitochondrial metabolic activity test and by counting cells with stained nuclei. The interaction of NDs with cells was monitored by phase contrast live-cell imaging in real time. For both types of oxygen-terminated HPHT NDs, the cell viability and the cell number remained almost the same for concentrations up to 100 μg/mL within the whole range of ND diameters tested. The uptake of hydrogen-terminated detonation NDs caused the viability and the cell number to decrease by 80–85%. The oxidation of the NDs hindered the decrease, but on day 7, a further decrease was observed. While the O-terminated NDs showed mechanical obstruction of cells by agglomerates preventing cell adhesion, migration and division, the H-terminated detonation NDs exhibited rapid penetration into the cells from the beginning of the cultivation period, and also rapid cell congestion and a rapid reduction in viability. These findings are discussed with reference to relevant properties of NDs such as surface chemical bonds, zeta potential and nanoparticle types.

Introduction

Carbon-based materials in the form of nanostructures are showing great promise as engineering and biomedical materials [1]. Moreover, diamond represents a new class of material with properties that are tailorable on demand [2]. This work investigates the use of diamond nanomaterials, or nanodiamonds (NDs), especially in life sciences, tissue engineering and regen-

erative medicine [3-6]. Diamond is biocompatible [7,8], and for advanced biomedical applications, it is particularly promising in its nanostructured forms (nanoparticles, nanostructured diamond films and composite scaffolds) [9].

ND particles can act in the single particle form (bioimaging and biosensing) [10,11], can serve as a stable delivery platform for therapeutic antibodies [12], or can be incorporated into various materials, for example, films for potential implant coatings [13]. Nanodiamond-based drug delivery has been mainly developed for advanced tumour therapies and for localized drug delivery [3,14]. Due to their stable and controllable photoluminescence, NDs are also highly promising for advanced photonic and bioimaging techniques [15,16] and for nanoscale sensing [17,18].

There are various types of NDs, but two main groups can be identified on the basis of their synthesis procedure. The first group of NDs are those synthesized by the detonation method [19], where even sub-nanometer detonation nanodiamond particles (DNDs) are produced [20]. A typical size distribution has a maximum DND diameter of around 5 nm. The second group of NDs are prepared by mechanical grinding of high-pressure high-temperature (HPHT) diamond crystals [21]. The HPHT ND particle size distribution can be mechanically controlled down to approximately 20 nm, or by further post-processing down to 1 nm, as has recently been reported [22].

NDs typically contain impurities, such as other carbon allotropes, various oxides or carbides (i.e., carriers of various functional surface groups) [3,23]. Therefore, for use in biological or biomedical studies, NDs need to be extensively purified. Numerous methods exist for removing non-diamond carbon components based on treatment with various oxidizers, such as peroxides, acids and ozone-enriched air [3,24,25]. Oxidation in air at elevated temperature is a good method for effective sp^2 carbon removal [26,27], particle size reduction [22] and surface oxidation (i.e., the surface is covered by defined starting functional groups).

The cytotoxicity of NDs depends on their origin (i.e., DNDs or HPHT NDs), their size (distribution), their tendency to form aggregates (surface charge), the presence of impurities, and surface functionalization groups. Adverse effects on cell viability have been reported when using DNDs [24,28-32], while HPHT NDs often appear to be nontoxic [33,34]. Factors influencing the cytotoxicity of nanoparticles are their size [24,35,36] and surface functionalization [37].

In this work, we focus on cytotoxicity studies of NDs as a function of their synthesis route (DNDs versus HPHT NDs), their concentration in the medium (from 10 to 1000 mg/mL, 3 to 300 µg/cm^2), their size (5 nm DND, 18–210 nm HPHT NDs) and their surface potential/termination (as-received and oxygen-terminated). The cytotoxicity of NDs against the SAOS-2 human osteoblastic cell line is evaluated in this work by counting adherent cells and by a mitochondrial metabolic activity test (MTS) after 3 and 7 days. Both the cell count and mitochondrial activity are positively correlated with the cell viability and are negatively correlated with the material cytotoxicity. The live-cell imaging method was used for observing the intake of NDs into the cells. The results were evaluated on the basis of particle size, surface potential, surface functional groups, and the concentration of the ND suspension.

Results and Discussion

Influence of particle size and concentration

Figure 1 shows the results of a cell mitochondrial activity test (upper row) and a cell nuclei count (lower row) after 3 days of cultivation for three different concentrations of 10, 100 and 1000 µg/mL (3, 30, and 300 µg/cm^2) as a function of HPHT ND (labeled as MR-xx) particle size. Both tests proved almost no ND size or concentration dependence on cell viability after 3 days of cultivation within the measurement error. Only at the highest concentration of NDs (1000 µg/mL, 300 µg/cm^2), the mitochondrial activity and the cell number showed a tendency to decrease in certain ND groups. However, these differences were not statistically significant. This decrease could be due to the obstruction of access to nutrients or scavenging of nutrients and growth factors from the cultivation medium by the NDs. A high ND concentration can also express chemical toxicity based on the production of reactive oxygen species.

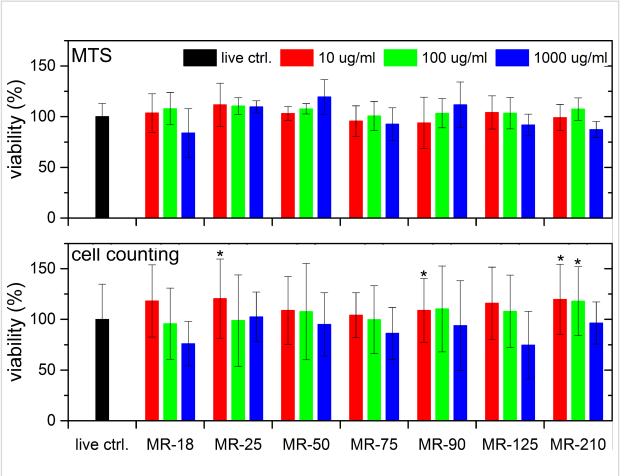

Figure 1: Viability of SAOS-2 cells incubated with HPHT NDs for three concentrations as a function of the mean particle diameter after 3 days. (Upper row) results of an MTS assay, (lower row) results of cell counting after cell staining. The results are given as the mean ± SD from 3 experiments, each performed in sextuplicate. ANOVA, Tukey HSD post-hoc test. "*" indicates a significant difference from MR-18 at a concentration of 1000 µg/mL ($p < 0.05$).

Figure 2 shows the results of a cell mitochondrial activity test (upper row) and counting of the cell nuclei (lower row) after 7 days of cultivation for three different concentrations of 10, 100 and 1000 µg/mL (3, 30, 300 µg/cm^2) as a function of HPHT ND particle size. Again, no dependence of the ND size or concentration was observed for 10 and 100 µg/mL (3 and 30 µg/cm^2) suspension concentrations after 7 days. However, a concentration-dependent toxic effect of HPHT NDs was revealed after 7 days of cultivation, where the viability of the cells cultivated in the 1000 µg/mL (300 µg/cm^2) suspension reduced by 25% when evaluated by MTS and by 35% when evaluated by the cell counting experiment. This pronounced effect may have been caused by the previously mentioned obstruction of access to nutrients by nutrient scavenging or by reactive oxygen species. Alternatively, it could have been caused just by mechanical obstruction of the cell adhesion and division by ND agglomerates, as confirmed by live-cell imaging. A similar effect was also observed in human osteoblast-like MG 63 cells cultured in a medium with multi-walled carbon nanotubes (MWCNTs) at concentrations of 4, 40, 400, 4000 and 40000 µg/mL. On days 1, 3 and 7 after seeding, the number of MG 63 in the media with 4 and 40 µg/mL of MWCNTs was similar to or even higher than in the control cultures without MWCNTs, while at higher concentrations of MWCNTs, it decreased in a concentration-dependent manner. This was explained by the fact that MWCNTs at higher concentrations covered most of the bottom of the culture well and left only limited space for cell attachment and spreading [38].

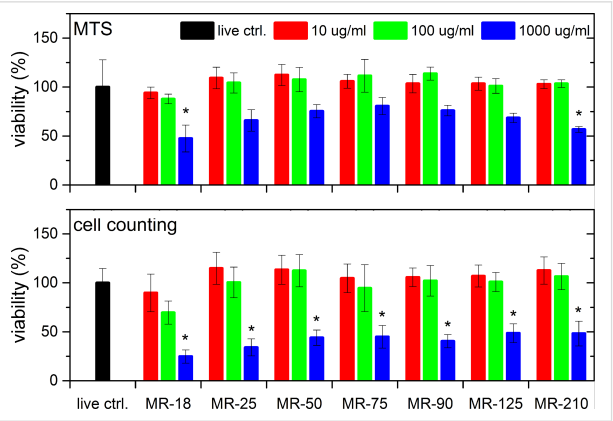

Figure 2: Viability of SAOS-2 cells incubated with HPHT NDs at three concentrations as a function of the mean particle diameter after 7 days. (Upper row) results of the MTS assay; (lower row) results of cell counting after cell staining. The results are given as the mean ± SD from 3 experiments, each performed in sextuplicate. ANOVA, Tukey HSD post-hoc test. "*" indicates a significant difference from MR-18 at a concentration of 1000 µg/mL ($p < 0.05$).

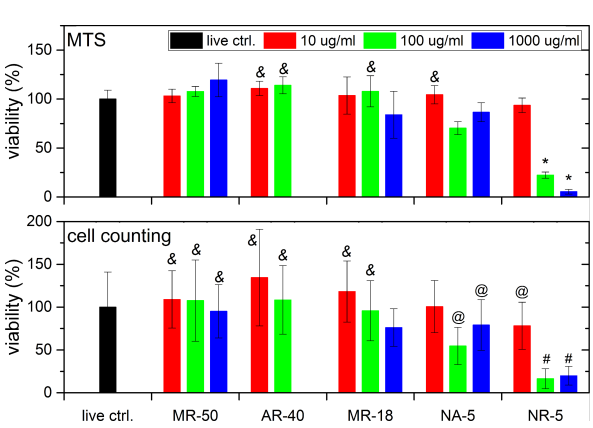

Figure 3: Viability of SAOS-2 cells incubated with NDs at three concentrations as a function of ND type and surface treatment after 3 days. (Upper row) results of the MTS assay; (lower row) results of cell counting after nuclei staining. The results are given as the mean ± SD from 3 experiments, each performed in sextuplicate. ANOVA, Tukey HSD post-hoc test. "&" - significant difference from NA-5 100 µg/mL ($p < 0.05$), "*" - significant difference from all other measurements ($p < 0.01$), "#" - significant difference from all other measurements except for NA-5 100 µg/mL ($p < 0.01$), "@" - significant difference from MR-50 10 and 100 µg/mL, AR-40 10 µg/mL ($p < 0.05$).

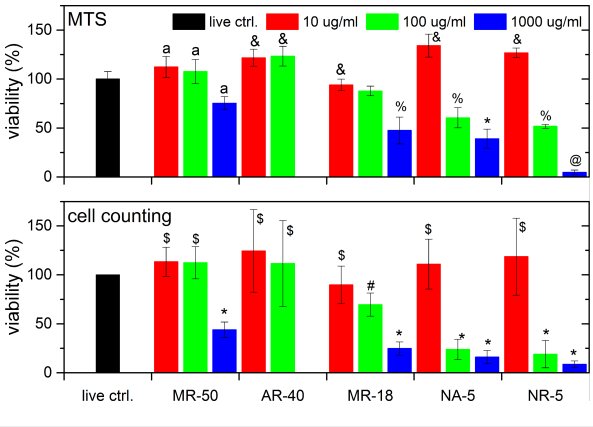

Figure 4: Viability of SAOS-2 cells incubated with NDs for three concentrations as a function of ND type and surface treatment after 7 days. (Upper row) results of the MTS assay; (lower row) results of cell counting after nuclei staining. The results are given as the mean ± SD from 3 experiments, each performed in sextuplicate. ANOVA, Tukey HSD post-hoc test. "a" - significant difference from NA-5 1000 µg/mL and NR-5 1000 µg/mL $p < 0.01$, "&" - significant difference from MR-18 1000 µg/mL, NA-5 100 and 1000 µg/mL, NR-5 100 and 1000 µg/mL ($p < 0.05$), "%" - significant difference from AR-40, MR-18 10 µg/mL, NA-5 10 µg/mL and NR-5 10 µg/mL ($p < 0.05$), "*" - significant difference from control, all 10 µg/mL measurements and all MR and AR 100 µg/mL measurements ($p < 0.01$), @ - same as "*" + MR-50 1000 µg/mL ($p < 0.01$), "$" - significant difference from 1000 µg/mL ($p < 0.01$), "#" - significant difference from all AR-40 and from all 100 and 1000 µg/mL concentrations, with the exception of MR-50 ($p < 0.05$).

Influence of particle type

Figure 3 and Figure 4 show a comparison between the cell metabolic activity test (upper row) and counting of the cell nuclei (lower row) for three different concentrations of 10, 100 and 1000 µg/mL (3, 30 and 300 µg/cm^2) as a function of ND type and surface treatment after 3 days (Figure 3) and 7 days

(Figure 4) of cultivation. Three ND types with differing characteristics were selected: non-luminescent HPHT NDs of two diameters as described in the previous section (MR-18 and MR-50), HPHT NDs with photoluminescent nitrogen-vacancy (N-V) centers (AR-40), and detonation NDs with hydrogen termination (NR-5, as-received) and with oxygen termination (NA-5, annealed).

First, we compared the photoluminescent HPHT NDs (AR-40) with non-luminescent HPHT NDs of similar size (MR-50) and of smaller size (MR-18). The photoluminescent NDs AR-40 were available only in two concentrations: 10 and 100 μg/mL (3 and 30 μg/cm^2). Both HPHT ND types were oxidized. Neither of the HPHT NDs are cytotoxic in low and medium concentrations after 3 and 7 days of cultivation. A visible decrease in cell viability can be observed with the highest ND concentration of MR-50 and 18. The decrease was statistically insignificant after 3 days (Figure 3). However, after 7 days the cell viability had decreased significantly (Figure 4) in comparison with the control cells in the pure culture medium and in comparison with the other concentrations of MR. The similar cytotoxicity of these HPHT NDs is probably caused by the similar production method, which results in oxidized surface termination and surface energy of the NDs. The presence of photoluminescent N-V centers had no negative effect on cell viability in the concentrations studied (3 μg/cm^2 and 30 μg/cm^2).

Similar to the other HPHT NDs with an oxidized surface, the NDs with N-V optical centers expressed no significant toxicity when compared with the ND-free living control (i.e., cells grown in polystyrene wells in a medium without diamond nanoparticles). Similar results were also obtained in a study by Vaijayanthimala et al. [11], in which the proliferation of HeLa cells and 3T3-L1 pre-adipocytes exhibited no significant difference in cultures exposed and unexposed to photoluminescent nanodiamonds. This positive effect can be attributed to the fact that the mechanism of the ND uptake was clathrin-mediated endocytosis, that is, a physiological cellular mechanism for internalization of various bioactive substances from the extracellular environment. The negligible difference in cytotoxicity is caused by the similar production method, surface termination and energy of the NDs.

The surface termination of the two HPHT ND types is similar, despite the fact that the photoluminescent NDs were further postprocessed utilising methods influencing the bulk of the NDs (formation of vacancies, and N-V sites supported by high-temperature annealing in vacuum) [39]. This was confirmed by the fact that there was no obvious difference in the FTIR spectra between the MR-18 sample and the AR-40 sample. The zeta potential of MR-type NDs were negative, typically in the range of −20 to −40 mV [40,41], comparable with the −37 mV zeta potential value of the AR-40 sample. The stock concentration of AR-40 did not allow us to test the effect of the highest ND concentration (1000 μg/mL, 300 μg/cm^2).

Next, we compared the influence of surface treatment by evaluating NR-5 and NA-5 samples (i.e., samples of detonation NDs as-received and treated by annealing, respectively). These detonation NDs in their as-received state have a positive zeta potential, which is characteristic for hydrogenated NDs. The XPS analysis indicated a mixture of hydrogen and oxygen states on the surface. They were fully oxygenated by annealing at high temperature. The viability of the cells cultivated with NR-5 (100 and 1000 μg/mL, 30 and 300 μg/cm^2) had already reduced by 80–85% after 3 days of cultivation. However, the annealing of these DNDs (NA-5) reduced their toxicity significantly by 30%. This effect could still be observed after 7 days of cultivation, where the cytotoxicity of air-annealed DNDs decreased by 25% for a 100 μg/mL (30 μg/cm^2) suspension, and by 30% for a 1000 μg/mL (300 μg/cm^2) suspension. The particle size should be same as these samples are produced from the same batch of DND powder. The main difference lies in the surface termination and energy. The surface termination differs mainly in antisymmetric and symmetric CH_2, CH_3 (decrease), C═O (increase) and strong overlapping C–O, C–C bonds with air oxidation [42]. The oxidation of DNDs has a strong impact on their zeta potential, which influences the aggregation or the selection of adhered proteins from the culture medium. The as-received DNDs have a strongly positive zeta potential of ≈40 mV, while oxidation reverses it to approximately −40 mV [41].

The cell surface charge is influenced by the actual biochemical composition of the cytoplasmic membrane and the state of the cell. It is an important biophysical parameter influencing the interaction with the cell surroundings.

The cell surface charge (zeta potential) of human cells was between −20 and −30 mV caused by the presence of nonionogenic groups within phospholipids, proteins, and their polysaccharide conjugates [43]. Thus, we can expect similar zeta potential values for SAOS-2 cells, which are comparable with HPHT NDs and annealed DNDs, (i.e., negatively charged nanoparticles). It is known that negatively charged nanoparticles are less attractive for binding to the cell membrane than positively charged nanoparticles, which can be internalized more rapidly [44]. Positively charged nanoparticles have been reported to improve the efficacy of imaging, gene transfer and drug delivery. However, at the same time, negative effects like impaired integrity of cytoplasmic membrane and damage of other membranous organelles like mitochondria and lysosomes were observed. Also, more autophagosomes were produced by

the cells cultivated with positively charged nanoparticles ([45] or for a review see [46]). Hydrogenated positively charged ND particles impaired the radio-resistance of cancer cells and potentiated radiation-caused DNA damage and the generation of cytotoxic reactive oxygen species [47]. Thus, the positive charge of our as-received DNDs could, at least partly, explain their more pronounced cytotoxic effect than that observed in negatively charged annealed DNDs.

Finally, we can compare the NDs produced by mechanical grinding and by the detonation method, MR-18 and NR-5, respectively. Here, the main differences are in the production method and the particle size (18 nm and 5 nm), while the effect of surface termination is minimized due to air annealing [42]. We have shown that air annealing of as-received DNDs reduced mainly bands in the 2800–3000 cm^{-1} region corresponding to CH_2 and CH_3 stretching vibrations, and they give rise to a C═O stretch at 1775 cm^{-1}, C–O stretch at 1294 cm^{-1}, and a C–O–C stretch at 1077 cm^{-1}.

This produces surface termination similar to that of the as-received HPHT NDs (compare Figs. 1 in [42] and [40]). The zeta potentials have almost the same value of −40 mV for both ND types [41]. This explains the similarity in cytotoxic behaviour, where annealing of DNDs reduced their toxicity significantly. A decrease in the cytotoxicity is still observable after 7 days of cultivation (a 40% reduction), likely because some CH_2, CH_3 and C–H stretch bands remain and some differences in particle diameter. Finally, the dependence of the concentration on the cell viability was again most pronounced for the highest concentration (1000 µg/mL, 300 µg/cm^2).

Live-cell imaging of diamond nanoparticle uptake

Live-cell imaging (see Supporting Information File 1 and Supporting Information File 2 for full experimental data) confirmed the formation of DND aggregates in the suspension (10 µg/mL, 3 µg/cm^2). Particle aggregates are collected by cells from their surroundings. DNDs then accumulate on their surface and are endocytosed during the experiment. The accumulation and the cytotoxicity of the DNDs in the cell depends on their surface termination.

Live-cell imaging of SAOS-2 cells with as-received DNDs (NR-5, see Supporting Information File 1) reveals rapid uptake of NDs by the cells. The DNDs penetrated the cells early in the experiment. The video begins with six living cells. The cells are soon congested by the nanoparticles then their viability drops rapidly. Five cells undergo cytokinesis, but at least half of the cells are dead at the end of the experiment. In at least one or two of the cases of cell death, an expelled cytoplast can be seen exiting the cell membrane. This indicates uncontrolled cell death and rupture. The remaining living cells have an elongated shape due to the accumulated NDs which mechanically restrain their spreading and migration [38].

Unlike NR-5, the air-annealed DND aggregates (NA-5, see Supporting Information File 2) are not taken up by the cells as rapidly as their non-annealed counterparts. The video starts with a similar number of living cells as described above. The cells undergo 14 cytokineses, and most of them survive until the end of the video sequence. Only two or three cell death events can be recognized in the video.

Photoluminescence of diamond nanoparticles

Figure 5 shows fluorescence phase contrast images of osteoblasts and photoluminescent NDs (AR-40, 100 µg/mL, 30 µg/cm^2) grown for 3 and 7 days. The images reveal the presence of NDs in the cells. The red photoluminescence signal around the outside of the cell nuclei indicate that the NDs could not penetrate the nuclear envelope and stay in the cytoplasm. A certain amount of NDs are present outside the cells, probably in the loose serum protein/ND aggregates or in cell debris. The

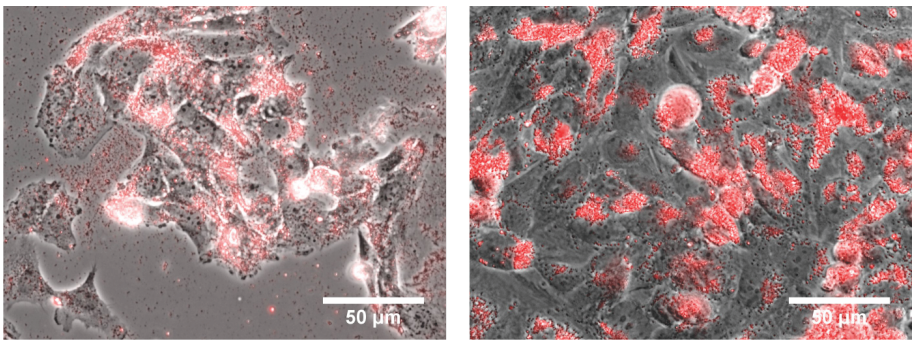

Figure 5: Phase contrast images of photoluminescent NDs (AR-40, 100 µg/mL) incubated with SAOS-2 cells after 3 days (left) and after 7 days (right).

well-spread osteoblasts are homogeneously and confluently distributed. Good cell adhesion and division confirms the viability of the cells with photoluminescent NDs (AR-40).

Conclusion

A comparison of cell viability with various types of NDs (HPHT, HPHT PL, DND) and surface termination and energy showed that the toxicity is mostly dependent on particle surface modification. In our study, oxygen termination emerges as the best surface modification for ND particles from the point-of-view of their biocompatibility. The viability of cells cultivated with positively charged as-received DNDs (100 and 1000 μg/mL, 30 and 300 μg/cm^2) had already decreased after 3 days of cultivation. However, annealing these NDs reduced their toxicity significantly. This effect could still be observed after 7 days of cultivation.

A concentration-dependent toxic effect of HPHT NDs was revealed after 7 days of cultivation when the viability of the cells cultivated at a 1000 μg/mL (300 μg/cm^2) concentration reduced by 25–30% in comparison with 100 μg/mL and 10 μg/mL (30 μg/cm^2 and 3 μg/cm^2). This was associated with the mechanical obstruction by NDs preventing cell adhesion, migration and division.

In comparison with the results of our previous studies, the air annealing of as-received DNDs reduced bands mainly corresponding to CH_2 and CH_3 stretching vibrations, and gave rise to C═O, CO and C–O–C stretch bands [41,42]. The zeta potential was also reversed from positive values to negative values. Thus the surface state of as-received DNDs is rendered similar to the state of HPHT NDs with similar cytotoxicity results. A decrease in viability was still observable after 7 days of cultivation, mostly due to the remaining CH_2, CH_3 and C–H stretching bands. The dependence of concentration on cell viability was again observed.

The comparison of the viability of the cells cultivated with various types of NDs indicates that the toxicity of NDs is probably dependent on the surface functional groups and the zeta potential rather than on the diameter of the particles.

Live-cell imaging showed that as-received DNDs penetrated rapidly into cells and caused rupture. O-terminated DNDs aggregated into large clusters, and the cells internalized them at a slower rate with a low impact on their viability for the first 3 days. After 7 days of cultivation, the MTS test revealed lower cell viability for ND concentrations of 100 μg/mL and 1000 μg/mL (30 μg/cm^{2}and 300 μg/cm^2). Nevertheless, O-termination increases the biocompatability of diamond nanoparticles and can be considered an advantageous modification.

Experimental

Origin and surface modification of diamond nanoparticles

Nanodiamond particles produced by two different methods were used: NanoAmando DNDs (NanoCarbon Research Institute, Japan) with a nominal diameter of 5 nm, HPHT NDs (Microdiamant AG, Switzerland) with median sizes from 18–210 nm, and 40 nm HPHT NDs with N-V-based photoluminescence (Adámas Nanotechnologies, USA). The particles were used either as-received or were oxidised by air annealing at 450 °C for 30 min [48]. For the detonation nanodiamonds purchased from NanoCarbon, the as-received nanodiamonds had a mixture of hydrogen and oxygen states on the surface with a positive zeta potential (characteristic for hydrogenated NDs). A fully oxidized state was achieved by air annealing, which resulted in oxygen-termination. The other diamond nanoparticles, namely high-pressure high-temperature (HPHT) DNPs and photoluminescent HPHT NDs, were oxidized in their as-delivered state.

Characterization of diamond nanoparticles

The size of the ND particles and their zeta potential was determined by dynamic light scattering (DLS) measurements in water at 25 °C using a Nano-ZetaSizer (Malvern, UK) equipped with an He-Ne laser. A separate disposable folded capillary cell was used for each set of ND measurements to eliminate sample cross contamination.

A Nicolet 8700 FTIR spectrometer (Thermo Scientific, USA) was equipped with N_2 purging, a KBr beamsplitter and an MCT detector cooled by liquid nitrogen. 50 μL of the water suspension with NDs was applied on the Au mirror by the drop-casting method just prior to the grazing angle reflectance FTIR measurements. The optical absorbance was calculated in standard absorbance units as $A = -\log(R/R_0)$, where R is the spectrum measured with NDs and R_0 is the reference (background) spectrum recorded using the clean Au mirror before the NDs were applied. In all cases, the spectra represent an average of 128 scans recorded with a resolution of 4 cm^{-1}.

The basic characteristics and the notation of the NDs that were used are summarized in Table 1. More data on ND characterization by FTIR and XPS can be found in our previous works [42,49].

Evaluation of cell viability

The cell viability upon exposure to the NDs was evaluated using the SAOS-2 human osteoblastic cell line (European Collection of Cell Cultures, Salisbury, UK, Cat. No. 89050205). The SAOS-2 cell line was used for biocompatibility experiments based on cell anchorage dependency and homogeneity.

Table 1: Characteristics and notation of diamond nanoparticle (ND) samples.

ND type	Particle size [nm]	Treatment	Notation
	18		MR-18
	25		MR-25
	50		MR-50
HPHT NDs	75	as-received	MR-75
	90		MR-90
	125		MR-125
	210		MR-210
DNDs	5	as-received	NR-5
	5	annealed	NA-5
HPHT PL NDs	40	as-received	AR-40

Two complementary methods were used. The first method was based on the mitochondrial metabolic activity test (MTS), while the second method was based on counting adherent cells. The cells were cultivated in the recommended McCoy's 5A medium (Sigma-Aldrich, USA) with 15% fetal bovine serum (FBS, Sigma-Aldrich, USA). The cells were seeded at a density of 15000 cells/cm^2 in a sterile 96-well plate (TPP, Switzerland) and were cultivated for 24 h before the nanoparticles were added. Cells from the 82nd passage to the 86th passage were used for the experiments. The NDs were sonicated in a UP 100H sonicator (Hielscher, Germany) in sterile distilled water in a stock concentration of 10 mg/mL, at 80 W for 30 min. The stock ND suspension was sterilized by exposure to UVC light (Esco germicidal lamp, spectrum peak at 253.7 nm) for 30 min. The working concentrations of 10, 100 and 1000 µg/mL were then diluted in the cultivation medium with FBS. The original medium was aspired off the cells, and the medium with NDs was pipetted onto the cells. The cells were cultivated with the NDs for 3 and 7 days under standard cultivation conditions (37 °C, 5% CO_2). The cell metabolic activity (a marker of cell viability and growth) was measured using the colorimetric MTS test (CellTiter 96® - Promega, USA). The absorbance of the colorimetric MTS test was measured at 490 nm, and a reference measurement was taken at 650 nm. This experiment was repeated three times in sextuplicate for each experimental group. The cells on the samples were then washed with phosphate buffered saline and were fixed with 4% paraformaldehyde for 10 min. The nuclei of the fixed cells were then stained using Hoechst 33258 dye for cell counting. Micrographs of the stained nuclei were acquired using an IX71 microscope (Olympus, Japan) with a 10× lens. 12 micrographs were taken for each sample. The cell nuclei were automatically counted using open source ImageJ image processing software. Photoluminescence microphotographs of fixed cells co-cultivated with photoluminescent NDs (AR-40), 100 µg/mL (30 µg/cm^2), were also taken using an IX71 microscope (Olympus, Japan) with a 40× lens. The AR-40 NDs were excited by green excitation light, and their red photoluminescence was collected through a U-MWG2 filter cube (Olympus, Japan).

The statistical significance of the differences in the cell metabolic activity and in cell number among the samples was evaluated using ANOVA with the Tukey HSD post-hoc test.

Live-cell imaging

The live-cell imaging method was used for observing the ND uptake in the cells. Live-cell imaging was again performed on the SAOS-2 cell line. The cells were seeded on a 35 mm diameter Petri dish with a 0.17 mm glass bottom and were cultivated for 24 h. The ND suspension was prepared in the same way as for the viability test. For live-cell imaging, only 10 µg/mL and 100 µg/mL concentrations were used. The live-cell imaging was performed on the TE2000 microscope with 40× magnification, (Nikon, Japan), Plan Fluor, ELWD objective (Nikon, Japan) with phase contrast installed. The microscope was equipped with a cell incubation chamber (Solent Scientific, UK) with humidity regulation (95%), controlled temperature (37 °C) and CO_2 concentration (5%). The cells were photographed for 72 h at 2 min intervals for the first 6 h and thereafter at 10 min intervals.

Supporting Information

Supporting Information File 1

Live-cell imaging of NR-5 (10 µg/mL, 3 µg/cm^2) uptake by the SAOS-2 cells.
[http://www.beilstein-journals.org/bjnano/content/supplementary/2190-4286-8-165-S1.avi]

Supporting Information File 2

Live-cell imaging of NA-5 (10 µg/mL, 3 µg/cm^2) uptake by the SAOS-2 cells.
[http://www.beilstein-journals.org/bjnano/content/supplementary/2190-4286-8-165-S2.avi]

Supporting Information File 3

FTIR comparison of MR-18 and AR-40 nanodiamonds.
[http://www.beilstein-journals.org/bjnano/content/supplementary/2190-4286-8-165-S3.png]

Supporting Information File 4

Live-cell imaging of SAOS-2 cells after three days without nanodiamonds.
[http://www.beilstein-journals.org/bjnano/content/supplementary/2190-4286-8-165-S4.avi]

Acknowledgements

This work was financially supported by the Czech Science Foundation research project 17-19968S (Š.P.). The work also received support from project No. LD15003 (Ministry of Education, Youth and Sports) within the frame of the COST Action MP1403 "Nanoscale Quantum Optics". This work was carried out in the framework of the LNSM infrastructure. The biological part of this work was supported by the Czech Health Research Council, Ministry of Health of the Czech Republic, project No. 15-32497A (A.B., L.B.). Mr. Robin Healey (Czech Technical University in Prague) is gratefully acknowledged for his language revision of the manuscript.

References

1. Monaco, A. M.; Giugliano, M. *Beilstein J. Nanotechnol.* **2014,** *5,* 1849–1863. doi:10.3762/bjnano.5.196
2. May, P. W. *Philos. Trans. R. Soc., A* **2000,** *358,* 473–495. doi:10.1098/rsta.2000.0542
3. Kaur, R.; Badea, I. *Int. J. Nanomed.* **2013,** *8,* 203–220. doi:10.2147/IJN.S37348
4. Ho, D., Ed. *Nanodiamonds: applications in biology and nanoscale medicine;* Springer: Berlin, Germany, 2010.
5. Bacakova, L.; Kopova, I.; Stankova, L.; Liskova, J.; Vacik, J.; Lavrentiev, V.; Kromka, A.; Potocky, S.; Stranska, D. *Phys. Status Solidi A* **2014,** *211,* 2688–2702. doi:10.1002/pssa.201431402
6. Bacakova, L.; Broz, A.; Liskova, J.; Stankova, L.; Potocky, S.; Kromka, A. The Application of Nanodiamond in Biotechnology and Tissue Engineering. In *Diamond and Carbon Composites and Nanocomposites;* Aliofkhazraei, M., Ed.; InTech: Rijeka, Croatia, 2016. doi:10.5772/63549
7. Tang, L.; Tsai, C.; Gerberich, W. W.; Kruckeberg, L.; Kania, D. R. *Biomaterials* **1995,** *16,* 483–488. doi:10.1016/0142-9612(95)98822-V
8. Paget, V.; Sergent, J. A.; Grall, R.; Altmeyer-Morel, S.; Girard, H. A.; Petit, T.; Gesset, C.; Mermoux, M.; Bergonzo, P.; Arnault, J. C.; Chevillard, S. *Nanotoxicology* **2014,** *8,* 46–56. doi:10.3109/17435390.2013.855828
9. Mochalin, V. N.; Shenderova, O.; Ho, D.; Gogotsi, Y. *Nat. Nanotechnol.* **2012,** *7,* 11–23. doi:10.1038/nnano.2011.209
10. Liu, K.-K.; Wang, C.-C.; Cheng, C.-L.; Chao, J.-I. *Biomaterials* **2009,** *30,* 4249–4259. doi:10.1016/j.biomaterials.2009.04.056
11. Vaijayanthimala, V.; Tzeng, Y.-K.; Chang, H.-C.; Li, C.-L. *Nanotechnology* **2009,** *20,* 425103. doi:10.1088/0957-4484/20/42/425103
12. Yan, L.; Yang, Y.; Zhang, W.; Chen, X. *Adv. Mater.* **2014,** *26,* 5533–5540. doi:10.1002/adma.201305683
13. Lam, R.; Ho, D. *Expert Opin. Drug Delivery* **2009,** *6,* 883–895. doi:10.1517/17425240903156382
14. Vaijayanthimala, V.; Lee, D. K.; Kim, S. V.; Yen, A.; Tsai, N.; Ho, D.; Chang, H.-C.; Shenderova, O. *Expert Opin. Drug Delivery* **2015,** *12,* 735–749. doi:10.1517/17425247.2015.992412
15. Chao, J.-I.; Perevedentseva, E.; Chung, P.-H.; Liu, K.-K.; Cheng, C.-Y.; Chang, C.-C.; Cheng, C.-L. *Biophys. J.* **2007,** *93,* 2199–2208. doi:10.1529/biophysj.107.108134
16. Aharonovich, I.; Neu, E. *Adv. Opt. Mater.* **2014,** *2,* 911–928. doi:10.1002/adom.201400189
17. Balasubramanian, G.; Lazariev, A.; Arumugam, S. R.; Duan, D.-w. *Curr. Opin. Chem. Biol.* **2014,** *20,* 69–77. doi:10.1016/j.cbpa.2014.04.014
18. Schirhagl, R.; Chang, K.; Loretz, M.; Degen, C. L. *Annu. Rev. Phys. Chem.* **2014,** *65,* 83–105. doi:10.1146/annurev-physchem-040513-103659
19. Dolmatov, V. Yu. *Russ. Chem. Rev.* **2007,** *76,* 339–360. doi:10.1070/RC2007v076n04ABEH003643
20. Ōsawa, E. *Pure Appl. Chem.* **2008,** *80,* 1365–1379. doi:10.1351/pac200880071365
21. Boudou, J.-P.; Curmi, P. A.; Jelezko, F.; Wrachtrup, J.; Aubert, P.; Sennour, M.; Balasubramanian, G.; Reuter, R.; Thorel, A.; Gaffet, E. *Nanotechnology* **2009,** *20,* 235602. doi:10.1088/0957-4484/20/23/235602
22. Stehlik, S.; Varga, M.; Ledinsky, M.; Jirasek, V.; Artemenko, A.; Kozak, H.; Ondic, L.; Skakalova, V.; Argentero, G.; Pennycook, T.; Meyer, J. C.; Fejfar, A.; Kromka, A.; Rezek, B. *J. Phys. Chem. C* **2015,** *119,* 27708–27720. doi:10.1021/acs.jpcc.5b05259
23. Krueger, A.; Stegk, J.; Liang, Y.; Lu, L.; Jarre, G. *Langmuir* **2008,** *24,* 4200–4204. doi:10.1021/la703482v
24. Keremidarska, M.; Ganeva, A.; Mitev, D.; Hikov, T.; Presker, R.; Pramatarova, L.; Krasteva, N. *Biotechnol. Biotechnol. Equip.* **2014,** *28,* 733–739. doi:10.1080/13102818.2014.947704
25. Schrand, A. M.; Hens, S. A. C.; Shenderova, O. A. *Crit. Rev. Solid State Mater. Sci.* **2009,** *34,* 18–74. doi:10.1080/10408430902831987
26. Pichot, V.; Comet, M.; Fousson, E.; Baras, C.; Senger, A.; Le Normand, F.; Spitzer, D. *Diamond Relat. Mater.* **2008,** *17,* 13–22. doi:10.1016/j.diamond.2007.09.011
27. Shenderova, O.; Petrov, I.; Walsh, J.; Grichko, V.; Grishko, V.; Tyler, T.; Cunningham, G. *Diamond Relat. Mater.* **2006,** *15,* 1799–1803. doi:10.1016/j.diamond.2006.08.032
28. Puzyr', A. P.; Tarskikh, S. V.; Makarskaya, G. V.; Chiganova, G. A.; Larionova, I. S.; Detkov, P. Ya.; Bondar, V. S. *Dokl. Biochem. Biophys.* **2002,** *385,* 201–204. doi:10.1023/A:1019959322589
29. Puzyr, A. P.; Neshumaev, D. A.; Tarskikh, S. V.; Makarskaia, G. V.; Dolmatov, V. I.; Bondar, V. S. *Biofizika* **2005,** *50,* 101–106.
30. Xing, Y.; Xiong, W.; Zhu, L.; Ōsawa, E.; Hussin, S.; Dai, L. *ACS Nano* **2011,** *5,* 2376–2384. doi:10.1021/nn200279k
31. Zhu, Y.; Li, W.; Zhang, Y.; Li, J.; Liang, L.; Zhang, X.; Chen, N.; Sun, Y.; Chen, W.; Tai, R.; Fan, C.; Huang, Q. *Small* **2012,** *8,* 1771–1779. doi:10.1002/smll.201102539
32. Wierzbicki, M.; Sawosz, E.; Grodzik, M.; Hotowy, A.; Prasek, M.; Jaworski, S.; Sawosz, F.; Chwalibog, A. *Int. J. Nanomed.* **2013,** *8,* 3427–3435. doi:10.2147/IJN.S49745
33. Xing, Z.; Pedersen, T. O.; Wu, X.; Xue, Y.; Sun, Y.; Finne-Wistrand, A.; Kloss, F. R.; Waag, T.; Krueger, A.; Steinmüller-Nethl, D.; Mustafa, K. *Tissue Eng., Part A* **2013,** *19,* 1783–1791. doi:10.1089/ten.tea.2012.0336
34. Eidi, H.; David, M.-O.; Crépeaux, G.; Henry, L.; Joshi, V.; Berger, M.-H.; Sennour, M.; Cadusseau, J.; Gherardi, R. K.; Curmi, P. A. *BMC Med.* **2015,** *13,* 144. doi:10.1186/s12916-015-0388-2
35. Solarska, K.; Gajewska, A.; Bartosz, G.; Mitura, K. *J. Nanosci. Nanotechnol.* **2012,** *12,* 5117–5121. doi:10.1166/jnn.2012.4952
36. Landgraf, L.; Müller, I.; Ernst, P.; Schäfer, M.; Rosman, C.; Schick, I.; Köhler, O.; Oehring, H.; Breus, V. V.; Basché, T.; Sönnichsen, C.; Tremel, W.; Hilger, I. *Beilstein J. Nanotechnol.* **2015,** *6,* 300–312. doi:10.3762/bjnano.6.28

37. Wehling, J.; Dringen, R.; Zare, R. N.; Maas, M.; Rezwan, K. *ACS Nano* **2014,** *8,* 6475–6483. doi:10.1021/nn502230m
38. Lombardi, S. L., Ed. *Nanoparticles: new research;* Nova Science Publishers: New York, NY, U.S.A., 2008.
39. Chang, Y.-R.; Lee, H.-Y.; Chen, K.; Chang, C.-C.; Tsai, D.-S.; Fu, C.-C.; Lim, T.-S.; Tzeng, Y.-K.; Fang, C.-Y.; Han, C.-C.; Chang, H.-C.; Fann, W. *Nat. Nanotechnol.* **2008,** *3,* 284–288. doi:10.1038/nnano.2008.99
40. Kozak, H.; Artemenko, A.; Čermák, J.; Švrček, V.; Kromka, A.; Rezek, B. *Vib. Spectrosc.* **2016,** *83,* 108–114. doi:10.1016/j.vibspec.2016.01.010
41. Jirásek, V.; Čech, J.; Kozak, H.; Artemenko, A.; Černák, M.; Kromka, A. *Phys. Status Solidi A* **2016,** *213,* 2680–2686. doi:10.1002/pssa.201600184
42. Kromka, A.; Jira, J.; Stenclova, P.; Kriha, V.; Kozak, H.; Beranova, J.; Vretenar, V.; Skakalova, V.; Rezek, B. *Phys. Status Solidi B* **2016,** *253,* 2481–2485. doi:10.1002/pssb.201600237
43. Bondar, O. V.; Saifullina, D. V.; Shakhmaeva, I. I.; Mavlyutova, I. I.; Abdullin, T. I. *ActaNaturae* **2012,** *4,* 78–81.
44. Platel, A.; Carpentier, R.; Becart, E.; Mordacq, G.; Betbeder, D.; Nesslany, F. *J. Appl. Toxicol.* **2016,** *36,* 434–444. doi:10.1002/jat.3247
45. Carmona-Ribeiro, A. M.; Dias de Melo Carrasco, L. *Int. J. Mol. Sci.* **2013,** *14,* 9906–9946. doi:10.3390/ijms14059906
46. Fröhlich, E. *Int. J. Nanomed.* **2012,** *7,* 5577–5591. doi:10.2147/IJN.S36111
47. Grall, R.; Girard, H.; Saad, L.; Petit, T.; Gesset, C.; Combis-Schlumberger, M.; Paget, V.; Delic, J.; Arnault, J.-C.; Chevillard, S. *Biomaterials* **2015,** *61,* 290–298. doi:10.1016/j.biomaterials.2015.05.034
48. Kozak, H.; Remes, Z.; Houdkova, J.; Stehlik, S.; Kromka, A.; Rezek, B. *J. Nanopart. Res.* **2013,** *15,* 1568. doi:10.1007/s11051-013-1568-7
49. Kromka, A.; Čech, J.; Kozak, H.; Artemenko, A.; Ižák, T.; Čermák, J.; Rezek, B.; Černák, M. *Phys. Status Solidi B* **2015,** *252,* 2602–2607. doi:10.1002/pssb.201552232

License and Terms